Natural Resources Research Institute

University of Minnesota Duluth

Driven to Discover℠

NRRI TECHNICAL REPORT

Continuous Pilot-Scale Demonstration of Ilmenite Processing Technology

Submitted by:

George J. Hudak, Shashi Rao, and Dean Peterson (NRRI)

Jonathan Chen, V.I. Lakshmanan, Ram Sridhar, and Eugen Gluck (PRO)

Date: May 2021

Report Number: NRRI/TR-2021/19

Funding:

University of Minnesota Permanent University Trust Fund

PROCESS RESEARCH ORTECH Inc.

Website: www.nrri.umn.edu

NRRI Duluth // Laboratories and Admin // 5013 Miller Trunk Highway, Duluth, MN 55811 // (218) 788-2694

NRRI Coleraine // Laboratories // P.O. Box 188 // One Gayley Avenue, Coleraine, MN 55722 // (218) 667-4201

Visit our website for access to NRRI publications (http://www.nrri.umn.edu/publications).

Recommended citation:
Hudak, G.J., Rao, S., Peterson, D., Chen, J., Lakshmanan, V.I., Sridhar, R., and Gluck, E. 2021. Continuous pilot-scale demonstration of ilmenite processing technology. Natural Resources Research Institute, University of Minnesota Duluth, Technical Report NRRI/TR-2021/19, 229 p. + Appendices.

Natural Resources Research Institute
University of Minnesota, Duluth
5013 Miller Trunk Highway
Duluth, MN 55811-1442
Telephone: 218.788.2694
e-mail: nrri-reports@umn.edu

EXECUTIVE SUMMARY

The Natural Resources Research Institute (NRRI) and Process Research Ortech (PRO) have completed a combined characterization effort and hydrometallurgical testing program on an ilmenite mineral concentrate produced by the NRRI Coleraine Lab in 2016 (Mlinar et al., 2017). The ilmenite mineral concentrate used for this study was derived from the 1999 Longnose oxide ultramafic intrusion (OUI) bulk sample. The work described in this report comprises a follow-up study to the batch hydrometallurgical test work program conducted by PRO and NRRI that has been described in NRRI Technical Report NRRI/TR-2017/25, "Pilot-Scale Demonstration of Ilmenite Processing Technology" (Mlinar et al., 2017).

This research builds on the findings from the previous study by performing additional steady-state pilot operations to examine the following:

- How variation in feed composition affects solvent extraction (SX) processes;
- The effect(s) of incorporation of recycled streams such as SX process raffinates and filtrates from precipitation stages;
- Evaluate impurity buildup in the circuit from integrated operation (for example, recycling of raffinates) on the final Fe_2O_3 and TiO_2 products and potential bleed effluents;
- Characterize Fe_2O_3 and TiO_2 product quality from mineralogical, textural, and mineral chemical/bulk chemical analyses;
- Determine mass balance of the system at steady state.

Detailed characterization of random grab samples of the 1999 Longnose bulk sample, 2016 Longnose ilmenite concentrate, magnetite-rich low-intensity magnetic separator (LIMS) concentrate, and rougher spiral tails produced during the Mlinar et al. (2017) report were performed prior to hydrometallurgical processing for this study. Analyses in the characterization included hand sample lithological characterization (bulk sample only), petrographic analysis (bulk sample only), x-ray diffraction mineralogical analysis, whole rock major and trace element analysis, and/or mineral chemical analysis of various oxide and silicate mineral phases present in these materials by means of electron microprobe analyses.

Lithological classification of 12 grab samples of the 1999 Longnose bulk sample indicated the presence of four lithologies, including semi-massive oxide, semi-massive to massive oxide, oxide-bearing peridotite, and oxide bearing dunite/peridotite. Overall, the bulk sample mineralogy was dominated by olivine, clinopyroxene, hornblende, chlorite, serpentine, ilmenite, magnetite (including titanomagnetite), with lesser silicate, oxide, and locally sulfide mineral phases. Electron microprobe studies indicate that ilmenite contains between 2.0 and 4.0 weight percent MgO. Magnetite and titanomagnetite in the bulk sample contain up to 2.5 weight percent V_2O_3. Silicate phases identified during electron microprobe studies include amphiboles (pargasite to magnesioriebeckite), clinochlore, biotite, phlogopite, olivine and serpentine. Whole rock major- and trace-element analyses of the bulk sample indicate it is primarily composed of Fe_2O_3 (33–55 weight percent), TiO_2 (9–39 weight percent), MgO (33–55 weight percent), and SiO_2 (2–29 weight percent). Sulfur contents ranged from 0.02–0.15 weight percent (average 0.07 weight percent). Average compositions of selected trace elements include As (1.05 ppm), Co (194 ppm), Cr (650ppm), Cu (1692 ppm), Ni (638 ppm), Pb (8 ppm), Sb (0.06 ppm), V (1658 ppm), and Zn (195 ppm). Chondrite-normalized rare earth element (REE) concentrations range from 0.1–10 times chondritic values. Relative to primitive mantle compositions, Longnose bulk samples

tend to be enriched in Nb (15–70 times), zirconium (4–20 times), hafnium (4–20 times), titanium (40–200 times), and vanadium (80–130 times).

Three mineral concentrates produced during the Mlinar et al. (2017) study include an ilmenite concentrate (which was the hydrometallurgical process feed in the current study), a magnetite/titanomagnetite-enriched low intensity magnetic separator (LIMS) concentrate, and silicate-mineral-rich rougher spiral tails.

- X-ray diffraction analyses of the ilmenite concentrate indicate the presence of ilmenite, antigorite, and zircon, whereas electron microprobe analyses indicate the presence of magnetite and rare rutile. Ilmenite in the ilmenite concentrate contains 2.6–4.0 weight percent MgO. Magnetite/titanomagnetite contains between 0.8–6.2 weight percent TiO_2 and up to 2.4 weight percent V_2O_3.
- Whole rock major and trace element analysis of the three concentrates indicates that SiO_2, Al_2O_3, CaO, MgO, Na_2O, K_2O, P_2O_5, S, and LOI are most highly concentrated in the rougher spiral tails; FeO, Cr_2O_3, and SrO are most highly concentrated in the LIMS concentrate; and TiO_2, MnO, and BaO are most highly concentrated in the ilmenite concentrate. As well, Co, Cu, and Ni are most highly concentrated in the rougher spiral tails; Cr, Pb, Sb, V, and Zn are most highly concentrated in the LIMS concentrate; and As is most highly concentrated in the ilmenite concentrate. Chondrite-normalized REE concentrations are higher in the rougher spiral tails (6–9 times chondritic values) relative to the ilmenite concentrate (1.5–4 times chondritic values) and the LIMS concentrate (0.5 to 3 times chondritic values). Primitive mantle-normalized values are highest for Th, La, Ce, Pr, Nd, Sm, Gd, Tb, Dy, Y, Er, Yb, Lu, and Al in the rougher spiral tails; V is most highly concentrated in the LIMS concentrate; and Nb, Zr, Hf, Ti, and Sc are most highly concentrated in the ilmenite concentrate.

Three pilot-scale hydrometallurgical campaigns were conducted for this study.

- Campaign 1 included setup of the pilot circuit and buildup of solutions in the various SX circuits so that examination of the effects of impurity buildup in the circuit from subsequent integrated operations could be established.
- Campaign 2 focused on impurity buildup and steady-state operation with recycling of evaporated Ti-raffinate. Additionally, bench testing was conducted on developing a proprietary technology for the production of an iron oxide product and regenerate HCl. The purpose of the bench tests was to establish operating conditions and determine potential HCl grade and quality.
- Campaign 3 involved continued pilot circuit operations with recycling streams from Campaign 2 (Ti-raffinate) along with implementation of recycling of the TiO_2 precipitation filtrate stream into the circuit as Ti SX barren strip. The focus of the Campaign 3 operation was on impurity buildup and steady-state operation along with determining the effects of impurity buildup on the selectivity of the SX separation circuits. Further bench-scale testing of the proprietary technology continued to produce a Fe_2O_3 product and establish the quality of the HCl.

It was found that recycling of $MgCl_2$ contained in the Ti raffinate to the leach operation did not adversely affect leach recoveries, with average Ti recovery remaining consistent over the three campaigns (~70%). It was found that particle size played a key role in the leach efficiency, and grinding of the material to a particle size of +90% -43 µm improved Ti leaching to levels of ~90%.

Additionally, operation of the SX circuits was not adversely affected by the buildup of impurities such as V, Cr, Al, and Ca. It was found that selectivity was maintained in both the Fe- and Ti-SX circuits, with high purity pregnant strip solutions produced in each campaign. The resultant products Fe_2O_3 (hematite) and TiO_2 (rutile) produced from the pregnant strip solutions were of high purity (96.7%–98.6% Fe_2O_3; 98.7%–99.7% TiO_2).

A TiO_2 rutile product with a purity of ~99.5% TiO_2 was produced from both Campaigns 2 and 3 that can be used as a precursor for pigment manufacture. An Fe_2O_3 (hematite) product of >95% Fe_2O_3 was produced from Campaigns 2 and 3 and can be used as a feed stock for direct reduced iron (DRI) processes, other metallurgical processes, or as a precursor for pigment.

Non-calcined and calcined TiO_2 products from Campaign 2 were characterized by means of x-ray diffraction studies, electron microprobe mineral chemistry studies, and lithogeochemical studies. The x-ray diffraction study results indicate the presence of rutile in both the non-calcined and calcined TiO_2 products. Electron microprobe analysis indicates that both non-calcined and calcined Campaign 2 TiO_2 rutile precipitates occur in a variety of rounded, oval, platy, and agglomerated textures. Within the calcined Campaign 2 TiO_2 rutile precipitates, rare curvilinear elongate fragments were locally observed. Electron microprobe mineral chemical analyses indicate that Campaign 2 TiO_2 precipitates are nearly stoichiometric rutile (TiO_2). Campaign 2 calcined TiO_2 precipitates have a normalized purity of 99.8 weight percent based on lithogeochemical analysis utilizing x-ray fluorescence.

Non-calcined and calcined TiO_2 products from Campaign 3 were characterized by means of x-ray diffraction studies, electron microprobe mineral chemistry studies, and lithogeochemical studies. The x-ray diffraction study results indicate the presence of rutile in both the non-calcined and calcined TiO_2 products. Electron microprobe analyses indicate that non-calcined and calcined Campaign 3 TiO_2 rutile precipitates occur in a variety of textures, including zoned rounded to oval rutile grains as well as composite fragments composed of agglomerates of round and locally elongate rutile grains. Locally, elongate grains were also present. Rounded to oval rutile grains in the calcined sample appear to have more porosity than similar grains in the non-calcined sample. Mineral chemical analyses performed during electron microprobe studies of the Campaign 2 TiO_2 precipitates indicate the precipitates are nearly stoichiometric rutile (TiO_2). Non-calcined and calcined Campaign 3 TiO_2 precipitates are composed primarily of TiO_2 and LOI. Campaign 3 calcined TiO_2 precipitates have a normalized purity of 98.7 weight percent based on lithogeochemical analysis utilizing x-ray fluorescence.

Non-calcined and calcined iron oxide precipitates from Campaign 2 were characterized by means of x-ray diffraction studies, electron microprobe mineral chemistry studies, and lithogeochemical studies. X-ray diffraction studies indicate the presence of hematite, possibly zircon, and an unknown phase within the non-calcined iron oxide precipitate. Hematite was the sole phase identified in the calcined iron oxide precipitate. Electron microprobe studies show that the non-calcined and calcined iron oxide precipitates occur in a variety of textures including composites of massive hematite lathes, amorphous composites, and polygonal composites. Whole-rock major and trace element lithogeochemical analyses indicate that both the non-calcined and calcined Campaign 2 iron oxide precipitates are primarily composed of Fe_2O_3, TiO_2, and LOI, with Fe_2O_3 contents being higher in the calcined sample and TiO_2 and LOI contents being higher in the non-calcined sample. Sulfur contents in the non-calcined and calcined samples were equivalent (<0.1 weight percent). Campaign 2 calcined Fe_2O_3 precipitates have a normalized purity of 98.5 weight percent based on lithogeochemical analysis utilizing x-ray fluorescence.

Non-calcined and calcined iron oxide precipitates from Campaign 3 were characterized by means of x-ray diffraction studies, electron microprobe mineral chemistry studies, and lithogeochemical studies. X-ray diffraction study results indicate the presence of hematite in both the non-calcined and calcined samples of Campaign 3 iron oxide precipitates. Electron microprobe analysis of the Campaign 3 iron oxide precipitates, assuming all iron as Fe^{3+}, indicates the presence of three types of precipitates, including: 1) precipitates that are nearly stoichiometric hematite (Fe_2O_3); 2) precipitates that contain greater than 0.5 weight percent TiO_2 and most likely represent titanohematite solid solution; and 3) precipitates composed of an iron- and titanium-bearing phase that may be ulvöspinel or titanohematite solid solution. Additional mineral chemical analysis will be required to better characterize these iron- and titanium-bearing phases. Both non-calcined and calcined Campaign 3 iron oxide precipitates are composed primarily of Fe_2O_3, TiO_2, and LOI. Sulfur contents in the non-calcined and calcined samples were 0.05 and 0.01 weight percent, respectively. Campaign 3 calcined Fe_2O_3 precipitates have a normalized purity of 96.84 weight percent based on lithogeochemical analysis utilizing x-ray fluorescence.

Samples of Campaign 1 (non-recycled), Campaign 2 (half-recycled), and Campaign 3 (recycled sample and two reground to 90% passing 400 mesh (38 µm) / two-stage leach samples) were characterized by means of x-ray diffraction studies, electron microprobe mineral chemistry studies, and lithogeochemical studies.

X-ray diffraction study results indicate that Campaign 1 leach residues contain ilmenite, zircon, and hornblende. X-ray diffraction study results indicate that Campaign 2 (half-recycled) leach residues contain ilmenite, augite, and zircon. X-ray diffraction study results indicate that Campaign 3 (recycled) leach residues contain ilmenite, zircon, and hornblende, whereas the Campaign 3 two-stage leach residues contain ilmenite, rutile, clinochlore, hornblende, and zircon. Electron microprobe studies identified ilmenite, rutile, actinolite, clinochlore, and possibly quartz in the Campaign 1 leach residues, and ilmenite, pargasite, augite, and possibly quartz in the Campaign 2 leach residues. Electron microprobe analysis of the Campaign 3 leach residues shows that the single-stage leach residues contain ilmenite, augite, actinolite, sepiolite, and possibly quartz. Electron microprobe analysis of the Campaign 3 two-stage leach residues indicates the presence of ilmenite, rutile, augite, actinolite, tremolite, clinochlore, and possibly plagioclase feldspar and quartz.

Major element lithogeochemical comparison between the Campaign 1 leach residue (no recycling) and Campaign 2 leach residue (half-recycled) samples indicate that the Campaign 1 leach residue had higher concentrations of SiO_2, Al_2O_3, LOI, S, Cu, Pb, and Sb, whereas the Campaign 2 leach residues had higher concentrations of Fe_2O3, MgO, TiO_2, MnO, P_2O_5, and Cr. Concentrations of CaO, Na_2O, K_2O, Cr_2O_3, SrO, BaO, and S were similar in the Campaign 1 and Campaign 2 leach residues.

Major element lithogeochemical comparison between the Campaign 2 leach residue (half-recycled) and Campaign 3 leach residue (recycled) samples indicate that the Campaign 2 leach residue (half-recycled) had higher concentrations of SiO_2, Al_2O_3, CaO, Na_2O, K_2O, MnO, LOI, and sulfur, whereas the Campaign 3 leach residue (recycled) was enriched in Fe_2O_3, MgO, TiO_2, and P_2O_5 relative to the Campaign 2 leach residue (half-recycled). Concentrations of Cr_2O_3 were similar in both samples.

Major element lithogeochemical comparison between the Campaign 3 leach residue (recycled) and the two Campaign 3 reground to 90% passing 400 mesh (38 µm)/two-stage leach samples indicates that the Campaign 3 leach residue (recycled) had higher concentrations of Fe_2O_3, Cr_2O_3, TiO_2, MnO, and P_2O_5,

whereas the two Campaign 3 reground and two-stage leach samples had higher concentrations of SiO_2, Al_2O_3, CaO, MgO, Na_2O, K_2O, LOI, and sulfur.

The Campaign 3 single-stage leach residues contain higher concentrations of Fe_2O_3, Cr_2O_3, TiO_2, and MnO. The Campaign 3 two-stage leach residues contain higher concentrations of SiO_2, Al_2O_3, CaO, MgO, Na_2O, K_2O, LOI, and S.

Chondrite-normalized REE values for Er were higher in the Campaign 1 sample, whereas the Campaign 2 sample was enriched in Ce, Pr, and Yb. Primitive mantle-normalized trace element values were higher in the Campaign 1 non-recycled sample than in the Campaign 2 half-recycled sample for Hf, Y, Er, and Al. Primitive mantle-normalized trace element values were higher in the half-recycled Campaign 2 (half-recycled) sample than the non-recycled Campaign 1 sample for Nb, La, Ce, Pr, Nd, Ti, V, Sc, and Zr. Both samples had similar values for Th, Sm, Eu, Gd, Tb, Dy, Yb, and Lu.

Chondrite-normalized REE values were higher in the Campaign 2 (half-recycled) sample for Ce, Pr, Nd, Tb, and Dy relative to the Campaign 3 (recycled) sample. The Campaign 3 (recycled) sample was enriched in Eu, Gd, and Er. Similar REE values were found in both samples for Sm, Gd, Ho, Yb, and Lu. Primitive mantle-normalized trace element values were higher in the Campaign 2 (half-recycled) sample for Th, La, Ce, Pr, Nd, Sm, Eu, Gd, Tb, Dy, Y, Er, Al, and Sc relative to the Campaign 3 (recycled) sample, whereas the Campaign 3 (recycled) sample was enriched in Nb, Zr,Ti, and V relative to the Campaign 2 (half-recycled) sample.

Chondrite-normalized REE values were consistently higher in the Campaign 3 reground and two-stage leach samples than in the Campaign 3 (recycled) sample. Primitive mantle-normalized trace element concentrations were higher for Th, La, Ce, Pr, Nd, Sm, Eu, Gd, Tb, Dy, Y, Er, Yb, and Al for the Campaign 3 reground and two-stage leach samples than for the Campaign 3 (recycled) sample, whereas the Campaign 3 (recycled) sample illustrated higher concentrations of Zr, Hf, and V than the Campaign 3 reground and two-stage leach samples.

Ontario Regulation 558 metals and inorganic testing was conducted on samples of leach residues from Campaigns 1, 2, and 3 of this study. Results indicate that these samples are considered environmentally inert relative to this standard. When compared with Minnesota Rules 7045.0131 Characteristics of Hazardous Waste (revisor.mn.gov/rules/78045.0131), the results obtained for the campaign 1, 2 and 3 residues, as well as the Campaign 3 ground residue, are below the maximum concentrations listed for arsenic, barium, cadmium, chromium, lead, mercury, selenium, and silver. No maximum concentrations are indicated for boron, uranium, flouride, cyanide, or (nitrate/nitrite) as N leachate in Minnesota Rules 7045.0131.

The CTL process was benchmarked against existing process technologies according to some of the major process parameters (Table i).

Table i. Benchmarking of CTL process to major competitors.

Parameter	Chloride	Sulphate	CTL	Upgraded Slag
Raw material	High cost	Low cost	Lowest cost	Medium Cost
($/ton of TiO_2 feed)	($2000 +)	Ilmenite ($250)	Ilmenite ($250)	Ilmenite ($250)
TiO_2 product	High value	Low value	High value	Low Value intermediate
($/ton of TiO_2)	+$3000		+$3000	
Capex	Highest (including front-end)	Medium	Lowest	Medium
Opex	Highest (including front-end)	Medium	Lowest	Medium
Environmental	Medium challenges	Major challenges	Most environmentally friendly	Medium challenges
Raw material	High cost, rutile	Low cost, ilmenite	Lower cost, ilmenite	Low cost, ilmenite
Flexibility in processing raw material	Limitation (Mn, Mg, size)	Limitation (Cr, V)	Can process (Flexible)	Limitation on Ca, Mg content
Process Condition	High Temp. Chlorine (800-1000°C)	High Temp. (140-180°C)	Atmospheric Mixed Chloride (70°C)	High temp. (1600°C)
Technology	Old	Old	Patented, New	Old
End to end in one location	Not practiced	Possible	Possible	Not practiced
Pigment production	Rutile	Rutile/Anatase	Rutile/Anatase	
Commercially Proven process	In practice	In practice	In Development	In practice
Environmental challenges	Disposal of iron and other byproduct chlorides	Disposal of large iron sulphate product and dilute acid	Minimum environmental impact, Iron oxide as byproduct Inert residue	Intermediate process to either sulphate or chloride processes
Safety Requirements	High (Cl_2 at high and low temperature)	High (High temperature acid digestion)	Low (No pressurized vessel and low temperature)	Medium (High temperature melting)
Chlorine and carbon/ carbon containing chemicals at high temperature	Challenges to handle	N/A	N/A	N/A
Energy consumption	High	High	Efficient	High
Sulfur price	No effect	Substantial effect	No effect	No effect

The technology in its present state has been applied to the Longnose deposit in Minnesota and shown to be successful in producing high-grade titanium and iron oxide products. The steady state piloting conducted was successful in demonstrating the robustness of the process with respect to impurity buildup and was capable of producing a high-purity TiO_2 product and relatively high-purity iron oxide (hematite) powder.

As a result of the recycling of reagents and process streams, a buildup of value impurities such as V takes place and can be a valuable byproduct. From the continuous pilot operation, levels as high as 450 ppm V were found in the Ti raffinate produced. This is equivalent to ~$78/t of V_2O_5 value per ton of ilmenite ore when using a cost of $6/lb for V_2O_5, which is significant considering the V has already been solubilized during the leach process and only requires an SX separation step to produce a high-purity V bearing stream for subsequent processing to produce a V product such as V_2O_5. Vanadium has been identified as an element of strategic importance by the USA, Japan, EU, and Australia, with applications in alloy steels, specialty chemicals (ammonium metavanadate), and high-capacity batteries. Further study to recover additional value can be considered.

TABLE OF CONTENTS

EXECUTIVE SUMMARY i
LIST OF TABLES iii
LIST OF FIGURES vi
INTRODUCTION 1
GEOLOGICAL SETTING OF THE LONGNOSE DEPOSIT 4
Oxide Ultramafic Intrusions 4
Geology of the Longnose Peridotite 5
MATERIAL CHARACTERIZATION 9
Methods 9
Concentrate Sample Source 9
Petrographic Analysis 9
Lithogeochemical Analysis 10
X-Ray Diffraction Analysis 12
Electron Microprobe Analysis 12
Hydrometallurgical Sampling 13
Chemical Analysis 14
Solid Analysis – 3-Acid Digestion 14
Solid Analysis – Peroxide Fusion 14
Calculation 14
Leaching Efficiency 14
Material Balance 14
Head/Residue Balance 15
Solution/Head Balance 15
SX Efficiency 15
Product Recovery 15
Longnose Bulk Sample 15
Petrographic Analysis 15
Mineral Chemical Analysis (Electron Microprobe Analysis) 18
Lithogeochemical Analysis 32
Longnose Mineral Concentrates 38
X-ray Diffraction Analysis 38
Mineral Chemical Analysis 40
Lithogeochemical Analysis 50
OVERALL PROCESS FLOWSHEET 57
Mineral Processing Steps 59
Beneficiation Flowsheet Selection 60
Mixed Chloride Leaching 60
Oxidation 60
Iron Solvent Extraction 61
Titanium Solvent Extraction 61
Titanium Dioxide Precipitation 61
Pyrohydrolysis/hydrohydrolysis 61
Aqueous Stream Recycle 61

MINERAL PROCESSING 62
Pilot-Scale Beneficiation Testing 62
Pilot High Pressure Grinding Roll (HPGR) Testing 62
Pilot Spiral Separator Testing 64
Pilot Ball Mill Regrind Testing 65
Pilot Low-Intensity Magnetic Separation (LIMS) Testing 66
Composite Metallurgical Balance 67
MINI PILOT PLANT (MPP) TESTING 67
Materials of Construction 67
Mixer-Settler Design 68
Pumps and Tubing 68
Mixers and Impellers 68
Campaign 1 69
Leaching 69
Oxidation 71
Iron Solvent Extraction 73
Titanium Solvent Extraction 74
Summary 76
Campaign 2 76
Leaching 77
Raffinate Evaporation and Recycling 78
Oxidation 80
Iron Solvent Extraction 81
Titanium Solvent Extraction 86
Titanium Dioxide Precipitation Testing 92
Experimental 93
Titanium Dioxide Product 95
Mineralogical Analysis (XRD) 96
Mineral Chemical Analysis 96
Lithogeochemical Analysis 101
Campaign 2 Summary 108
Campaign 3 109
Leaching 110
Raffinate Evaporation and Recycling 110
Oxidation 111
Iron Solvent Extraction 112
Titanium Solvent Extraction 116
TiO_2 Precipitation 121
Experimental 121
Titanium Dioxide Product 122
Mineralogical Analysis 123
Mineral Chemical Analysis 124
Lithogeochemical Analysis 132
Campaign 3 Summary 137
Fe-Product and HCl Regeneration Bench Testing 138
Experimental 139

Acid Regeneration and Recycling 139
Iron Oxide Product – Campaign 2 139
Mineralogical Analysis (XRD) 140
Mineral Chemical Analysis 140
Lithogeochemical Analysis 150
Iron Oxide Product – Campaign 3 154
Mineralogical Analysis (XRD) 154
Mineral Chemical Analysis 155
Lithogeochemical Analysis 167
Summary 173
Operation Summary 174
TAILING CHARACTERIZATION 175
Introduction 175
Mineralogical Analysis 175
Mineral Chemical Analysis (EMPA) 175
Lithogeochemical Analysis 189
Environmental Testing 201
MASS BALANCE 202
Feed 206
Model 206
Leach 206
Oxidation 207
Iron Removal 207
Iron Recovery 207
Titanium Recovery 208
Raffinate Recycle 208
Numerical Results 208
Leach 208
Solvent Extraction 208
Acid Recovery 209
Production 210
OVERALL FLOWSHEET 210
PROCESS BENCHMARKING 213
CONCLUSION 214
FUTURE CONSIDERATIONS 224
ACKNOWLEDGEMENTS 224
REFERENCES 225
LIST OF APPENDICES 229

LIST OF TABLES

Table i. Benchmarking of CTL process to major competitors. vi
Table 1. Drill holes within the Longnose peridotite 6
Table 2. Sample numbers and descriptions for samples associated with this study 9
Table 3. Rare earth element and trace element normalizing values 12

Table 4. Summary of petrographic analyses performed on randomly selected hand samples of the 1999 Longnose bulk sample 16
Table 5. Electron microprobe analyses of bulk sample ilmenites 22
Table 6. Electron microprobe analyses of bulk sample ilmenites 27
Table 7. Results of lithogeochemical analyses on hand samples from the Longnose bulk sample 33
Table 8. X-ray diffraction analyses for ilmenite mineral concentrate, various PRO hydrometallurgical process powders and residues, and titanium- and iron-oxide precipitates produced during this study 39
Table 9. Electron microprobe analyses of Longnose ilmenite concentrate ilmenites 42
Table 10. Electron microprobe analyses of Longnose ilmenite concentrate magnetites 46
Table 11. Electron microprobe analyses of Longnose ilmenite concentrate rutile 50
Table 12. Results of lithogeochemical analysis on Longnose mineral concentrates 52
Table 13. Chemical analysis of ilmenite concentrate sample comparing PRO analyses (ICP-OES) with NRRI lithogeochemical analysis 57
Table 14. Steady state HPGR calculations 63
Table 15. Pilot spiral testing metallurgical balance 65
Table 16. Pilot spiral testing metallurgical balance (single tailing product) 65
Table 17. Pilot UMS testing metallurgical balance 67
Table 18. Composite titanium dioxide balance from pilot-scale testing 67
Table 19. Mixer settler design 68
Table 20. Leach parameters 70
Table 21. Campaign 1 leaching PLS analysis 71
Table 22. Iron solvent extraction organic composition 73
Table 23. Initial MPP iron circuit stages 73
Table 24. Initial iron circuit operating conditions 74
Table 25. Iron SX solutions – Campaign 1 average elemental analysis 74
Table 26. Titanium SX extractant composition 75
Table 27. Initial MPP titanium circuit stages 75
Table 28. Initial titanium circuit operating conditions 76
Table 29. Titanium SX process solution – Campaign 1 average elemental analysis 76
Table 30. Campaign 2 leach parameters 77
Table 31. Campaign 2 average PLS analysis 78
Table 32. Titanium raffinate evaporation balance (EV-14) 79
Table 33. Leaching condition 80
Table 34. Iron solvent extraction organic composition 81
Table 35. Initial MPP iron circuit stages 81
Table 36. Initial iron circuit operating conditions 81
Table 37. Iron SX solutions – Campaign 2 average elemental analysis sample set 51 86
Table 38. Titanium SX extractant composition 87
Table 39. Initial MPP titanium circuit stages 87
Table 40. Initial titanium circuit operating conditions 87
Table 41. Titanium SX process Campaign 2 average solution analysis 92
Table 42. Comparison of titanium pregnant strip solution quality from prior study (PRO 16-05) and current study (PRO 18-02) 94
Table 43. Calcined titanium dioxide, Campaign 2, test 10 95
Table 44. Electron microprobe analyses of Campaign 2 sample 1802-P10-1 (ML-66) 98

Table 45. Electron microprobe analyses of Campaign 2 sample 1802-P10-2 (ML-67) 100
Table 46. Results of lithogeochemical analyses on Campaign 2 titanium dioxide precipitates 103
Table 47. Chemical analyses of titanium dioxide products produced during pilot-scale demonstration of ilmenite processing technology 104
Table 48. Campaign 2 average PLS analysis 110
Table 49. Leaching parameters 110
Table 50. Ti raffinate evaporation balance (EV-54) 110
Table 51. PLS analysis 111
Table 52. Fe solvent extraction organic composition 112
Table 53. Initial MPP iron circuit stages 112
Table 54. Initial iron circuit operating conditions 112
Table 55. Fe SX solutions – average analysis of Campaign 3 116
Table 56. Ti SX extractant composition 117
Table 57. Initial MPP titanium circuit stages 117
Table 58. Initial titanium circuit operating conditions 117
Table 59. Ti SX process solution average analysis of Campaign 3 121
Table 60. Calcined titanium dioxide, Campaign 3, PRO test 17 123
Table 61. Electron microprobe analyses of Campaign 3 sample 1802-P17-1 (ML-68) 126
Table 62. Electron microprobe analyses of Campaign 3 sample 1802-P17-2 (ML-69) 130
Table 63. Results of lithogeochemical analyses on Campaign 3 titanium dioxide precipitates 133
Table 64. Iron oxide calcined Campaign 2 product - Test 6 139
Table 65. Electron microprobe analyses of Campaign 2 non-calcined iron oxide precipitate hematite from sample 1802-T6NC/ML-73 143
Table 66. Electron microprobe analyses of Campaign 2 non-calcined magnesium- and chlorine-bearing unknown from sample 1802-T6NC/ML-73. Values are in weight percentages. 143
Table 67. Electron microprobe analyses of Campaign 2 non-calcined iron- and chlorine-bearing unknown from sample 1802-T6NC/ML-73 144
Table 68. Electron microprobe analysis of iron oxide precipitate (hematite) from Campaign 2 calcined sample 1802-T6C/ML-74. Values are in weight percentages 147
Table 69. Electron microprobe analyses of SiO_2-FeO-Al_2O_3-bearing unknown from Campaign 2 calcined iron oxide precipitate sample 1802-T6C/ML-74 148
Table 70. Results of lithogeochemical analyses on Campaign 2 iron oxide precipitates 151
Table 71. Iron oxide calcined campaign 3 product - Test 6 154
Table 72. Electron microprobe analyses of hematite in Campaign 3 non-calcined iron oxide precipitate sample 1802-T7NC (ML-75). Values are in weight percentages 157
Table 73. Electron microprobe analyses of iron- and titanium-bearing unknown phase in Campaign 3 non-calcined iron oxide precipitate sample 1802-T7NC (ML-75) 159
Table 74. Electron microprobe analyses of Campaign 3 calcined iron oxide precipitate (hematite) that contains greater than 0.5% (by weight) TiO_2 from sample 1802-T7C/ML-76 165
Table 75. Electron microprobe analyses of iron- and titanium-bearing unknown phase in Campaign 3 calcined iron oxide precipitates from sample 1802-T7C/ML-76 167
Table 76. Results of lithogeochemical analyses of Campaign 3 iron oxide precipitates 169
Table 77. Average leaching recovery over the three campaigns 174
Table 78. Leach recovery versus particle size 174
Table 79. Minerals identified during electron microprobe analysis of Campaign 2 leach residues 176
Table 80. Electron microprobe analyses of ilmenite from sample 1802-BL10-1 (ML-71) 179

Table 81. Electron microprobe analyses of ilmenite from sample 1802-BL6 (ML-70) 179
Table 82. Electron microprobe analyses of ilmenite from sample 1802-BL19 (ML-72) 180
Table 83. Minerals identified during electron microprobe analysis of Campaign 3 two-stage leach residues 182
Table 84. Electron microprobe analyses of ilmenite in Campaign 3 two-stage leach residues. Values are in weight percentages 183
Table 85. Electron microprobe analyses of ilmenite grains with low analytical totals from Campaign 3 two-stage leach residues 184
Table 86. Electron microprobe analyses of grains tentatively identified as rutile from Campaign 3 two-stage leach residues 185
Table 87. Results of lithogeochemical analyses on single stage leach residues 190
Table 88. Results of lithogeochemical analyses on two-stage leach residues 194
Table 89. TCLP. O. Reg. 558 Metals and Inorganics test on residue of campaigns 1, 2, and 3 201
Table 90. TCLP. O. Reg. 558 Metals and Inorganics test on the residue of Campaign 3 ground residue re-leached 202
Table 91. Leach 207
Table 92. Iron removal 207
Table 93. Predicted leach data 208
Table 94. Solvent extraction data, g/L 209
Table 95. Acid recovery 209
Table 96. Makeup acid requirement 210
Table 97. Results of lithogeochemical analyses on two-stage leach residues 210
Table 98. Benchmarking of CTL process to major competitors 213

LIST OF FIGURES

Figure 1. Flowsheet for the mineral processing of ilmenite 3
Figure 2. Flowsheet for the hydrometallurgical process of ilmenite 4
Figure 3. Location map of the Duluth Complex Cu-Ni and TiO_2 resources 5
Figure 4. Geology map of the Longnose peridotite area with cross section lines 7
Figure 5. Geologic cross section of the Partridge River Intrusion and the Longnose peridotite 7
Figure 6. Geologic cross sections through the Longnose TiO_2 deposit 8
Figure 7. Electron microprobe backscatter images of sample 1802-3765 19
Figure 8. Electron microprobe backscatter images of samples 1802-3766 20
Figure 9. Electron microprobe backscatter images of sample 1802-3769 21
Figure 10. Ternary diagrams illustrating the chemical compositions of ilmenites from the Longnose bulk sample 26
Figure 11. Ternary diagrams illustrating the chemical compositions of magnetites from the Longnose bulk sample 30
Figure 12. Ternary diagrams illustrating the chemical compositions of magnetites occurring in veins from the Longnose bulk sample 31
Figure 13. Chondrite-normalized and primitive mantle-normalized spider diagrams for all hand samples from the Longnose bulk sample 37
Figure 14. Electron microprobe backscatter images of Longnose ilmenite concentrate samples 1802-MIM-5 (ML-64) and 1802-ILMC (ML-79) 40

Figure 15. Ternary diagrams illustrating the chemical compositions of ilmenites from the Longnose ilmente concentrate 44
Figure 16. Ternary diagrams illustrating the chemical compositions of magnetites from the Longnose ilmenite concentrate 49
Figure 17. Ternary diagrams illustrating the chemical compositions of rutile from the Longnose ilmenite concentrate 51
Figure 18. Chondrite-normalized and primitive mantle-normalized spider diagrams for Longnose ilmenite concentrate, magnetic LIMS concentrate, and rougher spiral tails 56
Figure 19. Mineral processing flowsheet 58
Figure 20. PRO pilot plant hydrometallurgical process flowsheet 59
Figure 21. HPGR feed and screen product sizing 63
Figure 22. HPGR screen undersize by cycle 64
Figure 23. Pilot-scale ball mill discharge sizing per run 66
Figure 24. Leach tank 69
Figure 25. Filter press 70
Figure 26. Oxidation columns 72
Figure 27. Conversion rate of Fe^{2+} to Fe^{3+} during oxidation 72
Figure 28. Iron SX circuit 73
Figure 29. Titanium SX circuit 75
Figure 30. Impurity content in the leach 78
Figure 31. Titanium raffinate evaporation setup 79
Figure 32. Conversion rate of Fe^{2+} to Fe^{3+} during oxidation 80
Figure 33. Iron solvent extraction circuit schematic 82
Figure 34. Iron circuit iron analysis 83
Figure 35. Iron circuit titanium analysis 83
Figure 36. Iron circuit magnesium analysis 84
Figure 37. Iron circuit chromium analysis 84
Figure 38. Iron circuit vanadium analysis 85
Figure 39. Iron circuit manganese analysis 85
Figure 40. Iron circuit aluminum analysis 86
Figure 41. Titanium solvent extraction circuit schematic 88
Figure 42. Titanium circuit titanium analysis 89
Figure 43. Titanium circuit magnesium analysis 89
Figure 44. Titanium circuit vanadium analysis 90
Figure 45. Titanium circuit manganese analysis 90
Figure 46. Titanium circuit chromium analysis 91
Figure 47. Titanium circuit aluminum analysis 91
Figure 48. Block flow diagram for TiO_2 thermal precipitation and calcination 93
Figure 49. Precipitation kinetic in Campaign 2 94
Figure 50. Titanium dioxide impurities content in Campaign 2 95
Figure 51. Electron microprobe backscatter images of Campaign 2 titanium dioxide (rutile) precipitates in sample 1802-P10-1 (ML-66) 97
Figure 52. Electron microprobe backscatter image of Campaign 2 titanium dioxide (rutile) precipitates in sample 1802-P10-2 (ML-77), a calcined sample of Campaign 2 titanium dioxide precipitates 99

Figure 53. Ternary diagrams illustrating the chemical composition of titanium dioxide (TiO_2, rutile) precipitates from Campaign 2 102
Figure 54. Chondrite- and primitive mantle-normalized rare earth element spider diagram for Campaign 2 TiO_2 precipitates 107
Figure 55. Impurity content in leach 111
Figure 56. Fe circuit Fe analysis 113
Figure 57. Fe circuit Ti analysis 113
Figure 58. Fe circuit Mg analysis 114
Figure 59. Fe circuit Cr analysis 114
Figure 60. Fe circuit V analysis 115
Figure 61. Fe circuit Mn analysis 115
Figure 62. Fe circuit Al analysis 116
Figure 63. Ti circuit Ti analysis 118
Figure 64. Ti circuit Mg analysis 118
Figure 65. Ti circuit V analysis 119
Figure 66. Ti circuit Mn analysis 119
Figure 67. Ti Circuit Cr analysis 120
Figure 68. Ti circuit Al analysis 120
Figure 69. Ti content in preg strip during precipitation process in Campaign 3 122
Figure 70. Titanium impurities content in Campaign 3 per PRO analyses 123
Figure 71. Electron microprobe backscatter image of Campaign 3 non-calcined titanium dioxide (rutile) precipitates in sample 1802-P17-1 (ML-68) 125
Figure 72. Ternary diagrams illustrating the chemical composition of titanium dioxide (TiO_2, rutile) precipitates from sample 1802-P17-1, which represents the non-calcined titanium dioxide precipitate from Campaign 3 127
Figure 73. Electron microprobe backscatter image of Campaign 3 titanium dioxide (rutile) precipitates in sample 1802-P17-2 (ML69), a calcined sample of Campaign 3 titanium dioxide precipitates 129
Figure 74. Ternary diagram illustrating the chemical composition of titanium dioxide (TiO_2, rutile) precipitates from sample 1802-P17-2, which represents the calcined titanium dioxide precipitate from Campaign 3 131
Figure 75. Chondrite- and primitive mantle-normalized spider diagrams for Campaign 3 TiO_2 precipitates 136
Figure 76. Comparison of PRO and NRRI analyses of calcined Campaign 2 and Campaign 3 TiO_2 precipitates 138
Figure 77. Fe_2O_3 impurities content in Campaign 2 140
Figure 78. Electron microprobe backscatter image of Campaign 2 non-calcined iron oxide precipitate (sample 1802-T6NC/ML-73) 142
Figure 79. Ternary diagram illustrating the chemical compositions of iron oxide precipitates (hematite) from Campaign 2 non-calcined sample 1802-T6NC/ML-73 145
Figure 80. Electron microprobe backscatter images of Campaign 2 calcined iron oxide precipitate (sample 1802-T6C/ML-74) 146
Figure 81. Ternary diagram illustrating the chemical composition of iron oxide precipitate (hematite) from Campaign 2 calcined sample 1802-T6C/ML-74 149
Figure 82. Chondrite- and primitive mantle-normalized spider diagrams for Campaign 2 iron oxide precipitates 153

Figure 83. Campaign 3 calcined Fe_2O_3 products impurities 154
Figure 84. Electron microprobe backscatter image of Campaign 3 non-calcined iron oxide precipitates (sample 1802-T7NC (ML-75)) 156
Figure 85. Ternary diagram illustrating the chemical compositions of iron oxide precipitates (hematite) from Campaign 3 non-calcined sample 1802-T7NC (ML-75) 158
Figure 86. Ternary diagram illustrating the chemical compositions of TiO_2-bearing (TiO_2>0.5% by weight) iron oxide precipitates (hematite) from Campaign 3 non-calcined sample 1802-T7NC (ML-75) 160
Figure 87. Ternary diagram illustrating the chemical compositions of TiO_2-bearing (TiO2.0.5% by weight) iron oxide precipitates (hematite) from Campaign 3 non-calcined sample 1802-T7NC (ML-75) 162
Figure 88. Electron microprobe backscatter images of Campaign 3 calcined iron oxide precipitates from sample 1802-T7C (ML-76) 163
Figure 89. Ternary diagrams illustrating the chemical composition of iron oxide precipitate (hematite) from calcined Campaign 3 sample 1802-T7C/ML-76 164
Figure 90. Ternary diagram illustrating the chemical composition of the titanium-bearing (TiO_2>0.5% by weight) iron oxide (hematite) precipitate from Campaign 3 calcined iron oxide precipitate sample 1802-T7C/ML-76 166
Figure 91. Ternary diagram illustrating the chemical composition of the iron- and titanium-bearing unknown phase from the calcined Campaign 3 iron oxide precipitate sample 1802-T7C/ML-76 168
Figure 92. Chondrite- and primitive mantle-normalized spider diagrams for Campaign 3 iron oxide precipitates 172
Figure 93. Comparison of PRO and NRRI analyses of calcined Campaign 2 and Campaign 3 iron oxide precipitates 173
Figure 94. Electron microprobe backscatter images of Campaign 1, Campaign 2, and Campaign 3 leach residue samples 178
Figure 95. Ternary diagram illustrating the chemical composition of ilmenites from samples 1802-BL-10-1 (ML-71), 1802-BL-6 (ML-70), and 1802-BL-19 (ML72) 181
Figure 96. Ground- and two-stage leach residue samples 1802-L19R (ML-77) and 1802-L20R (ML-78) from Campaign 3 182
Figure 97. Ternary diagrams illustrating the mineral chemical compositions of ilmenite grains from Campaign 3 re-ground and two-stage leach samples 1802-L19R (ML-77) and 1802-L20R (ML-78) 187
Figure 98. Ternary diagrams illustrating the mineral chemical compositions of a mineral phase tentatively identified as rutile in the Campaign 3 two-stage leach residue samples 188
Figure 99. Chondrite- and primitive mantle-normalized spider diagrams for Campaign 1 leach residues (no recycling) 197
Figure 100. Chondrite- and primitive mantle-normalized spider diagrams compaing Campaign 2 and Campaign 3 leach residues (1802-BL6 (ML-70, Campaign 2, half-recycled) and sample 1802-BL-19 (ML-72, Campaign 3, recycled) 198
Figure 101. Chondrite- and primitive mantle normalized spider diagrams for Campaign 3 recycled and reground and two-stage leach residues, respectively 200
Figure 102a. Mass balance 203
Figure 102b. Mass balance (continued) 203
Figure 102c. Mass balance (continued) 204

Figure 102d. Mass balance (continued) 204
Figure 102e. Mass balance (continued)..... 205
Figure 102f. Mass balance (continued) 205
Figure 102g. Mass balance (continued)..... 206
Figure 103. PRO TiO2 process flowsheet..... 211
Figure 104. Process solutions and solids 212

INTRODUCTION

Process Research Ortech Inc. (PRO) has developed an innovative process for the production of high-purity TiO_2 directly from ilmenite ore. The PRO process is protected by several patents in North America and abroad (US Patent No. 7,803,336 B2, Canadian Patent No. 2,513,309, and Australian Patent No. 2004291568). The process consists of atmospheric chloride leach followed by solvent extraction of Fe, Ti, and V successively. A high-purity, Ti-bearing strip solution is produced and can be used to produce Ti products dependent on the end market use such as high-purity TiO_2 for pigments, pharmaceutical, and food industries. Other products that can be obtained from the process are Fe_2O_3, which is of high purity and can be used for pigment or iron production, and V_2O_5 if the ore contains vanadium. PRO process can produce an anatase or rutile product as required by controlling the process parameters. The PRO process employs commercially proven unit operations. The PRO process is flexible, as it can be applied to a wide range of feedstocks, especially those with Mg, V, and Cr not treatable by current methods. It is an energy-efficient process, and there is potential for further reduction in energy requirements with the newly developed hydrothermal HCl recycle technology. The PRO process is also economically attractive, as it potentially requires lower capital and operating costs and may offer the opportunity for early startup. In addition, the process is environmentally friendly, as the reagents are recycled and the residue is inert. As such, the residues can become useful byproducts of the process, including potential utilization for road fill or other specialty materials. There is no need to handle chlorine and carbon/carbon-containing chemicals at high temperature like existing plants in the USA. The entire processing scheme, from ore to end product, can be done in one location, and this scheme has the ability to produce Ti materials with physical properties to match end-user needs.

The ilmenite deposits associated with oxide ultramafic intrusions (OUIs) available in northeastern Minnesota contains alkaline-earth elements like Mg, which makes the ore unsuitable for slag making and the chlorination process currently used in the USA. However, this ore can be treated by the PRO process to produce high-purity, Ti-bearing solutions that can be used to produce TiO_2 pigment.

A joint project with the Natural Resources Research Institute (NRRI) at the University of Minnesota Duluth and PRO was initiated. In the initial work performed by NRRI and PRO on an ilmenite concentrate sample, bench testing and mini-pilot operation were performed to test the unit process steps involved on a batch continuous operation and produce samples of TiO_2 product for market evaluation (Mlinar et al., 2017). During that program, high-purity TiO_2 (99.3%) and Fe2O3 (98.5%) products were produced, and a sample of leach tailings analyzed by Ontario Regulation 558 (Standards for Metals and Inorganic Discharge) was found to be an inert waste stream.

In the current program, an oxide-rich bulk sample containing ilmenite and magnetite from the Longnose peridotite oxide ultramafic intrusion (Longnose OUI) located in northeastern Minnesota was examined. This funnel-shaped Mesoproterozoic intrusion was formed late in the history of the development of the Duluth Complex and contains numerous oxide-rich mineral horizons associated with ultramafic rocks (dunite, peridotite, feldspathic peridotite). The sample utilized for this study comprised remaining ilmenite concentrate that was produced for the previous hydrometallurgical study conducted by Mlinar et al. (2017). Mineral processing (gravity separation followed by low-intensity magnetic separation) was performed by NRRI by Mlinar et al. (2017) on a 1999 bulk sample acquired by American Shield from an outcrop exposure of the mineralization at the prospect.

Characterization of the bulk sample for this study included transmitted and reflected light petrography, whole rock major and trace element lithogeochemical characterization, x-ray diffraction (XRD)

mineralogy studies, and electron microprobe analysis (EMPA) to determine the chemistries of individual mineral species present in the rock. Products and process residues from the hydrometallurgical processing of the concentrate were characterized by means of lithogeochemical, x-ray diffraction, and EMPA analysis.

For the hydrometallurgical study, setup and operation of a pilot circuit were performed to test the various process steps, which included leaching, solid/liquid separation, solvent extraction (SX), and precipitation in an integrated circuit. The program was divided into campaigns that systematically integrated the unit operations to examine the impurity buildup in the circuit from integrated operation of specific streams.

The focus of this project was to build on the information acquired from the previous studies (Process Research Ortech Inc., 2017) conducted in 2016 by performing additional steady-state piloting to incorporate the following:

- Examine variation in feed composition and effect on subsequent SX separation processes;
- Incorporation of recycled streams such as SX process raffinates and filtrates from precipitation stages;
- Examine a potential proprietary process developed by PRO and NRRI for the production of Fe_2O_3 and determination of the quality of regenerated acid during the processing of ilmenite;
- Examine impurity buildup in the circuit from integrated operation (i.e. recycling of raffinate) on the quality of Fe_2O_3, TiO_2 product and potential bleed effluent;
- Evaluate TiO_2 quality from the integrated operation; and
- Perform mass balance of the system at steady state.

The mineral processing and hydrometallurgical flowsheets being developed are presented in Figures 1 and 2, and the areas of development for each campaign in the project are highlighted.

The targets of each pilot campaign were as follows:

In Campaign 1, the following elements were performed:

- Perform setup and operation of the pilot circuit to build up solutions in the various SX circuits in preparation of subsequent campaigns, which will examine the impurity buildup in the circuit from integrated operation of specific streams; and
- Generation of Ti raffinate for recycling in subsequent campaigns was targeted.

In Campaign 2, the elements being examined include the following:

- Continued operation of the Fe and Ti SX circuits with the generation of Ti raffinate for recycling;
- Recycling of the Ti SX raffinate into the leach;
- Monitor impurity buildup and assess the impact on pregnant strip solutions of Fe and Ti; and
- Continue testing and evaluation of proprietary technology to examine the quality of Fe_2O_3, HCl products, and determine process design criteria.

In Campaign 3, the following elements were evaluated in the flowsheet:

- Continued operation of the Fe and Ti SX circuits with the generation of Ti raffinate for recycling;
- Recycling of the Ti SX raffinate into the leach;

- Recycling of the TiO_2 precipitation filtrate into the circuit (Ti strip); and
- Monitor impurity buildup and assess the impact on pregnant strip solutions of Fe and Ti.

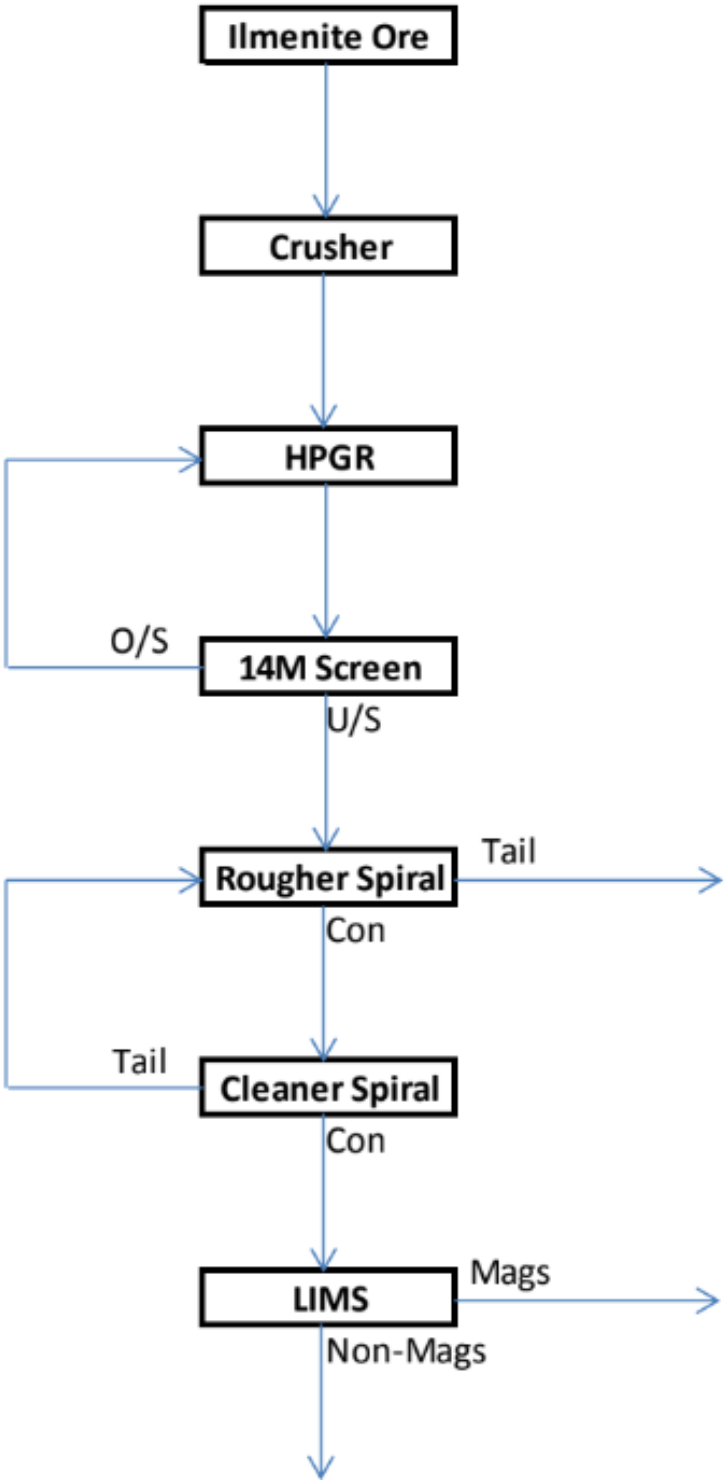

Figure 1. Flowsheet for the mineral processing of ilmenite**. The ilmenite concentrate is the non-magnetic (non-mags) portion resulting from the LIMS process.**

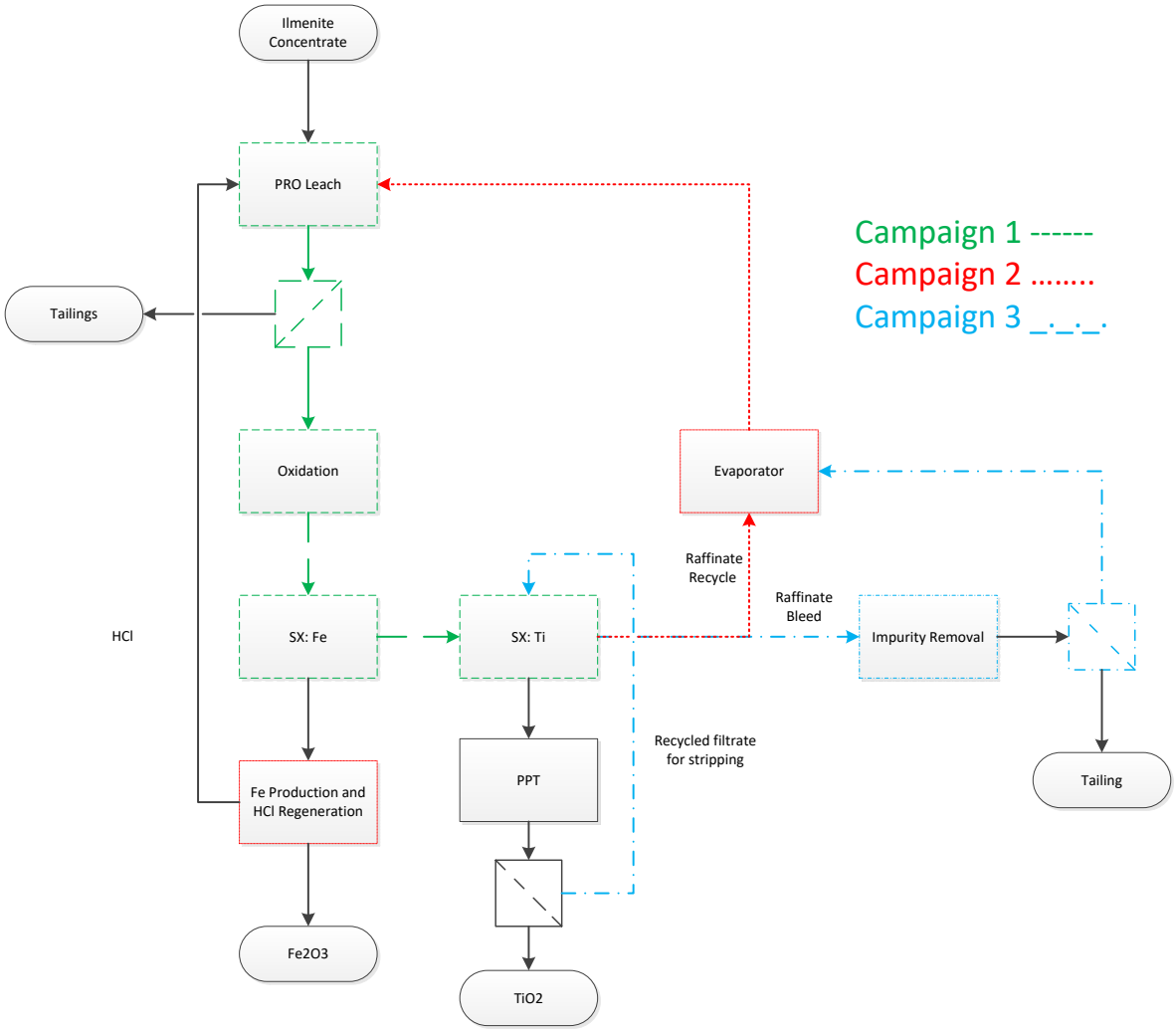

Figure 2. Flowsheet for the hydrometallurgical process of ilmenite. Areas of each pilot campaign highlighted.

GEOLOGICAL SETTING OF THE LONGNOSE DEPOSIT

Oxide Ultramafic Intrusions

Beginning in the mid-1950s, numerous mining companies flew airborne magnetic-electromagnetic surveys over the Duluth Complex to better understand the geology and focus work on developing the Cu-Ni mineral potential of the district. One result of these geophysical surveys was the discovery of numerous conductive magnetic anomalies. Many of these geophysical anomalies, which were initially drilled based on massive Fe-Cu-Ni sulfide mineralization targeting concepts, turned out to be oxide-bearing ultramafic intrusions (OUIs) with Fe-Ti ± V oxide mineral potential. Throughout several decades on mineral exploration, 13 oxide ultramafic intrusions were intersected in drill holes subparallel to the basal contact of the Duluth Complex. Detailed drilling to define potential Fe-Ti ± V resources has taken place at the Longnose, Titac (formerly Section 34), and Water Hen localities (Fig. 3).

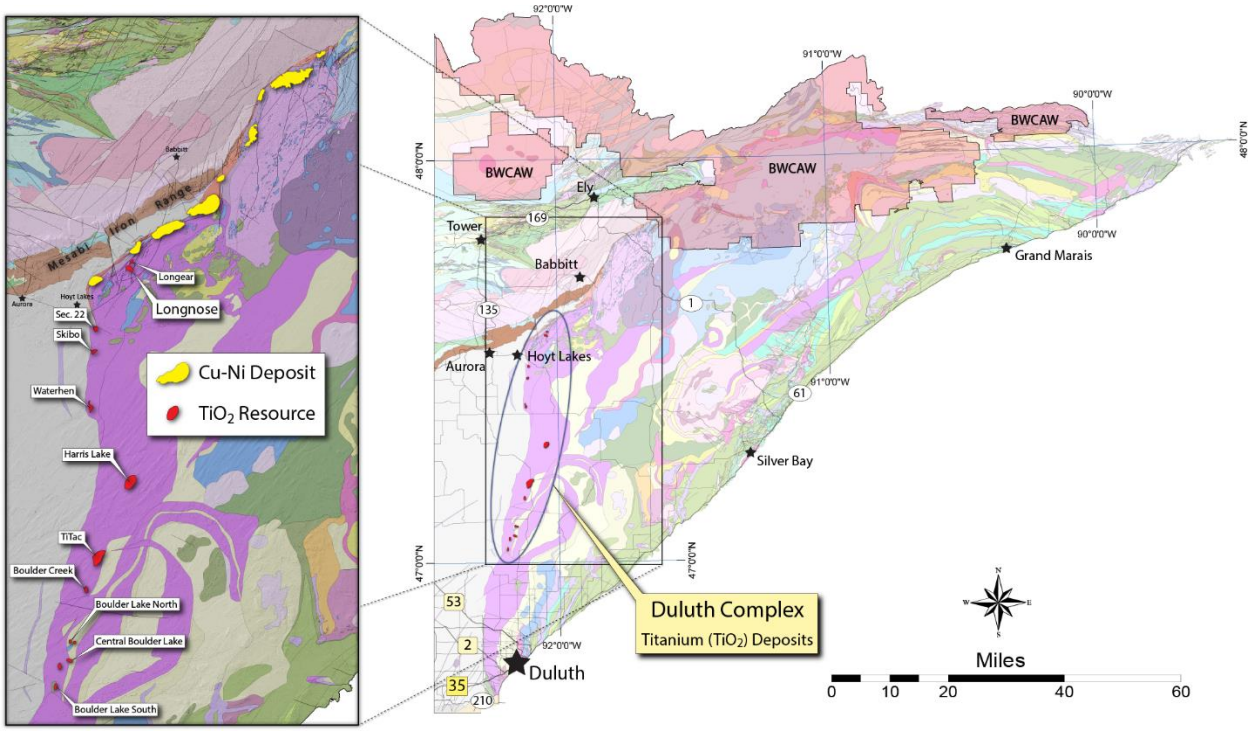

Figure 3. Location map of the Duluth Complex Cu-Ni and TiO_2 resources.

In general, OUIs are dominantly composed of coarse-grained to pegmatitic clinopyroxenite, peridotite, dunite, melatroctolite, and minor melagabbro that all contain approximately 10–40% iron-titanium oxide mineralization, commonly as disseminated to net-textured ilmenite-magnetite with lesser titaniferous magnetite. Irregular zones of semi-massive to massive iron-titanium oxide are present in many of the OUIs, and many also contain abundant fractionated copper > nickel sulfide mineralization. The intrusive morphology of the OUIs are varied in shape (sheet-, funnel-, dike- and pipe-like geometries) and inclination (flat-lying, moderately-dipping, and sub-vertical) and commonly have irregular apophyses along their margins. OUIs intrude and crosscut troctolitic rocks of the Partridge River, Western Margin, and Boulder Lake intrusions. Generally, OUIs are spatially arranged along linear trends subparallel to the strike of the hosting troctolitic intrusion, suggesting structural and/or stratigraphic control may be important to their genesis, which remains poorly understood (Woodruff et al., 2010). Some oxide ultramafic intrusions exhibit a crude zonation from an olivine-rich core (dunite, peridotite, and melatroctolite) to an outer clinopyroxenite margin, whereas others consist of only one dominant rock type. Detailed descriptions of the oxide ultramafic intrusions are found in Mainwaring (1975), Mainwaring and Naldrett (1977), Severson and Hauck (1990), Linscheid (1991), Miner and Pasteris (1994), Miner (1995), and Severson (1995).

Geology of the Longnose Peridotite

The Longnose peridotite (Longnose) is one of 13 known OUIs that intruded into layered series troctolitic intrusions of the Duluth Complex (Fig. 4; Minnesota Minerals Coordinating Committee, 2016). The ultramafic intrusion was geophysically discovered by Bear Creek Mining Company in 1955 as a result of an airborne magnetic/electromagnetic survey. Bear Creek first drilled the geophysical anomaly in 1958 (drill hole A1-1) and thus first truly discovered the TiO_2 mineralization at Longnose. Sporadic drilling over

the subsequent 53 years by numerous companies has provided the foundation upon which all geologic information that exists today on the deposit was built (Table 1).

Table 1. Drill holes within the Longnose peridotite.

Year	Number of Drill Holes	Drill Hole Names	Footage (feet)	Lessee
1958	1	A1-1	416	Bear Creek Mining
1969	1	Ba-6	3,085	Humble Oil
1975	1	LN-01	634	American Shield / Nicor
1984	9	LN-02 – LN-10	4,615	American Shield / Nicor
2010	6	LNG-01 – LNG-06	3,087	Cardero Iron Ore
2011	9	LNG-07 – LNG-15	8,288	Cardero Iron Ore
Total	***27***		***20,125***	

The Longnose peridotite is a roughly funnel-shaped, late-stage ultramafic intrusion that shallowly down-cuts the Partridge River intrusion to the southeast (Figs. 4 and 5). The intrusion contains abundant disseminated, semi-massive, and massive oxides (ilmenite, titanomagnetite, magnetite) within a crudely concentrically zoned ultramafic body. Olivine-rich rocks (dunite, peridotite, feldspathic peridotite) host the majority of the Ti – Fe oxide mineralization and form the core of the intrusion that grades downward and outwards into oxide-pyroxenite. Sulfides are a minor constituent at Longnose (trace to 2%), with chalcopyrite ($CuFeS_2$) accounting for upwards of 99% of the sulfide mineral assemblage (Linscheid, 1991). A series of cross sections through Longnose are presented in Figure 6. These cross sections clearly display an upper zone of olivine-rich rocks (labeled PR) that grade downwards into pyroxenite (labeled PX). Zones of semi-massive to massive oxide (labeled MX) occur dominantly within the upper olivine-rich core of the intrusion but can occur in the lower pyroxenite zone.

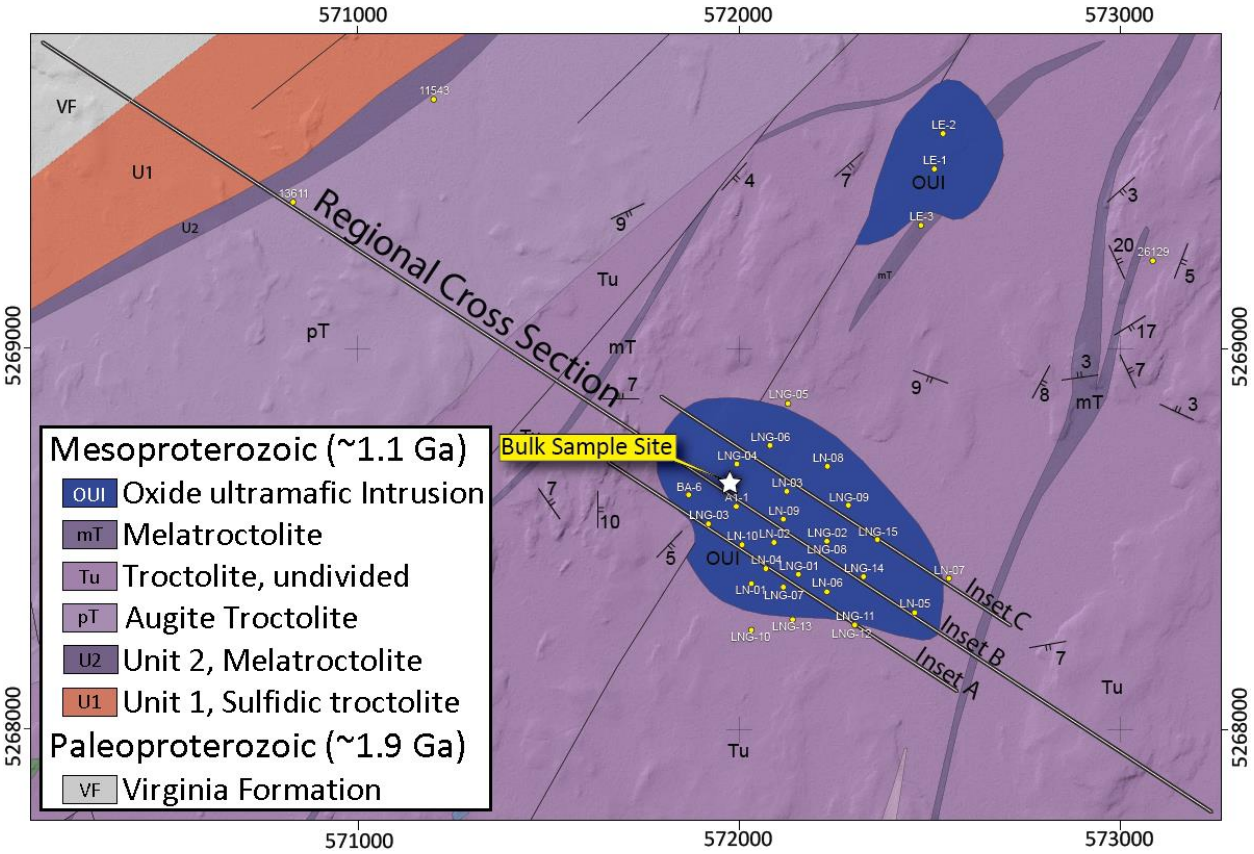

Figure 4. Geology map of the Longnose peridotite area with cross section lines (presented in Figs. 5 and 6).

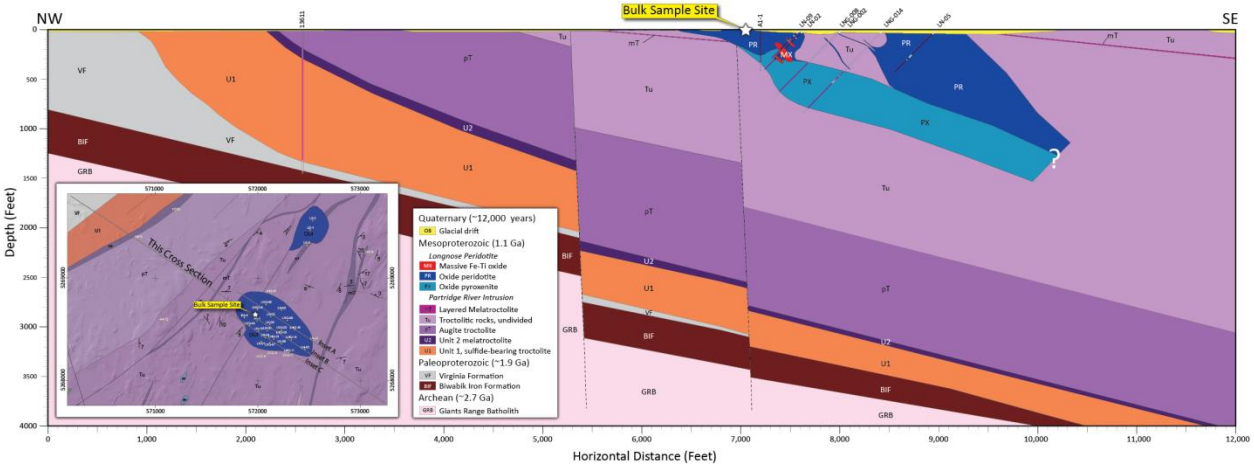

Figure 5. Geologic cross section of the Partridge River Intrusion and the Longnose peridotite.

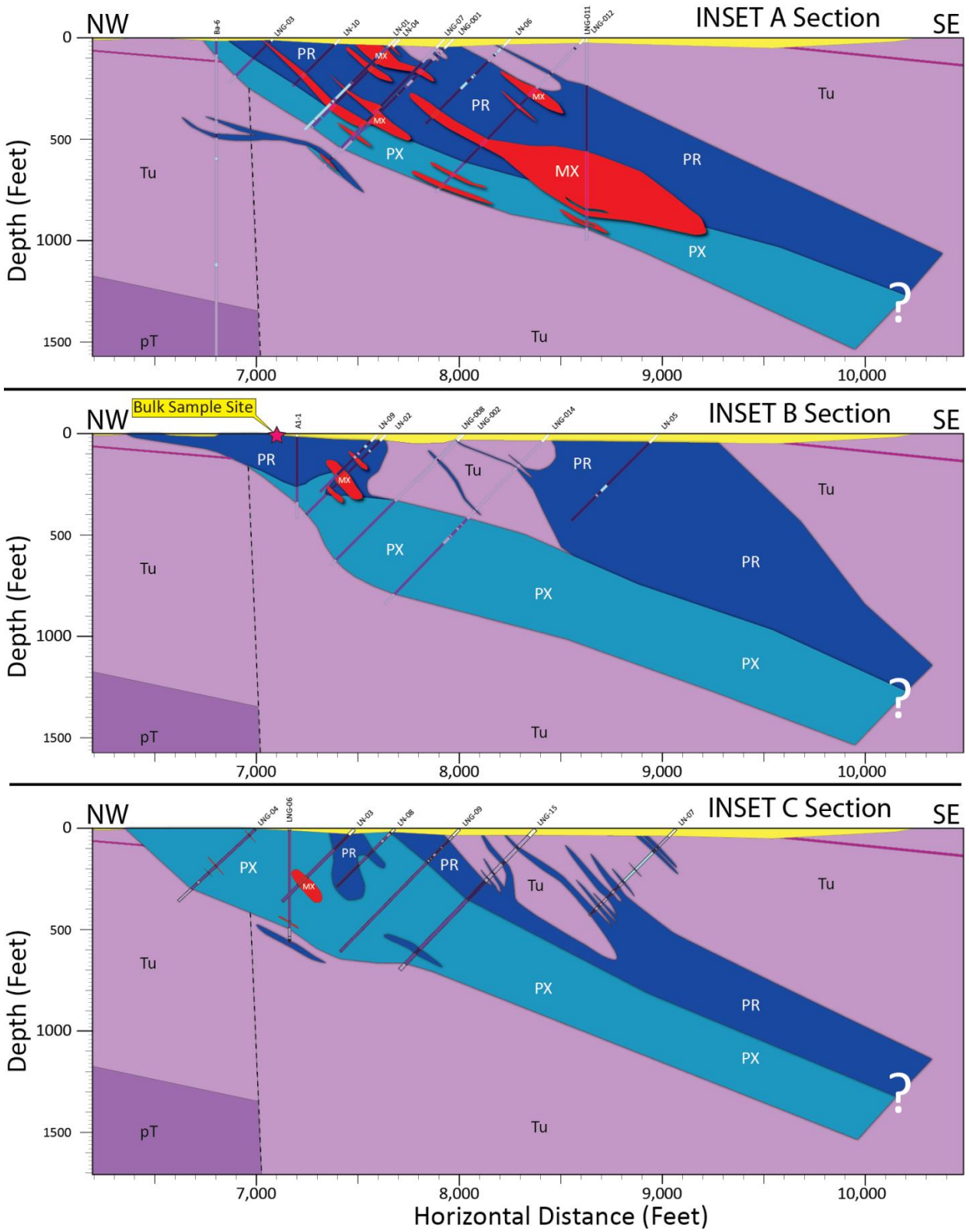

Figure 6. Geologic cross sections through the Longnose TiO_2 deposit.

MATERIAL CHARACTERIZATION

Methods

Concentrate Sample Source

The sample used for this study comprises part of an approximately 100-ton bulk sample collected from the Longnose OUI in 1999. The location of the Longnose bulk sample has Universe Transverse Mercator (UTM) Zone 15 North (NAD83 Zone 15N) coordinates 572026E and 5268651 N.

The Longnose concentrate utilized for this study was generated during the previous study by Mlinar et al. (2017). The concentrate was produced by gravity and magnetic separation of an approximately ten metric ton sample (located at the NRRI Coleraine Laboratory in Coleraine, Minnesota) obtained from the bulk sample. Further details related to the production of this sample are described in Mlinar et al. (2017).

Petrographic Analysis

Transmitted and reflected light petrographic analyses were conducted on 12 polished thin sections of the Longnose OUI bulk sample by a Minnesota Licensed Professional Geologist at NRRI (Table 2). Petrographic analyses were performed using an Olympus BX-51 petrographic microscope equipped with Olympus SWH10X eyepieces, an Olympus PlanApo 2X objective, UPlanFL 10x, 20x, and 40x objectives, and an Olympus DP71 1.41 megapixel digital microscope camera. Polished thin sections for these analyses were prepared by Quality Thin Sections (Tucson, Arizona).

Table 2. Sample numbers and descriptions for samples associated with this study. “NA” represents not applicable. “X” represents that a sample of that type was made and evaluated for this study.

PRO Sample Number	Coleraine Sample Number	Sample Round	Analysis Certificate	Description	Material Type	Polished Thin Section	Polished Puck	Lithogeo-chemistry	X-Ray Diffraction	Electron Microprobe
1802-T6-RES	NA	1	NA	Hydrohydrolysis iron powder	Powder	NA	NA	X	X	NA
1802-MIM-5	ML-64	1	TB19114510	PRO Ilmenite Concentrate	Powder	NA	X	X	X	X
1802-BL-10	NA	1	TB19114510	Leach residue, campaign 1, no recycling	Powder	NA	NA	X	X	NA
1802-BL-11	NA	1	TB19114509	Leach residue, campaign 2, after recycling	Powder	NA	NA	X	X	NA
1802-BL12	NA	1	TB19114509	Leach residue, campaign 2, after recycling duplicate	Powder	NA	NA	X	NA	NA
1802-P10-1	ML66	2	TB19150942	Ti-oxide precipitate Campaign 2 – not calcined	Powder	NA	X	X	NA	X
1802-P10-2	ML67	2	TB19150942	Ti-oxide precipitate Campaign 2 - calcined	Powder	NA	X	X	NA	X
1802-P17-1	ML68	2	TB19150942	Ti-oxide precipitate Campaign 3 – not calcined	Powder	NA	X	X	NA	X
1802-P17-2	ML69	2	TB19150942	Ti-oxide precipitate Campaign 3 - calcined	Powder	NA	X	X	NA	X
1802-BL-6	ML70	2	TB19150942	Leach residue, Campaign 2, half-recycled	Powder	NA	X	X	NA	X
1802-BL-10	ML71	2	TB19150942	Leach residue, Campaign 1, no recycling	Powder	NA	X	X	NA	X
1802-BL-19	ML72	2	TB19150942	Leach residue, Campaign 3, after recycling	Powder	NA	X	X	NA	X
1802-BL-66	NA	2	TB19150942	BL-6 Leach residue, Campaign 2, half-recycled, duplicate	Powder	NA	NA	X	NA	NA
1802-T6NC	ML73	2	TB19150942	Fe-oxide precipitate, Campaign 2, not calcined	Powder	NA	X	X	NA	X
1802-T6C	ML74	2	TB19150942	Fe-oxide precipitate, Campaign 2, calcined	Powder	NA	X	X	NA	X
1802-T7NC	ML75	2	TB19150942	Fe-oxide precipitate, Campaign 3, not calcined	Powder	NA	X	X	NA	X
1802-T7C	ML76	2	TB19150942	Fe-oxide precipitate, Campaign 3, calcined	Powder	NA	X	X	NA	X
1802-L19R	ML77	3	TB19173773	BL-19 Leach residue, Campaign 3, ground and 2-stage leach	Powder	NA	X	X	NA	X
1802-L20R	ML78	3	TB19173773	BL-20 Leach residue, Campaign 3, ground and 2-stage leach	Powder	NA	X	X	NA	X

Table 2 (continued).

PRO Sample Number	Coleraine Sample Number	Sample Round	Analysis Certificate	Description	Material Type	Polished Thin Section	Polished Puck	Lithogeo-chemistry	X-Ray Diffraction	Electron Microprobe
1802-ILMC	ML-79	4	TB19216336	Coleraine ilmenite concentrate	Powder	NA	X	X	NA	X
1802-3765	NA	1	TB19114510	Longnose Bulk Sample – Semi-massive Oxide	Rock	X	NA	X	X	X
1802-3766	NA	1	TB19114510	Longnose Bulk Sample – Semi-massive Oxide	Rock	X	NA	X	X	X
1802-3767	NA	1	TB19114510	Longnose Bulk Sample – Semi-massive Oxide	Rock	X	NA	X	X	NA
1802-3768	NA	1	TB19114510	Longnose Bulk Sample – Oxide-bearing Peridotite	Rock	X	NA	X	X	X
1802-3769	NA	1	TB19114510	Longnose Bulk Sample – Semi-massive to Massive Oxide	Rock	X	NA	X	X	X
1802-3770	NA	1	TB19114510	Longnose Bulk Sample – Oxide-bearing Dunite/Peridotite	Rock	X	NA	X	X	NA
1802-3771	NA	1	TB19114510	Longnose Bulk Sample – Semi-massive Oxide	Rock	X	NA	X	X	NA
1802-3772	NA	1	TB19114510	Longnose Bulk Sample – Semi-massive Oxide	Rock	X	NA	X	X	NA
1802-3773	NA	1	TB19114510	Longnose Bulk Sample – Semi-massive Oxide	Rock	X	NA	X	X	NA
1802-3774	NA	1	TB19114510	Longnose Bulk Sample – Massive Oxide	Rock	X	NA	X	X	NA
1802-3775	NA	1	TB19114510	Longnose Bulk Sample – Semi-massive Oxide	Rock	X	NA	X	X	NA
1802-3776	NA	1	TB19114510	Longnose Bulk Sample – Semi-massive Oxide	Rock	X	NA	X	X	NA
1802-ILM2	NA	5	TB19241464	Coleraine Ilmenite Low Intensity Magnetic Separator Magnetic Concentrate	Powder	NA	NA	X	NA	NA
1802-RST	NA	5	TB19241464	Coleraine Longnose Bulk Sample Rougher Spiral Tails	Powder	NA	NA	X	NA	NA
Quality Control Samples										
1802-BL13	NA	1	TB19114509	NIST Obsidian Rock 278 STANDARD	Powder	NA	NA	X	NA	NA
1802-BL14	NA	1	TB19114509	Nurserymen's Preferred Play Sand BLANK	Sand	NA	NA	X	NA	NA
1802-BL24	NA	2	TB19150942	Nurserymen's Preferred Play Sand BLANK	Sand	NA	NA	X	NA	NA
1802-BL67	NA	2	TB19150942	NIST Obsidian Rock 278 STANDARD	Powder	NA	NA	X	NA	NA
1802-BL68	NA	3	TB19173773	NIST Obsidian Rock 278 STANDARD	Powder	NA	NA	X	NA	NA
1802-BL69	NA	4	TB19216336	NIST Obsidian Rock 278 STANDARD	Powder	NA	NA	X	NA	NA
1802-BL70	NA	5	TB19241464	NIST Obsidian Rock 278 STANDARD	Powder	NA	NA	X	NA	NA

Prior to polished thin section preparation, all hand samples were briefly described and lithologically classified (Appendix 1). Modal analysis, mineral and rock texture observations, and geological interpretations based on petrographic observations were recorded on standardized data sheets developed at NRRI (Appendix 2).

Lithogeochemical Analysis

Twelve samples of the Longnose OUI bulk sample and 18 hydrometallurgical process samples (including NRRI ilmenite concentrate, NRRI ilmenite LIMS magnetic concentrate, NRRI rougher spiral tails, PRO leach residues, and non-calcined and calcined PRO products) were submitted to ALS Laboratories (Thunder Bay, Ontario) for major and trace element lithogeochemical analysis. Five duplicate samples, two blanks (Nurseryman's Preferred Play Sand; http://www.tccmaterials.com/pdf/NPplaysandmsds.pdf), and five standard samples (NIST Obsidian Rock 278 Standard, https://www-s.nist.gov/srmors/certificates/278.pdf (NIST, 1992)) were included in the analyses for quality control purposes. A list of the samples analyzed can be found in Table 2. ALS Laboratory analytical certificates containing analytical results and analytical detection limits can be found in Appendix 3. Quality Assurance/Quality Control certificates are available upon request.

ALS Laboratory analytical methods employed during this study included:

- Major element oxides reported in percent using ALS Method ICPO6 were performed for SiO_2, Al_2O_3, Fe_2O_3, CaO, MgO, Na_2O, K_2O, Cr_2O_3, TiO_2, MnO, P_2O_5, SrO, and BaO.
- Seven TiO_2, Fe_2O_3, and process residue samples that reported low analytical totals via ALS Method ICP-06 were reanalyzed for major element oxides (percents) via ALS Method ME-XRF06.

- Loss on ignition analyses (LOI) reported in percent were determined using method OA-GRA05. For samples reanalyzed using ALS Method ME-XRF06, LOI was redetermined via ALS Method LOI Sulfur analyses reported in percent were determined using method S-IR08.
- Selected trace elements reported in parts per million were determined via method ME-4ACD81. Trace elements analyzed using this method include Ag, As, Cd, Co, Cu, Li, Mo, Ni, Pb, Sc, Tl, and Zn.
- Selected trace elements reported in parts per million were determined via method ME-MS42. Trace elements analyzed using this method include Ag, As, Be, Bi, Cd, Ce, Co, Cs, Cu, Ga, Hf, Hg, In, La, Li, Mo, Nb, Ni, Pb, Rb, Sb, Sc, Sn, Sr, Ta, Te, Th, Tl, U, W, Y, and Zr.
- Selected trace elements reported in parts per million were determined via method ME-MS81. Trace element analyzed using this method include Ba, Ce, Cr, Cs, Dy, Er, Eu, Ga, Gd, Hf, Ho, La, lu, Nb, Nd, Pr, Rb, Re, Se, Sm, Sn, Sr, Ta, Tb, Th, Tm, U, V, W, Y, Yb, and Zr for ME-XRF06.

Detailed descriptions of these ALS analytical methods can be found at https://www.alsglobal.com/en-us/services-and-products/geochemistry/geochemistry-downloads.

To illustrate relative concentrations of rare earth elements and trace elements, chondrite normalized rare earth element diagrams and primitive mantle normalized spider diagrams have been constructed. Chondrite rare earth element and trace element values used for normalization were obtained from Sun and McDonough (1989). Primitive mantle elemental values used for normalization were obtained from Sun and McDonough (1989) and Kerrich and Wyman (1996). Table 3 contains the rare earth element and trace element normalizing values utilized to construct the chondrite normalized rare earth element diagrams and primitive mantle normalized spider diagrams contained in this study.

Table 3. Rare earth element and trace element normalizing values (Sun and McDonough, 1989; Kerrich and Wyman, 1996).

Element / Component	Chondrite Value[1] (ppm)	Primative Mantle Value[2] (ppm)	Element / Component	Chondrite Value[1] (ppm)	Primative Mantle Value[1] (ppm)	Element / Component	Chondrite Value[1] (ppm)	Primative Mantle Value[1] (ppm)
SiO_2	NA	44.9	Rb	2.32	0.635	Tm	0.0255	0.074
TiO_2	NA	0.217	Sr	7.26	21.1	Yb	0.17	0.493
$Al2O_3$	NA	4.63	Ba	2.41	6.99	Lu	0.0254	0.074
FeO	NA	7.85	Nb	0.246	0.713	Pb	2.47	0.185
MnO	NA	0.13	Zr	3.87	11.2	Th	0.029	0.085
MgO	NA	37.2	Hf	0.1066	0.309	U	0.008	0.021
CaO	NA	3.73	Y	1.57	4.55	Li	1.57	1.6
Na_2O	NA	0.369	La	0.237	0.687	Be	NA	NA
K_2O	NA	0.03	Ce	0.612	1.78	Ga	NA	4
P_2O_5	NA	0.022	Pr	0.095	0.276	As	NA	NA
Sc	NA	17.1	Nd	0.467	1.35	Mo	0.92	0.063
V	NA	82	Sm	0.153	0.444	Ag	NA	0.006
Cr	NA	2940	Eu	0.058	0.168	Cd	NA	NA
Co	NA	110	Gd	0.2055	0.596	Te	NA	NA
Ni	NA	1890	Tb	0.0374	0.108	Ta	0.014	0.041
Cu	NA	30	Dy	0.254	0.737	Tl	0.14	0.005
Zn	NA	56	Ho	0.0566	0.164	Bi	NA	0.002
Cs	0.188	0.032	Er	0.1655	0.48	W	0.095	NA

[1] Values from Sun and McDonough, 1989.

[2] Values from Sun and McDonough, 1989, Kerrich and Wyman, 1996

X-Ray Diffraction Analysis

Eighteen powdered samples including NRRI concentrates (ilmenite concentrate, magnetic fraction of the ilmenite concentrate obtained by low intensity magnetic separation processing), PRO process leach residues, and non-calcined and calcined titanium oxide and iron oxide powders were analyzed for mineralogy using the Bruker D2 Phaser x-ray diffractometer at NRRI's Coleraine facility. Mineral phase identification utilized Bruker AXS – Diffrac.Eva V4.3.1.2 phase identification software, the ICCD-PDF-4+ 2019 powder diffraction database, with Rietveld refinement utilizing Sietronics PTY Ltd – Siroquant V4.0 software. Table 2 contains a list of samples investigated by x-ray diffraction analysis at the NRRI.

Electron Microprobe Analysis

Electron microprobe analysis (EMPA) was carried out utilizing a field emission JOEL JXA-8350FPlus Electron Probe Microanalyzer located at the Electron Microscopy Laboratory (EML) in the Department of Earth Sciences at the University of Minnesota Twin Cities (UMTC). This instrument is equipped with an SXES detector, five automated wave-dispersive spectrometers (WDS), and an energy dispersive spectrometer (EDS) for rapid mineral chemistry analysis. Elemental analysis of mineral phases from polished sections of the Longnose OUI bulk sample and from polished puck samples of the Longnose ilmenite concentrate, PRO leach residues, and titanium oxide and iron oxide products were performed.

Dr. Anette von der Handt (EML-UMTC Lab Manager) performed all analyses with the guidance of a Minnesota Licensed Professional Geologist.

Table 2 contains a list of samples investigated using EMPA at the UMTC Electron Microprobe Lab. Analytical results can be found in Appendix 4. Standards utilized for analysis of silicate minerals include the following: silica (Albite, Taylor); titanium (Ilmenite, NMNH 96189); aluminum (Anorthite, NMNH 137041); vanadium (V-metal, MM); chromium (Chromite, NMNH 117075): iron (Magnetite, NMNH 114887); nickel (Ni-olivine, synthetic Ni_2SiO_4); manganese (Mn-olivine, synthetic, Mn_2SiO_4); magnesium (Chromite, NMNH 117075); calcium (Flourapatite, NMNH 104021); potassium (Orthoclase, Taylor); and chlorine (Tugtupite, CIT-8080 GRR153). Standards used for analysis of oxide minerals include the following: silica (Albite, Taylor); titanium (Ilmenite, NMNH 96189; rutile, Taylor TiO_2); aluminum (Anorthite, NMNH 137041); vanadium (V-metal, MM); chromium (Chromite, NMNH 117075): iron (Ilmenite, MNNH 96189); nickel (Ni-olivine, synthetic Ni_2SiO_4); manganese (Mn-olivine, synthetic, Mn_2SiO_4); magnesium (Chromite, NMNH 117075); and chlorine (Tugtupite, CIT-8080 GRR153) EMPA elemental analyses were converted into weight percent oxides using Probe for EMPA v. 12.8.0 software (available at Probesoft.com). Weight percent oxide values were utilized to calculate mineral stoichiometry. This included utilization of a variety of Microsoft Excel-based spreadsheets available at Gabbrosoft.com, including AMPH15.xls (for amphiboles), ILMNCALC.xls (for ilmenite), MICACALC.xls (for serpentine group and clay minerals), OLICALC.xls (for olivine compositions), SPINCALC.xls (for magnetite), and RUTCALC.xls (for rutile). The spreadsheet AMPHNAMES.xls (Gabbrosoft.com) was utilized for naming amphibole species according to the classification of Leake et al. (1997). Pyroxene mineral stoichiometry was calculated using methodology described by Klein and Hurlbut (1999). Chlorite mineral stoichiometry and classification according to Wiewiora and Wiess (1990) was determined using WinCcac software (Yavuz et al., 2015).

Hydrometallurgical Sampling

Sampling of solid and liquid samples was performed with efforts to obtain the most representative samples possible.

Feed to the circuit was obtained by mixing the drum of material in the slurry form with a pneumatically powered agitator to bring the particles into suspension. A double diaphragm pump was then used to pump the slurry into batches that could then be further processed (i.e. filtered and weighed) for preparation to leach.

Sampling of solid residue and product streams was performed by splitting the sample through a riffle splitter. The material is sub divided with each pass through the riffle splitter, with portions being discarded (set aside) from alternate sides until a portion of suitable size is obtained for analysis.

Solution samples from the various process steps are taken by thoroughly mixing the bulk solution and drawing off an aliquot for analysis. Where samples are divided up in several containers, the containers are sampled separately and combined in equivalent proportion to the bulk to form a composite.

Chemical Analysis

Analysis of samples was performed in house where possible, and confirmatory analysis was performed by accredited third-party laboratories. A description of the analytical techniques performed at PRO is presented in the following section.

Solid Analysis – 3-Acid Digestion

A prepared sample (0.25 g) is digested with nitric, hydrofluoric, and boric acids. The solution is evaporated to dryness and then re-diluted with nitric acid. This solution is quantitatively diluted and processed through the Inductively Coupled Plasma – Optical Emission Spectroscopy (ICP-OES), model Thermo Fisher iCAP 6000 ICP-OES.

While very aggressive, the solubility of some elements can be dependent on the mineral species present, and as such, data reported from the 3-acid digestion should be considered as representing only the leachable portion of a particular analyte. Some elements show poor recovery due to volatilization.

Blanks, sample replicates, and duplicates are routinely used as part of PRO's quality assurance.

Solid Analysis – Peroxide Fusion

A prepared sample (0.25 g) is fused with sodium peroxide and sodium hydroxide in a zirconium crucible heated by a bunsen burner. The resultant melt is dissolved in weak hydrochloric acid and quantitatively diluted with de-ionized water. This solution is through the Inductively Coupled Plasma – Optical Emission Spectroscopy (ICP-OES), model Thermo Fisher iCAP 6000 ICP-OES.

Blanks, sample replicates, and duplicates are routinely used as part of PRO's quality assurance.

Calculation

To determine the effectiveness of the recovery processes, calculation of efficiencies can be defined in several ways. This section explains the various methods used in this study to determine process recoveries.

Leaching Efficiency

Material Balance

The material balance for leach recovery was calculated using the following equation:

$$Leach\ Efficiency_{MB} = \frac{(Solution\ Volume_{PLS} * concentration_{PLS})}{Solution\ Volume_{PLS} * concentration_{PLS} + Residue\ mass * concentration_{Res}}$$

Head/Residue Balance

The Head/Residue Balance is determined as follows:

$$Leach\ Efficiency_{H/R} = \frac{(mass\ residue * concentration_{res})}{inital\ mass * concentration_{init}}$$

Solution/Head Balance

The solution/head balance is determined as follows:

$$Leach\ Efficiency_{S/H} = \frac{(Volume\ Solution\ PLS * concentration_{PLS})}{inital\ mass * concentration_{init}}$$

SX Efficiency

The efficiency of the SX recovery is determined as follows:

$$SX\ Extraction\ Eff = \frac{(Volume\ Solution_{\ Feed} * concentration_{Feed} - Vol\ Solution_{\ raffinate} * Concentration_{raffinate})}{Volume\ Solution_{\ Feed} * concentration_{Feed}}$$

Product Recovery

The determination of product recovery from a process such as precipitation of TiO_2 is determined as follows:

$$Product\ Recovery\ Eff = \frac{(Volume\ Solution_{\ Feed} * concentration_{Feed} - Vol\ Solution_{\ filtrate} * Concentration_{filtrate})}{Volume\ Solution_{\ Feed} * concentration_{Feed}}$$

Longnose Bulk Sample

Petrographic Analysis

Twelve samples from the 1999 Longnose bulk sample were described in hand sample (Appendix 1). The Longnose bulk samples were classified into four lithology types based on the relative proportions of silicate and oxide minerals as observed in hand sample. These included: 1) semi-massive oxide; 2) semi-massive to massive oxide; 3) oxide-bearing peridotite; and 4) oxide-bearing dunite-peridotite.

Polished thin sections made from these samples subsequently underwent transmitted- and reflected-light petrographic analysis at the NRRI. All mineral percentages indicated below represent modal percentages (percent by area). Modal percentages indicated as “rare” or “trace” represent abundances of less than 0.1% and between 0.1% to 0.5%, respectively.

The results of these analyses are shown in Table 4. All samples of the bulk sample varied from medium-grained to coarse-grained.

Table 4. Summary of petrographic analyses performed on randomly selected hand samples of the 1999 Longnose bulk sample. Detailed petrographic descriptions are included in Appendix 2.

Sample No.		1802-3765	1802-3766	1802-3767	1802-3768	1802-3769	1802-3770	1802-3771	1802-3772	1802-3773	1802-3774	1802-3775	1802-3776
Deposit		Longnose	Longnose	Longnose	Longnose	Longnose	Longnose	Longnose	Longnose	Longnose	Longnose	Longnose	Longnose
Sample Description		Longnose 1999 Bulk Sample	Longnose 1999 Bulk Sample	Longnose 1999 Bulk Sample	Longnose 1999 Bulk Sample	Longnose 1999 Bulk Sample	Longnose 1999 Bulk Sample	Longnose 1999 Bulk Sample	Longnose 1999 Bulk Sample	Longnose 1999 Bulk Sample	Longnose 1999 Bulk Sample	Longnose 1999 Bulk Sample	Longnose 1999 Bulk Sample
Chemisty		Yes	Yes	Yes	Yes	Yes	Yes	Yes	Yes	Yes	Yes	Yes	Yes
XRD		Yes	Yes	Yes	Yes	Yes	Yes	Yes	Yes	Yes	Yes	Yes	Yes
Microprobe		Yes	Yes	No	Yes	Yes	No	No	No	No	No	No	No
Rock Type		Semi-Massive Oxide	Semi-Massive Oxide	Semi-Massive Oxide	Oxide-Bearing Peridotite	Semi-Massive to Massive Oxide	Oxide-Bearing Dunite-Peridotite	Semi-Massive Oxide	Semi-Massive Oxide	Semi-Massive Oxide	Semi-Massive Oxide	Semi-Massive Oxide	Semi-Massive Oxide
Textures	Course-Grained(>5mm)	50	50	50	50	50	50	50	50	50	50	50	50
	Medium-Grained (5mm-1mm)	50	50	50	50	50	50	50	50	50	50	50	50
	Fine-Grained (<1mm)	0	0	0	0	0	0	0	0	0	0	0	0
Cumulate Phases		***60***	***20***	***35***	***85***	***20***	***50***	***95***	***70***	***55***	***40***	***65***	***70***
Silicates	Plagioclase	0	0	0	0	0	0	0	0	0	0	0	0
	Olivine	15	2	12	50	8	25	60	40	25	15	18	40
	Clinopyroxene	5	Trace	Trace	5	Trace	Trace	10	3	3	4	25	0
	Orthopyroxene	0	0	0	0	0	0	0	0	0	0	0	0
	Iddingsite	1	0	1	1	Trace	Trace	Trace	Trace	Trace	0	Trace	0
Intercumulate Phases		***40***	***80***	***65***	***15***	***80***	***50***	***5***	***30***	***45***	***60***	***35***	***30***
Silicates	Plagioclase	0	0	0	0	0	0	0	00	0	0	0	0
	Olivine	0	0	0	0	0	0	0	00	0	0	0	0
	Clinopyroxene	0	0	0	0	0	0	0	00	0	0	0	0
	Orthopyroxene	0	0	0	0	0	0	0	00	0	0	0	0
	Biotite	6	1	2	4	1	1	1	11	3	1	2	Rare
	Hornblende	0	0	0	6	Trace	0	10	rare	Trace	3	15	Trace
	Actinolite	Trace	Trace	Trace	Trace	Trace	0	0	0	Trace	0	0	0
	Ferroactinolite	0	0	0	0	0	0	0	0	0	0	0	0
	Tremolite	0	0	0	0.5	Trace	0	0	0	0	0	Rare	0
	Cummingtonite/ Grunerite	0	0	0	Trace	0	Trace	0	0	0	0	0	0
	Anthophyllite	0	0	0	1	0	0	0	0	Trace	0	Trace	12
	Chlorite	3	4	3	3	Trace	4	2	8	8	5	2	16
	Serpentine	25	6	15	10	3	12	8	8	12	8	2	0
	Sericite/ Muscovite	2	Trace	Trace	2	Trace	3	2	2	2	1.5	1	1
	Vermiculite	1	5	0.5	0	0	2	Trace	Trace	Trace	1	0	Trace
	Epidote	0	Trace	Trace	1	0.5	Trace	Trace	Trace	Trace	1	0	0
	Clay Minerals	0	Trace	0	0	Trace	0	0	Trace	Trace	Trace	0	0
Carbonates	Calcite	2	Trace	0	1	0	2	2	2	Trace	0	0	0
Phosphates	Apatite	0	0	0	1	0	0	0	0	0	0	0	28
Oxides	Ilmenite	0	78	60	14	78	45	4.5	25	30	50	20	2
	Magnetite	38	2	5	1	2	4	0.5	4	15	10	14	Rare
	Ulvospinel	2	0	Rare	Rare	Rare	Trace	Rare	Rare	Rare	Rare	Rare	Rare
	Rutile	Rare	0	0	1	1	0	0	Trace	0	Rare	0	0
	Hercynite	0	0	0	0	0	0	Rare	0	0	Rare	Rare	Trace
Sulfides	Chalcopyrite	Rare	0	Trace	Rare	Rare	0.5	0.5	Trace	Trace	Rare	0.5	0
	Pyrrhotite	Rare	0	0	0	0	0	0	0	0	0	Rare	0
	Cubanite	0	0	0	0	0	0	0	0	0	0	Rare	0
	Pentlandite	0	0	0	0	0	Rare	0	Rare	Rare	0	Rare	0
	Bornite	0	0	0	Rare	Rare	0	Rare	Trace	0	0	Trace	0
	Covellite	0	0	0	0	0	Trace	Rare	Trace	0	0	0	0
	Digenite	0	0	0	0	0	0	0	Rare	0	0	0	0
Sulfosalts	Enargite	0	0	0	0	0	0	0	Rare	0	0	0	0
Total Without Trace + Rare		***100.0***	***98.0***	***98.5***	***99.5***	***99.5***	***98.5***	***100.5***	***93.0***	***98.0***	***99.5***	***99.5***	***99.0***
Total With Trace + Rare		***100***	***100***	***100***	***100***	***100***	***100***	***100***	***100***	***100***	***100***	***100***	***100***

Semi-massive oxide comprised 9 of the 12 samples analyzed based on hand-sample-based classification. Interpretations of textures indicates that original "cumulate" phases in this unit varied from 20% to 95%. Many of these phases appear to have undergone varying degrees of alteration, which decreased the modal abundance of the original "cumulate" phases. At present, these "cumulate" phases include olivine (2%–60%), clinopyroxene (trace–24%), and iddingsite (an alteration product of olivine, 0–1 modal percent). "Intercumulus" phases include silicate minerals that originally formed in the interstices of the "cumulate" phases and include alteration phases of the "cumulate" phases. These comprise 5%–80% modal abundances of the rocks evaluated and include biotite (1%–6%), hornblende (rare to 15%), actinolite (trace), tremolite (rare), anthophyllite (trace), chlorite (2%–12%), serpentine (2%–25%), sericite/muscovite (0%–2%), vermiculite (0%–5%), epidote (0%–1%), and clay minerals (trace). Carbonate minerals were identified in four of the nine samples in abundances ranging from trace to 2%. Oxide minerals occurred in all nine samples of this lithology and included ilmenite (0%–78%) and magnetite (1%–38%). Rutile (0%–1%) was observed in three samples and rare hercynite was observed in two samples from this unit. Sulfide minerals identified petrographically include chalcopyrite (rare to 0.5% in eight samples), pyrrhotite (rare in two samples), cubanite (rare in one sample), pentlandite (rare in three samples), bornite (rate to trace in three samples), covellite (rare to trace in two samples), and digenite (rare in one sample).

One sample (1802-3769) was classified as Semi-Massive to Massive Oxide based on hand sample observation. "Cumulate" phases comprise 20% of this sample and include olivine (8%) and clinopyroxene and iddingsite (both in trace abundances). Intercumulus phases make up 80% of the sample and comprise biotite (1.5%), serpentine (3%), vermiculite (5%), and epidote (0.5%). Intercumulus phases occurring in trace abundances include hornblende, actinolite, tremolite, chlorite, sericite/muscovite, and clay minerals. Oxide phases present include ilmenite (78%), magnetite (2%), and rare ulvospinel. No sulfide phases were identified in this sample.

Based on hand sample observation, one sample (1802-3770) was classified as Oxide-Bearing Dunite/Peridotite. "Cumulate" phases originally comprised 50% of this sample and now comprise olivine (50%), clinopyroxene (trace), and iddingsite (trace). "Intercumulate" phases identified include biotite (1%), chlorite (4%), serpentine (12%), sericite/muscovite (3%), and vermiculite (2%). "Intercumulate" phases occurring in trace abundances include cummingtonite/grunerite and epidote. Calcite made up two percent of the sample. Oxide phases identified include ilmenite (45%), magnetite (4%), and ulvospinel (trace). Sulfide phases observed include chalcopyrite (0.5%), trace abundances of covellite, and rare pentlandite.

One sample (1802-3768) was classified as Oxide-Bearing Peridotite based on hand sample observation. "Cumulate" phases originally comprised 85% of this sample and now include olivine (50%), clinopyroxene (5%), and iddingsite (1%). "Intercumulate" phases identified petrographically include biotite (4%), hornblende (6%), tremolite (0.5%), anthophyllite (1%), chlorite (3%), serpentine (10%), sericite/muscovite (2%), and epidote (0.5%). "Intercumulate" phases occurring in trace abundances include actinolite and cummingtonite/grunerite. Calcite comprised one percent of the sample. Oxide phases present include ilmenite (14%), magnetite (1%), and rare ulvospinel and rutile. Sulfide phases occur in rare abundances and include chalcopyrite and bornite.

Mineral Chemical Analysis (Electron Microprobe Analysis)

Four hand samples obtained from the Longnose bulk sample underwent mineral chemistry analysis utilizing the Electron Probe Microanalyzer located at the EML in the Department of Earth Sciences at the UMTC. These include samples 1802-3765 (semi-massive oxide), 1802-3766 (semi-massive oxide), 1802-3768 (oxide-bearing peridotite), and 1802-3769 (semi-massive to massive oxide). Electron microprobe backscatter images of these samples are found in Figures 7—9.

Oxide mineral phases identified within the four bulk samples include ilmenite (Table 5; Appendix 4: Table A4-1) and magnetite (Table 6; Appendix 4: Table A4-2). Ilmenite has a general chemical formula of $FeTiO_3$ but can be more representatively expressed as (Fe, Mg, Mn)TiO_3, as substitutions of Mg^{2+} and Mn^{2+} for Fe^{2+} are common (Deer et al., 1992). As well, the majority of natural ilmenites can contain up to 5%–6% Fe^{3+} (as Fe_2O_3) within their crystal structures (Deer et al., 1992; Klein and Hurlbut, 1999). Trace amounts of V^{3+}, Al^{3+}, and Cr^{3+} may also be present and are believed to substitute for Fe^{3+} in the mineral structure.

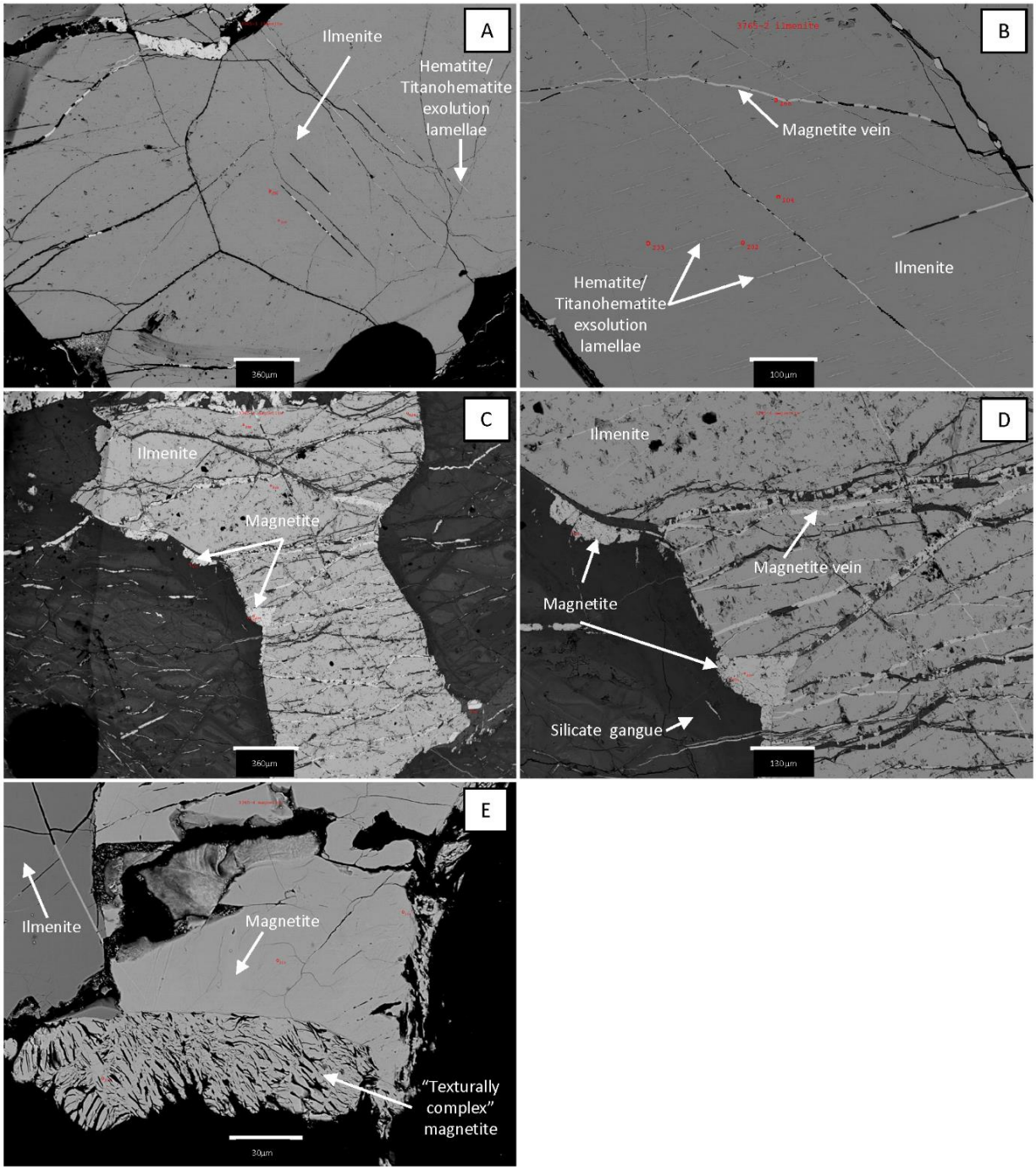

Figure 7. Electron microprobe backscatter images of sample 1802-3765 (Longnose bulk sample semi-massive oxide). A) Annealed ilmenite with <1–5 µm wide magnetite veins and ~1–3 µm exsolution lamellae believed to be hematite/titanohematite. Scale bar is 360 µm. B) Close-up of massive ilmenite with ~1–4 µm wide exsolution lamellae believed to be hematite/titanohematite. Scale bar is 100 µm. C) Mottled ilmenite grain with local magnetite along its grain boundary. Scale bar is 360 µm. D) Close-up of magnetite along the ilmenite grain boundary in Figure 7C. Scale bar is 130 µm. E) Massive magnetite with texturally complex magnetite. Scale bar is 30 µm. Red numbers and circles in images are analysis locations.

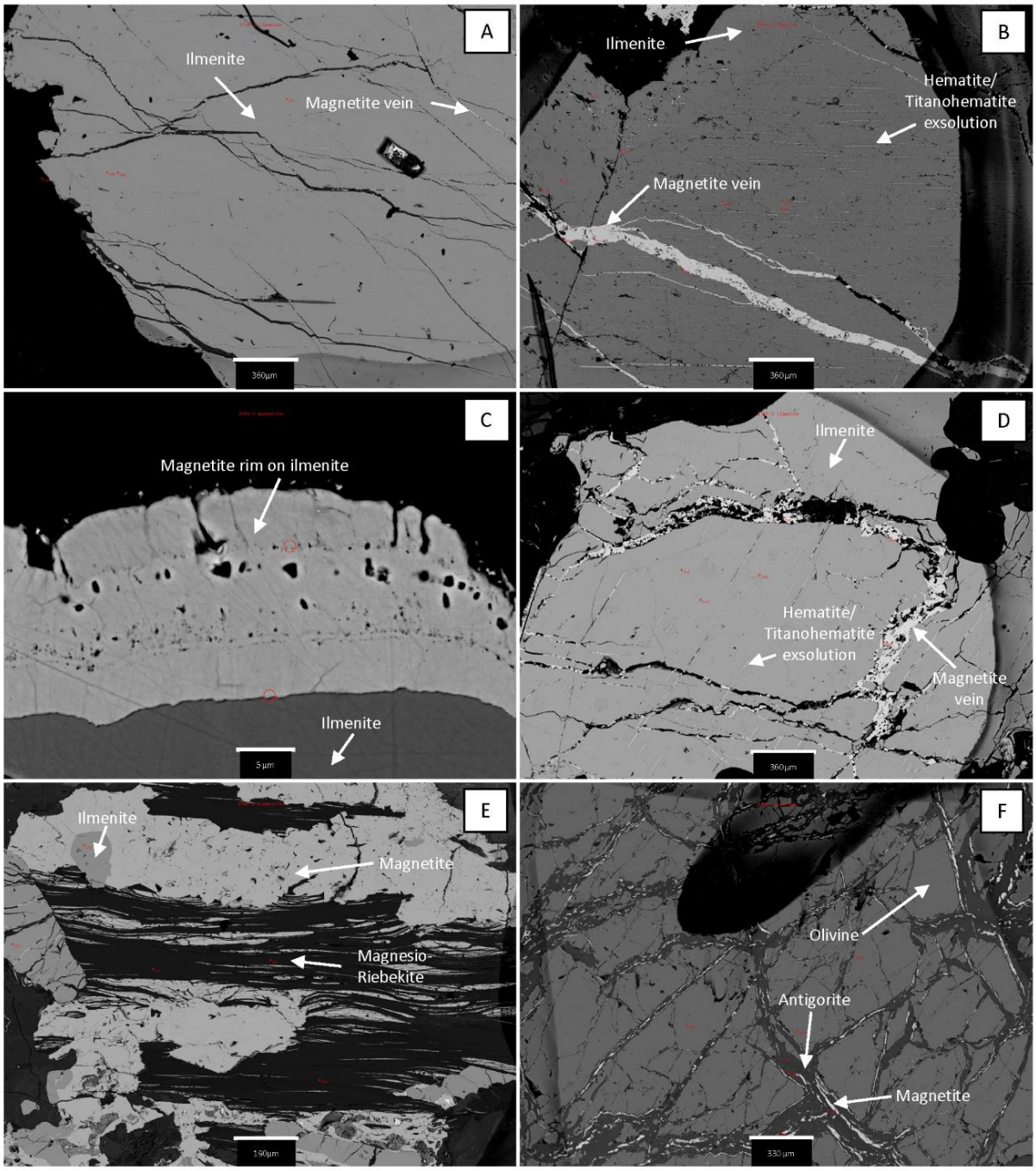

Figure 8. Electron microprobe backscatter images of samples 1802-3766 (semi-massive oxide) and 1802-3768 (oxide-bearing peridotite) obtained from the Longnose bulk sample. A) Inclusion-free massive ilmenite from sample 1802-3766. Scale bar is 360 µm. B) Massive ilmenite from sample 1802-3766 that is cross-cut by a 10–60 µm wide magnetite vein and contains ~1–4 µm exsolution lamellae (believed to be hematite/titanohematite). Scale bar is 360 µm. C) Close-up of zoned magnetite rim (light colored) on ilmenite grain (dark colored) from sample 1802-3766. Scale bar is 5 µm. D) Massive ilmenite grain with exsolution lamellae (hematite/titanohematite?) and cross-cutting magnetite veins, sample 1802-3768. Scale bar is 360 µm. E) Ilmenite (dark colored), magnetite (light colored) and amphiboles (tremolite, magnesio-reibeckite) from sample 1802-3768. Scale bar is 190 µm. F) Olivine grain cross-cut by veins of serpentine (antigorite) locally with local magnetite veins from sample 1802-3768. Scale bar is 330 µm. Red numbers and circles in images are analysis locations.

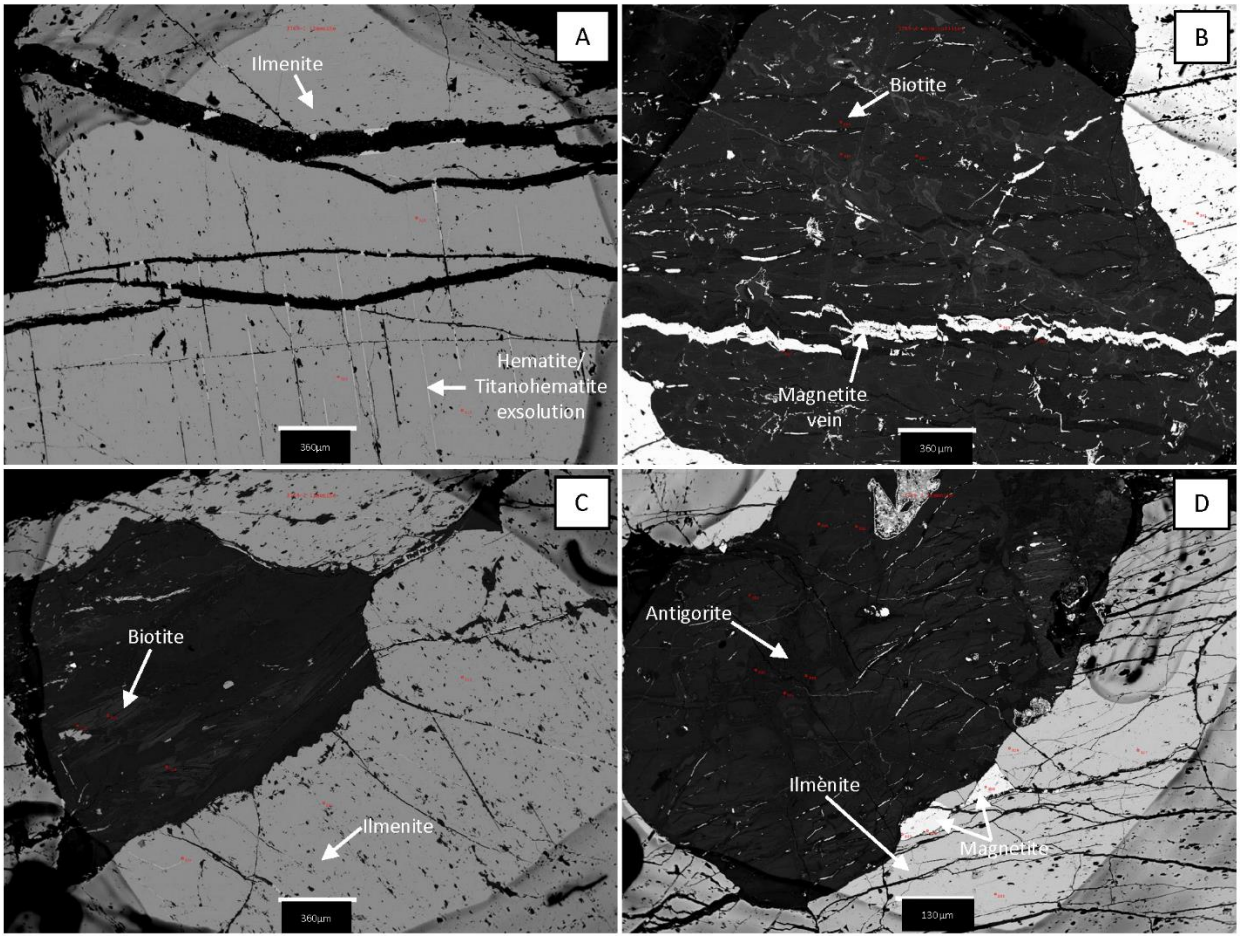

Figure 9. Electron microprobe backscatter images of sample 1802-3769 (Longnose bulk sample semi-massive to massive oxide). A) Massive ilmenite exsolution lamellae believed to be hematite/ titanohematite. Scale bar is 360 µm. B) Biotite with cross-cutting magnetite veins adjacent to magnetite grains. Scale bar is 360 µm. C) Ilmenite with local exsolution lamellae (hematite/titanohematite?) and biotite. Scale bar is 360 µm. D) Ilmenite (medium gray), magnetite (light gray), and serpentine (antigorite). Scale bar is 130 µm. Red numbers and circles in images are analysis locations.

Ilmenite occurs in a wide variety of textures, including massive ilmenite, inclusion-poor ilmenite, inclusion-bearing ilmenite, and ilmenites with inclusion-poor fresh cores and rims. Ilmenite compositions were dominated by titanium- and iron-oxides, which ranged from 48.602% to 50.944% (average 49.699%) TiO_2 and 43.785% to 46.911% (average 45.353%) FeO, respectively. MgO ranged from 1.965% to 3.968% (average 3.165%), MnO varied from 0.342% to 0.627% (average 0.420%), V_2O_3 ranged from 0.203% to 0.428% (average 0.334%), Cr_2O_3 varied from 0.015% to 0.129% (average 0.075%), and NiO ranged from 0.000% to 0.117% (average 0.037%). Exsolution lamellae, presumably composed of hematite/titanohematite, occur in <1 µm–5 µm discontinuous straight parallel lines along a preferred crystallographic orientation, perhaps parallel to (0001) as identified in the Allard Lake hemo-ilmenite ores (McEnroe et al., 2007).

Table 5. Electron microprobe analyses of bulk sample ilmenites. Values are in weight percent.

Electron Microprobe Analysis – Bulk Sample Ilmenites (n = 50)													
Sample	Description	Phase	SiO_2	TiO_2	Al_2O_3	FeO	MnO	MgO	V_2O_3	Cr_2O_3	NiO	Cl	Total
3765-2-6-202-1	Massive	Ilmenite	0.000	48.704	0.024	45.940	0.405	3.179	0.383	0.094	0.028	0.000	98.758
3765-2-6-203-2	Massive	Ilmenite	0.000	49.161	0.037	45.622	0.396	3.166	0.365	0.092	0.070	0.000	98.910
3765-2-6-204-3	Massive	Ilmenite	0.017	49.060	0.061	45.532	0.382	3.186	0.376	0.119	0.039	0.000	98.772
3765-3i-8-207-1	Inclusion – Hematite?	Ilmenite	0.009	50.077	0.014	45.222	0.442	3.163	0.321	0.070	0.019	0.000	99.337
3765-3-8-208-1	No Inclusions	Ilmenite	0.000	49.802	0.070	45.347	0.394	3.114	0.308	0.107	0.056	0.000	99.198
3765-3ii-10-209-1	Inclusion-Hematite?	Ilmenite	0.005	48.602	0.041	44.481	0.390	3.276	0.315	0.103	0.000	0.067	97.281
3765-4-11-210-1	No Inclusions	Ilmenite	0.003	49.340	0.074	46.828	0.525	2.238	0.338	0.083	0.013	0.000	99.441
3765-4-11-211-2	No Inclusions	Ilmenite	0.000	49.413	0.056	46.611	0.523	2.238	0.322	0.115	0.042	0.000	99.319
3765-6-18-221-1	Fresh	Ilmenite	0.000	49.386	0.019	45.471	0.418	3.036	0.338	0.129	0.041	0.000	98.838
3765-6-18-222-2	Fresh	Ilmenite	0.003	49.858	0.032	45.502	0.425	3.091	0.296	0.084	0.020	0.000	99.311
3765-6-18-223-3	Fresh – Rim	Ilmenite	0.000	49.940	0.038	45.397	0.443	3.056	0.320	0.093	0.055	0.000	99.343
3765-5-28-232-1	Inclusions	Ilmenite	0.024	49.583	0.031	45.355	0.414	3.047	0.319	0.103	0.006	0.000	99.882
3765-5-28-234-3	Inclusions	Ilmenite	0.000	50.008	0.033	45.012	0.472	3.052	0.317	0.095	0.065	0.000	99.053
3766-1-29-235-1	Massive	Ilmenite	0.000	49.632	0.054	44.720	0.351	3.827	0.347	0.030	0.013	0.000	98.975
3766-1-29-236-2	Massive	Ilmenite	0.008	49.814	0.048	44.695	0.357	3.854	0.352	0.114	0.022	0.000	99.264
3766-1-29-237-3	Massive	Ilmenite	0.012	49.839	0.041	44.363	0.383	3.886	0.408	0.075	0.065	0.000	99.072
3766-1-29-238-4	Rim	Ilmenite	0.002	49.883	0.063	44.557	0.395	3.753	0.380	0.088	0.017	0.000	99.137
3766-3-36-267-1	Massive	Ilmenite	0.000	49.312	0.050	44.328	0.410	3.930	0.428	0.104	0.008	0.000	98.571
3766-3-36-268-2	Massive	Ilmenite	0.000	49.628	0.044	44.357	0.376	3.958	0.377	0.029	0.049	0.000	98.817

Table 5 (continued).

Electron Microprobe Analysis – Bulk Sample Ilmenites (n = 50; continued)													
Sample	Description	Phase	SiO_2	TiO_2	Al_2O_3	FeO	MnO	MgO	V_2O_3	Cr_2O_3	NiO	Cl	Total
3766-3-36-269-3	Inclusion-Hematite?	Ilmenite	0.000	49.756	0.275	43.997	0.372	3.968	0.393	0.081	0.028	0.000	98.872
3766-3I-38-273-1	Massive	Ilmenite	0.000	49.996	0.046	44.244	0.371	3.885	0.405	0.092	0.117	0.000	99.157
3766-3I-38-274-2	Massive	Ilmenite	0.000	50.425	0.057	44.656	0.357	3.909	0.348	0.063	0.069	0.000	99.883
3766-3I-38-275-3	Massive	Ilmenite	0.000	50.163	0.030	46.042	0.408	2.369	0.299	0.050	0.023	0.000	99.384
3766-4-42-282-1	Massive	Ilmenite	0.000	49.830	0.025	44.700	0.375	3.765	0.324	0.071	0.037	0.000	99.127
3766-4-42-283-2	Massive	Ilmenite	0.008	50.177	0.042	44.756	0.389	3.523	0.284	0.072	0.055	0.000	99.306
3766-4-42-284-3	Massive	Ilmenite	0.000	50.593	0.043	44.890	0.398	2.899	0.203	0.054	0.052	0.000	99.132
3768-3-46-294-1	Massive	Ilmenite	0.000	49.345	0.043	44.678	0.579	1.981	0.336	0.105	0.055	0.000	99.123
3768-3-46-295-2	Massive	Ilmenite	0.021	49.649	0.037	46.911	0.604	1.978	0.335	0.069	0.051	0.000	99.655
3768-3-46-296-3	Massive	Ilmenite	0.008	49.632	0.011	46.595	0.627	1.965	0.298	0.089	0.051	0.000	99.277
3768-5-51-309-1	Massive	Ilmenite	0.000	49.014	0.028	46.343	0.398	2.758	0.338	0.086	0.035	0.000	98.999
3768-5-51-310-2	Massive	Ilmenite	0.037	49.170	0.058	46.380	0.357	2.779	0.361	0.125	0.057	0.000	99.326
3768-5-51-311-3	Massive	Ilmenite	0.018	49.117	0.022	46.129	0.408	2.753	0.383	0.048	0.056	0.000	98.934
3768-6-53-315-1	Massive	Ilmenite	0.000	49.563	0.023	45.988	0.408	2.929	0.312	0.032	0.001	0.000	99.256
3768-6-53-316-2	Massive	Ilmenite	0.001	49.986	0.033	45.755	0.473	2.916	0.342	0.023	0.048	0.000	98.578
3768-6-53-317-3	Massive	Ilmenite	0.000	49.513	0.056	45.575	0.391	2.993	0.360	0.082	0.039	0.000	99.009
3769-1-54-318-1	Massive	Ilmenite	0.002	50.580	0.050	44.394	0.398	3.756	0.280	0.051	0.000	0.000	99.511
3769-1-54-319-2	Massive	Ilmenite	0.012	49.719	0.049	44.778	0.420	3.668	0.352	0.074	0.016	0.000	99.087
3769-1-54-320-3	Massive	Ilmenite	0.000	50.944	0.039	43.785	0.410	3.790	0.330	0.015	0.044	0.006	99.365

Table 5 (continued).

Electron Microprobe Analysis – Bulk Sample Ilmenites (n = 50; continued)													
Sample	Description	Phase	SiO_2	TiO_2	Al_2O_3	FeO	MnO	MgO	V_2O_3	Cr_2O_3	NiO	Cl	Total
3769-2-55-321-1	Massive	Ilmenite	0.000	49.973	0.030	45.118	0.388	3.283	0.281	0.048	0.051	0.000	99.172
3769-2-55-322-2	Massive	Ilmenite	0.088	50.289	0.024	45.260	0.390	3.267	0.293	0.039	0.053	0.000	99.704
3769-2-55-323-3	Massive	Ilmenite	0.107	49.702	0.020	45.280	0.424	3.330	0.323	0.045	0.004	0.000	99.235
3769-3-57-327-1	Massive	Ilmenite	0.000	49.352	0.031	45.866	0.424	2.754	0.333	0.065	0.015	0.000	98.839
3769-3-57-328-2	Massive	Ilmenite	0.025	48.803	0.549	45.970	0.433	3.228	0.209	0.059	0.038	0.000	99.314
3769-3-57-329-3	Massive	Ilmenite	0.000	50.720	0.029	44.911	0.461	2.899	0.224	0.027	0.047	0.000	99.318
3769-4-61-339-1	Massive	Ilmenite	0.000	49.267	0.025	46.347	0.466	2.706	0.344	0.113	0.029	0.000	99.297
3769-4-61-340-2	Massive	Ilmenite	0.000	49.640	0.061	45.709	0.397	3.009	0.324	0.053	0.013	0.000	99.205
3769-4-61-341-3	Massive	Ilmenite	0.000	49.446	0.040	46.117	0.463	2.761	0.315	0.074	0.062	0.000	99.278
3769-5-64-348-1	Massive	Ilmenite	0.000	49.967	0.042	44.836	0.365	3.480	0.361	0.042	0.049	0.000	99.142
3769-5-64-349-2	Massive	Ilmenite	0.005	49.804	0.077	45.170	0.342	3.473	0.383	0.069	0.050	0.000	99.371
3769-5-64-350-3	Massive	Ilmenite	0.016	49.774	0.054	45.140	0.387	3.438	0.403	0.101	0.000	0.000	99.312
		Minimum	***0.000***	***48.602***	***0.011***	***43.785***	***0.342***	***1.965***	***0.203***	***0.015***	***0.000***	***0.000***	***98.281***
		Maximum	***0.107***	***50.944***	***0.549***	***46.911***	***0.627***	***3.968***	***0.428***	***0.129***	***0.117***	***0.067***	***99.883***
		Average	***0.009***	***49.699***	***0.056***	***45.353***	***0.420***	***3.165***	***0.334***	***0.075***	***0.037***	***0.001***	***99.149***
		Median	***0.000***	***49.710***	***0.041***	***45.314***	***0.402***	***3.165***	***0.336***	***0.074***	***0.040***	***0.000***	***99.202***
		St.Deviation	***0.020***	***0.491***	***0.079***	***0.778***	***0.061***	***0.539***	***0.046***	***0.029***	***0.023***	***0.009***	***0.368***

Figure 10 illustrates the chemical compositions of various textures of ilmenite from the Longnose bulk sample in terms of weight percent (FeO, TiO_2, MgO, and V_2O_3) and mol percent (Fe^{2+}, Ti^{4+}, and Fe^{3+}). Figures 10A and 10B illustrate the compositions of various textures of ilmenites from the Longnose bulk sample in terms of FeO, TiO_2, and MgO. Ilmenite compositions plot to the right of the FeO-TiO_2 compositional boundary as a result of the presence of magnesium in the ilmenite structure (Fig. 10A). Figure 10B, in which five times the ilmenite MgO contents are plotted relative to FeO and TiO_2, illustrates compositional differences between the various textures of ilmenite in terms of MgO contents. It appears that massive textured and inclusion-poor ilmenites contain slightly less MgO than inclusion-bearing ilmenites. Figures 10C and 10D show ilmenite compositions in terms of FeO, TiO_2, and V_2O_3. These plots illustrate the relatively low vanadium contents of the ilmenites from the Longnose bulk sample. Figure 10E illustrates the ilmenite compositions from the Longnose bulk sample in terms of molar Fe^{2+}, Ti^{4+}, and Fe^{3+} based on stoichiometric calculations of electron microprobe analyses utilizing ILMNCALC software (Gabbrosoft.com). Ilmenite compositions consistently plot to the right of the Fe^{2+} - Ti^{4+} compositional boundary and above the titanohematite solid solution line. This results from the presence of Mg^{2+} substituting for Fe^{2+} in the ilmenite structure (Deer et al., 1992; Klein and Hurlbut, 1999) and the presence of Fe^{3+} within the crystal structure.

Magnetite has a general chemical formula Fe_3O_4, which can be more correctly written as $Fe^{2+}(Fe^{3+})_2O_4$. Structurally, magnetite has an inverse spinel structure, and structurally the chemical formula may be written as $Fe^{3+}(Fe^{2+}, Fe^{3+})O_4$ (Klein and Hurlbut, 1999). Substitution of small amounts of Al^{3+}, Cr^{3+}, and V^{3+} can substitute for Fe^{3+}, and Ca^{2+}, Mn^{2+}, Mg^{2+}, Ni^{2+}, Co^{2+}, and Zn^{2+} can replace Fe^{2+} within the crystalline structure (Deer et al., 1992; Klein and Hurlbut, 1999). As well, a considerable amount of Ti^{4+} can substitute for Fe^{3+} within the magnetite crystalline structure such that a solid solution exists between magnetite and ulvöspinel (Fe_2TiO_4). Such titanium-bearing magnetites plot along a solid solution line between magnetite and ulvöspinel (the ulvöspinel – magnetite series) and are known as titanomagnetite.

Magnetite occurs in a variety of textures when observed using the electron microprobe (Figs. 7–9). These included massive magnetite, euhedral magnetite, massive magnetite rims along the margin of ilmenite grains, colloform, inclusion-rich magnetite rims, a complex “platy”-textured magnetite, and cross-cutting magnetite veins.

Thirty-five electron microprobe analyses of magnetites from the Longnose bulk sample are contained in Table 6. Magnetite compositions were dominated by iron-oxide, which ranged from 83.197% to 93.491% (average 89.979%) FeO, respectively. Titanium dioxide (TiO_2) contents ranged from 0.000% to 3.375% (average 0.937%), indicating the presence of titanomagnetites. MgO ranged from 0.001% to 2.491% (average 0.241%), MnO varied from 0.000% to 1.594% (average 0.196%), V_2O_3 ranged from 0.001% to 2.491% (average 0.604%), Cr_2O_3 varied from 0.000% to 2.593% (average 0.516%), and NiO ranged from 0.000% to 0.234% (average 0.056%). Minor SiO_2 (ranging from 0.000% to 2.244%, average 0.474%) and Al_2O_3 (ranging from 0.000% to 1.977%, average 0.276%) were also identified.

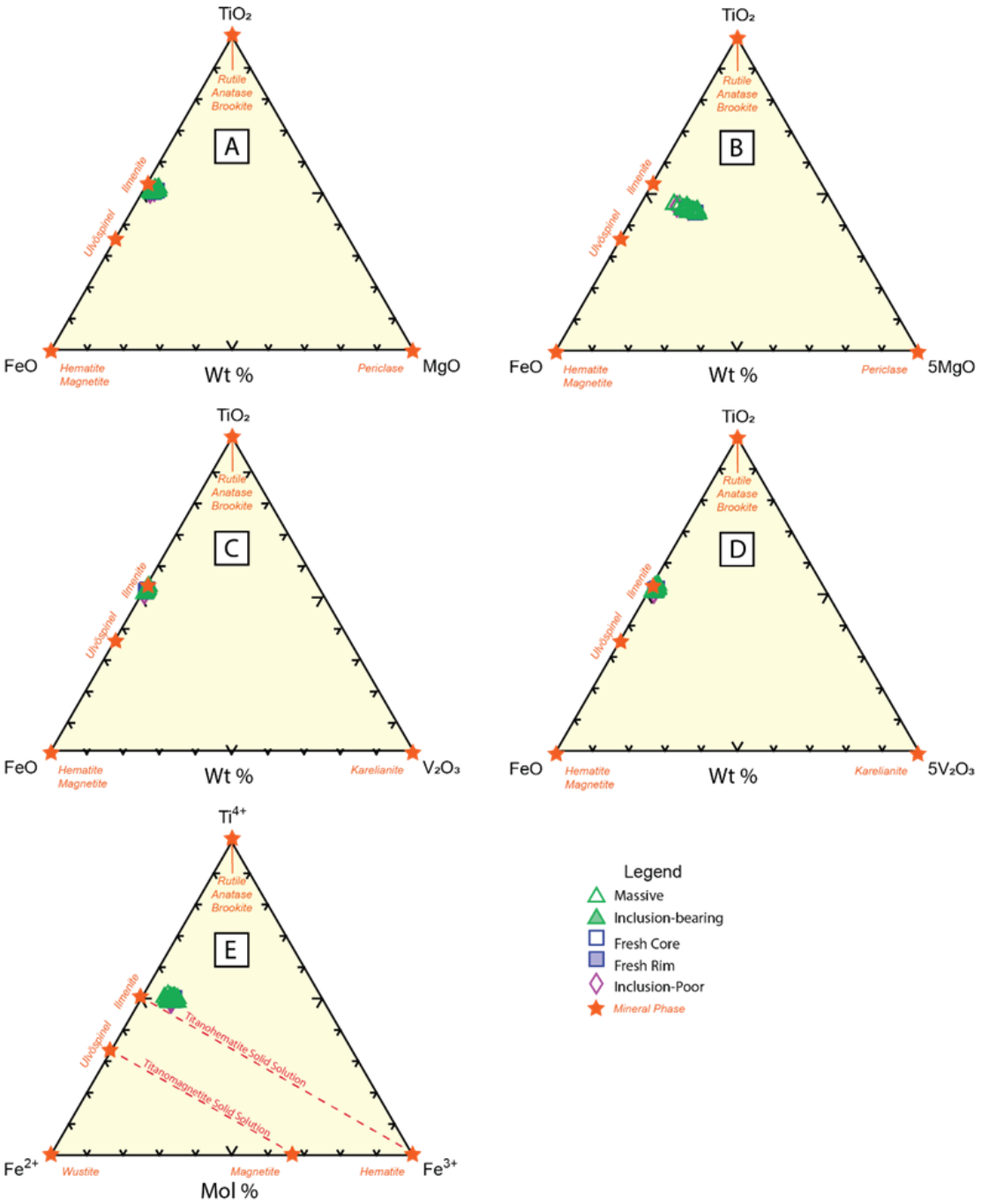

Figure 10. Ternary diagrams illustrating the chemical compositions of ilmenites from the Longnose bulk sample. A) FeO-TiO_2-MgO ternary diagram. Note that ilmenite composition plot off the FeO-TiO_2 compositional boundary in the direction of MgO. B) FeO-TiO_2-5MgO ternary diagram that emphasizes the magnesium contents of the Longnose bulk sample ilmenite composition. C) FeO-TiO_2-V_2O_3 ternary diagram. Note that ilmenite compositions plot very close to the FeO-TiO_2 compositional boundary. D) FeO-TiO_2-5V_2O_3 ternary diagram that emphasizes the relatively low concentration of V_2O_3 in the Longnose bulk sample ilmenites. E) Fe^{2+}-Ti^{4+}-Fe^{3+} ternary diagram (modified after Klein and Hurlbut, 1999; Meinhold, 2010) based on stoichiometric calculations of ilmenite compositions utilizing ILMNCALC (Gabbrosoft.com). Note that Longnose bulk sample ilmenites plot above the titanohematite solid solution line that results from substitution of Mg^{2+} for Fe^{2+} in the ilmenite structure. Wt % is weight percent, Mol % is molar percent.

Table 6. Electron microprobe analyses of bulk sample ilmenites. Values are in weight percent.

Electron Microprobe Analysis – Bulk Sample Magnetite (n = 35)													
Sample	Description	Phase	SiO_2	TiO_2	Al_2O_3	FeO	MnO	MgO	V_2O_3	Cr_2O_3	NiO	Cl	Total
3765-2-7-205-1	Magnetite-Vein	Magnetite	0.296	2.621	0.033	91.219	0.105	0.064	0.054	0.000	0.000	0.007	94.399
3765-2-7-206-2	Magnetite-Vein	Magnetite	0.288	1.164	0.000	90.440	0.830	0.382	0.040	0.007	0.012	0.000	93.164
3765-4-12-212-1	Magnetite-Massive	Magnetite	0.013	2.099	0.441	86.017	0.063	0.380	2.415	2.423	0.078	0.000	93.929
3765-4-13-213-1	Magnetite-Massive	Magnetite	0.023	3.375	1.059	83.197	0.112	0.607	2.480	2.412	0.200	0.035	93.501
3765-4-13-214-2	Magnetite-Rim	Magnetite	0.026	1.388	0.050	85.545	0.056	0.320	2.213	2.593	0.108	0.019	92.317
3765-4-13-215-3	Magnetite-Textured	Magnetite	0.177	0.196	0.023	93.491	0.000	0.007	0.033	0.019	0.004	0.037	93.988
3765-6-19-224-1	Magnetite-Massive	Magnetite	0.000	2.566	1.977	83.432	0.116	0.659	2.491	2.421	0.161	0.000	93.822
3765-6-21-225-1	Magnetite-Textured	Magnetite	0.006	0.098	0.032	93.210	0.000	0.015	0.069	0.049	0.000	0.000	93.478
3765-6-21-226-2	Magnetite-Textured	Magnetite	0.416	0.038	0.091	92.445	0.019	0.035	0.012	0.000	0.025	0.000	93.080
3765-6-22-227-1	Magnetite-Massive	Magnetite	0.059	2.029	0.491	87.369	0.065	0.302	1.665	1.290	0.120	0.022	93.411
3766-1-30-239-1	Magnetite-Massive	Magnetite	0.624	0.002	0.046	91.519	0.274	0.189	0.004	0.000	0.000	0.000	92.658
3766-1-30-240-2	Magnetite-Massive	Magnetite	0.452	0.044	0.037	92.429	0.137	0.309	0.001	0.000	0.047	0.000	93.457
3766-1-30-241-3	Magnetite-Textured	Magnetite	0.127	0.020	0.020	92.980	0.000	0.013	0.011	0.000	0.000	0.000	93.171
3766-3-37-270-1	Magnetite-Vein	Magnetite	0.173	0.176	0.015	91.551	0.513	0.261	0.019	0.000	0.000	0.031	92.738
3766-3-37-271-2	Magnetite-Vein	Magnetite	0.125	0.097	0.000	91.421	0.526	0.255	0.010	0.000	0.004	0.025	92.464
3766-3-37-222-3	Magnetite-Vein	Magnetite	0.179	0.153	0.023	90.727	1.594	0.237	0.013	0.000	0.000	0.024	92.950
3766-4-40-277-	Magnetite-Massive	Magnetite	1.416	0.010	0.044	91.743	0.000	0.021	0.011	0.000	0.008	0.000	93.252
3766-4-40-278-2	Magnetite-Massive	Magnetite	1.066	0.007	0.000	92.612	0.012	0.022	0.005	0.006	0.000	0.014	93.744
3766-4-40-279-3	Magnetite-Massive	Magnetite	0.036	3.208	1.004	84.522	0.131	0.481	2.489	1.742	0.234	0.012	93.857

Table 6 (continued).

Electron Microprobe Analysis – Bulk Sample Magnetite (n = 35; continued)													
Sample	Description	Phase	SiO_2	TiO_2	Al_2O_3	FeO	MnO	MgO	V_2O_3	Cr_2O_3	NiO	Cl	Total
3766-4-41-280-1	Magnetite-Colloform	Magnetite	0.460	2.543	0.000	90.511	0.091	0.101	0.014	0.111	0.000	0.003	93.733
3766-4-41-281-2	Magnetite-Colloform	Magnetite	1.784	0.405	0.006	89.376	0.057	0.136	0.025	0.000	0.006	0.028	91.823
3768-1-43-285-1	Magnetite-Euhedral	Magnetite	0.181	0.457	0.030	92.401	0.047	0.202	0.088	0.038	0.142	0.004	93.589
3768-1-43-286-2	Magnetite-Euhedral	Magnetite	0.011	0.434	0.030	92.046	0.006	0.186	0.080	0.038	0.031	0.000	92.862
3768-1-43-287-3	Magnetite-Euhedral	Magnetite	0.103	0.433	0.036	91.832	0.065	0.182	0.065	0.036	0.126	0.000	92.878
3768-4-50-306-1	Magnetite-Vein	Magnetite	2.244	0.006	0.000	90.392	0.057	0.059	0.006	0.041	0.010	0.036	92.850
3768-4-50-308-3	Magnetite-Vein	Magnetite	1.679	0.001	0.000	91.482	0.079	0.072	0.010	0.017	0.000	0.000	93.340
3768-5-52-312-1	Magnetite-Vein	Magnetite	0.463	0.239	0.000	91.527	0.399	0.232	0.021	0.018	0.025	0.000	92.923
3768-5-52-313-2	Magnetite-Vein	Magnetite	0.826	0.579	0.000	91.330	0.275	0.304	0.020	0.016	0.010	0.041	93.401
3768-5-52-314-3	Magnetite-Vein	Magnetite	0.010	0.968	0.006	92.598	0.026	0.053	0.035	0.000	0.000	0.016	93.712
3769-3-60-336-1	Magnetite-Massive	Magnetite	0.003	2.671	1.944	84.944	0.113	0.652	2.312	1.653	0.175	0.029	94.496
3769-3-60-337-2	Magnetite-Massive	Magnetite	0.026	2.267	0.701	85.888	0.069	0.518	2.036	1.535	0.176	0.001	93.243
3769-3-60-338-3	Magnetite-Massive	Magnetite	0.199	2.510	1.533	84.798	0.100	0.587	2.366	1.635	0.169	0.000	93.897
3769-4-62-342-1	Magnetite-Vein	Magnetite	0.637	0.000	0.003	91.652	0.163	0.164	0.002	0.011	0.045	0.034	92.711
3769-4-62-343-2	Magnetite-Vein	Magnetite	1.786	0.003	0.000	90.848	0.560	0.221	0.015	0.012	0.031	0.022	93.498
3769-4-62-344-3	Magnetite-Vein	Magnetite	0.665	0.000	0.000	91.787	0.165	0.192	0.009	0.019	0.000	0.000	92.837
		Minimum	***0.000***	***0.000***	***0.000***	***83.197***	***0.000***	***0.007***	***0.001***	***0.000***	***0.000***	***0.000***	***91.823***
		Maximum	***2.244***	***3.375***	***1.977***	***93.491***	***1.594***	***0.659***	***2.491***	***2.593***	***0.234***	***0.041***	***94.496***
		Average	***0.474***	***0.937***	***0.276***	***89.979***	***0.196***	***0.241***	***0.604***	***0.516***	***0.056***	***0.013***	***93.291***
		Median	***0.181***	***0.405***	***0.030***	***91.421***	***0.096***	***0.202***	***0.025***	***0.017***	***0.012***	***0.004***	***93.340***
		St.Deviation	***0.601***	***1.114***	***0.546***	***3.059***	***0.305***	***0.190***	***0.992***	***0.885***	***0.071***	***0.010***	***0.568***

Figures 11 and 12 illustrate the chemical compositions of various textures of magnetite from the Longnose bulk sample in terms of weight percent (FeO, TiO_2, MgO, and V_2O_3) and mol percent (Fe^{2+}, Ti^{4+}, and Fe^{3+}). Figure 11 illustrates the compositions of all textures of magnetites from the Longnose bulk sample. Figure 12 illustrates the compositions of magnetites occurring in magnetite veins in the Longnose bulk sample.

Figures 11A and 11B illustrate the compositions of various textures of magnetite from the Longnose bulk sample in terms of FeO, TiO^2, and MgO. Magnetite compositions generally plot along the FeO-TiO_2 compositional boundary indicating substitution of Ti^{4+} in the magnetite structure (Fig. 11A) and the presence of titanomagnetite. Figure 11B, in which five times the magnetite MgO contents are plotted relative to FeO and TiO_2, illustrates that massive-textured magnetites tend to be enriched in MgO and TiO_2 relative to other textures of magnetite. Figures 11C and 11D show magnetite compositions in terms of FeO, TiO_2, and V_2O_3. Figure 11D clearly shows that Longnose bulk sample magnetites plot in two distinct populations based on V_2O_3 contents, with massive, platy-textured, and rim textures being locally enriched in V_2O_3 relative to other textures. Figure 11E illustrates the magnetite compositions from the Longnose bulk sample in terms of molar Fe^{2+}, Ti^{4+}, and Fe^{3+} based on stoichiometric calculations of electron microprobe analyses utilizing SPINCALC software (Gabbrosoft.com). Magnetite compositions plot along the titanomagnetite solid solution tie line, indicating the presence of titanomagnetites in the bulk sample. Longnose bulk sample magnetite veins contain magnetites that tend to be depleted in MgO and V_2O_3 relative to other textures of magnetites (Figs. 11A–11D). Longnose magnetite veins contain magnetites that plot along the titanomagnetite solid solution tie line, indicating the local presence of titanomagnetite within these veins.

A number of silicate phases from the Longnose bulk sample were also chemically characterized from the Longnose bulk sample. These included amphibole, chlorite, mica, olivine, and serpentine. Mineral chemical analyses discussed below are reported in weight percentages.

Amphibole (Appendix 4: Table A4-3) compositions range from pargasite to magnesio-riebeckite based on the amphibole classification scheme of Leake et al. (1997). Chlorite compositions (Appendix 4: Table A4-4) are enriched in magnesium (MgO ranging from 33.859% to 35.060%) relative to iron (FeO ranging from 6.851% to 7.627%) and are classified as clinochlore using both the Bayliss (1975) and Yavuz et al. (2015) chlorite classification schemes. Micas identified included biotite and phlogopite (Appendix 4: Table A4-5). Olivines (Appendix 4: Table A4-6) proved difficult to analyze, with only two of eight analyses having reasonable analytical totals (98%–102%). Those samples with reasonable totals are enriched in MgO (32.404%-32.504%) relative to FeO (30.760%–30.775%) and have fosterite (FO, Mg_2SiO_4) — fayalite (FA, Fe_2SiO_4) — tephroite (TP, Mn_2SiO_4) compositions ranging from $FO_{64.97}FA_{34.60}TP_{0.43}$ to $FO_{65.06}FA_{34.56}TP_{0.38}$, with an average composition of $FO_{65.02}FA_{34.58}TP_{0.40}$. Serpentines (Appendix 4: Table A4-7) were consistently identified as antigorite.

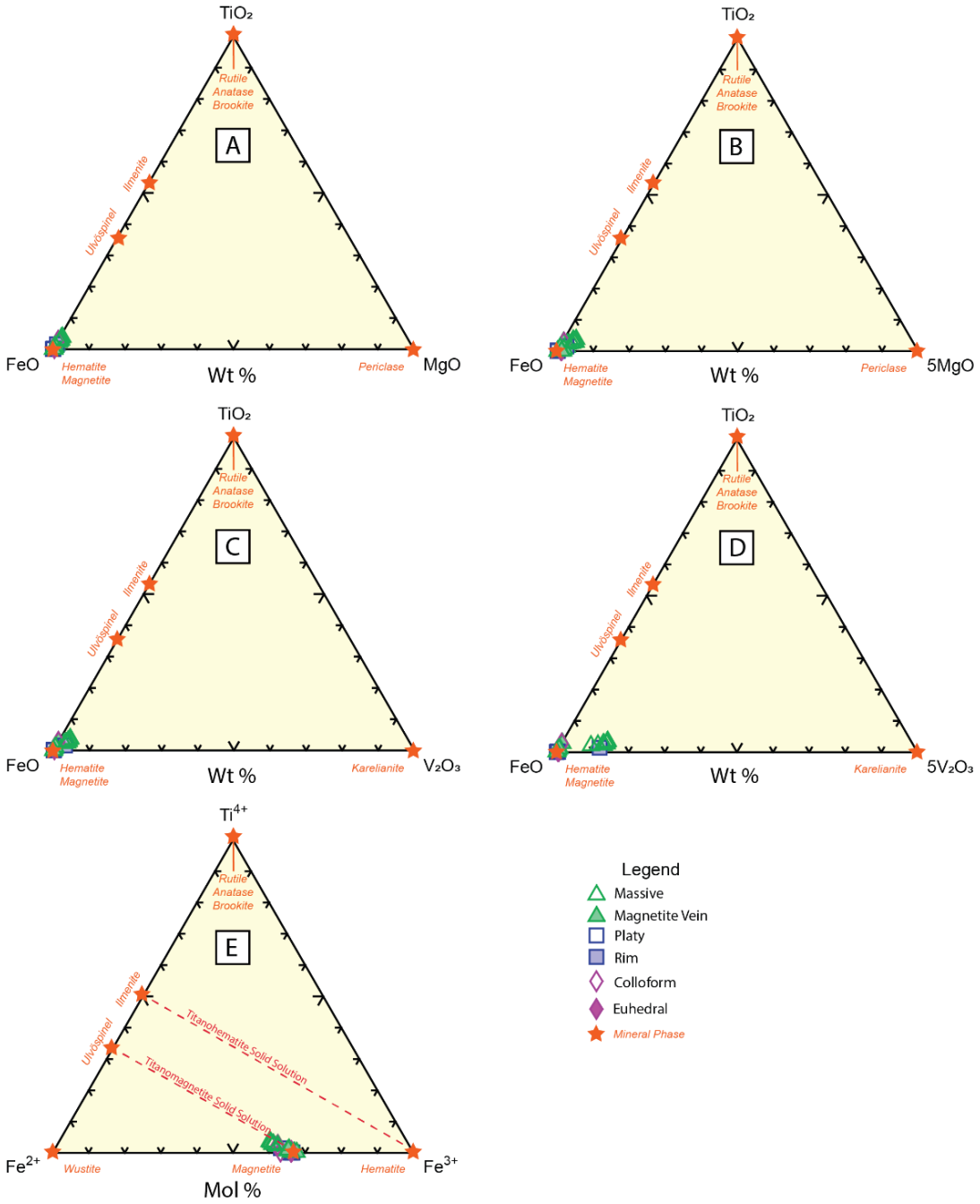

Figure 11. Ternary diagrams illustrating the chemical compositions of magnetites from the Longnose bulk sample. A) FeO-TiO_2-MgO ternary diagram. Note that magnetite compositions occur near the FeO-TiO_2 compositional boundary, indicating the local presence of titanomagnetite. B) FeO-TiO_2-5MgO ternary diagram that illustrates that massive magnetites tend to have slightly higher MgO and TiO_2 contents than other textures of magnetites. C) FeO-TiO_2-V_2O_3 ternary diagram. D) FeO-TiO_2-5V_2O_3 ternary diagram that illustrates that Longnose bulk sample magnetites plot in two distinct populations based on vanadium content, with massive, platy-textured, and rim textures being locally enriched in V_2O_3. E) Fe^{2+}-Ti^{4+}-Fe^{3+} ternary diagram (modified after Klein and Hurlbut, 1999; Meinhold, 2010) based on stoichiometric calculations of magnetite compositions utilizing SPINCALC (Gabbrosoft.com). Longnose bulk sample magnetites plot along the titanomagnetite solid solution tie line. Wt % is weight percent, Mol % is molar percent.

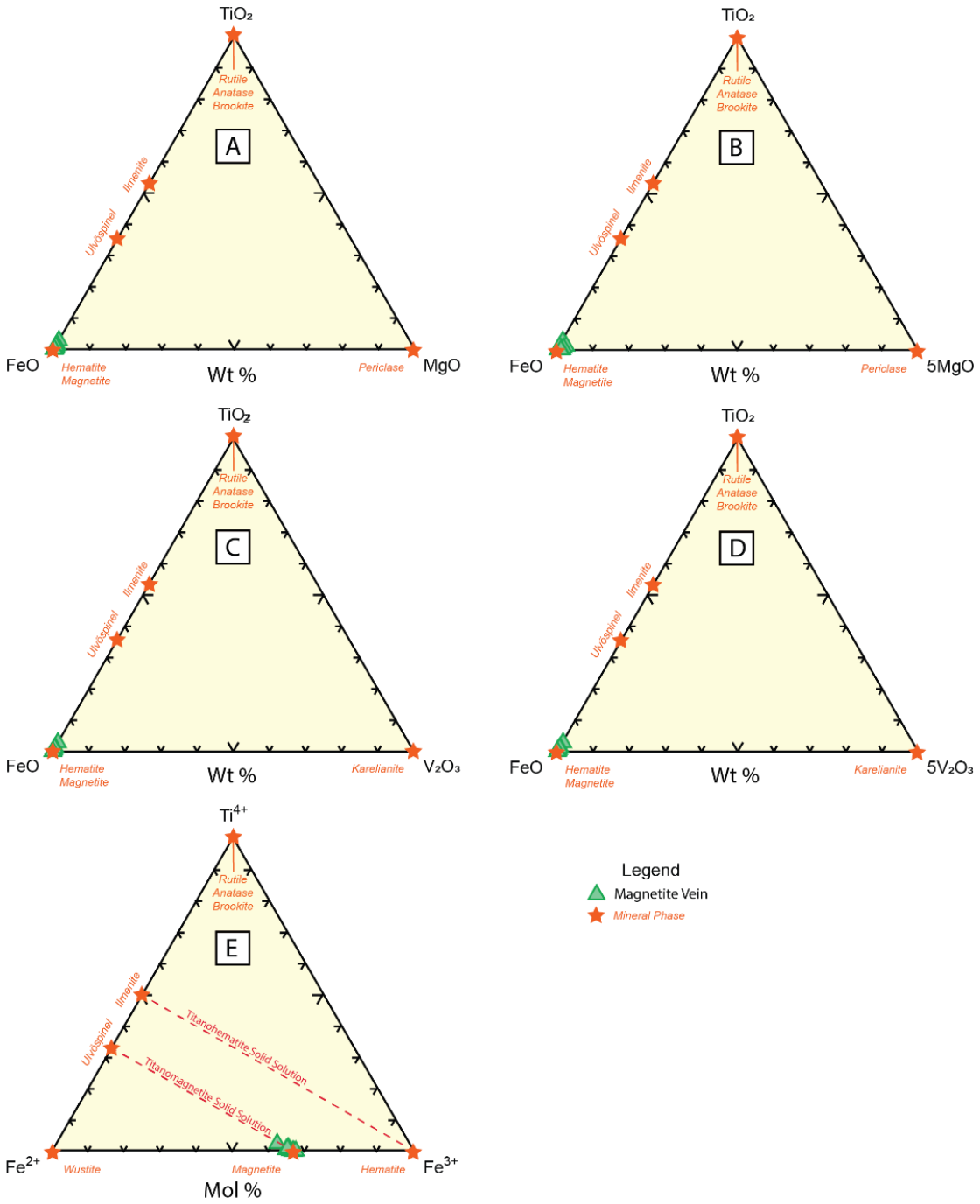

Figure 12. Ternary diagrams illustrating the chemical compositions of magnetites occurring in veins from the Longnose bulk sample. A) FeO-TiO_2-MgO ternary diagram. B) FeO-TiO_2-5MgO ternary diagram which illustrates that vein magnetite compositions tend to contain less MgO than other textures of magnetites in the Longnose bulk sample (refer to Fig. 11). C) FeO-TiO_2-V_2O_3 ternary diagram. Note that vein magnetite compositions plot very close to the FeO-TiO_2 compositional boundary. D) FeO-TiO_2-5V_2O_3 ternary diagram. Note that vein magnetites are V_2O_3-poor relative to other textures of magnetite in the Longnose bulk sample. E) Fe^{2+}-Ti^{4+}-Fe^{3+} ternary diagram (modified after Klein and Hurlbut, 1999; Meinhold, 2010) based on stoichiometric calculations of magnetite compositions utilizing SPINCALC (Gabbrosoft.com). Note that Longnose bulk sample magnetites plot along the titanomagnetite solid solution tie line. Wt % is weight percent, Mol % is molar percent.

Lithogeochemical Analysis

Whole rock lithogeochemical analyses were performed on the 12 random hand samples obtained from the Longnose bulk sample (samples 1802-3765 to 1802-3776). Samples that underwent lithogeochemical analysis are indicated in Table 2, and ALS Laboratory analytical certificates can be found in Appendix 3: Table A3-1 to Table A3-7. Lithogeochemical analyses have been summarized below (Table 7) in terms of their lithological classification.

Eight samples from the Longnose bulk sample have been classified as semi-massive oxide. Major element oxide results reported as weight percentages are as follows:

- SiO_2: Range from 4.60% to 23.40%, average 15.18%
- Al_2O_3: Range from 0.26% to 1.92%, average 0.76%
- Fe_2O_3 (total iron): Range from 34.6% to 47.9%, average 41.68%
- CaO: Range from 0.05% to 2.45%, average 0.82%
- MgO: Range from 7.17% to 17.35%, average 13.31%
- Na_2O: Range from <0.01% to 0.17%, average 0.06%
- K_20: Range from <0.01% to 0.03%, average 0.02%
- Cr_2O_3: Range from 0.046% to 0.112%, average 0.080%
- TiO_2: Range from 17.55% to 38.60%, average 26.02%
- MnO: Range from 0.25% to 0.40%, average 0.32%
- P_2O_5: Range from <0.01% to 0.03%, average 0.01%
- SrO: Consistently <0.01%
- BaO: Consistently <0.01%
- LOI: Range from -1.91% to 5.51%, average 1.27%
- Sulfur: Range from 0.03% to 0.15%, average 0.07%

Results of lithogeochemical analyses for selected trace elements from semi-massive oxide samples reported in parts per million (ppm) are as follows:

- As: Range from 0.10 to 2.9 ppm, average 0.94 ppm
- Co: Range from 187 to 206 ppm, average 195 ppm
- Cr: Range from 330 to 810 ppm, average 561 ppm
- Cu: Range from 829 to 4260 ppm, average 1907 ppm
- Ni: Range from 499 to 767 ppm, average 651 ppm
- Pb: Range from 4 to 11 ppm, average 7 ppm
- Sb: Range from <0.05 to 0.07 ppm, average 0.06 ppm
- V: Range from 1025 to 2080 ppm, average 1558 ppm
- Zn: Range from 109 to 370 ppm, average 198 ppm

Table 7. Results of lithogeochemical analyses on hand samples from the Longnose bulk sample.

		Sample	1802-3765	1802-3766	1802-3767	1802-3768	1802-3769	1802-3770	1802-3771	1802-3772	1802-3773	1802-3774	1802-3775	1802-3776	
		Sample Description	Longnose Bulk Sample - Semi-massive Oxide	Longnose Bulk Sample - Semi-massive Oxide	Longnose Bulk Sample - Semi-massive Oxide	Longnose Bulk Sample - Oxide-bearing Peridotite	Longnose Bulk Sample - Semi Massive to Massive Oxide	Longnose Bulk Sample - Oxide-bearing Dunite/ Peridotite	Longnose Bulk Sample - Semi-massive Oxide	Longnose Bulk Sample - Semi-massive Oxide	Longnose Bulk Sample - Semi-massive Oxide	Longnose Bulk Sample - Massive Oxide	Longnose Bulk Sample - Semi-massive Oxide	Longnose Bulk Sample - Semi-massive Oxide	Mlinar et al. 2017 Composite Head Sample
Analysis	Method	Detection Limit													
SiO2_%	ME-ICP06	0.01	22.1	4.6	7.05	28.7	2.49	19.25	23.4	16.7	19.9	4.12	12.5	15.2	16.60
Al2O3_%	ME-ICP06	0.01	0.97	0.26	0.46	1.76	0.31	0.87	1.92	0.8	0.72	1.02	0.66	0.26	1.05
Fe2O3_%	ME-ICP06	0.01	36.1	47.4	47.9	33.2	44.2	37.9	34.6	41.8	40.5	54.7	43.3	41.8	.20
CaO_%	ME-ICP06	0.01	0.7	0.05	0.23	1.09	0.1	1.08	2.45	2.26	0.65	0.09	0.17	0.07	0.92
MgO_%	ME-ICP06	0.01	17.35	7.17	8	22.5	5.1	16.05	17.25	12.85	16.6	6.18	12.4	14.85	13.80
Na2O_%	ME-ICP06	0.01	0.1	<0.01	0.01	0.18	0.01	0.07	0.17	0.06	0.05	<0.01	0.02	0.01	0.02
K2O_%	ME-ICP06	0.01	0.03	<0.01	<0.01	0.05	0.01	0.02	0.03	0.01	0.01	<0.01	0.01	<0.01	0.05
Cr2O3_%	ME-ICP06	0.002	0.052	0.093	0.087	0.034	0.085	0.076	0.046	0.112	0.099	0.252	0.078	0.071	0.01
TiO2_%	ME-ICP06	0.01	17.55	38.6	36.6	8.86	37.3	20.1	17.7	25.7	17.6	34.4	28.5	25.9	25.40
MnO_%	ME-ICP06	0.01	0.25	0.4	0.39	0.27	0.42	0.29	0.29	0.32	0.29	0.4	0.34	0.31	0.32
P2O5_%	ME-ICP06	0.01	0.01	0.01	<0.01	0.01	<0.01	0.01	0.03	0.01	<0.01	<0.01	<0.01	0.01	0.02
SrO_%	ME-ICP06	0.01	<0.01	<0.01	<0.01	<0.01	<0.01	<0.01	<0.01	<0.01	<0.01	<0.01	<0.01	<0.01	<0.01
BaO_%	ME-ICP06	0.01	<0.01	<0.01	<0.01	<0.01	<0.01	<0.01	<0.01	<0.01	<0.01	<0.01	<0.01	<0.01	<0.01
LOI_%	OA-GRA05	0.01	5.51	-1.91	-0.96	4.19	-3.01	2.9	2.16	-0.91	2.84	-2.06	1.59	1.83	2.17
Total_%	TOT-ICP06	0.01	100.72	96.67	99.77	100.84	87.03	98.62	100.05	99.71	99.26	99.1	99.57	100.31	101.00
S_%	S-IR08	0.01	0.04	0.07	0.04	0.05	0.05	0.12	0.07	0.13	0.03	0.02	0.15	0.06	0.01
Ag_ppm	ME-4ACD81	0.5	1.1	2	1.5	0.6	1.4	1.2	1	1.3	0.9	1.3	3.1	1.2	<0.5
Ag_ppm	ME-MS42	0.01	0.46	1.06	0.3	0.26	0.49	0.51	0.41	0.5	0.24	0.32	1.88	0.35	NA
As_ppm	ME-4ACD81	5	<5	5	<5	<5	<5	13	5	<5	13	8	8	<5	NA
As_ppm	ME-MS42	0.1	2.9	0.1	0.2	0.3	<0.1	3.6	0.9	0.4	1.4	0.1	1.1	0.5	<1
Ba_ppm	ME-MS81	0.5	19	<0.5	0.9	21.9	0.5	11.4	12	3.4	7.7	1.2	5.3	1.9	11.00
Be_ppm	ME-MS42	0.05	0.05	<0.05	<0.05	0.06	<0.05	<0.05	<0.05	<0.05	<0.05	<0.05	<0.05	<0.05	3.90
Bi_ppm	ME-MS42	0.01	0.02	0.05	0.04	0.01	0.04	0.04	0.02	0.04	0.02	0.01	0.06	0.03	<1
Cd_ppm	ME-4ACD81	0.5	3.5	8.3	7.6	2.7	7.7	4.4	3.9	5.6	3.9	8.2	5.4	4.6	<0.5
Cd_ppm	ME-MS42	0.01	0.04	0.25	0.07	0.03	0.03	0.08	0.05	0.11	0.05	0.04	0.12	0.04	NA
Ce_ppm	ME-MS42	0.02	2.07	0.19	0.42	2.52	0.18	1.45	1.55	0.51	0.84	0.18	0.65	0.23	NA
Ce_ppm	ME-MS81	0.1	5.1	0.4	0.6	7	0.8	3.5	4	2.3	1.9	0.2	1.2	0.5	44.0
Co_ppm	ME-4ACD81	1	196	188	191	203	173	201	187	196	206	191	197	196	169.00
Co_ppm	ME-MS42	0.1	132	57	75	157	35.4	121	123	97.7	138.5	68.6	101	121	NA
Cr_ppm	ME-MS81	10	360	590	610	240	670	550	330	810	720	1850	550	520	589.00
Cs_ppm	ME-MS42	0.05	0.08	<0.05	<0.05	0.08	<0.05	0.06	0.06	0.05	0.05	<0.05	0.06	<0.05	NA
Cs_ppm	ME-MS81	0.01	0.11	0.01	0.04	0.06	<0.01	0.09	0.08	0.06	0.04	0.01	0.04	0.04	NA
Cu_ppm	ME-4ACD81	1	1655	3220	1030	895	1735	1880	1285	1935	829	537	4260	1040	1770.00
Cu_ppm	ME-MS42	0.2	>250	>250	>250	>250	>250	>250	>250	>250	>250	>250	>250	>250	NA
Dy_ppm	ME-MS81	0.05	0.97	0.15	0.25	1.4	0.08	0.84	1.17	0.76	0.56	0.09	0.31	0.09	NA
Er_ppm	ME-MS81	0.03	0.62	0.31	0.19	0.84	0.2	0.52	0.61	0.43	0.37	0.14	0.38	0.21	NA
Eu_ppm	ME-MS81	0.03	0.21	<0.03	0.03	0.34	0.03	0.17	0.29	0.19	0.07	<0.03	0.05	<0.03	NA
Ga_ppm	ME-MS42	0.05	2.05	3.28	4.49	2.85	4.03	4.06	2.76	6.23	5.23	12.4	4.38	3	<5
Ga_ppm	ME-MS81	0.01	4.3	5	6.8	5.4	6.5	6.9	5.7	9.9	8.1	18.9	7.1	4.9	NA
Gd_ppm	ME-MS81	0.05	0.95	0.08	0.09	1.51	<0.05	0.87	1.07	0.73	0.48	0.06	0.33	0.1	NA
Hf_ppm	ME-MS42	0.02	0.12	0.31	0.4	0.14	0.49	0.13	0.17	0.21	0.18	0.21	0.19	0.18	NA
Hf_ppm	ME-MS81	0.2	2.7	4.9	4.5	1.3	5.5	2.7	2.6	3.5	2.5	4	3.9	3.5	NA
Hg_ppm	ME-MS42	0.005	<0.005	<0.005	<0.005	<0.005	0.008	<0.005	<0.005	<0.005	<0.005	<0.005	<0.005	<0.005	NA
Ho_ppm	ME-MS81	0.01	0.21	0.06	0.04	0.26	0.04	0.18	0.25	0.16	0.1	0.04	0.09	0.02	NA
In_ppm	ME-MS42	0.005	0.035	0.037	0.031	0.026	0.036	0.037	0.031	0.04	0.032	0.029	0.046	0.028	24.00
La_ppm	ME-MS42	0.2	0.8	<0.2	0.2	0.9	<0.2	0.6	0.8	0.2	0.5	<0.2	0.3	<0.2	<2
La_ppm	ME-MS81	0.1	1.9	0.4	0.5	2.7	0.5	1.5	1.6	0.9	1.1	0.4	0.8	0.4	NA
Li_ppm	ME-4ACD81	10	<10	<10	<10	<10	<10	<10	10	<10	<10	<10	<10	<10	5.0
Li_ppm	ME-MS42	0.1	1.5	0.5	0.7	2.3	0.6	1.2	3.7	1.4	1.4	1.2	1.6	1.1	NA
Lu_ppm	ME-MS81	0.01	0.12	0.09	0.09	0.09	0.1	0.09	0.1	0.11	0.08	0.08	0.1	0.07	NA
Mo_ppm	ME-4ACD81	1	<1	<1	1	<1	1	1	<1	1	1	1	<1	1	<0.5
Mo_ppm	ME-MS42	0.05	0.07	0.11	0.11	0.1	0.06	0.09	0.11	0.13	0.24	0.12	0.12	0.12	NA
Nb_ppm	ME-MS42	0.05	0.12	0.52	0.33	0.12	0.33	0.12	0.33	0.67	0.16	0.16	0.19	0.22	NA
Nb_ppm	ME-MS81	0.2	21.3	36.1	42	10.9	42.1	23.4	21.2	28.9	19.6	35.4	34.7	30.6	NA
Nd_ppm	ME-MS81	0.1	3.4	0.3	0.5	5	0.4	2.8	2.7	2.2	1.6	0.2	0.7	0.2	NA
Ni_ppm	ME-4ACD81	1	767	501	499	784	433	700	689	671	727	539	689	662	633.00
Ni_ppm	ME-MS42	0.2	>250	210	>250	>250	146	>250	>250	>250	>250	>250	>250	>250	NA
Pr_ppm	ME-MS81	0.03	0.72	0.04	0.1	0.97	0.1	0.54	0.55	0.37	0.29	0.04	0.14	0.05	NA
Pb_ppm	ME-4ACD81	2	7	10	11	3	14	6	4	8	8	8	5	6	75.00
Pb_ppm	ME-MS42	0.2	1.4	1	0.8	0.6	0.6	1	0.8	1	0.7	0.6	1.4	0.7	NA
Rb_ppm	ME-MS42	0.1	0.6	0.1	0.2	1.2	0.2	0.5	0.6	0.5	0.4	0.1	0.9	0.3	NA
Rb_ppm	ME-MS81	0.2	0.8	<0.2	0.2	1.6	<0.2	0.7	1	0.9	0.4	<0.2	1	0.4	12.00
Re_ppm	ME-MS42	0.001	<0.001	<0.001	0.001	<0.001	<0.001	0.001	<0.001	0.001	<0.001	0.001	<0.001	<0.001	NA
Sb_ppm	ME-MS42	0.05	<0.05	<0.05	0.05	<0.05	<0.05	0.09	0.07	<0.05	0.05	<0.05	0.05	<0.05	<1
Sc_ppm	ME-4ACD81	1	35	57	51	28	60	42	44	51	34	48	45	37	39.00
Sc_ppm	ME-MS42	0.1	10.5	6.3	9.1	11.3	8.1	9.5	9.4	7	9.9	4.9	7.7	6.7	NA
Se_ppm	ME-MS42	0.2	0.4	0.2	<0.2	0.3	0.2	0.4	0.2	0.2	0.2	0.3	0.4	0.2	<10
Sm_ppm	ME-MS81	0.03	0.84	0.05	0.15	1.18	0.04	0.81	0.82	0.64	0.35	0.09	0.2	0.03	NA
Sn_ppm	ME-MS42	0.2	<0.2	0.2	0.2	<0.2	0.2	<0.2	<0.2	0.2	0.2	0.3	0.2	<0.2	NA
Sn_ppm	ME-MS81	1	1	1	1	<1	2	1	1	1	1	1	1	1	<5
Sr_ppm	ME-MS42	0.2	5.5	0.5	1.6	9.1	0.6	3	8.4	2.1	3.5	0.6	2	1.9	13.00
Sr_ppm	ME-MS81	0.1	10	0.8	2.1	17.1	0.9	6.3	16.3	5.2	5.1	0.7	3.1	2.2	NA
Ta_ppm	ME-MS42	0.01	0.01	0.01	0.02	0.01	0.01	0.01	0.02	0.04	0.01	0.01	0.02	0.02	NA
Ta_ppm	ME-MS81	0.1	2	3	3.7	1.1	3.7	2.3	2.2	2.8	2	3.2	3.2	2.9	<10
Tb_ppm	ME-MS81	0.01	0.17	0.02	0.02	0.23	0.01	0.11	0.18	0.08	0.09	0.01	0.05	0.02	NA
Te_ppm	ME-MS42	0.01	<0.01	<0.01	<0.01	0.01	<0.01	<0.01	<0.01	0.01	<0.01	<0.01	<0.01	<0.01	<10
Th_ppm	ME-MS42	0.2	<0.2	<0.2	<0.2	<0.2	<0.2	<0.2	<0.2	<0.2	<0.2	<0.2	<0.2	<0.2	<5
Th_ppm	ME-MS81	0.05	0.18	0.05	0.06	0.21	0.07	0.18	0.21	0.08	0.1	<0.05	0.07	0.05	NA
Tl_ppm	ME-4ACD81	10	<10	<10	<10	<10	<10	<10	<10	<10	<10	<10	<10	10	<5
Tl_ppm	ME-MS42	0.02	0.03	<0.02	<0.02	<0.02	<0.02	<0.02	<0.02	<0.02	<0.02	<0.02	<0.02	<0.02	NA
Tm_ppm	ME-MS81	0.01	0.09	0.06	0.04	0.1	0.05	0.07	0.07	0.07	0.05	0.03	0.08	0.03	NA
U_ppm	ME-MS42	0.05	0.05	<0.05	<0.05	<0.05	0.06	<0.05	<0.05	<0.05	<0.05	<0.05	<0.05	<0.05	<5
U_ppm	ME-MS81	0.05	0.1	0.07	0.06	<0.05	0.08	0.06	<0.05	0.05	0.05	<0.05	0.06	<0.05	NA
V_ppm	ME-MS81	5	1025	1885	2080	663	2200	1335	1030	1815	1420	3230	1775	1435	1270.00
W_ppm	ME-MS42	0.05	<0.05	<0.05	<0.05	<0.05	<0.05	<0.05	<0.05	<0.05	<0.05	<0.05	<0.05	<0.05	NA
W_ppm	ME-MS81	1	<1	<1	<1	<1	<1	<1	<1	<1	<1	<1	<1	<1	<1
Y_ppm	ME-MS42	0.05	2.16	0.63	0.7	2.83	0.37	1.71	1.49	0.69	1.27	0.41	1.2	0.4	NA
Y_ppm	ME-MS81	0.1	4.8	1	1	7.2	0.5	4.2	5.2	3.8	2.8	0.6	2.1	0.7	<1
Yb_ppm	ME-MS81	0.03	0.76	0.44	0.36	0.75	0.44	0.6	0.51	0.5	0.39	0.3	0.59	0.38	NA
Zn_ppm	ME-4ACD81	2	109	370	182	148	167	170	150	222	172	277	226	152	186.00
Zr_ppm	ME-MS42	0.5	5.7	15.3	18.4	5.2	21.3	5.6	7.1	9.9	7.7	9.1	8.8	8.6	NA
Zr_ppm	ME-MS81	2	97	184	182	54	210	102	95	127	83	152	150	128	104.00

Two samples from the Longnose bulk sample have been classified as oxide-bearing peridotite or oxide-bearing dunite/peridotite. Major element oxide results reported as weigh percentages are as follows:

- SiO_2: Range from 19.25% to 28.70%, average 23.98%
- Al_2O_3: Range from 0.87% to 1.76%, average 1.32%
- Fe_2O_3 (total iron): Range from 33.2% to 37.9%, average 35.55%
- CaO: Range from 1.08% to 1.09%, average 1.09%
- MgO: Range from 16.05% to 22.50%, average 19.28%
- Na_2O: Range from 0.07% to 0.18%, average 0.13%
- K_20: Range from 0.02% to 0.05%, average 0.04%
- Cr_2O_3: Range from 0.034% to 0.076%, average 0.055%
- TiO_2: Range from 8.86% to 20.10%, average 14.48%
- MnO: Range from 0.27% to 0.29%, average 0.28%
- P_2O_5: Consistently 0.01%
- SrO: Consistently <0.01%
- BaO: Consistently <0.01%
- LOI: Range from 2.90% to 4.19%, average 3.55%
- Sulfur: Range from 0.05% to 0.12%, average 0.09%

Results of lithogeochemical analyses for selected trace elements from oxide-bearing peridotite or oxide-bearing dunite/peridotite samples are as follows:

- As: Range from 0.30 to 3.60 ppm, average 1.95 ppm
- Co: Range from 201 to 203 ppm, average 202 ppm
- Cr: Range from 240 to 550 ppm, average 395 ppm
- Cu: Range from 895 to 1880 ppm, average 1388 ppm
- Ni: Range from 700 to 784 ppm, average 742 ppm
- Pb: Range from 3 to 6 ppm, average 5 ppm
- Sb: Range from <0.05 to 0.09 ppm, average 0.09 ppm
- V: Range from 663 to 1335 ppm, average 999 ppm
- Zn: Range from 148 to 170 ppm, average 159 ppm

Two samples from the Longnose bulk sample have been classified as semi-massive oxide/massive oxide or massive oxide. Major element oxide results reported in weight percentages are as follows:

- SiO_2: Range from 2.49% to 4.12%, average 3.31%
- Al_2O_3: Range from 0.31% to 1.02%, average 0.67%
- Fe_2O_3 (total iron): Range from 44.20% to 54.70%, average 49.45%
- CaO: Range from 0.09% to 0.10%, average 0.10%
- MgO: Range from 5.10% to 6.18%, average 5.64%
- Na_2O: Range from <0.10% to 0.01%, average 0.01%
- K_20: Range from <0.01% to 0.01%, average 0.01%

- Cr_2O_3: Range from 0.095% to 0.252%, average 0.174%
- TiO_2: Range from 34.40% to 37.3%, average 35.85%
- MnO: Range from 0.40% to 0.42%, average 0.41%
- P_2O_5: Consistently 0.01%
- SrO: Consistently <0.01%
- BaO: Consistently <0.01%
- LOI: Range from -3.01% to -2.06%, average -2.54%
- Sulfur: Range from 0.02% to 0.05%, average 0.04%

Results of lithogeochemical analyses for selected trace elements from semi-massive oxide/massive oxide or massive oxide samples are as follows:

- As: Range from <0.10 to 0.10 ppm, average 0.10 ppm
- Co: Range from 173 to 191 ppm, average 182 ppm
- Cr: Range from 670 to 1850 ppm, average 1260 ppm
- Cu: Range from 537 to 1735 ppm, average 1136 ppm
- Ni: Range from 433 to 539 ppm, average 486 ppm
- Pb: Range from 8 to 14 ppm, average 11 ppm
- Sb: Consistently <0.05 ppm
- V: Range from 2200 to 3230 ppm, average 2715 ppm
- Zn: Range from 167 to 277 ppm, average 222 ppm

Combining the analyses of all lithogeochemical analyses on hand samples from the Longnose bulk sample, major oxide element results in weight percentages are as follows:

- SiO_2: Range from 2.49% to 28.7%, average 14.67%
- Al_2O_3: Range from 0.26% to 1.92%, average 0.83%
- Fe_2O_3 (total iron): Range from 33.20% to 54.70%, average 41.95%
- CaO: Range from 0.09% to 2.45%, average 0.75%
- MgO: Range from 5.10% to 22.5%, average 13.03%
- Na_2O: Range from <0.10% to 0.18%, average 0.07%
- K_20: Range from <0.01% to 0.05%, average 0.02%
- Cr_2O_3: Range from 0.034% to 0.252%, average 0.091%
- TiO_2: Range from 8.86% to 38.6%, average 25.73%
- MnO: Range from 0.25% to 0.42%, average 0.33%
- P_2O_5: Range from <0.01% to 0.03%, average 0.01%
- SrO: Consistently <0.01%
- BaO: Consistently <0.01%
- LOI: Range from -3.01% to 5.51%, average 1.01%
- Sulfur: Range from 0.02% to 0.15%, average 0.07%

Results of lithogeochemical analyses for selected trace element in all hand samples from the Longnose bulk sample are as follows:

- As: Range from <0.10 to 3.6 ppm, average 1.05 ppm
- Co: Range from 173 to 206 ppm, average 194 ppm
- Cr: Range from 240 to 1850 ppm, average 650 ppm
- Cu: Range from 537 to 4260 ppm, average 1692 ppm
- Ni: Range from 433 to 784 ppm, average 638 ppm
- Pb: Range from 3 to 14 ppm, average 8 ppm
- Sb: Range from <0.05 to 0.09 ppm, average 0.06 ppm
- V: Range from 663 to 3230 ppm, average 1658 ppm
- Zn: Range from 109 to 370 ppm, average 195 ppm

In order to evaluate element enrichment factors, the values of selected trace elements from the Longnose bulk sample have been plotted relative to chondritic and primitive mantle compositions found in Table 3 (Fig. 13). Figure 13A is a chondrite-normalized rare earth element plot that illustrates that rare earth element contents of the Longnose bulk sample vary from 0.1 to just over 10 times chondritic concentrations. Note that the sample classified as “semi-massive oxide” generally has lower concentrations of the rare earth elements than other rock types associated with the bulk sample that contain a higher percentage of silicate minerals. Figure 13B is a spider diagram showing trace element concentrations relative to primitive mantle compositions. In general, most elements have normalized elemental abundances ranging from approximately 0.1 to 10 times primitive mantle values, with relative enrichments in niobium (approximately 15–70 times primitive mantle values), zirconium (approximately 4–20 times primitive mantle values), hafnium (4–20 times primitive mantle values), titanium (approximately 40–200 times primitive mantle values) and vanadium (approximately 80–130 times primitive mantle values).

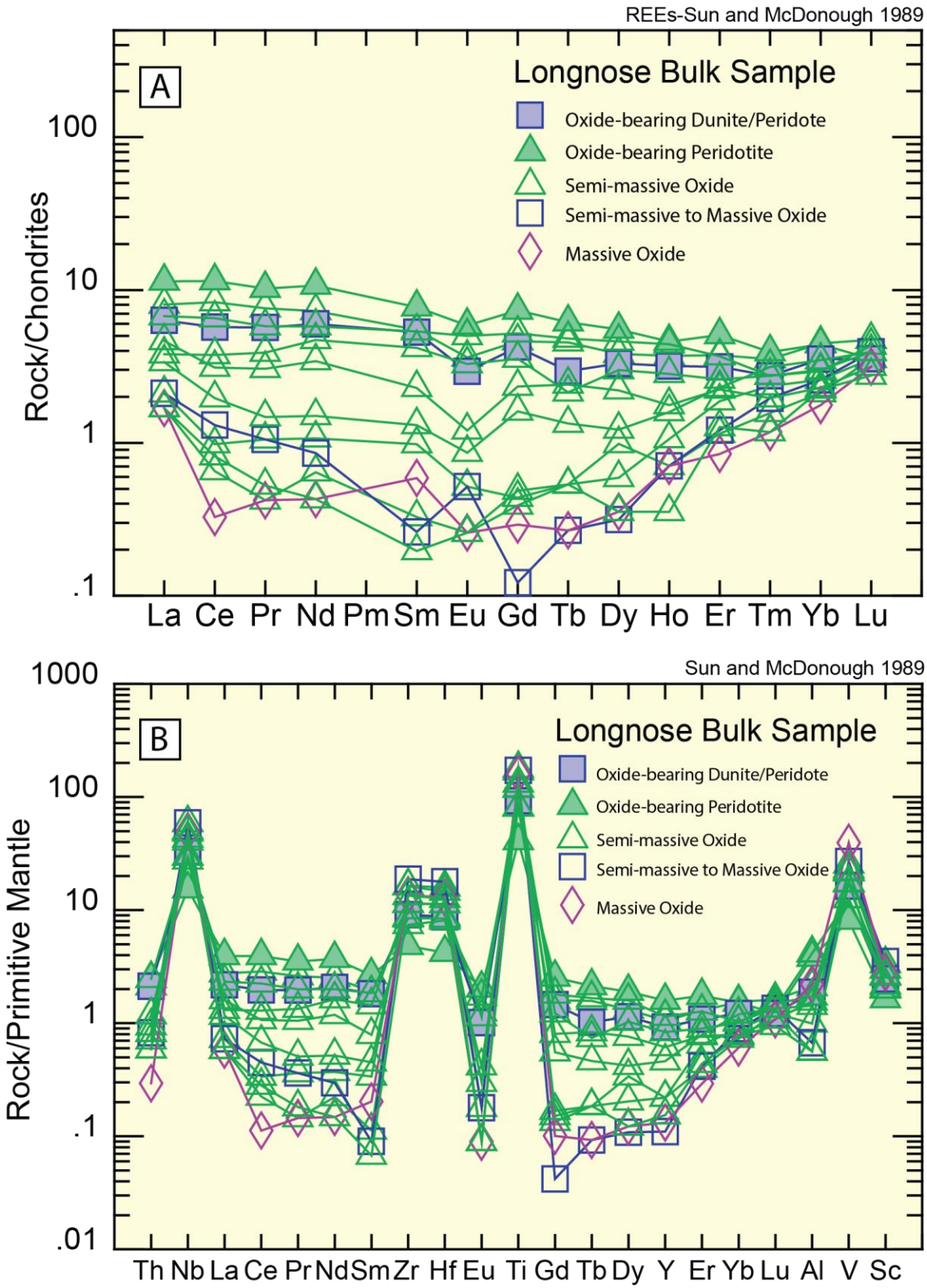

Figure 13. Chondrite-normalized and primitive mantle-normalized spider diagrams for all hand samples from the Longnose bulk sample. Chondrite and primitive mantle normalizing values from Sun and McDonough (1989) and Kerrich and Wyman (1996) can be found in Table 3.

Longnose Mineral Concentrates

Four Longnose mineral concentrate samples have undergone characterization during this study. These include: a) the ilmenite concentrate (hydrometallurgical process feed) provided to PRO (samples 1802-MIM-5 (ML-64) and 1802-ILMC (ML-79)); b) the low-intensity magnetic separator (LIMS) concentrate (magnetite-rich oxide mineral concentrate) that was produced during mineral processing activities for the Mlinar et al. (2017) study (sample 1802-ILM2); and c) the rougher spiral tails produced during mineral processing activities for the Mlinar et al. (2017) study (sample 1802-RST). The mineralogy of the ilmenite concentrate as determined by QEMSCAN analysis can be found in Table 5 of Mlinar et al. (2017). The results indicate that the sample is dominated by ilmenite and olivine, with minor (1–6%) amounts of serpentine, iron oxides, pyroxene/amphibole, chlorite and talc, and trace (<1%) quantities of quartz, calcite, feldspar, copper sulfides, muscovite, and rutile/anatase.

X-ray Diffraction Analysis

X-ray diffraction analysis was performed on the ilmenite concentrate (hydrometallurgical process feed) that was provided to PRO for the hydrometallurgical experiment. The results of this analysis are provided in Table 8. Ilmenite, antigorite, and zircon were identified in this sample.

Table 8. X-ray diffraction analyses for ilmenite mineral concentrate, various PRO hydrometallurgical process powders and residues, and titanium- and iron-oxide precipitates produced during this study.

PRO Sample Number	NRRI Sample Number	Sample Round	Description	Material	Mineralogy
1802-T6RES	ML-64	1	Hydrohydrolysis iron powder	Powder	Hematite, zircon, antigorite
1802-MIM-5	ML-65	1	PRO ilmenite concentrate (feed)	Powder	Ilmenite, zircon, antigorite
1802-BL10	ML-62	1	BL-10 leach residue, Campaign 1, no recycling	Powder	Ilmenite, hornblende, zircon
1802-BL11	ML-63	1	Leach residue, Campaign 1, after recycling	Powder	Ilmenite, hornblende, zircon
1802-P-10-1	ML-66	2	Ti-oxide precipitate, Campaign 2, not calcined	Powder	Rutile
1802-P-10-2	ML-67	2	Ti-oxide, precipitate, Campaign 2, calcined	Powder	Rutile
1802-P-17-1	ML-68	2	Ti-oxide precipitate, Campaign 3, not calcined	Powder	Rutile
1802-P-17-2	ML-69	2	Ti-oxide, precipitate, Campaign 3, calcined	Powder	Rutile
1802-BL-6	ML-70	2	BL-6 leach residue, Campaign 2, half-recycled	Powder	Ilmenite, augite, zircon
1802-BL-10	ML-71	2	BL-10 leach residue, Campaign 1, no recycling (duplicate)	Powder	Ilmenite, zircon, hornblende
1802-BL-19	ML-72	2	BL-19 leach residue, Campaign 3, after recycling	Powder	Ilmenite, zircon, hornblende
1802-T6NC	ML-73	2	Fe-oxide precipitate, Campaign 2, not calcined	Powder	Hematite, zircon?
1802-T6C	ML-74	2	Fe-oxide precipitate, Campaign 2, calcined	Powder	Hematite
1802-T7NC	ML-75	2	Fe-oxide precipitate, Campaign 3, not calcined	Powder	Hematite
1802-T7C	ML-76	2	Fe-oxide precipitate, Campaign 3, calcined	Powder	Hematite
1802-L19R	ML-77	3	BL-19 leach residue, Campaign 3, ground and 2-stage leach	Powder	Ilmenite, rutile, clinochlore, hornblende, zircon
1802-L20R	ML-78	3	BL-19 leach residue, Campaign 3, ground and 2-stage leach	Powder	Ilmenite, rutile, zircon, hornblende

Mineral Chemical Analysis

Two samples of the Longnose ilmenite concentrate underwent mineral chemistry analysis utilizing the Electron Probe Microanalyzer located at the Electron Microscopy Laboratory (EML) in the Department of Earth Sciences at the UMTC. These include samples 1802-MIM-5 (ML64) and 1802-ILMC (ML-79). Electron microprobe backscatter images of these samples are found in Figure 14. The backscatter images illustrate the angular nature of fragments within the concentrate resulting from crushing during mineral processing. Also note the presence of local agglomerates composed of smaller, angular fragments of crushed materials.

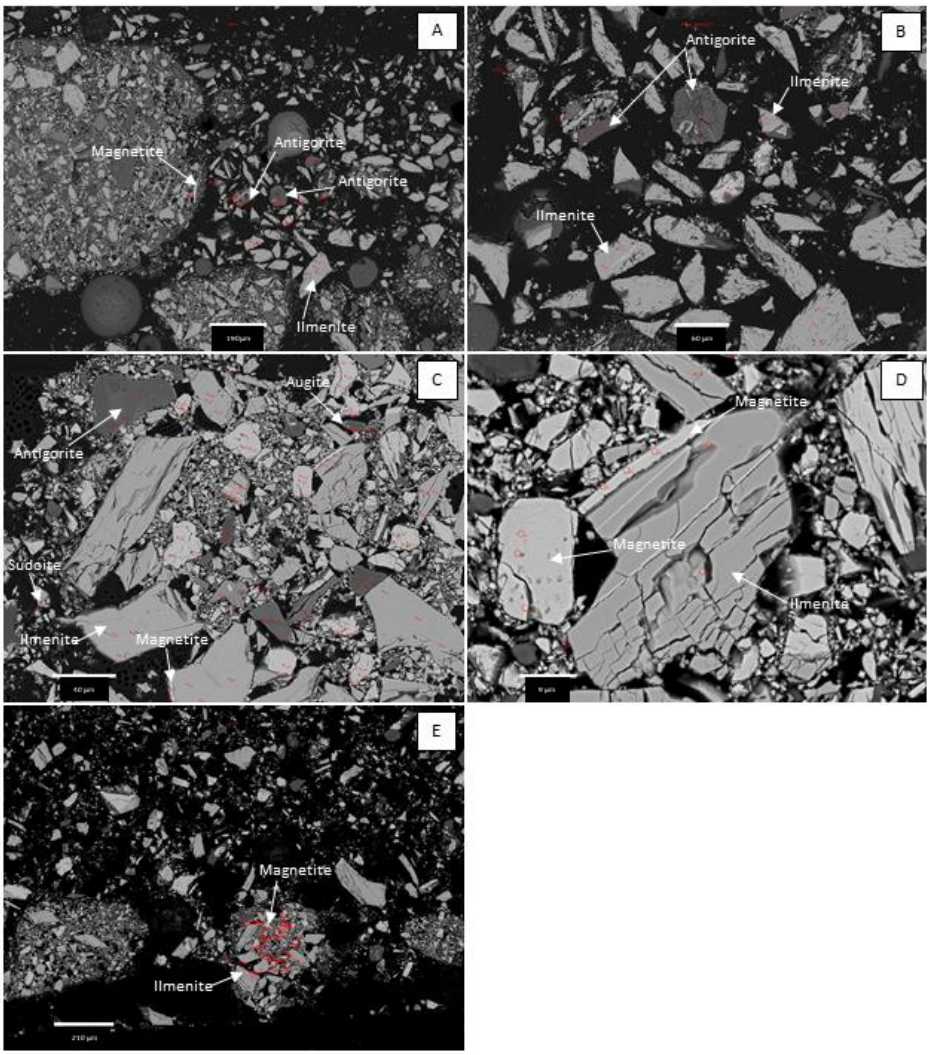

Figure 14. Electron microprobe backscatter images of Longnose ilmenite concentrate samples 1802-MIM-5 (ML-64) and 1802-ILMC (ML-79). A) Sample 1802-MIM-5 (ML-64). Ilmenite, magnetite, and antigorite. Scale bar is 190 µm. B) Sample 1802-MIM-5 (ML-64). Note angular nature of the concentrate resulting from sample crushing. Scale bar is 60 µm. C). Sample 1802-ILMC (ML-79). Ilmenite, magnetite, antigorite, augite, and sudoite within ilmenite mineral concentrate. Note magnetite rim on ilmenite grain in the lower central part of the image. Scale bar is 40 µm. D) Sample 1802-ILMC (ML-79). Close-up of ilmenite and magnetite grains in the ilmenite concentrate. Scale bar is 9 µm. E) Sample 1802-ILMC (ML-79). Ilmenite and magnetite grains highlighted. Note angular nature of fragments due to crushing and local agglomerates of finely-crushed materials. Scale bar is 210 µm. Red numbers and circles in images are analysis locations.

Oxide mineral phases identified in the Longnose ilmenite concentrate include ilmenite, magnetite, and rutile. Results of electron microprobe mineral chemical analysis and stoichiometric calculations are included in Appendix 4: Tables A4-8 – A4-10.

Ilmenite occurs in a wide variety of textures, including angular fragments, blocky fragments, elongate broken fragments, and massive fragments, which locally exhibited magnetite exsolution (Fig. 14). Mineral chemical analyses of ilmenites from the Longnose ilmenite mineral concentrate are shown in Table 9. Ilmenite compositions (weight percentages) are dominated by titanium- and iron-oxides, which range from 48.584% to 51.494% (average 49.625%) TiO_2 and 41.478% to 47.181% % (average 45.333%) FeO, respectively. MgO ranges from 2.567% to 3.990% (average 3.272%), MnO varies from 0.357% to 0.549% (average 0.431%), V_2O_3 ranges from 0.141% to 0.341% (average 0.238%), Cr_2O_3 varies from 0.008% to 0.129% (average 0.070%), and NiO ranges from 0.000% to 0.076% (average 0.020%).

Figure 15 illustrates the chemical compositions of various textures of ilmenite from the Longnose ilmenite concentrate in terms of weight percent (FeO, TiO_2, MgO, and V_2O_3) and mol percent (Fe^{2+}, Ti^{4+}, and Fe^{3+}). Figures 15A and 15B illustrate the compositions of the various textures of ilmenites from the Longnose ilmenite concentrate in terms of FeO, TiO_2, and MgO. Ilmenite compositions plot to the right of the FeO-TiO_2 compositional boundary as a result of the presence of magnesium in the ilmenite structure (Fig. 15A). Figure 15B, in which five times the ilmenite MgO contents are plotted relative to FeO and TiO_2, illustrates that the various textures of ilmenites analyzed in the Longnose ilmenite concentrate have similar magnesium contents. Figures 15C and 15D show ilmenite compositions in terms of FeO, TiO_2, and V_2O_3. These plots illustrate the relatively low vanadium contents of the ilmenites within the Longnose ilmenite mineral concentrate. Figure 15E illustrates the ilmenite compositions from the Longnose ilmenite concentrate in terms of molar Fe^{2+}, Ti^{4+}, and Fe^{3+} based on stoichiometric calculations of electron microprobe analyses utilizing ILMNCALC software (Gabbrosoft.com). Massive fragments with exsolution contain higher contents of Fe^{3+} relative to other textures of ilmenites in the ilmenite concentrate, consistent with the presence of exsolution lamellae of magnetite and/or hematite.

Table 9. Electron microprobe analyses of Longnose ilmenite concentrate ilmenites. Values are in weight percent.

Electron Microprobe Analysis – Titanium Concentrate Ilmenites (n = 29)													
Sample	Description	Phase	SiO_2	TiO_2	Al_2O_3	FeO	MnO	MgO	V_2O_3	Cr_2O_3	NiO	Cl	Total
ML-64-5-43-1	Ilmenite Concentrate	Ilmenite	0.000	50.975	0.054	41.853	0.407	3.733	0.199	0.010	0.000	0.000	97.231
ML-64-5-44-2	Ilmenite Concentrate	Ilmenite	0.000	510494	0.042	41.478	0.407	3.656	0.161	0.008	0.014	0.000	97.280
ML-64-6-46-1	Ilmenite Concentrate	Ilmenite	0.008	49.495	0.043	45.984	0.451	2.644	0.253	0.050	0.000	0.000	98.878
ML-64-6-47-2	Ilmenite Concentrate	Ilmenite	0.000	49.652	0.023	45.815	0.438	2.582	0.238	0.097	0.040	0.000	98.884
ML-64-6-48-3	Ilmenite Concentrate	Ilmenite	0.000	49.595	0.022	45.970	0.448	2.567	0.253	0.035	0.005	0.000	98.896
ML-64-7-49-1	Ilmenite Concentrate	Ilmenite	0.000	49.994	0.051	44.405	0.357	3.425	0.193	0.056	0.017	0.000	98.498
ML-64-7-50-2	Ilmenite Concentrate	Ilmenite	0.022	49.535	0.049	44.393	0.409	3.460	0.213	0.044	0.076	0.000	98.200
ML-64-7-51-3	Ilmenite Concentrate	Ilmenite	0.006	50.084	0.037	44.178	0.363	3.436	0.176	0.067	0.048	0.000	98.394
ML-79-9-85-1	Ilmenite Concentrate	Ilmenite	0.000	49.549	0.000	45.574	0.549	3.394	0.290	0.129	0.000	0.000	98.485
ML-79-9-86-2	Ilmenite Concentrate	Ilmenite	0.000	49.881	0.000	45.635	0.413	3.438	0.294	0.071	0.000	0.000	99.731
ML-79-9-87-3	Ilmenite Concentrate	Ilmenite	0.000	49.372	0.021	45.672	0.423	3.317	0.291	0.081	0.023	0.000	99.200
ML-79-10-88-1	Ilmenite Concentrate	Ilmenite	0.000	50.575	0.000	45.837	0.468	3.341	0.141	0.040	0.000	0.000	100.401
ML-79-10-89-2	Ilmenite Concentrate	Ilmenite	0.000	49.934	0.000	45.567	0.450	3.173	0.149	0.060	0.000	0.000	99.333
ML-79-10-90-3	Ilmenite Concentrate	Ilmenite	0.000	49.968	0.000	45.699	0.422	3.197	0.165	0.065	0.000	0.000	99.515
ML-79-11-91-1	Ilmenite Concentrate	Ilmenite	0.000	50.699	0.000	44.172	0.409	3.990	0.218	0.039	0.029	0.000	99.557
ML-79-11-92-2	Ilmenite Concentrate	Ilmenite	0.006	49.187	0.019	44.818	0.390	3.742	0.341	0.075	0.063	0.000	98.647
ML-79-11-93-3	Ilmenite Concentrate	Ilmenite	0.015	51.047	0.000	43.764	0.436	3.924	0.150	0.075	0.041	0.000	99.467
ML-79-12-94-1	Ilmenite Concentrate	Ilmenite	0.000	49.416	0.000	46.005	0.414	3.328	0.259	0.045	0.000	0.000	99.468
ML-79-12-95-2	Ilmenite Concentrate	Ilmenite	0.000	49.304	0.019	45.609	0.435	3.212	0.243	0.067	0.030	0.000	98.921

Table 9 (continued).

Electron Microprobe Analysis – Titanium Concentrate Ilmenites (n = 29; continued)													
Sample	Description	Phase	SiO_2	TiO_2	Al_2O_3	FeO	MnO	MgO	V_2O_3	Cr_2O_3	NiO	Cl	Total
ML-79-12-96-3	Ilmenite Concentrate	Ilmenite	0.007	49.057	0.000	46.079	0.463	3.172	0.220	0.077	0.009	0.000	99.090
ML-79-13-97-1	Ilmenite Concentrate	Ilmenite	0.000	49.387	0.000	45.709	0.410	3.435	0.196	0.070	0.043	0.000	99.251
ML-79-13-98-2	Ilmenite Concentrate	Ilmenite	0.001	49.033	0.000	46.156	0.436	3.327	0.250	0.089	0.019	0.000	99.312
ML-79-13-99-3	Ilmenite Concentrate	Ilmenite	0.293	49.225	0.240	45.713	0.436	3.256	0.240	0.064	0.003	0.000	99.804
ML-79-14-100-1	Ilmenite Concentrate	Ilmenite	0.000	49.288	0.000	45.805	0.405	3.246	0.266	0.096	0.022	0.000	99.128
ML-79-14-101-2	Ilmenite Concentrate	Ilmenite	0.000	48.697	0.000	45.777	0.406	3.208	0.320	0.095	0.045	0.000	98.549
ML-79-14-102-3	Ilmenite Concentrate	Ilmenite	0.000	48.704	0.000	45.989	0.388	3.249	0.326	0.107	0.044	0.000	98.806
ML-79-16-106-1	Ilmenite Concentrate	Ilmenite	0.000	48.584	0.000	46.943	0.470	2.735	0.326	0.086	0.000	0.000	99.143
ML-79-16-1707-2	Ilmenite Concentrate	Ilmenite	0.000	48.741	0.006	46.886	0.496	2.883	0.261	0.106	0.007	0.000	99.385
ML-79-16-108-3	Ilmenite Concentrate	Ilmenite	0.000	48.720	0.006	47.181	0.499	2.826	0.286	0.124	0.004	0.000	99.646
		Minimum	***0.000***	***48.584***	***0.000***	***41.478***	***0.357***	***2.567***	***0.141***	***0.008***	***0.000***	***0.000***	***97.231***
		Maximum	***0.293***	***51.494***	***0.240***	***47.181***	***0.549***	***3.990***	***0.341***	***0.129***	***0.076***	***0.000***	***100.401***
		Average	***0.012***	***49.625***	***0.022***	***45.333***	***0.431***	***3.272***	***0.238***	***0.070***	***0.020***	***0.000***	***99.037***
		Median	***0.000***	***49.445***	***0.000***	***45.709***	***0.423***	***3.317***	***0.243***	***0.070***	***0.014***	***0.000***	***99.143***
		St.Deviation	***0.053***	***0.740***	***0.045***	***1.276***	***0.040***	***0.359***	***0.057***	***0.029***	***0.021***	***0.000***	***0.672***

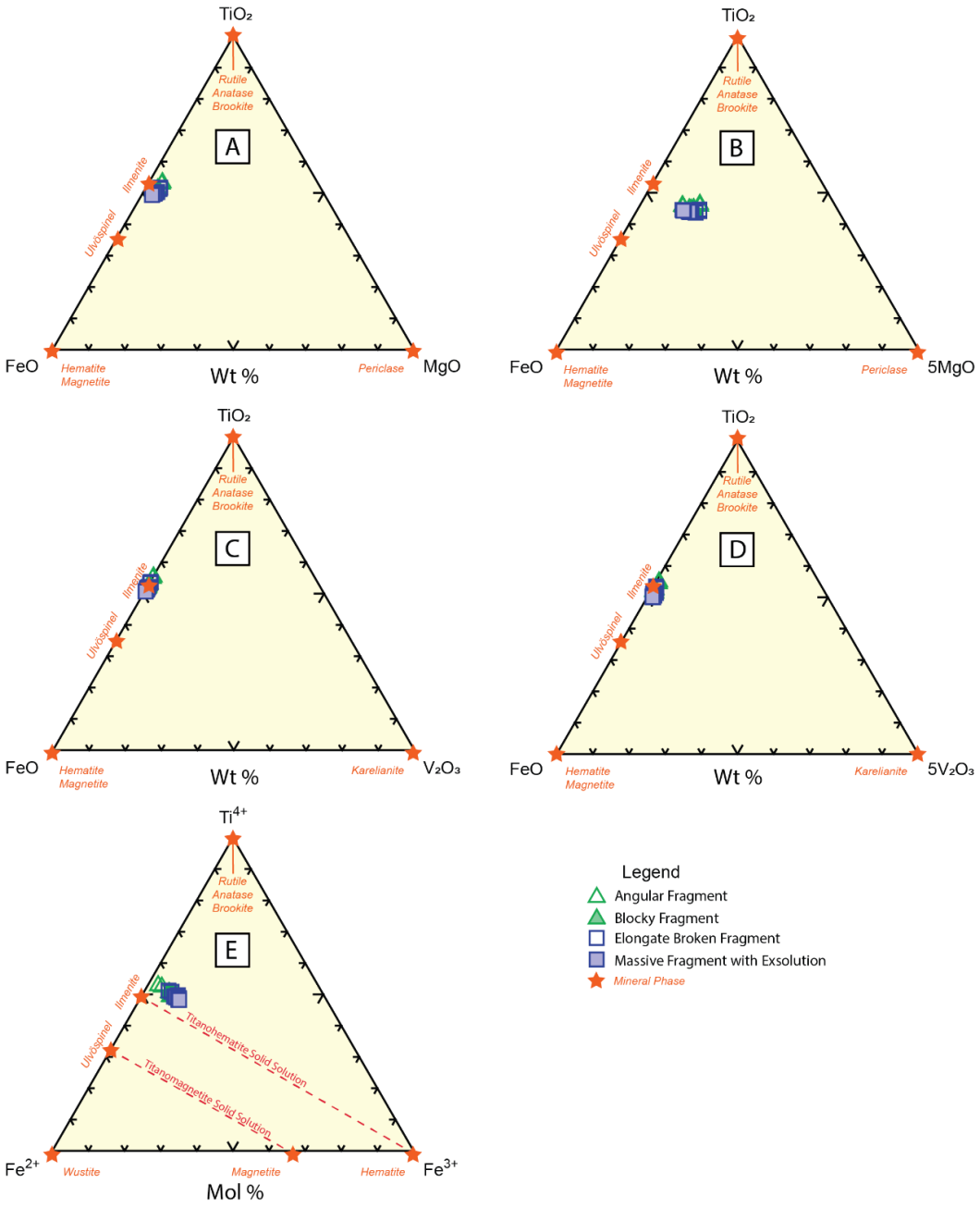

Figure 15. Ternary diagrams illustrating the chemical compositions of ilmenites from the Longnose ilmente concentrate. A) FeO-TiO_2-MgO ternary diagram. Note that ilmenite composition plot off the FeO-TiO_2 compositional boundary in the direction of MgO. B) FeO-TiO_2-5MgO ternary diagram that emphasizes the magnesium contents of the Longnose ilmenite concentrate ilmenite compositions. C) FeO-TiO_2-V_2O_3 ternary diagram. Note that ilmenite compositions plot near the FeO-TiO_2 compositional boundary. D) FeO-TiO_2-5V_2O_3 ternary diagram that emphasizes the relatively low concentration of V_2O_3 in the Longnose ilmenite concentrate ilmenites. E) Fe^{2+}-Ti^{4+}-Fe^{3+} ternary diagram (modified after Klein and Hurlbut, 1999; Meinhold, 2010) based on stoichiometric calculations of ilmenite compositions utilizing ILMNCALC (Gabbrosoft.com). Note that massive fragments with exsolution contain more Fe^{3+} than other textures of ilmenite identified in the ilmenite concentrate samples. Wt % is weight percent, Mol % is molar percent.

Magnetite occurs in a variety of textures when observed using the electron microprobe (Fig. 14). These include rounded fragments, angular fragments, exsolution lamellae, massive fragments, massive blocky fragments, and massive broken fragments.

Mineral chemical analyses of magnetites from the Longnose ilmenite mineral concentrate are shown in Table 10. Magnetite compositions (weight percentages) were dominated by iron-oxide, which ranged from 80.786% to 92.660% (average 87.643%) FeO, respectively. Titanium dioxide (TiO_2) contents ranged from 0.770% to 6.209% (average 2.449%), indicating the presence of titanomagnetites. MgO ranged from 0.000% to 1.424% (average 0.0.340%), MnO varied from 0.000% to 1.283% (average 0.248%), V_2O_3 ranged from 0.028% to 2.418% (average 0.795%), Cr_2O_3 varied from 0.000% to 1.668% (average 0.542%), and NiO ranged from 0.000% to 0.214% (average 0.063%). Minor SiO_2 (ranging from 0.000% to 2.984%, average 0.480%) and Al_2O_3 (ranging from 0.000% to 2.965%, average 0.439%) were also identified.

Figure 16 illustrates the chemical compositions of various textures of magnetite from the Longnose ilmenite mineral concentrate in terms of weight percent (FeO, TiO_2, MgO, and V_2O_3) and mol percent (Fe^{2+}, Ti^{4+}, and Fe^{3+}). Figures 16A and 16B illustrate the compositions of various textures of magnetite from the Longnose ilmenite concentrate in terms of FeO, TiO_2, and MgO. Magnetite compositions generally plot along the FeO-TiO_2 compositional boundary, indicating substitution of Ti^{4+} and a lack of Mg^{2+} in the magnetite structure. Figure 16B, in which five times the magnetite MgO contents are plotted relative to FeO and TiO2, indicates that massive fragments tend to be slightly enriched in both TiO_2 and MgO relative to other textures of magnetite that were analyzed. Figures 16C and 16D show magnetite compositions in terms of FeO, TiO_2, and V_2O_3. Figure 16D, in which five times the magnetite V_2O_3 contents are plotted relative to FeO and TiO2, indicates that magnetite exsolution lamellae are depleted in V_2O_3 relative to other textures of magnetite in the ilmenite concentrate sample. As well, massive fragments, massive broken fragments, and massive blocky fragments of magnetite in the Longnose ilmenite concentrate tend to be enriched in vanadium relative to other textures of magnetite identified (although it is clear that there are vanadium-enriched and vanadium-poor massive broken fragments). Figure 16E indicates that Longnose ilmenite concentrate magnetites plot along the titanomagnetite solid solution line.

Table 10. Electron microprobe analyses of Longnose ilmenite concentrate magnetites. Values are in weight percent.

Electron Microprobe Analysis – Ilmenite Concentrate Magnetite (n = 37)													
Sample	Description	Phase	SiO_2	TiO_2	Al_2O_3	FeO	MnO	MgO	V_2O_3	Cr_2O_3	NiO	Cl	Total
ML-64-12-64-1	Light Gray Rounded	Magnetite	0.067	0.770	0.016	89.996	0.005	0.124	0.095	0.000	0.060	0.047	91.180
ML-64-12-65-2	Light Gray Rounded	Magnetite	0.102	0.801	0.023	89.653	0.043	0.144	0.104	0.005	0.058	0.032	90.964
ML-64-12-66-3	Light Gray Rounded	Magnetite	0.120	0.908	0.000	89.322	0.012	0.134	0.160	0.021	0.082	0.000	90.760
ML-64-13-67-1	Light Gray Angular	Magnetite	0.000	0.984	0.154	86.449	0.000	0.012	0.033	0.000	0.022	0.000	87.664
ML-64-13-68-2	Light Gray Angular	Magnetite	0.027	0.963	0.187	86.752	0.037	0.000	0.029	0.042	0.000	0.000	88.038
ML-64-13-69-3	Light Gray Angular	Magnetite	0.007	1.031	0.185	86.387	0.001	0.000	0.028	0.006	0.000	0.019	87.665
ML-79-15-103-1	Exsolution in Gray Massive	Magnetite	0.728	2.507	0.000	89.886	1.283	0.405	0.086	0.061	0.000	0.000	94.955
ML-79-15-104-2	Exsolution in Gray Massive	Magnetite	0.893	2.622	0.000	90.082	0.604	0.813	0.081	0.056	0.000	0.000	95.151
ML-79-15-105-3	Exsolution in Gray Massive	Magnetite	0.701	3.864	0.000	89.214	1.255	0.521	0.077	0.042	0.000	0.000	95.673
ML-79-19-115-1	Light Gray Blocky Massive	Magnetite	0.334	5.642	0.217	83.288	0.045	0.057	1.150	1.252	0.214	0.000	92.198
ML-79-19-116-2	Light Gray Blocky Massive	Magnetite	0.578	5.733	0.237	82.404	0.056	0.174	1.222	1.139	0.154	0.000	91.698
ML-79-19-117-3	Light Gray Blocky Massive	Magnetite	0.161	2.143	0.616	87.482	0.071	0.447	1.369	1.182	0.133	0.000	93.604
ML-79-20-118-1	Light Gray Massive Broken	Magnetite	0.000	3.276	0.896	85.468	0.079	0.506	2.224	1.352	0.134	0.000	93.935
ML-79-20-119-2	Light Gray Massive Broken	Magnetite	0.004	2.511	0.641	86.196	0.040	0.401	2.267	1.375	0.179	0.000	93.615
ML-79-20-120-3	Light Gray Massive Broken	Magnetite	0.036	2.641	0.720	85.316	0.096	0.432	2.094	1.303	0.157	0.000	92.795

Table 10 (continued).

Electron Microprobe Analysis – Ilmenite Concentrate Magnetite (n = 37; continued)													
Sample	Description	Phase	SiO_2	TiO_2	Al_2O_3	FeO	MnO	MgO	V_2O_3	Cr_2O_3	NiO	Cl	Total
ML-79-21-121-1	Light Gray Massive	Magnetite	0.000	6.209	1.010	85.529	0.186	0.711	2.188	1.358	0.126	0.000	94.318
ML-79-21-122-2	Light Gray Massive	Magnetite	0.007	4.064	0.878	85.580	0.154	0.536	1.964	1.320	0.117	0.000	94.620
ML-79-21-123-3	Light Gray Massive	Magnetite	0.032	5.279	2.965	82.985	0.184	1.290	2.005	1.361	0.135	0.000	96.234
ML-79-22-125-2	Light Gray Massive	Magnetite	0.346	3.198	0.553	83.193	0.082	0.530	1.554	1.393	0.094	0.000	90.942
ML-79-22-126-3	Light Gray Massive	Magnetite?	1.567	4.040	0.900	82.357	0.081	0.339	1.811	1.668	0.104	0.000	92.867
ML-79-22-127-1	Light Gray Massive Broken	Magnetite	0.732	1.093	0.000	91.890	0.000	0.000	0.092	0.042	0.000	0.000	93.850
ML-79-23-128-2	Light Gray Massive Broken	Magnetite	0.678	1.299	0.070	90.466	0.030	0.080	0.079	0.037	0.000	0.000	92.739
ML-79-23-129-3	Light Gray Massive Broken	Magnetite?	1.055	0.927	0.063	91.126	0.014	0.012	0.074	0.031	0.000	0.000	93.303
ML-79-24-130-1	Light Gray Massive	Magnetite	0.377	1.769	0.000	91.241	0.653	0.168	0.043	0.030	0.000	0.000	94.281
ML-79-24-131-2	Light Gray Massive	Magnetite	0.466	1.500	0.000	90.841	0.681	0.181	0.056	0.009	0.000	0.000	93.734
ML-79-24-132-3	Light gray Massive	Magnetite	0.421	1.899	0.000	91.094	0.668	0.177	0.049	0.000	0.000	0.000	94.308
ML-79-25-133-1	Light Gray Massive	Magnetite	0.172	1.039	0.000	91.868	0.660	0.307	0.065	0.034	0.000	0.000	94.145
ML-79-25-134-2	Light Gray Massive	Magnetite	0.375	1.046	0.022	91.907	0.279	0.415	0.076	0.060	0.000	0.000	94.181
ML-79-25-135-3	Light Gray Massive	Magnetite	0.200	1.003	0.000	92.247	0.659	0.316	0.076	0.001	0.034	0.000	94.535
ML-79-26-136-1	Light Gray Massive Broken	Magnetite	0.389	0.773	0.051	92.660	0.245	0.245	0.064	0.030	0.000	0.000	94.457
ML-79-26-137-2	Light Gray Massive Broken	Magnetite?	2.984	0.843	0.576	86.673	0.211	0.194	0.069	0.048	0.000	0.000	91.601

Table 10 (continued).

Electron Microprobe Analysis – Ilmenite Concentrate Magnetite (n = 37; continued)													
Sample	Description	Phase	SiO_2	TiO_2	Al_2O_3	FeO	MnO	MgO	V_2O_3	Cr_2O_3	NiO	Cl	Total
ML-79-26-138-3	Light Gray Massive Broken	Magnetite?	1.370	0.882	0.000	87.620	0.115	1.424	0.069	0.013	0.000	0.000	91.494
ML-79-27-139-1	Light Gray Massive Broken	Magnetite	0.101	1.257	0.000	91.805	0.040	0.096	0.417	0.095	0.019	0.000	93.829
ML-79-27-140-2	Light Gray Massive Broken	Magnetite	0.384	1.425	0.000	91.491	0.029	0.117	0.443	0.083	0.033	0.000	94.006
ML-79-28-142-1	Light Gray Massive Broken	Magnetite	0.001	5.013	1.579	83.005	0.214	0.474	2.405	1.567	0.160	0.000	94.418
ML-79-28-143-2	Light Gray Massive Broken	Magnetite?	1.160	4.629	1.747	81.538	0.188	0.357	2.418	1.537	0.151	0.000	93.274
ML-79-28-144-3	Light Gray Massive Broken	Magnetite?	1.196	5.034	1.929	80.786	0.182	0.450	2.370	1.519	0.177	0.000	93.643
		Minimum	***0.000***	***0.770***	***0.000***	***80.786***	***0.000***	***0.000***	***0.028***	***0.000***	***0.000***	***0.000***	***87.654***
		Maximum	***2.984***	***6.209***	***2.965***	***92.660***	***1.283***	***1.424***	***2.418***	***1.668***	***0.214***	***0.047***	***96.234***
		Average	***0.480***	***2.449***	***0.439***	***87.643***	***0.248***	***0.340***	***0.795***	***0.542***	***0.063***	***0.003***	***93.003***
		Median	***0.346***	***1.769***	***0.070***	***87.620***	***0.096***	***0.307***	***0.095***	***0.056***	***0.033***	***0.000***	***93.724***
		St.Deviation	***0.595***	***1.704***	***0.668***	***3.612***	***0.327***	***0.317***	***0.928***	***0.660***	***0.069***	***0.009***	***2.038***

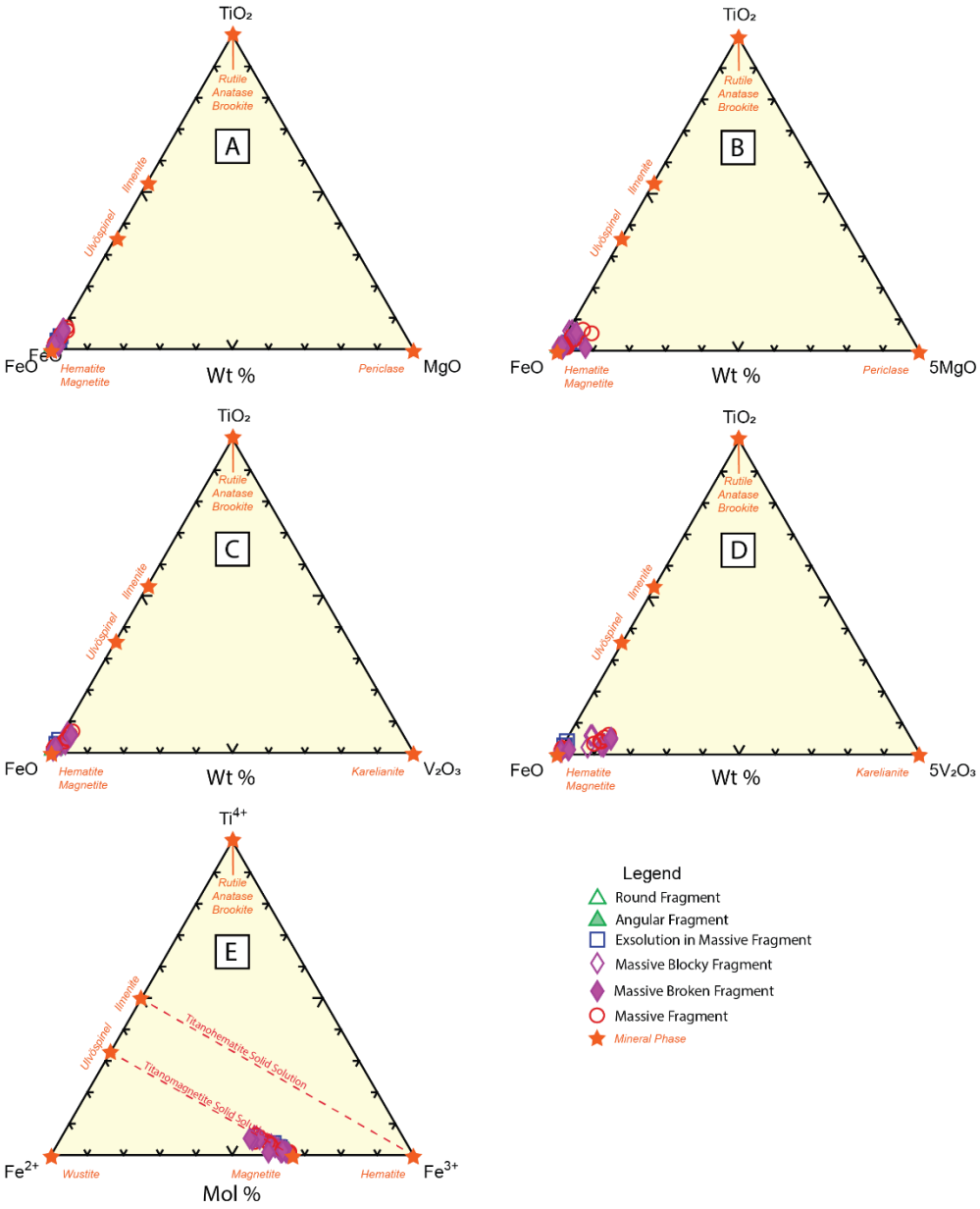

Figure 16. Ternary diagrams illustrating the chemical compositions of magnetites from the Longnose ilmenite concentrate. A) FeO-TiO_2-MgO ternary diagram illustrating that Longnose ilmenite concentrate magnetites are dominated by iron and titanium. B) FeO-TiO_2-5MgO ternary diagram that illustrates that massive broken fragments are slightly more Mg-enriched relative to other textures of magnetites analyzed. C) FeO-TiO_2-V_2O_3 ternary diagram. Note that magnetite compositions plot near the FeO-TiO_2 compositional boundary but are slightly offset in the direction of the V_2O_3 apex due to the presence of vanadium. D) FeO-TiO_2-5V_2O_3 ternary diagram. Note that exolution lamellae in ilmenite are iron-enriched relative to other textures of magnetite analyzed. Also note that massive fragments and massive blocky fragments are generally more V_2O_3-enriched than other textures of magnetites analyzed. E) Fe^{2+}-Ti^{4+}-Fe^{3+} ternary diagram (modified after Klein and Hurlbut, 1999; Meinhold, 2010) based on stoichiometric calculations of magnetite compositions utilizing SPINCALC (Gabbrosoft.com). Note that Longnose ilmenite concentrate magnetites plot along the titanomagnetite solid solution tie line. Wt % is weight percent, Mol % is molar percent.

One analyzed grain within the Longnose ilmenite concentrate was identified as rutile (general chemical formula TiO_2). This is consistent with the presence of minor amounts of rutile identified via petrography in several of the Longnose bulk sample hand samples (refer to Table 4 and Appendix 2). The rutile grain was dominated by the presence of TiO_2 (range from 97.074% to 97.340%, average 97.189%) and FeO (range from 2.321% to 2.721%, average 2.580%). Minor concentrations of SiO_2, MnO, MgO, V_2O_3, and Cr_2O_3 were also present in this grain (Table 11).

Table 11. Electron microprobe analyses of Longnose ilmenite concentrate rutile. Values are in weight percent.

Electron Microprobe Analysis – Ilmenite Concentrate Rutile (n = 3)													
Sample	Description	Phase	SiO_2	TiO_2	Al_2O_3	FeO	MnO	MgO	V_2O_3	Cr_2O_3	NiO	Cl	Total
ML-79-8-82-1	Rutile?	Rutile	0.000	97.074	0.000	2.697	0.025	0.049	0.176	0.023	0.000	0.000	100.044
ML-79-8-83-2	Rutile?	Rutile	0.021	97.153	0.000	2.721	0.014	0.022	0.080	0.057	0.000	0.000	100.068
ML-79-8-84-3	Rutile?	Rutile	0.006	97.340	0.000	2.321	0.000	0.012	0.262	0.070	0.000	0.000	100.012
		Minimum	*0.000*	*97.074*	*0.000*	*2.321*	*0.000*	*0.012*	*0.080*	*0.023*	*0.000*	*0.000*	*100.012*
		Maximum	*0.021*	*97.340*	*0.000*	*2.721*	*0.025*	*0.049*	*0.262*	*0.070*	*0.000*	*0.000*	*100.068*
		Average	*0.009*	*97.189*	*0.000*	*2.580*	*0.013*	*0.028*	*0.173*	*0.050*	*0.000*	*0.000*	*100.041*
		Median	*0.006*	*97.153*	*0.000*	*2.697*	*0.014*	*0.022*	*0.176*	*0.057*	*0.000*	*0.000*	*100.044*
		St.Deviation	*0.009*	*0.112*	*0.000*	*0.183*	*0.010*	*0.016*	*0.075*	*0.020*	*0.000*	*0.000*	*0.023*

Figure 17 illustrates the chemical composition of the rutile grain analyzed from the Longnose ilmenite mineral concentrate in terms of weight percent (FeO, TiO_2, MgO, and V_2O_3) and mol percent (Fe^{2+}, Ti^{4+}, and Fe^{3+}). In summary, the composition of this rutile grain plots near the stoichiometric composition of TiO_2, with minor substitution of Fe^{2+} for Ti^{4+} in the crystal structure (see Deer et al., 1992).

Lithogeochemical Analysis

Whole rock lithogeochemical analyses were performed on three mineral concentrates produced during the Mlinar et al. (2017) study. These included the Longnose ilmenite mineral concentrate (sample 1802-MIM-5), the Longnose LIMS concentrate (sample 1802-ILM2), and the Longnose rougher spiral tails (sample 1802-RST). The Longnose ilmenite mineral concentrate produced during the Mlinar et al. (2017) study was used for the hydrometallurgical experiments performed by PRO during this study. The results of these analyses are shown in Table 12, and ALS Laboratory analytical certificates can be found in Appendix 3: Tables A3-1 to A3-7.

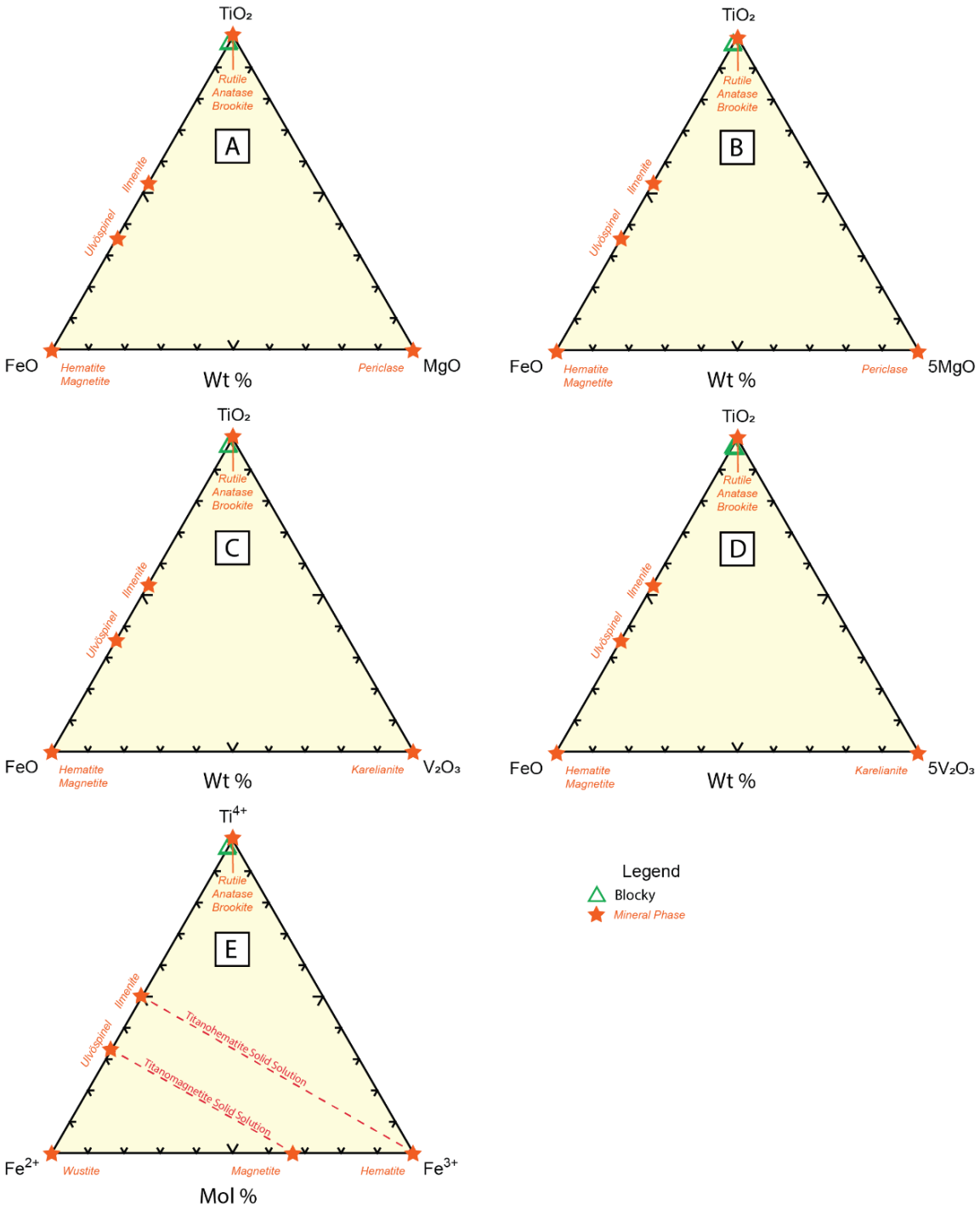

Figure 17. Ternary diagrams illustrating the chemical compositions of rutile from the Longnose ilmenite concentrate. A) FeO-TiO_2-MgO ternary diagram. B) FeO-TiO_2-5MgO ternary diagram that illustrates that the rutile grain analyzed plots along the FeO-TiO_2 compositional boundary and lacks significant MgO. C) FeO-TiO_2-V_2O_3 ternary diagram. D) FeO-TiO_2-5V_2O_3 ternary diagram. Note that the rutile grain analyzed plots along the FeO-TiO_2 compositional boundary and lacks significant V_2O_3. E) Fe^{2+}-Ti^{4+}-Fe^{3+} ternary diagram (modified after Klein and Hurlbut, 1999; Meinhold, 2010) based on stoichiometric calculations of rutile compositions utilizing RUTCALC (Gabbrosoft.com). Wt % is weight percent, Mol % is molar percent.

Table 12. Results of lithogeochemical analysis on Longnose mineral concentrates.

		Sample	1802-MIMS	1802-ILM2	1802-RST	Milnor et al., 2017	Milnor et al., 2017
		Sample Description	PRO Ilmenite Feed	Ilmenite LIMS Mags	Longnose Rougher SpiralTails	PRO Ilmenite Feed (NRRI)	PRO Ilmenite Feed (AGAT)
Analysis	Method	Detection Limit					
SiO2_%	ME-ICP06	0.01	7.03	5.41	31.7	6.43	7.49
Al2O3_%	ME-ICP06	0.01	0.54	0.79	2.18	NA	0.57
Fe2O3_%	ME-ICP06	0.01	44.5	64.6	27.1	NA	45.0
CaO_%	ME-ICP06	0.01	0.53	0.19	2.03	NA	0.59
MgO_%	ME-ICP06	0.01	7.54	6.03	23.2	7.57	8.0
Na2O_%	ME-ICP06	0.01	0.05	0.01	0.24	NA	0.02
K2O_%	ME-ICP06	0.01	0.03	0.02	0.13	NA	0.02
Cr2O3_%	ME-ICP06	0.002	0.069	0.324	0.034	NA	0.06
TiO2_%	ME-ICP06	0.01	37.5	24.1	7.23	38.93	40.10
MnO_%	ME-ICP06	0.01	0.41	0.34	0.19	NA	0.43
P2O5_%	ME-ICP06	0.01	0.01	0.01	0.06	NA	0.01
SrO_%	ME-ICP06	0.01	<0.01	0.01	<0.01	NA	0.01
BaO_%	ME-ICP06	0.01	<0.01	<0.01	<0.01	NA	<0.01
LOI_%	OA-GRA05	0.01	-1.71	-1.48	7.5	NA	<0.01
Total_%	TOT-ICP06	0.01	96.5	100.35	101.59	NA	102
S_%	S-IR08	0.01	0.05	0.04	0.06	NA	NA
Ag_ppm	ME-4ACD81	0.5	1.2	0.9	0.5	NA	NA
Ag_ppm	ME-MS42	0.01	0.3	0.62	0.64	NA	NA
As_ppm	ME-4ACD81	5	14	<5	7	NA	NA
As_ppm	ME-MS42	0.1	0.4	0.6	5.9	NA	<0.005
Ba_ppm	ME-MS81	0.5	12.1	7	37.8	NA	NA
Be_ppm	ME-MS42	0.05	<0.05	<0.05	0.06	NA	NA
Bi_ppm	ME-MS42	0.01	0.03	0.07	0.04	NA	NA
Cd_ppm	ME-4ACD81	0.5	7.4	1.3	<0.5	NA	NA
Cd_ppm	ME-MS42	0.01	0.06	0.04	0.11	NA	NA
Ce_ppm	ME-MS42	0.02	1.16	0.7	2.46	NA	NA
Ce_ppm	ME-MS81	0.1	2.3	1.1	4.8	NA	NA
Co_ppm	ME-4ACD81	1	177	170	189	NA	NA
Co_ppm	ME-MS42	0.1	48.7	84.7	149	NA	0.017
Cr_ppm	ME-MS81	10	460	2360	260	NA	0.044
Cs_ppm	ME-MS42	0.05	<0.05	<0.05	0.14	NA	NA
Cs_ppm	ME-MS81	0.01	0.04	0.15	0.18	NA	NA
Cu_ppm	ME-4ACD81	1	1045	1200	1810	NA	NA
Cu_ppm	ME-MS42	0.2	>250	>250	>250	NA	0.01
Dy_ppm	ME-MS81	0.05	0.27	0.18	1	NA	NA
Er_ppm	ME-MS81	0.03	0.28	0.15	0.6	NA	NA
Eu_ppm	ME-MS81	0.03	0.07	0.03	0.22	NA	NA
Ga_ppm	ME-MS42	0.05	1.67	17.5	3.03	NA	NA
Ga_ppm	ME-MS81	0.01	3.7	24.3	6	NA	NA
Gd_ppm	ME-MS81	0.05	0.27	0.15	0.96	NA	NA
Hf_ppm	ME-MS42	0.02	0.29	0.14	0.06	NA	NA
Hf_ppm	ME-MS81	0.2	5.3	2.8	1.3	NA	NA
Hg_ppm	ME-MS42	0.005	<0.005	<0.005	<0.005	NA	NA
Ho_ppm	ME-MS81	0.01	0.05	0.05	0.21	NA	NA
In_ppm	ME-MS42	0.005	0.022	0.031	0.039	NA	NA
La_ppm	ME-MS42	0.2	0.7	0.3	1.2	NA	NA
La_ppm	ME-MS81	0.1	1.2	0.5	2.1	NA	NA
Li_ppm	ME-4ACD81	10	<10	10	10	NA	NA
Li_ppm	ME-MS42	0.1	1.4	1.9	7.4	NA	<0.01
Lu_ppm	ME-MS81	0.01	0.08	0.07	0.09	NA	NA
Mo_ppm	ME-4ACD81	1	2	3	<1	NA	NA
Mo_ppm	ME-MS42	0.05	0.79	2.21	0.11	NA	0.008
Nb_ppm	ME-MS42	0.05	0.37	0.14	<0.05	NA	NA
Nb_ppm	ME-MS81	0.2	45.8	31.8	9.4	NA	NA
Nd_ppm	ME-MS81	0.1	1.2	0.5	3.1	NA	NA
Ni_ppm	ME-4ACD81	1	449	646	790	NA	NA
Ni_ppm	ME-MS42	0.2	186.5	>250	>250	NA	0.042
Pr_ppm	ME-MS81	0.03	0.26	0.12	0.66	NA	NA
Pb_ppm	ME-4ACD81	2	8	15	8	NA	NA
Pb_ppm	ME-MS42	0.2	2.6	1.4	1.7	NA	<0.005
Rb_ppm	ME-MS42	0.1	0.4	0.2	1.3	NA	NA
Rb_ppm	ME-MS81	0.2	1	0.7	4.2	NA	NA
Re_ppm	ME-MS42	0.001	0.001	0.001	0.001	NA	NA
Sb_ppm	ME-MS42	0.05	0.08	0.21	0.08	NA	NA
Sc_ppm	ME-4ACD81	1	56	32	28	NA	NA
Sc_ppm	ME-MS42	0.1	6.4	3.3	9.4	NA	NA
Se_ppm	ME-MS42	0.2	0.2	0.5	0.7	NA	NA
Sm_ppm	ME-MS81	0.03	0.38	0.16	0.89	NA	NA
Sn_ppm	ME-MS42	0.2	0.4	1.3	0.2	NA	<0.005
Sn_ppm	ME-MS81	1	2	2	1	NA	NA
Sr_ppm	ME-MS42	0.2	3.6	2.5	8.2	NA	NA
Sr_ppm	ME-MS81	0.1	8.1	3.6	30.9	NA	NA
Ta_ppm	ME-MS42	0.01	0.01	0.01	<0.01	NA	NA
Ta_ppm	ME-MS81	0.1	3.6	2.6	0.8	NA	NA
Tb_ppm	ME-MS81	0.01	0.04	0.02	0.15	NA	NA
Te_ppm	ME-MS42	0.01	<0.01	<0.01	0.01	NA	NA
Th_ppm	ME-MS42	0.2	<0.2	<0.2	0.2	NA	NA
Th_ppm	ME-MS81	0.05	0.18	0.11	0.33	NA	NA
Tl_ppm	ME-4ACD81	10	<10	<10	<10	NA	NA
Tl_ppm	ME-MS42	0.02	<0.02	<0.02	0.03	NA	NA
Tm_ppm	ME-MS81	0.01	0.04	0.03	0.10	NA	NA
U_ppm	ME-MS42	0.05	0.06	0.07	0.11	NA	NA
U_ppm	ME-MS81	0.05	0.21	0.11	0.17	NA	NA
V_ppm	ME-MS81	5	1775	3640	605	NA	0.141
W_ppm	ME-MS42	0.05	<0.05	<0.05	1.1	NA	<0.01
W_ppm	ME-MS81	1	<1	19	3	NA	NA
Y_ppm	ME-MS42	0.05	0.7	0.57	2.43	NA	NA
Y_ppm	ME-MS81	0.1	1.6	0.9	5.4	NA	NA
Yb_ppm	ME-MS81	0.03	0.37	0.27	0.62	NA	NA
Zn_ppm	ME-4ACD81	2	179	265	155	NA	0.025
Zr_ppm	ME-MS42	0.5	13.5	5.0	2.2	NA	NA
Zr_ppm	ME-MS81	2	199	104	43	NA	NA

Relative results for the three mineral concentrate samples in terms of major element oxide compositions (weight percentages) are described below:

- SiO_2: Longnose rougher spiral tails (31.70%) > PRO ilmenite feed (7.03%) > Ilmenite LIMS concentrate (5.41%) — explained by more silicates in the rougher spiral tails
- Al_2O_3: Longnose rougher spiral tails (31.70%) > Ilmenite LIMS concentrate (0.79%) > PRO ilmenite feed (0.54%) — explained by aluminum-bearing silicates (e.g. feldspar, micas) in the rougher spiral tails
- Fe_2O_3: Ilmenite LIMS concentrate (64.6%) > PRO ilmenite feed (44.5%) > Longnose rougher spiral tails (27.1%) — explained by the higher concentration of magnetite in the LIMS concentrate
- CaO: Longnose rougher spiral tail (2.03%) > PRO ilmenite feed (0.53%) > Ilmenite LIMS concentrate (0.19%) — explained by the greater abundance of calcium-bearing silicates (e.g. augite, amphiboles) in the rougher spiral tails
- MgO: Longnose rougher spiral tails (23.20%) > PRO ilmenite feed (7.54%) > Ilmenite LIMS concentrate (6.03%) — explained by the higher abundance of magnesium-bearing silicates (e.g. augite, olivine, serpentine) in the rougher spiral tails
- Na_2O: Longnose rougher spiral tails (0.24%) > PRO ilmenite feed (0.05%) > Ilmenite LIMS concentrate (0.01%) — possibly explained by the higher abundance of sodium-bearing silicate minerals (e.g. plagioclase) in the rougher spiral tails
- K_2O: Longnose rougher spiral tails (0.13%) > PRO ilmenite feed (0.03%) > Ilmenite LIMS concentrate (0.02%) — possibly explained by the higher abundance of potassium-bearing silicates (e.g. micas) in the rougher spiral tails
- Cr_2O_3: Ilmenite LIMS concentrate (0.324%) > PRO ilmenite feed (0.069%) > Longnose rougher spiral tails (0.034%) — explained by the higher abundance of magnetite in the LIMS concentrate
- TiO_2: PRO ilmenite feed (37.5%) > Ilmenite LIMS concentrate (24.10%) > Longnose rougher spiral tails (7.23%) — explained by the higher concentration of ilmenite in the ilmenite feed (concentrate)
- MnO: PRO ilmenite feed (0.41%) > Ilmenite LIMS concentrate (0.34%) > Longnose rougher spiral tails (0.19%) — explained by the higher average concentration of MnO in ilmenite relative to magnetites (see Tables 5 and 6)
- P_2O_5: Longnose rougher spiral tails (0.06%) > PRO ilmenite feed (0.01%) = Ilmenite LIMS concentrate (0.01%) — explained by the presence of phosphorus-bearing minerals (apatite?) in the rougher spiral tails
- SrO: Ilmenite LIMS concentrate (0.01%) > PRO ilmenite feed (<0.01%) = Longnose rougher spiral tails (<0.01%) — generally attributed to strontium substitution in calcium-bearing silicate minerals such as plagioclase feldspar
- BaO: PRO ilmenite feed (<0.01%) = Ilmenite LIMS concentrate (<0.01) = Longnose rougher spiral tails (<0.01%) — perhaps explained by apparent lack of barium substitution in micas
- LOI: Longnose rougher spiral tails (7.50%) > Ilmenite LIMS concentrate (-1.48%) > PRO ilmenite feed (-1.71%) — explained by the higher concentration of hydrous silicate minerals (micas, serpentine) in the Longnose rougher spiral tails. Note that negative LOI values may result from oxidation of Fe^{2+} to Fe^{3+} during LOI analysis at 1000°C (Potts, 1987; Lechler and Desilets (1987))

- Sulfur: Longnose rougher spiral tails (0.06%) > PRO ilmenite feed (0.05%) > Ilmenite LIMS concentrate (0.04%) — may be explained by higher abundance of sulfide minerals in the rougher spiral tails

Relative results for the three mineral concentrate samples in terms of selected trace element compositions are described below:

- As: PRO ilmenite feed (14 ppm) > Longnose rougher spiral tails (7 ppm) > Ilmenite LIMS concentrate (<5 ppm) — perhaps presence of traces of arsenic-bearing minerals (arsenides) in PRO ilmenite feed?
- Co: Longnose rougher spiral tails (189 ppm) > PRO ilmenite feed (177ppm) > Ilmenite LIMS concentrate (170 ppm) — perhaps presence of sulfide minerals in Longnose rougher spiral tails?
- Cr: Ilmenite LIMS concentrate (2360 ppm) > PRO ilmenite feed (460 ppm) > Longnose rougher spiral tails (260 ppm) — higher concentration of chromium in magnetite relative to ilmenite and silicate mineral (see Tables 5, 6, 9, and 10)
- Cu: Longnose rougher spiral tails (1810 ppm) > Ilmenite LIMS concentrate (1200 ppm) > PRO ilmenite feed (1045 ppm) — presence of copper-bearing sulfide minerals in Longnose rougher spiral tails
- Ni: Longnose rougher spiral tails (790 ppm) > Ilmenite LIMS concentrate (646 ppm) > PRO ilmenite feed (449 ppm) — may be explained by nickel substitution in olivines which report to rougher spiral tails
- Pb: Ilmenite LIMS concentrate (15 ppm) > PRO ilmenite feed (8 ppm) = Longnose rougher spiral tails (8 ppm) — perhaps traces of stibnite in LIMS concentrate
- Sb: Ilmenite LIMS concentrate (0.21 ppm) > PRO ilmenite feed (0.08 ppm) = Longnose rougher spiral tails (0.08 ppm) — perhaps traces of stibnite in LIMS concentrate
- V: Ilmenite LIMS concentrate (3640 ppm) > PRO ilmenite feed (1775 ppm) > Longnose rougher spiral tails (605 ppm) — explainable by higher concentration of vanadium in magnetite relative to ilmenite and silicate minerals (see Tables 5, 6, 9, and 10)
- Zn: Ilmenite LIMS concentrate (265 ppm) > PRO ilmenite feed (179 ppm) > Longnose rougher spiral tails (155 ppm) — perhaps minor Zn^{2+} substitution for Fe^{2+} within the spinel structure of magnetite

In order to evaluate element enrichment factors, the values of selected trace elements from the Longnose ilmenite mineral concentrate have been plotted relative to chondritic and primitive mantle compositions in Table 3 (Fig. 18). Figure 18A is a chondrite-normalized rare earth element plot that illustrates that the Longnose rougher spiral tails are enriched in rare earth elements (approximately 2 to 9 times chondritic values) relative to the Longnose ilmenite concentrate (approximately 1 to 4 times chondritic values) and the Longnose magnetic LIMS concentrate (approximately 0.5 to 2 times chondritic values). This is not unexpected, as the Longnose rougher spiral tails contain a higher proportion of silicate minerals that commonly contain higher rare earth element contents (e.g. olivines, pyroxenes, plagioclase) than the oxide minerals found in the LIMS and ilmenite concentrates (Rollinson, 1993).

Figure 18B is a spider diagram showing trace element concentrations in the Longnose ilmenite concentrate, LIMS concentrate and rougher spiral tails relative to primitive mantle compositions. The diagram illustrates that the rougher spiral tails concentrate consistently contains higher concentrations of the indicated trace elements with the exception of the elements niobium, zirconium, hafnium, titanium, and vanadium. In the case of these five elements, the Longnose ilmenite concentrate has higher abundances of niobium, zirconium, hafnium, and titanium than the Longnose LIMS concentrate; the Longnose LIMS concentrate has higher concentrations of vanadium than either the Longnose ilmenite concentrate or the Longnose rougher spiral tails. The results for titanium and vanadium can be explained in terms of the higher concentration of ilmenite (titanium) in the Longnose ilmenite concentrate than in the LIMS concentrate and the higher concentration of magnetite (which contains more vanadium than ilmenite, see Tables 5, 6, 9, and 10) in the LIMS concentrate than in the ilmenite concentrate. The higher values of niobium, zirconium, and hafnium in the ilmenite concentrate relative to the LIMS concentrate may indicate that these elements are preferentially enriched in ilmenite relative to magnetite. This was found to be the case for coexisting ilmenites and magnetites within the Sept Iles intrusion (Méric, 2011; Dare et al., 2014). Further microprobe analysis will be required to test this hypothesis.

NRRI provided several samples of the ilmenite concentrate prepared at NRRI's Coleraine research lab. Six 200 L drums were provided and included the upgraded concentrate fraction.

Chemical analysis (ICP-OES) of the samples is presented in Table 13. Material from Drum 5 was used in the testing performed in this phase of the program. These values correspond favorably with values obtained by NRRI for lithogeochemical analysis of sample 1802-MIM-5.

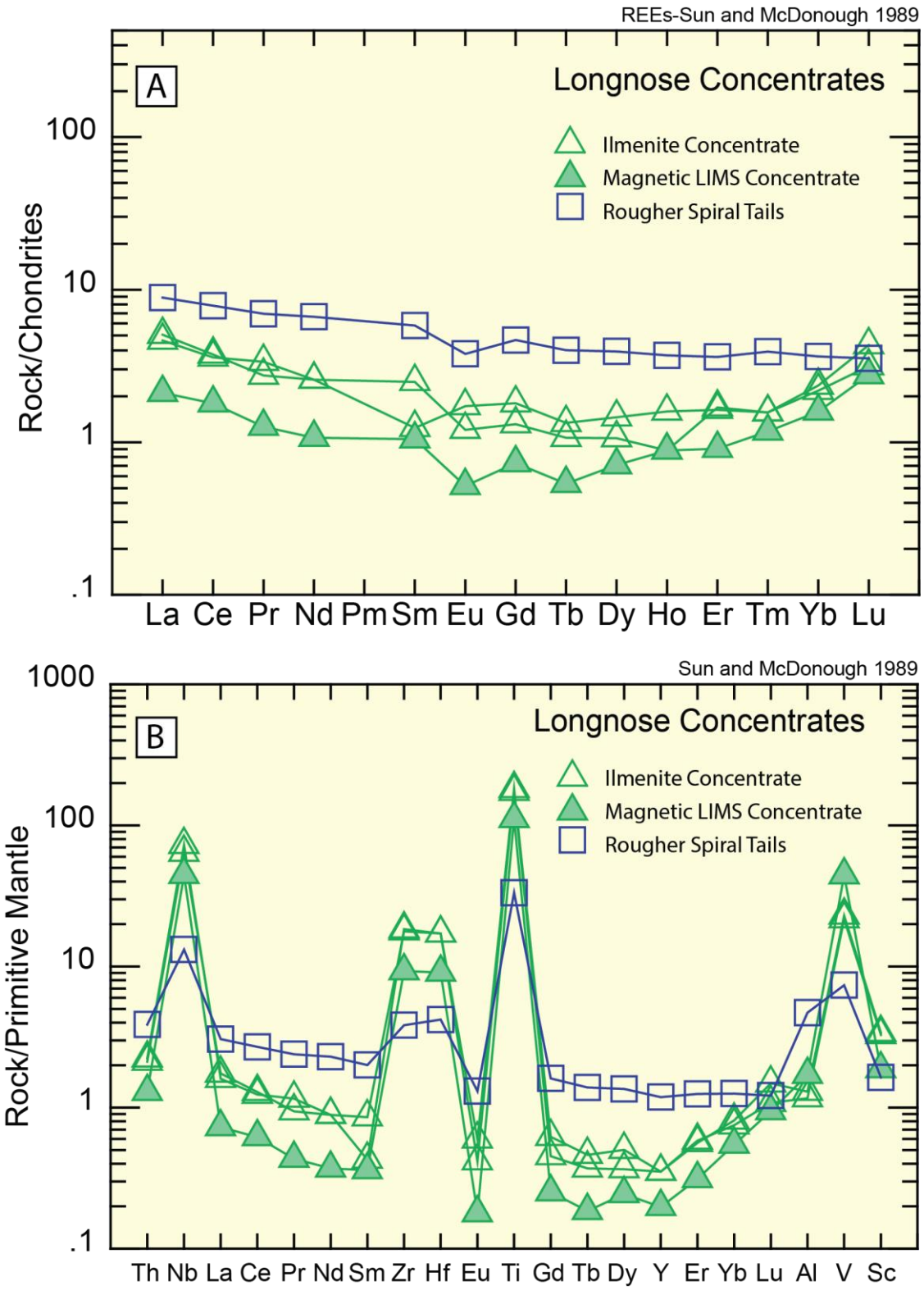

Figure 18. Chondrite-normalized and primitive mantle-normalized spider diagrams for Longnose ilmenite concentrate, magnetic LIMS concentrate, and rougher spiral tails. Chondrite- and primitive mantle-normalizing values from Sun and McDonough (1989) and Kerrich and Wyman (1996) can be found in Table 3.

Table 13. Chemical analysis of ilmenite concentrate sample comparing PRO analyses (ICP-OES) with NRRI lithogeochemical analysis (various methods, see Table 12). Values in weight percent.

	Al	As	Ca	Co	Cr	Cu	Fe	K
Sample Description	**%**	**%**	**%**	**%**	**%**	**%**	**%**	**%**
Detection Limit								
PRO 16-05 Ilmenite Conc	0.28	<0.005	0.20	0.02	0.04	0.10	30.00	<0.05
PRO 18-02 Ilmenite Conc Drum 1	<DL	<DL	<DL	0.03	0.21	0.07	43.64	<DL
PRO 18-02 Ilmenite Conc Drum 2	<DL	<DL	0.46	<DL	0.12	0.07	37.87	<DL
PRO 18-02 Ilmenite Conc Drum 3 (XRF)	0.186		0.339			0.10	36.99	
PRO 18-02 Ilmenite Conc Drum 5		<DL	<DL	<DL	<DL	0.06	30.24	<DL
NRRI Sample 1802-MIM-5	0.28	0.0014	0.38	0.0177	0.0460	0.1045	31.24	0.025

	Mg	Mn	Mo	Ni	Pb	Ti	V	Zn
Sample Description	%	%	%	%	%	%	%	%
Detection Limit								
PRO 16-05 Ilmenite Conc	4.40	0.35	0.01	0.04	<0.005	23.40	0.14	0.03
PRO 18-02 Ilmenite Conc Drum 1	3.36	0.20	<DL	0.04	<DL	14.36	0.27	0.08
PRO 18-02 Ilmenite Conc Drum 2	4.47	0.18	<DL	0.03	<DL	18.67	0.17	0.01
PRO 18-02 Ilmenite Conc Drum 3 (XRF)	1.26	0.21		0.05		13.31	0.45	0.03
PRO 18-02 Ilmenite Conc Drum 5	4.07	0.23	<DL	<DL	<DL	22.77	0.15	<DL
NRRI Sample 1802-MIM-5	4.55	0.32	0.0002	0.1865	0.0008	22.48	0.1775	0.0179

OVERALL PROCESS FLOWSHEET

The overall process flowsheets are shown for the beneficiation of ilmenite performed by NRRI (Fig. 19) and the hydrometallurgical recovery of value metals from ilmenite concentrate performed by PRO (Fig. 20). The process flowsheet can be divided into the following steps:

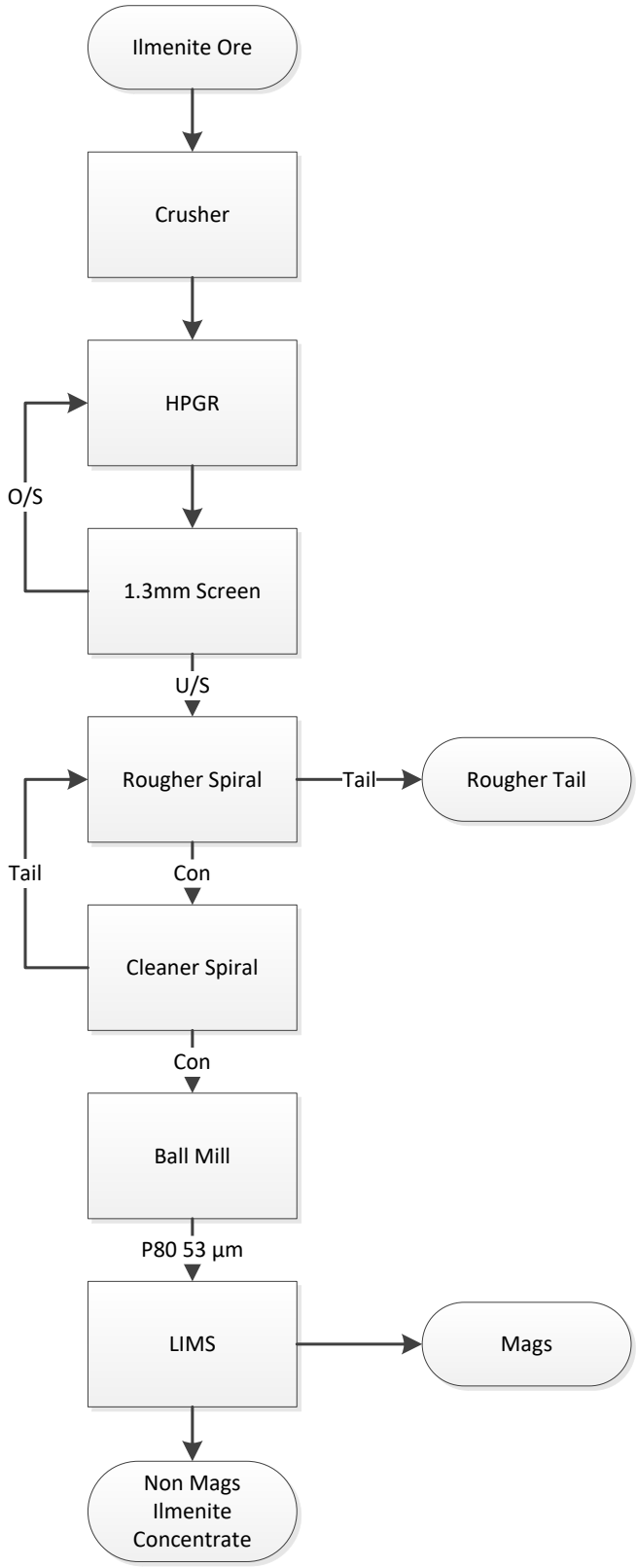

Figure 19. Mineral processing flowsheet (after Mlinar et al., 2017).

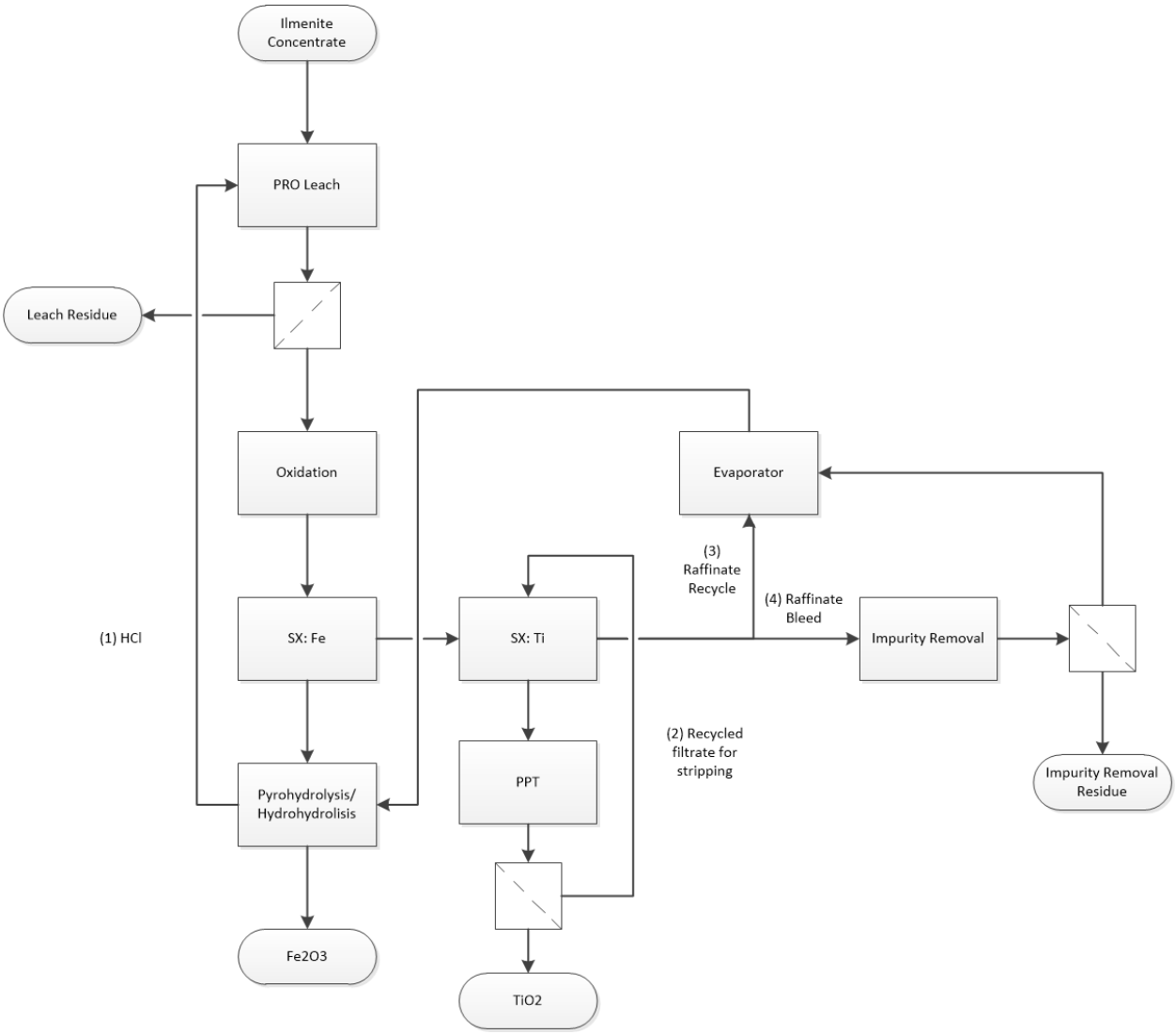

Figure 20. PRO pilot plant hydrometallurgical process flowsheet.

Mineral Processing Steps

The ilmenite concentrate used for this study was produced during the previous study by Mlinar et al. (2017) and is summarized below. For specific details related to mineral processing (e.g. metallurgical balance), the reader is referred to that study.

An approximate 100-ton stockpile of Longnose bulk sample material located at the NRRI Coleraine Laboratory (Coleraine, Minnesota) was the sample chosen for testing. The stockpile comprised Longnose deposit materials remaining from previous metallurgical studies that were conducted in the 1990s and 2000s (SRK Consulting, 2012).

Previous research conducted by NRRI researchers produced an ilmenite concentrate with a grade of ~40% TiO_2. TiO_2 recovery greater than 60% was produced with the following flowsheet (Niles, 1996):

1. Crude ore crushing;
2. Single-stage high pressure grinding roll (HPGR) processing;
3. Two-stage spiral separation; and
4. Single-stage low intensity magnetic separation.

Details can be found in the following section.

Beneficiation Flowsheet Selection

The following processing flowsheet was considered at NRRI for pilot-scale processing in 2016:

1. Single-stage gyratory crushing to approximately 25 mm (one inch);
2. Single-stage high pressure grinding roll (HPGR) processing with a 1.3 mm closing screen;
3. Two-stage spiral separation with cleaner tails recirculation to the rougher spiral;
4. Ball milling to specified leach target (80% passing 53 µm);
5. Single-stage low intensity magnetic separation (LIMS); and
6. Solid/liquid separation via decanting.

The proposed pilot block diagram for producing the ilmenite concentrate for hydrometallurgical testing can be seen in (Fig. 19) In this flowsheet the “Non Mags” stream is the ilmenite concentrate, the “LIMS Mags” stream is the magnetite concentrate, and the “Rougher Tail” stream is the final tailings.

The beneficiation scheme chosen for pilot-scale testing was relatively simple and straightforward. Crushing and grinding was necessary to liberate the ilmenite from the other gangue minerals. The silicate gangue minerals were then removed from the higher specific gravity oxide minerals by means of gravity separation. The spiral separator cleaner concentrate was reground using an open-circuit ball mill to liberate additional ilmenite units and to reduce particle size for the leaching in a single unit operation. Regrinding in open-circuit rather than in closed-circuit was chosen for simplicity and to allow for a wide size distribution of particles for hydrometallurgical testing. The final beneficiation process, magnetic separation, was necessary to remove the magnetite that would create a higher iron SX/hydrohydrolysis cost in the hydrometallurgical process.

Mixed Chloride Leaching

The ground ore is leached at atmospheric pressure at 70°C in a mixed chloride lixiviant (Fig. 20). The slurry is then filtered and the tailings are properly disposed of. Pregnant leach solution (PLS) obtained from leaching undergoes oxidation for the conversion of ferrous chloride to ferric chloride. Following oxidation successive solvent extraction stages are conducted to recover iron and titanium.

Oxidation

Following the filtration of the PLS, it is pumped into columns into which oxygen gas (O_2) is sparged to oxidize Fe^{2+} to Fe^{3+}.

Iron Solvent Extraction

The PLS is contacted with an organic extractant to selectively extract iron into the organic phase according to reaction (1) where the organic phase is represented by (S) containing a solvating extractant. The loaded organic is scrubbed with a high iron-containing solution and then stripped by contacting with a stripping solution to generate iron-rich strip liquor.

$$H^+FeCl_4^- + 2\,S = H^+FeCl_4^-.2\,S \quad (1)$$

Titanium Solvent Extraction

The raffinate from iron solvent extraction is contacted with an organic extractant to selectively extract titanium into the organic phase according to reaction (2) where the organic Tri-alkyl phosphine oxide (TRPO-Cyanex 923) is represented. The loaded organic is scrubbed with high titanium-containing solution and then stripped by contacting with a stripping solution to generate titanium-rich strip liquor.

$$TiOCl_2 + 2TRPO = TiOCl_2\,.2TRPO \quad (2)$$

Titanium Dioxide Precipitation

Titanium dioxide is precipitated from titanium-rich pregnant strip liquor by thermal precipitation.

Pyrohydrolysis/hydrohydrolysis

It is proposed to produce iron oxide and regenerate hydrochloric acid by pyrohydrolysis or hydrohydrolysis of iron-rich pregnant strip liquor. Magnesium oxide is produced, and hydrochloric acid is regenerated by pyrohydrolysis of a bleed stream from the raffinate of titanium solvent extraction. Regenerated hydrochloric acid is recycled to the process.

Pyrohydrolysis was not part of the pilot plant test work. Pyrohydrolysis is a well understood, fully commercialized unit operation. Pyrohydrolysis units are available from commercial vendors and can be designed based on the iron pregnant strip quality and volumetric flow rate for iron pyrohydrolysis and titanium solvent extraction raffinate quality and corresponding volumetric flow rate for magnesium pyrohydrolysis.

Hydro-hydrolysis is an alternative process that can be used for the production of Fe_2O_3 and regeneration of HCl from the Fe pregnant strip solution via the following reaction:

$$2FeCl_3 + 3H_2O = Fe_2O_3 + 6HCl$$

Past research performed by PRO has indicated that under specific conditions, the concentration of HCl produced has achieved upwards of 10N.

Aqueous Stream Recycle

The PRO flowsheet is based on the recycling of aqueous streams. After the pregnant leach solution has passed through both extraction circuits, it needs to be brought to the same lixiviant compositions that

are used for leaching. This will be achieved in the commercial plant by using appropriate levels of evaporation, bleeding, and acid addition.

MINERAL PROCESSING

Pilot-Scale Beneficiation Testing

Pilot High Pressure Grinding Roll (HPGR) Testing

A total of approximately 10 tons of ilmenite material was ground in a Weir/KHD high-pressure grinding roll (HPGR) to prepare the material for spiral separation. Benner (2001) found single-stage HPGR crushing at 40 bar and a 1.4 mm (14 mesh) closing screen resulted in low generation of fine HPGR product compared to rod mills. Minimizing the amount of minus 105 µm (150 mesh) HPGR product is important to reduce the amount of misplaced ilmenite particles that report to the spiral tails. Therefore, this flowsheet and pressure was chosen for processing the material.

Each HPGR product was dry screened on a 1.3 mm screen, with the screen oversize being recycled to the new feed. The 1.3 mm undersize material was stored in drums for spiral feed. The steady-state feed and screen product sizing is presented in Figure 21.

Average power consumption for the single-stage HPGR closed with a 1.3 mm screen was 1.6 kWh/t of HPGR feed and a recirculating load of 141%. Other characteristics of the HPGR circuit in steady state is presented in Table 14.

The lock-cycle testing continued until the new HPGR feed had been fully used. Figure 22 displays the HPGR screen undersize size distribution by cycle. As can be seen in the figure, the screen undersize size distribution matched the Benner (2001) results relatively closely; however, the results of the current study showed slightly coarser sizing of the coarse particles and slightly finer sizing of the fine particles.

FOOTNOTE: The Sweco 14 mesh panel has opening measurements of 1.295 mm.

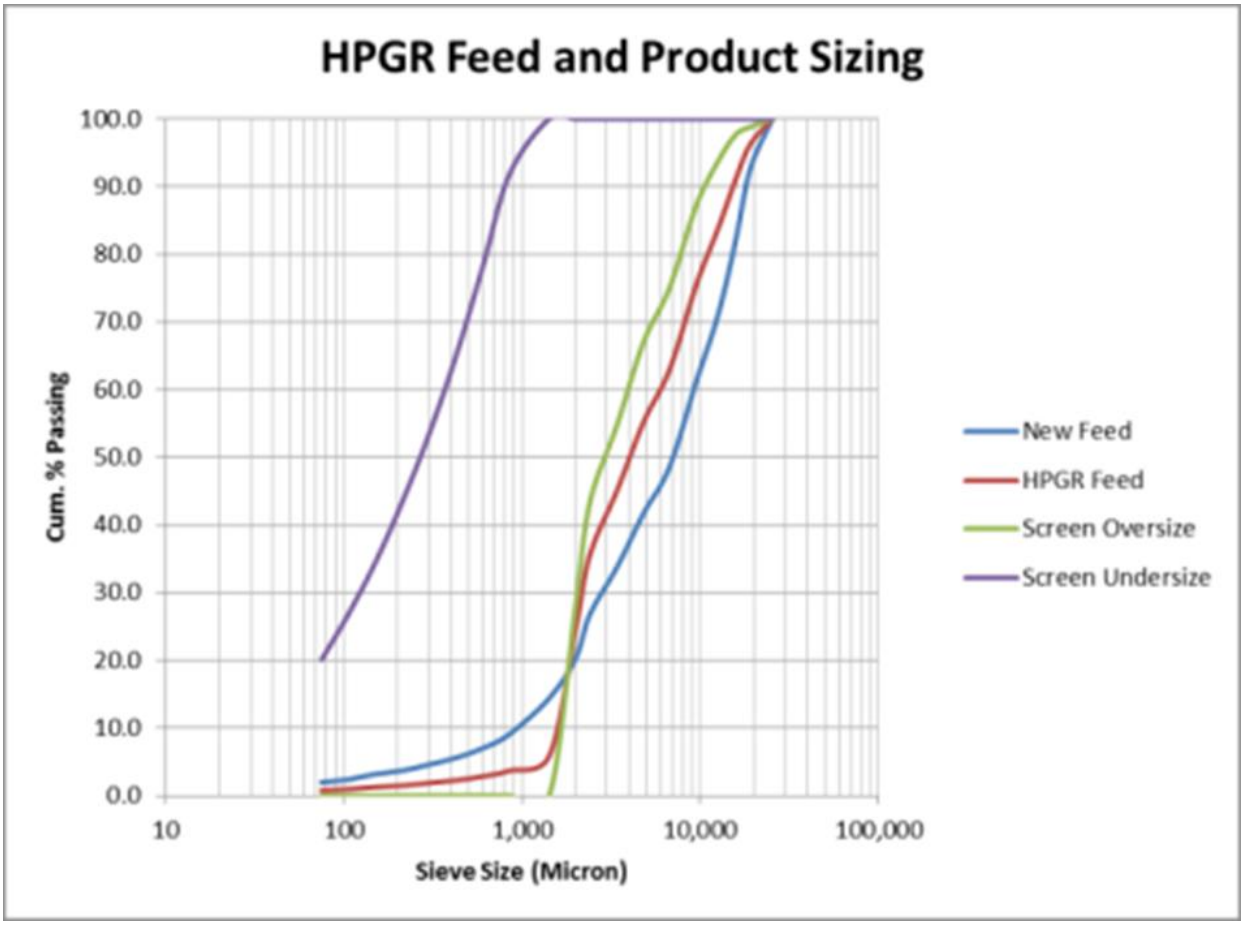

Figure 21. HPGR feed and screen product sizing.

Table 14. Steady state HPGR calculations.

Parameters	Cycle 4	Cycle 5	Cycle 6	Average
Specific power, Net, kWh/t	1.56	1.65	1.63	1.61
P80, mm	0.64	0.62	0.65	0.64
Screen Oversize (+1.3 mm), %	58.5	57.5	59.5	58.5
Screen Undersize (-1.3 mm), %	41.5	42.5	40.5	41.5
Recirculating Load, %	141.0	135.3	146.9	141.1

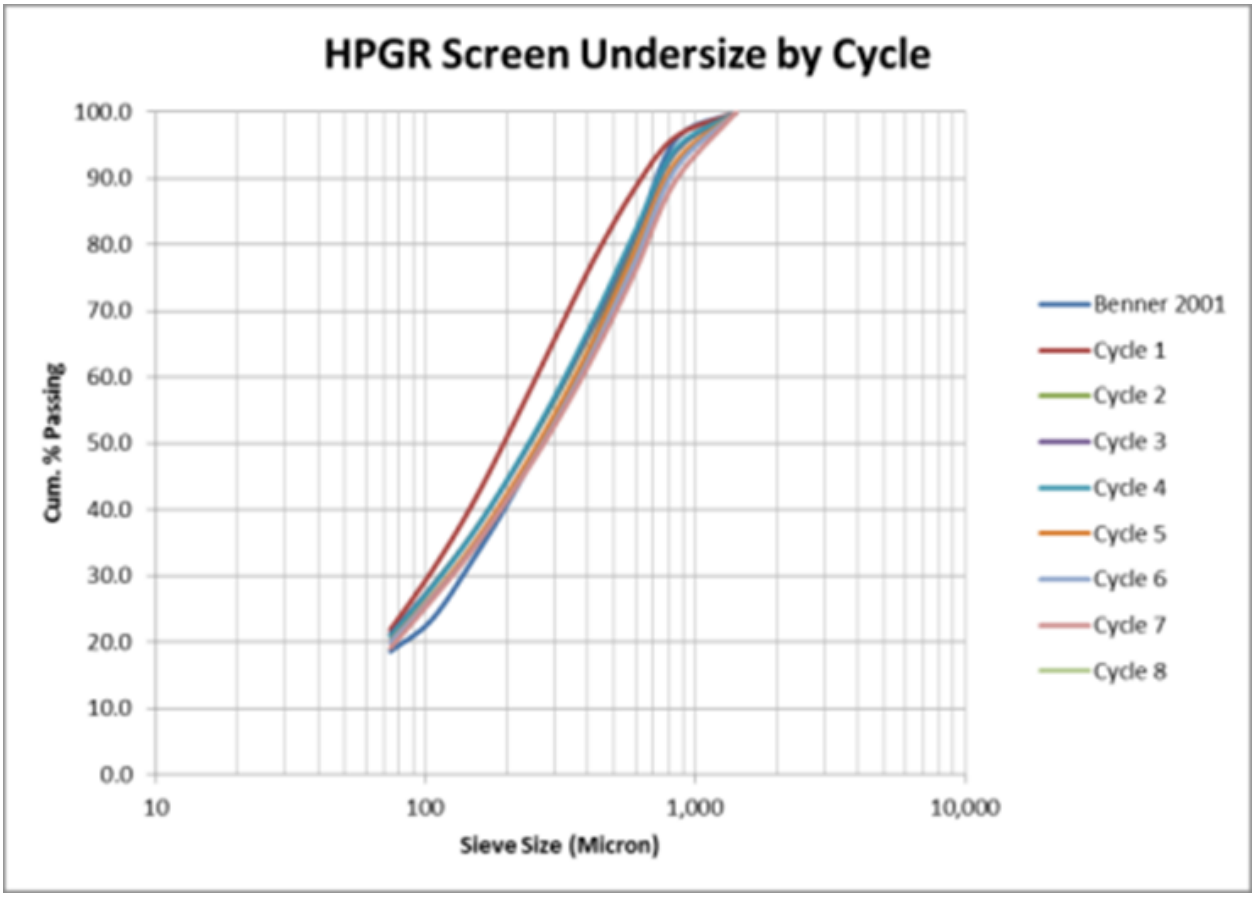

Figure 22. HPGR screen undersize by cycle.

Pilot Spiral Separator Testing

The 1.3 mm screen undersize from the HPGR circuit was then homogenized and prepared for spiral separation. The flowsheet chosen was a rougher-cleaner spiral separation, where rougher tailings reported to final tailings, cleaner tailings were recycled to rougher feed, and cleaner concentrate was the final concentrate in this circuit. A spiral classifier was used to dewater the sand fraction of the spiral separator tailings. The overflow (coarse fraction) of the spiral classifier tailings was retained in barrels and the underflow (fine fraction) was disposed. The cleaner concentrate was retained in barrels for the next regrinding step in the process plant.

Four pilot-scale spiral separation tests were conducted to produce spiral concentrate and spiral tailings from the HPGR product feed. The feed to the rougher spiral was approximately 1.5 tons per hour at 35% solids by weight (new feed basis). Flush water for the rougher and cleaner spirals were 21 lpm (5.5 gpm) and 25 lpm (6.5 gpm), respectively.

A weighted average was used to estimate the metallurgical balance for the pilot spiral separation based upon individual cut samples and hours per run. Each pilot operation ranged from one to four hours. The estimated metallurgical balance for the pilot spiral testing is presented in Table 15.

Table 15. Pilot spiral testing metallurgical balance.

Sample	Weight Dist (%)	TiO_2 (%)	TiO_2 Dist (%)
Rougher Spiral Feed	100.0	25.67	100.0
Rougher Spiral Tails (Sand)	15.8	7.72	5.0
Rougher Spiral Tails (Water)	29.3	12.32	14.3
Cleaner Spiral Concentrate	55.0	36.78	80.6

Combining the sand and water tailings together shows a simplified metallurgical balance; these results are presented in Table 16.

Table 16. Pilot spiral testing metallurgical balance (single tailing product).

Sample	Weight Dist (%)	TiO_2 (%)	TiO_2 Dist (%)
Rougher Spiral Feed	100.0	25.67	100.0
Rougher Spiral Tails	45.0	10.71	19.4
Cleaner Spiral Concentrate	55.0	36.78	80.6

The spiral separator cleaner concentrate TiO_2 grade was 2.4% higher, but the TiO_2 recovery was 5.6% lower than from the Benner (2001) study.

Pilot Ball Mill Regrind Testing

A ball mill Bond Work Index (BWI) test was conducted on the spiral cleaner concentrate to generate an energy consumption value for scale-up calculation purposes. The spiral separator cleaner concentrate ball mill BWI was found to be 20.4 kWh/t (18.5 kWh per short ton).

The spiral cleaner concentrate was reground in open circuit using a pilot-scale ball mill at approximately 1.4 kg/min (3 lbs/min) at 65% solids by weight (Fig. 23). The target ball mill discharge was 80% passing 53 µm (270 mesh) per recommendation of PRO.

Using the measured ball mill BWI value of 20.4 kWh/t, the estimated energy consumption for secondary ball mill grinding was 19.5 kWh/t. Therefore, the total grinding energy for HPGR and ball milling was 21.1 kWh per ton for grinding from 80% passing 15,205 µm to 80% passing 53 µm.

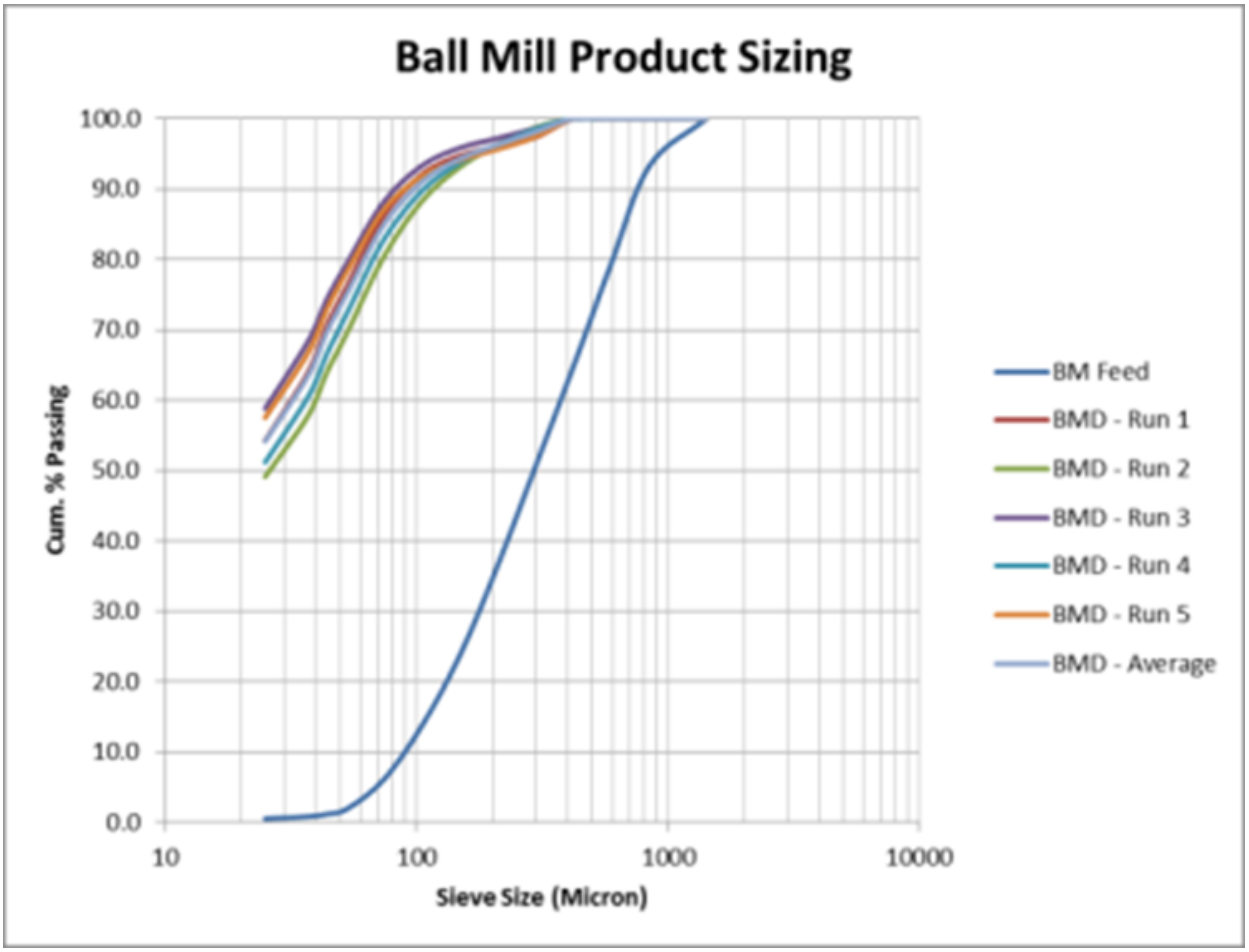

Figure 23. Pilot-scale ball mill discharge sizing per run.

Pilot Low-Intensity Magnetic Separation (LIMS) Testing

Five pilot-scale spiral low-intensity magnetic separation (LIMS) tests were conducted to produce a magnetic and non-magnetic product. Leaching of non-ilmenite iron-bearing material such as magnetite drastically increases the costs of the hydrometallurgical process. Therefore, to reduce the leaching cost process, the magnetite was removed from the ilmenite via LIMS per recommendation of PRO.

A single counter-rotation pilot-scale LIMS finisher drum was used for all the runs except for “Run 2”; Run 2 utilized a double-drum circuit. The double-drum operation was abandoned after the second run due to the high amount of water usage required for a relatively low amount of mags product. There was difficulty in operating the LIMS circuit as the heavy ilmenite particles created plugging issues in the non-mags overflow weirs of the pilot-scale LIMS unit.

A weighted average was used to estimate the metallurgical balance for the pilot LIMS based upon individual cut samples and estimated non-magnetic weight production per run. The non-mags stream represented approximately 83% of the feed weight with 89% of the TiO_2 with a grade of approximately 39% TiO_2. The estimated metallurgical balance for the pilot LIMS testing is presented in Table 17.

Table 17. Pilot UMS testing metallurgical balance.

Product	Weight Dist (%)	TiO_2 (%)	TiO_2 Dist (%)
Feed	100.0	36.44	100.0
Mags	17.1	24.40	11.5
Non-Mags	82.9	38.93	88.5

Approximately 1.5 tons of ilmenite concentrate sample was sent to PRO for hydrometallurgical testing, while the remainder of the ilmenite concentrate, magnetite/titanomagnetite concentrate, and high silica tailings were retained at NRRI for additional characterization and testing.

Composite Metallurgical Balance

A titanium balance was conducted using the cut samples from the pilot-scale testing. This balance can be seen in Table 18. The final LIMS Non-Mag product was found to contain approximately 39% TiO_2 at 45.5% weight recovery and 71.3% TiO_2 recovery.

Table 18. Composite titanium dioxide balance from pilot-scale testing.

Product	Weight Dist (%)	TiO_2 (%)	TiO_2 Dist (%)
Rougher Spiral Feed	100.0	25.67	100.0
Rougher Spiral Tails (Sand)	15.8	7.72	5.0
Rougher Spiral Tails (Water)	29.3	12.32	14.3
Cleaner Spiral Concentrate	55.0	36.78	80.6
Ball Mill Discharge (LIMS Feed)	55.0	36.78	80.6
LIMS Mags	9.4	24.40	9.3
LIMS Non-Mags	45.5	38.93	71.3

MINI PILOT PLANT (MPP) TESTING

Materials of Construction

In general, the materials used to contain, transfer, and mix fluids through the system must be compatible with both the organic phase (usually composed of an extractant, an alcohol-based modifier, and CF-231) and the aqueous phase (usually an acid chloride solution). Other than specialty alloys (Hastelloy B, C) or exotic metals (zirconium, niobium, and tantalum), plastics, ceramics, and glass are the only materials that are suitable for long-term acid chloride service. In general, plastics and glass were the primary materials exposed to the process solutions during pilot plant operations. The specific plastics used include polyethylene, polypropylene, and PVC. Highly chemically resistant flexible tubing materials such as Tygon® and PharMed®BPT were also part of the system. When considering the surrounding environment, it is important to note that HCl vapor from the acid chloride solutions will corrode most exposed metal surfaces.

Mixer-Settler Design

Custom, polypropylene solvent extraction cells were fabricated for PRO for the pilot program. Polypropylene provides good chemical resistance to the organic solvents and acids being used in the process. Each solvent extraction cell includes a mixer box and settler stage, and two sizes were used for the circuit (see Table 19).

During operation, aqueous and organic flow into a given mixer box through a "T" connection in the bottom. In the mixer box, organic and aqueous are mixed to form an emulsion, which overflows over a first baffle, travels downwards, and exits into the settler under a second baffle. The emulsion separates back into the distinct organic and aqueous phases in the settler, with the less dense organic phase rising to the top, and the denser aqueous phase moving to the bottom. The organic is collected from the top of the settler through a trough that is connected through the bottom of the tank with a fixed standpipe. The aqueous phase flows underneath a dam at the far end of the settler into a chamber containing an adjustable standpipe. By adjusting the height of the standpipe, the interface-level in the settler can be set.

Table 19. Mixer settler design.

Circuit	Square Mixer Box (cm)	Mixer Box Volume (L)	Settler Length (cm)	Settler Width (cm)	Settler Surface Area (cm^2)	Settler Volume (L)
Fe	8.89	0.70	10.16	8.89	90.3	0.80
Ti	12.7	2.05	20.32	12.7	258.1	3.28

Pumps and Tubing

Aqueous and organic feed flows and recycle flows were pumped using Masterflex® peristaltic pump drives and heads. The pump heads were fitted with peristaltic tubing in a variety of materials and sizes, depending upon the flowrate and solution being pumped. In general, Tygon Fuel & Lubricant® tubing was used for organic phases and Pharmed BPT® tubing was used for aqueous phases. Masterflex® pumps and tubing were also used to drive the hot water circulation system used to maintain temperature in the mixer-settlers.

Polyethylene was used to carry both aqueous and organic process solutions. In all the peristaltic pump heads, the appropriate tubing (Tygon or PharMed) was used to pump the solutions.

Mixers and Impellers

To provide mixing in the solvent extraction cells, IKA RW-20® adjustable rpm mixers were paired with pump-mix impellers. The impeller blade used had a diameter of 2" and was generally positioned near the bottom of the mixer box chamber to generate the required amount of vacuum to draw the aqueous and organic phases into the mixer box.

Campaign 1

In this phase of the program, setup of the pilot circuit was performed, and buildup of solutions in the various SX circuits was achieved in the preparation of subsequent phases that examine the impurity buildup in the circuit from integrated operation of specific streams which include the following:

- Ti SX raffinate which will build in impurities after each cycle of recycling and be reintroduced back to the leach stage
- TiO_2 precipitation filtrate which will contain residual impurities from the Ti pregnant strip and will result in build up of potentially deleterious elements with respect to TiO_2 purity.

Leaching

Leaching for the mini pilot plant (MPP) was conducted in a 45L mixing tank fitted with a water-cooled condenser, air-powered agitator, and 3kW Teflon-coated immersion heater (Fig. 24).

Figure 24. Leach tank.

Operating conditions for leaching were determined based on results from the prior program conducted in 2016 (PRO 16-05). The parameters are presented in Table 20. In this campaign, four leaches have been completed using those parameters that produced ~220 L of PLS for the filling and operation of the solvent extraction circuits to an initial steady state. Leach solution compositions are presented in

Table 20. The initial leach was performed with a sample from the 2016 study, as the new sample of ilmenite concentrate was not available at startup. Subsequent leaches were performed with Drum 5 material.

Table 20. Leach parameters.

Pulp Density	HCl Concentration	$MgCl_2$ Concentration	Temperature	Duration	Particle Size
10%	6M	220g/L	70°C	4h	P80 – 38µm

Once the leach was complete, the slurry was filtered using a 152.4 mm x 152.4 mm (6” x 6”) plate and frame filter press. The press contained four frames, for a total of 0.19 m^2 (288 in^2) of surface area. The solution was pumped through the press using an air-powered diaphragm pump with Teflon internals. A filtration cloth was used between the plate and frames to recover the solid residue material. The filter press is presented in Figure 25.

Figure 25. Filter press.

Upon completion of filtration, the wet cake is blown down with air to remove as much PLS as possible. The residue is then washed in the filter press using 2M HCl, and the residue is once again blown down. The acid wash solution is blended with the PLS to be processed in the solvent extraction circuits. The residue is then washed with water to remove any excess HCl, after which it is once again blown down. The residue is then removed from the filter press and placed in an oven to dry to determine the weight of the recovered residue. Samples were taken, and the analyses are contained in Table 21.

Table 21. Campaign 1 leaching PLS analysis.

	Analysis Result PPM							
Campaign 1 Average PLS	**Al**	**As**	**Ca**	**Co**	**Cr**	**Cu**	**Fe**	**K**
	179	<5	3942.9	<5	56.28	113.15	34473.8	1164.8
	Mg	**Mn**	**Mo**	**Ni**	**Ti**	**V**	**Zn**	**FAT**
	69159	336.1	<5	43.6	24590	17.7	189	2

Oxidation

After the PLS is filtered, it is pumped into the oxidation columns displayed in Figure 26 for the conversion of Fe^{2+} to Fe^{3+} and has a capacity of ~45 L in each column and is filled with media to increase surface area. Oxygen is sparged from the bottom of the column. For this study, only one column was utilized. The gas flowrate was set at 4 L/min of oxygen. Samples were taken at regular intervals to determine the extent of oxidation. Based on the results, it required ~32 hours for complete oxidation to take place at ambient temperature, as shown in Figure 27.

Following the oxidation step, the solution was pumped out of the columns and through a polishing filter with a 1 µm cartridge filter to remove any fine particulates in preparation for the solvent extraction stage.

Figure 26. Oxidation columns.

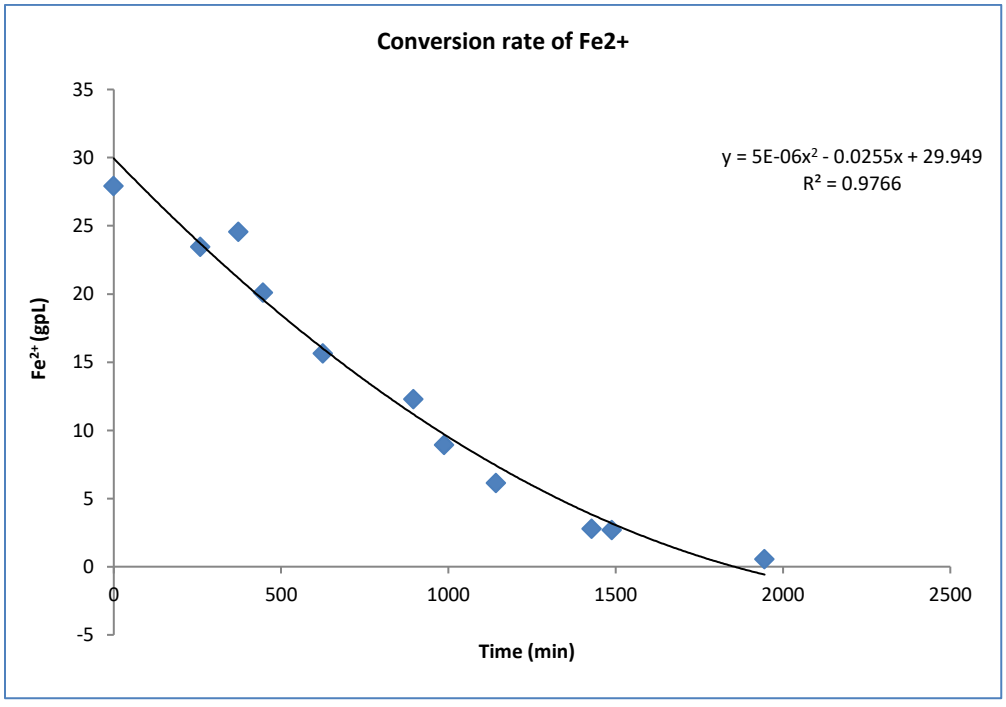

Figure 27. Conversion rate of Fe^{2+} to Fe^{3+} during oxidation.

Iron Solvent Extraction

The iron circuit (Fig. 28) was set up based on the study performed in 2016. The extractant organic composition is presented in Table 22. The circuit staging is presented in Table 23. The circuit operated for 112 hours using the PLS produced from the MPP leaching. Initial operating conditions are presented in Table 24.

Figure 28. Iron SX circuit.

Table 22. Iron solvent extraction organic composition.

Component	Volume Fraction
2-Tridecanone	20%
2-Octanol	20%
Exxal-13	20%
Cansol D80	40%

Table 23. Initial MPP iron circuit stages.

Section	# of Stages
Extraction	5
Scrubbing	1
Stripping	7

Table 24. Initial iron circuit operating conditions.

Stream	Flowrate (ml/min)	O:A
Organic	50	-
Feed	30	1.5:1
Scrub Feed	2.5	15:01
Strip Feed	7.5	5.5:1

The average operational profiles of the solutions in the Fe SX circuit are presented in Table 25. Results indicate that Fe is selectively extracted and results in ~63 ppm in the Fe raffinate. A pregnant strip solution with an average composition of ~93 g/lFe was produced during Campaign 1. Full details of the operation of the Fe SX circuit including operational log sheets and assays of sample sets are presented in Appendix 6 and 12, respectively.

Table 25. Iron SX solutions – Campaign 1 average elemental analysis.

Campaign 1	Analysis results (ppm)						
	Al	Cr	Fe	Mg	Mn	Ti	V
Feed (ppm)	164	47	30285	58994	296	22699	175
Iron raff (ppm)	175	49	63	61752	310	23288	180
Iron preg strip (ppm)	12	5	93769	920	8	401	6

Titanium Solvent Extraction

The titanium circuit (Fig. 29) was set up based on the study performed in 2016. The extractant organic composition is presented in Table 26. The circuit staging is presented in Table 27. In this phase, the circuit operated for 95 hours using the Fe raffinate produced from the Fe SX. Initial operating conditions are presented in Table 28.

Figure 29. Titanium SX circuit.

Table 26. Titanium SX extractant composition.

Component	Volume Fraction
Cyanex 923	20%
Exxal-13	20%
Cansol D80	60%

Table 27. Initial MPP titanium circuit stages.

Section	# of Stages
Extraction	4
Scrubbing	2
Stripping	8

Table 28. Initial titanium circuit operating conditions.

Stream	Flowrate (ml/min)	O:A
Organic	75	-
Feed	28	2.8:1
Scrub Feed	7.5	10:1
Strip Feed	15	5:1

Operational profile of solutions in the Ti SX circuit is presented in Table 29. Results indicate that Ti is selectively extracted and results in ~277 ppm of Ti in the Ti raffinate. The average composition of the pregnant strip solution produced was ~42 g/l Ti in Campaign 1. Full details of the operation of the Ti SX circuit, including operational log sheets and assays of sample sets, are presented in Appendix 7 and 13, respectively.

Table 29. Titanium SX process solution – Campaign 1 average elemental analysis.

Campaign 1	Analysis results (ppm)						
	Al	Cr	Fe	Mg	Mn	Ti	V
Feed (ppm)	178	50	16	61820	304	23614	173
Ti raff (ppm)	151	41	19	50812	218	278	59
Ti preg strip (ppm)	84	23	17	18751	158	42356	166

During operation of the Ti circuit, it was observed that the Mg levels in the strip solution were increasing. It was determined that the cause of the impurity was due to entrainment of aqueous scrub solution in the organic phase in the scrubbing cells. To improve the phase disengagement, an aqueous recycle to the mixer box was implemented to increase the O:A to 1. At high O:A ratios in the mixer box, fine droplets of aqueous are produced, and they are more difficult to coalesce; an O:A closer to 1 in the mixer box helps to mitigate this. The effect of this change was monitored in the next campaign.

Summary

The Campaign 1 MPP operation was successfully implemented with stable operation in both the Fe and Ti SX circuits in preparation for Campaign 2 with no upset conditions, either mechanical or chemical, during the run. There was no observable crud or emulsion formation, and a consistent product and effluent was produced.

Raffinate from the Ti SX circuit was collected in sufficient quantity and quality to be cycled back into the process to observe the effect of impurity buildup, which is the focus in Campaign 2.

Campaign 2

In this campaign, the focus of the operation was on impurity buildup and steady-state operation with the recycling of evaporated Ti raffinate. This was done to determine the effect of impurity buildup on

the robustness of the SX separation of the Fe and Ti circuits along with the subsequent impact on product quality. In addition, hydro-hydrolysis bench testing was continued to establish operating conditions and determine the potential HCl grade/quality.

Leaching

Leaching for the MPP Campaign 2 was conducted in the same apparatus as Campaign 1, which consists of a 45 L mixing tank fitted with a water-cooled condenser, air-powered agitator, and 3kW Teflon coated immersion heater.

Operating conditions were maintained from the previous campaign, and operational parameters are presented in Table 30. However, the bulk of the $MgCl_2$ is recovered from the Ti raffinate stream and recycled back to the leach after evaporation to maintain a water balance. In this phase, a total of seven leaches have been completed, with leaches 5–12 utilizing recycled Ti raffinate. In total, ~440 L of PLS has been produced for the filling and operation of the solvent extraction circuits to an initial steady state and complete recycling of evaporated Ti raffinate. The impurities content in different leaches is shown in Figure 30, and average leach solution compositions in this campaign are presented in Table 31. Full analyses of the PLS are presented in Appendix 5.

Once the leach was complete, the slurry was filtered using a 152.4 mm x152.4 mm (6” x 6”) plate and frame filter press. The press contained four frames for a total of 0.19 m^2 (288 in^2) of surface area.

Table 30. Campaign 2 leach parameters.

Pulp Density	HCl Concentration	$MgCl_2$ Concentration	Temperature	Duration	Particle Size
10%	5.8N	220 g/L	70°C	4h	P80 – 38µm

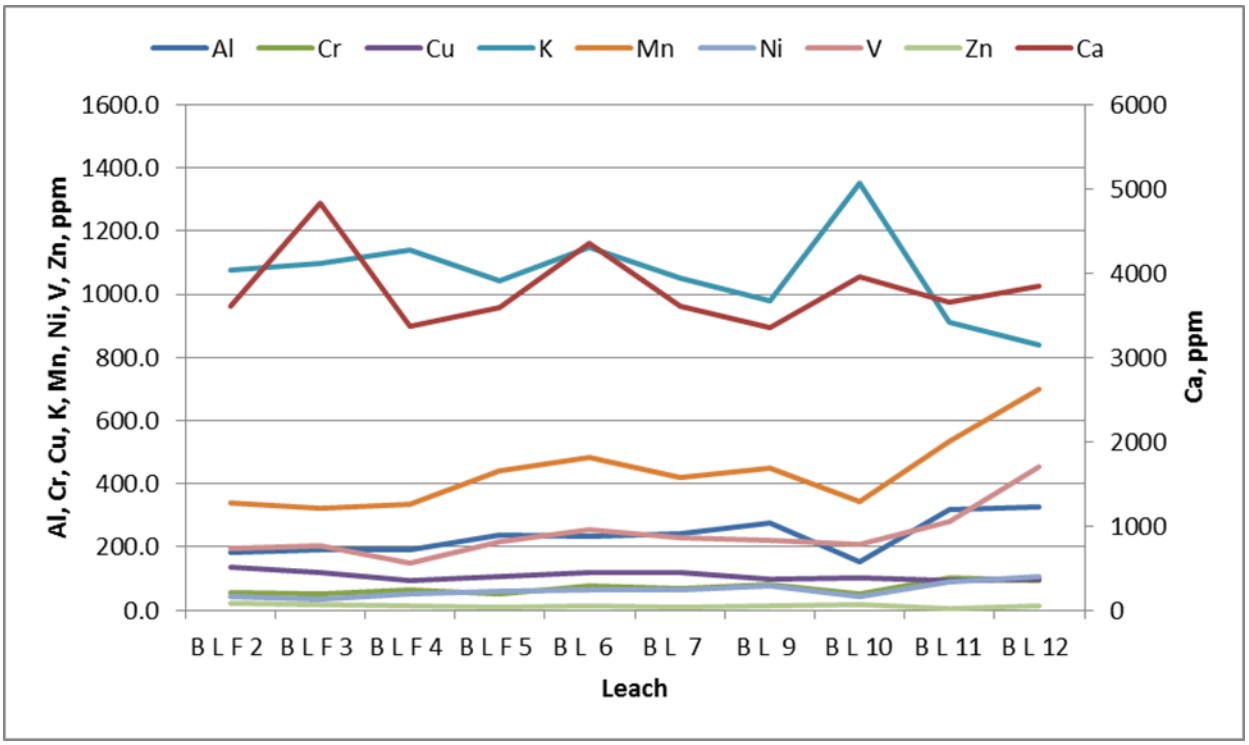

Figure 30. Impurity content in the leach.

Table 31. Campaign 2 average PLS analysis.

Campaign 2 Average PLS	Analysis Result ppm							
	Al	**As**	**Ca**	**Co**	**Cr**	**Cu**	**Fe**	**K**
	273.1	<5	3732.3	<5	80.02	106.2	31570	995.7
	Mg	**Mn**	**Mo**	**Ni**	**Ti**	**V**	**Zn**	**FAT**
	60933.3	505	<5	77	22067	276	11.13	1.9

Raffinate Evaporation and Recycling

Evaporation of the Ti raffinate was performed in a glass evaporation unit and is presented in Figure 31. There are two units in operation, and each unit has a capacity of 12 L of raffinate. The volume of the raffinate is reduced by half to achieve the volume and water balance requirement for subsequent leaching, and a typical analysis of a batch (i.e. feed solution, concentrate, and condensate) is presented in Table 32. The composition of the condensate that is recovered contains no metals but has a free acid level of ~1N HCl. This solution can be recycled in the circuit where dilute acid is required, such as in strip sections for Fe and Ti.

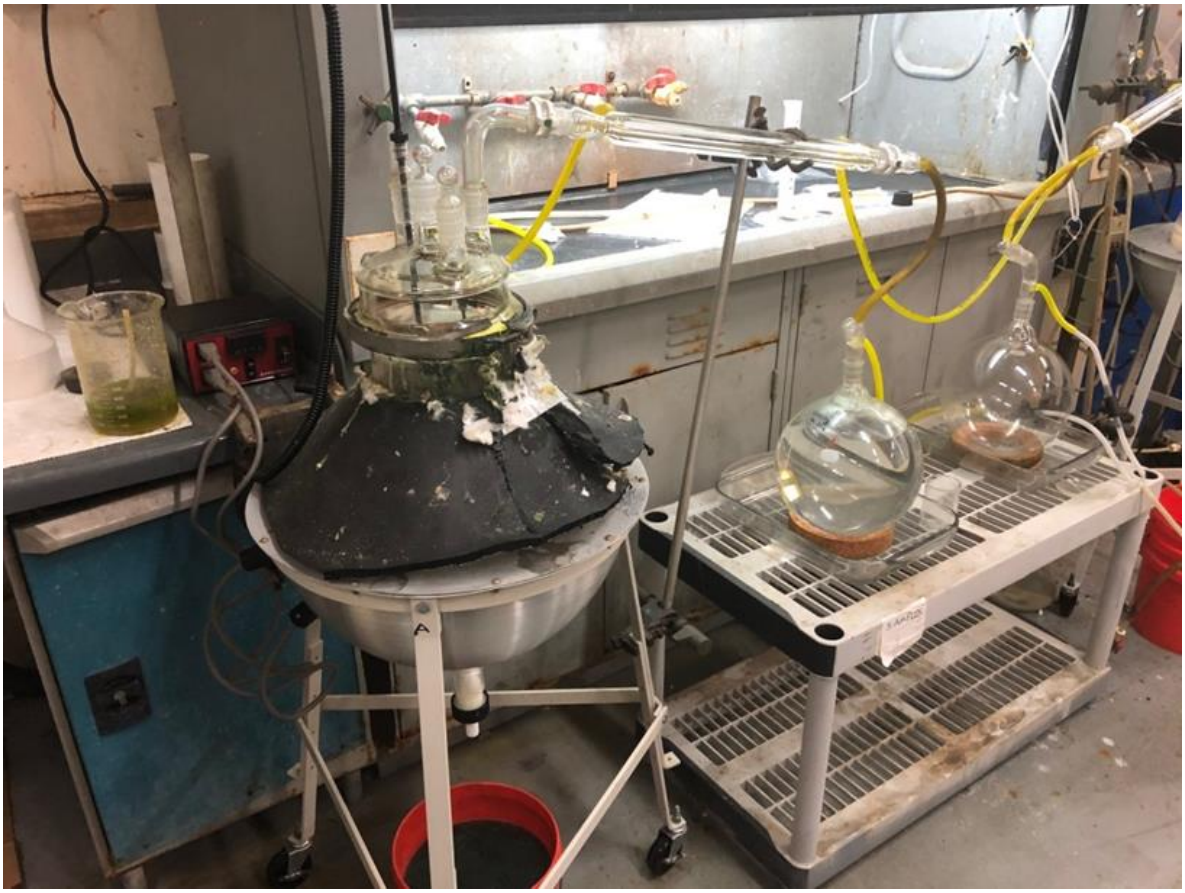

Figure 31. Titanium raffinate evaporation setup.

Table 32. Titanium raffinate evaporation balance (EV-14).

Evaporation Balance (EV-14)	Wt	Analysis Result PPM													
	kg	Al	Ca	Cr	Cu	Fe	K	Mg	Mn	FAT	Ni	Pb	Ti	V	Zn
Feed Ti Raff	14.4	209	4020	69	6	18	1211	67140	277	0.8	63	19	37	135	17
Concentrated Raff (Calculated)	8.3	363	6965	119	10	31	2098	116320	479	-	109	32	64	234	29
Condensate	6.1	-	-	-	-	-	-	-	-	2	-	-	-	-	-

Recycling of evaporated Ti raffinate was initiated from bulk leach 5 with ~50% raffinate recycling, and it has reached ~100% of recycled raffinate from leach 8 onward, which was the expectation in Campaign 2. A typical leach condition with the incorporation of recycled raffinate is presented in Table 33. After recycling of the raffinate to the leach in Campaign 2, there are increases in some of the impurities, notably K, Mn, and V as shown in Figure 30.

Table 33. Leaching condition.

Feed	HCl (31%)	Ti. Raff Evap (kg)		% Solids w/w
8.57 kg	35.89 kg	32.15 kg		10%
		$MgCl_2$	**H_20**	
		11.39	2.76	

Oxidation

After the PLS is filtered, it is pumped into the oxidation columns for the conversion of Fe^{2+} to Fe^{3+} and has a capacity of ~45 L in each column. For this study, only one column was utilized. Two procedures for oxidation were followed:

1. Dynamic: where the solution was circulated through the column in conjunction with O_2 gas sparging.
2. Static: where only O_2 gas was sparged into the column.

The gas flowrate was set at 4 L/min in both cases. Dynamic oxidation was performed when operators of the circuit were present, as supervision was required and was performed in the initial samples BL3 to BL10. Static oxidation was performed with no direct supervision and, as seen in BL 5 and BL 10, typically displayed longer oxidation times to achieve the conversion of Fe^{2+} to Fe^{3+} as seen in Figure 32. A target of <50 ppm Fe^{2+} was established for the oxidation step. Following the oxidation step, the solution was pumped out of the columns and through a polishing filter, with a 1 µm pore size in preparation for the solvent extraction stage.

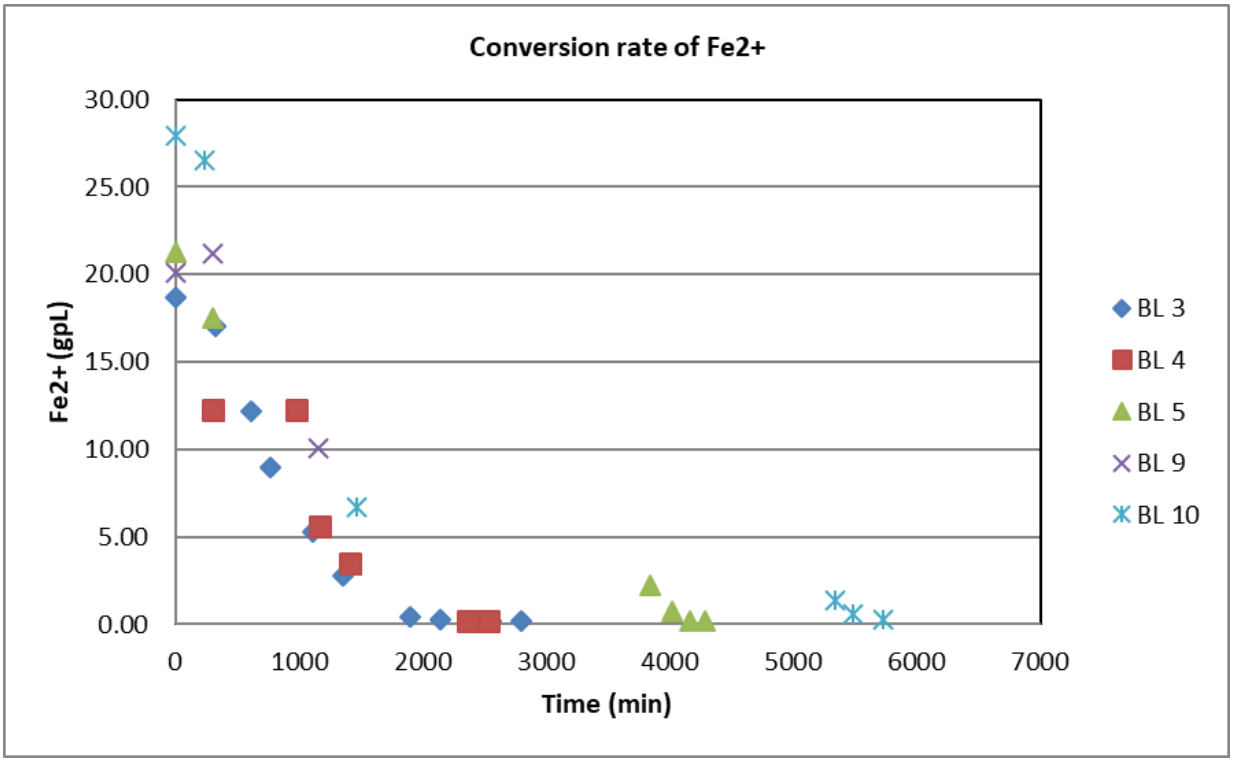

Figure 32. Conversion rate of Fe^{2+} to Fe^{3+} during oxidation.

Iron Solvent Extraction

Campaign 2 has a total operation time of ~237 hours. The combined operation time of the Iron circuit over Campaign 1 and 2 has totaled ~387 hours using the PLS produced from the MPP leaching. The operational conditions of the circuit have not been changed from those used in Campaign 1. The extractant organic composition is presented in Table 34. The circuit staging is presented in Table 35. Initial operating conditions are presented in Table 36. Based on the circuit volume, the estimated number of organic turnovers is ~100 times. Full details of the operation of the Fe SX circuit, including operational log sheets and assays of sample sets, are presented in Appendix 8.

Table 34. Iron solvent extraction organic composition.

Component	Volume Fraction
2-Tridecanone	20%
2-Octanol	20%
Exxal-13	20%
Cansol D80	40%

Table 35. Initial MPP iron circuit stages.

Section	# of Stages
Extraction	5
Scrubbing	1
Stripping	7

Table 36. Initial iron circuit operating conditions.

Stream	Flowrate (ml/min)	O:A
Organic	50	-
Feed	30	1.5:1
Scrub Feed	2.5	15:01
Strip Feed	7.5	5.5:1

The profile of key elements of interest in the Fe SX circuit in the feed, raffinate, and strip streams are presented in Figures 33–40. The results show selective and consistent extraction of Fe over the course of the campaign and a buildup of impurities such as Cr, V, and Mn.

During initial operation of the Fe circuit, high Mg levels were being observed in the Fe pregnant strip solution. The cause of this was due to entrainment of aqueous scrub in the organic being carried over to the stripping section. Entrainment is due to poor phase disengagement in the scrub cell, which can be due to several factors, including:

- High O:A phase ratio in the mixer box
- Long mixing time
- Insufficient settling time
- Low temperatures reducing the kinetics

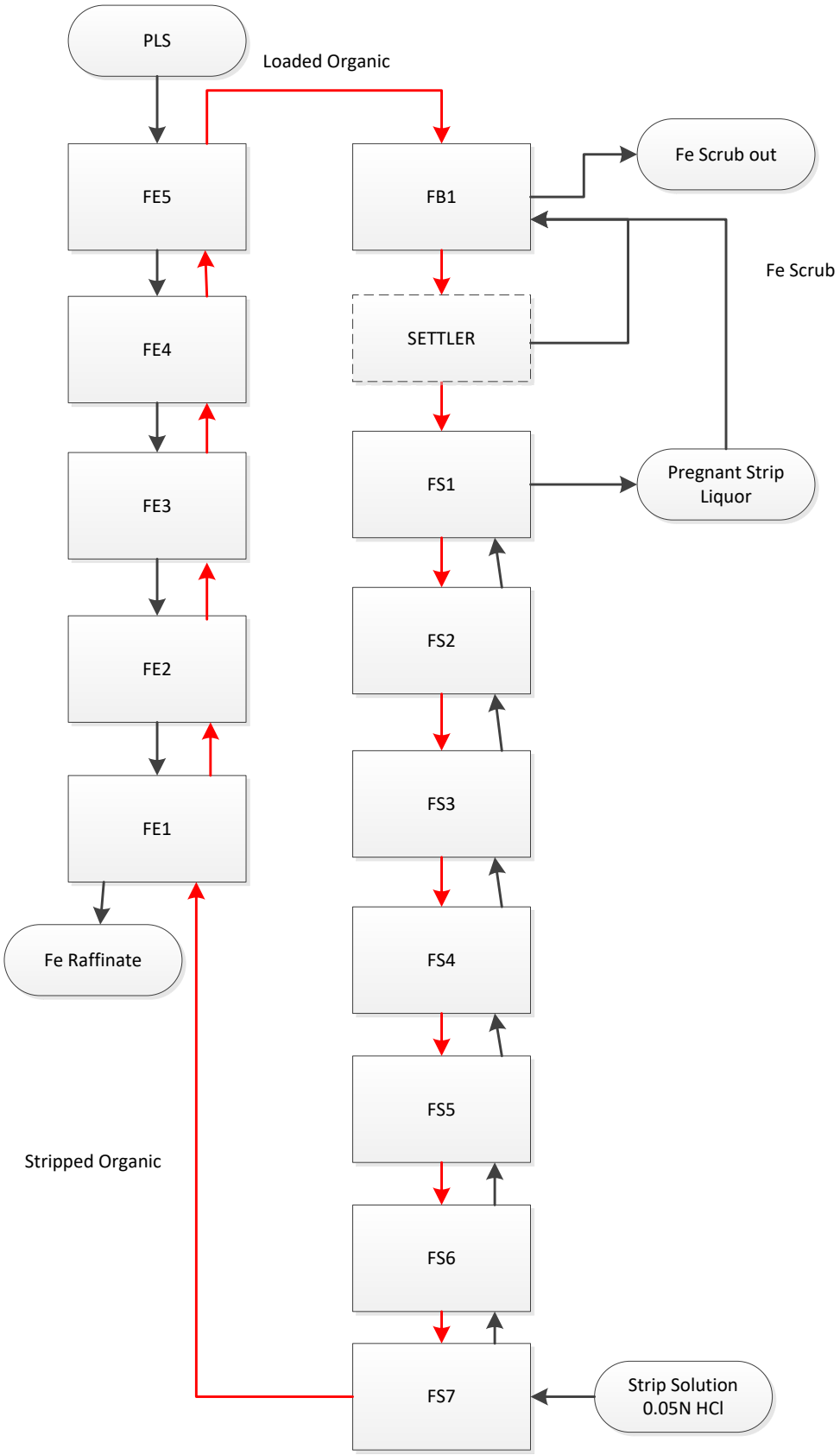

Figure 33. Iron solvent extraction circuit schematic.

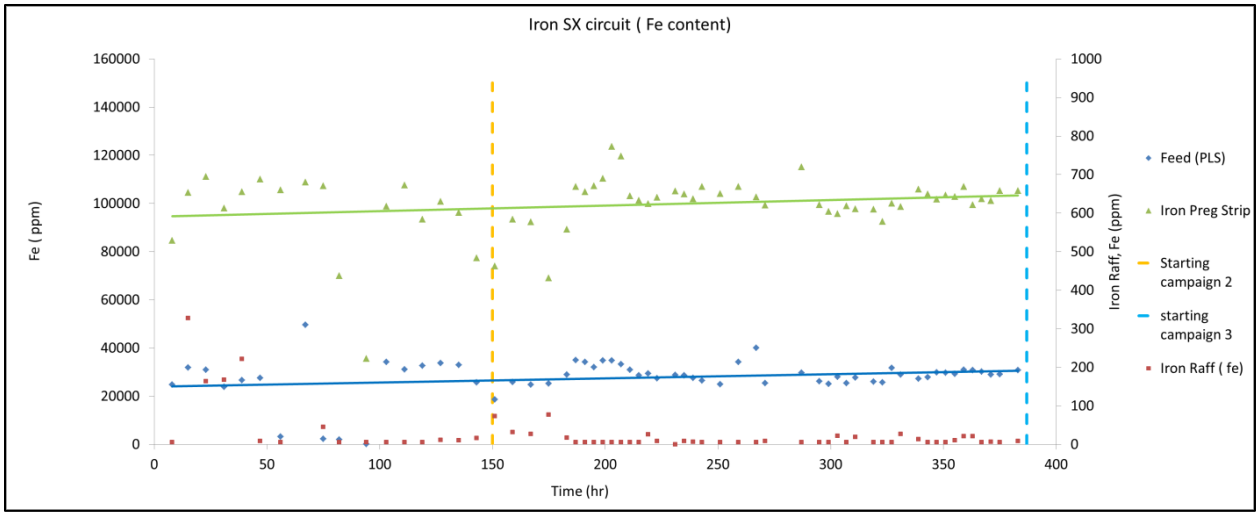

Figure 34. Iron circuit iron analysis.

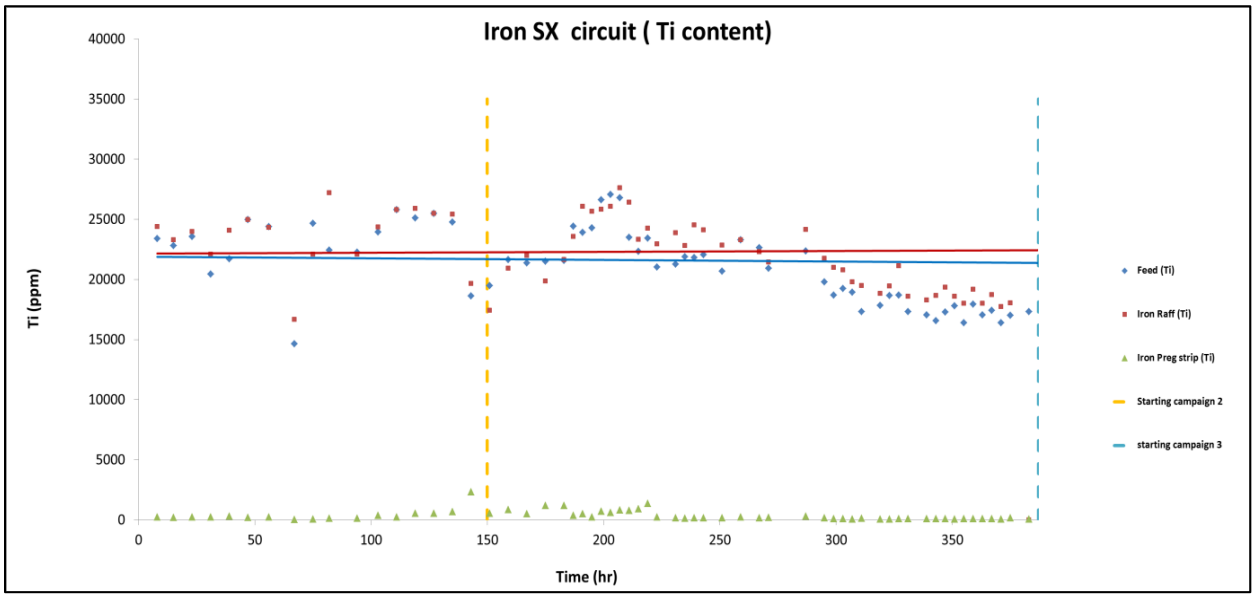

Figure 35. Iron circuit titanium analysis.

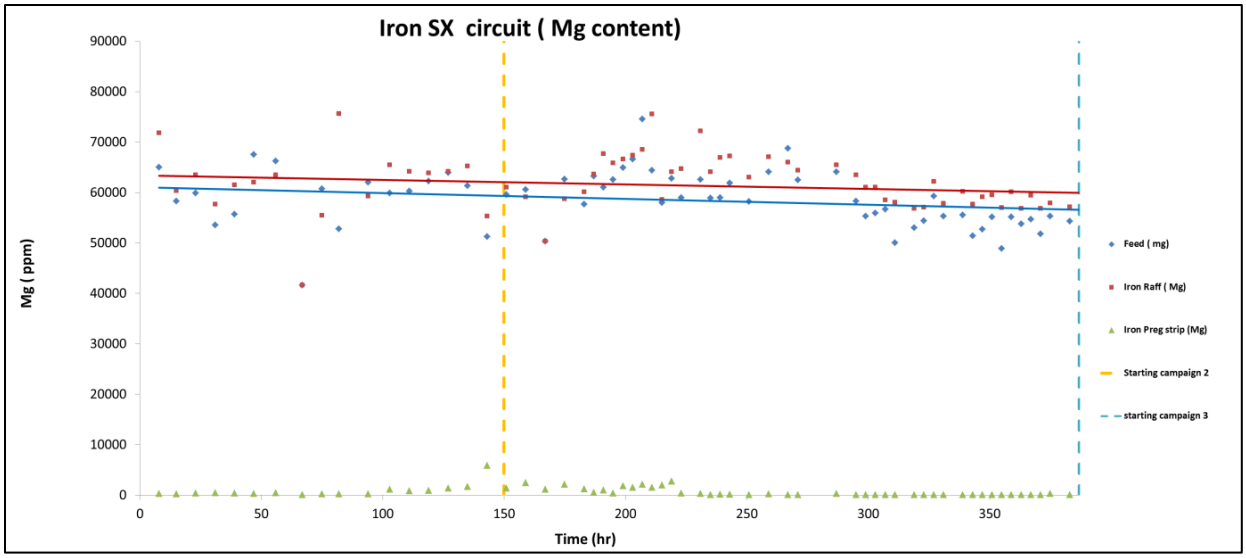

Figure 36. Iron circuit magnesium analysis.

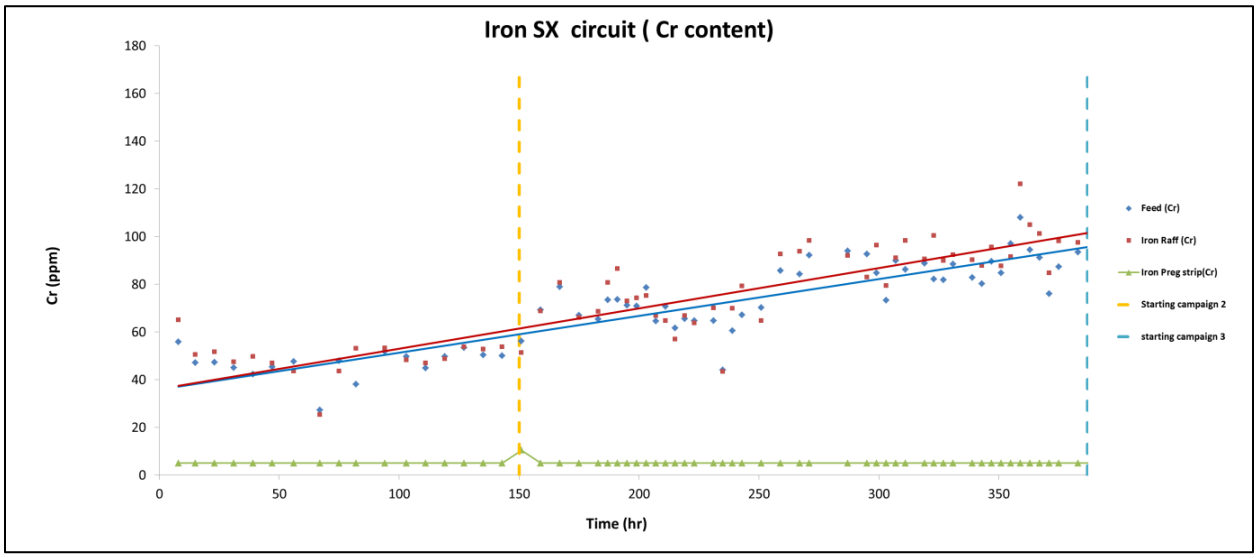

Figure 37. Iron circuit chromium analysis.

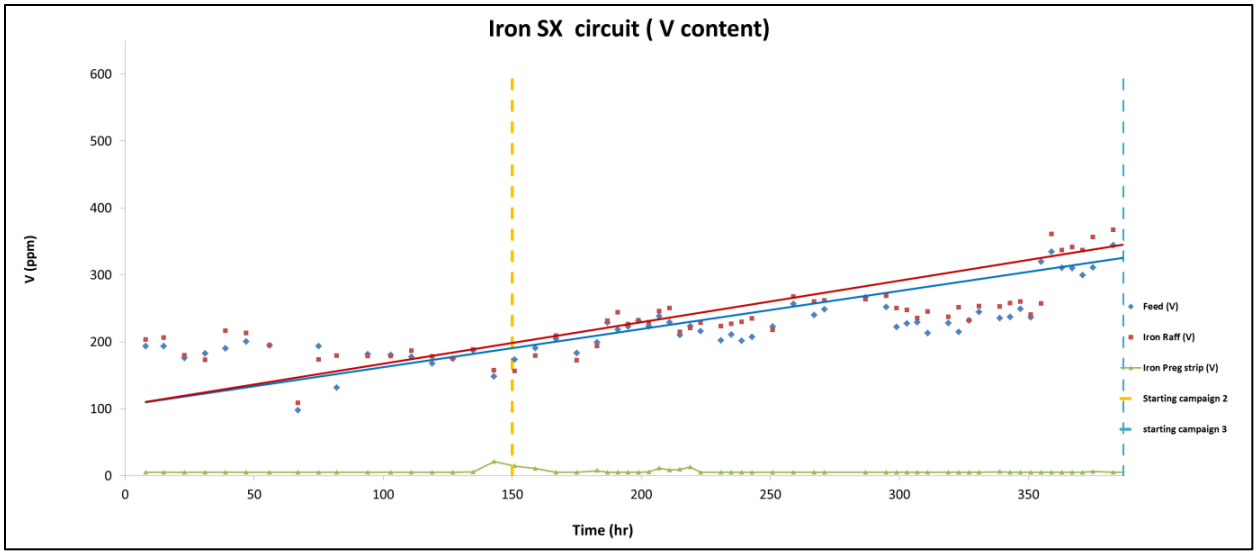

Figure 38. Iron circuit vanadium analysis.

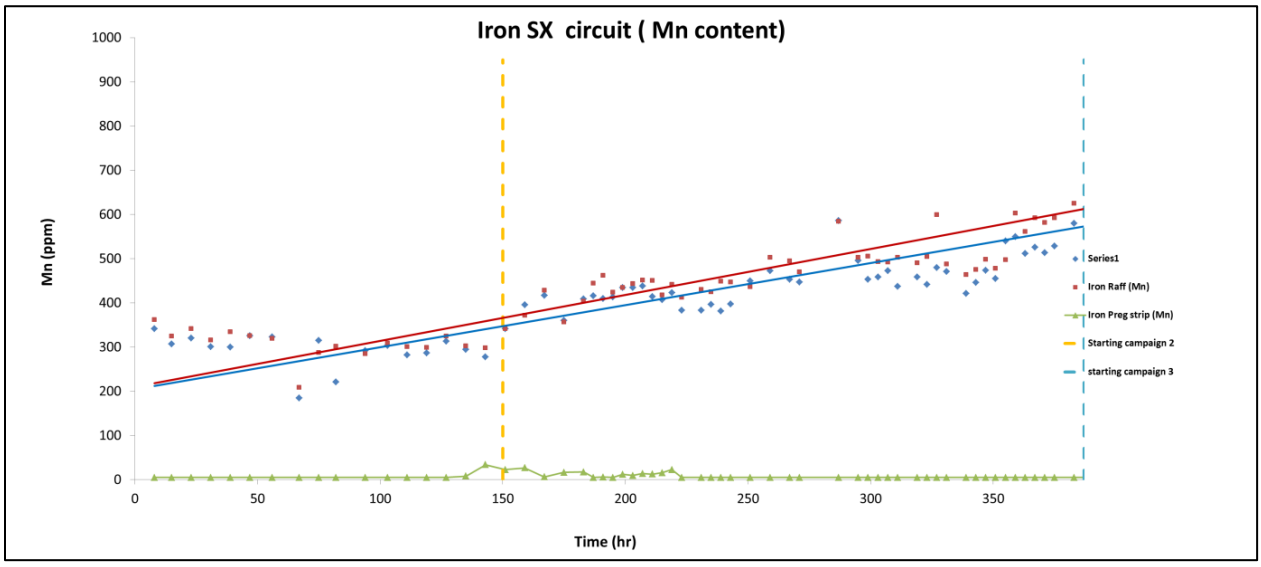

Figure 39. Iron circuit manganese analysis.

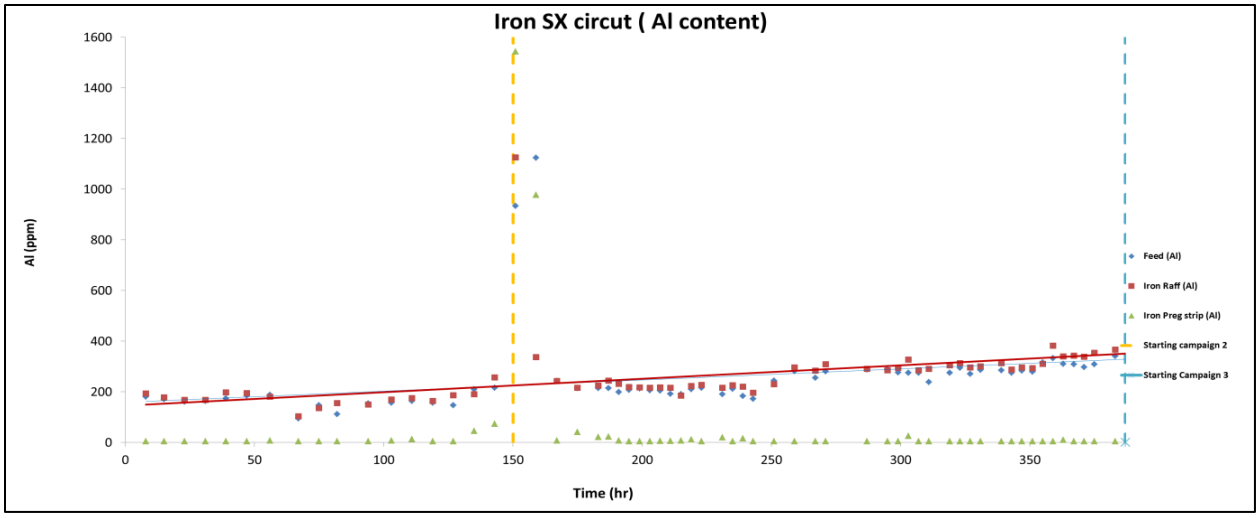

Figure 40. Iron circuit aluminum analysis.

The initial modification to the circuit that was implemented at the end of Campaign 1 was the addition of a raffinate recycle stream to decrease the O:A ratio in the mixer box to improve phase disengagement. This had limited success, and to remedy the situation an after-settler was introduced after the scrub cell to increase the settling time, which resulted in a significant decrease in Mg in the Fe pregnant strip solution. A schematic of the revised circuit is shown in Figure 33.

An average current operational profile of solutions in the Fe SX circuit is presented in Table 37. Results indicate that Fe is selectively extracted and results in 11.5 ppm in the Fe raffinate. A pregnant strip solution of >100 g/l Fe is currently being produced, which is being used in the hydro-hydrolysis test program. As it is indicated in Figures 37–39, the content of Cr, V, and Mn has started to build up after recycling of evaporated Ti raffinate (Campaign 2).

Table 37. Iron SX solutions – Campaign 2 average elemental analysis sample set 51.

Campaign 2	Analysis results (ppm)						
	Al	Cr	Fe	Mg	Mn	Ti	V
Feed (ppm)	254	79	29301	58487	452	20493	240
Iron raff (ppm)	274	83	11	61974	482	21686	252
Iron preg strip (ppm)	8	5	101936	553	7	322	6

Titanium Solvent Extraction

The operational conditions of the circuit in Campaign 2 were maintained from those used in Campaign 1. The extractant organic composition is presented in Table 38. The circuit staging is presented in Table 39. Initial operating conditions are presented in Table 40. The circuit has been in operation for a total of 335

hours over Campaigns 1 and 2 using the PLS produced from the MPP leaching. The Ti SX circuit in Campaign 2 commenced at the 95-hour mark and was in operation for ~240 hours. Based on the circuit volume, the estimated number of organic turnovers is ~35 times.

Table 38. Titanium SX extractant composition.

Component	Volume Fraction
Cyanex 923	20%
Exxal-13	20%
Cansol D80	60%

Table 39. Initial MPP titanium circuit stages.

Section	# of Stages
Extraction	4
Scrubbing	2
Setteler	1
Stripping	8

Table 40. Initial titanium circuit operating conditions.

Stream	Flowrate (ml/min)	O:A
Organic	75	-
Feed	28	2.8:1
Scrub Feed	7.5	10:1
Strip Feed	15	5:1

During operation of the Ti circuit, it was observed that the Mg levels in the Ti strip solution were increasing, with levels as high as 24 g/l Mg. It was determined that the cause of the impurity was due to entrainment of the aqueous scrub solution in the organic phase based on the Ti concentration remaining stable as the Mg concentration dropped. Several operational adjustments were made and included the following:

- To improve the phase disengagement, an aqueous recycle to the mixer box was initially implemented to decrease the O:A to 1. At higher O:A ratios in the mixer box, fine droplets of aqueous are produced, and they are more difficult to coalesce; an O:A closer to 1 in the mixer box helps to mitigate this.
- Volume reducers were added into the scrub mixer box to reduce the mixing time in the mixer box. Excess mixing residence time could result in emulsification and increase the phase disengagement time.
- An after-settler was added to increase the time for phase disengagement and minimize aqueous carry over.

These modifications resulted in a significant reduction of Mg in the Ti pregstrip, as seen in Figure 43, with levels of ~ 2 g/l Mg in the Ti pregnant strip solution. A schematic of the revised Ti circuit is shown in Figure 41.

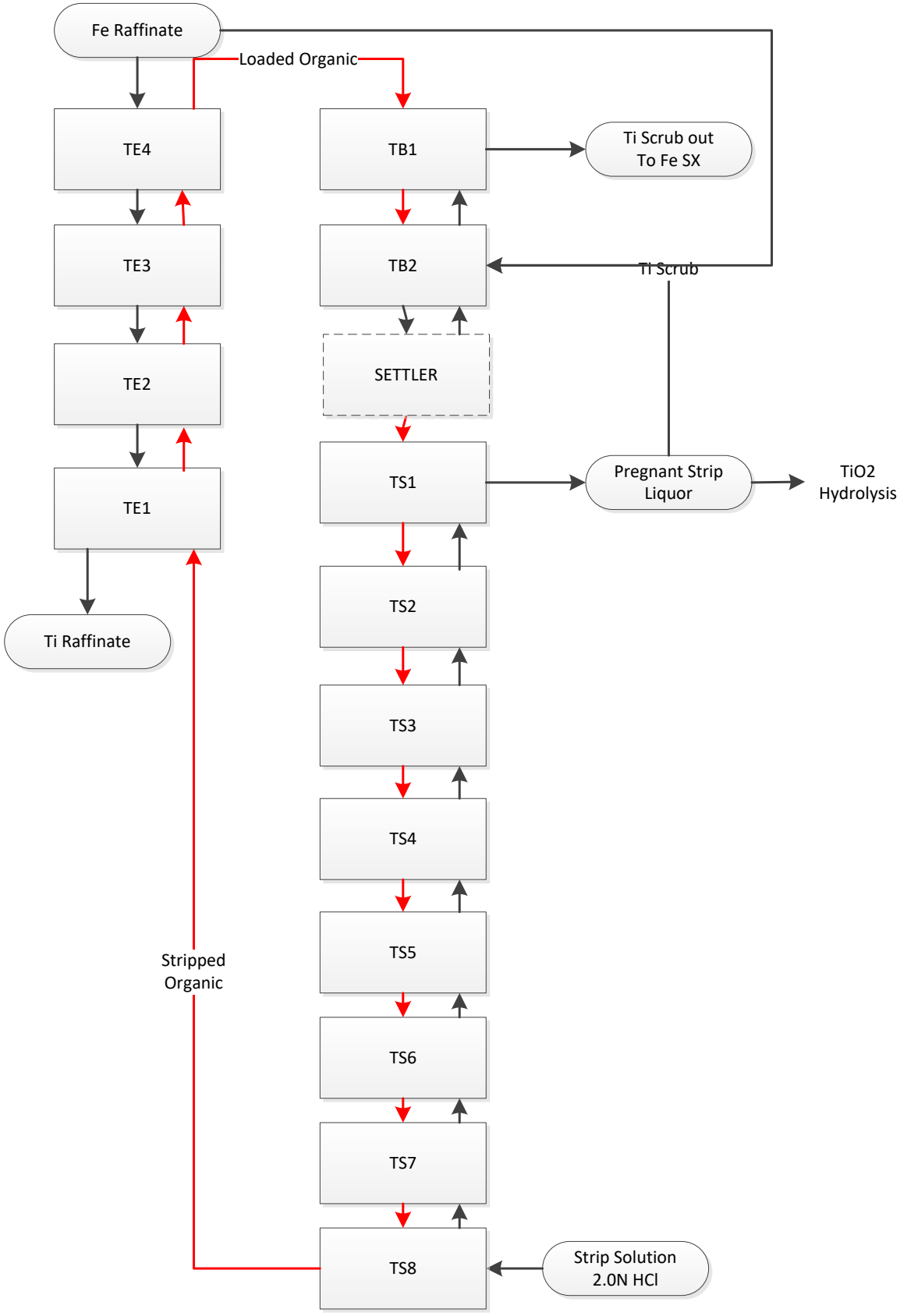

Figure 41. Titanium solvent extraction circuit schematic.

The profiles of key elements of interest in the Ti SX circuit in the feed, raffinate, and strip streams are presented in Figures 42–47. The results show selective and consistent extraction of Ti over the course of the campaign and a buildup of impurities such as Cr, V, and Mn in the Ti raffinate stream.

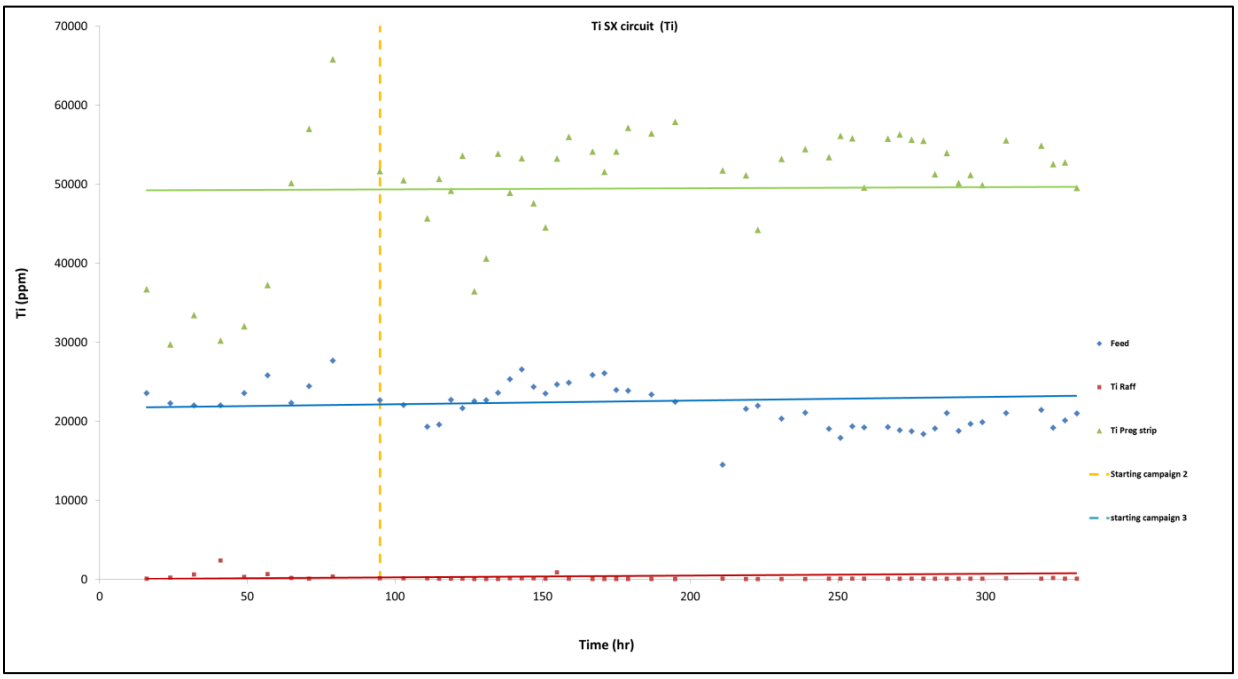

Figure 42. Titanium circuit titanium analysis.

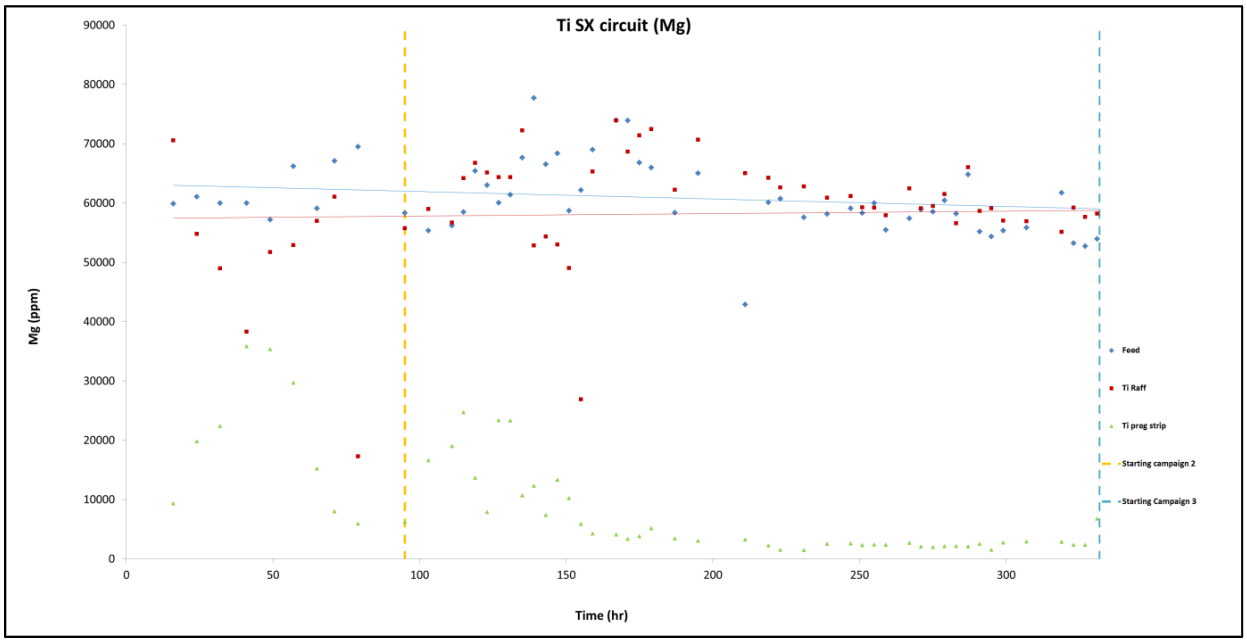

Figure 43. Titanium circuit magnesium analysis.

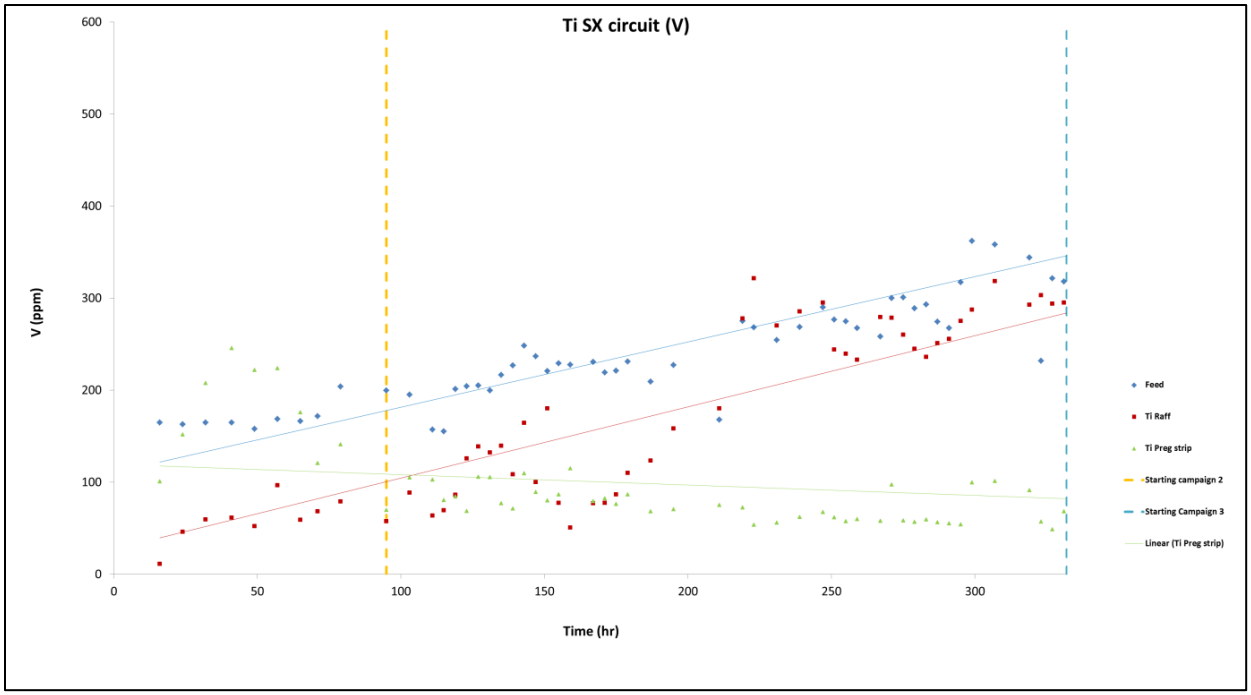

Figure 44. Titanium circuit vanadium analysis.

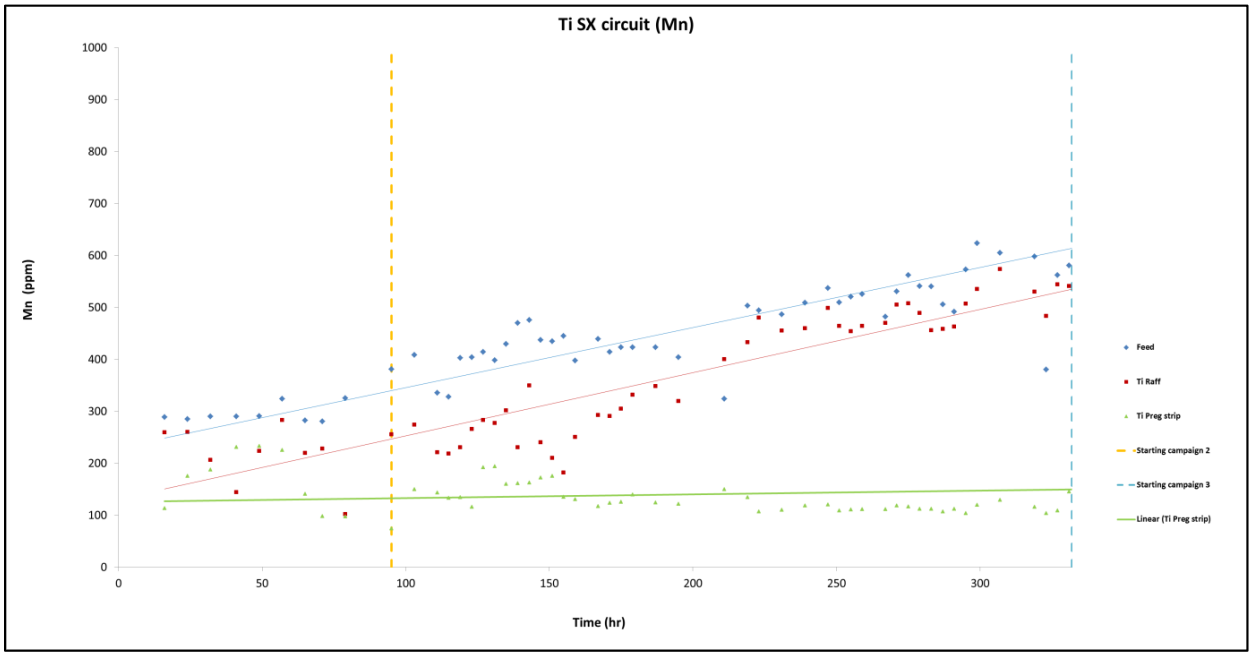

Figure 45. Titanium circuit manganese analysis.

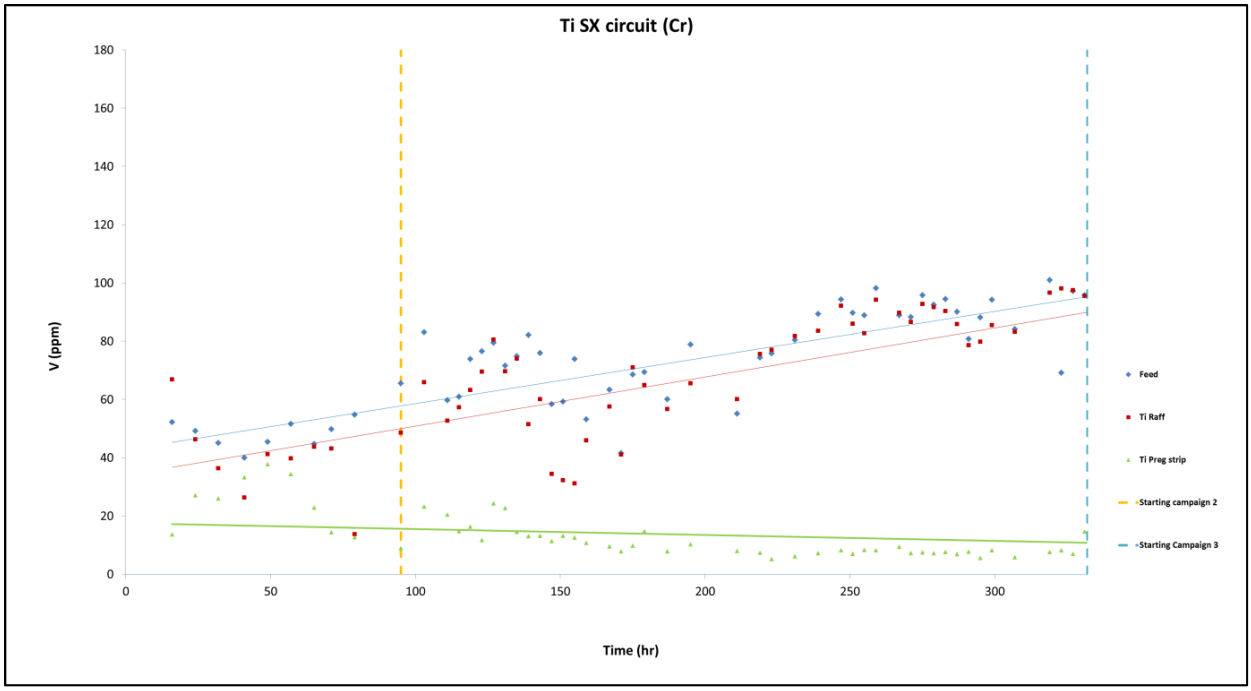

Figure 46. Titanium circuit chromium analysis.

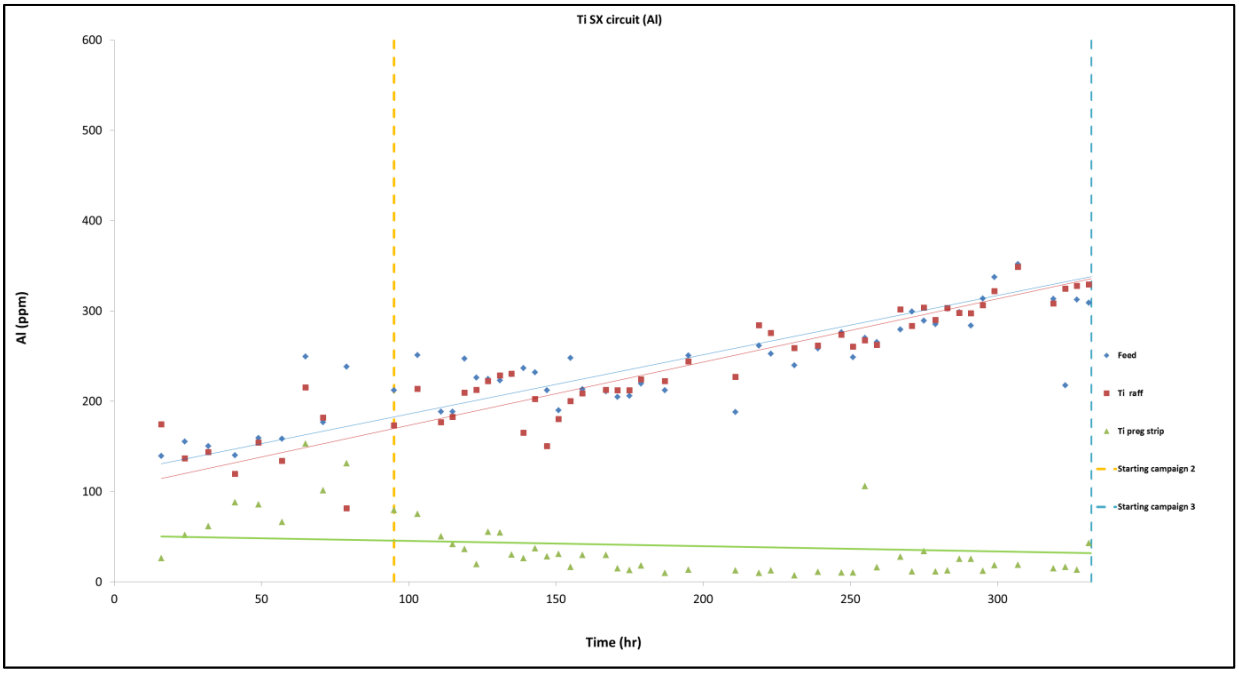

Figure 47. Titanium circuit aluminum analysis.

An average composition of the solutions in the Ti SX circuit over Campaign 2 is presented in Table 41. Results indicate that Ti is selectively extracted and results in 94 ppm of Ti in the Ti raffinate. A pregnant strip solution of ~52 g/l Ti was produced.

Table 41. Titanium SX process Campaign 2 average solution analysis.

Campaign 2	Analysis results (ppm)						
	Al	Cr	Fe	Mg	Mn	Ti	V
Feed (ppm)	253	81	21	59606	501	21867	274
Ti raff (ppm)	271	76	9	59925	428	94	227
Ti preg strip (ppm)	26	10	8	5627	129	52127	76

Titanium Dioxide Precipitation Testing

Titanium strip liquor from Campaign 2 undergoes pre-treatment prior to precipitation. These pre-treatment steps are essential and have been an important technology development during the pilot campaigns.

Precipitation occurs in an agitated vessel maintained at 95–100°C. Greater than 99% precipitation of Ti strip liquor values has been achieved in pilot plant operations. The reaction for the thermal precipitation of the product is presented below:

$$TiOCl_2\ (aq) + 2H_2O\ (l) \rightarrow TiO(OH)_2\ (s) + 2HCl\ (aq)\ \text{(Precipitation)}$$

$$TiO(OH)_2\ (s) \rightarrow TiO_2\ (s) + H_2O\ (l)\ \text{(Calcination)}$$

$$\textbf{Net Rxn: } \mathbf{TiCl_4 + 2H_2O \rightarrow TiO_2 + 4HCl}$$

After the precipitation reaction, the TiO_2 slurry proceeds to filtration and product post-treatment. The post-treatment procedure involves further washing and filtration. Finally, the treated TiO_2 is dried and calcined. The calcined product can go to a surface treatment step, depending on the end-user's application. A block flow diagram for TiO_2 production from pregnant strip solution is presented in Figure 48.

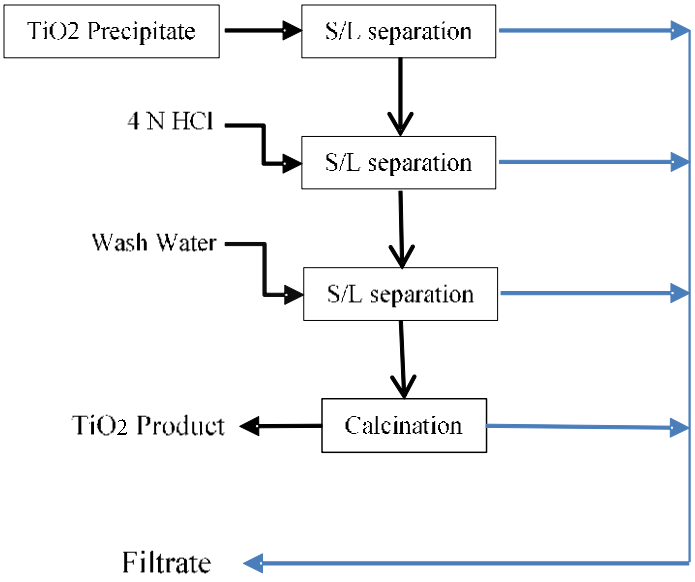

Figure 48. Block flow diagram for TiO_2 thermal precipitation and calcination.

Experimental

Ti pregnant strip solution from Campaign 2 (Table 42) was used to produce TiO_2 by thermal precipitation and calcination, and a total of 13 batches were run to produce a TiO_2 precipitate. Kinetics of the precipitation reaction are presented in Figure 49 for precipitation tests 8 and 13 and indicate that titanium precipitation is completed after nine hours, where greater than 98% of the Ti in pregnant strip solution is recovered.

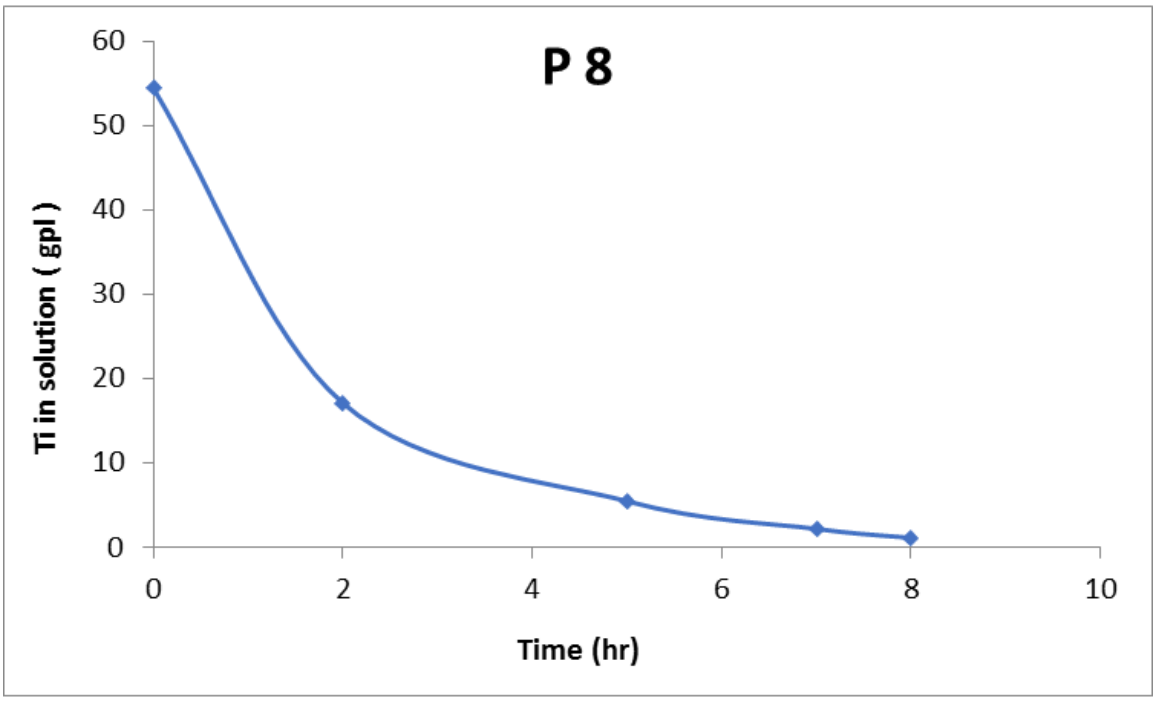

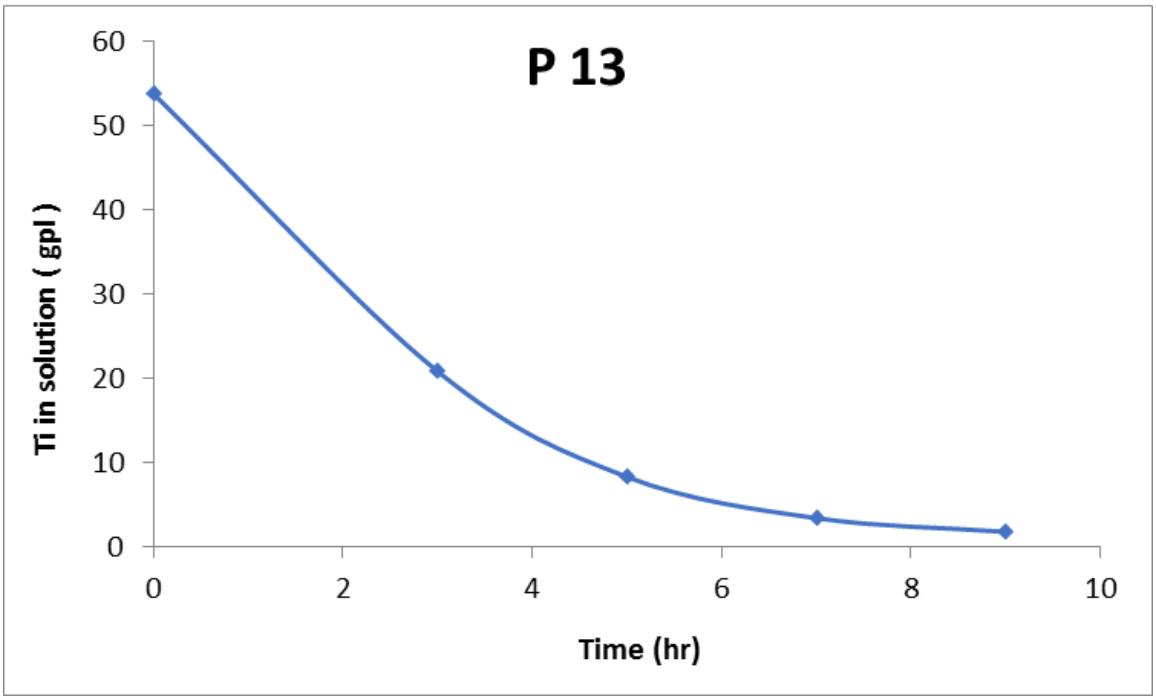

Figure 49. Precipitation kinetic in Campaign 2.

Table 42. Comparison of titanium pregnant strip solution quality from prior study (PRO 16-05) and current study (PRO 18-02).

Sample Description	Analysis Result PPM															
	Al	As	Ca	Co	Cr	Cu	Fe	K	Mg	Mn	Mo	Ni	Pb	Ti	V	Zn
PRO 16-05 Ti Preg Strip	12	2	116	42	8	154	11	177	4060	108	<0.05	4	1	44700	37	3
PRO 18-02 Ti Preg Strip (SS 36)	25	<5	191	<5	7	85	24	453	2040	107	<5	<5	<5	53900	57	9

Titanium Dioxide Product

The quality of calcined titanium dioxide that was produced in this campaign was examined. The impurities in the sample are shown in Table 43 and Figure 50. The purity of titanium dioxide is 99.56%.

The calcined and non-calcined products were also examined by mineralogical, mineral chemical, and lithogeochemical analysis methods.

Table 43. Calcined titanium dioxide, Campaign 2, test 10.

Assay Impurities in the iron oxide product (%)							
Ag_2O	Al_2O_3	CuO	P_2O_5	SO_2	Others	Total impurity	TiO_2
0.0009	0.2267	0.00088	0.0916	0.0798	0.036	0.4359	99.56

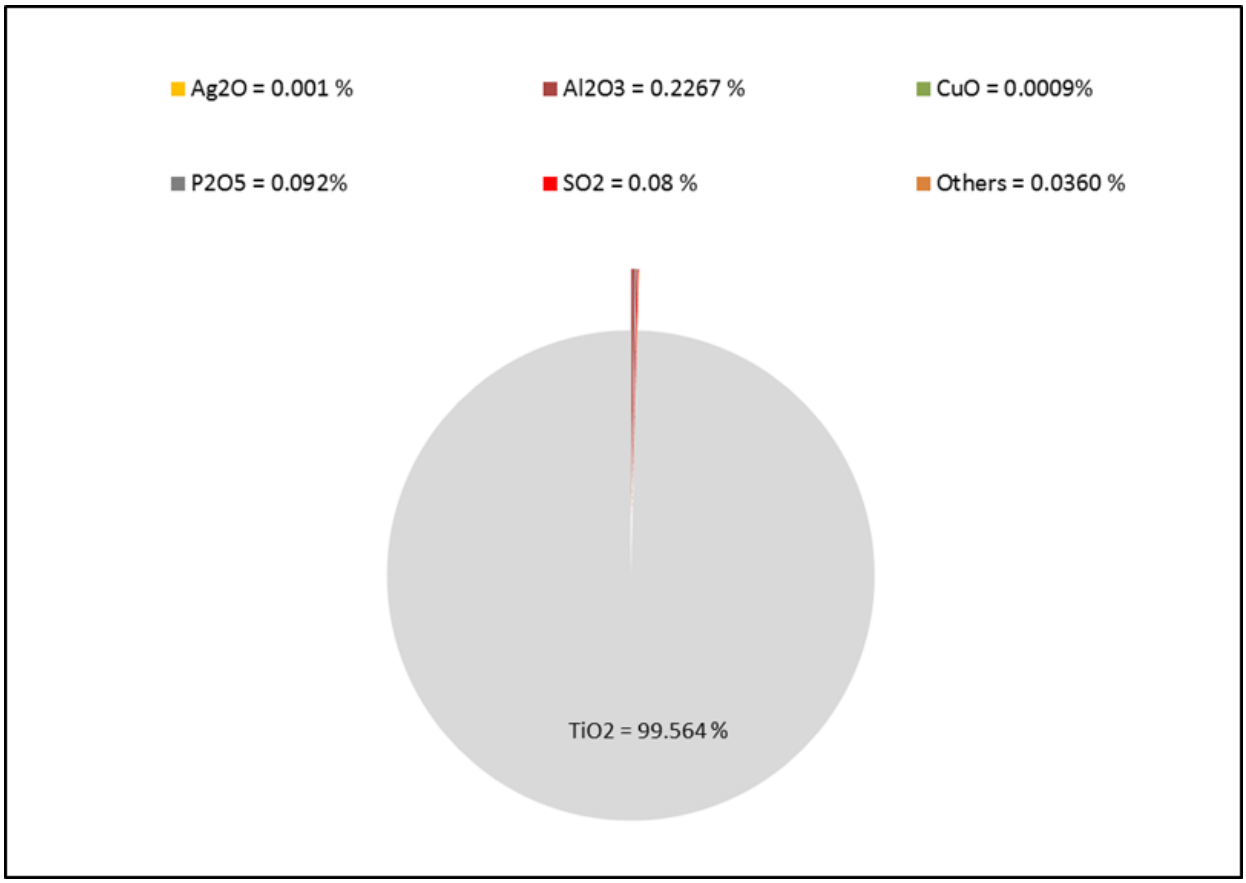

Figure 50. Titanium dioxide impurities content in Campaign 2.

Mineralogical Analysis (XRD)

Mineralogical analysis of the Campaign 2 titanium dioxide precipitates was performed utilizing x-ray diffraction analysis. Two samples of Campaign 2 titanium dioxide precipitates were evaluated. These included the non-calcined sample 1802-P-10-1 (NRRI sample number ML-66) and calcined sample 1802-P10-2 (NRRI sample number ML-67). As indicated in Table 8, the mineralogy of these precipitates was determined to be rutile.

Mineral Chemical Analysis

Two samples of Campaign 2 titanium dioxide precipitates underwent mineral chemistry analysis at the Electron Probe Microanalyzer located at the EML at UMTC. These include samples 1802-P10-1 (NRRI sample number ML-66) and 1802-P10-2 (NRRI sample number ML-67), which represent non-calcined and calcined Campaign 2 titanium dioxide precipitates, respectively.

Rutile was the single mineral phase identified in the titanium dioxide precipitates from Campaign 2. Results of electron microprobe mineral chemical analysis and stoichiometric calculations are included in Appendix 4: Tables A4-27 and A4-28.

Figure 51 is a backscatter image of sample 1802-P10-1 (ML-66) obtained during EMPA analysis. Five types of titanium dioxide precipitate morphologies were identified: A) angular to subangular composite particles greater than 100 µm in diameter composed of numerous 1–30 µm diameter circular (presumably spherical in three dimensions) rutile precipitates that are locally concentrically zoned (Figs. 51A and 51B); B) elongate (possibly platy in the third dimension) rutile precipitates that have growth textures roughly perpendicular to the long axis of the particles that range from 30 µm to 150 µm in length and 5 µm to 10 µm in width (Figs. 51B and 51C); C) elongate composite rutile precipitates composed of elongate rutile particles such as described in (B) and round (presumable spherical in three dimensions), locally concentrically zoned rutile spheres ranging from 10 µm to 30 µm in diameter; D) individual, commonly concentrically zoned rutile spheres ranging from approximately 5 µm to 25 µm in diameter (Fig. 51A to 51E); and E) composite rounded to oval (presumable spherical to oblong in three dimensions) rutile spheres composed of a combination of one or more round (spherical) rutile spheres that range from 10 µm to 20 µm in diameter (Figure 51D). Low analytical totals (see Appendix 4) for the lighter gray material that forms the matrix to the composite fragments suggest that this may be composed of a combination of titanium dioxide and an organic compound. Further research should be conducted to fully characterize this material.

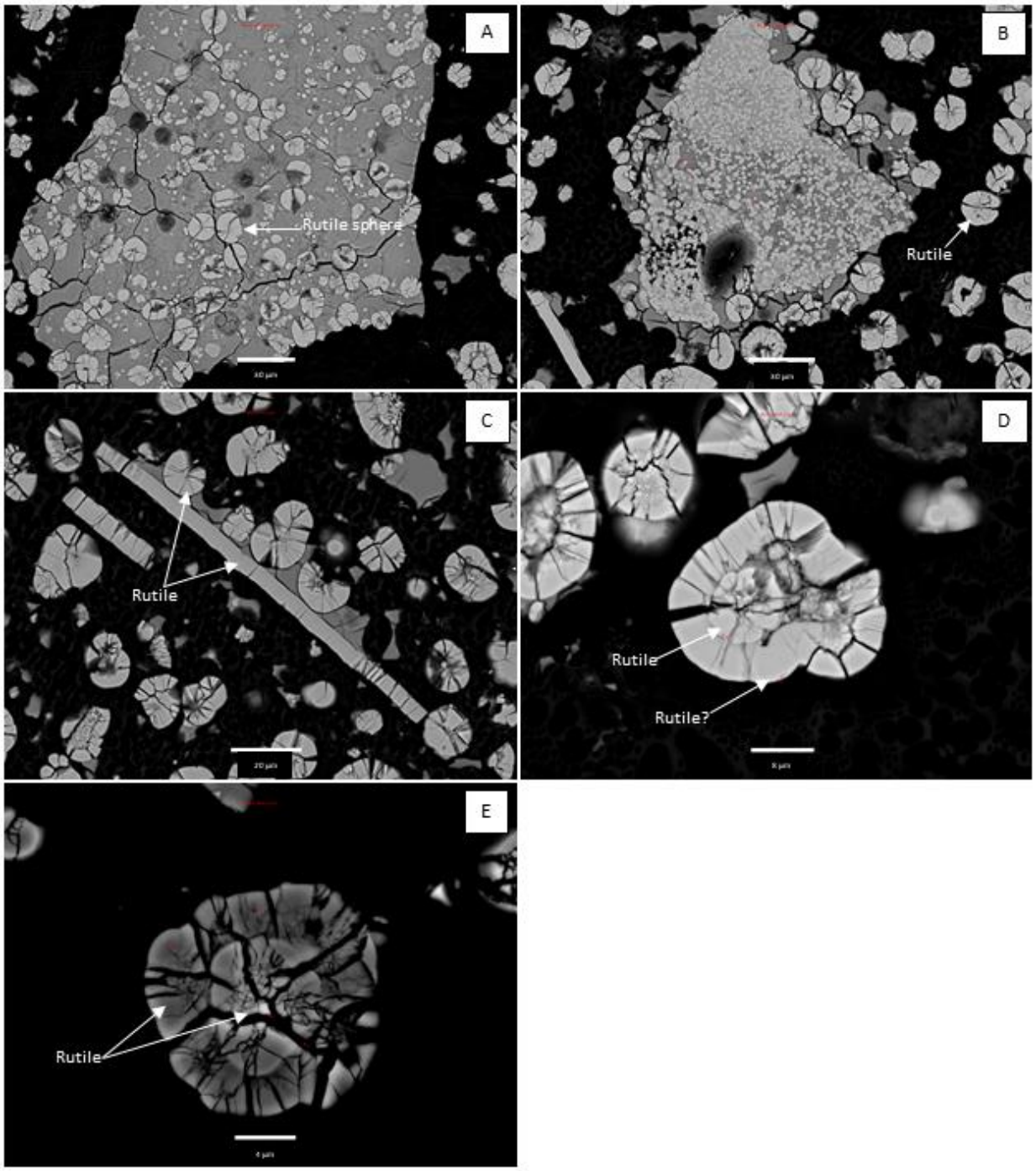

Figure 51. Electron microprobe backscatter images of Campaign 2 titanium dioxide (rutile) precipitates in sample 1802-P10-1 (ML-66). A) Composite fragment comprised of medium-gray matrix and 2 µm–10 µm rutile spheres. Scale bar is 30 µm. B) Composite fragment composed of light gray matrix with 1 µm–10 µm rutile spheres. Note elongate lathe-like rutile fragment in lower left hand corner of the photograph. Scale bar is 30 µm. C) Mixture of composite elongate rutile precipitate, elongate lathe-like rutile precipitate, and circular, locally concentrically zoned rutile spheres. Scale bar is 20 µm. D) Close-up of 10 µm–15 µm concentrically zoned rutile spheres and 15 µm–20 µm composite rutile precipitate. Scale bar is 8 µm. E) Close-up of concentrically zoned rutile spheres. Medium-gray cuspate fragments represent matrix of composite fragments. Scale bar is 4 µm. Red numbers and circles in images are analysis locations.

Mineral chemical analyses of non-calcined Campaign 2 titanium dioxide precipitates from sample 1802-P10-1 (ML-66) are shown in Table 44. Rutile was the sole mineral phase identified. The composition of the rutile was dominated by TiO_2 (97.580%–98.920%), with subordinate SiO_2 (0.026%–0.488%), FeO (0.000%–0.008%), MnO (0.000%–0.053%), MgO (0.027%–0.160%), V_2O_3 (0.000%–0.017%), Cr_2O_3 (0.000%–0.022%), NiO (0.004%–0.025%) and Cl (0.007%–0.051%). Overall, the TiO_2/Total ratio varied from 0.993 to 0.998.

Table 44. Electron microprobe analyses of Campaign 2 sample 1802-P10-1 (ML-66). This sample is non-calcined.

Electron Microprobe Analysis – TiO_2 Precipitate Rutile Campaign 2 Non-Calcined (n = 4)													
Sample	Description	Phase	SiO_2	TiO_2	Al_2O_3	FeO	MnO	MgO	V_2O_3	Cr_2O_3	NiO	Cl	Total
ML-66-5-59-2	Round Rutile Rim	Rutile	0.488	98.135	0.000	0.000	0.012	0.160	0.000	0.000	0.004	0.045	98.844
ML-66-6-61-2	Round Rutile Inner Rim	Rutile	0.126	97.580	0.000	0.000	0.008	0.064	0.000	0.000	0.004	0.051	97.834
ML-66-8-66-2	Round Rutile Outer Core	Rutile	0.026	97.727	0.000	0.000	0.053	0.027	0.014	0.000	0.025	0.007	97.879
ML-66-9-67-1	Elongate Rutile Lathe Core	Rutile	0.061	98.920	0.000	0.008	0.000	0.066	0.017	0.022	0.016	0.012	99.123
		Minimum	***0.026***	***97.580***	***0.000***	***0.000***	***0.000***	***0.027***	***0.000***	***0.000***	***0.004***	***0.007***	***97.834***
		Maximum	***0.488***	***98.920***	***0.000***	***0.008***	***0.053***	***0.160***	***0.017***	***0.022***	***0.025***	***0.051***	***99.123***
		Average	***0.175***	***98.091***	***0.000***	***0.002***	***0.018***	***0.079***	***0.008***	***0.006***	***0.012***	***0.029***	***98.420***
		Median	***0.094***	***97.931***	***0.000***	***0.000***	***0.010***	***0.065***	***0.007***	***0.000***	***0.010***	***0.029***	***98.362***
		St. Deviation	***0.184***	***0.520***	***0.000***	***0.003***	***0.021***	***0.049***	***0.008***	***0.010***	***0.009***	***0.019***	***0.572***

One analysis of the light gray matrix of the composite fragments was performed to evaluate the composition of this material. The results of this analysis can be found in Appendix 4: Table A4-28, Sample ML-66 Composite (Number 11, Line 71). The analytical result is questionable due to the low analytical total (91.616%). This material may represent a mix of titanium dioxide and an unknown organic phase with minor chlorine, although the analytical result indicates stoichiometric rutile. Further testing of this matrix material will be required.

Figure 52 is a backscatter image of sample 1802-P10-2 (ML-67) obtained during EMPA analysis. This sample represents titanium dioxide precipitates from Campaign 2 that have been calcined. Similar fragment types to those identified in sample 1802-P10-1 (ML-66) are present. As well, curvilinear elongate fragments composed of rutile ranging from approximately 60 µm to 150 µm in length and 5 µm to 15 µm in width were identified. Like the elongate fragments identified in 1802-P10-1 (ML-66), these fragments locally illustrate growth textures (locally herringbone-like) oriented approximately perpendicular to the length of the fragments. It is also worth noting that the central zones in the concentrically zoned round (presumably spherical in three dimensions) rutile precipitates commonly appeared to contain considerably more porosity than the central cores of concentrically zoned rutile precipitates in the non-calcined sample 1802-P10-1.

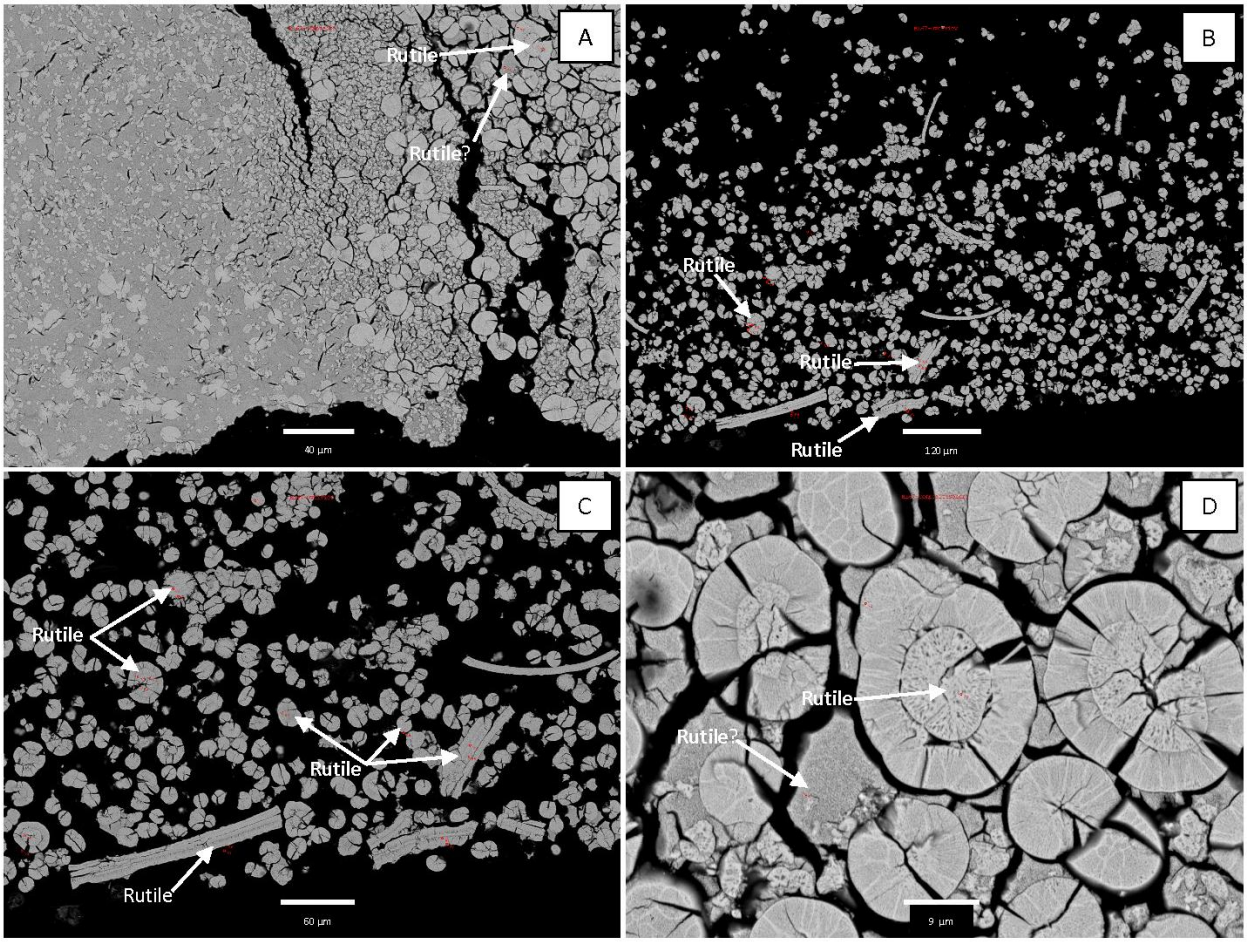

Figure 52. Electron microprobe backscatter image of Campaign 2 titanium dioxide (rutile) precipitates in sample 1802-P10-2 (ML-77), a calcined sample of Campaign 2 titanium dioxide precipitates. A) Large composite fragment composed of TiO_2-bearing matrix and approximately 10 µm–15 µm concentrically zoned circular (spherical) rutile precipitates. Scale bar is 40 µm. B) Abundant 3 µm–20 µm concentrically zoned rutile precipitates, local composite fragments of concentrically zoned rutile precipitates, elongate "lathe-like" rutile precipitates, and elongate curvilinear rutile precipitates. Scale bar is 120 µm. C) Close-up of Figure 51B showing details of the various types of rutile precipitates. Scale bar is 60 µm. D) Close-up of concentrically zoned rutile precipitates ranging from approximately 5 µm to 25 µm in diameter. Note the relative porosity in the cores of these concentric rutile precipitates relative to similar concentrically zoned precipitates in the non-calcined sample shown in Figure 50. Scale bar is 9 µm. Red numbers and circles in images are analysis locations.

Mineral chemical analyses of calcined Campaign 2 titanium dioxide precipitates from sample 1802-P10-2 (ML-67) are shown in Table 45. Rutile was the only mineral phase identified. As in the non-calcined sample, the composition of the rutile was dominated by TiO_2 (97.242%–101.926%) with subordinate SiO_2 (0.002%–0.404%), FeO (0.000%–0.034%), MnO (0.000%–0.030%), MgO (0.000%–0.010%), V_2O_3 (0.000%–0.132%), Cr_2O_3 (0.000%–0.028%), and NiO (0.000%–0.035%). No Cl was identified in these analyses. Overall, the TiO_2/Total ratio varied from 0.995 to 1.000.

Table 45. Electron microprobe analyses of Campaign 2 sample 1802-P10-2 (ML-67). This sample has been calcined. Analyses are in weight percentages.

Electron Microprobe Analysis – TiO_2 Precipitate Rutile Campaign 2 Calcined (n = 17)													
Sample	Description	Phase	SiO_2	TiO_2	Al_2O_3	FeO	MnO	MgO	V_2O_3	Cr_2O_3	NiO	Cl	Total
ML-67-12-73-2	Composite Sphere Core	Rutile	0.218	99.658	0.095	0.000	0.005	0.000	0.026	0.000	0.000	0.000	100.002
ML-67-13-75-2	Composite Sphere	Rutile	0.004	99.585	0.000	0.011	0.000	0.000	0.132	0.009	0.035	0.000	99.776
ML-67-14-76-1	Composite Sphere Core	Rutile	0.404	101.618	0.087	0.004	0.000	0.010	0.037	0.000	0.000	0.000	102.159
ML-67-16-78-1	Composite Sphere Rim	Rutile	0.002	98.520	0.000	0.034	0.004	0.000	0.114	0.025	0.007	0.000	98.706
ML-67-17-79-1	Composite Sphere Core	Rutile	0.368	101.926	0.093	0.000	0.000	0.010	0.028	0.009	0.000	0.000	102.434
ML-67-17-80-2	Composite Sphere Core	Rutile	0.018	98.558	0.000	0.000	0.000	0.000	0.000	0.000	0.000	0.000	98.576
ML-67-18-81-1	Composite Sphere Core	Rutile	0.301	100.723	0.052	0.023	0.020	0.010	0.048	0.014	0.010	0.000	101.202
ML-67-19-82-1	Composite Sphere Rim	Rutile	0.202	101.316	0.054	0.000	0.000	0.000	0.055	0.000	0.000	0.000	101.626
ML-67-20-83-1	Herringbone Rutile	Rutile	0.055	97.242	0.000	0.000	0.030	0.001	0.000	0.000	0.000	0.000	97.328
ML-67-21-84-1	Herringbone Rutile	Rutile	0.082	101.700	0.000	0.000	0.000	0.000	0.029	0.000	0.000	0.000	101.811
ML-67-22-85-1	Herringbone Rutile	Rutile	0.158	100.808	0.040	0.000	0.000	0.002	0.014	0.022	0.000	0.000	101.845
ML-67-23-86-1	Elongate Rutile Lathe Core	Rutile	0.013	97.910	0.000	0.007	0.000	0.000	0.000	0.024	0.000	0.000	97.953
ML-67-24-87-1	Elongate Rutile Lathe Rim	Rutile	0.203	100.039	0.041	0.009	0.000	0.005	0.000	0.000	0.006	0.000	100.303
ML-67-25-88-1	Elongate Rutile Lathe Core	Rutile	0.043	99.939	0.000	0.000	0.025	0.000	0.000	0.000	0.030	0.000	100.037
ML-67-26-89-1	Elongate Rutile Lathe Rim	Rutile	0.086	100.141	0.000	0.000	0.020	0.000	0.000	0.001	0.000	0.000	100.249
ML-67-27-90-1	Elongate Rutile Lathe Core	Rutile	0.024	97.785	0.000	0.000	0.015	0.000	0.034	0.000	0.000	0.000	97.858
ML-67-28-91-1	Elongate Rutile Lathe Rim	Rutile	0.055	97.955	0.000	0.020	0.010	0.000	0.000	0.028	0.000	0.000	98.070
		Minimum	***0.002***	***97.242***	***0.000***	***0.000***	***0.000***	***0.000***	***0.000***	***0.000***	***0.000***	***0.000***	***97.328***
		Maximum	***0.404***	***101.926***	***0.095***	***0.034***	***0.030***	***0.010***	***0.132***	***0.028***	***0.035***	***0.000***	***102.434***
		Average	***0.132***	***99.731***	***0.027***	***0.006***	***0.008***	***0.002***	***0.030***	***0.008***	***0.005***	***0.000***	***99.950***
		Median	***0.082***	***99.939***	***0.000***	***0.000***	***0.000***	***0.000***	***0.026***	***0.000***	***0.000***	***0.000***	***100.037***
		St. Deviation	***0.127***	***1.467***	***0.036***	***0.010***	***0.010***	***0.004***	***0.038***	***0.010***	***0.010***	***0.000***	***1.582***

Figure 53 illustrates the chemical compositions of the various textures of titanium dioxide (rutile) precipitates from both non-calcined and calcined samples produced during Campaign 2 based on EMPA mineral chemical analysis. In terms of weight percent oxides, the precipitates are nearly pure TiO_2 with little MgO or V_2O_3 contents (Figs. 53A–53D). Figure 53E illustrates the chemistry of the titanium dioxide precipitates in terms of molar Fe^{2+}, Ti^{4+}, and Fe^{3+}. Molar ratios of these cations were calculated using RUTCALC.xls (Gabbrosoft.com), which assumes all iron in rutile is Fe^{2+}. As indicated, the precipitates from both non-calcined (1802-P10-1/ML66) and calcined (1802-P10-2/ML67) samples are stoichiometrically rutile.

Lithogeochemical Analysis

Whole rock lithogeochemical analyses were performed on the non-calcined (1802-P10-1/ML66) and calcined (1802-P10-2/ML67) titanium dioxide precipitates produced during Campaign 2. The results of these analyses are shown in Table 46, and ALS Laboratory analytical certificates can be found in Appendix 3: Tables A3-1 to A3-7. Table 47 indicates the chemical compositions of titanium dioxide precipitates produced during the pilot-scale demonstration of ilmenite processing technology study performed by Mlinar et al. (2017).

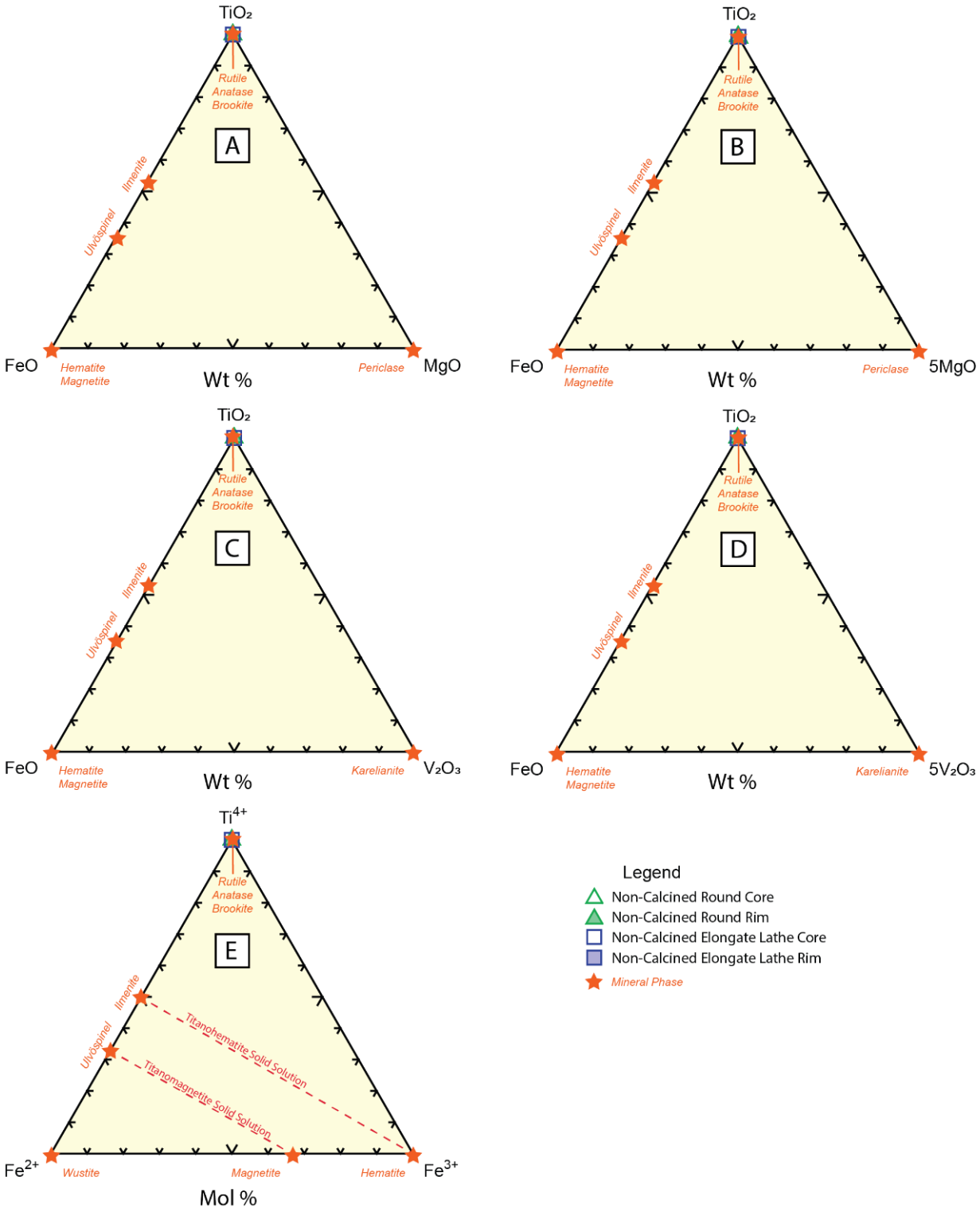

Figure 53. Ternary diagrams illustrating the chemical composition of titanium dioxide (TiO_2, rutile) precipitates from Campaign 2. Figures 53A–53D represent ternary diagrams in the FeO-TiO_2-MgO, FeO-TiO_2-5MgO, FeO-TiO_2-V_2O_3, and FeO-TiO_2-$5V_2O_3$ systems. Note that both non-calcined and calcined Campaign 2 titanium dioxide precipitates are nearly pure TiO_2. Figure 53E is an Fe^{2+}-Ti^{4+}-Fe^{3+} ternary diagram (modified after Klein and Hurlbut, 1999; Meinhold, 2010) showing that both the non-calcined and calcined titanium dioxide precipitates from Campaign 2 are stoichiometrically rutile.

Table 46. Results of lithogeochemical analyses on Campaign 2 titanium dioxide precipitates. Note low analytical totals (weight percentages) for major elements using the ME-ICP06 analytical method. Samples were reanalyzed using the ME-XRF06 method per recommendations from ALS Laboratories, and analytical totals were found to be between 98% and 100%.

		Sample	1802-P10-1	1802-P10-2			Sample	1802-P10-1	1802-P10-2
		Sample Description	P-10 Ti Precipitates Campaign 2	P-10 Ti Precipitates Campaign 2 - Calcined			Sample Description	P-10 Ti Precipitates Campaign 2	P-10 Ti Precipitates Campaign 2 - CALCINED
Analysis	Method	Detection Limit			Analysis	Method	Detection Limit		
SiO2_%	ME-ICP06	0.01	0.17	0.11	SiO2_%	ME-XRF06	0.01	0.15	0.1
Al2O3_%	ME-ICP06	0.01	0.07	<0.01	Al2O3_%	ME-XRF06	0.01	0.06	<0.01
Fe2O3_%	ME-ICP06	0.01	<0.01	<0.01	Fe2O3_%	ME-XRF06	0.01	<0.01	<0.01
CaO_%	ME-ICP06	0.01	<0.01	<0.01	CaO_%	ME-XRF06	0.01	0.01	0.01
MgO_%	ME-ICP06	0.01	<0.01	<0.01	MgO_%	ME-XRF06	0.01	0.01	0.01
Na2O_%	ME-ICP06	0.01	<0.01	<0.01	Na2O_%	ME-XRF06	0.01	<0.01	<0.01
K2O_%	ME-ICP06	0.01	<0.01	<0.01	K2O_%	ME-XRF06	0.01	<0.01	<0.01
Cr2O3_%	ME-ICP06	0.002	<0.002	<0.002	Cr2O3_%	ME-XRF06	0.002	<0.01	<0.01
TiO2_%	ME-ICP06	0.01	23.2	12.35	TiO2_%	ME-XRF06	0.01	87.41	98.95
MnO_%	ME-ICP06	0.01	<0.01	<0.01	MnO_%	ME-XRF06	0.01	<0.01	<0.01
P2O5_%	ME-ICP06	0.01	0.08	0.03	P2O5_%	ME-XRF06	0.01	0.092	0.064
SrO_%	ME-ICP06	0.01	<0.01	<0.01	SrO_%	ME-XRF06	0.01	<0.01	<0.01
BaO_%	ME-ICP06	0.01	<0.01	<0.01	BaO_%	ME-XRF06	0.01	<0.01	<0.01
LOI_%	OA-GRA05	0.01	11.1	0.01	LOI_%	ME-XRF06	0.01	11.25	0.06
Total_%	TOT-ICP06	0.01	34.62	12.5	Total_%	ME-XRF06	0.01	98.98	99.19
S_%	S-IR08	0.01	0.02	<0.01	S_%	S-IR08	0.01	0.02	<0.01
Ag_ppm	ME-4ACD81	0.5	<0.5	<0.5	Ag_ppm	ME-4ACD81	0.5	<0.5	<0.5
Ag_ppm	ME-MS42	0.01	0.01	<0.01	Ag_ppm	ME-MS42	0.01	0.01	<0.01
As_ppm	ME-4ACD81	5	20	5	As_ppm	ME-4ACD81	5	20	5
As_ppm	ME-MS42	0.1	<0.1	0.4	As_ppm	ME-MS42	0.1	<0.1	0.4
Ba_ppm	ME-MS81	0.5	3.9	2.9	Ba_ppm	ME-MS81	0.5	3.9	2.9
Be_ppm	ME-MS42	0.05	<0.05	<0.05	Be_ppm	ME-MS42	0.05	<0.05	<0.05
Bi_ppm	ME-MS42	0.01	0.01	0.03	Bi_ppm	ME-MS42	0.01	0.01	0.03
Cd_ppm	ME-4ACD81	0.5	<0.5	<0.5	Cd_ppm	ME-4ACD81	0.5	<0.5	<0.5
Cd_ppm	ME-MS42	0.01	<0.01	<0.01	Cd_ppm	ME-MS42	0.01	<0.01	<0.01
Ce_ppm	ME-MS42	0.02	<0.02	<0.02	Ce_ppm	ME-MS42	0.02	<0.02	<0.02
Ce_ppm	ME-MS81	0.1	<0.1	<0.1	Ce_ppm	ME-MS81	0.1	<0.1	<0.1
Co_ppm	ME-4ACD81	1	<1	<1	Co_ppm	ME-4ACD81	1	<1	<1
Co_ppm	ME-MS42	0.1	<0.1	<0.1	Co_ppm	ME-MS42	0.1	<0.1	<0.1
Cr_ppm	ME-MS81	10	<10	<10	Cr_ppm	ME-MS81	10	<10	<10
Cs_ppm	ME-MS42	0.05	<0.05	<0.05	Cs_ppm	ME-MS42	0.05	<0.05	<0.05
Cs_ppm	ME-MS81	0.01	<0.01	<0.01	Cs_ppm	ME-MS81	0.01	<0.01	<0.01
Cu_ppm	ME-4ACD81	1	1	1	Cu_ppm	ME-4ACD81	1	1	1
Cu_ppm	ME-MS42	0.2	0.5	<0.2	Cu_ppm	ME-MS42	0.2	0.5	<0.2
Dy_ppm	ME-MS81	0.05	<0.05	<0.05	Dy_ppm	ME-MS81	0.05	<0.05	<0.05
Er_ppm	ME-MS81	0.03	<0.03	<0.03	Er_ppm	ME-MS81	0.03	<0.03	<0.03
Eu_ppm	ME-MS81	0.03	<0.03	<0.03	Eu_ppm	ME-MS81	0.03	<0.03	<0.03
Ga_ppm	ME-MS42	0.05	0.05	<0.05	Ga_ppm	ME-MS42	0.05	0.05	<0.05
Ga_ppm	ME-MS81	0.01	0.1	0.1	Ga_ppm	ME-MS81	0.01	0.1	0.1
Gd_ppm	ME-MS81	0.05	<0.05	<0.05	Gd_ppm	ME-MS81	0.05	<0.05	<0.05
Hf_ppm	ME-MS42	0.02	<0.02	<0.02	Hf_ppm	ME-MS42	0.02	<0.02	<0.02
Hf_ppm	ME-MS81	0.2	<0.2	<0.2	Hf_ppm	ME-MS81	0.2	<0.2	<0.2
Hg_ppm	ME-MS42	0.005	<0.005	<0.005	Hg_ppm	ME-MS42	0.005	<0.005	<0.005
Ho_ppm	ME-MS81	0.01	<0.01	<0.01	Ho_ppm	ME-MS81	0.01	<0.01	<0.01
In_ppm	ME-MS42	0.005	<0.005	<0.005	In_ppm	ME-MS42	0.005	<0.005	<0.005
La_ppm	ME-MS42	0.2	<0.2	<0.2	La_ppm	ME-MS42	0.2	<0.2	<0.2
La_ppm	ME-MS81	0.1	<0.1	<0.1	La_ppm	ME-MS81	0.1	<0.1	<0.1
Li_ppm	ME-4ACD81	10	<10	<10	Li_ppm	ME-4ACD81	10	<10	<10
Li_ppm	ME-MS42	0.1	0.1	0.1	Li_ppm	ME-MS42	0.1	0.1	0.1
Lu_ppm	ME-MS81	0.01	<0.01	<0.01	Lu_ppm	ME-MS81	0.01	<0.01	<0.01
Mo_ppm	ME-4ACD81	1	<1	<1	Mo_ppm	ME-4ACD81	1	<1	<1
Mo_ppm	ME-MS42	0.05	<0.05	<0.05	Mo_ppm	ME-MS42	0.05	<0.05	<0.05
Nb_ppm	ME-MS42	0.05	<0.05	<0.05	Nb_ppm	ME-MS42	0.05	<0.05	<0.05
Nb_ppm	ME-MS81	0.2	28.8	22.8	Nb_ppm	ME-MS81	0.2	28.8	22.8
Nd_ppm	ME-MS81	0.1	<0.1	<0.1	Nd_ppm	ME-MS81	0.1	<0.1	<0.1
Ni_ppm	ME-4ACD81	1	<1	<1	Ni_ppm	ME-4ACD81	1	<1	<1
Ni_ppm	ME-MS42	0.2	<0.2	<0.2	Ni_ppm	ME-MS42	0.2	<0.2	<0.2
Pr_ppm	ME-MS81	0.03	<0.03	<0.03	Pr_ppm	ME-MS81	0.03	<0.03	<0.03
Pb_ppm	ME-4ACD81	2	<2	<2	Pb_ppm	ME-4ACD81	2	<2	<2
Pb_ppm	ME-MS42	0.2	0.2	0.9	Pb_ppm	ME-MS42	0.2	0.2	0.9
Rb_ppm	ME-MS42	0.1	<0.1	<0.1	Rb_ppm	ME-MS42	0.1	<0.1	<0.1
Rb_ppm	ME-MS81	0.2	<0.2	<0.2	Rb_ppm	ME-MS81	0.2	<0.2	<0.2
Re_ppm	ME-MS42	0.001	<0.001	<0.001	Re_ppm	ME-MS42	0.001	<0.001	<0.001
Sb_ppm	ME-MS42	0.05	<0.05	<0.05	Sb_ppm	ME-MS42	0.05	<0.05	<0.05
Sc_ppm	ME-4ACD81	1	<1	<1	Sc_ppm	ME-4ACD81	1	<1	<1
Sc_ppm	ME-MS42	0.1	<0.1	<0.1	Sc_ppm	ME-MS42	0.1	<0.1	<0.1
Se_ppm	ME-MS42	0.2	<0.2	<0.2	Se_ppm	ME-MS42	0.2	<0.2	<0.2
Sm_ppm	ME-MS81	0.03	<0.03	<0.03	Sm_ppm	ME-MS81	0.03	<0.03	<0.03
Sn_ppm	ME-MS42	0.2	<0.2	<0.2	Sn_ppm	ME-MS42	0.2	<0.2	<0.2
Sn_ppm	ME-MS81	1	<1	<1	Sn_ppm	ME-MS81	1	<1	<1
Sr_ppm	ME-MS42	0.2	<0.2	<0.2	Sr_ppm	ME-MS42	0.2	<0.2	<0.2
Sr_ppm	ME-MS81	0.1	0.4	0.3	Sr_ppm	ME-MS81	0.1	0.4	0.3
Ta_ppm	ME-MS42	0.01	<0.01	<0.01	Ta_ppm	ME-MS42	0.01	<0.01	<0.01
Ta_ppm	ME-MS81	0.1	0.6	0.3	Ta_ppm	ME-MS81	0.1	0.6	0.3
Tb_ppm	ME-MS81	0.01	<0.01	<0.01	Tb_ppm	ME-MS81	0.01	<0.01	<0.01
Te_ppm	ME-MS42	0.01	<0.01	<0.01	Te_ppm	ME-MS42	0.01	<0.01	<0.01
Th_ppm	ME-MS42	0.2	<0.2	<0.2	Th_ppm	ME-MS42	0.2	<0.2	<0.2
Th_ppm	ME-MS81	0.05	<0.05	<0.05	Th_ppm	ME-MS81	0.05	<0.05	<0.05
Tl_ppm	ME-4ACD81	10	<10	10	Tl_ppm	ME-4ACD81	10	<10	10
Tl_ppm	ME-MS42	0.02	<0.02	0.03	Tl_ppm	ME-MS42	0.02	<0.02	0.03
Tm_ppm	ME-MS81	0.01	<0.01	<0.01	Tm_ppm	ME-MS81	0.01	<0.01	<0.01
U_ppm	ME-MS42	0.05	<0.05	<0.05	U_ppm	ME-MS42	0.05	<0.05	<0.05
U_ppm	ME-MS81	0.05	<0.05	<0.05	U_ppm	ME-MS81	0.05	<0.05	<0.05
V_ppm	ME-MS81	5	<5	<5	V_ppm	ME-MS81	5	<5	<5
W_ppm	ME-MS42	0.05	<0.05	<0.05	W_ppm	ME-MS42	0.05	<0.05	<0.05
W_ppm	ME-MS81	1	<1	<1	W_ppm	ME-MS81	1	<1	<1
Y_ppm	ME-MS42	0.05	<0.05	<0.05	Y_ppm	ME-MS42	0.05	<0.05	<0.05
Y_ppm	ME-MS81	0.1	<0.1	<0.1	Y_ppm	ME-MS81	0.1	<0.1	<0.1
Yb_ppm	ME-MS81	0.03	<0.03	<0.03	Yb_ppm	ME-MS81	0.03	<0.03	<0.03
Zn_ppm	ME-4ACD81	2	<2	2	Zn_ppm	ME-4ACD81	2	<2	2
Zr_ppm	ME-MS42	0.5	<0.5	<0.5	Zr_ppm	ME-MS42	0.5	<0.5	<0.5
Zr_ppm	ME-MS81	2	<2	<2	Zr_ppm	ME-MS81	2	<2	<2

Table 47. Chemical analyses of titanium dioxide products produced during pilot-scale demonstration of ilmenite processing technology (Mlinar et al., 2017). Also included is chemical analysis of a commercially available TiO_2 pigment produced by DuPont.

	PRO Test #15 Product	*PRO Test #18 Product*	*PRO Test #29 Product*	*DuPont™ Ti-Pure® R350*
	Mlinar et al. 2017 Ti-Product (surface modified)	*Mlinar et al. 2017 Ti-Product (w/ surface modified)*	*Mlinar et al. 2017 Ti-Product (w/o surface modifiers)*	*Commercially Available TiO_2 Powder*
Analysis				
SiO2_%*	0.02	0.04	0.13	1.84
Al2O3_%*	0.23	0.23	<0.02	1.55
Fe2O3_%*	<0.01	<0.01	<0.01	<0.01
CaO_%*	0.11	0.10	<0.07	0.13
MgO_%*	<0.02	<0.02	<0.02	<0.02
Na2O_%	NA	NA	NA	NA
K2O_%*	<0.06	<0.06	<0.06	<0.06
Cr2O3_%*	<0.01	<0.01	<0.01	<0.01
TiO2_%*	98.91	99.41	99.92	97.91
MnO_%*	<0.10	<0.10	<0.10	<0.10
P2O5_%*	0.69	0.69	0.02	0.14
S_%	<0.01	<0.01	<0.01	0.03
Ag_ppm	<1	<1	<1	<1
As_ppm	<30	<30	<30	<30
B_ppm	<20	<20	<20	<20
Ba_ppm	17.2	22.1	70.3	<0.5
Be_ppm	<5	<5	<5	<5
Bi_ppm	<0.1	<0.1	<0.1	<0.1
Cd_ppm	<0.2	<0.2	<0.2	<0.2
Ce_ppm	<0.1	<0.1	<0.1	<0.1
Co_ppm	0.8	0.6	0.5	<0.5
Cs_ppm	<0.1	<0.1	<0.1	44.6
Cu_ppm	<5	<5	311	<5
Dy_ppm	<0.05	<0.05	<0.05	<0.05
Er_ppm	<0.05	<0.05	<0.05	<0.05
Eu_ppm	<0.05	<0.05	<0.05	<0.05
Ga_ppm	0.15	0.17	0.11	0.82
Gd_ppm	<0.05	<0.05	<0.05	<0.05
Ge_ppm	<1	<1	<1	<1
Hf_ppm	<1	<1	<1	<1
Ho_ppm	<0.05	<0.05	<0.05	<0.05
In_ppm	<0.2	<0.2	<0.2	<0.2
La_ppm	<0.1	<0.1	<0.1	<0.1
Li_ppm	<10	<10	<10	<10
Lu_ppm	<0.05	<0.05	<0.05	<0.05
Mo_ppm	<2	<2	<2	<2
Nb_ppm	102	117	101	1
Nd_ppm	<0.1	<0.1	<0.1	<0.1
Ni_ppm	<5	<5	<5	<5
Pb_ppm	<5	<5	<5	<5
Pr_ppm	<0.05	<0.05	<0.05	<0.05
Rb_ppm	<0.2	<0.2	<0.2	<0.2
Sb_ppm	0.1	1.1	<0.1	<0.1
Sc_ppm	<5	<5	<5	<5
Sm_ppm	<0.1	<0.1	<0.1	<0.1
Sn_ppm	<1	<1	<1	<1
Sr_ppm	<0.1	<0.1	<0.1	<0.1
Ta_ppm	7.4	6.5	3.7	1.9
Tb_ppm	<0.05	<0.05	<0.05	<0.05
Th_ppm	<0.1	<0.1	<0.1	<0.1
Tl_ppm	<0.5	<0.5	<0.5	<0.5
Tm_ppm	<0.05	<0.05	<0.05	<0.05
U_ppm	<0.05	<0.05	<0.05	<0.05
V_ppm	23	17	14	<5
W_ppm	1	<1	1	<1
Y_ppm	<0.5	<0.5	<0.5	<0.5
Yb_ppm	<0.1	<0.1	<0.1	<0.1
Zn_ppm	15	22	43	<5

It is important to note that original lithogeochemical analyses on the Campaign 2 TiO_2 precipitates using ALS Laboratories analytical method ME-ICP06 resulted in low major element analytical totals (ranging from 12.5% to 34.62%). Discussions with ALS Laboratory personnel indicated that accurate analyses of such pure materials would be better achieved utilizing ALS Laboratory analytical method ME-XRF06. Reanalyses of the Campaign 2 TiO_2 precipitates using ALS Laboratory analytical method ME-XRF06 were conducted, and the analytical totals for major element oxides for the Campaign 2 TiO_2 precipitates ranged between 98% and 100%.

Relative results for the non-calcined (1802-P10-1/ML66) and calcined (1802-P10-2/ML67) Campaign 2 titanium dioxide precipitates in terms of major element oxide compositions (weight percentages) are described as follows:

- SiO_2: Higher in the non-calcined sample (0.15%) versus the calcined sample (0.10%)
- Al_2O_3: Higher in the non-calcined sample (0.06%) versus the calcined sample (below 0.01%)
- Fe_2O_3: Below 0.01% in both the non-calcined and calcined samples
- CaO: Equivalent in the non-calcined and calcined sample at 0.01%
- MgO: Equivalent in the non-calcined and calcined sample at 0.01%
- Na_2O: Below 0.01% in both the non-calcined and calcined samples
- K_2O: Below 0.01% in both the non-calcined and calcined samples
- Cr_2O_3: Below 0.01% in both the non-calcined and calcined samples
- TiO_2: Higher in the calcined sample (98.95%) versus the non-calcined sample (87.41%)
- MnO: Below 0.01% in both the non-calcined and calcined samples
- P_2O_5: Higher in the non-calcined sample (0.092%) than in the calcined sample (0.064%)
- SrO: Below 0.01% in both the non-calcined and calcined samples
- BaO: Below 0.01% in both the non-calcined and calcined samples
- LOI: Higher in the non-calcined sample (11.25%) versus the calcined sample (0.06%)
- Sulfur: Higher in the non-calcined sample (0.02%) versus the calcined sample (<0.01%)

Relative results for selected trace elements in the non-calcined and calcined Campaign 2 titanium dioxide precipitates are described as follows:

- As: The four-acid digestion method (Method ME-4ACD81) indicated higher arsenic in the non-calcined sample (20 ppm) than in the calcined sample (5 ppm). Analysis using mass spectrometry (Method ME-MS42) indicated a higher concentration of As in the calcined sample (4 ppm) versus the non-calcined sample (<0.1 ppm).
- Co: Below 1ppm for both samples using Method ME-4ACD81, and below 0.1 ppm for both samples using Method MEMS42.
- Cr: Below 10 ppm for both samples using mass spectrometry method ME-MS81.
- Cu: 1ppm for both samples using Method ME-4ACD81, and higher in the non-calcined sample (0.5 ppm) than the calcined sample (<0.2 ppm) using Method ME-MS42.
- Nb: Less than 0.05 ppm for both samples using Method ME-MS42, and higher in the non-calcined sample (28.8 ppm) than the calcined sample (22.8 ppm) using Method ME-MS81.

- Ni: Below 1ppm for both samples using Method 4ACD81, and below 0.2 ppm using Method ME-MS42.
- Pb: Less than 2 ppm for both samples using Method ME-4ACD81, and higher in the calcined sample (0.9 ppm) than the non-calcined sample (0.2 ppm) using Method ME-MS42.
- Sb: Below 0.05 ppm for both samples using Method ME-MS42.
- Ta: Less than 0.1 ppm for both samples using Method ME-MS42, and higher in the non-calcined sample (0.6 ppm) than the calcined sample (0.3 ppm) using Method ME-MS81.
- V: Less than 5 ppm for both samples using Method ME-MS81.
- Zn: Less than 2 ppm for both samples using Method ME-4ACD81.

Neither the non-calcined nor the calcined titanium dioxide products produced during this study were surface modified. Relative to calcined, non-surface modified TiO_2 products produced during the previous Mlinar et al. (2017) study, calcined TiO_2 products produced during Campaign 2 for this study have higher major element oxide concentrations of P_2O_5 and lower major element oxide concentrations of TiO_2 (98.95% (this study) versus 99.92% (Mlinar et al., 2017)). In terms of trace elements, calcined TiO_2 products produced for this study have higher concentrations (ppm) of Sr and lower concentrations (ppm) of Ba, Cu, Ga, Nb, Ta, V, and Zn relative to non-surface-modified TiO_2 products produced by Mlinar et al. (2017) (see Table 46 and Table 47). It is interesting to note that Nb and Ta may be incorporated into the rutile structure via substitution for Ti^{4+}. These results suggest that the rutile produced during this study has less substitution of these two elements than in rutile produced during the previous study (Mlinar et al., 2017).

Figure 54A is a chondrite-normalized rare earth element plot for both the non-calcined and calcined Campaign 2 TiO_2 precipitates. All rare earth elements analyzed were found to be in concentrations less than the analytical detection limits for both samples.

Figure 54B is a primitive mantle-normalized spider diagram showing selected trace element concentrations in the Campaign 2 TiO_2 precipitates. All elements with the exceptions of niobium, titanium, and aluminum were found to be in concentrations less than the analytical detection limits. Niobium was slightly more concentrated in the non-calcined sample (~40 times primitive mantle value) than the calcined sample (~30 times primitive mantle value). Titanium was slightly more concentrated in the calcined sample (~500 times primitive mantle value) relative to the non-calcined sample (~400 times primitive mantle value). Aluminum (as Al_2O_3) was found to be significantly higher in the non-calcined sample (between 10 and 20 times primitive mantle value) relative to the calcined sample (between 0.1 and 0.2 times primitive mantle value). The enrichments of niobium and titanium in the Campaign 2 TiO_2 precipitates is not surprising, as both titanium and niobium are commonly present in rutile (Deer et al., 1992; Klein and Hurlbut, 1999).

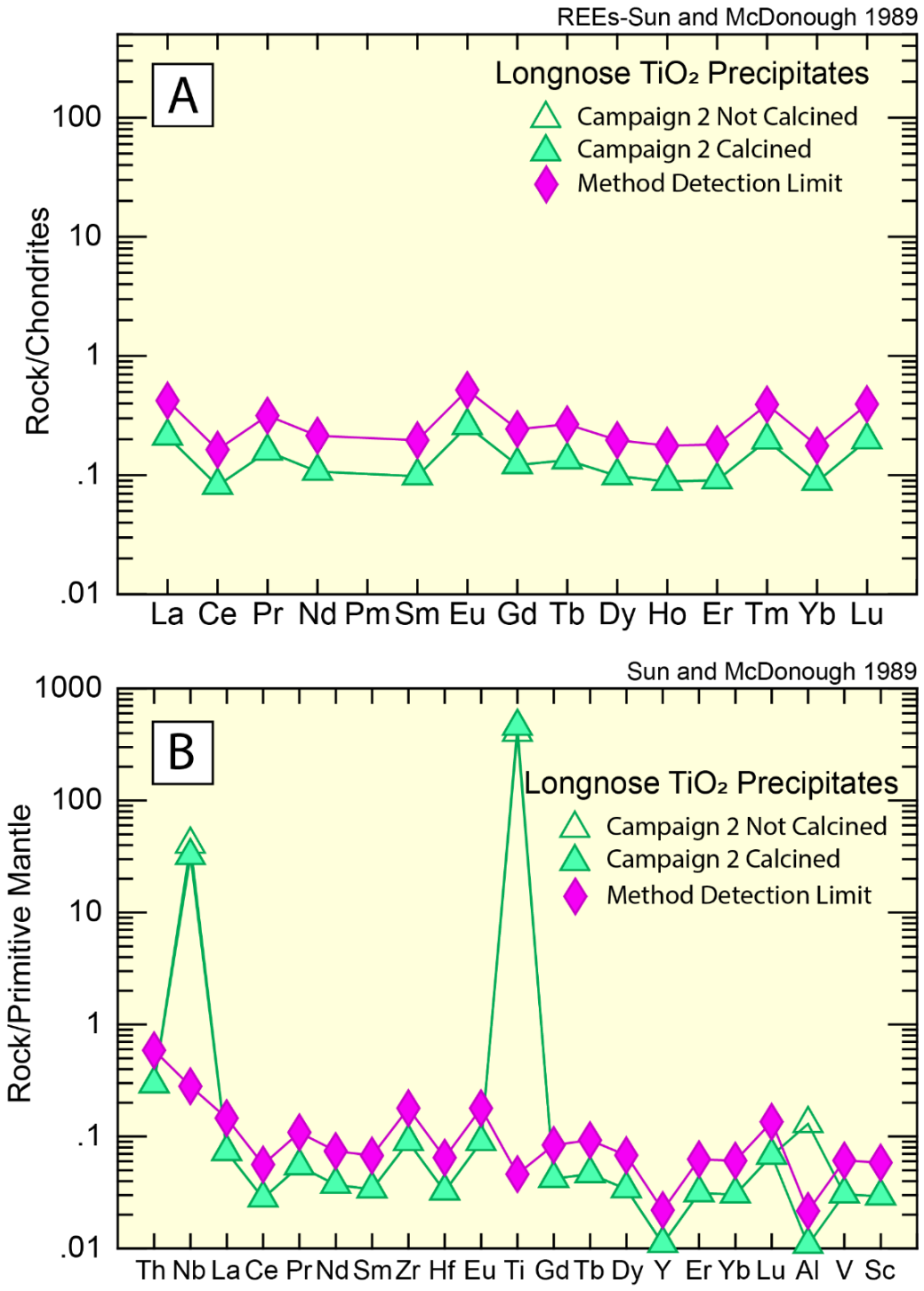

Figure 54. Chondrite- and primitive mantle-normalized rare earth element spider diagram for Campaign 2 TiO_2 precipitates. A) Chondrite-normalized rare earth element diagram. Note that all rare earth element values fall below the analytical detection limits. B) Primitive mantle-normalized spider diagram for Campaign 2 TiO_2 precipitates. Note niobium and titanium enrichment relative to the other trace elements plotted and differences in the aluminum content of the non-calcined and calcined products. For the purpose of plotting, all analyses below the detection limit have been set to values equal to one-half the value of the detection limit. Chondrite- and primitive-mantle normalizing values from Sun and McDonough (1989) and Kerrich and Wyman (1996).

Campaign 2 Summary

The Campaign 2 operation of the MPP has been successfully implemented to achieve impurity buildup and steady-state operation with recycling of evaporated Ti raffinate into the circuit. Both non-calcined and calcined TiO_2 precipitates were produced.

Operational highlights of Campaign 2:

- Evaporation of the Ti raffinate containing $MgCl_2$ and subsequent recycling to the PRO leach process.
- Recycled $MgCl_2$ bearing Ti raffinate does not affect leaching efficiency with estimated recovery of ~71% in the bulk pilot leaches.
- Total cumulative operation of the Fe circuit of ~350 hours, ~100 organic turnovers.
- Total cumulative operation of the Ti circuit of ~287hours, ~35 organic turnovers.
- After-settler installed in both Fe and Ti circuits after scrubbing section and have improved phase disengagement and reduced Mg carryover to subsequent stripping circuits with levels. Mg content in the Fe pregnant strip solution was reduced from 2 g/l to <50 ppm and from over 20 gpl g/l to 2 g/l in the Ti pregnant strip solution.
- High-purity Fe strip solution was produced with minimal increase in impurity content. Fe SX circuit displays selectivity for Fe with increased impurities in the feed.
- High-purity Ti strip solution was produced with no apparent increase in impurity content. Quality is comparable to that achieved in previous study without recycling of raffinate/impurity buildup. Ti SX circuit displays selectivity for Ti with increased impurities in the feed.
- Both non-calcined and calcined TiO_2 precipitates were produced during this campaign. The TiO_2 precipitates are composed of the mineral phase rutile. The morphologies of both of these precipitates are similar, comprising 1 µm–30 µm rounded, concentrically zoned rutile spheres. Elongate and elongate, locally curved rutile precipitates are locally present and range in size from 30 µm to 150 µm in length and 5 µm to 10 µm in width. Composite fragments composed on multiple rounded rutile spheres are also present. Other research has shown that precipitation of titanium dioxide from various types of solutions results in the formation of nanoparticles and microparticles that can have crystalline morphologies ranging from prismatic to needle-like (acicular) to wire-like to net-like to amorphous aggregates composed of wire-like or acicular nanoparticles (Tsuchida et al., 1982; Ookubo et al., 1989; Ohno et al., 2001; Yamabi and Imai, 2002; Li et al., 2008; Reyes-Coronado et al., 2008; Ismagilov et al., 2009; Akhgar et al., 2013; Wu et al., 2013; Mostafa et al., 2013; Mehdilo and Irannajad, 2013; Razeih et al., 2014) as well as spherical morphologies ranging from individual spheres to aggregates of spheres (Visca and Matijević, 1979; Gopal et al., 1997; Tadros et al., 1996; Park et al., 1997; Kim et al., 1999a; Alemany et al., 2000; Chen and Chen, 2003; Li et al., 2004; Lee and Yang, 2005; Šubrt et al., 2006; Lee et al., 2008; Li and Demopoulos, 2008; Deorsola and Vallauri, 2009; Kirillov et al., 2011; Thangavelu et al., 2013; Xu et al., 2013). These experiments indicate that the three TiO_2 polymorphs (rutile, brookite, and anatase) can all be produced, depending on the temperature conditions of precipitation and subsequent calcination. Numerous patents exist for the precipitation of spherical TiO_2 nanoparticles, microparticles, and crystalline aggregates (including, but not limited to, Montino and Spoto, 1989; Lawhorne, 1990; Karvinen, 1995; Kim et al., 1998; Kim et al., 1999b). Composite particles composed of a titanium dioxide core and a polymer rim have also been synthesized (Nakade et al., 2004; Werts et al., 2008).

- Lithogeochemical analysis of the TiO_2 precipitates illustrates that the precipitates are dominated by the component TiO_2. For sample 1802-P10-1 (ML-66, non-calcined), the TiO_2/Total ratio is 0.883, whereas for sample 1802-P10-2 (ML-77, calcined), the TiO_2/Total ratio is 0.998. These ratios reflect the higher LOI contents of the non-calcined sample (11.25 weight percent (wt. %)) relative to the LOI contents of the calcined sample (0.06 wt. %). This presumably reflects loss of hydration water and/or (OH)- surface groups from the precipitate during calcination (e.g. Alemany et al., 2000). Sulfur contents are also higher in the non-calcined sample (0.02 wt. %) than in the calcined sample (<0.01 wt. %). The rare earth element contents of both non-calcined and calcined samples were found to be below detection limits. Relative to primitive mantle normalizing values (Sun and McDonough, 1989; Kerrich and Wyman, 1996), both the non-calcined and calcined samples are enriched in niobium (~30–50 times primitive mantle values) and titanium (400 to 500 times primitive mantle values), with the non-calcined sample having a higher concentration of niobium than the calcined sample, and with the calcined sample having a higher concentration of titanium than the non-calcined sample. Aluminum (as Al_2O_3) was found to have a higher concentration in the non-calcined precipitate relative to the calcined precipitate.
- Hydro-hydrolysis bench-scale testing continued in this Campaign to examine parameters for regeneration of HCl and production of an Fe_2O_3 precipitate, which is described below (see "6.5.1.3 Iron oxide Product – Campaign 2"). Tests were performed to simulate steady-state operation of the process and determine the operational criteria with respect to feed composition, reactor composition, and operation temperature over time and the subsequent effect on HCl produced. Current testing has established that the reactor composition has a significant effect on the quality of HCl produced with higher concentration of Fe^{2+}/Fe^{3+} (>400 g/l) in the bath, resulting in higher HCl concentrations, with up to 11 N observed.

Campaign 3

In this campaign, operation continued with recycling of streams from Campaign 2 (Ti raffinate) with the addition of the implementation of recycling of TiO_2 precipitation filtrate stream into the circuit as Ti SX barren strip. The focus of operation was on impurity buildup and steady-state operation and determining the effects of impurity buildup on the selectivity in the SX separation circuits.

In addition, bench-scale hydro-hydrolysis continued to produce Fe_2O_3 product and establish quality of HCl. It was found that the results achieved during Campaign 3 were similar to those in Campaign 1 and Campaign 2:

- Leach: Ti recovery of ~71% in bulk leaching
- Fe Oxidation: Residence time ~32hrs, <50 ppm Fe^{2+}
- Fe SX: Raffinate contains <50 ppm Fe, >100 g/l Fe Pregnant strip solution
- Ti SX: ~56 g/l Ti Pregnant strip solution

Leaching

Leaching for the MPP Campaign 3 was conducted in the same apparatus as Campaigns 1 and 2, which consists of a 45 L mixing tank fitted with water-cooled condenser, air-powered agitator, and 3kW Teflon coated immersion heater. Average leach solution compositions in this campaign are presented in Table 48.

Table 48. Campaign 2 average PLS analysis.

	Analysis Result PPM							
Campaign 3 Average PLS	**Al**	**As**	**Ca**	**Co**	**Cr**	**Cu**	**Fe**	**K**
	400.9	<5	3358.0	<5	112.5	106	34640	932
	Mg	**Mn**	**Mo**	**Ni**	**Ti**	**V**	**Zn**	**FAT**
	58378	729	<5	115	23298	431	17	2

Operating conditions were maintained from the previous campaign, and operational parameters are presented in Table 49; however, the bulk of the $MgCl_2$ is recovered from the Ti raffinate stream and recycled back to the leach after evaporation to maintain a water balance. A total of 20 bulk leaches have been completed, with leaches 5–20 utilizing recycled Ti raffinate. In total, ~1000 L of PLS has been produced in all campaigns for the filling and operation of the solvent extraction circuits to an initial steady state and complete recycling of evaporated Ti raffinate.

Table 49. Leaching parameters.

Pulp Density	HCl Concentration	$MgCl_2$ Concentration	Temperature	Duration	Particle Size
10%	5.8N	220 g/l	70°C	4h	P80 – 38 µm

Raffinate Evaporation and Recycling

Raffinate evaporation was conducted in the same apparatus that was used in Campaign 2, and evaporated raffinate was recycled to the leach to satisfy the $MgCl_2$ requirement in the leach. A typical balance from the evaporation process is presented in Table 50.

Table 50. Ti raffinate evaporation balance (EV-54).

Evaporation Balance (EV-54)	Wt	Al	As	Ca	Co	Cr	Cu	Fe	K	Mg	Mn	Mo	FAT	Fe2+	Ni	Pb	Ti	V	Zn
	kg	ppm																	
Feed Ti Raff	14.3	428	<5	3650	<5	92	33	8	951	62240	736	<5	0.8	_	116	<5	1285	425	6
Concentrated Raff (Calculated)	7.96	772	<5	6577	<5	166	59	15	1713	112157	1325	<5		-	209	<5	64	765	11
Condensate	6.38	-	-	-	-	-	-	-	-	-	-	-	1.1	-	-	-	-	-	-

Leach solution compositions with respect to the main impurities are presented in Table 51. After recycling of the raffinate to the leach in Campaigns 2 and 3, it can be seen that there are increases in some of the impurities, notably K, Mn, and V, as shown in Figure 55.

Table 51. PLS analysis.

Sample ID	Sample Description	Analysis Result PPM																
		Al	As	Ca	Co	Cr	Cu	Fe	K	Mg	Mn	Mo	FAT	Ni	Pb	Ti	V	Zn
P- 19 - 135	BL2	181.3	<5	3614	<5	55.9	136.1	24820	1075	65020	341.1	<5	-	41.2	<5	23400	193.5	22.6
P- 19 - 257	BL3	189.5	<5	4833	<5	52.7	121.1	42875	1096	74575	323.8	<5	2.00	35.9	<5	26300	204.8	16.8
P- 19 - 507	BL4	193.4	<5	3372	<5	63.7	93.4	28100	1138	62620	336.8	<5	2.40	52.2	<5	18478	150.4	15.4
P- 19 - 564	BL5	239.9	<5	3594	<5	53.4	107.1	33100	1043	56360	442.6	<5	1.90	59.9	<5	22780	216.8	8.3
P- 19 - 643	BL6	232.1	<5	4350	<5	77.8	121.1	32740	1150	54100	485.5	<5	1.90	64.1	<5	24680	253.5	11.9
P- 19 - 645	BL7	243.3	<5	3600	<5	70.2	119.8	33360	1050	60760	420.0	<5	1.8	63.8	<5	22740	229.2	11.1
P-19 - 1095	BL9	274.0	<5	3350	<5	81.2	96.5	32460	980	71360	449	<5	2	76	<5	24360	221	13
P- 19 - 1118	BL10	151.9	<5	3953	<5	52.8	102	42100	1350	74420	343	<5	2	45	<5	30180	208	16
P- 19 - 1340	BL11	320.4	<5	3650	<5	103	92.5	26380	911	57760	533	<5	2	90	<5	17106	281	7
P- 19 - 1399	BL12	328.7	<5	3850	<5	94.5	99.9	31380	841	65260	699	<5	2	109	<5	20740	454	16
P- 19 - 1556	BL13	361.5	<5	3550.0	<5	80.2	91.8	31160.0	940.5	60680.0	638.5	<5	1.8	99.5	<5	20980	372.5	14.3
P- 19 - 1675	BL14	314.6	<5	3376.0	<5	106.3	86.6	36700.0	1000.0	64000.0	551.6	<5	1.7	90.6	<5	25020.0	343.8	15.8
P- 19 - 1809	BL15	384.0	<5	3200.0	<5	125.2	83.3	32120.0	1020.0	57440.0	621.5	<5	2.1	108.5	<5	21800	413.5	24.2
P- 19 - 2052	BL16	405.7	<5	3340.0	<5	129.1	59.3	38360.0	891.0	52960.0	753.7	<5	1.6	114.0	<5	25200.0	472.7	15.2
P- 19 - 2171	BL17	392.6	<5	3327.0	<5	110.3	153.9	37260.0	864.5	60380.0	836.6	<5	1.6	121.1	<5	25460.0	466.4	17.1
P- 19 - 2447	BL18	407.1	<5	3521.0	<5	91.0	161.2	37800.0	930.0	58500.0	824.4	<5	1.8	120.7	<5	25100.0	420.1	17.9
P- 19 - 2625	BL19	484.4	<5	3550.0	<5	135.5	133.9	33120.0	920.5	58140.0	872.5	<5	2.3	129.3	<5	22240.0	502.5	17.9
P- 19 - 2763	BL20	457.5	<5	3000.0	<5	122.4	80.9	30600.0	890.5	54920.0	735.4	<5	1.4	134.0	<5	20580.0	456.3	13.5

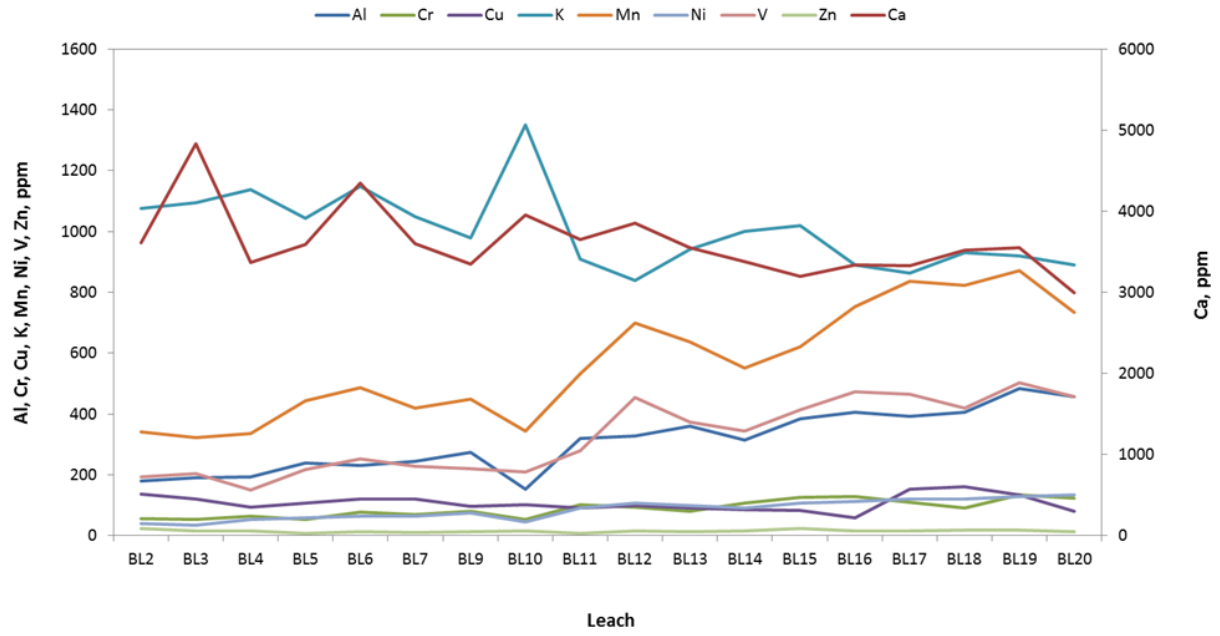

Figure 55. Impurity content in leach.

Once the leach was complete, the slurry was filtered and processed in subsequent SX operations.

Oxidation

After filtration of the PLS, oxidation was performed under the same conditions as in Campaign 2. There was a combination of oxidation procedures as follows to speed up production of oxidized PLS:

- Dynamic: where the solution was circulated through the column in conjunction with O_2 gas
- Static sparging: where only O_2 gas was sparged into the column

The gas flowrate was set at 4L/min in both cases. Dynamic oxidation was performed when operators of the circuit were present, as supervision was required while static oxidation was performed with no direct supervision.

Following the oxidation step, the solution was pumped out of the columns and through a polishing filter, a 1 µm cartridge filter, in preparation for the solvent extraction stage.

Iron Solvent Extraction

The iron circuit was in operation for a cumulative total of ~623 hours using the PLS produced from the MPP leaching. Campaign 3 commenced at hour 387 of the program operation. The operational conditions of the circuit were not changed from those used in Campaigns 1 and 2. The extractant organic composition is presented in Table 52. The circuit staging is presented in Table 53. Initial operating conditions are presented in Table 54. Based on the circuit volume, the estimated number of total organic turnovers was ~180 times.

Table 52. Fe solvent extraction organic composition.

Component	Volume Fraction
2-Tridecanone	20%
2-Octanol	20%
Exxal-13	20%
Cansol D80	40%

Table 53. Initial MPP iron circuit stages.

Section	# of Stages
Extraction	5
Scrubbing	1
Stripping	7

Table 54. Initial iron circuit operating conditions.

Stream	Flowrate (ml/min)	O:A
Organic	50	-
Feed	30	1.5:1
Scrub Feed	2.5	15:01
Strip Feed	7.5	5.5:1

The profile of key elements of interest in the Fe SX circuit in the feed, raffinate, and strip streams are presented in Figures 56–62.

Campaign 3 average operational profiles of solutions in the Fe SX circuit are presented in Table 55. Results indicate that Fe is selectively extracted and results in 30 ppm in the Fe raffinate. A pregnant strip solution of 100 g/l Fe is currently being produced that is being used in the Hydro-hydrolysis test program. As it is indicated in Figures 56–62, the content of Cr, V, and Mn has continued to build up after recycling of evaporated Ti raffinate (Campaigns 2 and 3). Even with the increase in impurities in the PLS, selectivity for Fe is displayed.

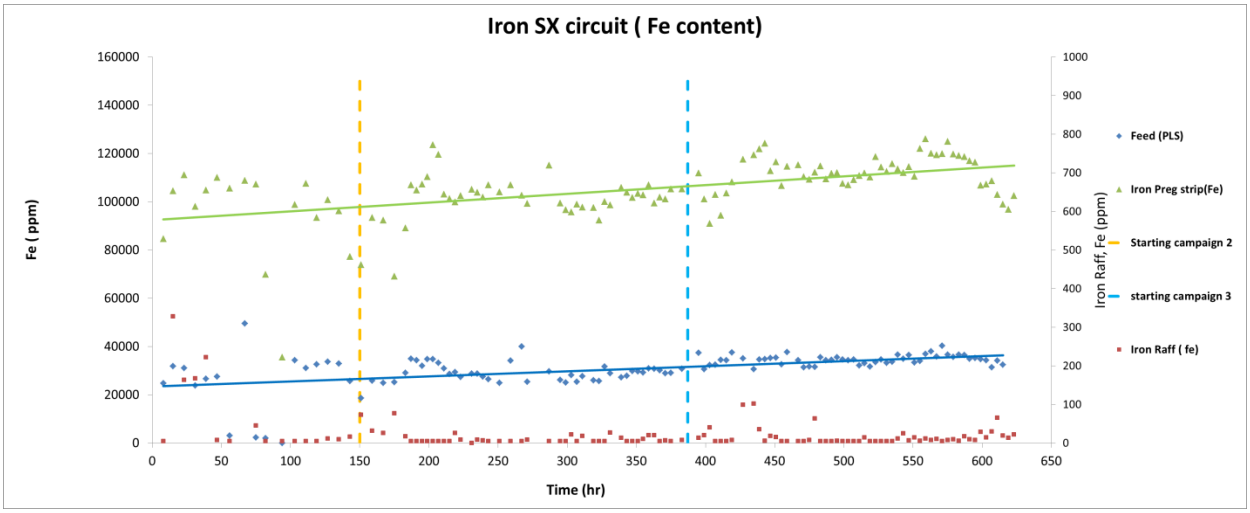

Figure 56. Fe circuit Fe analysis.

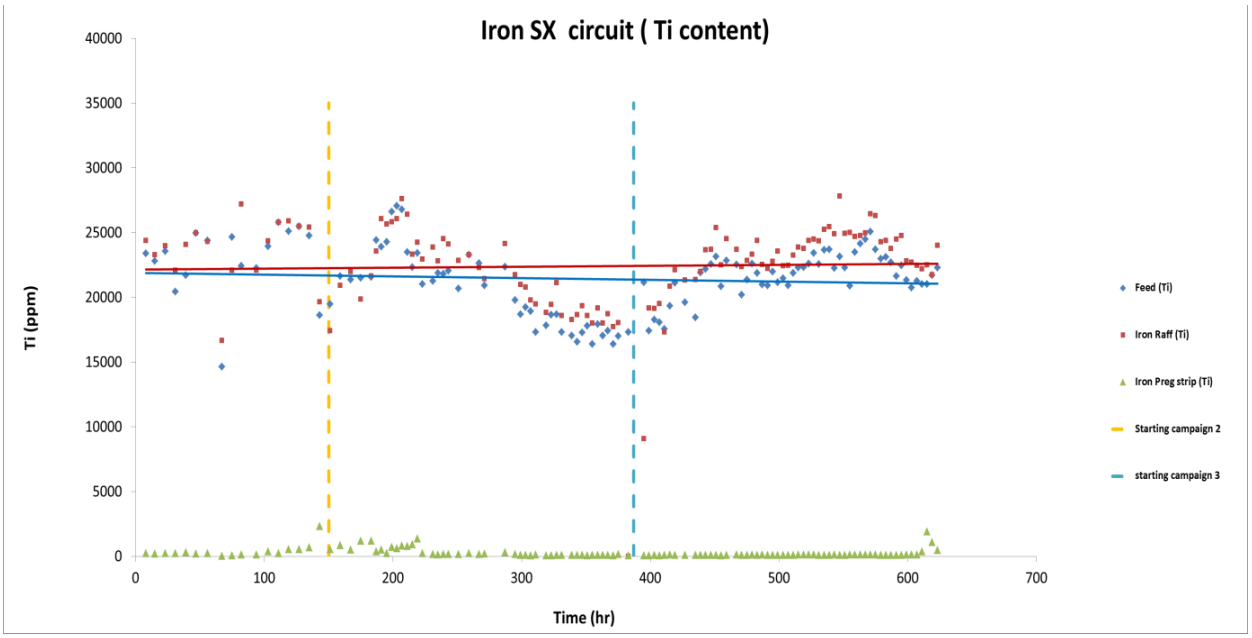

Figure 57. Fe circuit Ti analysis.

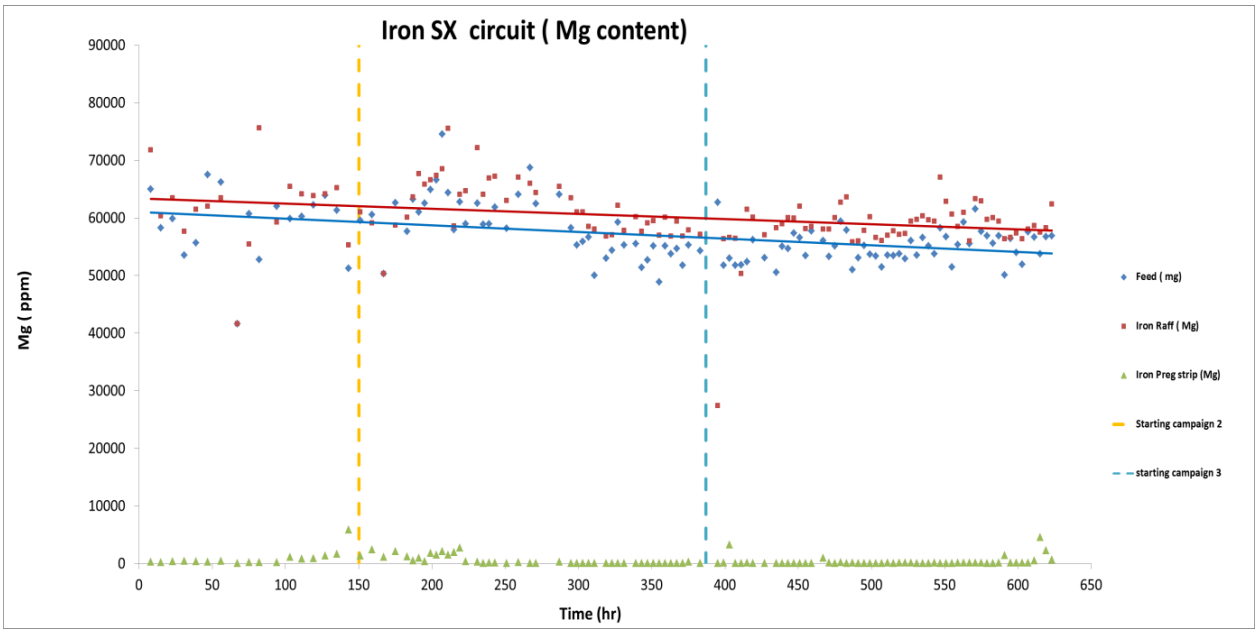

Figure 58. Fe circuit Mg analysis.

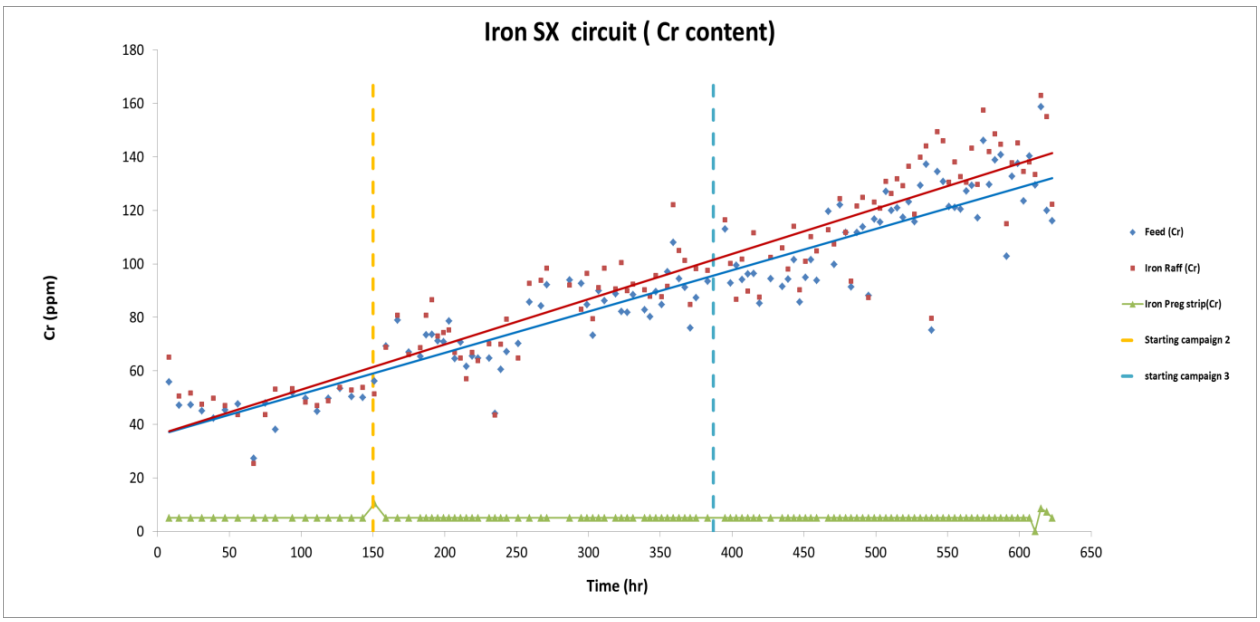

Figure 59. Fe circuit Cr analysis.

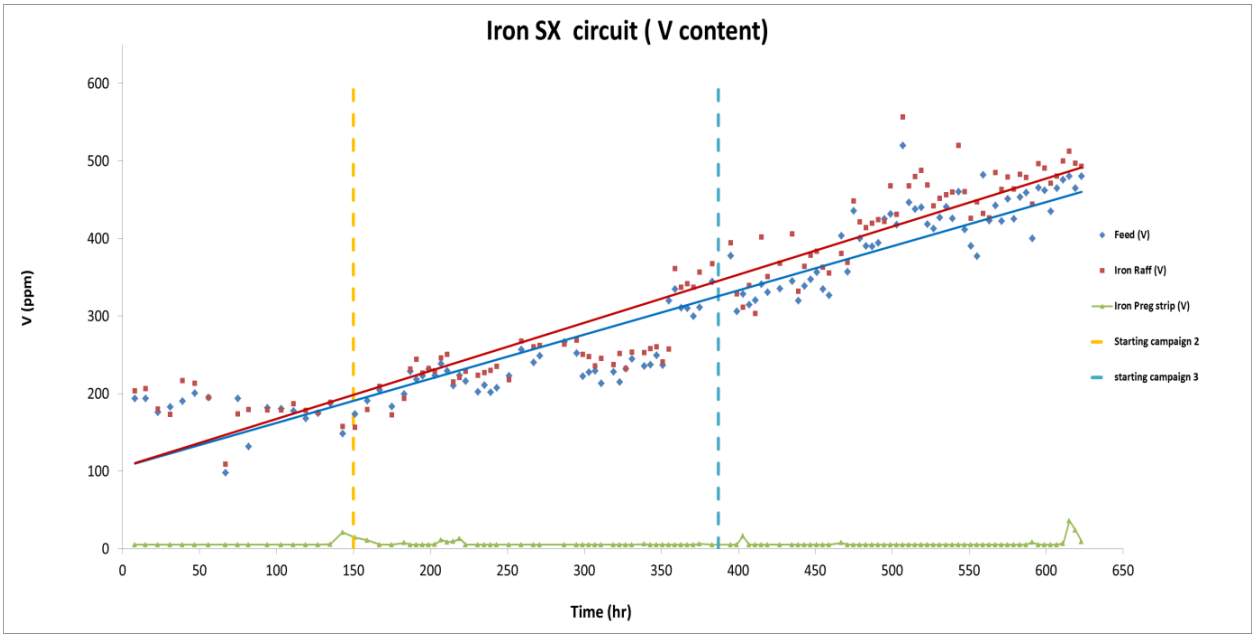

Figure 60. Fe circuit V analysis.

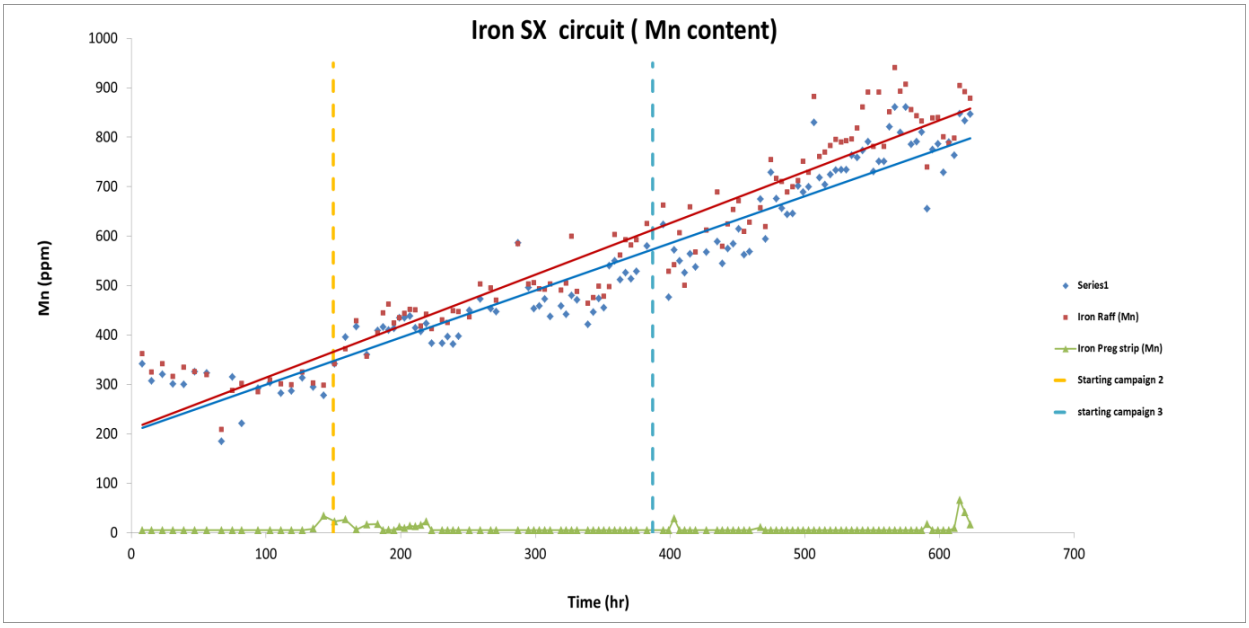

Figure 61. Fe circuit Mn analysis.

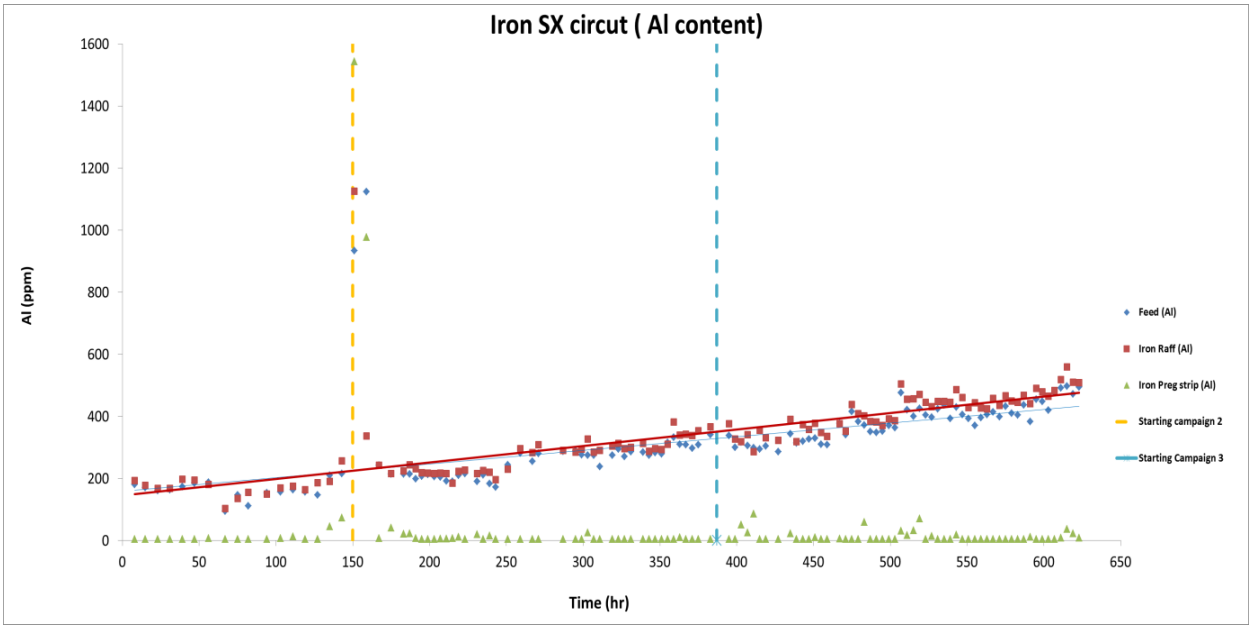

Figure 62. Fe circuit Al analysis.

Table 55. Fe SX solutions – average analysis of Campaign 3.

Campaign 3	Analysis results (ppm)						
	Al	Cr	Fe	Mg	Mn	Ti	V
Feed (ppm)	385	115	34395	55031	698	21729	406
Iron raff (ppm)	418	122	16	58319	748	23337	432
Iron preg strip (ppm)	13	5	111933	341	8	168	6

Titanium Solvent Extraction

The operational conditions of the Ti SX circuit were changed from those used in Campaigns 1 and 2. The extractant organic composition is presented in Table 56. The circuit staging and operation conditions are presented in Table 57 and Table 58. The circuit operated for 287 hours using the PLS produced from the MPP leaching. Initial operating conditions are presented in Table 57. Campaign 3 has started after 332 and finished at 523 hours of operation. Based on the circuit volume, the estimated number of organic turnovers is ~64 times.

Table 56. Ti SX extractant composition.

Component	Volume Fraction
Cyanex 923	20%
Exxal-13	20%
Cansol D80	60%

Table 57. Initial MPP titanium circuit stages.

Section	# of Stages
Extraction	4
Scrubbing	2
Settler	1
Stripping	8

Table 58. Initial titanium circuit operating conditions.

Stream	Flowrate (ml/min)	O:A
Organic	75	-
Feed	28	2.8:1
Scrub Feed	7.5	10:1
Strip Feed	15	5:1

The profile of key elements of interest in the Ti SX circuit in the feed, raffinate, and strip streams are presented in Figures 63–68.

The results show selective and consistent extraction of Ti over the course of the campaign and a buildup of impurities such as Cr, V, and Mn in the Ti raffinate stream.

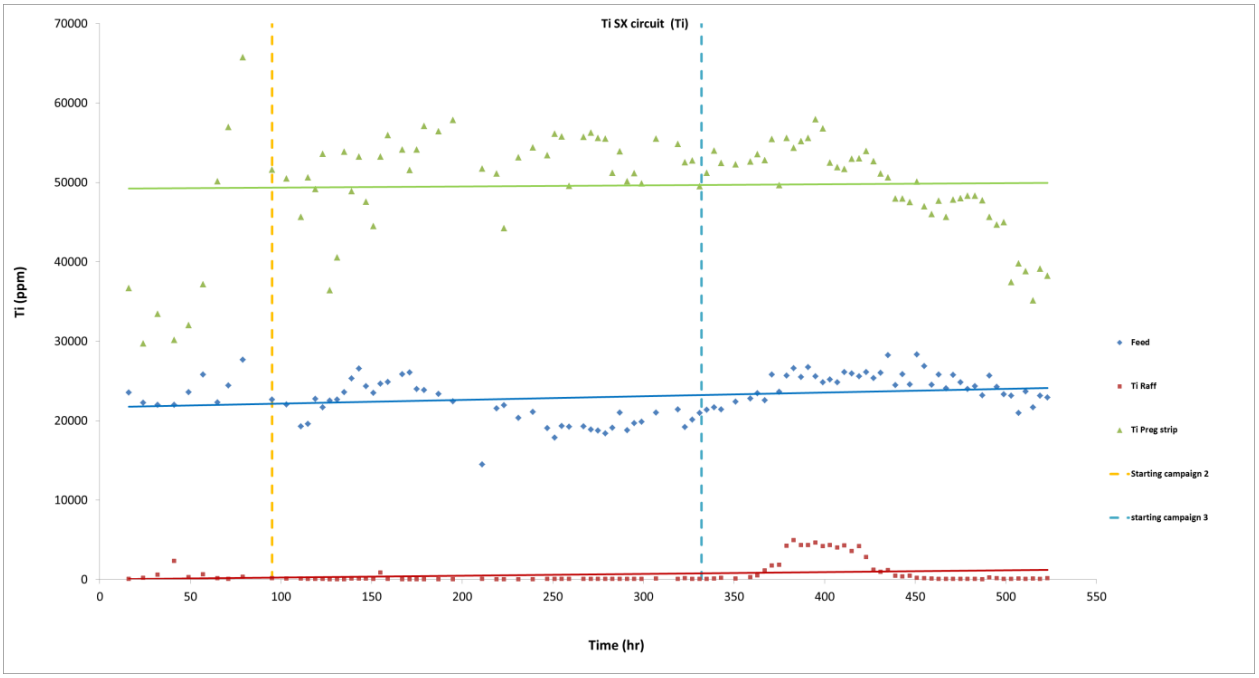

Figure 63. Ti circuit Ti analysis.

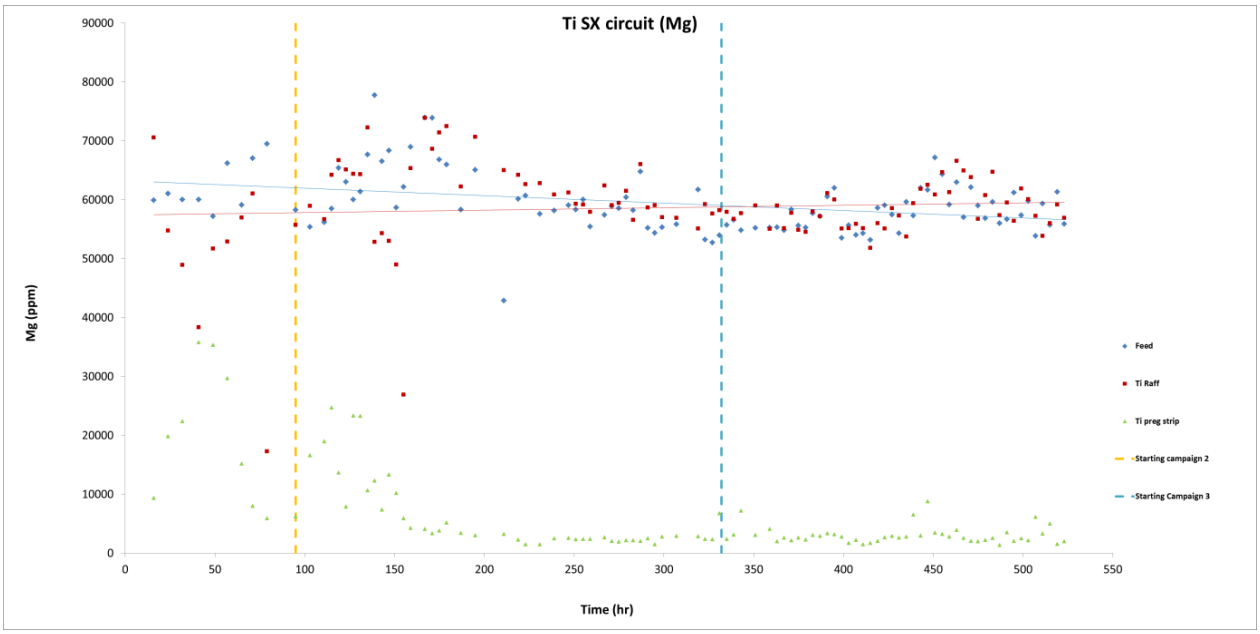

Figure 64. Ti circuit Mg analysis.

Figure 65. Ti circuit V analysis.

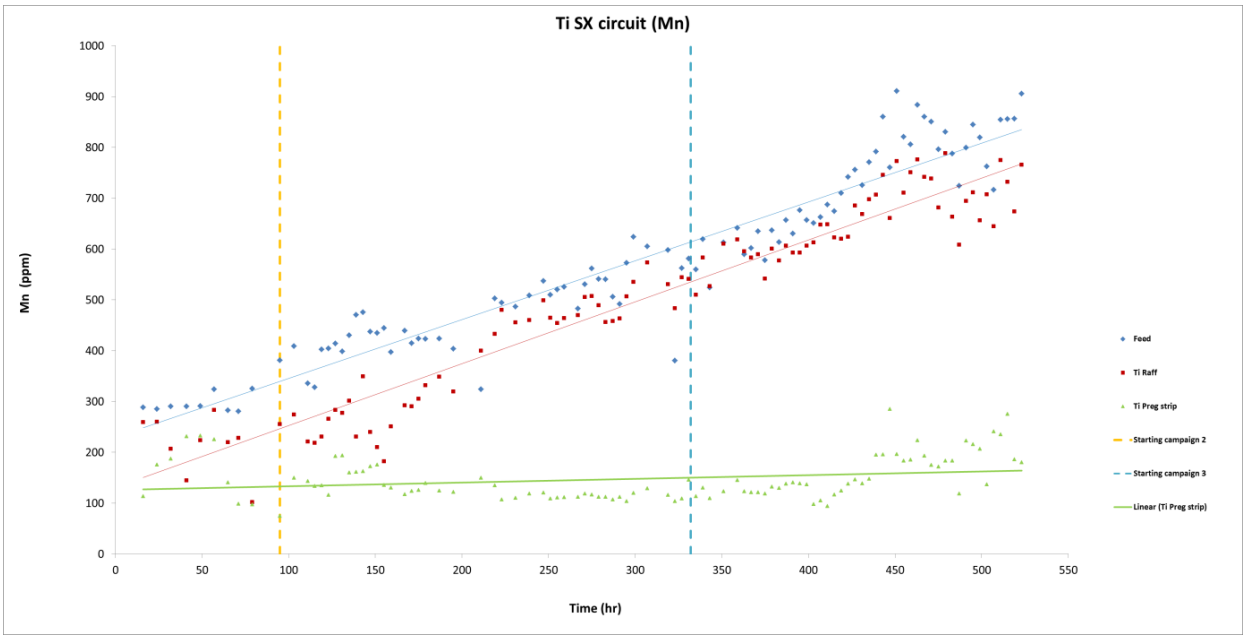

Figure 66. Ti circuit Mn analysis.

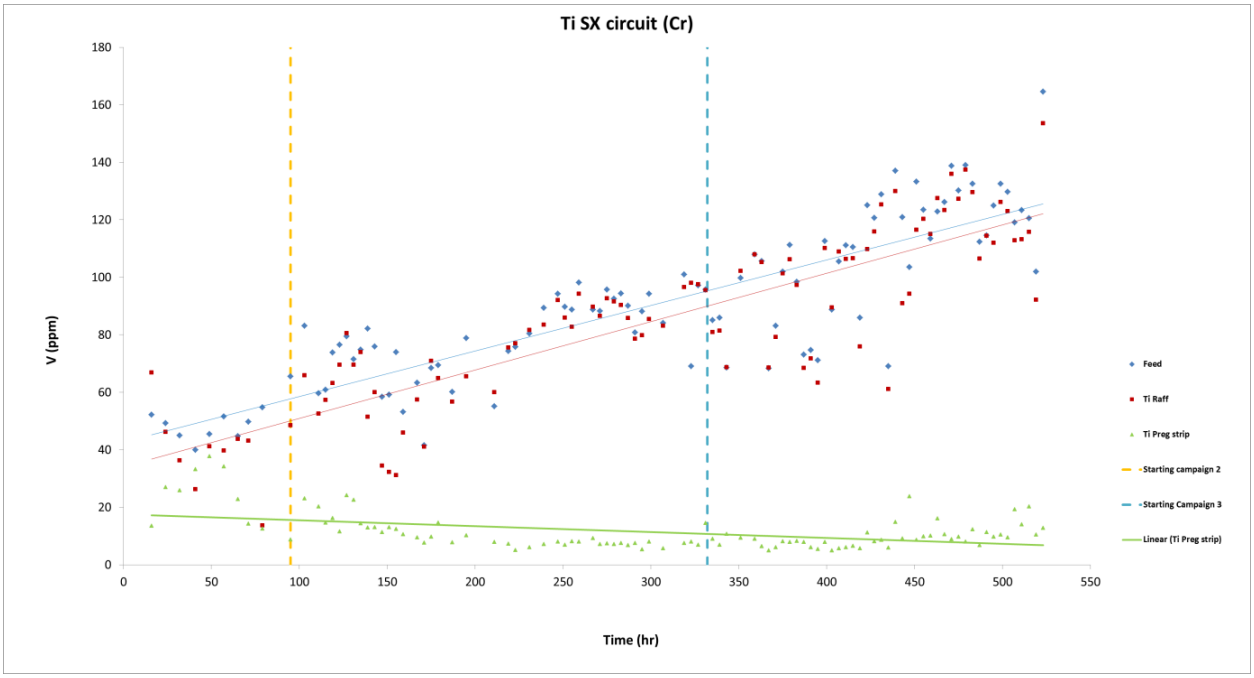

Figure 67. Ti Circuit Cr analysis.

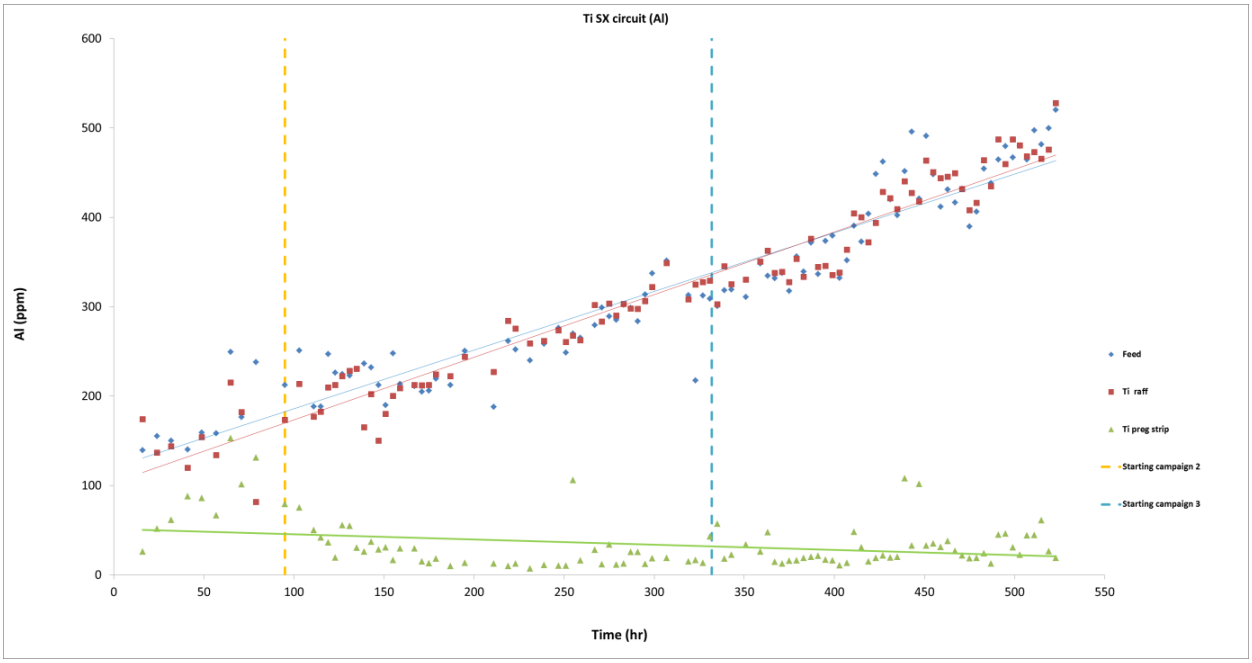

Figure 68. Ti circuit Al analysis.

Campaign 3 average operational profile of solutions in the Ti SX circuit is presented in Table 59. Results indicate that Ti is selectively extracted and results in 95 ppm of Ti in the Ti raffinate. A pregnant strip solution of ~48 g/l Ti was produced.

Table 59. Ti SX process solution average analysis of Campaign 3.

Campaign 3	Analysis results (ppm)						
	Al	Cr	Fe	Mg	Mn	Ti	V
Feed (ppm)	433	117	15	58490	778	24871	446
Ti raff (ppm)	429	111	12	58854	686	95	369
Ti preg strip (ppm)	32	10	21	2984	174	47767	79

During operation of the Ti circuit, it was observed that the Ti levels in the Ti raffinate solution were increasing with levels as high as 4 g/l Ti. It was determined that the cause of the variation was due to a high free acid level from a batch of solution. This promoted a strip condition rather than a load condition and resulted in incomplete extraction of Ti from the solution. Operation stabilized and returned to regular operation after that particular batch of solution passed through the system.

In Campaign 3, there was an increase in impurities such as Al, V, K, and Mn in the solution fed into the Ti SX circuit (Fe raffinate); however, there was not a significant increase in impurities in the Ti pregnant strip solution produced from the circuit. The results indicate that the Ti circuit is selective despite the increase in contained impurities with impurities being rejected in the Ti raffinate.

TiO_2 Precipitation

Precipitation was performed in an agitated vessel maintained at 95–100°C. Greater than 99% precipitation of Ti strip liquor values has been achieved in pilot plant operations.

For completion of Campaign 3, Ti precipitation filtrate cycled back into the circuit to further integrate the circuit with respect to recycling of process streams.

After the precipitation reaction, the TiO_2 slurry proceeds to filtration and product post-treatment. The post-treatment procedure involves further washing and filtration. Finally, the treated TiO_2 was dried and calcined.

Experimental

Ti pregnant strip solution from Campaign 3 was used to produce TiO_2 by thermal precipitation and calcination. A total amount of ~10kg of TiO_2 was produced in both Campaigns 2 and 3, and purity of the TiO_2 products was assessed. As shown in Figure 69, the kinetics of TiO_2 precipitation was similar to that of Campaign 2 and was complete after 9 hours, with greater than 98% of the contained Ti in the pregnant strip solution precipitated.

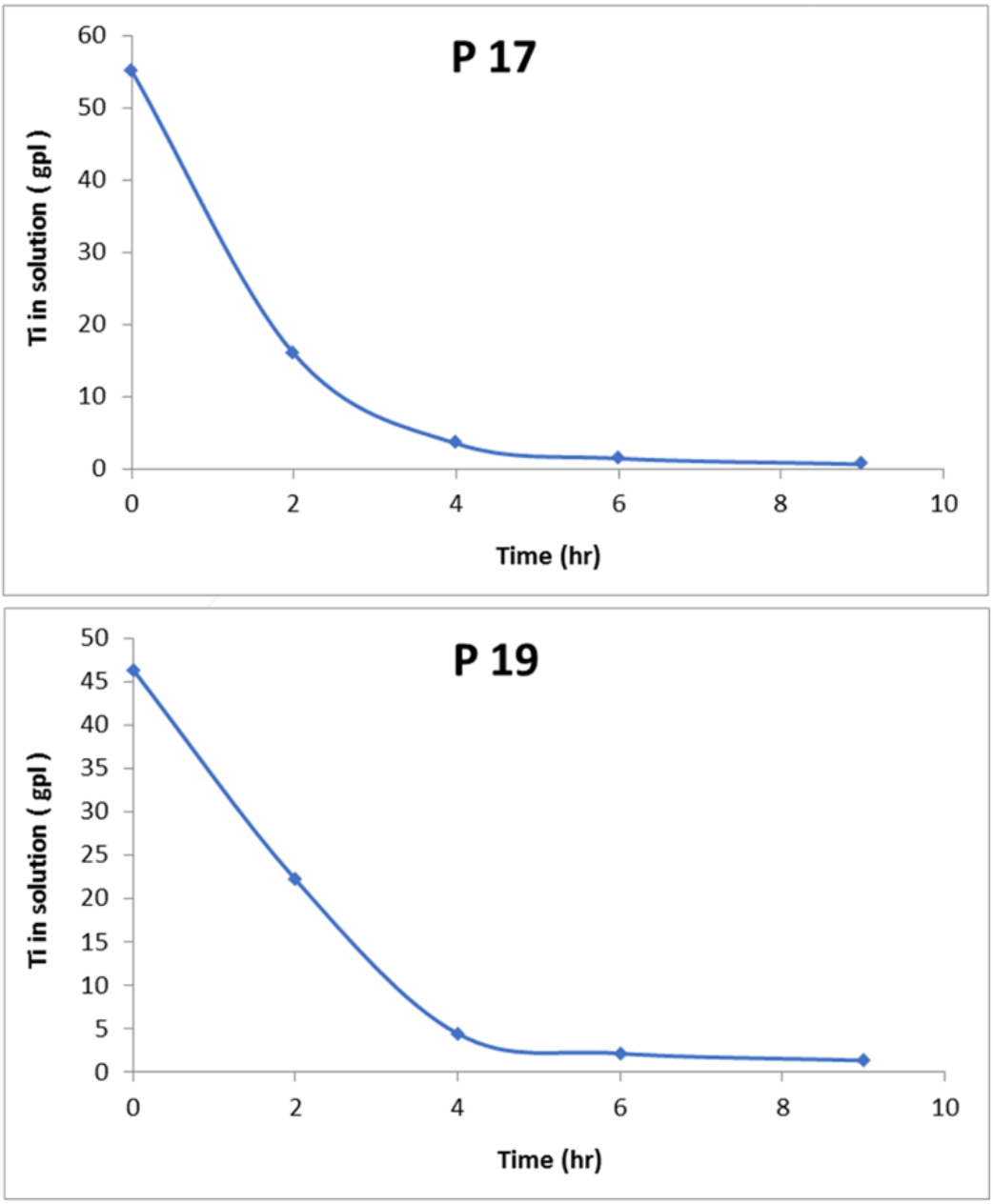

Figure 69. Ti content in preg strip during precipitation process in Campaign 3.

Titanium Dioxide Product

The quality of calcined titanium dioxide that was produced in Campaign 3 was examined. The impurities in the sample are shown in Table 60; the purity of Titanium dioxide is 99.51%. Titanium dioxide quality after calcination reached to ~99.51% and 99.56% in Campaigns 3 and 2, respectively (Fig. 70). It clearly shows that the quality of TiO_2 is not affected by the impurity buildup in the circuit caused by the integration of recycled process streams (i.e. Ti raffinate and Ti preciptation process filtrate) into the flowsheet.

Table 60. Calcined titanium dioxide, Campaign 3, PRO test 17.

Assay Impurities in the Titanium dioxide product (%)							
Ag_2O	Al_2O_3	CuO	P_2O_5	SO_2	Others	Total impurity	TiO_2
0.0005	0.2523	0.0013	0.0510	0.1334	0.0515	0.4899	99.51

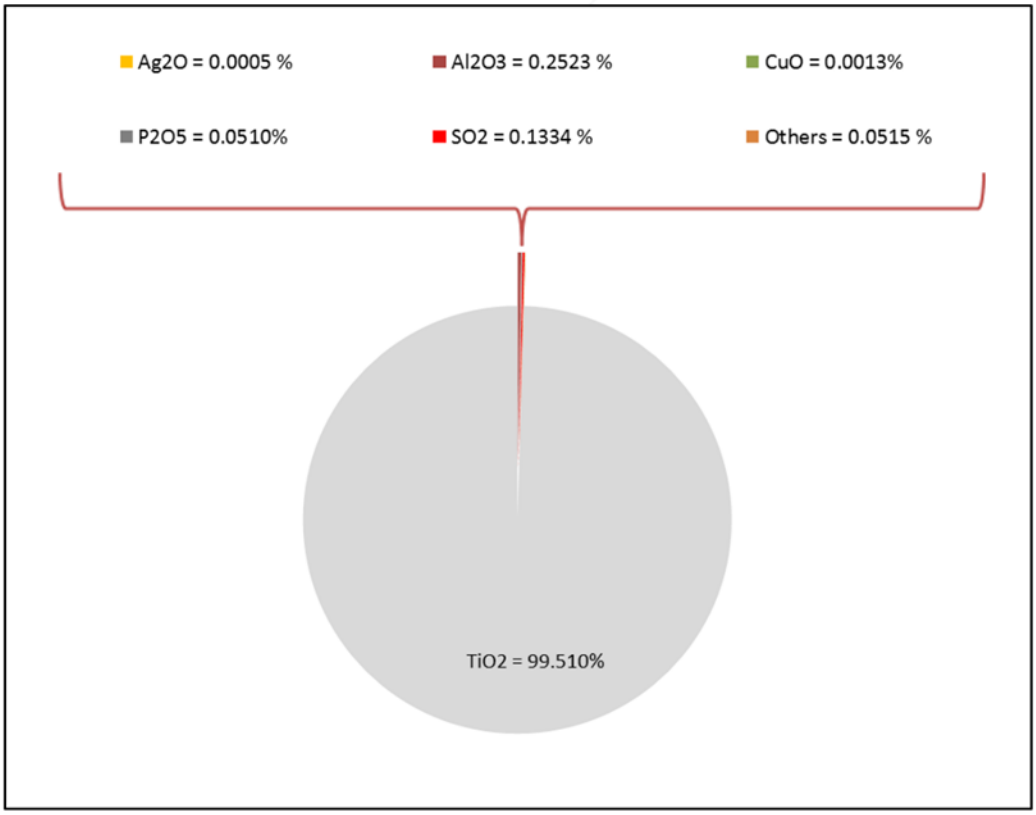

Figure 70. Titanium impurities content in Campaign 3 per PRO analyses.

The calcined and non-calcined products were also examined independently by NRRI using mineralogical, mineral chemical, and lithogeochemical analysis methods.

Mineralogical Analysis

Mineralogical analysis of the Campaign 3 titanium dioxide precipitates was performed utilizing x-ray diffraction analysis. Two samples of the Campaign 3 titanium dioxide precipitates were evaluated. These included the non-calcined sample 1802-P17-1 (ML-68) and the calcined sample 1802-P17-2 (ML-69). As indicated in Table 8, the mineralogy of these precipitates was determined to be rutile.

Mineral Chemical Analysis

Two samples of Campaign 3 titanium dioxide precipitates underwent mineral chemistry analysis at the Electron Probe Microanalyzer located at the EML at the UMTC. These included samples 1802-P17-1 (ML-68) and 1802-P17-2 (ML-69), which represent non-calcined and calcined Campaign 3 titanium dioxide precipitates, respectively.

Rutile was the single mineral phase identified in the titanium dioxide precipitates from Campaign 3. Results of electron microprobe mineral chemical analysis and stoichiometric calculations are included in Appendix 4: Tables A-27 and A-28.

Figure 71 is a backscatter image of sample 1802-P17-1 (ML-68) obtained during EMPA analysis. Four morphological types of titanium dioxide precipitates were identified: A) round (presumably spherical in three dimensions), locally concentrically zoned rutile spheres ranging from 2 µm to 20 µm in diameter, with concentric zoning occurring primarily in the larger spheres (Fig. 71A); B) elongate (possibly platy in the third dimension) rutile precipitates that have growth textures roughly perpendicular to the long axis of the particles that range from 30 µm to 60 µm in length and 10 µm to 20 µm in width (Figs. 71B and 71D); C) slightly curved, elongate rutile precipitates up to 60 µm in length and 10 µm–15 µm in width, characterized by one side that is composed of a fine layer of rutile that grades into the other side of the fragment, which is composed of a composite of semi-angular to rounded individual rutile precipitates that range from 1 µm to 4 µm in diameter (Fig. 71C); and D) elongate composite fragments up to 380 µm in length and ranging from 20 µm to 75 µm in length characterized by one side of the fragment that is composed of a fine layer of rutile with growth textures that are perpendicular to the long axis of the fragment, which abruptly transitions into a composite of 3 µm–15 µm diameter semi-angular rutile precipitates and rounded and locally concentrically zoned rutile spheres (Figs. 71 E and 71F). These composite fragments are believed to have precipitated at the edge of the precipitation vessel.

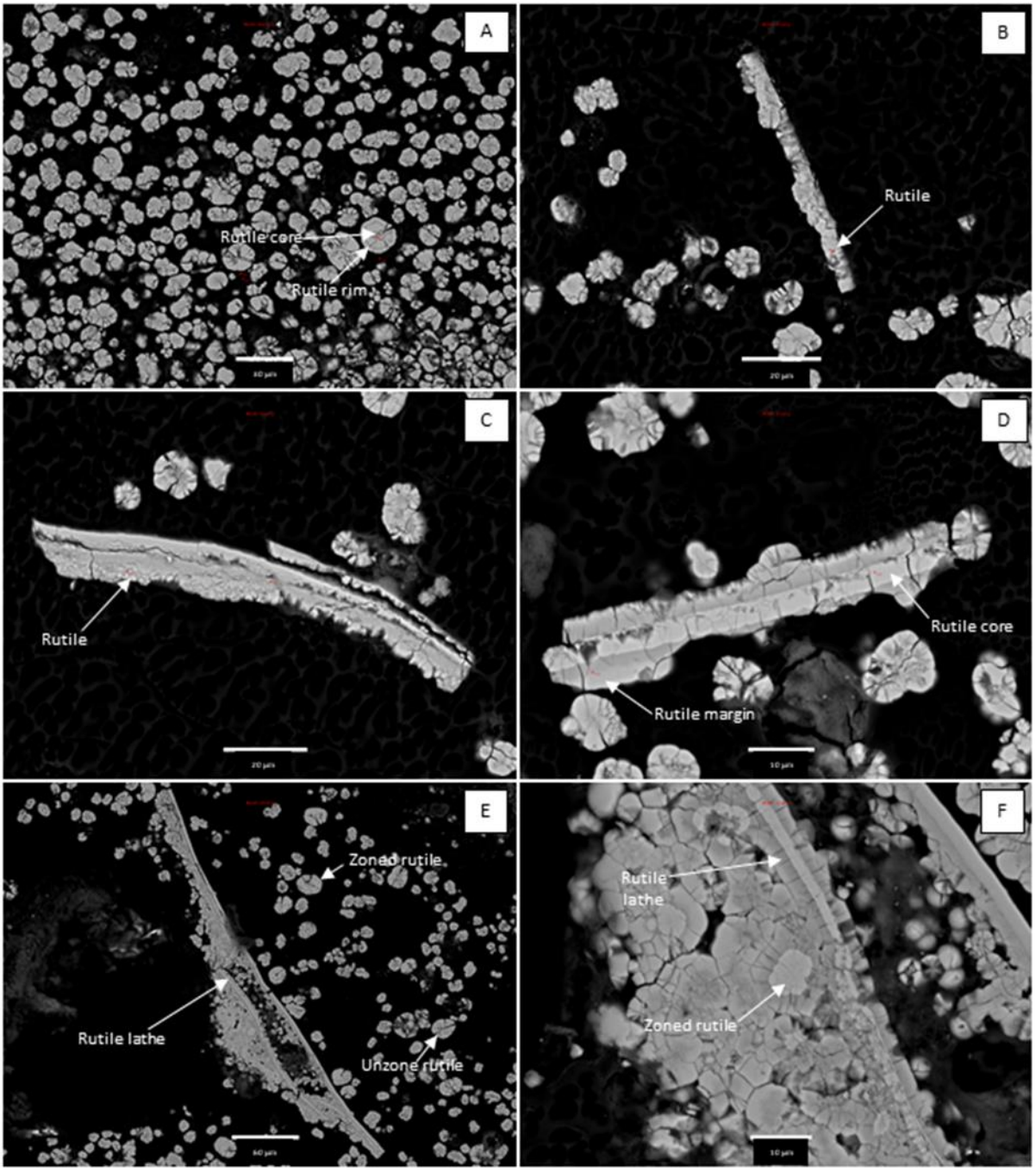

Figure 71. Electron microprobe backscatter image of Campaign 3 non-calcined titanium dioxide (rutile) precipitates in sample 1802-P17-1 (ML-68). A) Locally concentrically zoned rutile spheres. Scale bar is 20 µm. B) Rutile spheres with elongate rutile precipitate that has growth textures roughly perpendicular to the long axis of the fragment. Scale bar is 10 µm. C) Slightly curved fragment composed of a fine layer of rutile that grades into a composite of semi-angular to rounded, locally concentrically zoned rutile precipitates. Scale bar is 20 µm. D) Close-up of elongate rutile fragment illustrating well-defined core and margins. Scale bar is 10 µm. E) Elongate composite fragment comprising elongate rutile precipitate and a composite of semi-angular to rounded, locally concentrically zoned rutile spheres. Scale bar is 60 µm. F) Close-up view of elongate composite fragment in Figure 68E. Scale bar is 10 µm. Red numbers and circles in images are analysis locations.

Mineral chemical analysis of the non-calcined Campaign 3 titanium dioxide precipitates from sample 1802-P17-1 (ML-68) are shown in Table 61. Rutile was the sole mineral phase identified. The composition of the rutile was dominated by TiO_2 (96.394%–99.100%) with subordinate SiO_2 (0.022%–0.157%), FeO (0.000%–0.029%), MnO (0.000%–0.026%), MgO (0.001%–0.110%), V_2O_3 (0.024%–0.358%), Cr2O3 (0.000%–0.016%), NiO (0.000%–0.015%), and chlorine (0.000%–0.286%). Aluminum (as Al_2O_3) was not identified in the analyses. Overall, the TiO_2/Total ratio varied from 0.992 to 0.999, with that average TiO_2/Total ratio for the non-calcined sample being 0.995. Four samples that were analyzed were questionable due to low analytical totals (80.439%–96.750%; Appendix 4: Table A4-28).

Table 61. Electron microprobe analyses of Campaign 3 sample 1802-P17-1 (ML-68). This sample is non-calcined. Values are in weight percentages.

Electron Microprobe Analysis – TiO_2 Precipitate Rutile Campaign 3 Non-Calcined (n = 7)													
Sample	Description	Phase	SiO_2	TiO_2	Al_2O_3	FeO	MnO	MgO	V_2O_3	Cr_2O_3	NiO	Cl	Total
ML-68-30-92-1	Composite Rutile Sphere Core	Rutile	0.118	97.687	0.000	0.000	0.000	0.041	0.328	0.000	0.015	0.013	98.202
ML-68-31-93-1	Composite Rutile Sphere Rim	Rutile	0.157	97.852	0.000	0.016	0.000	0.110	0.358	0.000	0.005	0.085	98.583
ML-68-32-94-1	Composite Rutile Sphere Core	Rutile	0.022	98.924	0.000	0.004	0.026	0.001	0.024	0.000	0.012	0.038	99.050
ML-68-34-96-1	Composite Rutile Sphere Core	Rutile	0.034	97.525	0.000	0.025	0.018	0.017	0.136	0.016	0.000	0.058	97.829
ML-68-35-97-1	Composite Rutile Sphere Rim	Rutile	0.121	99.100	0.000	0.029	0.000	0.020	0.123	0.000	0.002	0.210	99.606
ML-68-39-101-1	Elongate Rutile Lathe Core	Rutile	0.082	98.445	0.000	0.000	0.002	0.035	0.133	0.007	0.000	0.000	98.704
ML-68-40-102-1	Elongate Rutile Lathe Rim	Rutile	0.108	96.394	0.000	0.014	0.000	0.048	0.186	0.013	0.000	0.286	97.050
		Minimum	*0.022*	*96.394*	*0.000*	*0.000*	*0.000*	*0.001*	*0.024*	*0.000*	*0.000*	*0.000*	*97.050*
		Maximum	*0.157*	*99.100*	*0.000*	*0.029*	*0.026*	*0.110*	*0.358*	*0.016*	*0.015*	*0.286*	*99.606*
		Average	*0.092*	*97.990*	*0.000*	*0.013*	*0.007*	*0.039*	*0.184*	*0.005*	*0.005*	*0.099*	*98.432*
		Median	*0.108*	*97.852*	*0.000*	*0.014*	*0.000*	*0.035*	*0.136*	*0.000*	*0.002*	*0.058*	*98.583*
		St. Deviation	*0.045*	*0.861*	*0.000*	*0.011*	*0.010*	*0.033*	*0.110*	*0.006*	*0.006*	*0.100*	*0.773*

Figure 72 illustrates the chemical compositions of the various textures of titanium dioxide (rutile) from the non-calcined Campaign 3 sample 1802-P17-1 (ML-68). In terms of weight percent oxides, the precipitates are nearly pure TiO_2 with little MgO or V_2O_3 contents (Figs. 71A–71D). Figure 71E illustrates the chemistry of the titanium dioxide precipitates in terms of molar Fe^{2+}, Ti^{4+}, and Fe^{3+}. Molar ratios of these cations were calculated using RUTCALC.xls (Gabbrosoft.com), which assumes all iron in the titanium dioxide precipitate is Fe^{2+}. As shown in Figure 69E, the titanium dioxide precipitates in the non-calcined sample 1802-P17-1 (ML-68) are stoichiometric rutile.

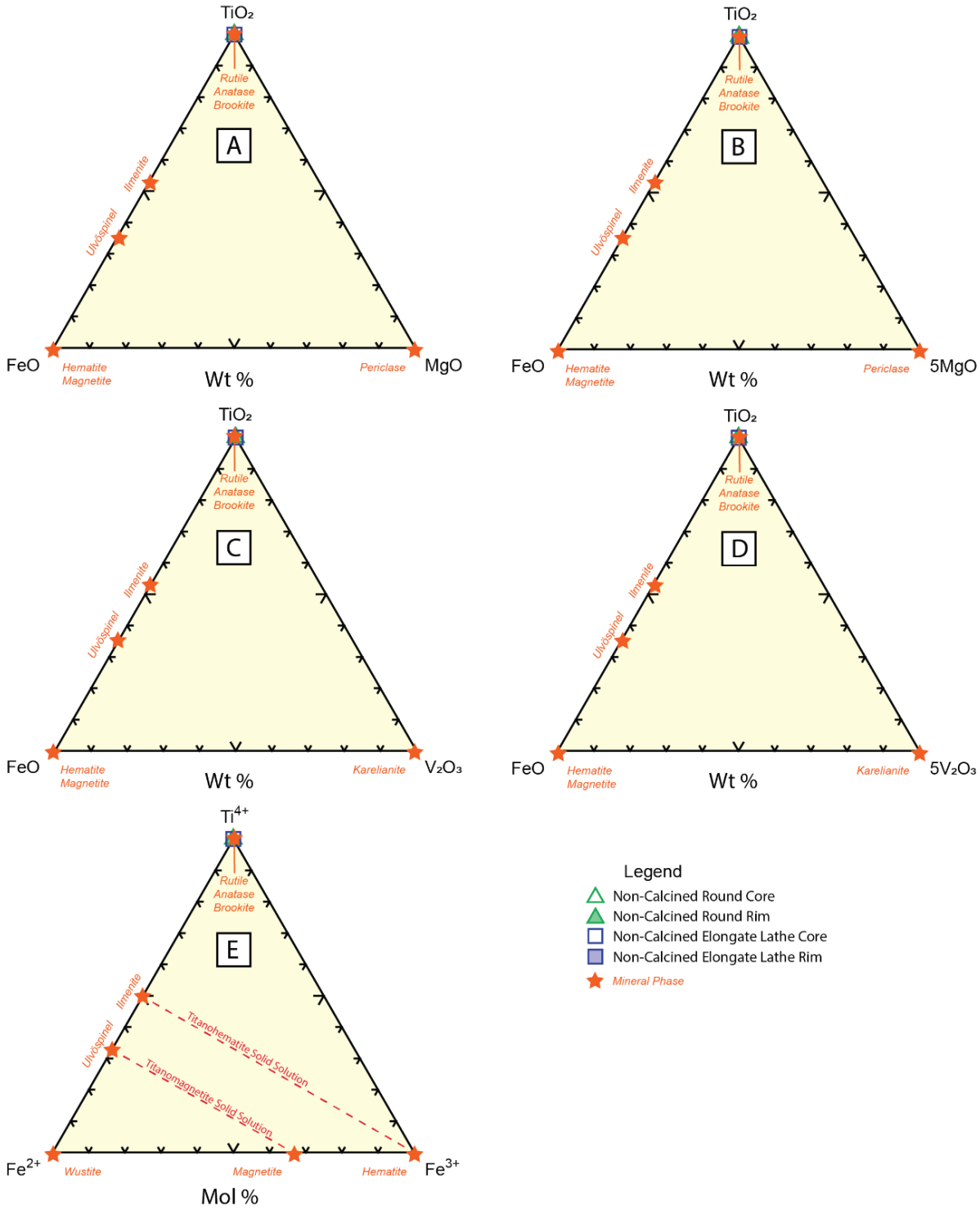

Figure 72. Ternary diagrams illustrating the chemical composition of titanium dioxide (TiO_2, rutile) precipitates from sample 1802-P17-1, which represents the non-calcined titanium dioxide precipitate from Campaign 3. Figures 72A–72D represent ternary diagrams in the FeO-TiO_2-MgO, FeO-TiO_2-5MgO, FeO-TiO_2-V_2O_3, and FeO-TiO_2-5V_2O_3 systems. Note that the titanium precipitate in this sample is nearly pure TiO_2. Figure 72E is a molar Fe^{2+}-Ti^{4+}-Fe^{3+} ternary diagram (modified after Klein and Hurlbut, 1999; Meinhold, 2010) showing that the non-calcined titanium dioxide precipitate is stoichiometric rutile.

Figure 73 is a backscatter image of sample 1802-P17-2 (ML-69) obtained during EMPA analysis. This sample represents titanium dioxide precipitates from Campaign 3 that have been calcined. Four morphological types of titanium dioxide precipitates were identified: A) round (presumably spherical in three dimensions), locally concentrically zoned rutile spheres ranging from 2 µm to 15 µm in diameter, locally with concentric zoning occurring primarily in the larger spheres (Fig. 73A); B) slightly curved, elongate rutile precipitates up to ~40 µm in length and 5 µm to 12 µm in width that display growth textures roughly perpendicular to the long axis of the particles. Note that rutile spheres appear to have considerable porosity (Fig. 73B); C) Slightly curved composite fragments comprising a core of an elongate rutile precipitate surrounded by 1 µm–5 µm diameter round to oval rutile structures (Fig. 73C); D) large (250 µm–300 µm in diameter) aggregate fragments comprised of 5 µm–30 µm rounded, locally concentrically zoned rutile spheres. Note that one concentrically zoned rutile sphere is approximately 60 µm in diameter (Figs. 73D, 73E, and 73F). In almost all photos, the calcined rutile spheres appear to have more porosity than spherical rutile structures in the non-calcined sample (refer to Fig. 52).

Mineral chemical analysis of the rutile precipitates from Campaign 3 calcined titanium dioxide precipitate sample 1802-P17-2 (ML-69) are shown in Table 62. Rutile was the only mineral phase identified. As in the non-calcined sample, the composition of the rutile in the calcined sample was dominated by TiO_2 (97.685–101.449%) with subordinate SiO_2 (0.000%–0.637%), Al_2O_3 (0.000%–0.184%), FeO (0.000%–0.044%), MnO (0.000%–0.029%), MgO (0.000%–0.004%), V_2O_3 (0.000%–0.195%), Cr_2O_3 (0.000%–0.042%), NiO (0.000%–0.017%), and chlorine (0.000%–0.059%). Note that the highest chlorine concentration in this calcined sample (0.059%) is considerably lower than the chlorine content in the non-calcined sample (0.286%; sample 1802-P17-1/ML68). Overall, the TiO_2/Total ratio for the calcined samples varied from 0.987 to 0.999. The average TiO_2/Total ratio for the calcined sample 1802-P17-2 (ML69) is 0.997. This is higher than the average TiO_2/Total ratio for the non-calcined sample 1802-P17-1 (ML-68) of 0.995.

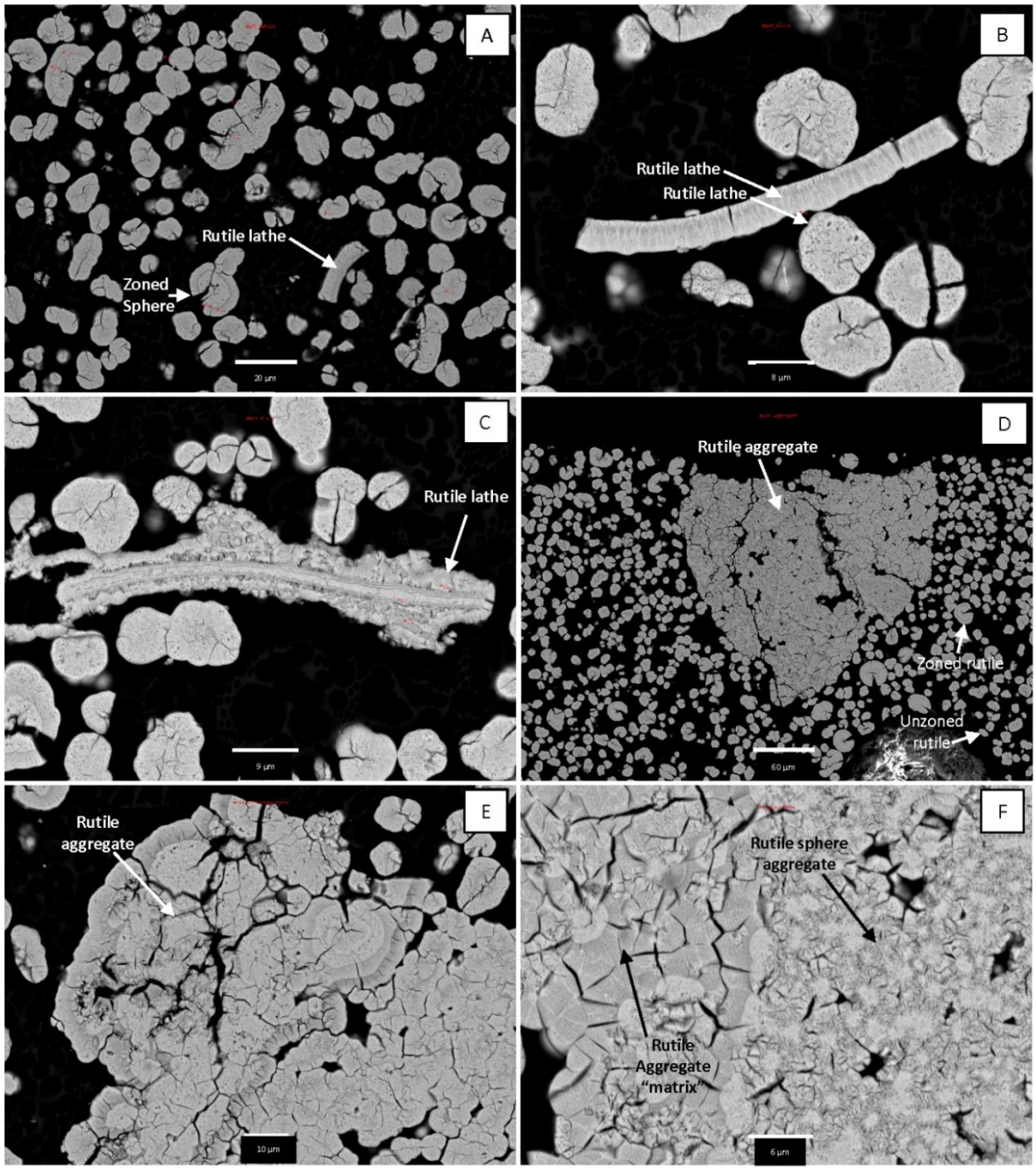

Figure 73. Electron microprobe backscatter image of Campaign 3 titanium dioxide (rutile) precipitates in sample 1802-P17-2 (ML69), a calcined sample of Campaign 3 titanium dioxide precipitates. A) Rutile spheres and lathes. Scale bar is 20 µm. B) Close-up of rutile spheres and lathes. Note growth textures perpendicular to long axis of the lathe. Also note faint concentric zoning and apparent porosity within the rutile spheres. Scale bar is 8 µm. C) Close-up of rutile spheres and lathe. Note well-defined zones in the lab and faint zoning and apparent porosity within the spheres. Scale bar is 9 µm. D) Rutile aggregate and rutile spheres. Note that spheres commonly exhibit a wedge-shaped indentation from the margin to the core of the sphere. Scale bar is 60 µm. E) Close-up of rutile aggregate composed of concentrically zoned rutile spheres. Scale bar is 10 µm. F) Close-up of rutile aggregate. Note radial growth textures around rutile spheres in area labeled as "rutile aggregate matrix." Scale bar is 6 µm. Red numbers and circles in images are analysis locations.

Table 62. Electron microprobe analyses of Campaign 3 sample 1802-P17-2 (ML-69). This sample is calcined. Values are in weight percentages.

Electron Microprobe Analysis – TiO_2 Precipitate Rutile Campaign 3 Calcined (n = 13)												
Sample	Description	Phase	SiO_2	TiO_2	Al_2O_3	FeO	MnO	MgO	V_2O_3	Cr_2O_3	NiO	Cl	Total
ML-69-41-103-1	Composite Rutile Sphere Core	Rutile	0.637	98.249	0.184	0.006	0.026	0.004	0.152	0.000	0.000	0.000	99.259
ML-69-42-104-1	Composite Rutile Sphere Rim	Rutile	0.102	99.067	0.000	0.001	0.007	0.000	0.173	0.000	0.004	0.000	99.354
ML-69-43-105-1	Composite Rutile Sphere Core	Rutile	0.253	100.864	0.033	0.022	0.000	0.000	0.096	0.000	0.017	0.026	101.311
ML-69-44-106-1	Composite Rutile Sphere Rim	Rutile	0.060	98.450	0.000	0.000	0.006	0.000	0.151	0.000	0.009	0.000	98.676
ML-69-45-107-1	Composite Rutile Sphere Core	Rutile	0.054	100.915	0.000	0.021	0.001	0.000	0.128	0.042	0.000	0.059	101.220
ML-69-46-108-1	Composite Rutile Sphere Rim	Rutile	0.207	98.771	0.014	0.000	0.000	0.002	0.138	0.000	0.007	0.000	99.138
ML-69-47-109-1	Non-Zoned Rutile Sphere	Rutile	0.086	101.449	0.000	0.026	0.000	0.000	0.195	0.000	0.000	0.000	101.756
ML-69-48-110-1	Non-Zoned Rutile Sphere	Rutile	0.000	96.731	0.000	0.000	0.000	0.000	0.196	0.032	0.041	0.000	97.009
ML-69-49-111-1	Non-Zoned Rutile Sphere	Rutile	0.028	99.617	0.000	0.044	0.002	0.000	0.162	0.000	0.001	0.000	99.854
ML-69-50-112-1	Elongate Rutile Lathe Core	Rutile	0.002	100.538	0.000	0.000	0.029	0.000	0.118	0.011	0.008	0.000	100.706
ML-69-51-113-1	Elongate Rutile Lathe Core	Rutile	0.053	101.415	0.000	0.025	0.004	0.000	0.048	0.026	0.010	0.000	101.582
ML-69-52-114-1	Elongate Rutile Lathe Rim	Rutile	0.000	97.685	0.000	0.011	0.000	0.000	0.086	0.003	0.000	0.000	97.785
ML-69-53-115-1	Elongate Rutile Lathe Rim	Rutile	0.012	99.924	0.000	0.007	0.000	0.000	0.000	0.000	0.017	0.000	99.960
		Minimum	***0.000***	***97.685***	***0.000***	***0.000***	***0.000***	***0.000***	***0.000***	***0.000***	***0.000***	***0.000***	***97.785***
		Maximum	***0.637***	***101.449***	***0.184***	***0.044***	***0.029***	***0.004***	***0.195***	***0.042***	***0.017***	***0.059***	***101.756***
		Average	***0.125***	***99.745***	***0.019***	***0.014***	***0.006***	***0.000***	***0.121***	***0.007***	***0.006***	***0.007***	***100.050***
		Median	***0.057***	***99.770***	***0.000***	***0.009***	***0.002***	***0.000***	***0.133***	***0.000***	***0.006***	***0.000***	***99.907***
		St. Deviation	***0.172***	***1.243***	***0.051***	***0.013***	***0.010***	***0.001***	***0.053***	***0.013***	***0.006***	***0.017***	***1.213***

Figure 74 illustrates the chemical compositions of the various textures of titanium dioxide (rutile) precipitates from Campaign 3 calcined sample 1802-P17-2(ML-69) based on EMPA mineral chemical analysis. In terms of weight percent oxides, the precipitates are nearly pure TiO_2, with little MgO or V_2O_3 contents (Figs. 74A–74D). Figure 74E illustrates the chemistry of the titanium dioxide precipitates in terms of molar Fe^{2+}, Ti^{4+}, and Fe^{3+}. Molar ratios of these cations were calculated using RUTCALC.xls (Gabbrosoft.com), which assumes all iron in rutile is Fe^{2+}. As indicated, the precipitates from the Campaign 3 calcined sample 1802-P17-2 (ML-69) are stochiometrically rutile.

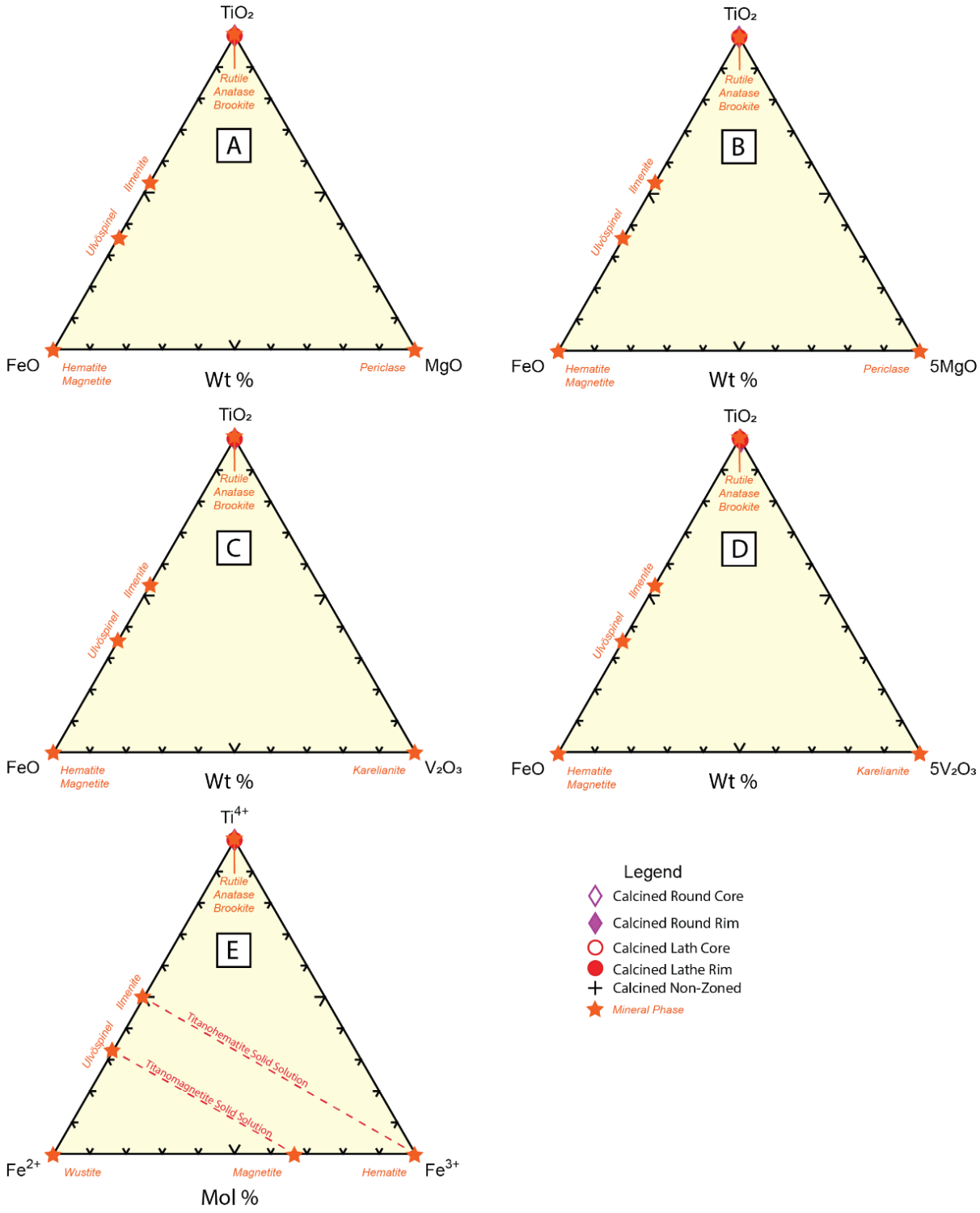

Figure 74. Ternary diagram illustrating the chemical composition of titanium dioxide (TiO_2, rutile) precipitates from sample 1802-P17-2, which represents the calcined titanium dioxide precipitate from Campaign 3. Figures 74A–74D represent ternary diagrams in the FeO-TiO_2-MgO, FeO-TiO_2-5MgO, FeO-TiO_2-V_2O_3, and FeO-TiO_2-5V_2O_3 systems. Note that the titanium precipitate in this sample is nearly pure TiO_2. Figure 74E is a molar Fe^{2+}-Ti^{4+}-Fe^{3+} ternary diagram (modified after Klein and Hurlbut, 1999; Meinhold, 2010) showing that the calcined titanium dioxide precipitate is stoichiometric rutile.

Lithogeochemical Analysis

Whole rock lithogeochemical analyses were performed on the non-calcined (1802-P17-2/ML-68) and calcined (1802-P17-2/ML-69) titanium dioxide precipitates produced during Campaign 3. The results of these analyses are shown in Table 63, and ALS Laboratory analytical certificates can be found in Appendix 3: Tables A3-1 to A3-7.

It is important to note that original lithogeochemical analyses on the Campaign 3 TiO_2 precipitates using ALS Laboratories analytical method ME-ICP06 resulted in low major element analytical totals (ranging from 9.36% to 30.54%). Discussions with ALS Laboratory personnel indicated that accurate analyses of such pure materials would be better achieved using ALS Laboratory analytical method ME-XRF06. Reanalysis of the Campaign 3 TiO_2 precipitates using ALS Laboratory analytical method ME-XRF06 were conducted, and the analytical totals for the major element oxides for the Campaign 3 TiO_2 precipitates ranged between 99.0% and 99.5%.

Relative results for the non-calcined (1802-P17-1/ML-68) and calcined (1802-P17-2/ML-69) Campaign 3 titanium dioxide precipitates in terms of major element oxide compositions (weight percentages) are described below:

- SiO_2: Higher in the non-calcined sample (0.07%) versus the calcined sample (0.03%)
- Al_2O_3: Below 0.01% in both the non-calcined and calcined samples
- Fe_2O_3: Higher in the calcined sample (0.01%) versus the non-calcined sample (<0.01%)
- CaO: Equivalent in the non-calcined and calcined sample at 0.01%
- MgO: Higher in the calcined sample (0.01%) versus the non-calcined sample (<0.01%)
- Na_2O: Below 0.01% in both the non-calcined and calcined samples
- K_2O: Below 0.01% in both the non-calcined and calcined samples
- Cr_2O_3: Below 0.01% in both the non-calcined and calcined samples
- TiO_2: Higher in the calcined sample (98.22%) versus the non-calcined sample (87.01%)
- MnO: Below 0.01% in both the non-calcined and calcined samples
- P_2O_5: Higher in the calcined sample (0.023%) than in the non-calcined sample (0.021%)
- SrO: Below 0.01% in both the non-calcined and calcined samples
- BaO: Below 0.01% in both the non-calcined and calcined samples
- LOI: Higher in the non-calcined sample (11.90%) versus the calcined sample (0.12%)
- Sulfur: Higher in the non-calcined sample (0.03%) versus the calcined sample (0.02%)

Table 63. Results of lithogeochemical analyses on Campaign 3 titanium dioxide precipitates. Note low analytical totals for major elements using the ME-ICP06 analytical method. Samples were reanalyzed using the ME-XRF06 method per recommendation from ALS Laboratories and analytical totals were found to be between 99% and 100%.

		Sample	1802-P17-1	1802-P17-2			Sample	1802-P17-1	1802-P17-2
		Sample Description	P-17 Ti Precipitates Campaign 3	P-17 Ti Precipitates Campaign 3 - Calcined			Sample Description	P-17 Ti Precipitates Campaign 3	P-17 Ti Precipitates Campaign 3 - CALCINED
Analysis	Method	Detection Limit			Analysis	Method	Detection Limit		
SiO2_%	ME-ICP06	0.01	0.08	0.07	SiO2_%	ME-XRF06	0.01	0.07	0.08
Al2O3_%	ME-ICP06	0.01	<0.01	<0.01	Al2O3_%	ME-XRF06	0.01	<0.01	<0.01
Fe2O3_%	ME-ICP06	0.01	<0.01	<0.01	Fe2O3_%	ME-XRF06	0.01	<0.01	0.01
CaO_%	ME-ICP06	0.01	<0.01	<0.01	CaO_%	ME-XRF06	0.01	0.01	0.01
MgO_%	ME-ICP06	0.01	<0.01	<0.01	MgO_%	ME-XRF06	0.01	<0.01	0.01
Na2O_%	ME-ICP06	0.01	<0.01	<0.01	Na2O_%	ME-XRF06	0.01	<0.01	<0.01
K2O_%	ME-ICP06	0.01	<0.01	<0.01	K2O_%	ME-XRF06	0.01	<0.01	<0.01
Cr2O3_%	ME-ICP06	0.002	<0.002	<0.002	Cr2O3_%	ME-XRF06	0.002	<0.01	<0.01
TiO2_%	ME-ICP06	0.01	19.35	9.28	TiO2_%	ME-XRF06	0.01	87.01	98.22
MnO_%	ME-ICP06	0.01	<0.01	<0.01	MnO_%	ME-XRF06	0.01	<0.01	<0.01
P2O5_%	ME-ICP06	0.01	0.01	0.01	P2O5_%	ME-XRF06	0.01	0.021	0.023
SrO_%	ME-ICP06	0.01	<0.01	<0.01	SrO_%	ME-XRF06	0.01	<0.01	<0.01
BaO_%	ME-ICP06	0.01	<0.01	<0.01	BaO_%	ME-XRF06	0.01	<0.01	<0.01
LOI_%	OA-GRA05	0.01	11.1	0	LOI_%	ME-XRF06	0.01	11.9	0.12
Total_%	TOT-ICP06	0.01	30.54	9.36	Total_%	ME-XRF06	0.01	99.01	99.47
S_%	S-IR08	0.01	0.03	0.02	S_%	S-IR08	0.01	0.03	0.02
Ag_ppm	ME-4ACD81	0.5	<0.5	<0.5	Ag_ppm	ME-4ACD81	0.5	<0.5	<0.5
Ag_ppm	ME-MS42	0.01	<0.01	<0.01	Ag_ppm	ME-MS42	0.01	<0.01	<0.01
As_ppm	ME-4ACD81	5	<5	<5	As_ppm	ME-4ACD81	5	<5	<5
As_ppm	ME-MS42	0.1	<0.1	<0.1	As_ppm	ME-MS42	0.1	<0.1	<0.1
Ba_ppm	ME-MS81	0.5	<0.5	<0.5	Ba_ppm	ME-MS81	0.5	<0.5	<0.5
Be_ppm	ME-MS42	0.05	<0.05	<0.05	Be_ppm	ME-MS42	0.05	<0.05	<0.05
Bi_ppm	ME-MS42	0.01	<0.01	<0.01	Bi_ppm	ME-MS42	0.01	<0.01	<0.01
Cd_ppm	ME-4ACD81	0.5	<0.5	<0.5	Cd_ppm	ME-4ACD81	0.5	<0.5	<0.5
Cd_ppm	ME-MS42	0.01	<0.01	<0.01	Cd_ppm	ME-MS42	0.01	<0.01	<0.01
Ce_ppm	ME-MS42	0.02	<0.02	<0.02	Ce_ppm	ME-MS42	0.02	<0.02	<0.02
Ce_ppm	ME-MS81	0.1	0.1	<0.1	Ce_ppm	ME-MS81	0.1	0.1	<0.1
Co_ppm	ME-4ACD81	1	<1	<1	Co_ppm	ME-4ACD81	1	<1	<1
Co_ppm	ME-MS42	0.1	<0.1	<0.1	Co_ppm	ME-MS42	0.1	<0.1	<0.1
Cr_ppm	ME-MS81	10	<10	<10	Cr_ppm	ME-MS81	10	<10	<10
Cs_ppm	ME-MS42	0.05	<0.05	<0.05	Cs_ppm	ME-MS42	0.05	<0.05	<0.05
Cs_ppm	ME-MS81	0.01	<0.01	<0.01	Cs_ppm	ME-MS81	0.01	<0.01	<0.01
Cu_ppm	ME-4ACD81	1	1	1	Cu_ppm	ME-4ACD81	1	1	1
Cu_ppm	ME-MS42	0.2	0.2	<0.2	Cu_ppm	ME-MS42	0.2	0.2	<0.2
Dy_ppm	ME-MS81	0.05	<0.05	<0.05	Dy_ppm	ME-MS81	0.05	<0.05	<0.05
Er_ppm	ME-MS81	0.03	<0.03	<0.03	Er_ppm	ME-MS81	0.03	<0.03	<0.03
Eu_ppm	ME-MS81	0.03	<0.03	<0.03	Eu_ppm	ME-MS81	0.03	<0.03	<0.03
Ga_ppm	ME-MS42	0.05	<0.05	<0.05	Ga_ppm	ME-MS42	0.05	<0.05	<0.05
Ga_ppm	ME-MS81	0.01	<0.1	<0.1	Ga_ppm	ME-MS81	0.01	<0.1	<0.1
Gd_ppm	ME-MS81	0.05	<0.05	<0.05	Gd_ppm	ME-MS81	0.05	<0.05	<0.05
Hf_ppm	ME-MS42	0.02	<0.02	<0.02	Hf_ppm	ME-MS42	0.02	<0.02	<0.02
Hf_ppm	ME-MS81	0.2	<0.2	<0.2	Hf_ppm	ME-MS81	0.2	<0.2	<0.2
Hg_ppm	ME-MS42	0.005	<0.005	<0.005	Hg_ppm	ME-MS42	0.005	<0.005	<0.005
Ho_ppm	ME-MS81	0.01	<0.01	<0.01	Ho_ppm	ME-MS81	0.01	<0.01	<0.01
In_ppm	ME-MS42	0.005	<0.005	<0.005	In_ppm	ME-MS42	0.005	<0.005	<0.005
La_ppm	ME-MS42	0.2	<0.2	<0.2	La_ppm	ME-MS42	0.2	<0.2	<0.2
La_ppm	ME-MS81	0.1	<0.1	<0.1	La_ppm	ME-MS81	0.1	<0.1	<0.1
Li_ppm	ME-4ACD81	10	<10	<10	Li_ppm	ME-4ACD81	10	<10	<10
Li_ppm	ME-MS42	0.1	<0.1	<0.1	Li_ppm	ME-MS42	0.1	<0.1	<0.1
Lu_ppm	ME-MS81	0.01	<0.01	<0.01	Lu_ppm	ME-MS81	0.01	<0.01	<0.01
Mo_ppm	ME-4ACD81	1	<1	<1	Mo_ppm	ME-4ACD81	1	<1	<1
Mo_ppm	ME-MS42	0.05	<0.05	<0.05	Mo_ppm	ME-MS42	0.05	<0.05	<0.05
Nb_ppm	ME-MS42	0.05	<0.05	<0.05	Nb_ppm	ME-MS42	0.05	<0.05	<0.05
Nb_ppm	ME-MS81	0.2	23	16.5	Nb_ppm	ME-MS81	0.2	23	16.5
Nd_ppm	ME-MS81	0.1	<0.1	<0.1	Nd_ppm	ME-MS81	0.1	<0.1	<0.1
Ni_ppm	ME-4ACD81	1	<1	<1	Ni_ppm	ME-4ACD81	1	<1	<1
Ni_ppm	ME-MS42	0.2	<0.2	<0.2	Ni_ppm	ME-MS42	0.2	<0.2	<0.2
Pr_ppm	ME-MS81	0.03	<0.03	<0.03	Pr_ppm	ME-MS81	0.03	<0.03	<0.03
Pb_ppm	ME-4ACD81	2	<2	<2	Pb_ppm	ME-4ACD81	2	<2	<2
Pb_ppm	ME-MS42	0.2	<0.2	0.2	Pb_ppm	ME-MS42	0.2	<0.2	0.2
Rb_ppm	ME-MS42	0.1	<0.1	<0.1	Rb_ppm	ME-MS42	0.1	<0.1	<0.1
Rb_ppm	ME-MS81	0.2	<0.2	<0.2	Rb_ppm	ME-MS81	0.2	<0.2	<0.2
Re_ppm	ME-MS42	0.001	<0.001	<0.001	Re_ppm	ME-MS42	0.001	<0.001	<0.001
Sb_ppm	ME-MS42	0.05	<0.05	<0.05	Sb_ppm	ME-MS42	0.05	<0.05	<0.05
Sc_ppm	ME-4ACD81	1	<1	<1	Sc_ppm	ME-4ACD81	1	<1	<1
Sc_ppm	ME-MS42	0.1	<0.1	<0.1	Sc_ppm	ME-MS42	0.1	<0.1	<0.1
Se_ppm	ME-MS42	0.2	<0.2	<0.2	Se_ppm	ME-MS42	0.2	<0.2	<0.2
Sm_ppm	ME-MS81	0.03	<0.03	<0.03	Sm_ppm	ME-MS81	0.03	<0.03	<0.03
Sn_ppm	ME-MS42	0.2	<0.2	<0.2	Sn_ppm	ME-MS42	0.2	<0.2	<0.2
Sn_ppm	ME-MS81	1	<1	<1	Sn_ppm	ME-MS81	1	<1	<1
Sr_ppm	ME-MS42	0.2	<0.2	<0.2	Sr_ppm	ME-MS42	0.2	<0.2	<0.2
Sr_ppm	ME-MS81	0.1	0.1	0.1	Sr_ppm	ME-MS81	0.1	0.1	0.1
Ta_ppm	ME-MS42	0.01	<0.01	<0.01	Ta_ppm	ME-MS42	0.01	<0.01	<0.01
Ta_ppm	ME-MS81	0.1	0.2	<0.1	Ta_ppm	ME-MS81	0.1	0.2	<0.1
Tb_ppm	ME-MS81	0.01	<0.01	<0.01	Tb_ppm	ME-MS81	0.01	<0.01	<0.01
Te_ppm	ME-MS42	0.01	<0.01	<0.01	Te_ppm	ME-MS42	0.01	<0.01	<0.01
Th_ppm	ME-MS42	0.2	<0.2	<0.2	Th_ppm	ME-MS42	0.2	<0.2	<0.2
Th_ppm	ME-MS81	0.05	<0.05	<0.05	Th_ppm	ME-MS81	0.05	<0.05	<0.05
Tl_ppm	ME-4ACD81	10	<10	10	Tl_ppm	ME-4ACD81	10	<10	10
Tl_ppm	ME-MS42	0.02	<0.02	<0.02	Tl_ppm	ME-MS42	0.02	<0.02	<0.02
Tm_ppm	ME-MS81	0.01	<0.01	<0.01	Tm_ppm	ME-MS81	0.01	<0.01	<0.01
U_ppm	ME-MS42	0.05	<0.05	<0.05	U_ppm	ME-MS42	0.05	<0.05	<0.05
U_ppm	ME-MS81	0.05	<0.05	<0.05	U_ppm	ME-MS81	0.05	<0.05	<0.05
V_ppm	ME-MS81	5	<5	<5	V_ppm	ME-MS81	5	<5	<5
W_ppm	ME-MS42	0.05	<0.05	<0.05	W_ppm	ME-MS42	0.05	<0.05	<0.05
W_ppm	ME-MS81	1	<1	<1	W_ppm	ME-MS81	1	<1	<1
Y_ppm	ME-MS42	0.05	<0.05	<0.05	Y_ppm	ME-MS42	0.05	<0.05	<0.05
Y_ppm	ME-MS81	0.1	<0.1	<0.1	Y_ppm	ME-MS81	0.1	<0.1	<0.1
Yb_ppm	ME-MS81	0.03	<0.03	<0.03	Yb_ppm	ME-MS81	0.03	<0.03	<0.03
Zn_ppm	ME-4ACD81	2	<2	<2	Zn_ppm	ME-4ACD81	2	<2	<2
Zr_ppm	ME-MS42	0.5	<0.5	<0.5	Zr_ppm	ME-MS42	0.5	<0.5	<0.5
Zr_ppm	ME-MS81	2	<2	<2	Zr_ppm	ME-MS81	2	<2	<2

Relative results for the non-calcined (1802-P17-1/ML-68) and calcined (1802-P17-2/ML-69) Campaign 3 titanium dioxide precipitates are described below:

- As: The four-acid digestion method (Method ME-4ACD81) yielded equivalent <5 ppm results for both the non-calcined and calcined samples. Analysis using mass spectrometry (Method ME-MS42) indicated equivalent results for the non-calcined and calcined samples, both having values <0.1 ppm
- Co: Below 1 ppm for both non-calcined and calcined samples using Method ME-4ACD81, and below 0.1 ppm for both non-calcined and calcined samples using Method MEMS42
- Cr: Below 10 ppm for both non-calcined and calcined samples using mass spectrometry method ME-MS81
- Cu: 1 ppm for both non-calcined and calcined samples using Method ME-4ACD81, and higher in the non-calcined sample (0.2 ppm) than the calcined sample (<0.2 ppm) using Method ME-MS42
- Nb: Less than 0.05 ppm for both non-calcined and calcined samples using Method ME-MS42, and higher in the non-calcined sample (223.0 ppm) than the calcined sample (16.5 ppm) using Method ME-MS81
- Ni: Below 1 ppm for both non-calcined and calcined samples using Method 4ACD81, and both non-calcined and calcined samples below 0.2 ppm using Method ME-MS42
- Pb: Less than 2 ppm for both non-calcined and calcined samples using Method ME-4ACD81, and higher in the calcined sample (0.2 ppm) than the non-calcined sample (<0.2 ppm) using Method ME-MS42
- Sb: Below 0.05 ppm for both non-calcined and calcined samples using Method ME-MS42
- Ta: Less than 0.1 ppm for both non-calcined and calcined samples using Method ME-MS42, and higher in the non-calcined sample (0.2 ppm) than the calcined sample (<0.1 ppm) using Method ME-MS81
- V: Less than 5 ppm for both non-calcined and calcined samples using Method ME-MS81
- Zn: Less than 2 ppm for both non-calcined and calcined samples using Method ME-4ACD81

Neither the non-calcined nor the calcined titanium dioxide products produced during this study were surface modified. Relative to calcined, non-surface modified TiO_2 products produced during the previous Mlinar et al. (2017) study, calcined TiO_2 products produced during Campaign 3 from this study have similar major element oxide concentrations of P_2O_5 and lower major element oxide concentrations of TiO_2 (98.22% (this study) versus 99.92% (Mlinar et al., 2017)). In terms of trace elements, calcined TiO_2 products produced for this study have higher concentrations (ppm) of Sr and lower concentrations (ppm) of Ba, Cu, Ga, Nb, Ta, W, and Zn relative to non-surface modified TiO_2 products produced by Mlinar et al. (2017) (see Tables 46 and 47). It is interesting to note that Nb and Ta may be incorporated into the rutile structure via substitution for Ti^{4+}.

Figure 75A is a chondrite-normalized rare earth element plot for both the non-calcined and calcined Campaign 3 TiO_2 precipitates. All rare earth elements analyzed were found to be in concentrations less than the analytical detection limits.

Figure 75B is a primitive mantle-normalized spider diagram showing selected trace element concentrations in the Campaign 3 TiO_2 precipitates. All elements with the exceptions of niobium and titanium were found to be in concentrations less than the analytical detection limits. Niobium is slightly more enriched in the non-calcined sample (~300 times primitive mantle values relative to ~250 times primitive mantle value for the calcined sample), and titanium is slightly more enriched in the calcined sample relative to the non-calcined sample (~500 times primitive mantle value relative to ~400 times primitive mantle value, respectively). The enrichments of niobium and titanium in the Campaign 3 TiO_2 precipitates is not surprising, as both titanium and niobium are commonly present in rutile (Deer et al., 1992; Klein and Hurlbut, 1999).

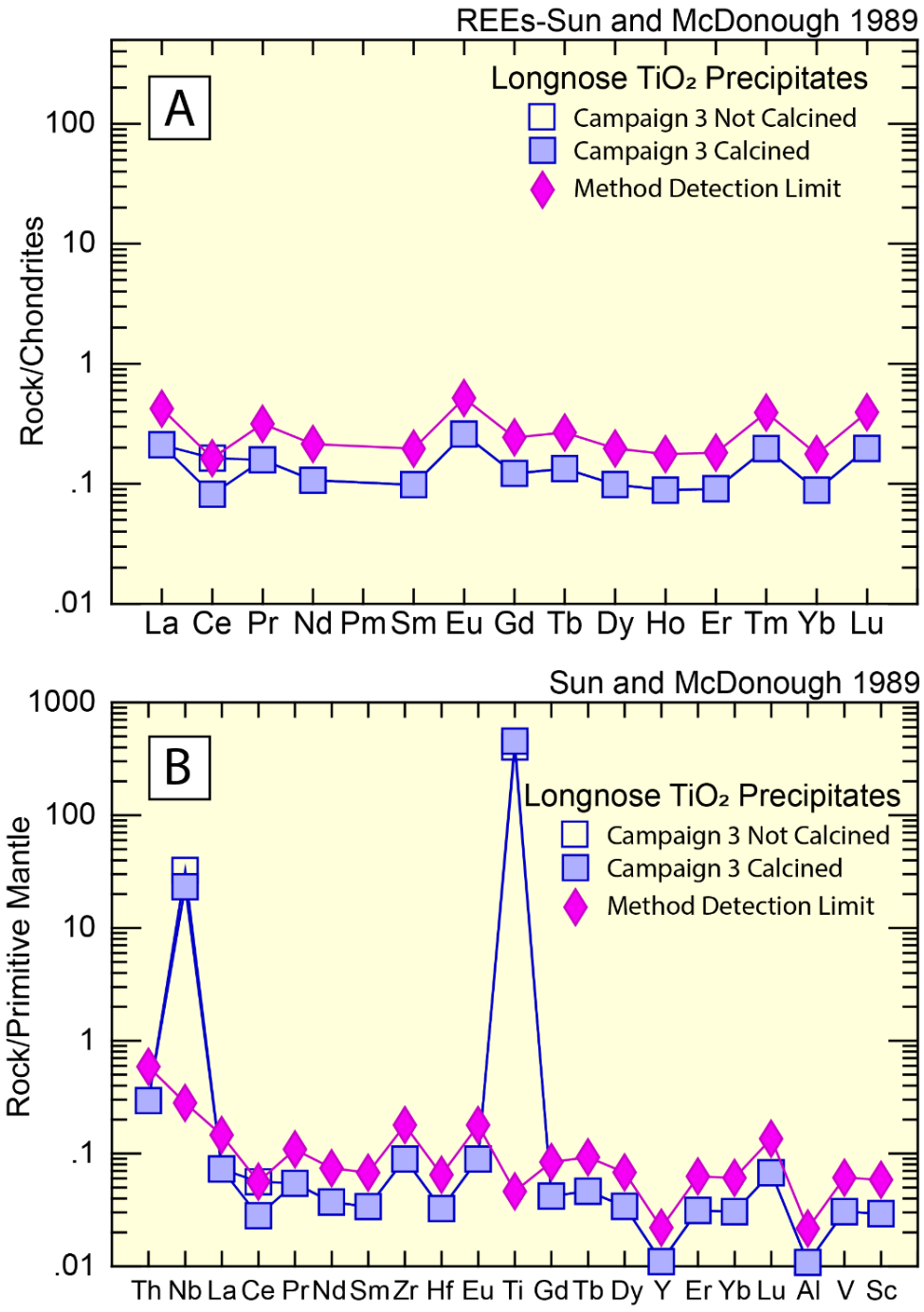

Figure 75. Chondrite- and primitive mantle-normalized spider diagrams for Campaign 3 TiO_2 precipitates. A) Chondrite-normalized rare earth element diagram. Note that all rare earth element values fall below the analytical detection limits. B) Primitive mantle-normalized spider diagram for Campaign 3 TiO_2 precipitates. Note that all elements except niobium and titanium have values below the detection limits. Niobium is slightly more enriched in the non-calcined sample, and titanium is slightly more enriched in the calcined sample. For the purposes of plotting, all analyses below the detection limit have been set to values one-half the value of the detection limit. Chondrite- and primitive mantle-normalizing values from Sun and McDonough (1989) and Kerrich and Wyman (1996).

Campaign 3 Summary

The Campaign 3 operation of the MPP was successfully implemented to determine impurity buildup and steady-state operation with recycling of the evaporated Ti raffinate and the TiO_2 filtrate stream into the circuit.

Operational highlights of Campaign 3 include:

- Evaporation of the Ti raffinate maintained water balance for the leach process.
- Recycled $MgCl_2$ bearing Ti raffinate did not affect leaching efficiency with estimated recovery of ~70% in the bulk pilot leaches.
- Cycling of the TiO_2 filtrate stream into the titanium striping circuit did not affect Ti extraction, and striping efficiency and selectivity of Ti was maintained.
- Total cumulative operation of the Fe circuit was ~623 hours, ~180 organic turnovers.
- Total cumulative operation of the Ti circuit was ~523 hours, ~64 organic turnovers.
- High-purity Fe strip solution was produced, with minimal increase in impurity content. Fe SX circuit displays selectivity for Fe with increased impurities in the feed.
- High-purity Ti strip solution was produced, with no apparent increase in impurity content. Quality is comparable to that achieved in previous study without recycling of raffinate/impurity buildup. Ti SX circuit displays selectivity for Ti with increased impurities in the feed.
- High-purity TiO_2 produced ~99.5% TiO_2.
  - Main impurities present: K (<0.05%) and V (<5 ppm)
  - TiO_2 level dependent on calcination
  - Purity confirmed by third-party analysis
- Both non-calcined and calcined TiO_2 precipitates were produced during Campaign 3. The TiO_2 precipitates are composed of the mineral phase rutile. The morphologies of both the non-calcined and calcined precipitates are similar, comprising 2 µm–20 µm, commonly concentrically zoned spheres. Elongate and elongate, locally curved rutile precipitates are also present and range in size from 30 µm to 60 µm in length and up to 20 µm in width. Composite fragments were identified in both the non-calcined and calcined samples, and these comprise elongate composite fragments up to 380 µm in length that vary from 10 µm to 20 µm in width that are made up of both spherical and elongate TiO_2 precipitates (non-calcined) and large (250 µm–300 µm diameter) aggregate fragments composed of 5 µm–30 µm rounded, locally concentrically zoned rutile spheres. In almost all photomicrographs, the calcined spherical rutile spheres appear to have more porosity than the spherical rutile structures in the non-calcined sample.
- Lithogeochemical analysis of the TiO_2 precipitates illustrates that the precipitates are dominated by the component TiO_2. For sample 1802-P17-1 (ML-68, non-calcined), the TiO_2/Total ratio is 0.878, whereas for sample 1802-P17-2 (ML-69, calcined), the TiO_2/Total ratio is 0.987. These ratios reflect the higher LOI contents of the non-calcined sample (11.90 wt. percent) relative to the LOI contents of the calcined sample (0.12 wt. percent). Sulfur contents were slightly higher in the non-calcined sample (0.03 wt. percent) than the calcined sample (0.02 wt. percent). The rare earth element contents of both the non-calcined and calcined Campaign 3 TiO_2 precipitates were found to be below detection limits. Relative to primitive mantle normalizing values (Sun and McDonough, 1989; Kerrich and Wyman, 1996), both the calcined and non-calcined samples are enriched in niobium

(~300 times primitive mantle values in the non-calcined sample versus ~250 times primitive mantle values in the calcined sample) and titanium (~500 times primitive mantle values in the calcined sample versus ~400 times primitive mantle values in the non-calcined sample). This is consistent with the common presence of niobium in the rutile crystal structure (Deer et al., 1992; Klein and Hurlbut, 1999). Aluminum values in the both the non-calcined and calcined Campaign 3 TiO_2 precipitates were below detection limits. PRO and NRRI independent analyses of calcined Campaign 2 and Campaign 3 TiO_2 precipitates yield similar compositional results using TiO_2/Total ratios for the NRRI lithogeochemical analyses (Fig. 76).

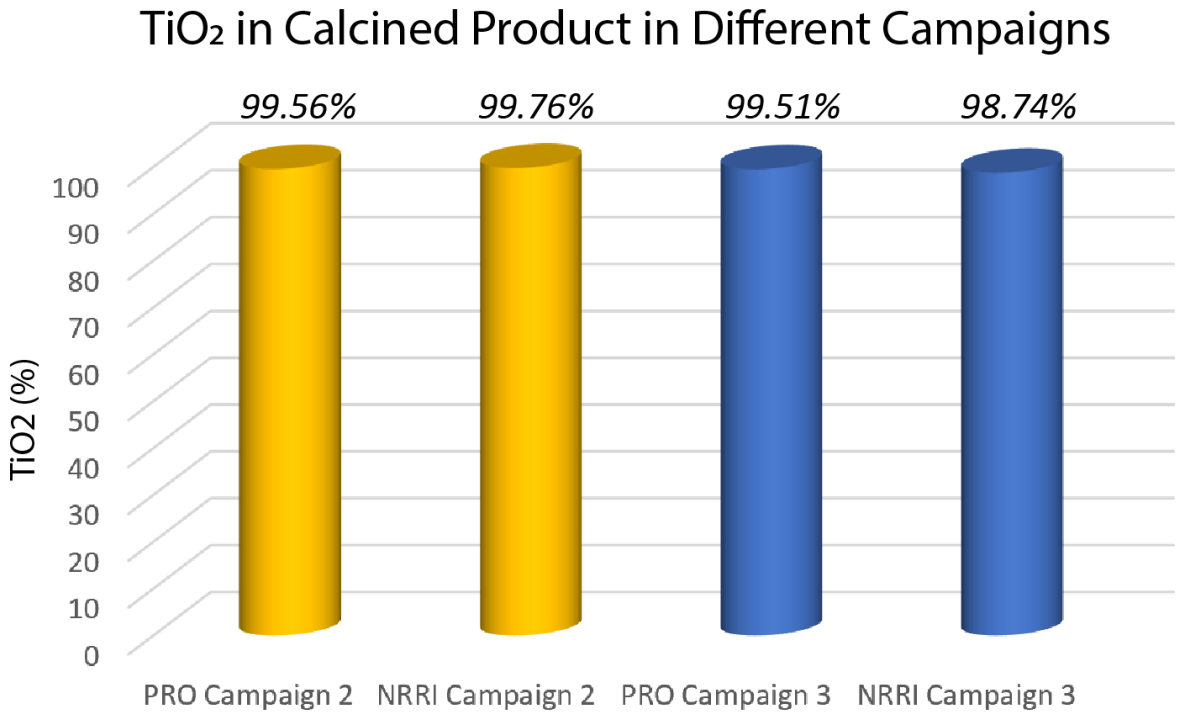

Figure 76. Comparison of PRO and NRRI analyses of calcined Campaign 2 and Campaign 3 TiO_2 precipitates.

Fe-Product and HCl Regeneration Bench Testing

The proprietary technology component of the flowsheet recovers the hydrochloric acid used in the leach, namely the acid that used to dissolve the iron present in the ore.

Current processes are available and used to recycle HCl acid, namely pyrohydrolysis, that uses harsh operating conditions running at a high temperature range of 900°C to 1200°C. [1] PRO's sustainable hydro-hydrolysis technology recycles HCl at substantially lower temperatures than pyrohydrolysis while maintaining effective recovery.

The PRO leach uses a lixiviant consisting of $MgCl_2$ and HCl. The pregnant liquor contains iron chloride, which is separated using solvent extraction. As a result, an iron pregnant strip is produced and used for acid recovery. The process is based on the following equation:

$$2FeCl_3 + 3H_2O \rightarrow Fe_2O_3 + 6HCl$$

An additional benefit of this process is the production of marketable iron oxide, used in pigments for cosmetics and paints (Rittner and Abraham, 1999).

Experimental

Details on the experimental setup and technology development are proprietary and are not disclosed in this report.

Acid Regeneration and Recycling

From the results obtained in this program, parameters for the operation of the system were developed that enabled study of steady-state operation. Experiments were performed in the continuous system to examine parameters for regeneration of HCl and production of Fe_2O_3. Experiments were performed to simulate steady-state operation of the process and determine the operational criteria with respect to feed composition, reactor composition, and operation temperature over time and the subsequent effect on HCl produced.

The experiments conducted have helped to establish the unit operations required for the continuous operation, potential commercialization of the technology, and subsequent application in chloride-based flowsheets such as in the processing of ilmenite and the regeneration of HCl from $FeCl_3$ solutions. The quality of HCl produced (10N) will reduce the amount of water returned to the leach operation in the process and help reduce the water balance.

Iron Oxide Product – Campaign 2

The quality of calcined iron oxide that was produced in Campaign 2 was examined independently by both PRO and the NRRI. The results of these studies will be discussed separately.

The impurities in the sample as analyzed by PRO are shown in Table 64 and Figure 77. Based on this analyses, the purity of iron oxide is 98.60%.

Table 64. Iron oxide calcined Campaign 2 product - Test 6.

Assay Impurities in the iron oxide product (%)											
Ag_2O	**Al_2O_3**	**As_2O_3**	**CaO**	**CoO**	**MgO**	**SO_2**	**TiO_2**	**V_2O_5**	**Others**	**Total**	**Fe_2O_3**
0.0004	0.0576	0.0017	0.0994	0.0001	0.0505	0.01997	0.6005	0.0137	0.56	1.40	98.60

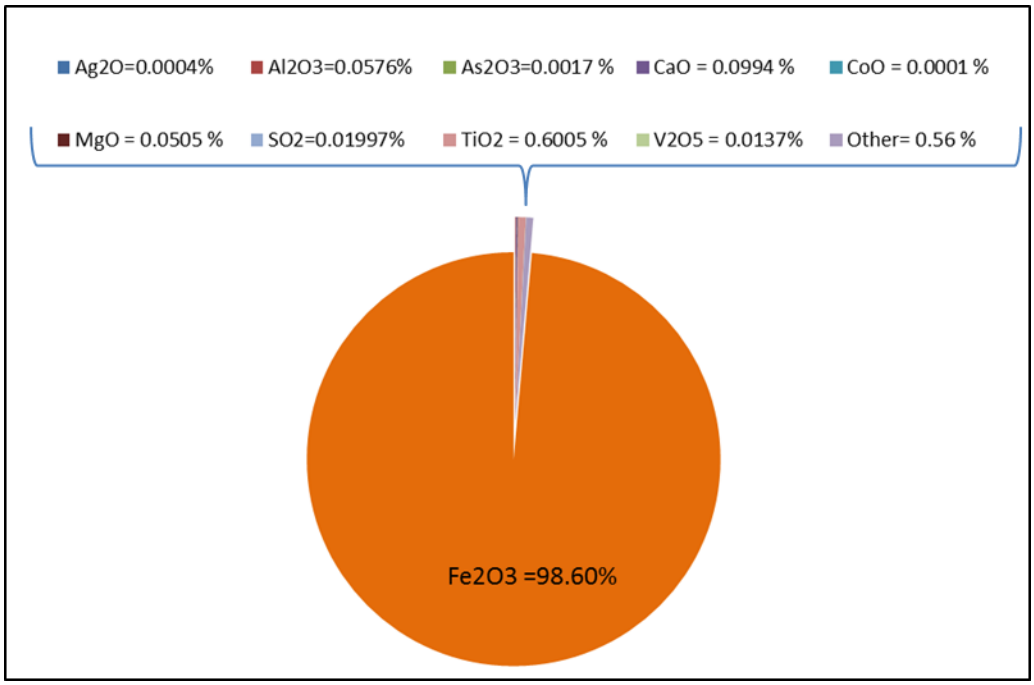

Figure 77. Fe_2O_3 impurities content in Campaign 2.

Mineralogical Analysis (XRD)

Mineralogical analysis of Campaign 2 iron oxide precipitates was performed using x-ray diffraction analysis. Two samples of Campaign 2 iron oxide precipitates were evaluated. These included the non-calcined sample 1802-T6NC (ML-73) and the calcined sample 1802-T6C (ML-74). For the non-calcined sample 1802-T6NC (ML-73), the mineral phase hematite, and possibly the mineral phase zircon, were identified. As well, an unknown phase that could account for 20%–40% of the material was observed (Dr. Rodney Johnson, personal communication, 2019). For the calcined sample 1802-T6C (ML-74), the mineral phase hematite was identified (refer to Table 8).

Mineral Chemical Analysis

Two samples of Campaign 2 iron oxide precipitates underwent mineral chemistry analysis at the Electron Probe Microanalyzer located at the EML at the UMTC. These include samples 1802-T6NC (ML-73) and 1802-T6C, which represent the non-calcined and calcined Campaign 2 iron oxide precipitates, respectively. Hematite, titanohematite solid solution (defined as hematite containing greater that 0.5 wt. percent TiO_2) are the oxide phases identified in sample 1802-T6NC (ML-73). As well, an iron-rich, chlorine-bearing unknown phase and a magnesium-rich, unknown phase, were also identified in this sample. Hematite and a SiO_2-rich, iron bearing unknown phase (quartz?) were identified in sample 1802-T6C. Results of electron microprobe mineral chemical analysis and stoichiometric calculations are included in Appendix 4: Tables A4-29 to A4-32.

Figure 78 is a backscatter image of samples 1802-T6NC (ML-73) obtained during EMPA analysis. A variety of morphological types were identified in this sample, including: A) composites composed of chain-like to massive hematite lathes (up to 1 µm in length) and six-sided trigonal cross-sections on the order of several hundred nanometers across (Fig. 78A); B) amorphous composites composed of micro-hematite that have lengths up to 125 µm and widths up to 60 µm (Fig. 78B); and C) massive micro-hematite comprising irregular shaped masses that are at least 60 µm in diameter (Fig. 78C); Figure 78D is an image of a magnesium- and chlorine-bearing unknown comprising irregular-shaped masses that are at least 40 µm in diameter that are characterized by a "swiss-cheese-like," vesicular texture. Figure 78E illustrates semi-spherical composites (up to 40 µm in length and 30 µm in width) that comprise an iron- and chlorine-bearing unknown and light-colored inclusions of titanium-bearing hematite. These semi-spherical composites comprise greater than 0.5% TiO_2 and over 1.3% chlorine.

Mineral chemical analysis of non-calcined Campaign 2 iron oxide precipitates (hematite) from sample 1802-T6NC/ML-73 are shown in Table 65. The composition of the hematite is dominated by FeO (82.856%–85.233%), with subordinate TiO_2 (0.055%–0.492%), SiO_2 (0.019%–0.167%), NiO (0.000%–0.056%), Al_2O_3 (0.000%–0.044%), MgO (0.000%–0.022%), MnO (0.000%–0.015%), and Cr_2O_3 (0.000%–0.010%). Analyses of the hematite indicates the presence of chlorine, ranging from 0.288% to 0.914%. With iron analyzed as FeO, analytical totals range from 83.906% to 86.231%, with an average analytical total of 85.347%. With iron recalculated at Fe_2O_3, analytical totals range from 93.111% to 95.698%, with an average analytical total of 94.738%. Overall, the FeO/Total ratio varied from 0.998 to 0.994, with an average FeO/Total ratio of 0.990.

Mineral chemical analyses of the magnesium- and chlorine-bearing unknown from sample 1802-T6NC/ML-73 are shown in Table 66. The composition of this material is dominated by MgO (78.490%–81.826%) and chlorine (3.711%–6.640%), with lesser amounts of TiO_2 (0.049%–0.358%), SiO_2 (0.008%–0.176%), NiO (0.000%–0.059%), Al_2O_3 (0.000%–0.048%), V_2O_3 (0.000%–0.040%), FeO (0.000%–0.016%), MnO (0.000%–0.009%), and Cr_2O_3 (0.000%–0.008%). The MgO/Total ratio varied from 0.921 to 0.949, with and average MgO/Total ratio of 0.935.

Mineral chemical analyses of the iron- and chlorine bearing unknown from sample 1802-T6NC/ML-73 are shown in Table 67. The composition of this material is dominated by FeO (76.428%–81-411%) and chlorine (2.213%–7.839%), with lesser amounts of TiO_2 (0.049%–0.097%), Al_2O_3 (0.000%–0.030%), SiO_2 (0.000%–0.019%), Cr_2O_3 (0.000%–0.017%), V_2O_3 (0.002%–0.016%), NiO (0.000%–0.015%), and MnO (0.000%–0.001%). MgO was not identified in this material. The FeO/Total ratio varied from 0.906 to 0.973, with an average FeO/Total ratio of 0.930.

A single analysis of sample 1802-T6NC/ML-73 indicates the presence of a titanium-bearing (greater than 0.5% TiO_2) hematite phase. This analysis yielded the following results: FeO (77.353%), Cl (1.358%), TiO_2 (0.747%), SiO_2 (0.296%), Al_2O_3 (0.156%), MgO (0.33%), NiO (0.25%), MnO (0.017%), and Cr_2O_3 (0.002%). No V_2O_3 was identified in the sample. With iron analyzed as FeO, the analytical total for this sample was 79.988%. With iron recalculated as Fe_2O_3 (Abbey, 1977), the analytical total is 88.597. The FeO/Total ratio of this sample is 0.967.

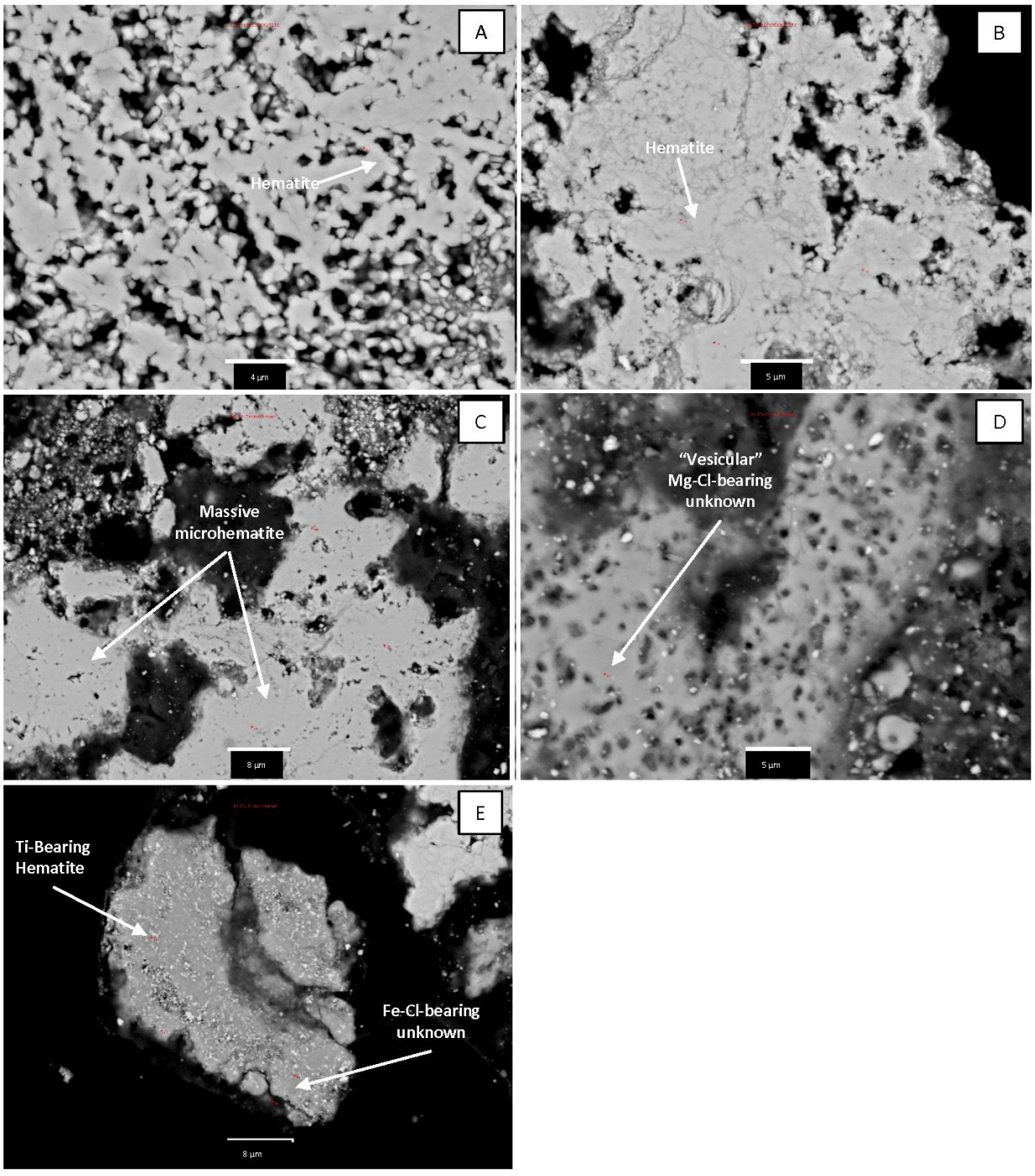

Figure 78. Electron microprobe backscatter image of Campaign 2 non-calcined iron oxide precipitate (sample 1802-T6NC/ML-73). A) Chain-like composite of massive hematite lathes with trigonal cross-sections. Scale bar is 4 µm. B) Amorphous hematite composite. Scale bar is 5 µm. C) Massive microhematite. Scale bar is 8 µm. D) Vesicular textured magnesium- and chlorine-bearing unknown. Scale bar is 5 µm. E) Semi-spherical composite comprising an iron- and chlorine-bearing unknown that locally contains titanium-bearing hematite (titanohematite). Scale bar is 8 µm. Red numbers and circles in images are analysis locations.

Table 65. Electron microprobe analyses of Campaign 2 non-calcined iron oxide precipitate hematite from sample 1802-T6NC/ML-73.

Electron Microprobe Analysis – Iron Oxide Precipitate Hematite Campaign 2 Non-Calcined (n = 17)													
Sample	Description	Phase	SiO_2	TiO_2	Al_2O_3	FeO	MnO	MgO	V_2O_3	Cr_2O_3	NiO	Cl	Total
ML-73-4-43-1	Microhematite Lathe Composite	Hematite	0.146	0.059	0.022	84.530	0.000	0.000	0.003	0.000	0.000	0.288	85.048
ML-73-4-44-2	Microhematite Lathe Composite	Hematite	0.065	0.066	0.010	84.528	0.009	0.000	0.000	0.000	0.010	0.395	85.083
ML-73-4-45-3	Microhematite Lathe Composite	Hematite	0.058	0.055	0.002	84.620	0.000	0.000	0.001	0.006	0.003	0.381	85.126
ML-73-5-46-1	Microhematite Amorphous Composite	Hematite	0.099	0.141	0.019	84.434	0.000	0.005	0.022	0.000	0.031	0.333	85.085
ML-73-5-47-2	Microhematite Amorphous Composite	Hematite	0.110	0.066	0.012	84.449	0.000	0.039	0.005	0.010	0.000	0.338	85.080
ML-73-5-48-3	Microhematite Amorphous Composite	Hematite	0.078	0.148	0.001	84.757	0.004	0.000	0.006	0.000	0.056	0.390	85.441
ML-73-10-58-1	Microhematite Semi-Sphere	Hematite	0.069	0.064	0.010	83.906	0.000	0.000	0.013	0.009	0.032	0.705	84.808
ML-73-10-59-2	Microhematite Lathe Composite	Hematite	0.056	0.064	0.000	82.856	0.008	0.000	0.008	0.000	0.000	0.914	83.906
ML-73-10-60-3	Microhematite Lathe Composite	Hematite	0.085	0.065	0.019	83.828	0.010	0.000	0.010	0.009	0.000	0.720	84.745
ML-73-12-64-1	Massive Microhematite	Hematite	0.062	0.098	0.024	85.233	0.001	0.000	0.000	0.010	0.007	0.596	86.032
ML-73-12-65-2	Massive Microhematite	Hematite	0.054	0.074	0.005	84.971	0.000	0.000	0.008	0.000	0.000	0.555	85.667
ML-73-12-66-3	Massive Microhematite	Hematite	0.019	0.082	0.028	85.140	0.015	0.000	0.009	0.003	0.000	0.493	85.788
ML-73-13-68-2	Microhematite Amorphous Composite	Hematite	0.167	0.072	0.006	85.207	0.002	0.000	0.011	0.008	0.000	0.759	86.231
ML-73-13-69-3	Microhematite Amorphous Composite	Hematite	0.103	0.082	0.016	84.812	0.007	0.000	0.002	0.008	0.000	0.770	85.800
ML-73-14-70-1	Microhematite Amorphous Composite	Hematite	0.131	0.071	0.018	85.147	0.000	0.000	0.000	0.000	0.000	0.729	85.096
ML-73-14-71-2	Microhematite Amorphous Composite	Hematite	0.103	0.098	0.000	84.644	0.000	0.000	0.013	0.000	0.000	0.724	85.582
ML-73-14-72-3	Microhematite Amorphous Composite	Hematite	0.122	0.492	0.044	83.900	0.000	0.000	0.008	0.000	0.011	0.804	85.383
		Minimum	*0.019*	*0.055*	*0.000*	*82.856*	*0.000*	*0.000*	*0.000*	*0.000*	*0.000*	*0.288*	*83.906*
		Maximum	*0.167*	*0.492*	*0.044*	*85.233*	*0.015*	*0.039*	*0.022*	*0.010*	*0.056*	*0.914*	*86.231*
		Average	*0.090*	*0.106*	*0.014*	*84.530*	*0.003*	*0.003*	*0.007*	*0.004*	*0.009*	*0.582*	*85.347*
		Mean	*0.085*	*0.072*	*0.012*	*84.620*	*0.000*	*0.000*	*0.008*	*0.000*	*0.000*	*0.596*	*85.383*
		St. Deviation	*0.037*	*0.100*	*0.011*	*0.601*	*0.005*	*0.009*	*0.006*	*0.004*	*0.015*	*0.193*	*0.567*
		Measurement Unit	*Wt. %*	*Wt. %*	*Wt. %*	*Wt. %*	*Wt. %*	*Wt. %*	*Wt. %*	*Wt. %*	*Wt. %*	*Wt. %*	*Wt. %*

Table 66. Electron microprobe analyses of Campaign 2 non-calcined magnesium- and chlorine-bearing unknown from sample 1802-T6NC/ML-73. Values are in weight percentages.

Electron Microprobe Analysis – Magnesium Chloride Unknown (n = 6)													
Sample	Description	Phase	SiO_2	TiO_2	Al_2O_3	FeO	MnO	MgO	V_2O_3	Cr_2O_3	NiO	Cl	Total
ML-73-8-54-1	Microhematite Semi-Sphere	Mg-Cl Unknown	0.079	0.239	0.000	0.000	0.000	80.016	0.010	0.000	0.036	4.071	84.451
ML-73-8-55-2	Microhematite Semi-Sphere	Mg-Cl Unknown	0.176	0.358	0.016	0.015	0.000	80.874	0.040	0.000	0.021	3.711	85.211
ML-73-8-56-3	Microhematite Semi-Sphere	Mg-Cl Unknown	0.164	0.272	0.048	0.010	0.000	81.826	0.000	0.000	0.059	3.963	86.342
ML-73-11-61-1	"Vesicular" Microhematite	Mg-Cl Unknown	0.008	0.054	0.005	0.002	0.000	79.012	0.009	0.000	0.025	6.640	85.755
ML-73-11-62-2	"Vesicular" Microhematite	Mg-Cl Unknown	0.060	0.049	0.026	0.006	0.009	78.723	0.000	0.000	0.000	6.504	85.377
ML-73-11-63-3	"Vesicular" Microhematite	Mg-Cl Unknown	0.022	0.049	0.005	0.016	0.000	78.490	0.028	0.008	0.001	6.465	85.084
		Minimum	*0.008*	*0.049*	*0.000*	*0.000*	*0.000*	*78.490*	*0.000*	*0.000*	*0.000*	*3.711*	*84.451*
		Maximum	*0.176*	*0.358*	*0.048*	*0.016*	*0.009*	*81.826*	*0.040*	*0.008*	*0.059*	*6.640*	*86.342*
		Average	*0.085*	*0.170*	*0.017*	*0.008*	*0.002*	*79.824*	*0.015*	*0.001*	*0.024*	*5.226*	*85.370*
		Mean	*0.070*	*0.147*	*0.011*	*0.008*	*0.000*	*79.514*	*0.010*	*0.000*	*0.023*	*5.268*	*85.294*
		St. Deviation	*0.065*	*0.125*	*0.016*	*0.006*	*0.003*	*1.211*	*0.015*	*0.003*	*0.020*	*1.316*	*0.584*
		Measurement Unit	*Wt. %*	*Wt. %*	*Wt. %*	*Wt. %*	*Wt. %*	*Wt. %*	*Wt. %*	*Wt. %*	*Wt. %*	*Wt. %*	*Wt. %*

Table 67. Electron microprobe analyses of Campaign 2 non-calcined iron- and chlorine-bearing unknown from sample 1802-T6NC/ML-73. Values are in weight percentages.

Electron Microprobe Analysis – Iron Chloride Unknown (n = 5)													
Sample	Description	Phase	SiO_2	TiO_2	Al_2O_3	FeO	MnO	MgO	V_2O_3	Cr_2O_3	NiO	Cl	Total
ML-73-6-49-1	Lathe-Shaped	Iron Chloride?	0.000	0.070	0.011	78.154	0.000	0.000	0.002	0.000	0.000	7.435	85.672
ML-73-6-50-2	Lathe-Shaped	Iron Chloride?	0.019	0.049	0.030	76.706	0.000	0.000	0.010	0.000	0.000	7.164	83.977
ML-73-6-51-3	Lathe-Shaped	Iron Chloride?	0.000	0.064	0.009	76.428	0.000	0.000	0.007	0.017	0.015	7.839	84.379
ML-73-7-52-1	Lathe-Shaped	Iron Chloride?	0.000	0.097	0.027	81.197	0.000	0.000	0.011	0.000	0.000	4.626	85.957
ML-73-7-53-2	Lathe-Shaped	Iron Chloride?	0.000	0.058	0.000	81.411	0.001	0.000	0.016	0.000	0.000	2.213	83.699
		Minimum	*0.000*	*0.049*	*0.000*	*76.428*	*0.000*	*0.000*	*0.002*	*0.000*	*0.000*	*2.213*	*83.699*
		Maximum	*0.019*	*0.097*	*0.030*	*81.411*	*0.001*	*0.000*	*0.016*	*0.017*	*0.015*	*7.839*	*85.957*
		Average	*0.004*	*0.068*	*0.015*	*78.779*	*0.000*	*0.000*	*0.009*	*0.003*	*0.003*	*5.855*	*84.737*
		Mean	*0.000*	*0.064*	*0.011*	*78.154*	*0.000*	*0.000*	*0.010*	*0.000*	*0.000*	*7.164*	*84.379*
		St. Deviation	*0.008*	*0.016*	*0.011*	*2.144*	*0.001*	*0.000*	*0.005*	*0.007*	*0.006*	*2.141*	*0.910*
		Measurement Unit	*Wt. %*	*Wt. %*	*Wt. %*	*Wt. %*	*Wt. %*	*Wt. %*	*Wt. %*	*Wt. %*	*Wt. %*	*Wt. %*	*Wt. %*

Figure 79 illustrates the chemical composition of the iron oxide (hematite) precipitates from non-calcined Campaign 2 sample 1802-T6NC/ML-73. In terms of weight percent oxides, these precipitates are nearly pure FeO with little MgO or V_2O_3 contents (Figs. 79A–79D). The molar ratio of Fe^{3+} was calculated by converting all FeO from the electron microprobe analysis into Fe_2O_3 using the method of Abbey (1977). As shown in Figure 79E, the iron oxide precipitates from sample 1802-T6NC/ML-73 are nearly stoichiometric Fe_2O_3 (hematite).

Figure 80 is a backscatter image of sample 1802-T6C (ML-74), a calcined sample of iron oxide precipitate from Campaign 2, obtained during EMPA analysis. The precipitates formed discrete angular to subangular particles ranging in size from 5 µm in length and 2–3 µm in width to large aggregates up to 500 µm in length and up to 450 µm in width (Fig. 80A). Two morphologies of iron oxide precipitates were identified, including: A) polygonal composite fragments up to approximately 90 µm in length and 50 µm in width that are composed of agglomerated hematite polygons ranging from 0.5 µm to 2.5 µm in diameter (Fig. 80B); and B) “vesicular” composite fragments comprising mostly agglomerated hematite lathes and 0.4 µm–3.0 µm in length and 0.2 µm–0.6 µm in width that are locally agglomerated with hematite polygons or spheres ranging from approximately 3 µm to 4 µm in diameter (Fig. 80C). As well, rare local agglomerates approximately 60 µm in length and up to 25 µm in width contain round (generally 1 µm–2 µm in diameter) to oval (1 µm–12 µm in length and 1 µm–2.5 µm in width) pale-gray SiO_2-Al_2O_3-FeO-bearing unknown surrounded by a darker gray, SiO_2-Fe_2O_3- Al_2O_3-bearing unknown matrix (Fig. 80D).

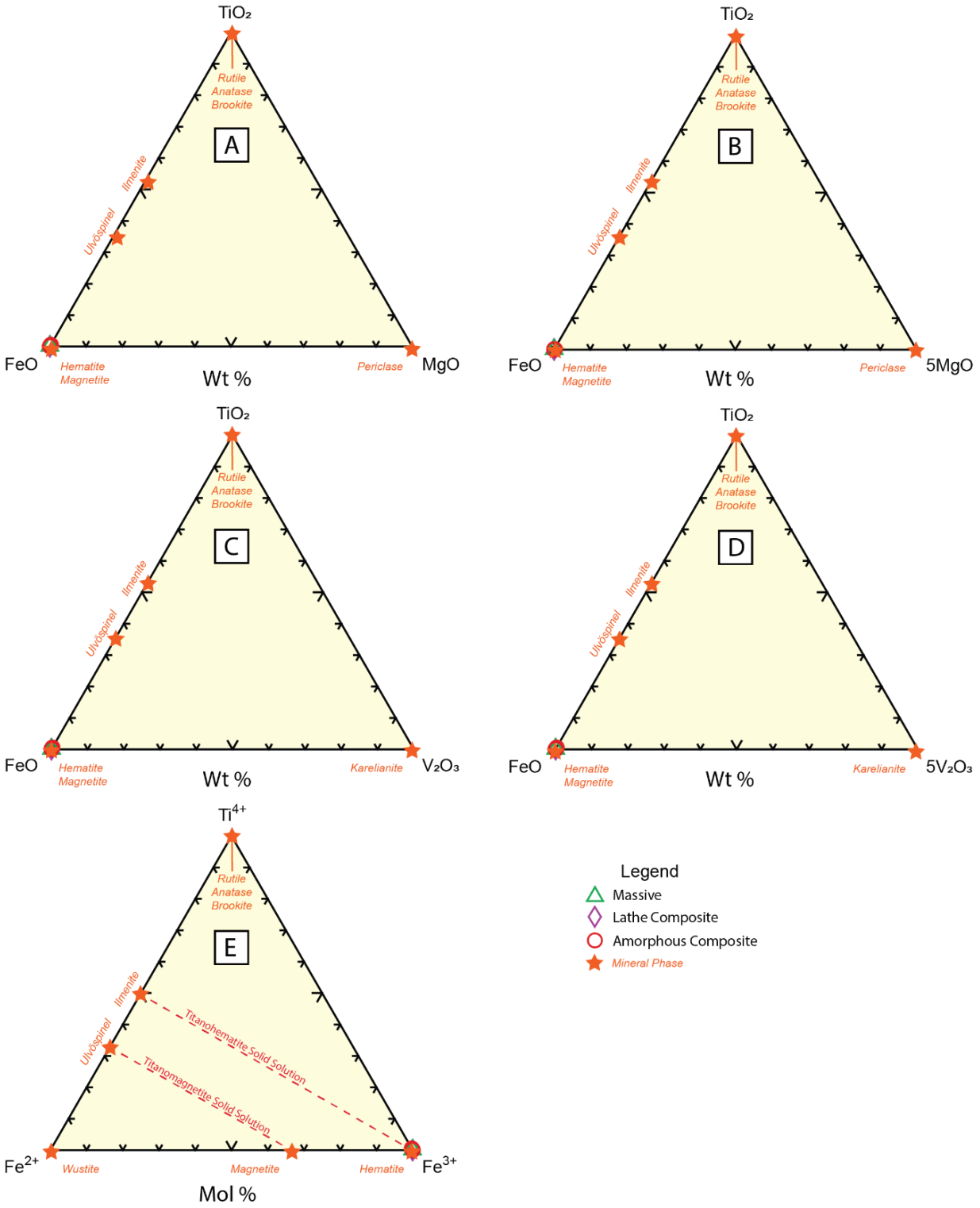

Figure 79. Ternary diagram illustrating the chemical compositions of iron oxide precipitates (hematite) from Campaign 2 non-calcined sample 1802-T6NC/ML-73. Figures 79A–79D represent ternary diagrams in the FeO-TiO_2-MgO, FeO-TiO_2-5MgO, FeO-TiO2-V_2O_3, and FeO-TiO_2-5V_2O_3 systems. Note that this iron oxide precipitate plots as nearly pure FeO. Figure 79E is a molar Fe^{2+}-Ti^{4+}-Fe^{3+} ternary diagram (modified after Klein and Hurlbut, 1999; Meinhold, 2010) showing that the iron oxide precipitate is stoichiometric hematite.

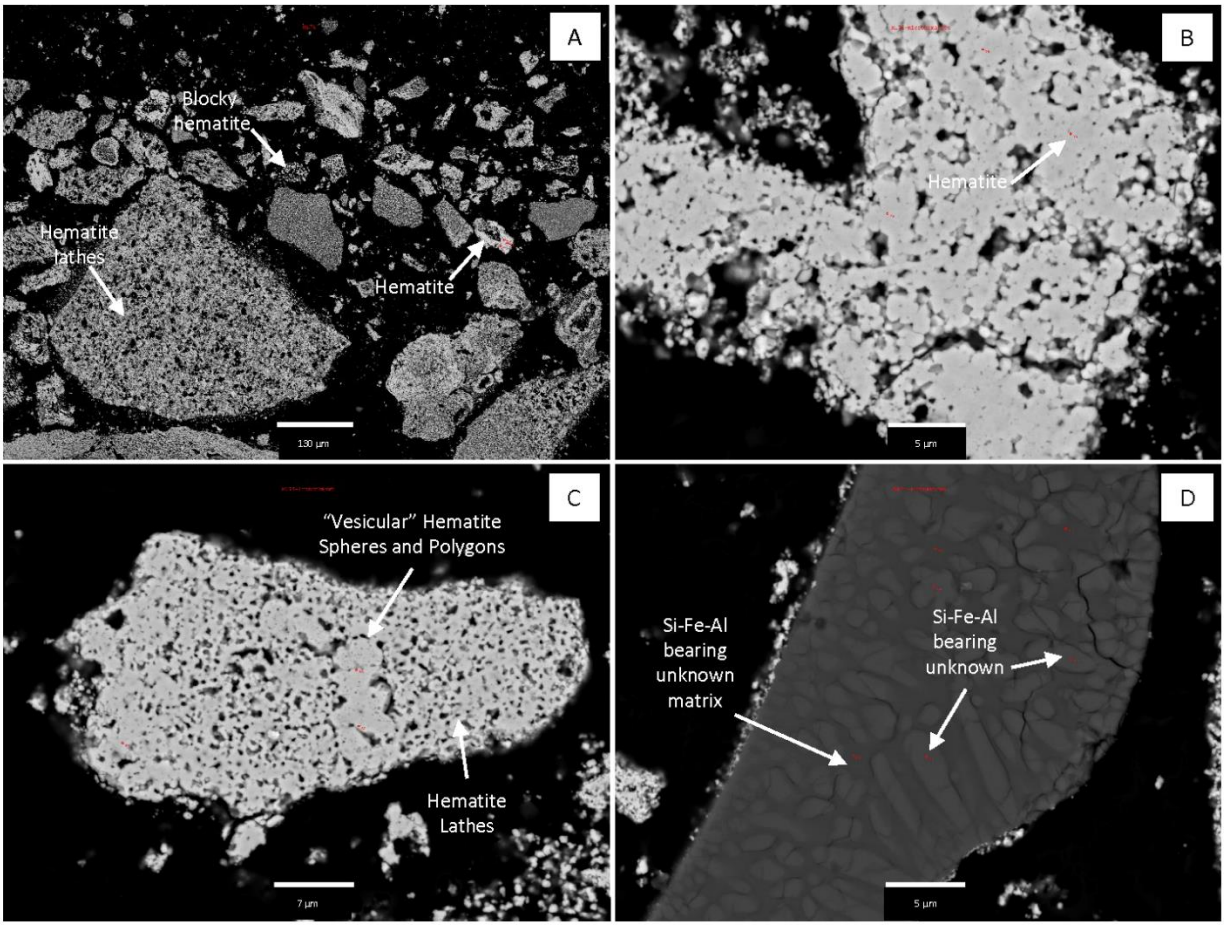

Figure 80. Electron microprobe backscatter images of Campaign 2 calcined iron oxide precipitate (sample 1802-T6C/ML-74). A) General appearance of iron-oxide precipitates. Scale bar is 130 µm. B) Polygonal composite fragment composed of hematite. Scale bar is 5 µm. C) Vesicular composite composed of discrete hematite spheres and polygons surrounded by a finer-grained matrix composed of agglomerated lathe-like hematite. Scale bar is 7 µm. D) Fragment comprising discrete rounded to oval SiO_2-FeO-Al_2O_3 particles in a darker gray SiO_2-FeO-Al_2O_3 matrix containing more Al_2O_3 than the rounded to oval particles. Scale bar is 5 µm. Red numbers and circles in images are analysis locations.

Mineral chemical analyses of calcined Campaign 2 iron oxide precipitates (hematite) from sample 1802-T6C/ML-74 are shown in Table 68. The composition of the iron-oxide precipitate is dominated by FeO (83.866%–86.560%), with lesser amounts of chlorine (0.88%–0.897%), TiO_2 (0.076–0.290%), SiO_2 (0.000%–0.292%), MgO (0.011%–0.210%), Al_2O_3 (0.000%–0.068%), NiO (0.000%–0.034%), V_2O_3 (0.000%–0.020%), MnO (0.000%–00.005%), and Cr_2O_3 (0.000%–0.002%). With iron analyzed as FeO, the analytical totals range from 84.118% to 87.264%, with an average of 86.350%. With iron recalculated as Fe_2O_3 (Abbey, 1977), the analytical totals range from 93.452% to 96.896, with an average of 95.870%. The FeO/Total ratio of this precipitate varies from 0.984 to 0.997, with an average FeO/Total ratio of 0.991.

Table 68. Electron microprobe analysis of iron oxide precipitate (hematite) from Campaign 2 calcined sample 1802-T6C/ML-74. Values are in weight percentages.

Electron Microprobe Analysis – Iron Oxide Precipitate Hematite Campaign 2 Non-Calcined (n = 6)													
Sample	Description	Phase	SiO_2	TiO_2	Al_2O_3	FeO	MnO	MgO	V_2O_3	Cr_2O_3	NiO	Cl	Total
ML-74-15-73-1	Microhematite Polygonal Composite	Hematite	0.000	0.143	0.000	86.560	0.000	0.094	0.015	0.001	0.000	0.088	86.901
ML-74-15-74-2	Microhematite Polygonal Composite	Hematite	0.292	0.160	0.063	86.543	0.003	0.077	0.020	0.000	0.000	0.106	87.264
ML-74-15-75-3	Microhematite Polygonal Composite	Hematite	0.118	0.163	0.053	85.636	0.003	0.191	0.009	0.001	0.004	0.471	86.646
ML-74-18-82-1	Microhematite "Vesicular" Composite	Hematite	0.000	0.161	0.012	85.040	0.000	0.094	0.000	0.000	0.000	0.897	86.205
ML-74-18-83-2	Microhematite "Vesicular" Composite	Hematite	0.110	0.290	0.068	85.569	0.000	0.210	0.010	0.000	0.034	0.678	86.968
ML-74-18-84-3	Microhematite "Vesicular" Composite	Hematite	0.028	0.076	0.033	83.866	0.005	0.011	0.000	0.002	0.004	0.095	84.118
		Minimum	*0.000*	*0.076*	*0.000*	*83.866*	*0.000*	*0.011*	*0.000*	*0.000*	*0.000*	*0.088*	*84.118*
		Maximum	*0.292*	*0.290*	*0.068*	*86.560*	*0.005*	*0.210*	*0.020*	*0.002*	*0.034*	*0.897*	*87.264*
		Average	*0.091*	*0.166*	*0.038*	*85.536*	*0.002*	*0.113*	*0.009*	*0.001*	*0.007*	*0.389*	*86.350*
		Mean	*0.069*	*0.161*	*0.043*	*85.603*	*0.002*	*0.094*	*0.010*	*0.001*	*0.002*	*0.289*	*86.774*
		St. Deviation	*0.107*	*0.054*	*0.028*	*0.594*	*0.001*	*0.056*	*0.007*	*0.000*	*0.013*	*0.317*	*0.355*
		Measurement Unit	*Wt. %*	*Wt. %*	*Wt. %*	*Wt. %*	*Wt. %*	*Wt. %*	*Wt. %*	*Wt. %*	*Wt. %*	*Wt. %*	*Wt. %*

Mineral chemical analyses of the SiO_2-Al_2O_3-FeO bearing unknown particles from sample 1802-T6C/ML-74 are shown in Table 69. The lighter gray-colored round to oval particles within the fragment contain less Al_2O_3 than the darker gray-colored matrix that surrounds these particles. The lighter colored particles are composed mostly of SiO_2 (90.610%–92.689%), with lesser amounts of Al_2O_3 (10138%–1.361%), FeO (1.072%–1.176%), TiO2 (0.087%–0.100%), MnO (0.002%–0.028%), NiO (0.000%–0.018%), chlorine (0.000%–0.016%), V_2O_3 (0.000%–0.006%), and Cr_2O_3 (0.000%–0.006%). No MgO was identified in the analysis of this fragment type. The average SiO_2/Total ratio, average FeO/Total ratio, and average Al2O3/Total ratio of these fragments are 0.973, 0.012, and 0.014, respectively. The darker-gray colored matrix is also composed mostly of SiO_2 (73.520%–78.063%), with lesser amounts of Al_2O_3 (2.886%–3.458%), FeO (1.307%–1.944%), TiO_2 (0.137%–0.155%), NiO (0.012%–0.028%), and V_2O_3 (0.009%–0.011%). No MgO, Cr_2O_3, or chlorine were identified in this matrix material. The average SiO_2/Total ratio, average FeO/Total ratio, and average Al_2O_3/Total ratio of these fragments is 0.956, 0.020, and 0.039, respectively. Note that the darker gray colored matrix has similar SiO_2/Total and FeO/Total ratios to the round-to-oval particle described above; however, the Al_2O_3/Total ratio for the matrix is over 2.5 times the Al_2O_3/Total ratio for the circular and oval particles that it surrounds.

Table 69. Electron microprobe analyses of SiO_2-FeO-Al_2O_3-bearing unknown from Campaign 2 calcined iron oxide precipitate sample 1802-T6C/ML-74.

Electron Microprobe Analysis – Iron Oxide Precipitate Silicate Unknown (n = 6)													
Sample	Description	Phase	SiO_2	TiO_2	Al_2O_3	FeO	MnO	MgO	V_2O_3	Cr_2O_3	NiO	Cl	Total
ML-74-16-76-1	Light Gray Elongate Core	Silica-Rich Unknown	92.689	0.098	1.138	1.176	0.002	0.000	0.006	0.006	0.002	0.011	95.127
ML-74-16-77-2	Light Gray Elongate Core	Silica-Rich Unknown	90.610	0.100	1.361	1.072	0.028	0.000	0.005	0.000	0.018	0.016	93.210
ML-74-16-78-3	Light Gray Elongate Core	Silica-Rich Unknown	91.343	0.087	1.296	1.142	0.009	0.000	0.000	0.001	0.000	0.000	93.878
ML-74-17-79-1	Dark Gray Matrix	Silica-Rich Unknown	78.063	0.137	2.886	1.307	0.000	0.000	0.009	0.000	0.028	0.000	82.431
ML-74-17-80-2	Dark Gray Matrix	Silica-Rich Unknown	73.520	0.155	3.458	1.944	0.000	0.000	0.011	0.000	0.012	0.000	79.100
ML-74-17-81-3	Dark Gray Matrix	Silica-Rich Unknown	77.429	0.147	3.141	1.674	0.000	0.000	0.011	0.000	0.013	0.000	82.416
		Minimum	*73.520*	*0.087*	*1.138*	*1.072*	*0.000*	*0.000*	*0.000*	*0.000*	*0.000*	*0.000*	*79.100*
		Maximum	*92.689*	*0.155*	*3.458*	*1.944*	*0.028*	*0.000*	*0.011*	*0.006*	*0.028*	*0.000*	*95.127*
		Average	*83.942*	*0.121*	*2.214*	*1.386*	*0.007*	*0.000*	*0.007*	*0.001*	*0.012*	*0.000*	*87.694*
		Mean	*84.337*	*0.119*	*2.124*	*1.242*	*0.001*	*0.000*	*0.007*	*0.000*	*0.012*	*0.000*	*87.821*
		St. Deviation	*7.760*	*0.027*	*0.965*	*0.317*	*0.010*	*0.000*	*0.004*	*0.002*	*0.009*	*0.000*	*6.498*
		Measurement Unit	*Wt. %*	*Wt. %*	*Wt. %*	*Wt. %*	*Wt. %*	*Wt. %*	*Wt. %*	*Wt. %*	*Wt. %*	*Wt. %*	*Wt. %*

Figure 81 illustrates the mineral chemical composition of the Campaign 2 calcined iron oxide (hematite) precipitates from sample 1802-T6C/ML-74. The hematite precipitates, when plotted in the FeO-TiO_2-MgO and FeO-TiO_2-V_2O_3 systems, are similar for hematite in the polygonal composite fragments and the "vesicular" composite fragments. In terms of weight percent oxides, hematite precipitates within the polygonal composite fragments are nearly pure FeO, with little or no MgO or V_2O_3 (Figs. 81A–81D). Hematite precipitates within the "vesicular" composite fragments are also nearly pure FeO with little or no V_2O_3; however, the MgO contents of hematite within the "vesicular" composite fragments contain slightly more MgO than hematite precipitates in the polygonal composite fragments (Figs. 81A and 81D). The molar ratio of Fe^{3+} was calculated by converting all FeO from the electron microprobe analysis into Fe_2O_3 using the method of Abbey (1977). As shown in Figure 81E, the iron oxide precipitates from sample 1802-T6NC/ML-73 are nearly stoichiometric Fe_2O_3 (hematite).

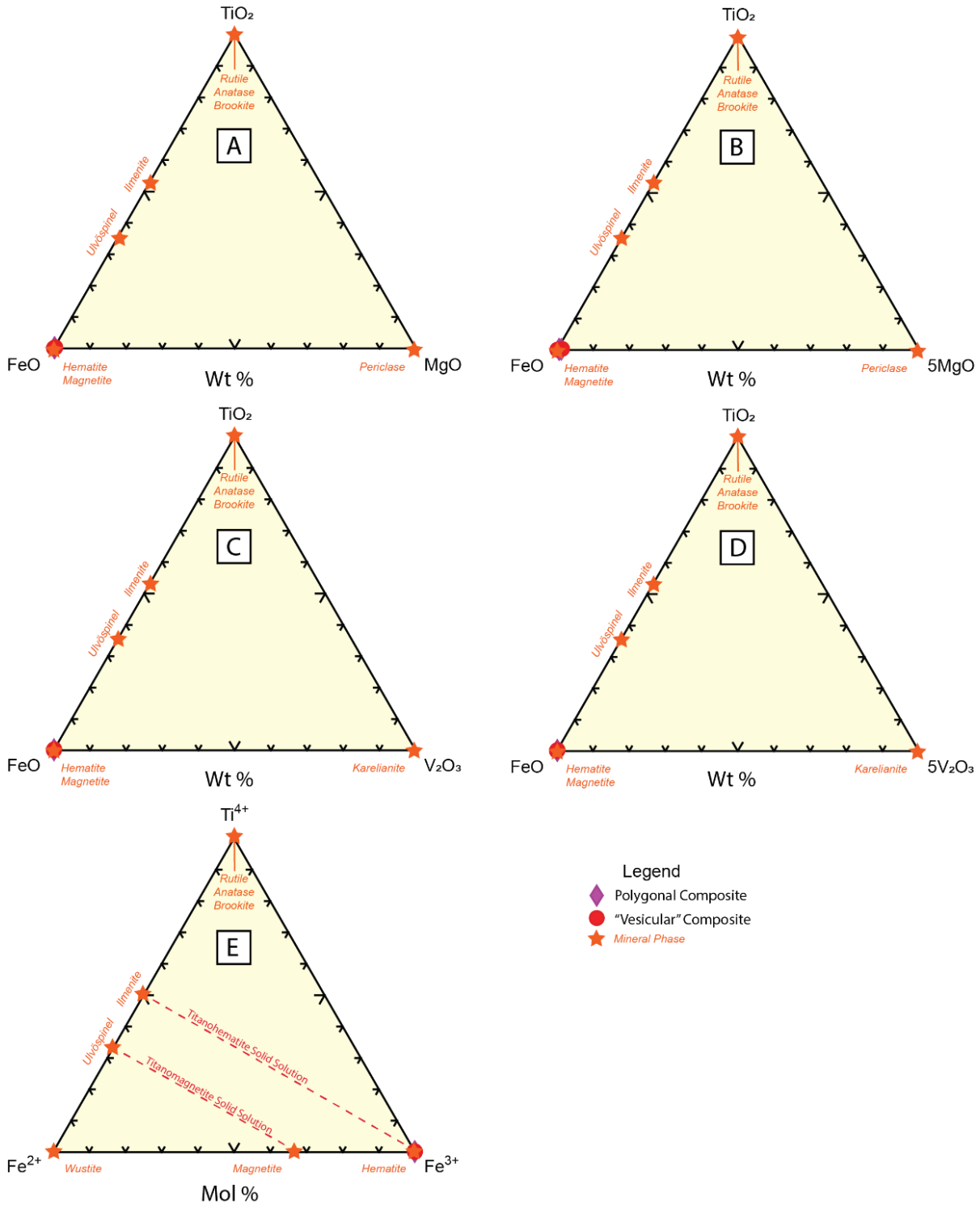

Figure 81. Ternary diagram illustrating the chemical composition of iron oxide precipitate (hematite) from Campaign 2 calcined sample 1802-T6C/ML-74. Figures 81A–81D represent ternary diagrams in the FeO-TiO_2-MgO, FeO-TiO_2-5MgO, FeO-TiO_2-V_2O_3, and FeO-TiO_2-5V_2O_3 systems. Note that the iron oxide (hematite) plots as nearly pure FeO, with the iron oxide precipitate in the "vesicular" composite samples containing slightly more MgO than in the polygonal composite samples. Figure 81E is a molar Fe^{2+}-Ti^{4+}-Fe^{3+} ternary diagram (modified after Klein and Hurlbut, 1999; Meinhold, 2010) showing that the iron oxide precipitate for both morphologies is stoichiometric hematite.

Lithogeochemical Analysis

Whole rock lithogeochemical analyses were performed on the non-calcined (1802-T6NC/ML-73) and calcined (1802-T6C/ML-74) iron oxide precipitate samples produced during Campaign 2. The results of these analyses are shown in Table 70, and ALS Laboratory analytical certificates can be found in Appendix 3: Tables A3-1 to A3-7.

It is important to note that original lithogeochemical analyses on the Campaign 2 iron oxide precipitates using ALS Laboratories analytical method ME-ICP06 resulted in low major element analytical totals (ranging from 53.82% to 92.23%). Discussions with ALS Laboratory personnel indicated that accurate analyses of such pure materials would be better achieved using ALS Laboratory analytical method ME-XRF06. Reanalysis of the Campaign 2 calcined iron oxide precipitates (sample 1802-T6C/ML-74) using ALS Laboratory analytical method ME-XRF06 was conducted, and the analytical totals for the major element oxides for this sample using this analytical methodology improved to 99.92%. A lack of sufficient Campaign 2 iron oxide precipitate (sample 1802-T6NC/ML-73) prevented reanalysis of this material using the ME-XRF06 method.

Relative results for the non-calcined (1802-T6NC/ML-73) and calcined (1802-T6C/ML-74) Campaign 2 iron oxide precipitates in terms of major element oxide compositions (weight percentages) are described below:

- SiO_2: Higher in the calcined sample (0.53%) versus the non-calcined sample (0.38%)
- Al_2O_3: Higher in the calcined sample (0.03%) versus the non-calcined sample (<0.01%)
- Fe_2O_3: Higher in the calcined sample (98.41%) versus the non-calcined sample (79.50%)
- CaO: Higher in the calcined sample (0.04%) versus the non-calcined sample (0.03%)
- MgO: Higher in the calcined sample (0.08%) versus the non-calcined sample (0.07%)
- Na_2O: Equivalent in the non-calcined and calcined samples (0.04%)
- K_2O: Equivalent in the non-calcined and calcined samples (0.01%)
- Cr_2O_3: Below 0.002% in the non-calcined sample; below 0.01% in the calcined sample
- TiO_2: Below 0.01% in both the non-calcined and calcined samples
- MnO: Below 0.01% in both the non-calcined and calcined samples
- P_2O_5: Below 0.01% in the non-calcined sample; below 0.001% in the calcined sample
- SrO: Below 0.01% in both the non-calcined and calcined samples
- BaO: Higher in the calcined sample (0.03%) than in the non-calcined sample (0.01%)
- LOI: Higher in the non-calcined sample (10.85%) versus the calcined sample (0.16%)
- Sulfur: Higher in the non-calcined sample (0.02%) versus the calcined sample (0.01%)

Table 70. Results of lithogeochemical analyses on Campaign 2 iron oxide precipitates. Note low analytical totals (weight percentages) for major elements using the ME-ICP06 analytical method. Sample 1802-T6C (ML-74) was reanalyzed using method ME-XRF-06 per recommendation by ALS Laboratories, and the major element analytical total improved to over 99%. Sample 1802-T6NC could not be reanalyzed due to insufficient sample remaining for the reanalysis.

		Sample	1802-T6NC	1802-T6C*			Sample	1802-T6C
		Sample Description	Iron Oxide Non Calcined Campaign 2	Iron Oxide Calcined Campaign 2			Sample Description	Iron Oxide Precipitate Campaign 2 - CALCINED
Analysis	Method	Detection Limit			Analysis	Method	Detection Limit	
SiO2_%	ME-ICP06	0.01	0.38	0.47	SiO2_%	ME-XRF05	0.01	0.53
Al2O3_%	ME-ICP06	0.01	<0.01	0.02	Al2O3_%	ME-XRF05	0.01	0.03
Fe2O3_%	ME-ICP06	0.01	79.5	52.6	Fe2O3_%	ME-XRF05	0.01	98.41
CaO_%	ME-ICP06	0.01	0.03	0.03	CaO_%	ME-XRF05	0.01	0.04
MgO_%	ME-ICP06	0.01	0.08	0.07	MgO_%	ME-XRF05	0.01	0.08
Na2O_%	ME-ICP06	0.01	0.04	0.04	Na2O_%	ME-XRF05	0.01	0.04
K2O_%	ME-ICP06	0.01	0.01	0.01	K2O_%	ME-XRF05	0.01	0.01
Cr2O3_%	ME-ICP06	0.002	<0.002	<0.002	Cr2O3_%	ME-XRF05	0.01	<0.01
TiO2_%	ME-ICP06	0.01	1.33	0.53	TiO2_%	ME-XRF05	0.01	0.58
MnO_%	ME-ICP06	0.01	<0.01	<0.01	MnO_%	ME-XRF05	0.01	<0.01
P2O5_%	ME-ICP06	0.01	<0.01	<0.01	P2O5_%	ME-XRF05	0.001	0.008
SrO_%	ME-ICP06	0.01	<0.01	<0.01	SrO_%	ME-XRF05	0.01	<0.01
BaO_%	ME-ICP06	0.01	0.01	0.01	BaO_%	ME-XRF05	0.01	0.03
LOI_%	OA-GRA05	0.01	10.85	0.04	LOI_%	ME-XRF05	0.01	0.16
Total_%	TOT-ICP06	0.01	92.23	53.82	Total_%	ME-XRF05	0.01	99.92
S_%	S-IR08	0.01	0.02	0.01	S_%	S-IR08	0.01	0.01
Ag_ppm	ME-4ACD81	0.5	<0.5	<0.5	Ag_ppm	ME-4ACD81	0.5	<0.5
Ag_ppm	ME-MS42	0.01	0.03	0.03	Ag_ppm	ME-MS42	0.01	0.03
As_ppm	ME-4ACD81	5	20	19	As_ppm	ME-4ACD81	5	19
As_ppm	ME-MS42	0.1	0.3	5.4	As_ppm	ME-MS42	0.1	5.4
Ba_ppm	ME-MS81	0.5	67.8	61.3	Ba_ppm	ME-MS81	0.5	61.3
Be_ppm	ME-MS42	0.05	<0.05	<0.05	Be_ppm	ME-MS42	0.05	<0.05
Bi_ppm	ME-MS42	0.01	0.02	0.01	Bi_ppm	ME-MS42	0.01	0.01
Cd_ppm	ME-4ACD81	0.5	<0.5	<0.5	Cd_ppm	ME-4ACD81	0.5	<0.5
Cd_ppm	ME-MS42	0.01	0.03	0.04	Cd_ppm	ME-MS42	0.01	0.04
Ce_ppm	ME-MS42	0.02	0.22	0.18	Ce_ppm	ME-MS42	0.02	0.18
Ce_ppm	ME-MS81	0.1	1.3	1	Ce_ppm	ME-MS81	0.1	1
Co_ppm	ME-4ACD81	1	<1	<1	Co_ppm	ME-4ACD81	1	<1
Co_ppm	ME-MS42	0.1	0.4	0.3	Co_ppm	ME-MS42	0.1	0.3
Cr_ppm	ME-MS81	10	10	10	Cr_ppm	ME-MS81	10	10
Cs_ppm	ME-MS42	0.05	<0.05	<0.05	Cs_ppm	ME-MS42	0.05	<0.05
Cs_ppm	ME-MS81	0.01	0.01	<0.01	Cs_ppm	ME-MS81	0.01	<0.01
Cu_ppm	ME-4ACD81	1	15	18	Cu_ppm	ME-4ACD81	1	18
Cu_ppm	ME-MS42	0.2	11.7	7.2	Cu_ppm	ME-MS42	0.2	7.2
Dy_ppm	ME-MS81	0.05	0.07	0.06	Dy_ppm	ME-MS81	0.05	0.06
Er_ppm	ME-MS81	0.03	0.03	<0.03	Er_ppm	ME-MS81	0.03	<0.03
Eu_ppm	ME-MS81	0.03	<0.03	<0.03	Eu_ppm	ME-MS81	0.03	<0.03
Ga_ppm	ME-MS42	0.05	4.78	2.06	Ga_ppm	ME-MS42	0.05	2.06
Ga_ppm	ME-MS81	0.01	5.4	3.5	Ga_ppm	ME-MS81	0.01	3.5
Gd_ppm	ME-MS81	0.05	0.07	0.06	Gd_ppm	ME-MS81	0.05	0.06
Hf_ppm	ME-MS42	0.02	0.02	0.02	Hf_ppm	ME-MS42	0.02	0.02
Hf_ppm	ME-MS81	0.2	<0.2	<0.2	Hf_ppm	ME-MS81	0.2	<0.2
Hg_ppm	ME-MS42	0.005	<0.005	<0.005	Hg_ppm	ME-MS42	0.005	<0.005
Ho_ppm	ME-MS81	0.01	0.01	0.01	Ho_ppm	ME-MS81	0.01	0.01
In_ppm	ME-MS42	0.005	<0.005	0.026	In_ppm	ME-MS42	0.005	0.026
La_ppm	ME-MS42	0.2	<0.2	<0.2	La_ppm	ME-MS42	0.2	<0.2
La_ppm	ME-MS81	0.1	2	1.5	La_ppm	ME-MS81	0.1	1.5
Li_ppm	ME-4ACD81	10	<10	<10	Li_ppm	ME-4ACD81	10	<10
Li_ppm	ME-MS42	0.1	0.1	1.5	Li_ppm	ME-MS42	0.1	1.5
Lu_ppm	ME-MS81	0.01	<0.01	<0.01	Lu_ppm	ME-MS81	0.01	<0.01
Mo_ppm	ME-4ACD81	1	6	6	Mo_ppm	ME-4ACD81	1	6
Mo_ppm	ME-MS42	0.05	0.6	3.88	Mo_ppm	ME-MS42	0.05	3.88
Nb_ppm	ME-MS42	0.05	0.09	0.17	Nb_ppm	ME-MS42	0.05	0.17
Nb_ppm	ME-MS81	0.2	1.4	0.7	Nb_ppm	ME-MS81	0.2	0.7
Nd_ppm	ME-MS81	0.1	0.6	0.4	Nd_ppm	ME-MS81	0.1	0.4
Ni_ppm	ME-4ACD81	1	<1	<1	Ni_ppm	ME-4ACD81	1	<1
Ni_ppm	ME-MS42	0.2	1.2	2.3	Ni_ppm	ME-MS42	0.2	2.3
Pr_ppm	ME-MS81	0.03	0.17	0.11	Pr_ppm	ME-MS81	0.03	0.11
Pb_ppm	ME-4ACD81	2	2	<2	Pb_ppm	ME-4ACD81	2	<2
Pb_ppm	ME-MS42	0.2	3.6	3.4	Pb_ppm	ME-MS42	0.2	3.4
Rb_ppm	ME-MS42	0.1	0.1	0.1	Rb_ppm	ME-MS42	0.1	0.1
Rb_ppm	ME-MS81	0.2	0.2	<0.2	Rb_ppm	ME-MS81	0.2	<0.2
Re_ppm	ME-MS42	0.001	0.005	0.001	Re_ppm	ME-MS42	0.001	0.001
Sb_ppm	ME-MS42	0.05	0.44	0.94	Sb_ppm	ME-MS42	0.05	0.94
Sc_ppm	ME-4ACD81	1	<1	<1	Sc_ppm	ME-4ACD81	1	<1
Sc_ppm	ME-MS42	0.1	0.1	0.1	Sc_ppm	ME-MS42	0.1	0.1
Se_ppm	ME-MS42	0.2	0.5	<0.2	Se_ppm	ME-MS42	0.2	<0.2
Sm_ppm	ME-MS81	0.03	0.06	0.06	Sm_ppm	ME-MS81	0.03	0.06
Sn_ppm	ME-MS42	0.2	1.3	0.5	Sn_ppm	ME-MS42	0.2	0.5
Sn_ppm	ME-MS81	1	1	1	Sn_ppm	ME-MS81	1	1
Sr_ppm	ME-MS42	0.2	2.1	2.2	Sr_ppm	ME-MS42	0.2	2.2
Sr_ppm	ME-MS81	0.1	3.6	3	Sr_ppm	ME-MS81	0.1	3
Ta_ppm	ME-MS42	0.01	<0.01	<0.01	Ta_ppm	ME-MS42	0.01	<0.01
Ta_ppm	ME-MS81	0.1	<0.1	<0.1	Ta_ppm	ME-MS81	0.1	<0.1
Tb_ppm	ME-MS81	0.01	0.01	0.01	Tb_ppm	ME-MS81	0.01	0.01
Te_ppm	ME-MS42	0.01	0.01	0.02	Te_ppm	ME-MS42	0.01	0.02
Th_ppm	ME-MS42	0.2	<0.2	<0.2	Th_ppm	ME-MS42	0.2	<0.2
Th_ppm	ME-MS81	0.05	<0.05	<0.05	Th_ppm	ME-MS81	0.05	<0.05
Tl_ppm	ME-4ACD81	10	<10	<10	Tl_ppm	ME-4ACD81	10	<10
Tl_ppm	ME-MS42	0.02	0.02	<0.02	Tl_ppm	ME-MS42	0.02	<0.02
Tm_ppm	ME-MS81	0.01	<0.01	0.01	Tm_ppm	ME-MS81	0.01	0.01
U_ppm	ME-MS42	0.05	<0.05	<0.05	U_ppm	ME-MS42	0.05	<0.05
U_ppm	ME-MS81	0.05	<0.05	<0.05	U_ppm	ME-MS81	0.05	<0.05
V_ppm	ME-MS81	5	59	47	V_ppm	ME-MS81	5	47
W_ppm	ME-MS42	0.05	<0.05	<0.05	W_ppm	ME-MS42	0.05	<0.05
W_ppm	ME-MS81	1	<1	1	W_ppm	ME-MS81	1	1
Y_ppm	ME-MS42	0.05	0.06	0.05	Y_ppm	ME-MS42	0.05	0.05
Y_ppm	ME-MS81	0.1	0.4	0.4	Y_ppm	ME-MS81	0.1	0.4
Yb_ppm	ME-MS81	0.03	<0.03	<0.03	Yb_ppm	ME-MS81	0.03	<0.03
Zn_ppm	ME-4ACD81	2	65	59	Zn_ppm	ME-4ACD81	2	59
Zr_ppm	ME-MS42	0.5	0.7	0.9	Zr_ppm	ME-MS42	0.5	0.9
Zr_ppm	ME-MS81	2	3	3	Zr_ppm	ME-MS81	2	3

Relative results for selected trace elements in the Campaign 2 non-calcined (1802-T6NC/ML-73) and calcined (1805-T6C/ML-74) iron oxide precipitates are described below:

- As: Higher in the non-calcined sample (20 ppm) versus the calcined sample (19 ppm) using the four-acid digestion method (Method ME-4ACD81). Analysis using mass spectrometry indicated a higher concentration (5.4 ppm) in the calcined sample relative to the non-calcined sample (0.3 ppm)
- Co: Equivalent values of <1 ppm for both the non-calcined and calcined samples using the four-acid digestion method (Method ME-4ACD81). Higher in the non-calcined sample (0.4 ppm) relative to the calcined sample (0.3 ppm) using mass spectrometry method ME-MS42
- Cr: Equivalent values of 10 ppm in both the non-calcined and calcined samples using mass spectrometry method ME-MS81
- Cu: Higher in the calcined sample (18 ppm) versus the non-calcined sample (15ppm) using the four-acid digestion method (Method ME-4ACD81). Higher in the non-calcined sample (11.7 ppm) versus the calcined sample (70 ppm) using mass spectrometry method ME-MS42
- Nb: Higher in the calcined (0.17 ppm) versus non-calcined sample (0.09 ppm) using mass spectrometry method ME-MS42. Higher in the non-calcined sample (1.4 ppm) versus the calcined sample (0.7 ppm) using mass spectrometry method ME-MS81
- Ni: Equivalent values of <1 ppm in both the non-calcined and calcined samples using the four-acid digestion method (Method ME-4ACD81). Higher in the calcined sample (2.3 ppm) versus the non-calcined sample (1.2 ppm) using mass spectrometry method ME-MS42
- Pb: Higher in the non-calcined sample (2 ppm) than the calcined sample (<2 ppm) using the four-acid digestion method (Method ME-4ACD81). Higher in the non-calcined sample (3.6 ppm) than the calcined sample (3.4 ppm) using mass spectrometry method ME-MS42
- Sb: Higher in the calcined sample (0.94 ppm) versus the non-calcined sample (0.44 ppm) using mass spectrometry method ME-MS42
- Ta: Equivalent below detection limit values (<0.01 ppm) using mass spectrometry method ME-MS42. Equivalent below detection limit values (<0.1 ppm) values using mass spectrometry method ME-MS81
- V: Higher in the non-calcined sample (59 ppm) than the calcined sample (47 ppm) using mass spectrometry method ME-MS81

Figure 82A is a chondrite-normalized rare earth element plot for both the non-calcined and calcined Campaign 2 iron oxide precipitates. Note that the light rare earth elements (La, Ce, Pr, Nd) are slightly enriched relative to chondritic values, with the non-calcined sample being slightly enriched in these elements relative to the calcined sample. All other elements have values less than chondritic values, with the non-calcined sample values generally slightly higher than the calcined sample values. The exception to this is for the element Tm (thulium), which is enriched in the calcined sample relative to the non-calcined sample.

Figure 82B is a primitive mantle-normalized spider diagram showing selected trace element concentrations in the Campaign 2 iron oxide precipitates. Relative to primitive mantle values (Sun and McDonough, 1989; Kerrich and Wyman, 1996), the Campaign 2 iron oxide precipitates are slightly enriched (less than 10 times primitive mantle values) in Nb (approximately 1 time primitive mantle value), La (2–3 times primitive mantle value), and titanium (2–7 times primitive mantle value), with the non-calcined sample having a higher concentration than the calcined sample.

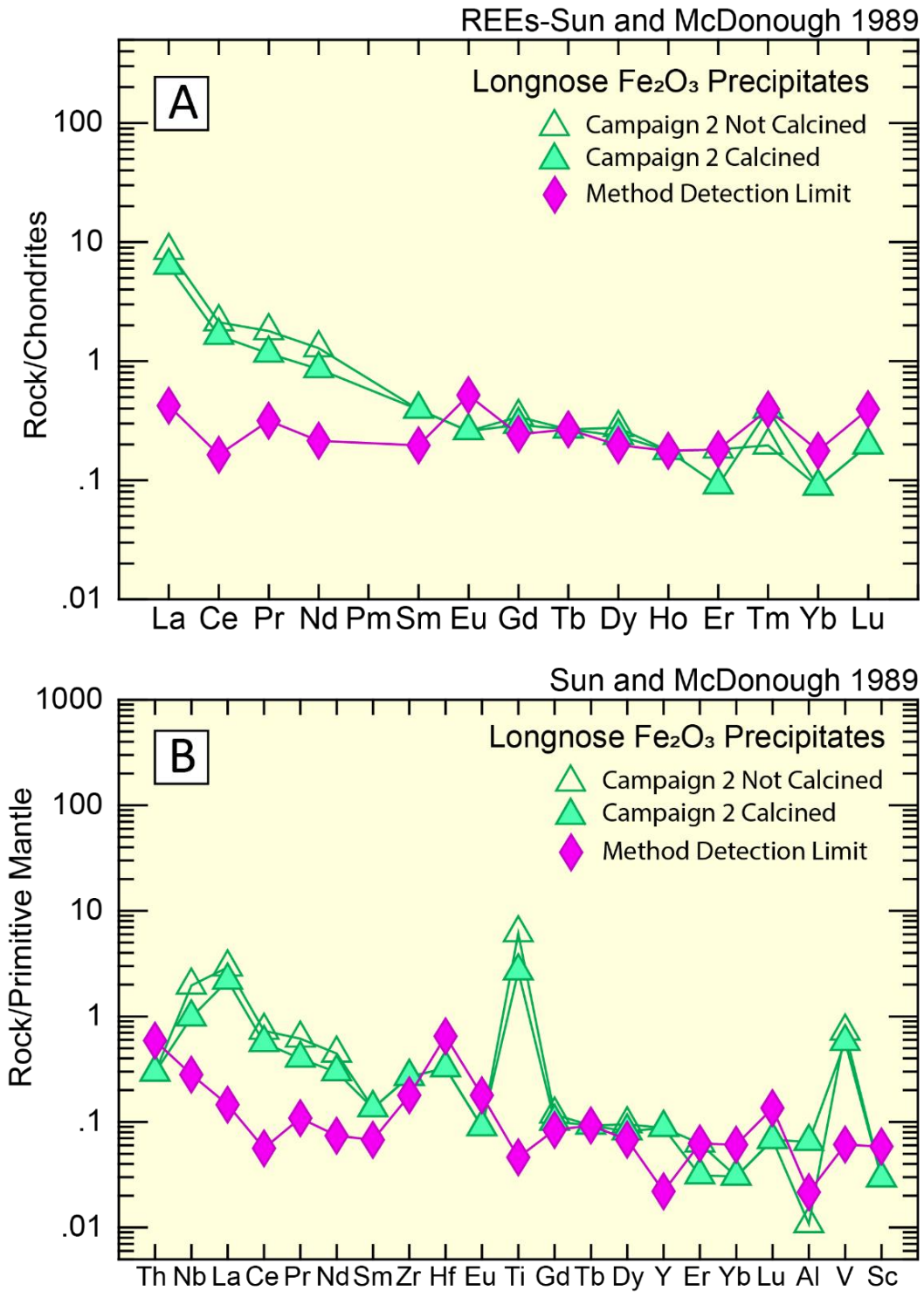

Figure 82. Chondrite- and primitive mantle-normalized spider diagrams for Campaign 2 iron oxide precipitates. A) Chondrite-normalized rare earth element diagram. Note that relative to chondritic values, both non-calcined and calcined Campaign 2 iron oxide precipitates are slightly enriched (2–9 times) in the light rare earth elements La, Ce, Pr, and Nd. B) Primitive mantle-normalized spider diagram for Campaign 2 iron oxide precipitates. Relative to primitive mantle normalizing values (Sun and Mcdonough, 1989; Kerrich and Wyman, 1996), the Campaign 2 iron oxide precipitates are slightly enriched (less than 10x) in niobium, lanthanum, and titanium.

Iron Oxide Product – Campaign 3

The quality of calcined Iron oxide that was produced in Campaign 3 was examined independently by PRO and NRRI. The results of these analyses will be discussed separately.

The impurities in the samples as analyzed by PRO are shown in Table 71 and Figure 83. The purity of the calcined iron oxide product from Campaign 3 has a purity of 96.72% Fe_2O_3.

The calcined and non-calcined products were also examined by mineralogical, mineral chemical, and lithogeochemical analysis methods which are presented in the following section.

Table 71. Iron oxide calcined campaign 3 product - Test 6.

Assay Impurities in the iron oxide product (%)											
Ag_2O	Al_2O_3	As_2o_3	CaO	CoO	MgO	SO_2	TiO_2	V_2O_5	Others	Total	Fe_2O_3
0.0004	0.1322	0.0033	0.098	0.0003	0.0166	0.01997	1.82	0.0213	1.167	3.28	96.72

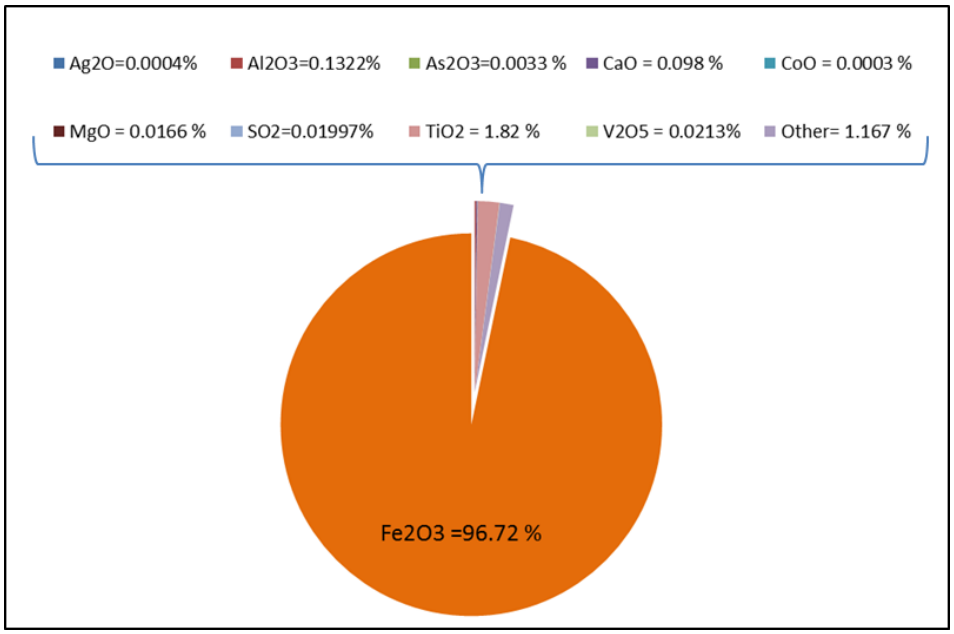

Figure 83. Campaign 3 calcined Fe_2O_3 products impurities.

Mineralogical Analysis (XRD)

Mineralogical analysis of Campaign 3 iron oxide precipitates were performed using X-ray diffraction analysis. Two samples of Campaign 3 iron oxide precipitates were evaluated. These included the non-calcined Campaign 3 iron oxide precipitate sample 1802-T7NC (ML-75) and the calcined Campaign 3 iron oxide precipitate sample 1802-T7C (ML-76). For both samples, the sole mineral phase identified in these precipitates was hematite (refer to Table 8).

Mineral Chemical Analysis

Two samples of Campaign 3 iron oxide precipitates underwent mineral chemical analysis at the Electron Probe Microanalyzer located at the EML at the UMTC. These included the non-calcined Campaign 3 iron oxide precipitate sample 1802-T7NC (ML-75) and the calcined Campaign 3 iron oxide precipitate sample 1802-T7C (ML-76).

Hematite, an iron-oxide precipitate containing greater than 0.5% (weight percent) TiO_2, and an iron- and titanium-bearing unknown were identified in both the non-calcined sample 1802-T7NC (ML-75) and the calcined sample 1802-T7C (ML-76). Results of the electron microprobe mineral chemical analyses of the iron oxide precipitates are included in Appendix 4: Tables A4-29 to A4-32.

Figure 84 is a backscatter image of sample 1802-T7NC (ML-75) obtained during EMPA analysis. Hematite occurred in several morphologies, including: A) rounded to locally polygonal to locally lathe-shaped nanoparticles of hematite ranging from approximately 0.4 µm to 0.8 µm in diameter or length (Figs. 84A–84D; these particles proved difficult to chemically analyze due to their small size); B) concentrically zoned microhematite spheres up to approximately 12 µm in diameter (Fig. 84A); and C) massive, amorphous microhematite composites ranging from 5 µm to 90 µm in diameter (Figs. 84A and 84B). As well, hematite containing greater than 0.5 weight percent TiO_2 occurred in patchy masses up to 15 µm in diameter composed of polygonal masses of hematite ranging from 0.8 µm to 2 µm in size and local larger polygonal grains and polygonal composites ranging from 4 µm to 10 µm in diameter (Fig. 84C). An iron- and titanium-bearing unknown was also identified and occurred in 5 µm–20 µm concentrically zoned spheres and ovoids associated with elongate, lathe-like particles of the same composition that are at least 12 µm in length and up to 6 µm in width (Fig. 84D).

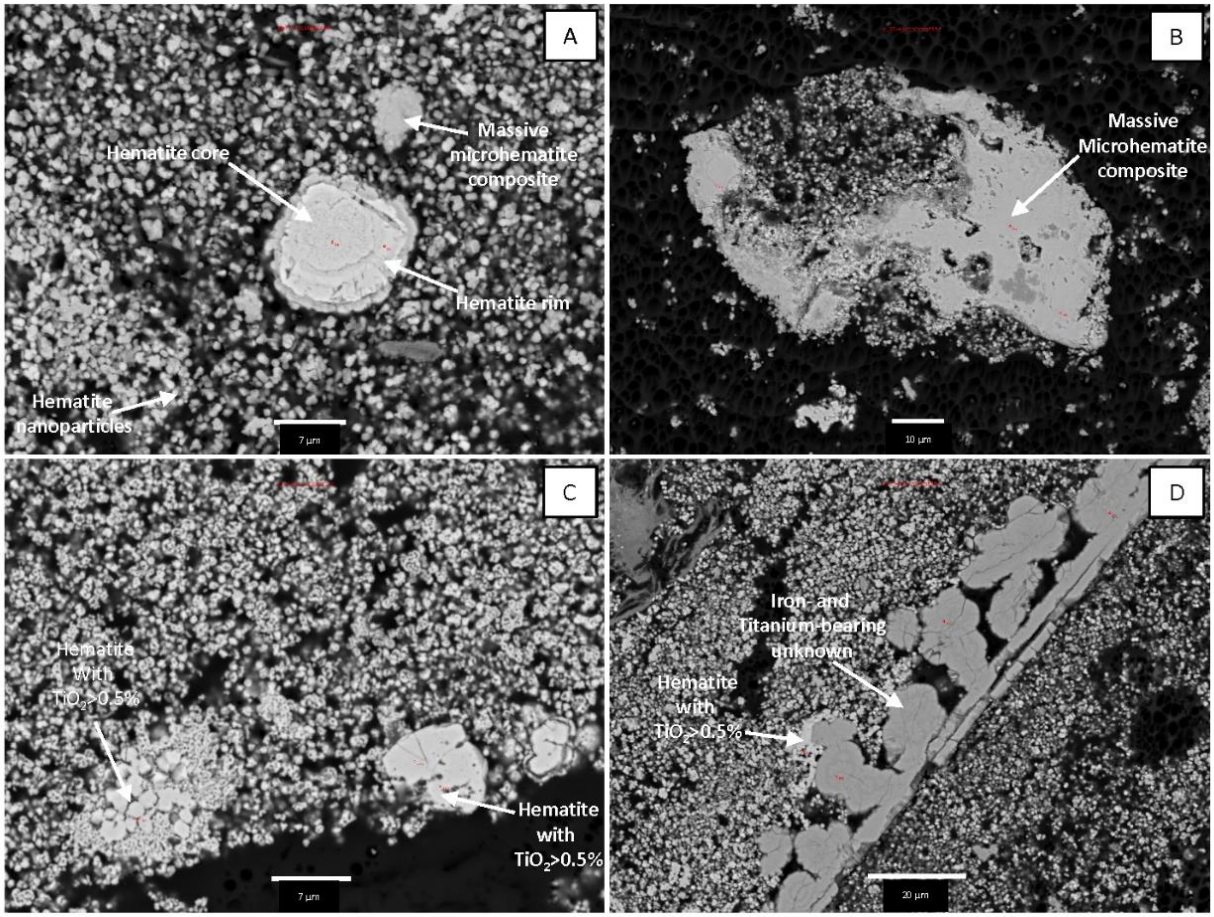

Figure 84. Electron microprobe backscatter image of Campaign 3 non-calcined iron oxide precipitates (sample 1802-T7NC (ML-75)). A). Matrix composed of hematite nanoparticles with concentrically-zoned hematite sphere and an ovoid composite of microhematite. Scale bar is 7 µm. B) Close-up of amorphous massive microhematite composite. Scale bar is 10 µm. C) Hematite nanoparticle matric containing polygonal particles of hematite containing greater than 0.5 weight percent TiO_2. Scale bar is 7 µm. D) Rounded- to lathe-shaped iron- and titanium-bearing unknown. Scale bar is 20 µm. Red numbers and circles in images are analysis locations.

Mineral chemical analyses of non-calcined Campaign 3 iron oxide precipitates (hematite) from sample 1802-T7NC (ML-75) are shown in Table 72. The composition of the hematite precipitate is dominated by FeO (81.773%-84.492%), with lesser amounts of TiO_2 (0.128%–0.351%), SiO_2 (0.079%–0.279%), MgO (0.000%–1.060%), Al_2O_3 (0.000%–0.084%), V_2O_3 (0.000%–0.037%), MnO (0.000%–0.012%), NiO (0.000%–0.009%), and Cr_2O_3 (0.000%–0.007%). Chlorine contents ranged from 0.567%–1.100%. Analytical totals ranged from 83.024%–86.900% with iron analyzed as FeO. When the FeO contents are recalculated as Fe_2O_3, the analytical totals range from 92.125% to 96.304%. The FeO/Total ratio of the sample varied from 0.972 to 0.987, with an average FeO/Total ratio of 0.982. The Fe_2O_3/Total ratio of the sample varied from 0.975 to 0.989, with an average Fe_2O_3/Total ratio of 0.983.

Table 72. Electron microprobe analyses of hematite in Campaign 3 non-calcined iron oxide precipitate sample 1802-T7NC (ML-75). Values are in weight percentages.

Electron Microprobe Analysis – Iron Oxide Precipitate Hematite Campaign 3 Non-Calcined (n = 5)													
Sample	Description	Phase	SiO_2	TiO_2	Al_2O_3	FeO	MnO	MgO	V_2O_3	Cr_2O_3	NiO	Cl	Total
ML-75-20-89-1	Microhematite Sphere Core	Hematite	0.160	0.128	0.074	83.994	0.012	0.598	0.008	0.000	0.000	1.100	86.074
ML-75-20-90-2	Microhematite Sphere Rim	Hematite	0.127	0.351	0.084	84.491	0.000	1.060	0.011	0.000	0.004	0.733	86.900
ML-75-21-91-1	Massive Microhematite	Hematite	0.079	0.294	0.005	83.662	0.000	0.000	0.035	0.006	0.006	0.639	84.726
ML-75-21-92-2	Massive Microhematite	Hematite	0.162	0.324	0.000	83.726	0.000	0.022	0.032	0.000	0.009	0.567	84.841
ML-75-21-93-3	Massive Microhematite	Hematite	0.279	0.277	0.030	81.773	0.000	0.041	0.037	0.007	0.002	0.578	83.024
		Minimum	*0.079*	*0.128*	*0.000*	*81.773*	*0.000*	*0.000*	*0.008*	*0.000*	*0.000*	*0.567*	*83.024*
		Maximum	*0.279*	*0.351*	*0.084*	*84.491*	*0.012*	*1.060*	*0.037*	*0.007*	*0.009*	*1.100*	*86.900*
		Average	*0.161*	*0.275*	*0.039*	*83.529*	*0.002*	*0.344*	*0.025*	*0.003*	*0.004*	*0.731*	*85.113*
		Mean	*0.160*	*0.294*	*0.030*	*83.726*	*0.000*	*0.041*	*0.032*	*0.000*	*0.004*	*0.639*	*84.841*
		St. Deviation	*0.066*	*0.078*	*0.035*	*0.925*	*0.005*	*0.422*	*0.012*	*0.003*	*0.003*	*0.198*	*1.319*
		Measurement Unit	*Wt. %*	*Wt. %*	*Wt. %*	*Wt. %*	*Wt. %*	*Wt. %*	*Wt. %*	*Wt. %*	*Wt. %*	*Wt. %*	*Wt. %*

Figure 85 illustrates the mineral composition of the Campaign 3 non-calcined iron oxide (hematite) precipitates from sample 1802-T7NC (ML-75). When plotted in the FeO-TiO_2-MgO and FeO-TiO_2-5MgO systems, it can be seen that these precipitates contain minor amounts of MgO, with round rims containing more MgO than round cores and massive hematite composites, respectively (Figs. 85A and 85B). When plotted in the FeO-TiO_2-V_2O_3 and FeO-TiO_2-5V_2O_3 systems, it is clear that these precipitates contain little V_2O_3 (Figs. 85C and 85D). For stoichiometric calculations, all FeO analyzed in the sample was converted to Fe_2O_3 using the Abbey (1977) calculation method. When plotted in Fe^{2+}-Ti^{4+}-Fe^{3+} space, the precipitates plot at or near stoichiometric hematite (Fig. 85E).

One analysis from Campaign 3 non-calcined iron oxide precipitate sample 1802-T7NC (ML-75) identified the presence of hematite containing greater than 0.5 weight percent TiO_2. The material is composed of FeO (80.938%), TiO_2 (3.648%), SiO_2 (0.126%), V_2O_3 (0.048%), Al_2O_3 (0.015%), Cr_2O_3 (0.015%), NiO (0.001%), and chlorine (0.795%). No MnO or MgO were detected in the analysis. The analytical total of the analysis was 85.587%, with iron analyzed as FeO. When FeO is recalculated as Fe2O3 (Abbey, 1977), the analytical total increases to 94.595%.

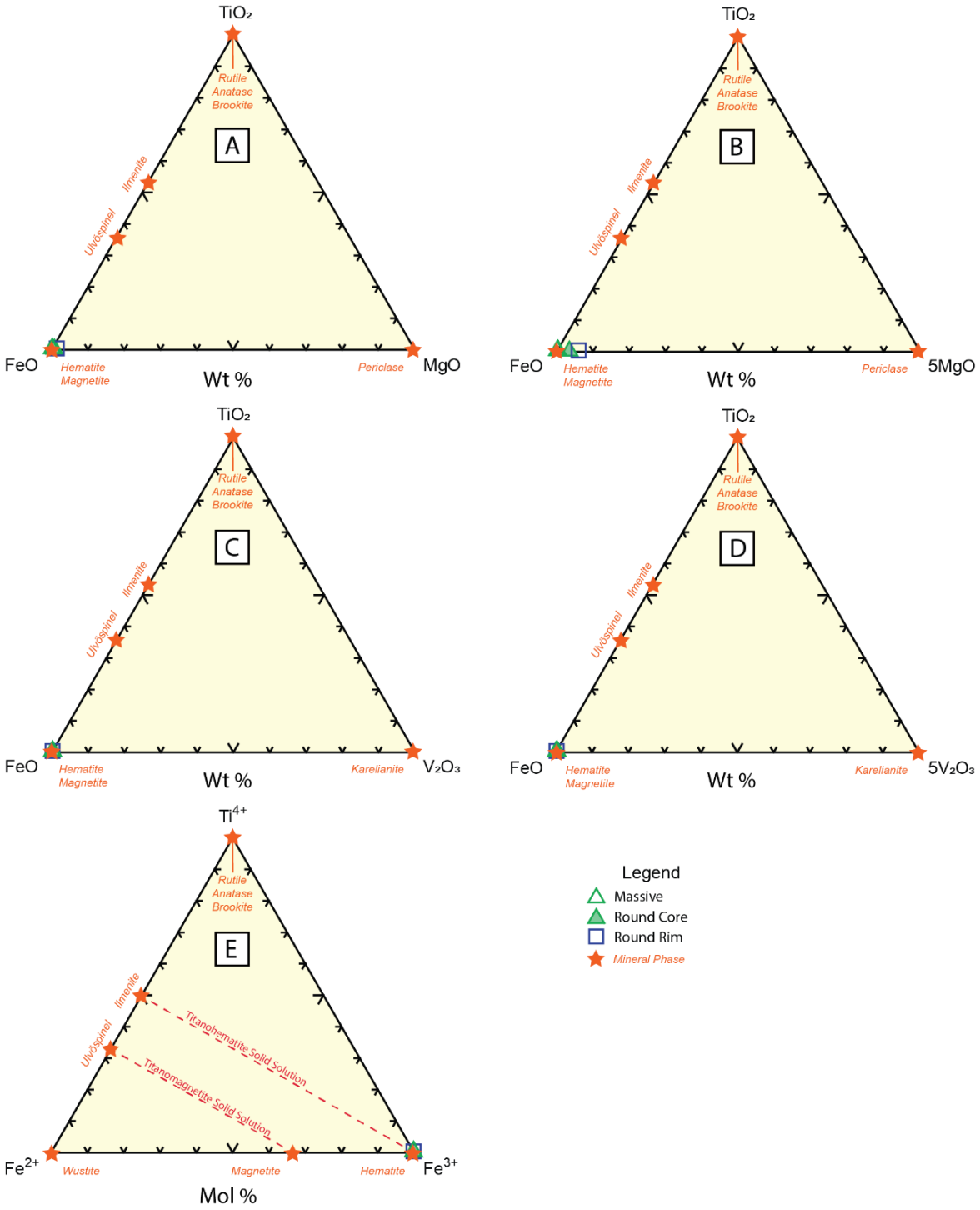

Figure 85. Ternary diagram illustrating the chemical compositions of iron oxide precipitates (hematite) from Campaign 3 non-calcined sample 1802-T7NC (ML-75). Figures 89A and 89B represent ternary diagrams in the FeO-TiO_2-MgO and FeO-TiO_2-5MgO systems and show that these iron oxide precipitates contain minor amounts of MgO. Figures 89C and 89D represent ternary diagrams in the FeO-TiO_2-V_2O_3 and FeO-TiO_2-5V_2O_3 systems, respectively. Both diagrams illustrate that the iron oxide precipitates contain little V_2O_3. Figure 89E is a molar Fe^{2+}-Ti^{4+}-Fe^{3+} ternary diagram (modified after Klein and Hurlbut, 1999; Meinhold, 2010) and shows that the composition of the precipitates plots near stoichiometric hematite after FeO is converted to Fe_2O_3 (Abbey, 1977).

Figure 86 illustrates the mineral composition of the Campaign 3 non-calcined iron oxide precipitates that contain greater than 0.5% by weight TiO_2 from sample 1802-T7NC (ML-75). When plotted in the FeO-TiO_2-MgO and FeO-TiO_2-5MgO, it can be seen that these precipitates contain little MgO and plot just above stoichometric hematite along the FeO-TiO_2 tie line (Figs. 86A and 86B). When plotted in the FeO-TiO_2-V_2O_3 and FeO-TiO_2-5V_2O_3 systems, it is clear that these precipitates contain little V_2O_3. The samples on these ternary diagrams also plot above stoichometric hematite along the FeO-TiO_2 tie line (Figs. 86C and 86D). For stoichiometric calculations, all FeO analyzed in the sample was converted to Fe_2O_3 using the Abbey (1977) calculation method. When plotted in Fe^{2+}-Ti^{4+}-Fe^{3+}, the precipitates plot at or near stoichiometric hematite (Fig. 86E) but are shifted toward Ti^{4+} along the Fe^{3+}-Ti^{4+} tie line.

Three analyses from Campaign 3 non-calcined iron oxide precipitate sample 1802-T7NC (ML-75) indicate the presence of an iron- and titanium-bearing unknown phase (Table 73). This material is primarily composed of TiO_2 (76.120%–79.639%), with lesser amounts of FeO (12.699%–15.909%), SiO_2 (0.399%–0.507%), V_2O_3 (0.026%–0.095%), MnO (0.003%–0.23%), Cr_2O_3 (0.001%–0.024%), Al_2O_3 (0.000%–0.041%), and NiO (0.000%–0.036%). MgO was not detected in the sample. Chlorine contents range from 0.178% to 0.233%. Analytical totals, when iron is analyzed as FeO, range from 91.756% to 93.010%; if all iron is accounted for as Fe_2O_3, the analytical totals range from 93.380% to 94.642%.

Table 73. Electron microprobe analyses of iron- and titanium-bearing unknown phase in Campaign 3 non-calcined iron oxide precipitate sample 1802-T7NC (ML-75). Values are in weight percentages.

Electron Microprobe Analysis – Iron- and Titanium-bearing Unknown (n = 6)													
Sample	Description	Phase	SiO_2	TiO_2	Al_2O_3	FeO	MnO	MgO	V_2O_3	Cr_2O_3	NiO	Cl	Total
ML-75-19-85-1	Spherical Core	Unknown Fe-Ti-Oxide	0.448	76.366	0.000	14.594	0.023	0.000	0.078	0.010	0.036	0.201	91.756
ML-75-19-86-2	Spherical Core	Unknown Fe-Ti-Oxide	0.507	76.120	0.020	15.909	0.019	0.000	0.095	0.024	0.000	0.178	92.871
ML-75-19-87-3	Spherical Core	Unknown Fe-Ti-Oxide	0.399	79.639	0.041	12.669	0.003	0.000	0.026	0.001	0.000	0.233	93.010
		Minimum	***0.399***	***76.120***	***0.000***	***12.699***	***0.003***	***0.000***	***0.026***	***0.001***	***0.000***	***0.178***	***91.756***
		Maximum	***0.507***	***79.639***	***0.041***	***15.909***	***0.023***	***0.000***	***0.095***	***0.024***	***0.036***	***0.233***	***93.010***
		Average	***0.451***	***77.375***	***0.020***	***14.391***	***0.015***	***0.000***	***0.066***	***0.012***	***0.012***	***0.204***	***92.546***
		Mean	***0.448***	***76.366***	***0.020***	***14.594***	***0.019***	***0.000***	***0.078***	***0.010***	***0.000***	***0.201***	***92.871***
		St. Deviation	***0.038***	***1.389***	***0.014***	***1.152***	***0.007***	***0.000***	***0.025***	***0.008***	***0.015***	***0.020***	***0.486***
		Measurement Unit	***Wt. %***	***Wt. %***	***Wt. %***	***Wt. %***	***Wt. %***	***Wt. %***	***Wt. %***	***Wt. %***	***Wt. %***	***Wt. %***	***Wt. %***

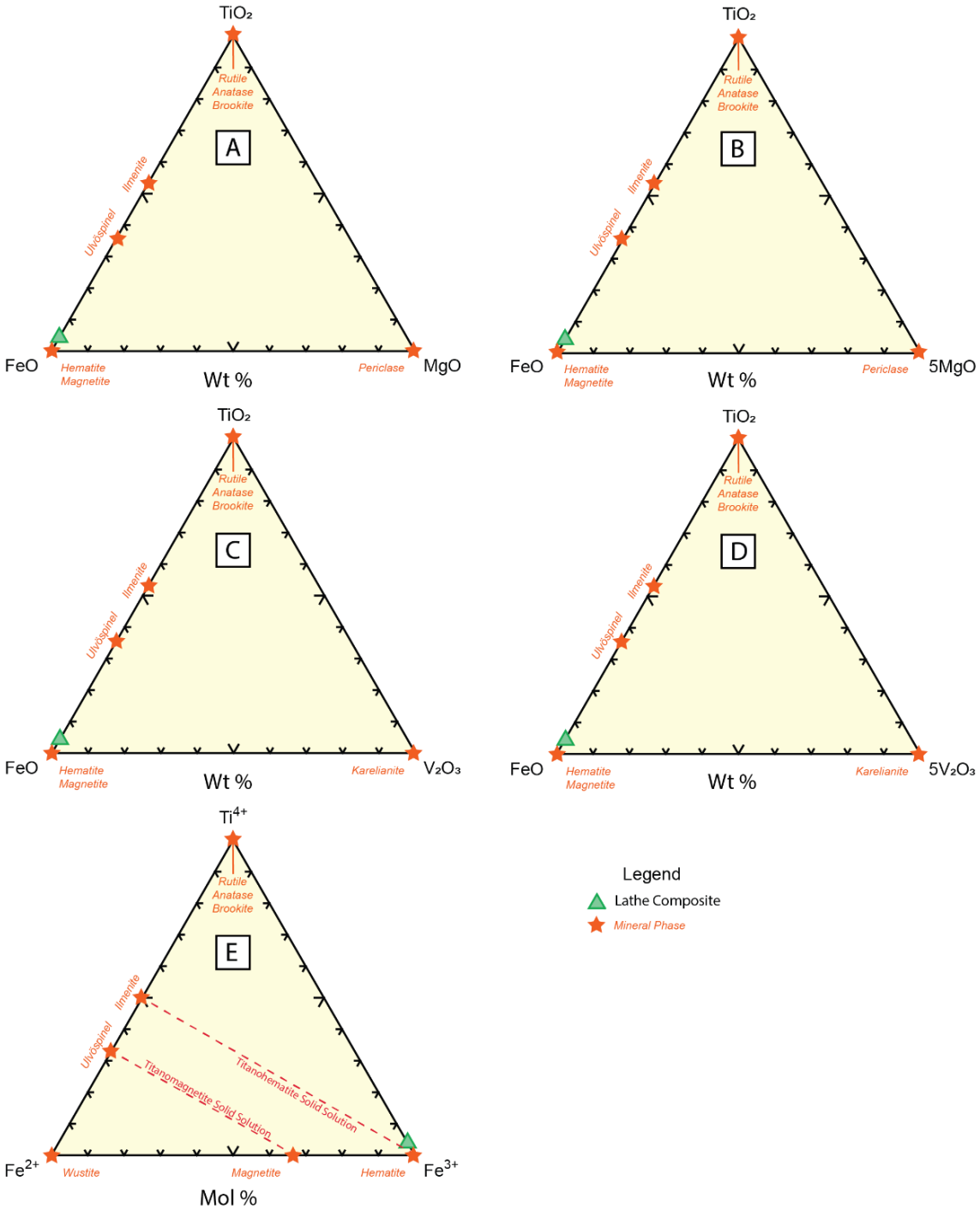

Figure 86. Ternary diagram illustrating the chemical compositions of TiO_2-bearing (TiO_2>0.5% by weight) iron oxide precipitates (hematite) from Campaign 3 non-calcined sample 1802-T7NC (ML-75). Figures 89A and 89B represent ternary diagrams in the FeO-TiO_2-MgO and FeO-TiO_2-5MgO systems and show that these iron oxide precipitates contain minor amounts of MgO. Figures 89C and 89D represent ternary diagrams in the FeO-TiO_2-V_2O_3 and FeO-TiO_2-5V_2O_3 systems, respectively. Both diagrams illustrate that the iron oxide precipitates contain little V_2O_3. Figure 89E is a molar Fe^{2+}-Ti^{4+}-Fe^{3+} ternary diagram (modified after Klein and Hurlbut, 1999; Meinhold, 2010) and shows that the composition of the precipitates plots near stoichiometric hematite after FeO is converted to Fe_2O_3 (Abbey, 1977).

Figure 87 illustrates the mineral chemical composition of the iron- and titanium-bearing unknown phase from Campaign 2 non-calcined sample 1802-T7NC (ML-75). Ternary diagrams in the FeO-TiO_2-MgO and FeO-TiO_2-5MgO systems illustrate that the unknown material contains little MgO and plots along the FeO-TiO_2 tie line between 80% and 90% TiO_2 (Figs. 87A and 87B). When plotted on ternary diagrams comprising the FeO-TiO_2-V_2O_3 and FeO-TiO_2-5V_2O_3 systems, it is also clear that this unknown phase contains little V_2O_3. The composition of this material plots along the FeO-TiO_2 tie line between 80% and 90% TiO_2 (Figs. 87C and 87D). As this material was primarily composed of TiO_2, stoichiometric calculation using the ILMNCALC.xls spreadsheet (Gabbrosoft.com) indicated an absence of Fe^{3+}, and therefore the composition of this material plotted in Fe^{2+}-Ti^{4+}-Fe^{3+} space occurs along the Fe^{2+}-Ti^{4+} tie line about 2/3 of the way toward stoichiometric rutile from stoichiometric ilmenite (Fig. 87E). Compositionally, the material may be a fine mixture of ilmenite and rutile and/or ferropseudobrookite and rutile. Further analysis will be required.

Figure 88 is a backscatter image of sample 1802-T7C (ML-76) obtained during EMPA analysis. This sample represents iron oxide precipitate from Campaign 3 that has been calcined. Hematite occurred in two morphologies, including: A) rounded to locally polygonal-shaped particles of hematite typically ranging from approximately 0.3 µm to 1 µm in diameter or length, but locally up to 2 µm in diameter or length (Fig. 88A; these particles proved difficult to chemically analyze due to their small size); and B) massive hematite composites composed of two or more individual hematite nanoparticles that range up to 2 µm to 4 µm in diameter (Fig. 88B). Hematite containing greater than 0.5 weight percent TiO_2 occurred in irregular- to chain-like masses ranging from approximately 5 µm to 50 µm in length and 3 µm to 25 µm in width, which comprise aggregates of <1 µm–6 µm polygonal grains (Figs. 88A and 88B) as well as individual polygonal grains ranging from 5 µm to 10 µm in diameter (Figs. 88A and 88B). As well, an iron- and titanium-bearing unknown was also identified and occurred in 5 µm–10 µm, rhomboid-like particles in elongate masses up to 60 µm in length and 30 µm in width (Fig. 88C).

One electron microprobe mineral chemical analysis from a massive composite grain of hematite was composed primarily of FeO (85.625%), with lesser amounts of MgO (0.371%), TiO_2 (0.151%), SiO_2 (0.045%), Cr_2O_3 (0.008%), MnO (0.007%), V_2O_3 (0.005%), and Al_2O_3 (0.003%). Nickel oxide (NiO) was not detected in the analysis. The chlorine contents were 0.920%. The analytical total of the analysis was 87.136%, with iron analyzed as FeO. When the FeO contents are recalculated as Fe_2O_3 (Abbey, 1977), the analytical total increases to 96.666%. The FeO/Total ratio of the sample is 0.983; the Fe_2O_3/Total ratio was found to be 0.984.

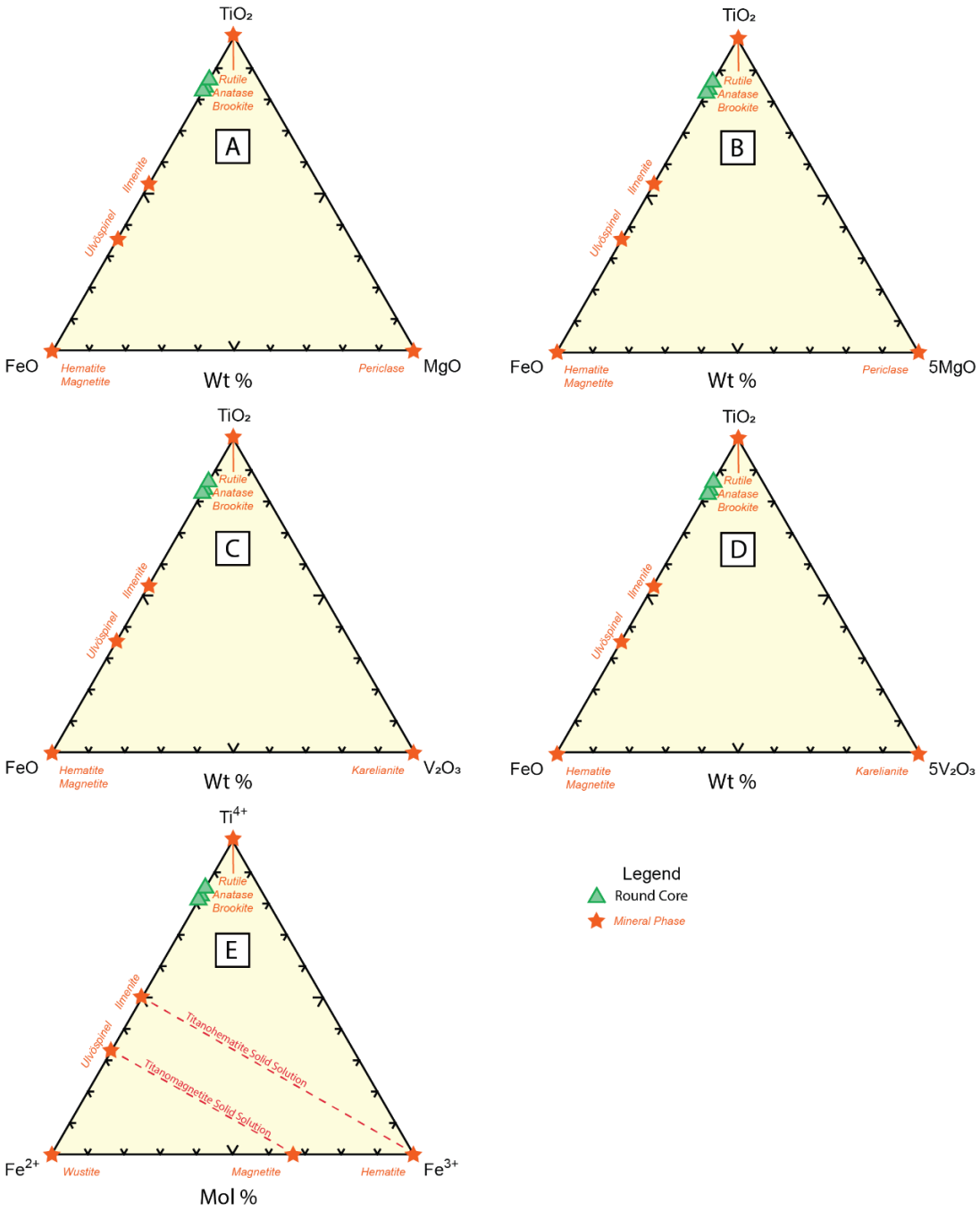

Figure 87. Ternary diagram illustrating the chemical compositions of TiO_2-bearing (TiO2.0.5% by weight) iron oxide precipitates (hematite) from Campaign 3 non-calcined sample 1802-T7NC (ML-75). Figures 89A and 89B represent ternary diagrams in the FeO-TiO_2-MgO and FeO-TiO_2-5MgO systems and show that these iron oxide precipitates are made up of FeO and TiO_2 without any MgO. Figures 89C and 89D represent ternary diagrams in the FeO-TiO_2-V_2O_3 and FeO-TiO_2-5V_2O_3 systems respectively and illustrate the low V_2O_3 contents of the material. Figure 89E is a molar Fe^{2+}-Ti^{4+}-Fe^{3+} ternary diagram (modified after Klein and Hurlbut, 1999; Meinhold, 2010) and shows that the composition of the precipitates plots about 2/3 toward stoichiometric rutile from the stoichiometric ilmenite composition along the Fe^{2+}-Ti^{4+} tie line, perhaps suggesting a fine mixture of ilmenite and rutile or ferropseudobrookite and rutile. Identification will require further analysis.

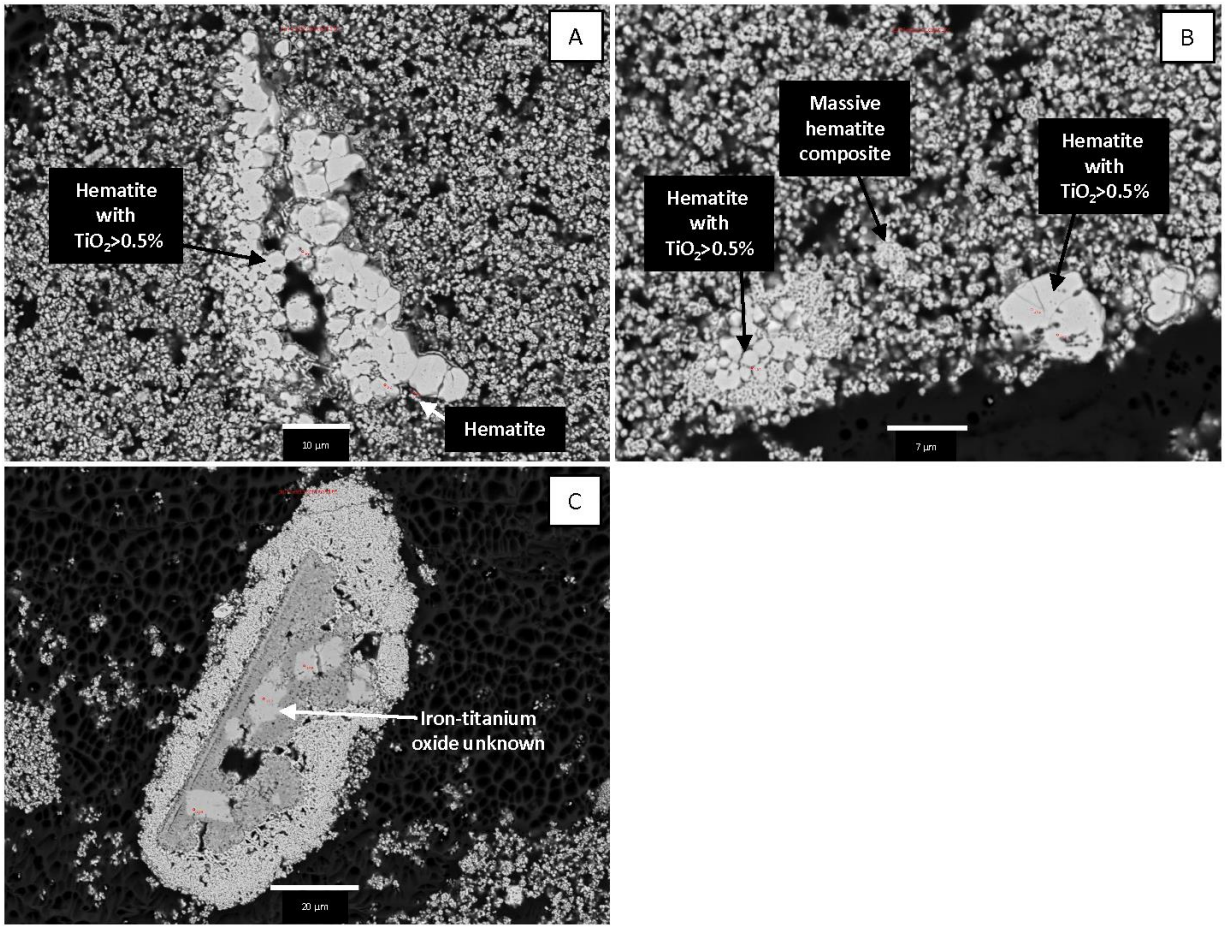

Figure 88. Electron microprobe backscatter images of Campaign 3 calcined iron oxide precipitates from sample 1802-T7C (ML-76). A) Fine-grained hematite matrix containing irregular, chain-like agglomerate of polygons of hematite containing greater than 0.5% (by weight) TiO_2. Scale bar is 10 µm. B) Fine-grained hematite matrix composed of individual oval hematite grains and local massive hematite composites. Also present are irregular polygonal agglomerates and individual crystals composed of hematite containing greater than 0.5% (by weight) TiO_2. Scale bar is 7 µm. C) Rhomboid-like iron- and titanium-bearing oxide unknown. Scale bar is 20 µm. Red numbers and circles in images are analysis locations.

Figure 89 illustrates the chemical composition of the iron oxide (hematite) precipitates from Campaign 3 calcined sample 1802-T7C (ML-76). When plotted in the FeO-TiO_2-MgO and FeO-TiO_2-5MgO systems, it is clear that the Campaign 2 calcined precipitates contain minor amounts of MgO (Figs. 89A and 89B). Ternary plots in the FeO-TiO_2-V_2O_3 and FeO-TiO_2-5V_2O_3 systems illustrate that the calcined Campaign 3 iron oxide precipitates contain little V_2O_3 (Figs. 89C and 89D). The molar ratio of Fe^{3+} was calculated by converting all FeO from the electron microprobe analysis into Fe_2O_3 using the method of Abbey (1977). As shown in Figure 89E, the iron oxide (hematite) precipitate from sample 1802-T7C (ML-76) is nearly stoichiometric hematite.

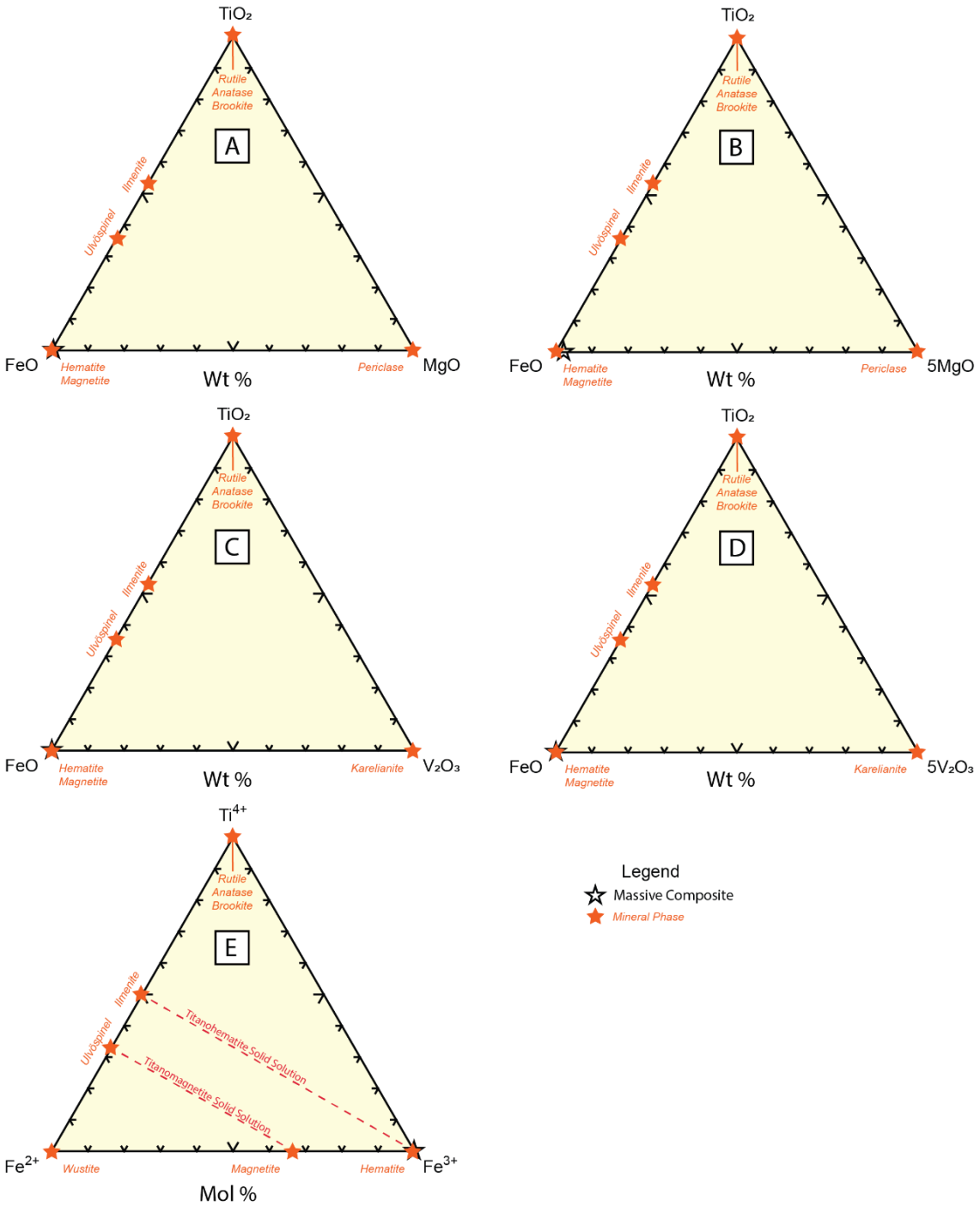

Figure 89. Ternary diagrams illustrating the chemical composition of iron oxide precipitate (hematite) from calcined Campaign 3 sample 1802-T7C/ML-76. Figures 93A and 93B show the composition of the iron oxide (hematite) precipitate plotted in the FeO-TiO_2-MgO and FeO-TiO_2-5MgO systems, respectively. These diagrams illustrate the minor MgO contents of the precipitate. Figures 93C and 93D show the composition of the iron oxide (hematite) precipitate plotted in the FeO-TiO_2-V_2O_3 and FeO-TiO_2-5V_2O_3 systems, respectively. These diagrams illustrate the low abundance of V_2O_3 in the precipitate. Figure 93E is a molar Fe^{2+}-Ti^{4+}-Fe^{3+} ternary diagram (modified after Klein and Hurlbut, 1999; Meinhold, 2010) showing that the calcined Campaign 3 iron oxide precipitate is stoichiometric hematite.

Several electron microprobe mineral chemical analyses from sample 1802-T7C (ML-76) identified the presence of a hematite precipitate that contained greater than 0.5% (by weight) TiO_2 (Table 74). This material is composed primarily of FeO (81.867%–85.882%), TiO_2 (0.503%–1.352%), MgO (0.069%–0.308%), V_2O_3 (0.001%–0.025%), SiO_2 (0.000%–0.126%), Al_2O_3 (0.000%–0.097%), MnO (0.000%–0.012%), NiO (0.000%–0.003%), and Cr_2O_3 (0.000%–0.002%). Chlorine contents varied from 0.258% to 0.668%). The analytical totals of the analyses with iron analyzed as FeO ranged from 83.155% to 87.385%. When FeO contents are recalculated as Fe_2O_3 (Abbey, 1977), the analytical totals range from 92.227% to 96.914%. The FeO/Total ratio of the samples ranges from 0.975 to 0.989, with an average FeO/Total of 0.981. The Fe_2O_3/Total ratio of the samples ranges from 0.977 to 0.990, with an average Fe_2O_3/Total of 0.983.

Table 74. Electron microprobe analyses of Campaign 3 calcined iron oxide precipitate (hematite) that contains greater than 0.5% (by weight) TiO_2 from sample 1802-T7C/ML-76. Values are in weight percentages.

Electron Microprobe Analysis – Iron Oxide Precipitate Hematite where TiO_2 > 0.500% (n = 5)													
Sample	Description	Phase	SiO_2	TiO_2	Al_2O_3	FeO	MnO	MgO	V_2O_3	Cr_2O_3	NiO	Cl	Total
ML-76-23-98-2	Large Massive Hematite Composite	Ti-bearing Hematite	0.000	0.503	0.000	85.882	0.000	0.101	0.010	0.002	0.000	0.381	86.880
ML-76-23-99-3	Large Massive Hematite Composite	Ti-bearing Hematite	0.126	0.696	0.022	85.616	0.000	0.308	0.010	0.000	0.002	0.605	87.385
ML-76-24-100-1	Microhematite Sphere Core	Ti-bearing Hematite	0.000	1.352	0.032	84.937	0.012	0.152	0.006	0.000	0.000	0.668	87.158
ML-76-24-101-2	Microhematite Sphere Core	Ti-bearing Hematite	0.015	1.095	0.097	85.481	0.000	0.069	0.001	0.001	0.003	0.520	87.282
ML-76-24-102-3	Microhematite Sphere Core	Ti-bearing Hematite	0.080	0.621	0.029	81.867	0.000	0.237	0.025	0.000	0.000	0.258	83.115
		Minimum	*0.000*	*0.503*	*0.000*	*81.867*	*0.000*	*0.069*	*0.001*	*0.000*	*0.000*	*0.258*	*83.155*
		Maximum	*0.126*	*1.352*	*0.097*	*85.882*	*0.012*	*0.308*	*0.025*	*0.002*	*0.003*	*0.668*	*87.385*
		Average	*0.044*	*0.853*	*0.036*	*84.757*	*0.002*	*0.173*	*0.010*	*0.001*	*0.001*	*0.486*	*86.364*
		Mean	*0.015*	*0.696*	*0.029*	*85.481*	*0.000*	*0.152*	*0.010*	*0.000*	*0.000*	*0.520*	*87.158*
		St. Deviation	*0.050*	*0.319*	*0.032*	*1.477*	*0.005*	*0.088*	*0.008*	*0.001*	*0.001*	*0.149*	*1.633*
		Measurement Unit	*Wt. %*	*Wt. %*	*Wt. %*	*Wt. %*	*Wt. %*	*Wt. %*	*Wt. %*	*Wt. %*	*Wt. %*	*Wt. %*	*Wt. %*

Figure 90 illustrates the chemical composition of the iron oxide (hematite) precipitates that contain greater than 0.5% (by weight TiO_2) from Campaign 3 calcined sample 1802-T7C (ML-76). When plotted in the FeO-TiO_2-MgO and FeO-TiO_2-5MgO systems, the presence of minor amounts of MgO in the precipitate are observed (Figs. 90A and 90B). Ternary plots in the FeO-TiO_2-V_2O_3 and FeO-TiO_2-5V_2O_3 illustrate the low contents of V_2O_3 in the precipitate (Figs. 90C and 90D). The molar ratio of Fe^{3+} was calculated by converting all FeO from the electron microprobe analysis into Fe_2O_3 using the method of Abbey (1977). As shown in Figure 90E, the titanium-bearing iron oxide (hematite) precipitate from sample 1802-T7C (ML-76) is nearly stoichiometric hematite.

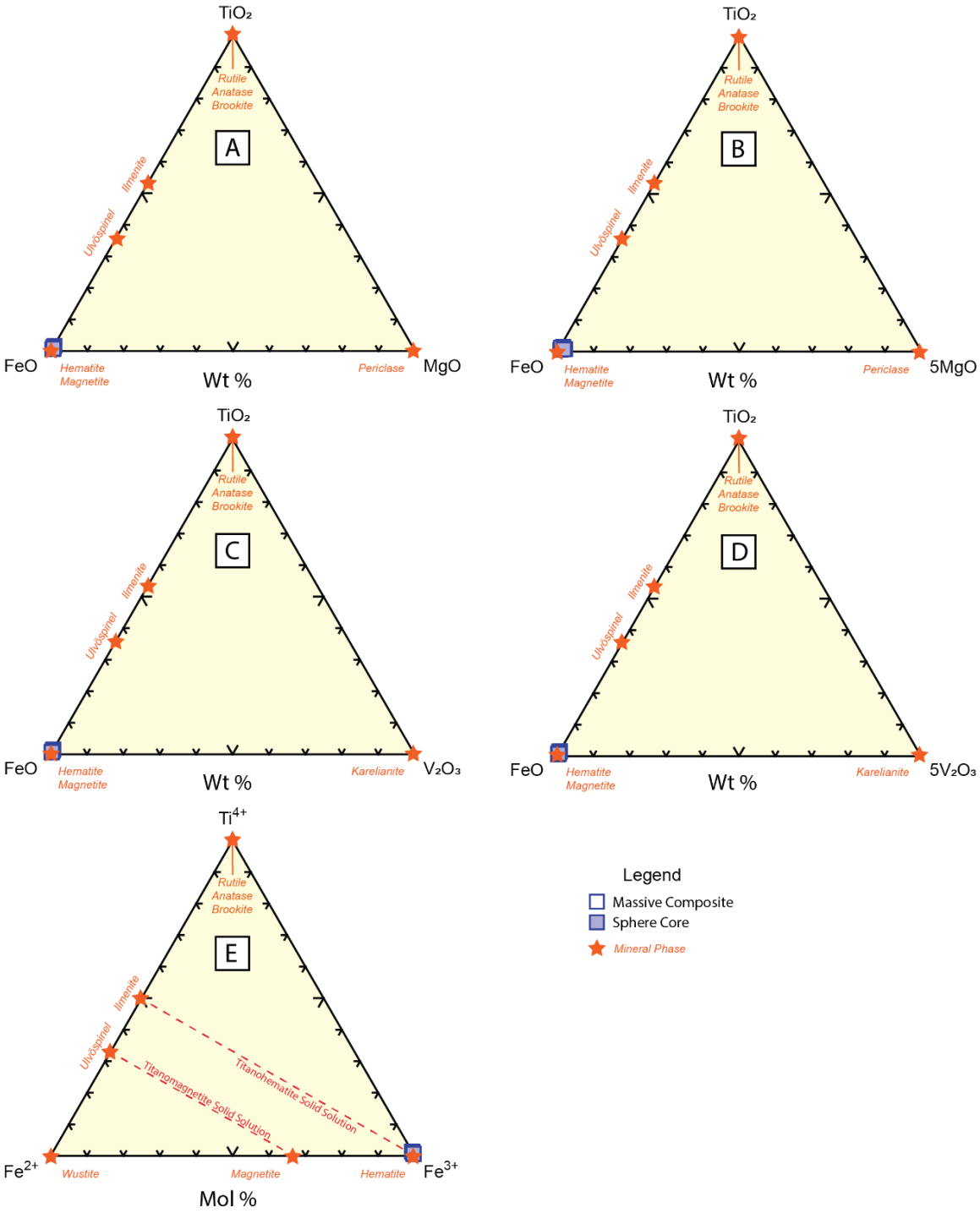

Figure 90. Ternary diagram illustrating the chemical composition of the titanium-bearing (TiO_2>0.5% by weight) iron oxide (hematite) precipitate from Campaign 3 calcined iron oxide precipitate sample 1802-T7C/ML-76. Figures 94A and 94B illustrate the composition of the precipitate in the FeO-TiO_2-MgO and FeO-TiO_2-5MgO systems. These plots illustrate the minor MgO contents of the precipitate. Figs. 94C and 94D illustrate the composition of the precipitate in the FeO-TiO_2-V_2O_3 and FeO-TiO_2-$5V_2O_3$ systems, respectively, and show that the precipitates contain little V_2O_3. Figure 94E is a molar Fe^{2+}-Ti^{4+}-Fe^{3+} ternary diagram (modified after Klein and Hurlbutt, 1999; Meinhold, 2010) and illustrates that these precipitates are nearly stoichiometric hematite.

A number of analyses from Campaign 3 calcined iron precipitate sample 1802-T7C (ML-76), an iron- and titanium-bearing unknown phase (Table 75). The material is composed primarily of FeO (53.934%–59.712%) and TiO_2 (33.727%–40.456%), with lesser amounts of SiO_2 (0.021%–0.154%), Al_2O_3 (0.005%–0.032%), NiO (0.000%–0.039%), V_2O_3 (0.000%–0.019%), and MnO (0.000%–0.004%). Non-detected components include MgO and Cr_2O_3. Chlorine contents in the material varied from 0.000% to 0.025%. With iron contents analyzed as FeO, analytical totals ranged from 90.321% to 100.343%. If all iron is accounted for as Fe_2O_3, the analytical totals range from 96.607% to 106.989%. The high analytical totals associated with the assumption that all iron is present as Fe_2O_3 suggests that this material may contain both Fe^{2+} and Fe^{3+} cations.

Table 75. Electron microprobe analyses of iron- and titanium-bearing unknown phase in Campaign 3 calcined iron oxide precipitates from sample 1802-T7C/ML-76. Values are in weight percentages.

Electron Microprobe Analysis – Campaign 3 Calcined Iron- and Titanium-bearing Unknown (n = 6)													
Sample	Description	Phase	SiO_2	TiO_2	Al_2O_3	FeO	MnO	MgO	V_2O_3	Cr_2O_3	NiO	Cl	Total
ML-76-25-103-1	Blocky Composite Core	Unknown Fe-Ti-Oxide	0.154	40.456	0.005	59.712	0.004	0.000	0.000	0.000	0.000	0.012	100.343
ML-76-25-104-2	Blocky Composite Core	Unknown Fe-Ti-Oxide	0.082	36.652	0.013	53.934	0.000	0.000	0.019	0.000	0.011	0.000	90.710
ML-76-25-105-3	Blocky Composite Core	Unknown Fe-Ti-Oxide	0.211	33.727	0.032	56.477	0.000	0.000	0.000	0.000	0.039	0.025	90.321
		Minimum	***0.021***	***33.727***	***0.005***	***53.934***	***0.000***	***0.000***	***0.000***	***0.000***	***0.000***	***0.000***	***90.321***
		Maximum	***0.154***	***40.456***	***0.032***	***59.712***	***0.004***	***0.000***	***0.019***	***0.000***	***0.039***	***0.025***	***100.343***
		Average	***0.086***	***36.945***	***0.017***	***56.708***	***0.001***	***0.000***	***0.006***	***0.000***	***0.017***	***0.012***	***93.791***
		Median	***0.082***	***36.652***	***0.013***	***56.477***	***0.000***	***0.000***	***0.000***	***0.000***	***0.011***	***0.012***	***90.710***
		St. Deviation	***0.054***	***2.755***	***0.011***	***2.364***	***0.002***	***0.000***	***0.009***	***0.000***	***0.016***	***0.010***	***4.635***
		Measurement Unit	***Wt. %***	***Wt. %***	***Wt. %***	***Wt. %***	***Wt. %***	***Wt. %***	***Wt. %***	***Wt. %***	***Wt. %***	***Wt. %***	***Wt. %***

Figure 91 illustrates the mineral chemical composition of the Campaign 3 iron oxide precipitate iron- and titanium-bearing unknown phase from sample 1802-T7C (ML-76). The unknown phase, when plotted in the FeO-TiO_2-MgO, FeO-TiO_2-5MgO, FeO-TiO_2-V_2O_3, and FeO-TiO_2-5V_2O_3 systems, has little MgO or V_2O_3 contents and has FeO/TiO_2 ratios that lie between the compositions of ulvöspinel and ilmenite (Figs. 91A–91D). As this material is composed primarily of FeO and TiO_2, the stoichiometry of the material was determined using the ILMNCALC.xls spreadsheet (Gabbrosoft.com), which is capable of determining both Fe^{2+} and Fe^{3+} stoichiometry of the material. When plotted on a ternary diagram plotting molar Fe^{2+}, Ti^{4+}, and Fe^{3+} (Fig. 91E), the material plots on the titanohematite solid solution line that lies between stoichiometric ilmenite and stoichiometric hematite. Additional electron microprobe analyses in which both Fe^{2+} and Fe^{3+} are analyzed may help to further identify this unknown phase.

Lithogeochemical Analysis

Whole rock lithogeochemical analyses were performed on the non-calcined (1802-T7NC/ML-75) and calcined (1802-T7C/ML-76) iron oxide precipitates produced during Campaign 3. The results of these analyses are shown in Table 76, and ALS Laboratory analytical certificates can be found in Appendix 3: Tables A3-1 to A3-7.

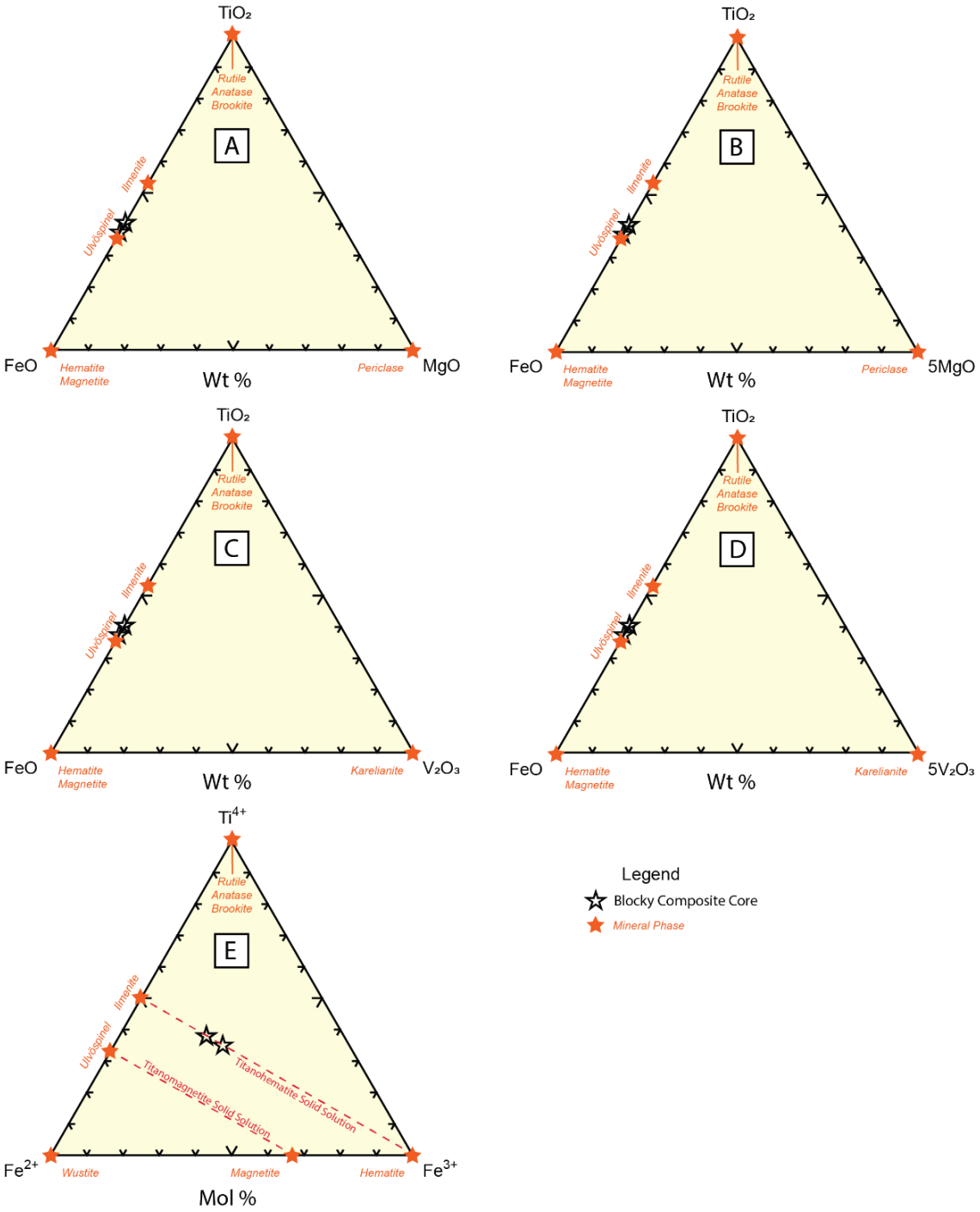

Figure 91. Ternary diagram illustrating the chemical composition of the iron- and titanium-bearing unknown phase from the calcined Campaign 3 iron oxide precipitate sample 1802-T7C/ML-76. Figures 95A–95D illustrate the composition of the precipitate in the FeO-TiO_2-MgO, FeO-TiO_2-5MgO, FeO-TiO_2-V_2O_3 and FeO-TiO_2-5V_2O_3 systems, respectively. These plots illustrate the minor MgO and V_2O_3 contents of the precipitate and that, within these component systems, the unknown phase has FeO/TiO_2 ratios that are similar to that within ulvöspinel. Figure 95E is a molar Fe^{2+}-Ti^{4+}-Fe^{3+} ternary diagram (modified after Klein and Hurlbutt, 1999; Meinhold, 2010) based on stoichiometric calculations of the phase using the ILMNCALC.xls spreadsheet (Gabbrosoft.com). In this system, the material plots as titanohematite solid solution.

Table 76. Results of lithogeochemical analyses of Campaign 3 iron oxide precipitates. Note low analytical totals for major element oxide using the ME-ICP06 method for sample 1802-T7C (ML-76). This sample was reanalyzed using method ME-XRF06 per recommendation by ALS Laboratories and the major element oxide analytical total improved to 99.98%.

		Sample	1802-T7NC	1802-T7C*			Sample	1802-T7C
		Sample Description	Iron Oxide Non Calcined Campaign 3	Iron Oxide Calcined Campaign 3			Sample Description	Iron Oxide Precipitate Campaign 3 - CALCINED
Analysis	Method	Detection Limit			Analysis	Method	Detection Limit	
SiO2_%	ME-ICP06	0.01	0.95	0.85	SiO2_%	ME-XRF06	0.01	0.89
Al2O3_%	ME-ICP06	0.01	0.08	0.05	Al2O3_%	ME-XRF06	0.01	0.08
Fe2O3_%	ME-ICP06	0.01	89.30	64.2	Fe2O3_%	ME-XRF06	0.01	96.82
CaO_%	ME-ICP06	0.01	0.02	0.02	CaO_%	ME-XRF06	0.01	0.02
MgO_%	ME-ICP06	0.01	<0.01	<0.01	MgO_%	ME-XRF06	0.01	0.04
Na2O_%	ME-ICP06	0.01	0.10	0.07	Na2O_%	ME-XRF06	0.01	0.06
K2O_%	ME-ICP06	0.01	0.03	0.03	K2O_%	ME-XRF06	0.01	0.03
Cr2O3_%	ME-ICP06	0.002	<0.002	<0.002	Cr2O3_%	ME-XRF06	0.01	<0.01
TiO2_%	ME-ICP06	0.01	1.76	1.41	TiO2_%	ME-XRF06	0.01	1.76
MnO_%	ME-ICP06	0.01	<0.01	<0.01	MnO_%	ME-XRF06	0.01	<0.01
P2O5_%	ME-ICP06	0.01	0.01	<0.01	P2O5_%	ME-XRF06	0.001	0.011
SrO_%	ME-ICP06	0.01	<0.01	<0.01	SrO_%	ME-XRF06	0.01	<0.01
BaO_%	ME-ICP06	0.01	0.05	0.05	BaO_%	ME-XRF06	0.01	0.07
LOI_%	OA-GRA05	0.01	5.72	0.02	LOI_%	ME-XRF06	0.01	0.20
Total_%	TOT-ICP06	0.01	98.02	66.7	Total_%	ME-XRF06	0.01	99.98
S_%	S-IR08	0.01	0.05	0.01	S_%	S-IR08	0.01	0.01
Ag_ppm	ME-4ACD81	0.5	<0.5	<0.5	Ag_ppm	ME-4ACD81	0.5	<0.5
Ag_ppm	ME-MS42	0.01	0.04	0.01	Ag_ppm	ME-MS42	0.01	0.01
As_ppm	ME-4ACD81	5	37	41	As_ppm	ME-4ACD81	5	41
As_ppm	ME-MS42	0.1	0.6	6.7	As_ppm	ME-MS42	0.1	6.7
Ba_ppm	ME-MS81	0.5	457	412	Ba_ppm	ME-MS81	0.5	412
Be_ppm	ME-MS42	0.05	<0.05	<0.05	Be_ppm	ME-MS42	0.05	<0.05
Bi_ppm	ME-MS42	0.01	0.01	0.23	Bi_ppm	ME-MS42	0.01	0.23
Cd_ppm	ME-4ACD81	0.5	<0.5	<0.5	Cd_ppm	ME-4ACD81	0.5	<0.5
Cd_ppm	ME-MS42	0.01	0.05	0.06	Cd_ppm	ME-MS42	0.01	0.06
Ce_ppm	ME-MS42	0.02	0.05	0.09	Ce_ppm	ME-MS42	0.02	0.09
Ce_ppm	ME-MS81	0.1	0.8	1.5	Ce_ppm	ME-MS81	0.1	1.5
Co_ppm	ME-4ACD81	1	<1	<1	Co_ppm	ME-4ACD81	1	<1
Co_ppm	ME-MS42	0.1	0.1	1.3	Co_ppm	ME-MS42	0.1	1.3
Cr_ppm	ME-MS81	10	10	10	Cr_ppm	ME-MS81	10	10
Cs_ppm	ME-MS42	0.05	<0.05	<0.05	Cs_ppm	ME-MS42	0.05	<0.05
Cs_ppm	ME-MS81	0.01	0.03	0.01	Cs_ppm	ME-MS81	0.01	0.01
Cu_ppm	ME-4ACD81	1	3	6	Cu_ppm	ME-4ACD81	1	6
Cu_ppm	ME-MS42	0.2	5.5	3.1	Cu_ppm	ME-MS42	0.2	3.1
Dy_ppm	ME-MS81	0.05	0.06	0.1	Dy_ppm	ME-MS81	0.05	0.1
Er_ppm	ME-MS81	0.03	0.03	0.05	Er_ppm	ME-MS81	0.03	0.05
Eu_ppm	ME-MS81	0.03	<0.03	<0.03	Eu_ppm	ME-MS81	0.03	<0.03
Ga_ppm	ME-MS42	0.05	2.08	1.5	Ga_ppm	ME-MS42	0.05	1.5
Ga_ppm	ME-MS81	0.01	2.2	2	Ga_ppm	ME-MS81	0.01	2
Gd_ppm	ME-MS81	0.05	<0.05	0.12	Gd_ppm	ME-MS81	0.05	0.12
Hf_ppm	ME-MS42	0.02	0.05	0.05	Hf_ppm	ME-MS42	0.02	0.05
Hf_ppm	ME-MS81	0.2	0.2	<0.2	Hf_ppm	ME-MS81	0.2	<0.2
Hg_ppm	ME-MS42	0.005	0.006	<0.005	Hg_ppm	ME-MS42	0.005	<0.005
Ho_ppm	ME-MS81	0.01	0.01	0.02	Ho_ppm	ME-MS81	0.01	0.02
In_ppm	ME-MS42	0.005	<0.005	0.013	In_ppm	ME-MS42	0.005	0.013
La_ppm	ME-MS42	0.2	<0.2	<0.2	La_ppm	ME-MS42	0.2	<0.2
La_ppm	ME-MS81	0.1	1.4	2.6	La_ppm	ME-MS81	0.1	2.6
Li_ppm	ME-4ACD81	10	<10	10	Li_ppm	ME-4ACD81	10	10
Li_ppm	ME-MS42	0.1	0.1	3.2	Li_ppm	ME-MS42	0.1	3.2
Lu_ppm	ME-MS81	0.01	<0.01	<0.01	Lu_ppm	ME-MS81	0.01	<0.01
Mo_ppm	ME-4ACD81	1	22	23	Mo_ppm	ME-4ACD81	1	23
Mo_ppm	ME-MS42	0.05	6.47	12.4	Mo_ppm	ME-MS42	0.05	12.4
Nb_ppm	ME-MS42	0.05	0.12	0.17	Nb_ppm	ME-MS42	0.05	0.17
Nb_ppm	ME-MS81	0.2	1.6	1.4	Nb_ppm	ME-MS81	0.2	1.4
Nd_ppm	ME-MS81	0.1	0.4	0.7	Nd_ppm	ME-MS81	0.1	0.7
Ni_ppm	ME-4ACD81	1	<1	<1	Ni_ppm	ME-4ACD81	1	<1
Ni_ppm	ME-MS42	0.2	12.6	1.4	Ni_ppm	ME-MS42	0.2	1.4
Pr_ppm	ME-MS81	0.03	0.11	0.2	Pr_ppm	ME-MS81	0.03	0.2
Pb_ppm	ME-4ACD81	2	87	45	Pb_ppm	ME-4ACD81	2	45
Pb_ppm	ME-MS42	0.2	86.1	37.5	Pb_ppm	ME-MS42	0.2	37.5
Rb_ppm	ME-MS42	0.1	0.1	0.3	Rb_ppm	ME-MS42	0.1	0.3
Rb_ppm	ME-MS81	0.2	0.9	0.7	Rb_ppm	ME-MS81	0.2	0.7
Re_ppm	ME-MS42	0.001	0.023	<0.001	Re_ppm	ME-MS42	0.001	<0.001
Sb_ppm	ME-MS42	0.05	1.51	0.81	Sb_ppm	ME-MS42	0.05	0.81
Sc_ppm	ME-4ACD81	1	<1	<1	Sc_ppm	ME-4ACD81	1	<1
Sc_ppm	ME-MS42	0.1	0.1	<0.1	Sc_ppm	ME-MS42	0.1	<0.1
Se_ppm	ME-MS42	0.2	0.7	<0.2	Se_ppm	ME-MS42	0.2	<0.2
Sm_ppm	ME-MS81	0.03	0.1	0.11	Sm_ppm	ME-MS81	0.03	0.11
Sn_ppm	ME-MS42	0.2	5.3	4	Sn_ppm	ME-MS42	0.2	4
Sn_ppm	ME-MS81	1	6	5	Sn_ppm	ME-MS81	1	5
Sr_ppm	ME-MS42	0.2	0.5	6.4	Sr_ppm	ME-MS42	0.2	6.4
Sr_ppm	ME-MS81	0.1	9.4	8.6	Sr_ppm	ME-MS81	0.1	8.6
Ta_ppm	ME-MS42	0.01	<0.01	<0.01	Ta_ppm	ME-MS42	0.01	<0.01
Ta_ppm	ME-MS81	0.1	<0.1	<0.1	Ta_ppm	ME-MS81	0.1	<0.1
Tb_ppm	ME-MS81	0.01	<0.01	0.01	Tb_ppm	ME-MS81	0.01	0.01
Te_ppm	ME-MS42	0.01	0.03	0.01	Te_ppm	ME-MS42	0.01	0.01
Th_ppm	ME-MS42	0.2	<0.2	<0.2	Th_ppm	ME-MS42	0.2	<0.2
Th_ppm	ME-MS81	0.05	0.06	0.07	Th_ppm	ME-MS81	0.05	0.07
Tl_ppm	ME-4ACD81	10	<10	<10	Tl_ppm	ME-4ACD81	10	<10
Tl_ppm	ME-MS42	0.02	0.03	<0.02	Tl_ppm	ME-MS42	0.02	<0.02
Tm_ppm	ME-MS81	0.01	<0.01	<0.01	Tm_ppm	ME-MS81	0.01	<0.01
U_ppm	ME-MS42	0.05	<0.05	<0.05	U_ppm	ME-MS42	0.05	<0.05
U_ppm	ME-MS81	0.05	<0.05	0.06	U_ppm	ME-MS81	0.05	0.06
V_ppm	ME-MS81	5	86	101	V_ppm	ME-MS81	5	101
W_ppm	ME-MS42	0.05	<0.05	<0.05	W_ppm	ME-MS42	0.05	<0.05
W_ppm	ME-MS81	1	1	1	W_ppm	ME-MS81	1	1
Y_ppm	ME-MS42	0.05	<0.05	<0.05	Y_ppm	ME-MS42	0.05	<0.05
Y_ppm	ME-MS81	0.1	0.4	0.7	Y_ppm	ME-MS81	0.1	0.7
Yb_ppm	ME-MS81	0.03	<0.03	<0.03	Yb_ppm	ME-MS81	0.03	<0.03
Zn_ppm	ME-4ACD81	2	403	324	Zn_ppm	ME-4ACD81	2	324
Zr_ppm	ME-MS42	0.5	2.4	2.2	Zr_ppm	ME-MS42	0.5	2.2
Zr_ppm	ME-MS81	2	7	7	Zr_ppm	ME-MS81	2	7

It is important to note that the original lithogeochemical analysis for Campaign 3 calcined iron oxide precipitate sample (1802-T7C/ML-76) using ALS Laboratories analytical method ME-ICP06 resulted in low major element oxide analytical totals (66.70%). Discussions with ALS Laboratory personnel indicated that accurate analysis of such pure materials would be better achieved using ALS analytical method ME-XRF06. Reanalysis of the Campaign 3 calcined iron oxide precipitate sample using ALS analytical method ME-XRF06 was conducted, and the analytical total for the major element oxides for this sample improved to 99.98%.

Relative results for the non-calcined (1802-T7NC/ML-75) and calcined (1802-T7C/ML-76) Campaign 3 iron oxide precipitates in terms of major element oxide compositions (weight percentages) are described below:

- SiO_2: Higher in the non-calcined sample (0.95%) versus the calcined sample (0.89%)
- Al_2O_3: Equivalent in the non-calcined and calcined samples (0.08%)
- Fe_2O_3: Higher in the calcined sample (96.82%) versus the non-calcined sample (89.30%)
- CaO: Equivalent in the non-calcined and calcined samples (0.02%)
- MgO: Higher in the calcined sample (0.04%) versus the non-calcined sample (<0.01%)
- Na_2O: Higher in the non-calcined sample (0.10%) than in the calcined sample (0.06%)
- K_2O: Equivalent in the non-calcined and calcined samples (0.03%)
- Cr_2O_3: Below 0.002% in the non-calcined sample; below 0.01% in the calcined sample
- TiO_2: Equivalent in the non-calcined and calcined samples (1.76%)
- MnO: Below 0.01% in both the non-calcined and calcined samples
- P_2O_5: Higher in the calcined sample (0.011%) than the non-calcined sample (<0.01%)
- SrO: Below 0.01% in both the non-calcined and calcined samples
- BaO: Higher in the calcined sample (0.07%) than in the non-calcined sample (0.05%)
- LOI: Higher in the non-calcined sample (5.72%) versus the calcined sample (0.20%)
- Sulfur: Higher in the non-calcined sample (0.05%) versus the calcined sample (0.01%)

Relative results for selected trace elements in the Campaign 3 non-calcined (1802-T7NC/ML-75) and calcined (1805-T7C/ML-76) iron oxide precipitates are described below:

- As: Higher in the calcined sample (41 ppm) versus the non-calcined sample (37 ppm) using the four-acid digestion method (Method ME-4ACD81). Analysis using mass spectrometry Method ME-MS-42 indicated a higher concentration in the calcined sample (6.7 ppm) relative to the non-calcined sample (0.6 ppm)
- Co: Equivalent values of <1ppm for both the non-calcined and calcined samples using the four-acid digestion method (Method ME-4ACD81). Higher in the calcined sample (1.3 ppm) relative to the non-calcined sample (0.1 ppm) using mass spectrometry method ME-MS42
- Cr: Equivalent values of 10ppm in both the non-calcined and calcined samples using mass spectrometry method ME-MS81
- Cu: Higher in the calcined sample (6 ppm) versus the non-calcined sample (3 ppm) using the four-acid digestion method (Method ME-4ACD81). Higher in the non-calcined sample (5.5 ppm) versus the calcined sample (3.1 ppm) using mass spectrometry method ME-MS42

- Nb: Higher in the calcined (0.17 ppm) than in the non-calcined sample (0.12 ppm) using mass spectrometry method ME-MS42. Higher in the non-calcined sample (1.6 ppm) versus the calcined sample (1.4 ppm) using mass spectrometry method ME-MS81
- Ni: Equivalent values of <1 ppm in both the non-calcined and calcined samples using the four-acid digestion method (Method ME-4ACD81). Higher in the non-calcined sample (12.6 ppm) versus the calcined sample (1.4 ppm) using mass spectrometry method ME-MS42
- Pb: Higher in the non-calcined sample (87 ppm) than the calcined sample (45 ppm) using the four-acid digestion method (Method ME-4ACD81). Higher in the non-calcined sample (86.1 ppm) than the calcined sample (37.5 ppm) using mass spectrometry method ME-MS42
- Sb: Higher in the non-calcined sample (1.51 ppm) versus the non-calcined sample (0.81 ppm) using mass spectrometry method ME-MS42
- Ta: Equivalent below detection limit values (<0.01 ppm) using mass spectrometry method ME-MS42. Equivalent below detection limit values (<0.1 ppm) values using mass spectrometry method ME-MS81
- V: Higher in the calcined sample (101 ppm) than the non-calcined sample (86 ppm) using mass spectrometry method ME-MS81

Figure 92A is a chondrite-normalized rare earth element plot for both the non-calcined and calcined Campaign 3 iron oxide precipitates. Note that the light rare earth elements (La, Ce, Pr, Nd) are slightly enriched (up to approximately 10 times) relative to chondritic values, with the calcined sample being slightly enriched in these elements relative to the non-calcined sample. All other rare earth elements have values less than chondritic values with the calcined sample values being generally slightly higher than, or equal to, the calcined sample values.

Figure 92B is a primitive mantle-normalized spider diagram showing selected trace element concentrations in the Campaign 3 iron oxide precipitates. Relative to primitive mantle values (Sun and McDonough, 1989; Kerrich and Wyman, 1996), the Campaign 3 iron oxide precipitates are slightly enriched (less than 10 times primitive mantle values) in Nb (approximately 1–2 times primitive mantle value), La (approximately 1–3 times primitive mantle value), and titanium (up to eight times primitive mantle value), with the non-calcined sample having a higher concentration than the calcined sample for the element niobium, the calcined sample having a slightly higher concentration than the non-calcined sample for the element lanthanum, and both the non-calcined and calcined samples having the same value for the element titanium.

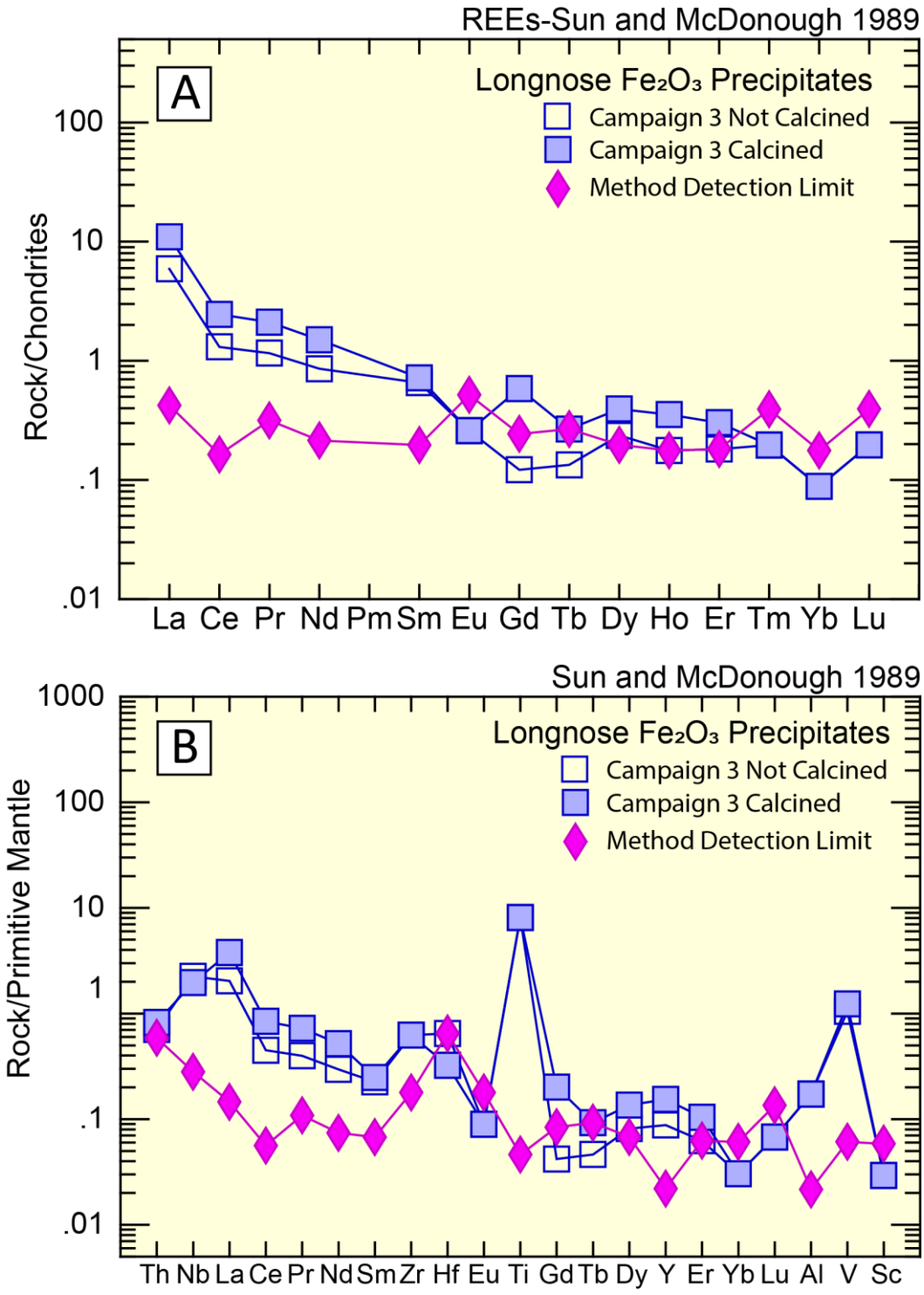

Figure 92. Chondrite- and primitive mantle-normalized spider diagrams for Campaign 3 iron oxide precipitates. A) Chondrite-normalized rare earth element diagram. Note enrichment relative to chondritic values (Sun and McDonough, 1989) for the elements lanthanum, cerium, and praseodymium. B) Primitive mantle-normalized spider diagram for Campaign 3 iron oxide precipitates. Niobium, lanthanum, and titanium are enriched relative to primitive mantle normalizing values (Sun and McDonough, 1989; Kerrich and Wyman, 1996). For the purposes of plotting, all analyses below the detection limit have been set to one-half the value of the detection limit.

Summary

Hydro-hydrolysis bench scale testing continued in this Campaign to examine parameters for regeneration of HCl and production of Fe_2O_3. A high-purity Fe_2O_3 product was produced.

- Fe_2O_3 precipitates were produced from the pregnant strip liquors produced from the operation of the MPP.
- Non-calcined Fe_2O_3 precipitates produced in Campaign 2 and Campaign 3 had purities of 86.20% Fe_2O_3 and 91.10% Fe_2O_3 based on NRRI lithogeochemical analyses and on Fe_2O_3/Total ratios.
- A high-purity calcined Fe_2O_3 precipitate was produced in Campaigns 2 and 3. PRO analyses of Campaign 2 and Campaign 3 calcined Fe_2O_3 precipitates indicate a purity of 98.60% in Campaign 2 and 96.72% in Campaign 3. NRRI lithogeochemical analysis of the calcined Fe_2O_3 precipitates indicates a purity of 98.49% Fe_2O_3 for Campaign 2 and 96.84% Fe_2O_3 in Campaign 3 based on Fe_2O_3/Total ratios in the analyses (Fig. 93).
- Four different phases were identified in the non-calcined iron oxide precipitate from Campaign 2. These include: 1) hematite; 2) hematite containing greater than 0.5 weight percent TiO_2 (titanohematite solid solution); 3) a magnesium- and chlorine-bearing unknown phase; and 4) an iron- and chlorine-bearing unknown phase.
- Two different phases were identified in the calcined iron-oxide precipitate from Campaign 2. These include: 1) hematite; and 2) an SiO_2-Al_2O_3-FeO-bearing unknown.
- Hematite, an iron-oxide precipitate containing greater than 0.5% (weight percent) TiO_2, and an iron- and titanium-bearing unknown (titanohematite?), were identified in the non-calcined (1802-T7NC (ML-75)) and calcined (1802-T7C (ML-76)) iron oxide precipitates from Campaign 3.

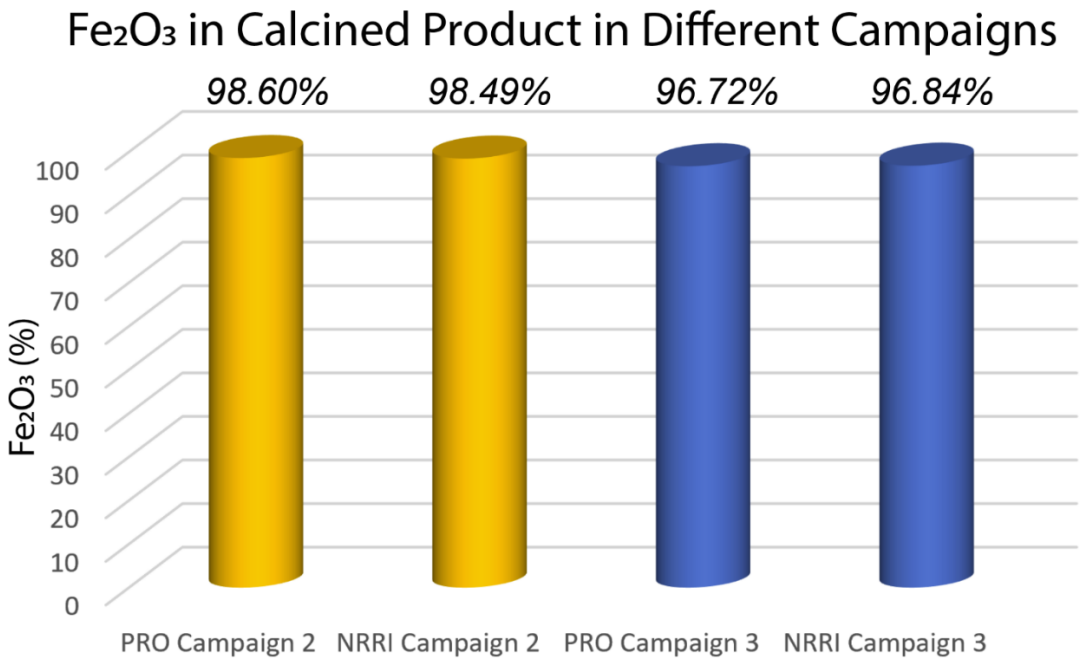

Figure 93. Comparison of PRO and NRRI analyses of calcined Campaign 2 and Campaign 3 iron oxide precipitates.

Operation Summary

Over the three MPP campaigns, the effect of integrated operation was studied along with the effect of impurity buildup. The overall leach recovery for each campaign was similar, as shown in Table 77. There was some decrease in the recovery at the end of Campaign 3, and this was due to segregation of the feed material *with coarser material being processed*. With the results of leaching for select tests in Campaign 3 as shown in Table 78, Ti efficiency in bulk leach number 19 and 20 were between 61% and 71%. In order to demonstrate the ability to achieve a higher efficiency, tests were performed where the residues were ground to 90% < 38 µm and re-leached. As it is shown in Table 81, the total recovery of titanium can be increased to around 89%–91%.

Table 77. Average leaching recovery over the three campaigns.

Campaign Average	# Batches	Recovery % (Material balance)		Recovery % (Res/Head)	
		Fe	Ti	Fe	Ti
Campaign 1	3	75.6	69.7	75.1	69.4
Campaign 2	7	76.9	71.2	76.0	71.1
Campaign 3	5	79.5	71.9	77.0	69.1

Table 78. Leach recovery versus particle size.

Leaching #	Efficiency Material balance %	
	Fe	Ti
BL19 (73% < 38 µm)	79.30	**70.41**
BL19 ground Residue leach (90% < 38 µm)	90.77	64.29
Total efficiency	98	**89.43**
BL20 (66% < 38 µm)	75.05	**61.87**
BL20 ground Residue leach (90% < 38 µm)	87.98	77.76
Total efficiency	97.01	**91.51**

As it is shown in Figure 76 and Figure 93 for TiO_2 and Fe_2O_3, respectively, the quality of final products in Campaigns 2 and 3 are similar, and the recycling did not affect the quality of the final products. A TiO_2 product with an average purity of ~99.25% (NRRI analyses) or ~99.54% (PRO analyses) ~TiO_2 was produced from both Campaigns 2 and 3 (refer to Fig. 75). An average Fe_2O_3 product of >97% Fe_2O_3 (NRRI average analysis of 97.67% Fe_2O_3, PRO average analysis of 97.66% Fe_2O_3) was produced from Campaigns 2 and 3, although the Campaign 3 Fe_2O_3 purity is slightly lower in Campaign 3 than in Campaign 2 (average NRRI and PRO analyses for Campaign 2 and Campaign 3 Fe_2O_3 of 98.55% and 96.78%, respectively).

TAILING CHARACTERIZATION

Introduction

During the operation of the process, solid and liquid waste was produced that will require proper disposal. Waste produced includes the tailings from the leaching process, a bleed stream from titanium raffinate recycling, and wash solutions produced from the precipitation process.

Analysis of Campaign 1 (no recycling), Campaign 2 (half-recycled), and Campaign 3 (recycled and reground, two-stage leach) leach residues were conducted to characterize the respective leach residues with respect to their mineral, mineral chemical, and lithogeochemical characteristics. Leach residues samples include (also refer to Table 2):

- Sample 1802-BL-10 (ML-71), which comprises Campaign 1 leach residue that has undergone no recycling with $MgCl_2$ solution (titanium raffinate)
- Sample 1802-BL-6 (ML-70), which comprises Campaign 2 leach residue that was half-recycled with $MgCl_2$ solution (titanium raffinate)
- Sample 1802-BL-19 (ML-72), which comprises Campaign 3 leach residue that has undergone recycling after a single-stage leach with $MgCl_2$ solution (titanium raffinate)
- Sample 1802-L19R (ML-77), which comprises Campaign 3 leach residues that have been re-ground to 90% passing 400 mesh (38 µm) and have been subjected to a two-stage leach with $MgCl_2$ solution (titanium raffinate)
- Sample 1802-L20R (ML-87), which comprises Campaign 3 leach residues that have been re-ground to 90% passing 400 mesh (38 µm) and have been subjected to a two-stage leach with $MgCl_2$ solution (titanium raffinate).

Mineralogical Analysis

Mineralogical analyses of Campaign 1, Campaign 2, and Campaign 3 leach samples were performed using X-ray diffraction analysis (refer to Table 8). Minerals identified in the Campaign 2 leach residues include:

- Sample 1802-BL-10 (ML-71) – Campaign 1, no recycling: ilmenite, zircon, hornblende
- Sample 1802-BL-6 (ML-70) – Campaign 2, half-recycled: ilmenite, augite, zircon
- Sample 1802-BL-19 (ML-72) – Campaign 3, fully-recycled: ilmenite, zircon, hornblende

Minerals identified in the Campaign 3 ground and two-stage leach residues include:

- Sample 1802-L19R (ML-77) - ilmenite, rutile, clinochlore, hornblende, and zircon
- Sample 1802-L20R (ML-78) - ilmenite, rutile, zircon, and hornblende

Mineral Chemical Analysis (EMPA)

Three samples of single-stage leach residues underwent mineral chemical analysis at the Electron Probe Microanalyzer located at the EML at the UMTC. These included sample 1802-BL10-1 (ML-71, no recycling), sample 1802-BL-6 (ML-70, half-recycled), and sample 1802-BL-19 (ML-72, fully recycled).

Minerals identified during electron microprobe analysis for the three single-stage leach residues are indicated in Table 79. Complete results of the electron microprobe mineral chemical analysis for single stage leach residues are included in Appendix 4: Table A4-14 Table A4-19.

Table 79. Minerals identified during electron microprobe analysis of Campaign 2 leach residues.

Mineral Species	1802-BL10-1 (ML-71)	1802-BL-6 (ML-70)	1802-BL-19 (ML-72)
Ilmenite	X	X	X
Rutile	X		
Actinolite	X		X
Pargasite		X	
Clinochlore	X		
Sepiolite (?)			X
Augite		X	X
Quartz (?)	X	X	X

The sole oxide mineral identified in the single-stage leach residues was ilmenite ($FeTiO_3$). Magnetite was not identified in any of the single stage leach residues and may be the result of one of two possibilities: 1) random sampling of minerals during electron microprobe analysis may have inadvertently excluded magnetite grains present in the samples; or 2) during hydrometallurgical processing, magnetite grains were broken down and leached more effectively than ilmenite grains. More analysis is needed to better constrain which of these two possibilities is correct.

Figure 94 is a series of backscatter images obtained during EMPA analysis of the three leach residue samples from Campaigns 1 through 3 described above. Figure 94A shows the nature of sample 1802-BL10-1 (ML-71), which comprises Campaign 1 leach residue that has not been recycled. Both individual mineral particles and large aggregates of particles can be observed. The large, rounded aggregates of particles are believed to be agglomerates of the leachate produced during preparation of the epoxy puck sample utilized during EMPA analysis. Rounded agglomerates range from 40 µm to >400 µm in diameter, and elongate agglomerates vary from ~130 µm to ~300 µm in length and <100 µm to 150 µm in width. Note the presence of the oxide mineral phase ilmenite as well as the silicate (amphibole-group) minerals actinolite (standard chemical formula $Ca_2(Mg,Fe)_5Si_8O_{22}(OH)_2$) and pargasite ($NaCa_2(Mg,Fe)_4Al(Si_6Al_2)O_{22}(OH)_2$) (Nickel and Nichols, 1991)). Note that pargasite has a chemical formula similar to hornblende (standard chemical formula $(Ca,Na)_{2\text{-}3}(Mg,Fe,Al)_5Si_6(Si,Al)_2O_{22}(OH)_2$ (Klein and Hurlbut, 1999)). Both actinolite and pargasite may form from the hydration of clinopyroxenes such as augite (Phillips and Griffen, 1981). Amphibole species identified during EMPA analysis were classified according to Leake et al. (2007) using the spreadsheet AMPHNAME.xls (Gabbrosoft.com).

Figures 94B and 94C are backscatter images obtained during EMPA analysis of sample 1802-BL-6 (ML-70), which is made up of Campaign 2 leach residue that has been half-recycled. As in the previous sample, both individual mineral particles and rounded to elongate agglomerates are present. Individual elongate mineral particles are up to about 60 µm in length and 20 µm–30 µm in width; more equant mineral particles are up to approximately 40 µm in diameter. Agglomerates are up to 220 µm in length and up to 130 µm in width. Figure 94C is a close-up of the agglomerates that occurs near the left margin of Figure 94B. Note the presence of ilmenite, augite, and possibly quartz (quartz?) in both figures.

Figures 94D and 94E are backscatter images obtained during EMPA analysis of sample 1802-BL-19 (ML-72), which is composed of Campaign 3 leach residues that have been recycled. The sample is composed primarily of individual equant mineral fragments that range from <10 µm to 60 µm in diameter and elongate, splinter-like particles that range from <10 µm to 60 µm in length and <10 µm to 40 µm in width. Locally, pseudofragments are present and can be up to 400 µm in length and 100 µm in width (see pseudofragment in lower right part of Fig. 94E). Minerals identified in Figures 94D and 94E include ilmenite, actinolite, and possibly quartz.

Mineral chemical analyses of ilmenites from sample 1802-BL10-1 (ML-71, Campaign 1) are shown in Table 80. The ilmenite grains in this sample occur as angular, blocky to elongate broken grains that range from <10 µm to ~40 µm in diameter (Fig. 94A). Locally, dark-colored, lens-shaped parallel zones ranging from a few microns in length and < 1 µm in width may represent areas of hematite or titanohematite that were leached during hydrometallurgical processing. The composition of the ilmenite is primarily TiO_2 (49.117%–51.814%) and FeO (42.554%–44.111%) and MgO (3.108%–3.528%), with lesser amounts of MnO (0.352%–0.507%), V_2O_3 (0.076%–0.384%), SiO_2 (0.026%–0.100%), Cr_2O_3 (0.007%–0.064%), Al_2O_3 (0.000%–0.067%), NiO (0.000%–0.057%), and chlorine (0.000%–0.028%). Analytical totals for ilmenites from this sample ranged from 96.305% to 99.010%.

Mineral chemical analyses of ilmenites from sample 1802-BL6 (ML-70, Campaign 2) are shown in Table 81. Ilmenite in this sample also occurs as angular, blocky to elongate broken grains that range from <10 µm to ~50 µm in diameter. Locally, dark-colored, lens-shaped parallel zones ranging from 2 µm to 3 µm in length and <1 µm in width may represent areas of hematite or titanohematite solid solution that were leached during hydrometallurgical processing (Figs. 98B and 98C). The ilmenite is composed mainly of TiO_2 (49.150%–50.974%), FeO (42.300%–45.015%), and MgO 2.935%–3.822%), with lesser MnO (0.345%–0.619%), V_2O_3 (0.239%–0.403%), Al_2O_3 (0.017%–0.053%), Cr_2O_3 (0.013%–0.066%), NiO (0.012%–0.096%), SiO_2 (0.003%–0.143%), and chlorine (0.000%–0.009%). Analytical totals for ilmenites from this sample ranged from 96.408% to 98.533%.

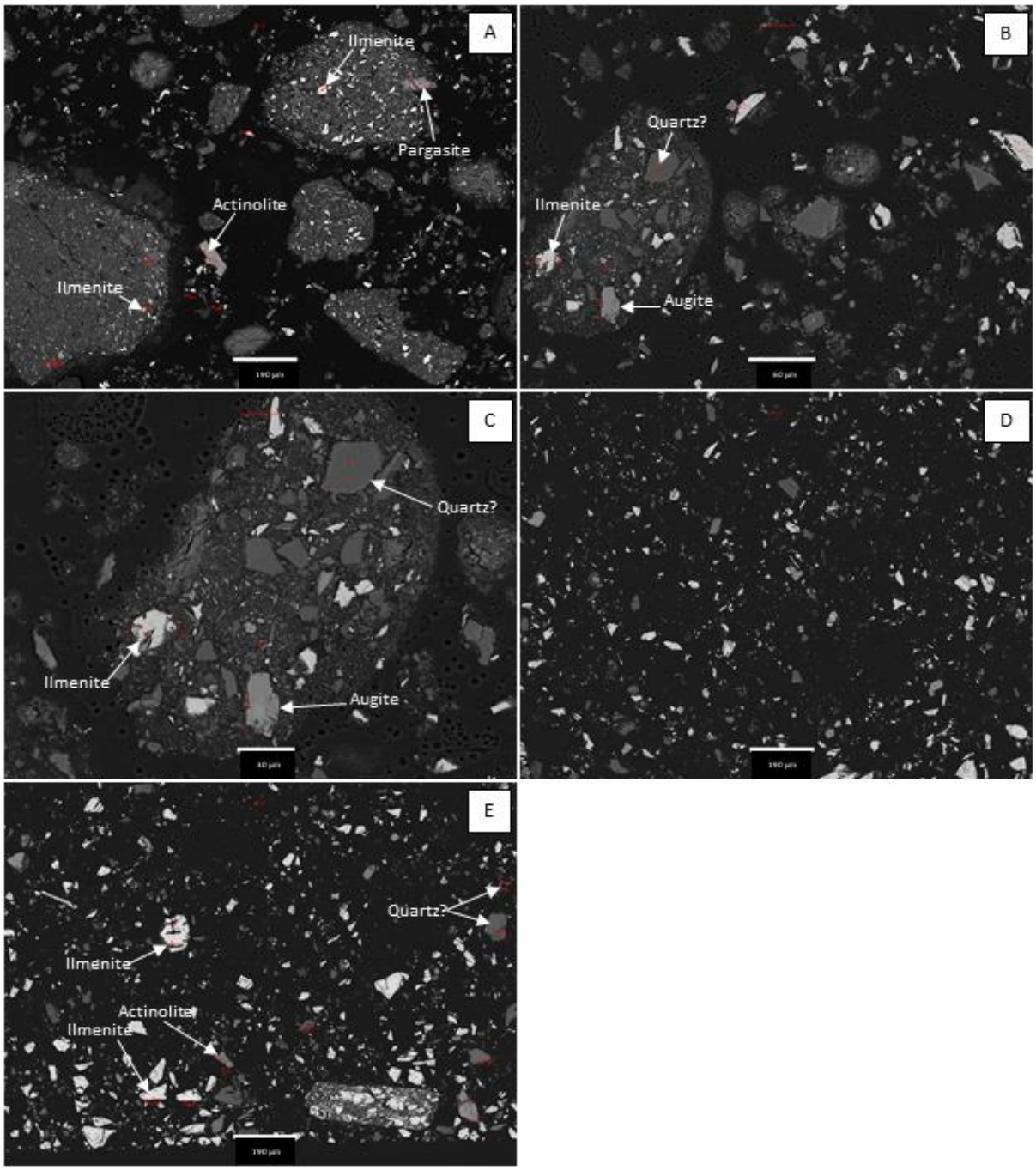

Figure 94. Electron microprobe backscatter images of Campaign 1, Campaign 2, and Campaign 3 leach residue samples. A) Sample 1802-BL10-1 (ML-71), which represents Campaign 1 leach residue that has not been recycled. The mineral phases ilmenite, actinolite, and pargasite are indicated. Scale bar is 190 µm. B) and C) Sample 1802-BL-6 (ML-70), which represents Campaign 2 leach residues that have been half-recycled. Note the presence of ilmenite, augite, and possibly quartz in the leach residue. Scale bars are 60 µm and 30 µm in Figures 94B and 94C, respectively. D) Sample 1802-BL-19 (ML-72), which represents Campaign 3 single stage recycled residues, showing the size ranges of the particles in the leach residue. Scale bar is 190 µm. E) Sample 1802-BL-19 (ML-72), Campaign 3 single-stage leach residues after recycling. Mineral phases present include ilmenite, actinolite, and possibly quartz. Red numbers and circles are analysis locations. Scale bar is 190 µm. Red numbers and circles in images are analysis locations.

Table 80. Electron microprobe analyses of ilmenite from sample 1802-BL10-1 (ML-71). Values are in weight percentages.

Electron Microprobe Analysis – Sample 1802-BL-10-1 (ML-71) - Leach Residue Ilmenite (n = 8)													
Sample	Description	Phase	SiO_2	TiO_2	Al_2O_3	FeO	MnO	MgO	V_2O_3	Cr_2O_3	NiO	Cl	Total
ML-71-31-119-1	Angular Chip	Ilmenite	0.042	49.140	0.067	43.331	0.379	3.310	0.376	0.064	0.057	0.000	96.766
ML-71-31-120-2	Angular Chip	Ilmenite	0.044	49.117	0.039	43.070	0.470	3.201	0.384	0.051	0.017	0.000	96.393
ML-71-31-121-3	Angular Chip	Ilmenite	0.034	49.141	0.035	43.017	0.352	3.305	0.360	0.033	0.000	0.028	96.305
ML-71-32-122-1	Angular Chip	Ilmenite	0.050	50.327	0.066	43.293	0.463	3.525	0.192	0.046	0.029	0.000	97.990
ML-71-32-124-3	Angular Chip	Ilmenite	0.026	50.125	0.017	42.854	0.460	3.528	0.215	0.026	0.035	0.000	97.285
ML-71-33-125-1	Blocky Chip	Ilmenite	0.044	51.020	0.033	43.961	0.463	3.179	0.090	0.007	0.002	0.000	98.799
ML-71-33-126-2	Blocky Chip	Ilmenite	0.073	51.036	0.037	44.111	0.477	3.108	0.138	0.013	0.018	0.000	99.010
ML-71-33-217-3	Blocky Chip	Ilmenite	0.100	51.814	0.000	42.924	0.507	3.194	0.076	0.020	0.012	0.000	98.649
		Minimum	***0.026***	***49.117***	***0.000***	***42.854***	***0.352***	***3.108***	***0.076***	***0.007***	***0.000***	***0.000***	***96.305***
		Maximum	***0.100***	***51.814***	***0.067***	***44.111***	***0.507***	***3.528***	***0.384***	***0.064***	***0.057***	***0.028***	***99.010***
		Average	***0.052***	***50.215***	***0.037***	***43.320***	***0.446***	***3.294***	***0.229***	***0.033***	***0.021***	***0.004***	***97.650***
		Median	***0.044***	***50.226***	***0.036***	***43.182***	***0.463***	***3.253***	***0.204***	***0.030***	***0.018***	***0.000***	***97.638***
		St.Deviation	***0.022***	***0.963***	***0.021***	***0.442***	***0.049***	***0.148***	***0.120***	***0.019***	***0.018***	***0.009***	***1.036***

Table 81. Electron microprobe analyses of ilmenite from sample 1802-BL6 (ML-70). Values are in weight percentages.

Electron Microprobe Analysis – Sample 1802-BL-6 (ML70) - Leach Residue Ilmenite (n = 8)													
Sample	Description	Phase	SiO_2	TiO_2	Al_2O_3	FeO	MnO	MgO	V_2O_3	Cr_2O_3	NiO	Cl	Total
ML-70-16-76-1	Elongate Chip	Ilmenite	0.016	49.178	0.041	45.015	0.415	3.031	0.239	0.013	0.012	0.000	97.961
ML-70-16-77-2	Elongate Chip	Ilmenite	0.008	49.204	0.053	44.792	0.345	2.955	0.270	0.021	0.035	0.000	97.681
ML-70-16-78-3	Elongate Chip	Ilmenite	0.033	49.154	0.027	44.823	0.395	2.935	0.275	0.042	0.054	0.000	97.738
ML-70-17-79-1	Elongate Chip	Ilmenite	0.011	50.541	0.017	43.561	0.388	3.579	0.305	0.064	0.068	0.000	98.533
ML-70-17-81-3	Elongate Chip	Ilmenite	0.003	50.974	0.045	42.844	0.378	3.556	0.336	0.056	0.021	0.000	98.213
ML-70-18-82-1	Toothlike-Fragment	Ilmenite	0.042	49.527	0.045	43.253	0.379	3.629	0.403	0.049	0.086	0.000	97.413
ML-70-18-83-2	Toothlike-Fragment	Ilmenite	0.049	49.416	0.044	43.042	0.559	3.822	0.389	0.058	0.096	0.000	97.475
ML-70-18-84-3	Toothlike-Fragment	Ilmenite	0.143	49.150	0.032	42.300	0.619	3.637	0.402	0.066	0.051	0.009	96.408
		Minimum	***0.003***	***49.150***	***0.017***	***42.300***	***0.345***	***2.935***	***0.239***	***0.013***	***0.012***	***0.000***	***96.408***
		Maximum	***0.143***	***50.974***	***0.053***	***45.015***	***0.619***	***3.822***	***0.403***	***0.066***	***0.096***	***0.009***	***98.533***
		Average	***0.038***	***49.643***	***0.038***	***43.704***	***0.435***	***3.393***	***0.327***	***0.046***	***0.053***	***0.001***	***97.678***
		Median	***0.025***	***49.310***	***0.043***	***43.407***	***0.392***	***3.568***	***0.321***	***0.053***	***0.053***	***0.000***	***97.710***
		St.Deviation	***0.043***	***0.665***	***0.011***	***0.970***	***0.092***	***0.334***	***0.061***	***0.018***	***0.028***	***0.003***	***0.594***

Mineral chemical analyses of ilmenites (in weight percentages) from sample 1802-BL19 (ML-72, Campaign 3) are shown in Table 82. Ilmenite occurs as equant, locally polygonal grains ranging from approximately 40 µm to 100 µm in diameter as well as broken, elongate grains ranging in length from <10 µm to 110 µm and in width from <5 µm to 60 µm (Figs. 94D and 94E). As seen in the previous samples, local dark-colored, lens-shaped parallel zones ranging up to 10 µm in length and a few micrometers in width may represent areas of hematite or titanohematite that were leached during hydrometallurgical processing. Ilmenites from this sample are also primarily composed of TiO_2 (49.839%–52.555%), FeO (41.346%–45.614%), and MgO (2.640%–4.178%), with lesser amounts of MnO (0.369%–0.530%), V_2O_3 (0.203%–0.340%), NiO (0.019%–0.080%), Al_2O_3 (0.016%–0.036%), Cr_2O_3 (0.013%–0.088%), and SiO_2 (0.000%–0.019%). Chlorine was not identified in the mineral chemical

analyses of ilmenites from this sample. Analytical totals for ilmenites from sample 1802-BL19 (ML-72) ranged from 96.408% to 98.533%.

Table 82. Electron microprobe analyses of ilmenite from sample 1802-BL19 (ML-72).

Electron Microprobe Analysis – Sample 1802-BL-19 (ML-72) - Leach Residue Ilmenite (n = 9)													
Sample	Description	Phase	SiO_2	TiO_2	Al_2O_3	FeO	MnO	MgO	V_2O_3	Cr_2O_3	NiO	Cl	Total
ML-72-41-149-1	Hexagaon-like Chip	Ilmenite	0.000	52.085	0.033	41.346	0.428	4.178	0.203	0.013	0.071	0.000	98.358
ML-72-41-150-2	Hexagon-like Chip	Ilmenite	0.000	52.555	0.029	41.566	0.411	4.152	0.213	0.038	0.038	0.000	99.002
ML-72-41-151-3	Hexagon-like Chip	Ilmenite	0.000	50.279	0.022	43.767	0.369	4.053	0.326	0.067	0.065	0.000	98.948
ML-72-41-152-4	Elongate Chip	Ilmenite	0.015	50.289	0.029	45.263	0.433	2.640	0.269	0.080	0.021	0.000	99.040
ML-72-41-153-5	Elongate Chip	Ilmenite	0.000	50.838	0.016	45.058	0.445	2.660	0.252	0.046	0.062	0.000	99.378
ML-72-41-154-6	Elongate Chip	Ilmenite	0.000	50.784	0.036	44.178	0.530	2.691	0.245	0.074	0.080	0.000	99.618
ML-72-42-155-1	Elongate Chip	Ilmenite	0.014	49.898	0.029	44.987	0.421	3.041	0.313	0.057	0.060	0.000	98.821
ML-72-42-156-2	Elongate Chip	Ilmenite	0.019	49.853	0.022	45.614	0.373	3.015	0.308	0.045	0.064	0.000	99.312
ML-72-42-157-3	Elongate Chip	Ilmenite	0.000	49.839	0.032	45.152	0.444	3.015	0.340	0.088	0.019	0.000	98.928
		Minimum	***0.000***	***49.839***	***0.016***	***41.346***	***0.369***	***2.640***	***0.203***	***0.013***	***0.019***	***0.000***	***98.358***
		Maximum	***0.019***	***52.555***	***0.036***	***45.614***	***0.530***	***4.178***	***0.340***	***0.088***	***0.080***	***0.000***	***99.378***
		Average	***0.005***	***50.713***	***0.028***	***44.103***	***0.428***	***3.272***	***0.274***	***0.056***	***0.053***	***0.000***	***98.934***
		Median	***0.000***	***50.289***	***0.029***	***44.987***	***0.428***	***3.015***	***0.269***	***0.057***	***0.062***	***0.000***	***98.948***
		St.Deviation	***0.008***	***0.933***	***0.006***	***1.512***	***0.044***	***0.624***	***0.047***	***0.022***	***0.021***	***0.000***	***0.298***

Figure 95 illustrates the chemical compositions of ilmenite grains in the Campaign 1, Campaign 2, and Campaign 3 leach residue samples 1802-BL-10-1 (ML-71), 1802-BL-6 (ML-70), and 1802-BL-19 (ML72), respectively. When plotted in the FeO-TiO_2-MgO or FeO-TiO_2-5MgO systems (Figs. 95A and 95B), it is clear that ilmenites from all three samples contain appreciable amounts of MgO. As well, it appears that samples 1802-BL-10-1 (ML-71) and 1802-BL-6 (ML-70) have ilmenites with similar compositions. Ilmenites from sample 1802-BL-19 (ML-72) also have similar compositions to the aforementioned samples, but the range of compositions in this sample have a broader range of MgO contents than samples 1802-BL-10-1 (ML-71) and 1802-BL-6 (ML-70). When plotted in the FeO-TiO_2-V_2O_3 and FeO-TiO_2-5V_2O_3 systems (Figs. 95C and 95D), it is clear that the ilmenites from all three samples have similar compositions (plotting near stoichiometric ilmenite) and contain minor amounts of V_2O_3. Ilmenites from sample 1802-BL-19 display the widest range of TiO_2/FeO ratios, which vary from 0.51 to 0.56. To plot the compositions in the molar Fe^{2+}-Ti^{4+}-Fe^{3}+ system (Fig. 95E), Fe^{2+} and Fe^{3+} values for the ilmenite grains were calculated using the spreadsheet ILMNCALC.xls (Gabbrosoft.com). All samples have similar compositions, plotting slightly above the titanohematite solid solution line due to the substitution of Mg^{2+} for Fe^{2+} within the crystal structure.

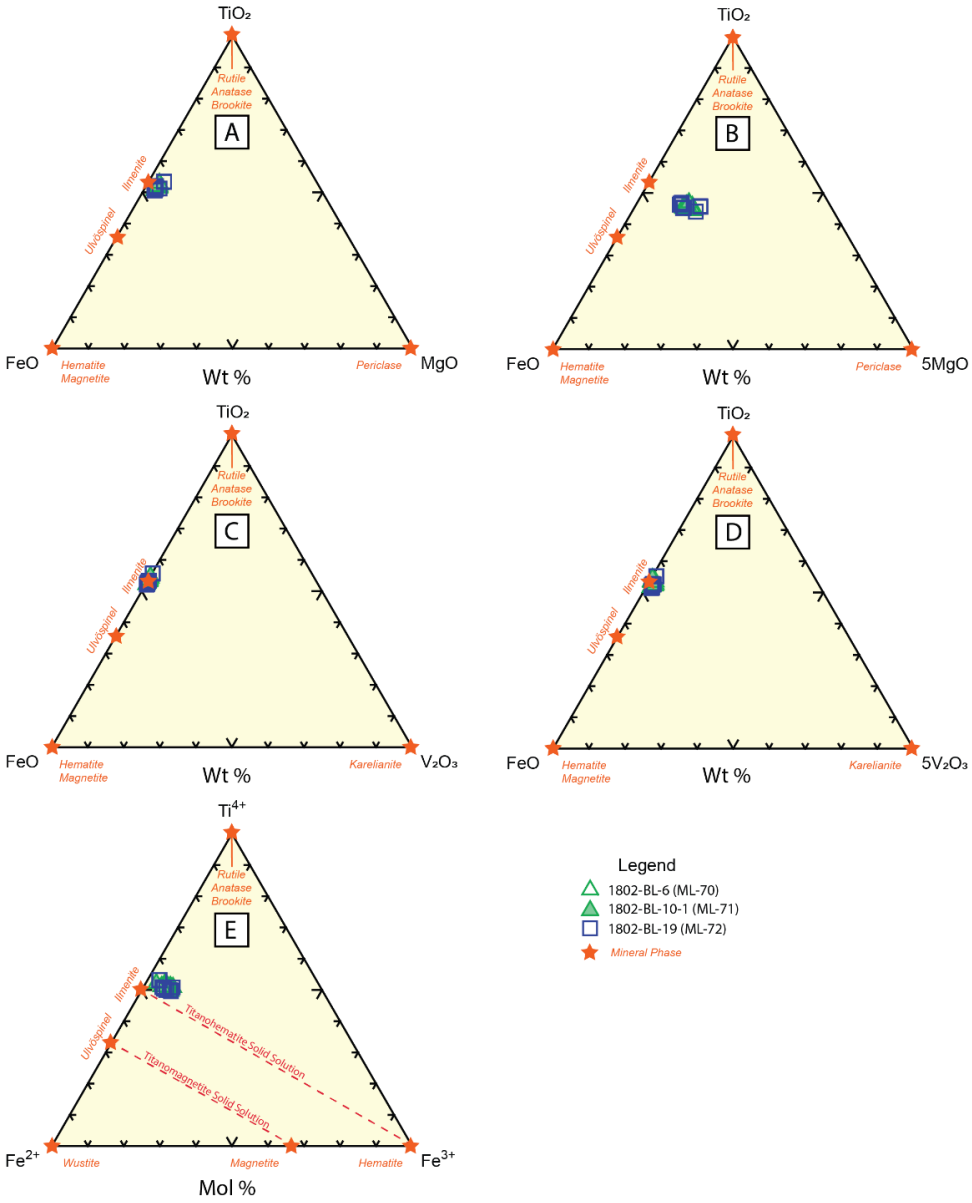

Figure 95. Ternary diagram illustrating the chemical composition of ilmenites from samples 1802-BL-10-1 (ML-71), 1802-BL-6 (ML-70), and 1802-BL-19 (ML72). These three samples represent leach residue derived from Campaign 1 that has not been recycled by $MgCl_2$ solution (titanium raffinate), leach residue derived from Campaign 2 that has been half-recycled recycled by $MgCl_2$ solution (titanium raffinate), and leach residue derived from Campaign 3 that has been recycled by $MgCl_2$ solution (titanium raffinate), respectively. Figures 95A and 95B illustrate the composition of ilmenite grains within the leach residues samples in the FeO-TiO_2-MgO and FeO-TiO_2-5MgO systems and illustrate the presence of appreciable MgO in these ilmenite grains. Figures 95C and 95D illustrate the compositions of the ilmenites in the FeO-TiO_2-V_2O_3 and FeO-TiO_2-$5V_2O_3$ systems. Note that the ilmenite grains from all three samples contain minor V_2O_3 and that ilmenite grains from sample 1802-BL-19 (ML-72) have the widest range of FeO and TiO_2 values. Figure 95E illustrates the compositions of the ilmenite grains in a molar Fe^{2+}-Ti^{4+}-Fe^{3+} ternary diagram. Ilmenite compositions in all three samples are similar and plot slightly above the titanohematite solid solution line due to substitution of Mg^{2+} for Fe^{2+} within the ilmenite crystal structure.

Two samples of Campaign 3 leach residues, which were reground to 90% passing 400 mesh (38 µm) and underwent a two-stage leach (samples 1802-L19R (ML-77) and 1802-L20R (ML-78)), were analyzed using the electron probe microanalyzer located at the EML at the UMTC. Figure 96 contains electron microprobe backscatter images of these samples. Results of electron microprobe mineral chemical analyses and stoichiometric calculations are included in Appendix 4: Tables A4-20 to A4-28.

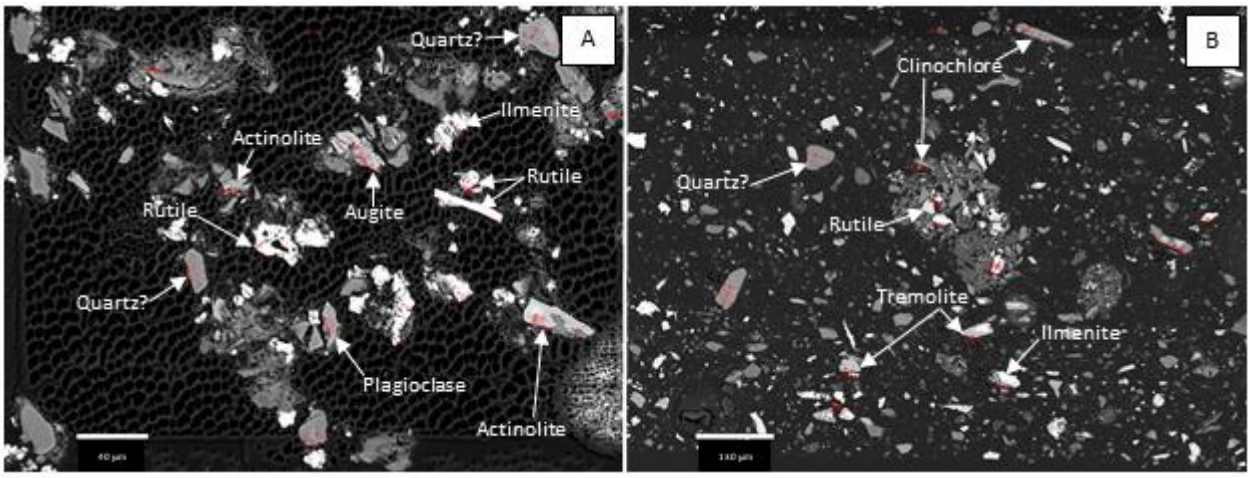

Figure 96. Ground- and two-stage leach residue samples 1802-L19R (ML-77) and 1802-L20R (ML-78) from Campaign 3. A) Sample 1802-L19R (ML-77). Note the angular fragments composed of ilmenite, rutile, actinolite, plagioclase, and possible quartz. Scale bar is 40 µm. B) Sample 1802-L20R (ML-78). Note the presence of ilmenite, rutile, tremolite, clinochlore, and possible quartz. Scale bar is 130 µm. Red numbers and circles in images are analysis locations.

Oxide mineral phases identified in the two samples include ilmenite and rutile (Table 83, Fig. 96). Ilmenite occurs as equant-to-elongate broken grains that are up to 30 µm in diameter and 10 µm–30 µm in length by 5 µm–20 µm in width. Rutile (?) occurs as blocky to elongate, often chip-like particles that are up to 25 µm in diameter or length. Magnetite was not identified during the electron microprobe analysis and may be the result of one of two possibilities: 1) random sampling of minerals during electron microprobe analysis may inadvertently have excluded magnetite grains present in the samples; or 2) during hydrometallurgical processing, magnetite grains were broken down and leached more effectively than ilmenite grains. More analysis is needed to better constrain which of these two possibilities is correct.

Table 83. Minerals identified during electron microprobe analysis of Campaign 3 two-stage leach residues.

Mineral Phase	1802-L19R (ML-77)	1802-L20R (ML-78)
Ilmenite	X	X
Rutile?	X	X
Actinolite	X	
Tremolite	X	X
Clinochlore		X
Augite	X	
Plagioclase Feldspar?	X	
Quartz?	X	X

Silicate minerals identified in the samples (Table 83, Fig. 96) include the pyroxene species augite, the amphibole species actinolite and tremolite, the chlorite species clinochlore, an unknown silicate mineral species with mineral stoichiometry similar to plagioclase feldspar (~$Na_{0.6}Ca_{0.4}Al_{1.4}Si_{2.6}O_8$: Appendix 4: Table A4-26), and an unknown SiO_2-, FeO-, MgO- and TiO_2-bearing phase with mineral stoichiometry similar to quartz (Appendix 4: Table A4-27). As well, several analyses of mineral phases originally believed to be augite or possible clay minerals yielded low analytical totals (Appendix 4: Table A4-28).

Augite occurs as columnar, locally broken grains ranging in length up to 30 µm and in width up to 15 µm. Actinolite occurs as broken, elongate particles that range from 10 µm to 40 µm in length and 5 µm to 10 µm in width. Actinolite grains are often wedge-shaped due to breaking along 60°–120° cleavages. Tremolite occurs as blocky to elongate, often wedge-shaped broken grains that range from 20 µm to 25 µm in diameter, 30 µ to 40 µm in length, and 15 µm to 20 µm in width. Chlinochlore occurs as platy, elongate mineral grains that are up to 5 µm in width and 20 µm to 35 µm in length. The silicate mineral species with stoichiometry similar to plagioclase feldspar (identified as plagioclase in Fig. 96A) occurs as elongate grains up to 25 µm in length and 5 µm to 10 µm in width. The unknown SiO_2-, FeO-, MgO- and TiO_2-bearing phase with mineral stoichiometry similar to quartz occurs as broken equant-to-elongate grains ranging from 30 µm to 40 µm in diameter, and 20 µm to 30 µm in length and 10 µm to 15 µm in width, respectively. None of the unknown SiO_2-, FeO-, MgO- and TiO_2-bearing phase display any apparent cleavage; some grains of this phase display crude conchoidal fracture.

Mineral chemical analyses of ilmenite grains identified in the Campaign 3 reground and two-stage leach residues are shown in Table 84. The compositions of the ilmenite grains (in weight percentages) are primarily composed of TiO_2 (48.077%–50.189%) and FeO (43.501%–44.569%), with lesser amounts of MgO (3.021%–3.635%), MnO (0.372%–0.567%), V_2O_3 (0.327–0.399%), NiO (0.020%–0.049%), Cr_2O_3 (0.007%–0.075%), SiO_2 (0.000%–0.067%), and Al_2O_3 (0.000%–0.021%). As well, SO_3 (0.000%–0.084%) and chlorine (0.000%–0.008%) occurred in trace amounts.

Table 84. Electron microprobe analyses of ilmenite in Campaign 3 two-stage leach residues. Values are in weight percentages.

Electron Microprobe Analysis – 2-Stage Leach Residue Ilmenite (n = 6)														
Sample	Description	Phase	SiO_2	TiO_2	Al_2O_3	FeO	MnO	MgO	V_2O_3	Cr_2O_3	NiO	SO_3	Cl	Total
ML-78-30-146-1	Ilmenite-Massive	Ilmenite	0.032	49.946	0.004	43.734	0.481	3.037	0.327	0.007	0.037	0.000	0.000	97.606
ML-78-30-147-2	Ilmenite-Massive	Ilmenite	0.034	49.571	0.015	43.886	0.513	3.021	0.399	0.055	0.049	0.000	0.000	97.543
ML-78-30-148-3	Ilmenite-Massive	Ilmenite	0.067	50.189	0.005	43.867	0.567	3.212	0.329	0.075	0.031	0.030	0.000	98.370
ML-78-31-149-1	Ilmenite-Blocky	Ilmenite	0.000	48.645	0.000	43.970	0.377	3.566	0.388	0.067	0.036	0.000	0.008	97.056
ML-78-31-150-2	Ilmenite-Blocky	Ilmenite	0.000	48.818	0.021	44.569	0.409	3.635	0.356	0.069	0.020	0.052	0.000	97.949
ML-78-31-151-3	Ilmenite-Blocky	Ilmenite	0.035	48.077	0.000	43.501	0.372	3.570	0.369	0.027	0.033	0.084	0.000	96.069
		Minimum	***0.000***	***48.077***	***0.000***	***43.501***	***0.372***	***3.021***	***0.327***	***0.007***	***0.020***	***0.000***	***0.000***	***96.069***
		Maximum	***0.067***	***50.189***	***0.021***	***44.569***	***0.567***	***3.635***	***0.399***	***0.075***	***0.049***	***0.084***	***0.008***	***98.370***
		Average	***0.028***	***49.208***	***0.007***	***43.921***	***0.453***	***3.340***	***0.362***	***0.050***	***0.034***	***0.028***	***0.001***	***97.432***
		Median	***0.033***	***49.194***	***0.004***	***43.876***	***0.445***	***3.389***	***0.363***	***0.061***	***0.035***	***0.015***	***0.000***	***97.574***
		St.Deviation	***0.023***	***0.751***	***0.008***	***0.326***	***0.073***	***0.258***	***0.027***	***0.025***	***0.009***	***0.032***	***0.003***	***0.729***

Several analyses of grains within the Campaign 3 reground and two-stage leach residue samples believed to be ilmenite were analyzed and yielded low analytical totals. These analyses and statistics associated with these analyses are included in Table 85.

Table 85. Electron microprobe analyses of ilmenite grains with low analytical totals from Campaign 3 two-stage leach residues. Values are in weight percentages.

Electron Microprobe Analysis – 2-Stage Leach Residue Ilmenite (Low Total, n =12)														
Sample	Description	Phase	SiO_2	TiO_2	Al_2O_3	FeO	MnO	MgO	V_2O_3	Cr_2O_3	NiO	SO_3	Cl	Total
ML-77-14-100-3	Ilmenite-Broken	Ilmenite	0.934	48.065	0.322	40.360	0.335	4.235	0.315	0.053	0.050	0.030	0.000	94.700
ML-77-13-96-2	Light Gray Broken	Ilmenite?	2.766	26.804	0.229	21.489	0.203	2.441	0.293	0.019	0.050	0.407	0.766	55.465
ML-77-12-92-1	Light Gray Elongate Broken	Ilmenite?	0.794	37.408	0.091	34.714	0.308	3.322	0.394	0.068	0.036	0.285	0.381	77.802
ML-77-12 12-93-2	Light Gray Elongate Broken	Ilmenite?	8.421	39.881	1.400	36.489	0.344	2.512	0.375	0.035	0.000	0.025	0.247	89.729
ML-77-12-94-3	Light Gray Elongate Broken	Ilmenite?	8.687	40.650	1.101	35.712	0.338	1.465	0.312	0.065	0.037	0.117	0.127	88.611
ML-77-13-95-1	Light Gray Broken	Ilmenite?	12.378	38.276	2.425	31.221	0.308	3.073	0.333	0.014	0.060	0.115	0.147	88.389
ML-77-13-97-3	Light Gray Broken	Ilmenite?	1.422	46.518	0.503	38.961	0.347	3.131	0.292	0.056	0.032	0.192	0.074	91.530
ML-77-14-98-1	Light Gray Broken	Ilmenite?	8.367	37.392	1.000	30.863	0.274	3.629	0.353	0.056	0.034	0.433	0.093	82.493
ML-77 14-99-2	Light Gray Broken	Ilmenite?	5.404	40.913	0.755	34.264	0.322	4.077	0.349	0.016	0.032	0.198	0.113	86.443
ML-78-32-152-1	Light Gray Massive	Ilmenite?	2.416	42.917	1.329	44.072	0.839	0.727	0.291	0.014	0.000	0.053	0.000	92.658
ML-78-32-153-2	Light Gray Massive	Ilmenite?	1.163	46.266	0.473	44.722	0.873	0.560	0.159	0.000	0.027	0.005	0.027	92.274
ML-78-32-154-3	Light Gray Massive	Ilmenite?	1.153	45.314	0.027	43.089	0.860	0.512	0.117	0.039	0.000	0.000	0.042	91.153
		Minimum	***0.794***	***26.804***	***0.027***	***21.489***	***0.203***	***0.512***	***0.117***	***0.000***	***0.000***	***0.000***	***0.000***	***55.465***
		Maximum	***12.378***	***46.518***	***2.425***	***44.722***	***0.873***	***4.077***	***0.394***	***0.068***	***0.060***	***0.433***	***0.766***	***94.274***
		Average	***4.816***	***40.213***	***0.848***	***35.963***	***0.456***	***2.313***	***0.297***	***0.035***	***0.028***	***0.170***	***0.183***	***85.322***
		Median	***2.766***	***40.650***	***0.755***	***35.712***	***0.338***	***2.512***	***0.312***	***0.035***	***0.032***	***0.155***	***0.113***	***88.611***
		St.Deviation	***3.844***	***5.308***	***0.675***	***6.502***	***0.249***	***1.233***	***0.082***	***0.023***	***0.019***	***0.146***	***0.211***	***10.459***

A phase tentatively identified as rutile was identified in Campaign 3 two-stage leach residue samples 1802-L19R (ML-77) and 1802-L20R (ML-78) (Table 86). All samples analyzed yielded low analytical totals, ranging from 83.309% to 96.914%. The phase is dominated by TiO_2 (71.066%–91.822%), SiO_2 (0.790%–5.904%), V_2O_3 (0.494%–1.432%), FeO (0.333%–3.127%), MgO (0.083%–.012%), Al_2O_3 (0.000%–0.612%), Cr_2O_3 (0.000%–0.172%), NiO (0.000%–0.063%), and MnO (0.000%–0.020%). Also present were SO_3 (0.893%–2.681%) and chlorine (0.000%–0.717%). Fe^{2+}, V^{3+}, and Cr^{3+} may occur in trace amounts within the mineral rutile (Deer et al., 1992; Klein and Hurlbut, 1999).

Table 86. Electron microprobe analyses of grains tentatively identified as rutile from Campaign 3 two-stage leach residues.

Electron Microprobe Analysis – 2-Stage Leach Residue Rutile (n = 20)														
Sample	Description	Phase	SiO_2	TiO_2	Al_2O_3	FeO	MnO	MgO	V_2O_3	Cr_2O_3	NiO	SO_3	Cl	Total
ML-77-9-83-1	Rutile Core	Rutile	1.139	86.908	0.029	0.633	0.020	1.275	0.658	0.067	0.000	0.893	0.315	91.937
ML-77-9-84-2	Rutile Core	Rutile	1.293	86.921	0.143	0.694	0.000	1.720	0.606	0.059	0.006	0.955	0.250	92.647
ML-77-9-85-3	Rutile Core	Rutile	2.232	83.463	0.100	1.040	0.016	2.012	0.494	0.058	0.000	1.118	0.421	90.954
ML-77-10-86-1	Rutile Rim	Rutile	5.904	71.066	0.302	1.801	0.018	1.686	0.535	0.033	0.000	1.246	0.717	83.309
ML-77-10-87-2	Rutile Rim	Rutile	5.717	75.236	0.612	3.127	0.002	1.740	0.592	0.000	0.000	1.131	0.662	88.820
ML-77-10-88-3	Rutile Rim	Rutile	0.911	89.432	0.000	0.632	0.000	1.459	0.651	0.045	0.019	1.108	0.187	94.353
ML-77-11-89-1	Rutile "Vesicular"	Rutile	1.144	80.228	0.179	0.822	0.000	0.974	0.898	0.080	0.000	2.024	0.142	86.492
ML-77-11-90-2	Rutile "Vesicular"	Rutile	2.309	84.046	0.362	0.895	0.015	1.230	0.822	0.172	0.036	1.609	0.067	91.563
ML-77-11-91-3	Rutile "Vesicular"	Rutile	0.790	90.280	0.081	0.719	0.000	1.016	1.035	0.058	0.063	1.199	0.038	95.278
ML-78-26-134-1	Rutile Core "Vesicular"	Rutile	2.068	89.309	0.110	0.415	0.004	0.098	1.259	0.138	0.000	1.810	0.000	95.212
ML-78-26-135-2	Rutile Core "Vesicular"	Rutile	2.429	84.526	0.138	0.485	0.006	0.130	1.092	0.066	0.000	2.020	0.068	90.959
ML-78-26-136-3	Rutile Core "Vesicular"	Rutile	1.849	89.835	0.120	0.409	0.000	0.085	1.239	0.056	0.022	1.681	0.000	95.256
ML-78-27-137-1	Rutile Rim "Vesicular"	Rutile	2.769	84.560	0.082	0.397	0.000	0.083	1.432	0.076	0.000	1.479	0.112	90.991
ML-78-27-138-2	Rutile Rim "Vesicular"	Rutile	4.622	86.969	0.165	0.400	0.000	0.103	1.251	0.072	0.022	1.633	0.010	95.249
ML-78-27-139-3	Rutile Rim "Vesicular"	Rutile	2.291	86.516	0.211	0.384	0.001	0.105	1.321	0.089	0.000	1.719	0.033	92.670
ML-78-28-140-1	Rutile Core	Rutile	1.699	91.192	0.047	0.336	0.015	0.146	0.888	0.038	0.000	1.376	0.056	95.773
ML-78-28-141-2	Rutile Core	Rutile	1.143	91.173	0.088	0.353	0.007	0.259	0.992	0.079	0.000	1.459	0.075	95.917
ML-78-28-142-3	Rutile Core	Rutile	1.219	91.822	0.142	0.333	0.000	0.462	0.969	0.124	0.016	1.541	0.000	96.628
ML-78-29-143-1	Rutile Core	Rutile	3.331	80.603	0.098	0.574	0.000	0.123	0.672	0.062	0.003	2.681	0.031	88.177
ML-78-29-144-2	Rutile Core	Rutile	1.768	91.504	0.020	0.485	0.000	0.088	0.532	0.063	0.000	2.246	0.009	96.914
		Minimum	***0.790***	***71.066***	***0.000***	***0.333***	***0.000***	***0.083***	***0.494***	***0.000***	***0.000***	***0.893***	***0.000***	***83.309***
		Maximum	***5.904***	***91.822***	***0.612***	***3.127***	***0.020***	***2.012***	***1.432***	***0.172***	***0.063***	***2.681***	***0.717***	***96.914***
		Average	***2.346***	***85.778***	***0.152***	***0.747***	***0.005***	***0.740***	***0.897***	***0.072***	***0.009***	***1.522***	***0.160***	***92.457***
		Median	***1.959***	***96.914***	***0.115***	***0.529***	***0.001***	***0.361***	***0.893***	***0.065***	***0.000***	***1.510***	***0.067***	***92.659***
		St.Deviation	***1.450***	***5.437***	***0.137***	***0.640***	***0.007***	***0.692***	***0.291***	***0.037***	***0.016***	***0.466***	***0.209***	***3.563***

Figure 97 illustrates the mineral chemical compositions of ilmenites analyzed within the Campaign 3 reground and two-stage leach residue samples. Figures 97A and 97B show the composition of the ilmenites when plotted in the FeO-TiO_2-MgO and FeO-TiO_2-5MgO systems, respectively. From these diagrams, it is apparent that the ilmenites in the reground and two-stage leach residues contain appreciable MgO. The compositions of the two-stage leach residue ilmenites are similar to compositions of ilmenites within the Longnose bulk sample samples (refer to Fig. 10) and the Longnose ilmenite concentrate that was derived by physical processing of the Longnose bulk sample (refer to Fig. 15). ***This result suggests that ilmenites in the Campaign 3 two-stage leach residues have not been appreciably impacted by hydrometallurgical processing.*** Figures 97C and 97D illustrate the compositions of ilmenite from the Campaign 3 reground and two-stage leach residues in the FeO-TiO_2-V_2O_3 and FeO-TiO_2-5V_2O_3 systems, respectively. The lack of appreciable V_2O_3 in the Campaign 3 two-stage leach residues is also similar to the V_2O_3 compositions of ilmenites from the Longnose bulk sample samples and Longnose ilmenite concentrate, again suggesting that the ilmenites in the Campaign 3 two-stage leach residues have not been appreciably affected by hydrometallurgical processing. Figure 97E illustrates the compositions of ilmenites from Campaign 3 two-stage leach residues in the molar Fe^{2+}-Ti^{4+}-Fe^{3+} system based on stoichiometric calculations utilizing ILMNCALC software (Gabbrosoft.com). Again, the results are similar to those from the Longnose bulk sample samples and the Longnose ilmenite concentrate, with compositions plotting above the titanohematite solid solution line, which indicates that Mg^{2+} has substituted into the ilmenite grains within structural sites typically associated with the presence of Fe^{2+}.

Figure 98 illustrates the composition of the mineral phase tentatively identified as rutile from the Campaign 3 reground and two-stage leach residue samples. Figures 98A and 98B show the compositions of this phase in the FeO-TiO_2-MgO and FeO-TiO_2-5MgO systems. The presence of both FeO and MgO in this phase is apparent. Figures 98C and 98D illustrate the composition of this phase in the FeO-TiO_2-V_2O_3 and FeO-TiO_2-5V_2O_3 systems. The presence of both FeO and V_2O_3 is indicated in these diagrams. Figure 98E is a molar Fe^{2+}-Ti^{4+}-Fe^{3+} ternary diagram based on stoichiometry calculated using RUTCALC.xls (Gabbrosoft.com). The mineral phase plots near stoichiometric rutile, and the presence of Fe^{2+} is indicated.

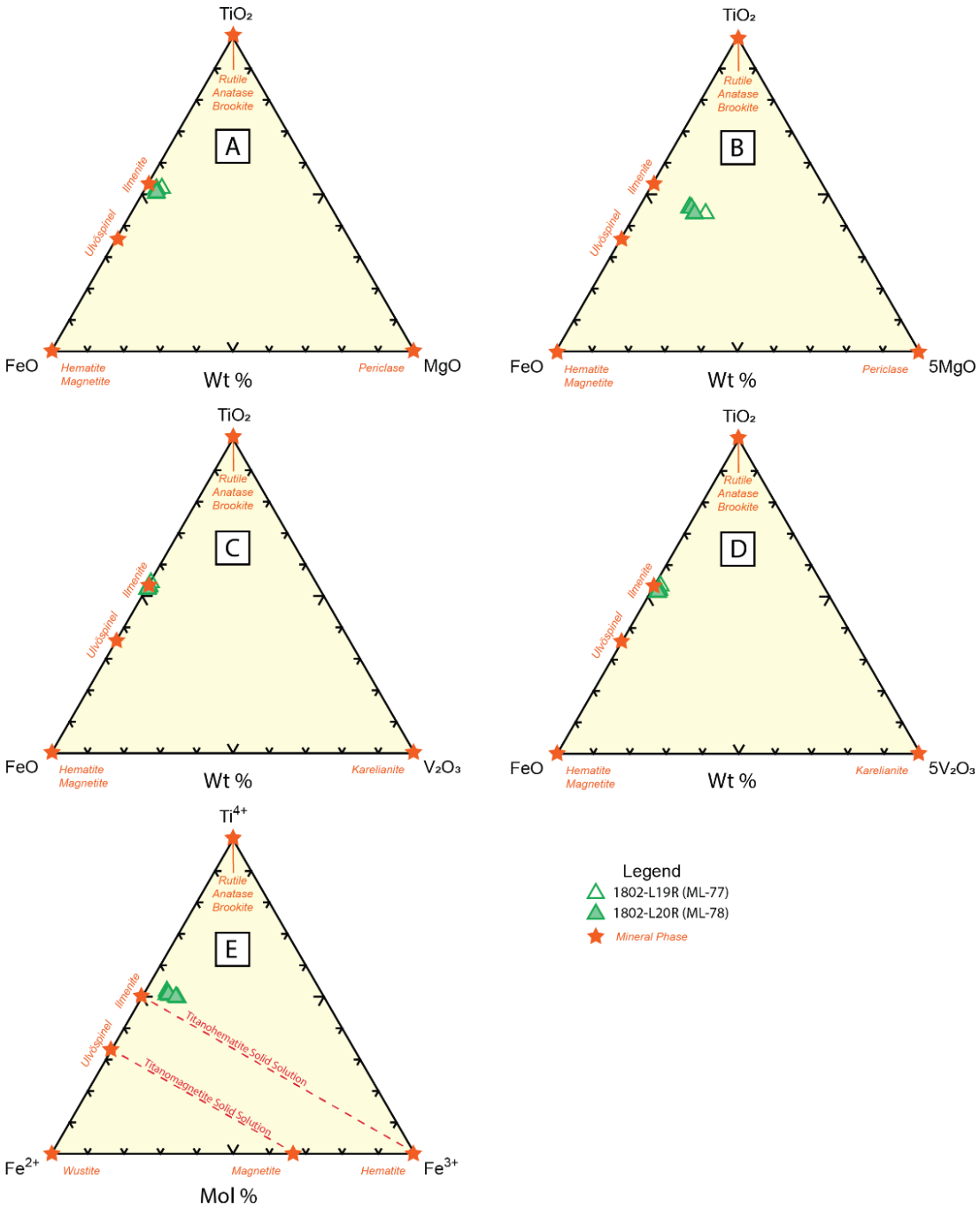

Figure 97. Ternary diagrams illustrating the mineral chemical compositions of ilmenite grains from Campaign 3 re-ground and two-stage leach samples 1802-L19R (ML-77) and 1802-L20R (ML-78). A) and B) Figures 97A and 97B represent ternary diagrams in the FeO-TiO_2-MgO and FeO-TiO_2-5MgO systems, respectively, and show that ilmenites from the two-stage leach residue samples contain appreciable MgO. C) and D) Figures 97C and 97D are ternary diagrams in the FeO-TiO_2-V_2O_3 and FeO-TiO_2-5V_2O_3 systems and illustrate the low V_2O_3 values within Campaign 3 two-stage leach residue samples. E) Molar Fe^{2+}-Ti^{4+}-Fe^{3+} ternary diagram (modified after Klein and Hurlbut, 1999; Meinhold, 2010) showing compositions of ilmenites from Campaign 3 two-stage leach residues based on stoichiometric calculations utilizing ILMNCALC.xls (Gabbrosoft.com). Note that two-stage leach ilmenites plot above the titanohematite solid solution line, a result indicating the substation of Mg^{2+} for Fe^{2+} within the ilmenite structure.

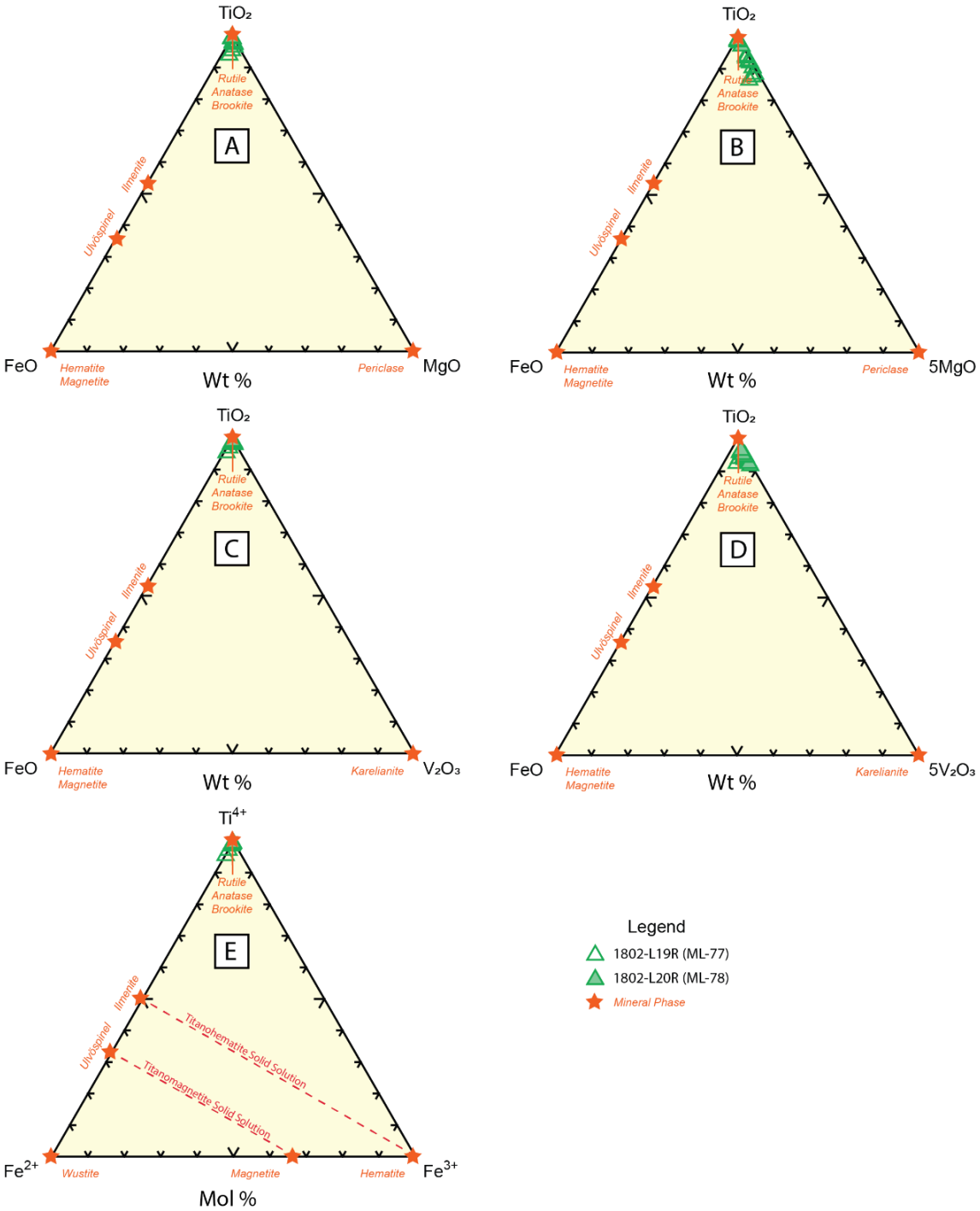

Figure 98. Ternary diagrams illustrating the mineral chemical compositions of a mineral phase tentatively identified as rutile in the Campaign 3 two-stage leach residue samples. Figures 98A and 98B illustrate the composition of the possible rutile phase in the FeO-TiO_2-MgO and FeO-TiO_2-5MgO systems, respectively. Note the presence of both FeO and MgO in this phase. Figures 98C and 98D show the composition of the possible rutile phase in the FeO-TiO_2-V_2O_3 and FeO-TiO_2-$5V_2O_3$ systems. The presence of both FeO and V_2O_3 is indicated in these diagrams. Figure 98E is a molar Fe^{2+}-$Ti^{4+}Fe^{3+}$ ternary diagram based on stoichiometry calculated using RUTCALC.xls (Gabbrosoft.com). The mineral phase plots near stoichiometric rutile, and the presence of Fe^{2+} is indicated.

Lithogeochemical Analysis

Whole rock lithogeochemical analyses were performed on three samples of Campaign 1, Campaign 2, and Campaign 3 leach residues. These include sample 1802-BL10-1 (ML-71, Campaign 1, no recycling), sample 1802-BL-6 (ML-70, Campaign 2, half-recycled), and sample 1802-BL-19 (ML-72, Campaign 3, recycled). The results of the lithogeochemical analyses are shown in Table 87 and are included in Appendix 3: Tables A3-1 to A3-7.

It is important to note that the original lithogeochemical analysis of sample 1802-BL19 (ML-72) using ALS Laboratories analytical method ME-ICP06 resulted in a low major element analytical total (84.83%). Discussions with ALS Laboratories personnel indicated that accurate analysis of this sample might be better achieved using ALS Laboratory analytical method ME-XRF06. Reanalysis of sample 1802-BL19 (ML-72) was performed using method ME-ICP06, and the major element analytical total improved to 99.60%.

As well, a blind duplicate analysis of sample 1802-BL6 (ML-70) was performed for quality control purposes. This sample was labeled 1802-BL66 and was subjected to the same lithogeochemical analysis using identical lithogeochemical methods. Duplicate analyses for major elements were duplicated within 2%, with the exceptions of K_2O (8%) and LOI (5.6%). Duplicate analyses for trace element were all within 5%, with the exceptions of Ag (ME-4ACD81 – 14%), Cd (ME-MS42 – 19%), Er (ME-MS81 – 14%), In (ME-MS42 – 7.6%), Mo (ME-MS42 – 33%), Sc (ME-MS42 – 6.3%), Sm (ME-MS81 – 11%), and Y (ME-MS42 – 7.4%).

Table 87. Results of lithogeochemical analyses on single stage leach residues. Note low analytical totals for major elements (weight percentages) using the ME-ICP06 method for sample 1802-BL-19 (ML-72). This sample was reanalyzed using analytical method ME-XRF-06 per recommendation from ALS Laboratories, and the analytical total improved to >98%.

		Sample	1802-BL6	1802-BL10	1802-BL19	1802-BL66	1802-L19R	1802-L20R			1802-BL19
		Sample Description	BL-6 Leach Residue Campaign 2 - Half Recycled	BL-10 Leach Residue Campaign 1 No Recycling	BL-19 Leach Residue Campaign 3 After Recyling	BL-6 Leach Residue Campaign 2-Half Recycled - DUPLICATE	BL19 Leach Residue Campaign 3 ground and 2-stage leach	BL20 Leach Residue Campaign 3 ground and 2-stage leach			BL19 Leach Residue Campaign 3 After Recycling - Reanalysis
Analysis	Method	Detection Limit							Analysis	Method	
SiO2_%	ME-ICP06	0.01	39.2	46	18.8	39.3	45.2	34.4	SiO2_%	ME-XRF06	19.04
Al2O3_%	ME-ICP06	0.01	1.38	1.45	0.85	1.38	2.01	1.43	Al2O3_%	ME-XRF06	0.85
Fe2O3_%	ME-ICP06	0.01	17.55	12.45	29.7	17.25	12.45	6.05	Fe2O3_%	ME-XRF06	30.18
CaO_%	ME-ICP06	0.01	1.22	1.21	0.79	1.21	2.1	1.61	CaO_%	ME-XRF06	0.85
MgO_%	ME-ICP06	0.01	4.91	3.66	3.3	4.89	4.65	6.33	MgO_%	ME-XRF06	3.15
Na2O_%	ME-ICP06	0.01	0.22	0.21	0.13	0.22	0.33	0.29	Na2O_%	ME-XRF06	0.12
K2O_%	ME-ICP06	0.01	0.12	0.11	0.06	0.11	0.16	0.15	K2O_%	ME-XRF06	0.06
Cr2O3_%	ME-ICP06	0.002	0.05	0.042	0.055	0.051	0.046	0.041	Cr2O3_%	ME-XRF06	0.05
TiO2_%	ME-ICP06	0.01	22.1	14.45	27.9	21.9	22.8	28.8	TiO2_%	ME-XRF06	41.24
MnO_%	ME-ICP06	0.01	0.15	0.11	0.26	0.15	0.11	0.06	MnO_%	ME-XRF06	0.27
P2O5_%	ME-ICP06	0.01	0.01	<0.01	0.04	0.01	0.01	0.07	P2O5_%	ME-XRF06	0.042
SrO_%	ME-ICP06	0.01	<0.01	<0.01	<0.01	<0.01	<0.01	0.01	SrO_%	ME-XRF06	<0.01
BaO_%	ME-ICP06	0.01	<0.01	<0.01	<0.01	<0.01	<0.01	<0.01	BaO_%	ME-XRF06	<0.01
LOI_%	OA-GRA05	0.01	11.35	18.35	2.94	12	10.3	18.85	LOI_%	ME-XRF06	3.75
Total_%	TOT-ICP06	0.01	98.26	98.04	84.83	98.47	100.17	98.09	Total_%	ME-XRF06	99.6
S_%	S-IR08	0.01	0.15	0.17	0.11	0.15	0.18	0.19	S_%	S-IR08	0.11
Ag_ppm	ME-4ACD81	0.5	0.7	0.8	1.1	0.8	<0.5	<0.5	Ag_ppm	ME-4ACD81	1.1
Ag_ppm	ME-MS42	0.01	0.06	0.13	0.08	0.06	0.06	0.12	Ag_ppm	ME-MS42	0.08
As_ppm	ME-4ACD81	5	<5	6	5	5	5	11	As_ppm	ME-4ACD81	5
As_ppm	ME-MS42	0.1	<0.1	<0.1	<0.1	<0.1	<0.1	<0.1	As_ppm	ME-MS42	<0.1
Ba_ppm	ME-MS81	0.5	23.2	24.4	38	22.2	46	40.5	Ba_ppm	ME-MS81	38
Be_ppm	ME-MS42	0.05	<0.05	<0.05	<0.05	<0.05	<0.05	<0.05	Be_ppm	ME-MS42	<0.05
Bi_ppm	ME-MS42	0.01	0.01	0.05	0.02	0.01	0.02	0.16	Bi_ppm	ME-MS42	0.02
Cd_ppm	ME-4ACD81	0.5	0.6	0.7	1.5	0.7	2	1.6	Cd_ppm	ME-4ACD81	1.5
Cd_ppm	ME-MS42	0.01	0.11	0.07	0.27	0.09	0.6	0.25	Cd_ppm	ME-MS42	0.27
Ce_ppm	ME-MS42	0.02	9.53	3.82	1	9.28	0.87	1.1	Ce_ppm	ME-MS42	1
Ce_ppm	ME-MS81	0.1	10.2	5	2.5	10.3	8.5	4.4	Ce_ppm	ME-MS81	2.5
Co_ppm	ME-4ACD81	1	95	93	127	92	90	52	Co_ppm	ME-4ACD81	127
Co_ppm	ME-MS42	0.1	39.7	49.3	27.9	38.1	44	31.8	Co_ppm	ME-MS42	27.9
Cr_ppm	ME-MS81	10	360	320	390	370	330	300	Cr_ppm	ME-MS81	390
Cs_ppm	ME-MS42	0.05	<0.05	<0.05	<0.05	<0.05	<0.05	<0.05	Cs_ppm	ME-MS42	<0.05
Cs_ppm	ME-MS81	0.01	0.07	0.07	0.04	0.07	0.14	0.12	Cs_ppm	ME-MS81	0.04
Cu_ppm	ME-4ACD81	1	162	385	124	157	207	57	Cu_ppm	ME-4ACD81	124
Cu_ppm	ME-MS42	0.2	150	>250	101.5	144.5	177.5	45.3	Cu_ppm	ME-MS42	101.5
Dy_ppm	ME-MS81	0.05	0.64	0.64	0.4	0.59	1.03	0.73	Dy_ppm	ME-MS81	0.4
Er_ppm	ME-MS81	0.03	0.35	0.39	0.28	0.4	0.56	0.42	Er_ppm	ME-MS81	0.28
Eu_ppm	ME-MS81	0.03	0.14	0.13	0.10	0.15	0.30	0.15	Eu_ppm	ME-MS81	0.10
Ga_ppm	ME-MS42	0.05	1.06	1.35	0.47	1.01	0.57	0.45	Ga_ppm	ME-MS42	0.47
Ga_ppm	ME-MS81	0.01	6.8	8	4.3	6.8	7.9	5.6	Ga_ppm	ME-MS81	4.3
Gd_ppm	ME-MS81	0.05	0.56	0.57	0.35	0.59	1.05	0.66	Gd_ppm	ME-MS81	0.35
Hf_ppm	ME-MS42	0.02	0.99	1.36	0.76	0.98	1.01	0.88	Hf_ppm	ME-MS42	0.76
Hf_ppm	ME-MS81	0.2	4.4	4.8	5.1	4.3	4.5	3.2	Hf_ppm	ME-MS81	5.1
Hg_ppm	ME-MS42	0.005	<0.005	0.012	0.006	<0.005	<0.005	<0.005	Hg_ppm	ME-MS42	0.006
Ho_ppm	ME-MS81	0.01	0.13	0.13	0.08	0.13	0.2	0.14	Ho_ppm	ME-MS81	0.08
In_ppm	ME-MS42	0.005	0.013	0.049	0.011	0.014	0.007	0.008	In_ppm	ME-MS42	0.011
La_ppm	ME-MS42	0.2	2	1.2	0.3	1.9	0.4	0.4	La_ppm	ME-MS42	0.3
La_ppm	ME-MS81	0.1	2.4	1.7	0.8	2.3	3.6	1.8	La_ppm	ME-MS81	0.8
Li_ppm	ME-4ACD81	10	<10	<10	<10	<10	<10	<10	Li_ppm	ME-4ACD81	<10
Li_ppm	ME-MS42	0.1	1.2	0.9	0.4	1.2	0.8	1.5	Li_ppm	ME-MS42	0.4
Lu_ppm	ME-MS81	0.01	0.07	0.07	0.07	0.07	0.08	0.05	Lu_ppm	ME-MS81	0.07
Mo_ppm	ME-4ACD81	1	1	1	4	<1	8	6	Mo_ppm	ME-4ACD81	4
Mo_ppm	ME-MS42	0.05	0.06	0.71	0.18	0.08	0.07	<0.05	Mo_ppm	ME-MS42	0.18
Nb_ppm	ME-MS42	0.05	<0.05	0.13	<0.05	<0.05	<0.05	<0.05	Nb_ppm	ME-MS42	<0.05
Nb_ppm	ME-MS81	0.2	28.3	21.9	50.3	28.5	35.5	74.4	Nb_ppm	ME-MS81	50.3
Nd_ppm	ME-MS81	0.1	2.9	2.4	1.4	2.9	4.7	2.5	Nd_ppm	ME-MS81	1.4
Ni_ppm	ME-4ACD81	1	206	189	262	187	174	110	Ni_ppm	ME-4ACD81	262
Ni_ppm	ME-MS42	0.2	73.5	95.9	72.8	72.7	66.4	49.3	Ni_ppm	ME-MS42	72.8
Pr_ppm	ME-MS81	0.03	0.78	0.57	0.31	0.77	1.12	0.56	Pr_ppm	ME-MS81	0.31
Pb_ppm	ME-4ACD81	2	3	9	14	3	10	19	Pb_ppm	ME-4ACD81	14
Pb_ppm	ME-MS42	0.2	3.2	7.7	6.9	3	4.1	14	Pb_ppm	ME-MS42	6.9
Rb_ppm	ME-MS42	0.1	0.7	0.6	0.6	0.7	4.9	4.1	Rb_ppm	ME-MS42	0.6
Rb_ppm	ME-MS81	0.2	2.4	2.6	1.8	2.5	1.5	1.4	Rb_ppm	ME-MS81	1.8
Re_ppm	ME-MS42	0.001	0.001	0.001	<0.001	0.001	<0.001	0.001	Re_ppm	ME-MS42	<0.001
Sb_ppm	ME-MS42	0.05	<0.05	0.07	<0.05	<0.05	0.06	<0.05	Sb_ppm	ME-MS42	<0.05
Sc_ppm	ME-4ACD81	1	37	26	50	36	29	17	Sc_ppm	ME-4ACD81	50
Sc_ppm	ME-MS42	0.1	9.6	5.1	5.4	9	4	4.1	Sc_ppm	ME-MS42	5.4
Se_ppm	ME-MS42	0.2	0.2	0.3	<0.2	<0.2	<0.2	<0.2	Se_ppm	ME-MS42	<0.2
Sm_ppm	ME-MS81	0.03	0.54	0.54	0.37	0.6	1.21	0.68	Sm_ppm	ME-MS81	0.37
Sn_ppm	ME-MS42	0.2	0.4	4.7	0.6	0.4	0.2	0.3	Sn_ppm	ME-MS42	0.6
Sn_ppm	ME-MS81	1	1	5	1	1	1	1	Sn_ppm	ME-MS81	1
Sr_ppm	ME-MS42	0.2	17.2	9.1	2.1	16.8	10.9	35.3	Sr_ppm	ME-MS42	2.1
Sr_ppm	ME-MS81	0.1	31	24.6	12.8	31.2	39	55.6	Sr_ppm	ME-MS81	12.8
Ta_ppm	ME-MS42	0.01	0.02	0.01	<0.01	0.02	<0.01	<0.01	Ta_ppm	ME-MS42	<0.01
Ta_ppm	ME-MS81	0.1	5.1	5.2	5	5	7.3	14.3	Ta_ppm	ME-MS81	5
Tb_ppm	ME-MS81	0.01	0.1	0.09	0.06	0.1	0.16	0.11	Tb_ppm	ME-MS81	0.06
Te_ppm	ME-MS42	0.01	<0.01	<0.01	<0.01	<0.01	<0.01	<0.01	Te_ppm	ME-MS42	<0.01
Th_ppm	ME-MS42	0.2	<0.2	<0.2	<0.2	<0.2	<0.2	<0.2	Th_ppm	ME-MS42	<0.2
Th_ppm	ME-MS81	0.05	0.16	0.14	0.14	0.16	0.45	0.22	Th_ppm	ME-MS81	0.14
Tl_ppm	ME-4ACD81	10	<10	<10	<10	10	<10	<10	Tl_ppm	ME-4ACD81	<10
Tl_ppm	ME-MS42	0.02	<0.02	0.03	<0.02	<0.02	<0.02	0.03	Tl_ppm	ME-MS42	<0.02
Tm_ppm	ME-MS81	0.01	0.06	0.06	0.05	0.06	0.08	0.05	Tm_ppm	ME-MS81	0.05
U_ppm	ME-MS42	0.05	0.05	0.09	0.07	0.05	<0.05	<0.05	U_ppm	ME-MS42	0.07
U_ppm	ME-MS81	0.05	0.1	0.14	0.11	0.1	0.13	0.08	U_ppm	ME-MS81	0.11
V_ppm	ME-MS81	5	915	580	1510	929	672	1140	V_ppm	ME-MS81	1510
W_ppm	ME-MS42	0.05	<0.05	<0.05	<0.05	<0.05	<0.05	<0.05	W_ppm	ME-MS42	<0.05
W_ppm	ME-MS81	1	1	1	<1	1	2	2	W_ppm	ME-MS81	<1
Y_ppm	ME-MS42	0.05	1.05	1.33	0.29	1.01	0.52	0.51	Y_ppm	ME-MS42	0.29
Y_ppm	ME-MS81	0.1	3.1	3.3	2	3	4.8	3.5	Y_ppm	ME-MS81	2
Yb_ppm	ME-MS81	0.03	0.43	0.42	0.4	0.42	0.58	0.39	Yb_ppm	ME-MS81	0.4
Zn_ppm	ME-4ACD81	2	333	428	269	326	435	303	Zn_ppm	ME-4ACD81	269
Zr_ppm	ME-MS42	0.5	39.6	56.6	30.5	39.6	38.3	32	Zr_ppm	ME-MS42	30.5
Zr_ppm	ME-MS81	2	154	156	190	155	154	110	Zr_ppm	ME-MS81	190

Relative results for samples 1802-BL-10 (ML-71, Campaign 1, no recycling) and sample 1802-BL-6 (ML-70, Campaign 2, half-recycled) in terms of major element oxide compositions are described below:

- SiO_2: Higher in the non-recycled sample (46.00%) than the half-recycled sample (39.20%, 39.30%)
- Al_2O_3: Higher in the non-recycled sample (1.45%) than in the half-recycled sample (1.38%, 1.38%)
- Fe_2O_3: Higher in the half-recycled sample (17.55%, 17.25%) than the non-recycled sample (12.45%)
- CaO: Nearly equivalent, but slightly higher in the half-recycled sample (1.22%, 1.21%) than the non-recycled sample (1.21%)
- MgO: Higher in the half-recycled sample (4.91%, 4.89%) than the non-recycled sample (3.66%)
- Na_2O: Nearly equivalent, but slightly higher in the half-recycled sample (0.22%, 0.22%) than the non-recycled sample (0.21%)
- K_2O: Nearly equivalent, but slightly higher in the half-recycled sample (0.12%, 0.11%) than the non-recycled sample (0.11%)
- Cr_2O_3: Higher in the half-recycled sample (0.050%, 0.051%) than the non-recycled sample (0.042%)
- TiO_2: Higher in the half-recycled sample (22.10%, 21.90%) than the non-recycled sample (14.45%)
- MnO: Higher in the half-recycled sample (0.15%, 0.15%) than the non-recycled sample (0.11%)
- P_2O_5: Higher in the half-recycled sample (0.01%, 0.01%) than the non-recycled sample (<0.01%)
- SrO: Below detection limit (<0.01%) in both the non-recycled and half-recycled samples
- BaO: Below detection limit (<0.01%) in both the non-recycled and half-recycled samples
- LOI: Higher in the non-recycled sample (18.35%) than the half-recycled sample (11.35%, 12.00%)
- Sulfur: Slightly higher in the non-recycled sample (0.17%) than the half-recycled sample (0.15%, 0.15%)

Relative results for samples 1802-BL-10 (ML-70, no recycling) and sample 1802-BL-6 (ML-71, half-recycled) in for selected trace element compositions are described below:

- As: Approximately equal in the non-recycled sample (6 ppm) and the non-recycled sample (<5 ppm, 5 ppm) using analytical method ME-4ACD81; equivalent in both samples (<0.1 ppm) using analytical method ME-MS42
- Co: Slightly higher in the half-recycled sample (95 ppm, 92 ppm) than the non-recycled sample (93 ppm) using analytical method ME-4ACD81; higher in the non-recycled sample (49.3 ppm) than the half-recycled sample (39.7 ppm, 38.1 ppm) using analytical method ME-MS42
- Cr: Higher in the half-recycled sample (360 ppm, 370 ppm) than the non-recycled sample (320 ppm) using analytical method ME-MS81
- Cu: Higher in the non-recycled sample (385 ppm) than the half-recycled sample (150 ppm, 144.5 ppm) using analytical method ME-4ACD81; higher in the non-recycled sample (>250 ppm) than in the half-recycled sample (150 ppm) using analytical method ME-MS42
- Nb: Higher in the non-recycled sample (0.13 ppm) than the half-recycled sample (<0.05 ppm, <0.05 ppm) using analytical method ME-MS42; higher in the half-recycled sample (28.3 ppm, 28.5 ppm) than the non-recycled sample (21.9 ppm) using analytical method ME-MS81
- Ni: Higher in the half-recycled sample (206 ppm, 187 ppm) than the non-recycled sample (189 ppm) using analytical method ME-4ACD81; higher in the non-recycled sample (95.9 ppm) than the half-recycled sample (73.5 ppm, 72.7 ppm) using analytical method ME-MS42

- Pb: Higher in the non-recycled sample (9 ppm) than the half-recycled sample (3 ppm, 3 ppm) using analytical method ME-4ACD81; higher in the non-recycled sample (7.7 ppm) than the half-recycled sample (3.2 ppm. 3.0 ppm) using analytical method ME-MS42
- Sb: Higher in the non-recycled sample (0.07 ppm) than the half-recycled sample (<0.05 ppm, <0.05 ppm) using analytical method ME-MS42
- Ta: Higher in the half-recycled sample (0.02 ppm, 0.02 ppm) than the non-recycled sample (0.01 ppm) using analytical method ME-MS42; approximately equal in the non-recycled sample (5.2 ppm) and the half-recycled sample (5.1 ppm, 5.0 ppm) using analytical method ME-MS81
- V: Higher in the half-recycled sample (915 ppm, 929 ppm) than the non-recycled sample (580 ppm) using analytical method ME-MS81

Relative results for sample 1802-BL-6 (ML-71, Campaign 2, half-recycled) and sample 1802-BL-19 (ML-72, Campaign 3, recycled) in terms of major element oxide compositions are described below:

- SiO_2: Higher in the half-recycled sample (39.20%, 39.30%) than in the recycled sample (19.04%)
- Al_2O_3: Higher in the half-recycled sample (1.38%, 1.38%) than in the recycled sample (0.85%)
- Fe_2O_3: Higher in the recycled sample (30.18%) than in the half-recycled sample (17.55%, 17.25%)
- CaO: Higher in the half-recycled sample (1.22%, 1.21%) than the recycled sample (0.85%)
- MgO: Higher in the half-recycled sample (4.91%, 4.89%) than the recycled sample (3.15%)
- Na_2O: Higher in the half-recycled sample (0.22%, 0.22%) than the recycled sample (0.12%)
- K_2O: Higher in the half-recycled sample (0.12%, 0.11%) than the recycled sample (0.06%)
- Cr_2O_3: Equivalent in the half-recycled sample (0.050%, 0.051%) and the recycled sample (0.050%)
- TiO_2: Higher in the recycled sample (41.24%) than in the half-recycled sample (22.10%, 21.90%)
- MnO: Higher in the recycled sample (0.27%) than the half-recycled sample (0.15%, 0.15%)
- P_2O_5: Higher in the recycled sample (0.042%) than the half-recycled sample (0.01%, 0.01%)
- SrO: Below detection limit (<0.01%) in both the recycled and half-recycled samples
- BaO: Below detection limit (<0.01%) in both the recycled and half-recycled samples
- LOI: Higher in the half-recycled sample (11.35%, 12.00%) than the recycled sample (3.75%)
- Sulfur: Higher in the half-recycled sample (0.15%, 0.15%) than the recycled sample (0.11%)

Relative results for sample 1802-BL-6 (ML-71, Campaign 2, half-recycled) and sample 1802-BL-19 (ML-72, Campaign 3, recycled) in terms of selected trace element compositions are described below:

- As: Equivalent in the non-recycled sample (<5 ppm, 5 ppm) and the recycled sample (5 ppm) using analytical method ME-4ACD81; equivalent in both samples (<0.1 ppm) using analytical method ME-MS42
- Co: Higher in the recycled sample (127 ppm) than the half-recycled sample (95 ppm, 92 ppm) using analytical method ME-4ACD81; higher in the half-recycled sample (39.7 ppm, 38.1 ppm) than the recycled sample (27.9 ppm) using analytical method ME-MS42
- Cr: Slightly higher in the recycled sample (390 ppm) than the half-recycled sample (360 ppm, 370 ppm) using analytical method ME-MS81

- Cu: Higher in the half-recycled sample (150 ppm, 144.5 ppm) than the recycled sample (124 ppm) using analytical method ME-4ACD81; potentially higher in the non-recycled sample (>250 ppm) than in the recycled sample (101.5 ppm) using analytical method ME-MS42
- Nb: Equivalent in the half-recycled sample (<0.05 ppm, <0.05 ppm) and the recycled sample (<0.05 ppm) using analytical method ME-MS42; higher in the recycled sample (50.3 ppm) than the half-recycled sample (28.3 ppm, 28.5 ppm) using analytical method ME-MS81
- Ni: Higher in the recycled sample (262 ppm) than the half-recycled sample (206 ppm, 187 ppm) using analytical method ME-4ACD81; nearly equivalent in the half-recycled sample (73.5 ppm, 72.7 ppm) and the recycled sample (72.8 ppm) using analytical method ME-MS42
- Pb: Higher in the recycled sample (14 ppm) than the half-recycled sample (3 ppm, 3 ppm) using analytical method ME-4ACD81; higher in the recycled sample (6.9 ppm) than the half-recycled sample (3.2 ppm. 3.0 ppm) using analytical method ME-MS42
- Sb: Equivalent in the half-recycled sample (<0.05 ppm, <0.05 ppm) and the recycled sample (<0.05 ppm) using analytical method ME-MS42
- Ta: Higher in the half-recycled sample (0.02 ppm, 0.02 ppm) than the recycled sample (<0.01 ppm) using analytical method ME-MS42; essentially equivalent in the half-recycled sample (5.1 ppm, 5.0 ppm) and the recycled sample (5.0 ppm) using analytical method ME-MS81
- V: Higher in the recycled sample (1510 ppm) than the half-recycled sample (915 ppm, 929 ppm) using analytical method ME-MS81

Table 88 contains the lithogeochemical results of analyses of two Campaign 3 leach residue samples 1802-L19R (ML-77) and 1802-L20R (ML-78) that have been reground and undergone two-stage leaching. Relative results for these samples in terms of major element oxide compositions (weight percentages) are described below:

- SiO_2: Higher in sample 1802-L19R (ML77, 45.2%) than in sample 1802-L19R (ML-78, 34.4%)
- Al_2O_3: Higher in sample 1802-L19R (ML77, 2.01%) than in sample 1802-L19R (ML-78, 1.43%)
- Fe_2O_3: Higher in sample 1802-L19R (ML77, 12.45%) than in sample 1802-L19R (ML-78, 6.05%)
- CaO: Higher in sample 1802-L19R (ML77, 2.10%) than in sample 1802-L19R (ML-78, 1.61%)
- MgO: Higher in sample 1802-L20R (ML-78, 6.33%) than in sample 1802-L19R (ML77, 4.65%)
- Na_2O: Higher in sample 1802-L19R (ML77, 0.33%) than in sample 1802-L19R (ML-78, 0.29%)
- K_2O: Higher in sample 1802-L19R (ML77, 0.16%) than in sample 1802-L19R (ML-78, 0.15%)
- Cr_2O_3: Higher in sample 1802-L19R (ML77, 0.046%) than in sample 1802-L19R (ML-78, 0.041%)
- TiO_2: Higher in sample 1802-L20R (ML-78, 28.80%) than in sample 1802-L19R (ML77, 22.80%)
- MnO: Higher in sample 1802-L19R (ML77, 0.11%) than in sample 1802-L19R (ML-78, 0.06%)
- P_2O_5: Higher in sample 1802-L20R (ML-78, 0.07%) than in sample 1802-L19R (ML77, 0.01%)
- SrO: Higher in sample 1802-L20R (ML-78, 0.01%) than in sample 1802-L19R (ML77, <0.01%)
- BaO: Equivalent (<0.01%) in samples 1802-L19R (ML-77) and 1802-L20R (ML-78)
- LOI: Higher in sample 1802-L20R (ML-78, 18.85%) than in sample 1802-L19R (ML77, 10.30%)
- Sulfur: Slightly higher in sample 1802-L20R (ML-78, 0.19%) than in sample 1802-L19R (ML-77, 0.18%)

Table 88. Results of lithogeochemical analyses on two-stage leach residues.

		Sample	1802-L19R (ML-77)	1802-L20R (ML-78)
		Sample Description	BL19 Leach Residue Campaign 3 ground and 2-stage leach	BL20 Leach Residue Campaign 3 ground and 2-stage leach
Analysis	Method	Detection Limit		
SiO2_%	ME-ICP06	0.01	45.20	34.40
Al2O3_%	ME-ICP06	0.01	2.01	1.43
Fe2O3_%	ME-ICP06	0.01	12.45	6.05
CaO_%	ME-ICP06	0.01	2.1	1.61
MgO_%	ME-ICP06	0.01	4.65	6.33
Na2O_%	ME-ICP06	0.01	0.33	0.29
K2O_%	ME-ICP06	0.01	0.16	0.15
Cr2O3_%	ME-ICP06	0.002	0.046	0.041
TiO2_%	ME-ICP06	0.01	22.8	28.8
MnO_%	ME-ICP06	0.01	0.11	0.06
P2O5_%	ME-ICP06	0.01	0.01	0.07
SrO_%	ME-ICP06	0.01	<0.01	0.01
BaO_%	ME-ICP06	0.01	<0.01	<0.01
LOI_%	OA-GRA05	0.01	10.3	18.85
Total_%	TOT-ICP06	0.01	100.17	98.09
S_%	S-IR08	0.01	0.18	0.19
Ag_ppm	ME-4ACD81	0.5	<0.5	<0.5
Ag_ppm	ME-MS42	0.01	0.06	0.12
As_ppm	ME-4ACD81	5	5	11
As_ppm	ME-MS42	0.1	<0.1	<0.1
Ba_ppm	ME-MS81	0.5	46	40.5
Be_ppm	ME-MS42	0.05	<0.05	<0.05
Bi_ppm	ME-MS42	0.01	0.02	0.16
Cd_ppm	ME-4ACD81	0.5	2	1.6
Cd_ppm	ME-MS42	0.01	0.6	0.25
Ce_ppm	ME-MS42	0.02	0.87	1.1
Ce_ppm	ME-MS81	0.1	8.5	4.4
Co_ppm	ME-4ACD81	1	90	52
Co_ppm	ME-MS42	0.1	44	31.8
Cr_ppm	ME-MS81	10	330	300
Cs_ppm	ME-MS42	0.05	<0.05	<0.05
Cs_ppm	ME-MS81	0.01	0.14	0.12
Cu_ppm	ME-4ACD81	1	207	57
Cu_ppm	ME-MS42	0.2	177.5	45.3
Dy_ppm	ME-MS81	0.05	1.03	0.73
Er_ppm	ME-MS81	0.03	0.56	0.42
Eu_ppm	ME-MS81	0.03	0.30	0.15
Ga_ppm	ME-MS42	0.05	0.57	0.45
Ga_ppm	ME-MS81	0.01	7.9	5.6
Gd_ppm	ME-MS81	0.05	1.05	0.66
Hf_ppm	ME-MS42	0.02	1.01	0.88
Hf_ppm	ME-MS81	0.2	4.5	3.2
Hg_ppm	ME-MS42	0.005	<0.005	<0.005
Ho_ppm	ME-MS81	0.01	0.2	0.14
In_ppm	ME-MS42	0.005	0.007	0.008
La_ppm	ME-MS42	0.2	0.4	0.4
La_ppm	ME-MS81	0.1	3.6	1.8
Li_ppm	ME-4ACD81	10	<10	<10
Li_ppm	ME-MS42	0.1	0.8	1.5
Lu_ppm	ME-MS81	0.01	0.08	0.05
Mo_ppm	ME-4ACD81	1	8	6
Mo_ppm	ME-MS42	0.05	0.07	<0.05
Nb_ppm	ME-MS42	0.05	<0.05	<0.05
Nb_ppm	ME-MS81	0.2	35.5	74.4
Nd_ppm	ME-MS81	0.1	4.7	2.5
Ni_ppm	ME-4ACD81	1	174	110
Ni_ppm	ME-MS42	0.2	66.4	49.3
Pr_ppm	ME-MS81	0.03	1.12	0.56
Pb_ppm	ME-4ACD81	2	10	19
Pb_ppm	ME-MS42	0.2	4.1	14
Rb_ppm	ME-MS42	0.1	4.9	4.1
Rb_ppm	ME-MS81	0.2	1.5	1.4
Re_ppm	ME-MS42	0.001	<0.001	0.001
Sb_ppm	ME-MS42	0.05	0.06	<0.05
Sc_ppm	ME-4ACD81	1	29	17
Sc_ppm	ME-MS42	0.1	4	4.1
Se_ppm	ME-MS42	0.2	<0.2	<0.2
Sm_ppm	ME-MS81	0.03	1.21	0.68
Sn_ppm	ME-MS42	0.2	0.2	0.3
Sn_ppm	ME-MS81	1	1	1
Sr_ppm	ME-MS42	0.2	10.9	35.3
Sr_ppm	ME-MS81	0.1	39	55.6
Ta_ppm	ME-MS42	0.01	<0.01	<0.01
Ta_ppm	ME-MS81	0.1	7.3	14.3
Tb_ppm	ME-MS81	0.01	0.16	0.11
Te_ppm	ME-MS42	0.01	<0.01	<0.01
Th_ppm	ME-MS42	0.2	<0.2	<0.2
Th_ppm	ME-MS81	0.05	0.45	0.22
Tl_ppm	ME-4ACD81	10	<10	<10
Tl_ppm	ME-MS42	0.02	<0.02	0.03
Tm_ppm	ME-MS81	0.01	0.08	0.05
U_ppm	ME-MS42	0.05	<0.05	<0.05
U_ppm	ME-MS81	0.05	0.13	0.08
V_ppm	ME-MS81	5	672	1140
W_ppm	ME-MS42	0.05	<0.05	<0.05
W_ppm	ME-MS81	1	2	2
Y_ppm	ME-MS42	0.05	0.52	0.51
Y_ppm	ME-MS81	0.1	4.8	3.5
Yb_ppm	ME-MS81	0.03	0.58	0.39
Zn_ppm	ME-4ACD81	2	435	303
Zr_ppm	ME-MS42	0.5	38.3	32
Zr_ppm	ME-MS81	2	154	110

Relative results for two-stage leach samples 1802-L19R (ML-77) and 1802-L20R (ML-78) in terms of selected trace element compositions are described below:

- As: Higher in sample 1802-L20R (ML-78, 11 ppm) than in sample 1802-L19R (ML-77, 5 ppm) using analytical method ME-4ACD81; equivalent in both samples (<0.1 ppm) using analytical method ME-MS42
- Co: Higher in sample 1802-L19R (ML-77, 90 ppm) than sample 1802-L20R (ML-78, 52 ppm) using analytical method ME-4ACD81; higher in sample 1802-L19R (ML-77, 44ppm) than sample 1802-L20R (ML-78, 31.8 ppm) using analytical method ME-MS42
- Cr: Higher in sample 1802-L19R (ML-77, 330 ppm) than in sample 1802-L20R (ML-78, 300 ppm) using analytical method ME-MS81
- Cu: Higher in sample 1802-L19R (ML-77, 207 ppm) than in sample 1802-L20R (ML-78, 57 ppm) using analytical method ME-4ACD81; higher in sample 1802-L19R (ML-77, 177.5 ppm) than in sample 1802-L20R (ML-78, 45.3 ppm) using analytical method ME-MS42
- Nb: Equivalent (<0.05 ppm) in samples 1802-L19R (ML-77) and 1802-L20R (ML-78) using analytical method ME-MS42; higher in sample 1802-L20R (ML-78, 74.4 ppm) than in sample 1802-L19R (ML-77, 35.5 ppm) using analytical method ME-MS81
- Ni: Higher in sample 1802-L19R (ML-77, 174 ppm) than in sample 1802-L20R (ML-78, 110 ppm) using analytical method ME-4ACD81; higher in sample 1802-L19R (ML-77, 66.4 ppm) than sample 1802-L20R (ML-78, 49.3 ppm) using analytical method ME-MS42
- Pb: Higher in sample 1802-L20R (ML-78, 19 ppm) than in sample 1802-L19R (ML-77, 10 ppm) using analytical method ME-4ACD81; higher in sample 1802-L20R (ML-78, 14 ppm) than sample 1802-L19R (ML-77, 4.1 ppm) using analytical method ME-MS42
- Sb: Higher in sample 1802-L19R (ML-77, 0.06 ppm) than sample 1802-L20R (ML-78, <0.05 ppm) using analytical method ME-MS42
- Ta: Equivalent (<0.01 ppm) in samples 1802-L19R (ML-77) and 1802-L20R (ML-78) using analytical method ME-MS42; higher in sample 1802-L20R (ML-78, 14.3 ppm) than sample 1802-L19R (ML-77, 7.3 ppm) using analytical method ME-MS81
- V: Higher in sample 1802-L20R (ML-78, 1140 ppm) than sample 1802-l19R (ML-77, 672 ppm) using analytical method ME-MS81

Figure 99A is a chondrite-normalized rare earth element plot for Campaign 1 leach residues (sample BL-10 (ML-71) that have not been recycled. As indicated in the diagram, all rare earth elements are slightly enriched (approximately 2.5–10 times) relative to chondritic values, with the light rare earth elements being slightly more enriched relative to the heavy rare earth elements.

Figure 99B is a primitive mantle-normalized spider diagram for Campaign 1 leach residues (sample BL-10 (ML-71) that have not been recycled. All of these trace elements have concentrations that are equivalent to or enriched relative to primitive mantle-normalized values with the exception of scandium. Trace elements with the highest enrichments relative to primitive mantle values (Sun and McDonough, 1989; Kerrich and Wyman, 1996) are niobium (30–40 times normalizing values), zirconium (10–20 times normalizing values), hafnium (10–20 times normalizing values), titanium (60–70 times normalizing values), aluminum (approximately 3 times normalizing values), and vanadium (6–7 times normalizing values).

Figure 100A is a chondrite-normalized rare earth element plot for single-stage leach residues associated with Campaign 2 (BL-6 (ML-70), half-recycled) and Campaign 3 ((BL-19, ML-72) recycled). Results are similar to the Campaign 1 leach residue results, with all rare earth elements being slightly enriched (approximately 2–20 times) relative to chondritic values. The Campaign 2 half-recycled sample consistently is enriched in rare earth elements relative to the Campaign 3 recycled sample. As with the Campaign 1 leach residues, the light rare earth elements are relatively enriched relative to the heavy rare earth elements in both the Campaign 2 and Campaign 3 samples.

Figure 100B is a primitive mantle-normalized spider diagram for single-stage leach residues associated with Campaign 2 (half-recycled) and Campaign 3 (recycled). Both samples illustrate similar primitive mantle-normalized trends, with the Campaign 2 (half-recycled) samples generally having higher primitive mantle-normalized trace element values with the exceptions of niobium, zirconium, halfnium, titanium, and vanadium. For the Campaign 2 (half-recycled) sample, nearly all these trace elements have concentrations that are equivalent to, or enriched, relative to primitive mantle-normalized values with the exception of dysprosium, yttrium, erbium, ytterbium, and scandium. The most enriched trace elements relative to primitive mantle values (Sun and McDonough, 1989; Kerrich and Wyman, 1996) are niobium (40–50 times normalizing values), zirconium (10–20 times normalizing values), hafnium (10–20 times normalizing values), titanium (100–200 times normalizing values), aluminum (approximately 3 times normalizing values), and vanadium (approximately 10 times normalizing values).

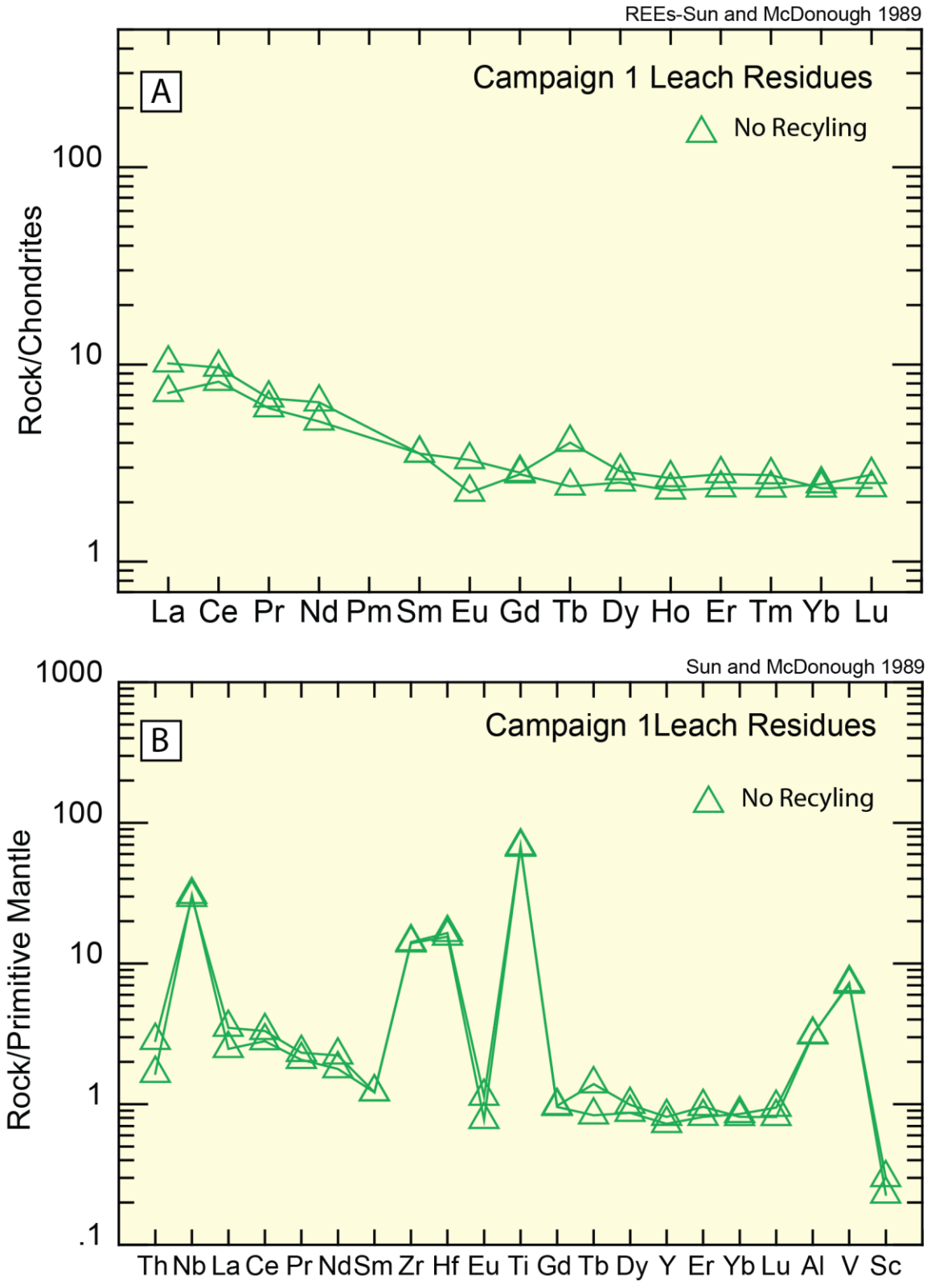

Figure 99. Chondrite- and primitive mantle-normalized spider diagrams for Campaign 1 leach residues (no recycling). A) Chondrite-normalized rare earth element diagram. B) Primitive mantle-normalized spider diagram. Chondrite- and primitive mantle-normalizing values from Sun and McDonough (1989) and Kerrich and Wyman (1996).

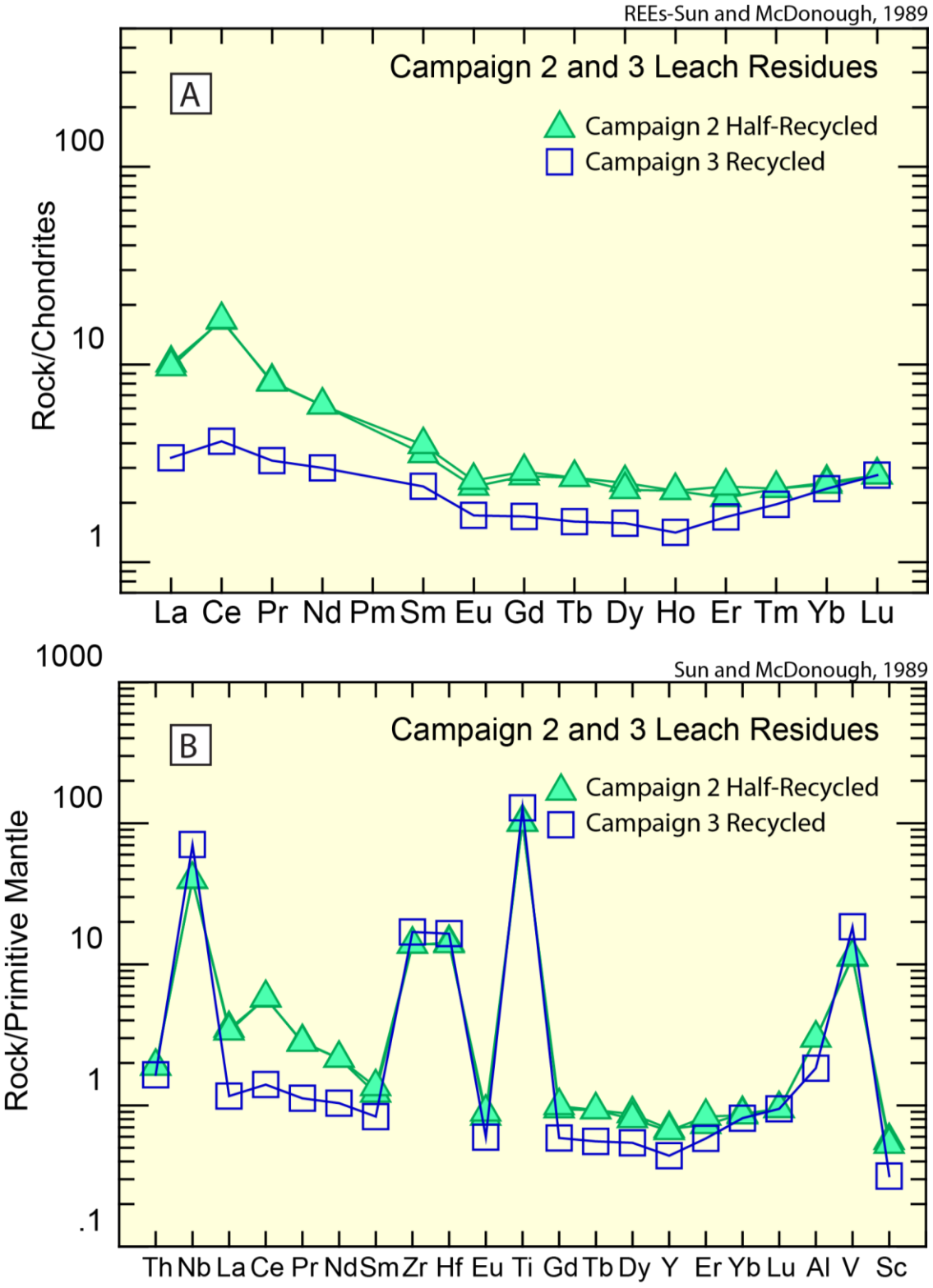

Figure 100. Chondrite- and primitive mantle-normalized spider diagrams compaing Campaign 2 and Campaign 3 leach residues (1802-BL6 (ML-70, Campaign 2, half-recycled) and sample 1802-BL-19 (ML-72, Campaign 3, recycled). A) Chondrite-normalized rare earth element diagram. B) Primitive mantle-normalized spider diagram. Chondrite- and primitive mantle-normalizing values from Sun and McDonough (1989) and Kerrich and Wyman (1996).

Figure 101A is a chondrite-normalized rare earth element plot comparing the concentrations of rare earth elements in the Campaign 3 recycled sample (BL-19 (ML-72)) with the concentrations of rare earth elements in the Campaign 3 reground and two-stage leach residues (L19R (ML-77) and L20R (ML-78)). Both Campaign 3 sample types are enriched in rare earth elements (~2–15 times) relative to chondrite-normalizing values, with the light rare earth elements being slightly enriched relative to the heavy rare earth elements. The reground, two-stage leach samples have higher chondrite-normalized rare earth element values than the single-stage leach residues.

Figure 101B is a primitive mantle-normalized spider diagram comparing the concentrations of rare earth elements in the single-stage leach sample with the concentrations of rare earth elements in the recycled, reground two-stage leach residues. In general, primitive mantle-normalized values in the reground, two-stage leach residues are higher than those in the single-stage leach residues with the exceptions of zirconium, vanadium, and scandium. Both types of Campaign 3 leach residues are enriched in niobium (50–100 times normalizing values), zirconium (10–20 times normalizing values), hafnium (10–20 times normalizing values), titanium (100–200 times normalizing values), aluminum (2–5 times normalizing values), and vanadium (7–20 times normalizing values).

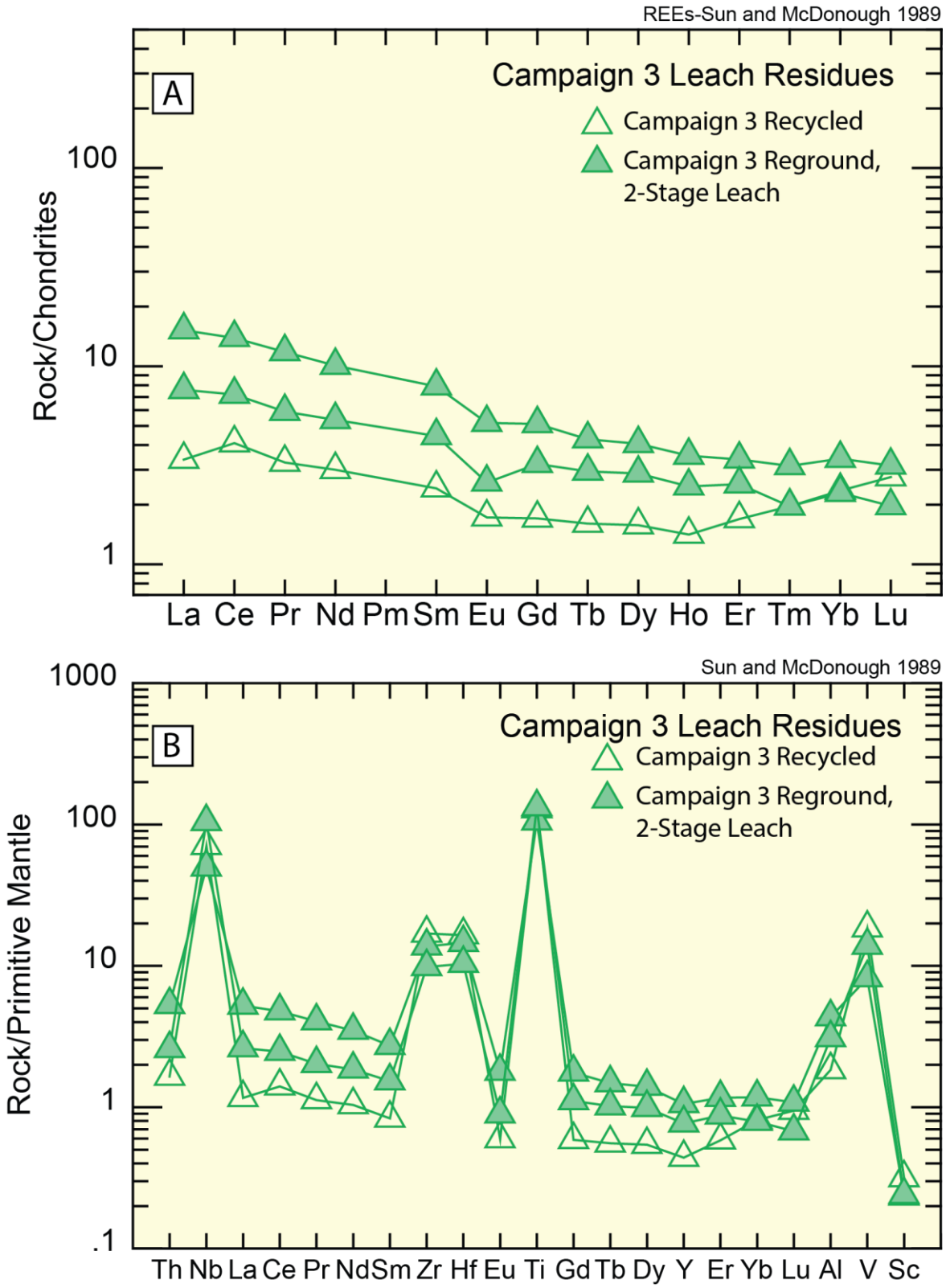

Figure 101. Chondrite- and primitive mantle normalized spider diagrams for Campaign 3 recycled and reground and two-stage leach residues, respectively. A) Chondrite-normalized rare earth element diagram. B) Primitive mantle-normalized spider diagram. Chondrite- and primitive mantle-normalizing values from Sun and McDonough (1989) and Kerrich and Wyman (1996).

Environmental Testing

Solid leach residues from the mini pilot were collected and analyzed to determine their composition. Selected bulk samples from each campaign and a sample that had undergone re-leach testing was submitted for Ontario regulation 558, metals and inorganics testing, by a third party to determine if it met environmental standards. By using the PRO mixed chloride leaching process, the tailings produced are environmentally inert (as shown in Table 89 and Table 90), as they are below the guideline/standard levels in all cases. When compared with Minnesota Rules 7045.0131 Characteristics of Hazardous Waste (revisor.mn.gov/rules/78045.0131), the results obtained for the campaign 1, 2, and 3 residues—as well as the Campaign 3 ground residue—are below the maximum concentrations listed for arsenic, barium, cadmium, chromium, lead, mercury, selenium, and silver. No maximum concentrations are indicated for boron, uranium, flouride, cyanide or (nitrate/nitrite) as N leachate in Minnesota Rules 7045.0131.

Table 89. TCLP. O. Reg. 558 Metals and Inorganics test on residue of campaigns 1, 2, and 3.

Sample Description				**BLR 06 Campaign 2**	**BLR 10 Campaign 1**	**BLR19 Campaign 3**
				Date Sampled		
				05/29/2019	**05/29/2019**	**05/29/2019**
Parameter	**Unit**	**G / S**	**RDL**	**240600**	**240633**	**240634**
Arsenic Leachate	mg/L	2.5	0.010	0.014	<0.010	<0.010
Barium Leachate	mg/L	100	0.100	0.165	0.178	0.516
Boron Leachate	mg/L	500	0.050	0.315	0.306	0.080
Cadmium Leachate	mg/L	0.5	0.010	<0.010	<0.010	<0.010
Chromium Leachate	mg/L	5	0.010	0.033	0.030	0.093
Lead Leachate	mg/L	5	0.010	<0.010	<0.010	<0.010
Mercury Leachate	mg/L	0.1	0.01	<0.01	<0.01	<0.01
Selenium Leachate	mg/L	1	0.010	0.070	0.033	0.010
Silver Leachate	mg/L	5	0.010	<0.010	<0.010	<0.010
Uranium Leachate	mg/L	10	0.050	<0.050	<0.050	<0.050
Fluoride Leachate	mg/L	150	0.05	<0.05	0.15	<0.05
Cyanide Leachate	mg/L	20	0.05	<0.05	<0.05	<0.05
(Nitrate + Nitrite) as N Leachate	mg/L	1000	0.70	<0.70	<0.70	<0.70
Comments: RDL - Reported Detection Limit; G / S - Guideline / Standard						

Table 90. TCLP. O. Reg. 558 Metals and Inorganics test on the residue of Campaign 3 ground residue re-leached.

Sample Description				19-0048 (BLRR20) Campaign 3
				Date Sampled 07/05/2019
Parameter	**Unit**	**G / S**	**RDL**	**334743**
Arsenic Leachate	mg/L	2.5	0.010	<0.010
Barium Leachate	mg/L	100	0.100	0.136
Boron Leachate	mg/L	500	0.050	0.278
Cadmium Leachate	mg/L	0.5	0.010	<0.010
Chromium Leachate	mg/L	5	0.010	0.022
Lead Leachate	mg/L	5	0.010	<0.010
Mercury Leachate	mg/L	0.1	0.01	<0.01
Selenium Leachate	mg/L	1	0.010	0.077
Silver Leachate	mg/L	5	0.010	<0.010
Uranium Leachate	mg/L	10	0.050	<0.050
Fluoride Leachate	mg/L	150	0.05	<0.05
Cyanide Leachate	mg/L	20	0.05	<0.05
(Nitrate + Nitrite) as N Leachate	mg/L	1000	0.70	<0.70
Comments: RDL - Reported Detection Limit; G / S - Guideline / Standard				

MASS BALANCE

Based on the data obtained during the operation of the mini-pilot circuit, a mass balance of the overall flowsheet was calculated. An ore flowrate of 1 tph was used for the calculations. Summaries of the main process steps are presented below and in Figures 102a through 102g.

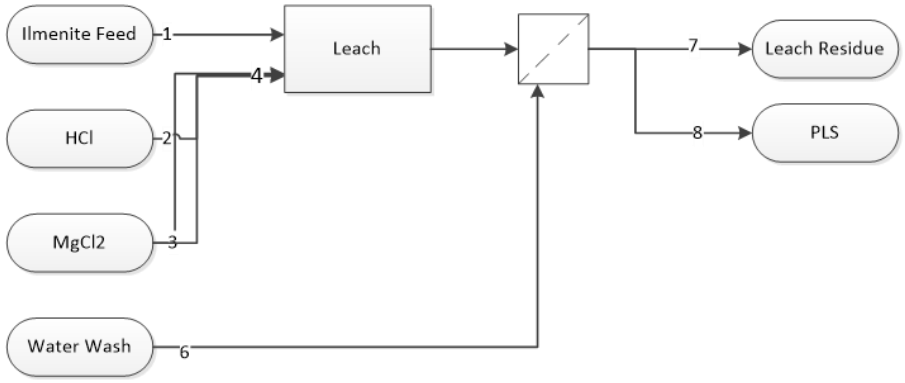

	Steam 1	Stream 2	Stream 3	Stream 4	Stream 5	Stream 6	Stream 7	Stream 8
	Ore	Hcl	MgCl2	Lixiviant	PLS	Water Wash	Leach Residue	Fiiltrate pls
Temperature (C)	ambient	ambient	ambient	ambient	70	ambient	35	35
Pressure (bar)	1	1	1	1	1	1	1	1
Mass Flowrate (tonne/h)	1.000	1.629	1.692	9.000		0.239	0.285	9.522
Mass Flowrate (M3/h)	0.514	1.357	0.729	7.200		0.335	0.119	7.439
Density	1.944	1.2	2.32	1.25		1	2.389	1.28
HCl (N)	0	5.8	0	6.2217		0	0	2
Ti (g/l)	442.56	0	0	0		0	0	26.797
Fe (g/l)	588.00	0	0	0		0	0	34.908
Mg (g/l)	79.14	0	55.5257	5.62539		0	0	63.192
Mn (g/l)	4.53	0	0	0		0	0	0.278
V (g/l)	2.92	0	0	0		0	0	0.168

Figure 102a. Mass balance.

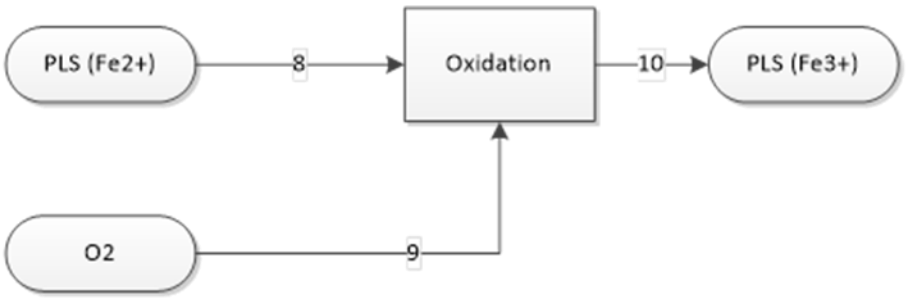

	Stream 8	Stream 9	Stream 10
	PLS	O2	Oxidized PLS
Temperature (C)	ambient	ambient	ambient
Pressure (bar)	1	1	1
Mass Flowrate (tonne/h)	9.522	0.024	9.522
Mass Flowrate (M3/h)	7.439		7.439
Density	1.280		1.280

Figure 102b. Mass balance (continued).

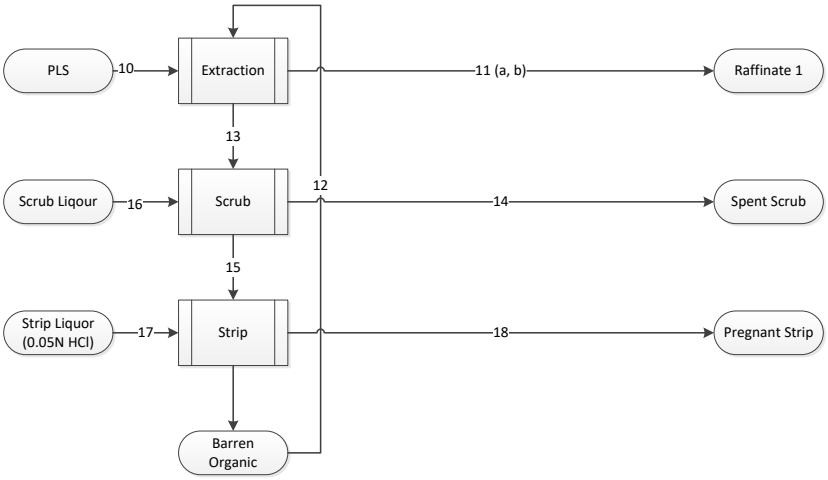

	Stream 10	Stream 11	Stream 12	Stream 13	Stream 14	Stream 15	Stream 16	Stream 17	Stream 18
	Oxidised PLS	Fe Raffinate	Fresh Organic	Loaded Organic	Scrub Liquor	Refined Organic	Scrub Solution	Barren Strip Solution	Fe Preg Strip
Temperature (C)	ambient	ambient	ambient	ambient	ambient	ambient	ambient	ambient	ambient
Pressure (bar)	1	1	1	1	1	1	1	1	1
Mass Flowrate (tonne/h)	9.522	9.299	9.038	9.150	0.922	9.485	0.945	2.029	2.556
Mass Flowrate (M3/h)	7.439	7.439	11.158	11.158	0.744	11.158	0.744	2.029	2.029
Density	1.28	1.25	0.81	0.82	1.24	0.85	1.27	1	1.26
HCl (N)	1.60	1.20	0.00	0.27	0.05	0.27	0.05	0.05	1.52
Ti (g/l)	26.787	26.787	0.000	0.170	0.170	0.170	2.550	0.000	0.935
Fe (g/l)	34.908	0.348	0.000	23.039	51.692	23.039	51.692	0.000	126.716
Mg (g/l)	63.182	63.182	0.470	0.047	0.047	0.047	0.700	0.000	0.257
Mn (g/l)	0.278	0.278	0.000	0.078	0.078	0.078	1.170	0.000	0.429
V (g/l)	0.168	0.168	0.000	0.035	0.035	0.035	0.531	0.000	0.195

Figure 102c. Mass balance (continued).

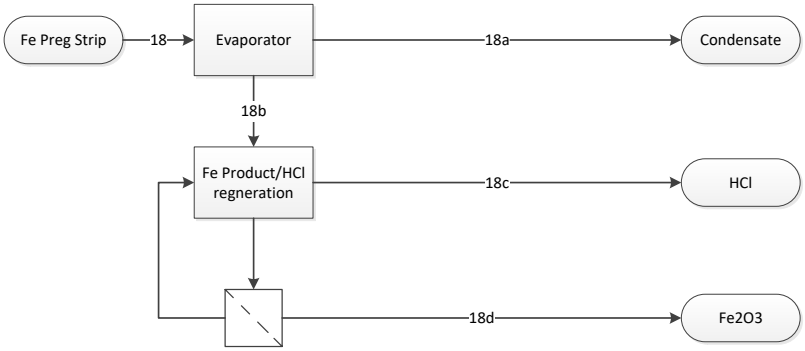

	Steam 18	Stream 18a	Stream 18b	Stream 18c	Stream 18d
	Fe preg strip	Condensate	Fe preg strip out	Filtrate	Fe2O3 cake
Temperature (C)	ambient	ambient	ambient	ambient	ambient
Pressure (bar)	1	1	1	1	1
Mass Flowrate (tonne/h)	2.556	0.869	1.687	1.320	0.367
Mass Flowrate (M3/h)	2.029	0.852	1.205	1.263	
Density	1.260	1.020	1.400	1.045	
HCl (N)	1.517	2.000	1.139	1.131	
Ti (g/l)	0.935	0.000	1.574	1.502	
Fe (g/l)	126.716	0.000	213.327	2.035	
Mg (g/l)	0.257	0.000	0.432	0.412	
Mn (g/l)	0.429	0.000	0.722	0.689	
V (g/l)	0.195	0.000	0.328	0.313	

Figure 102d. Mass balance (continued).

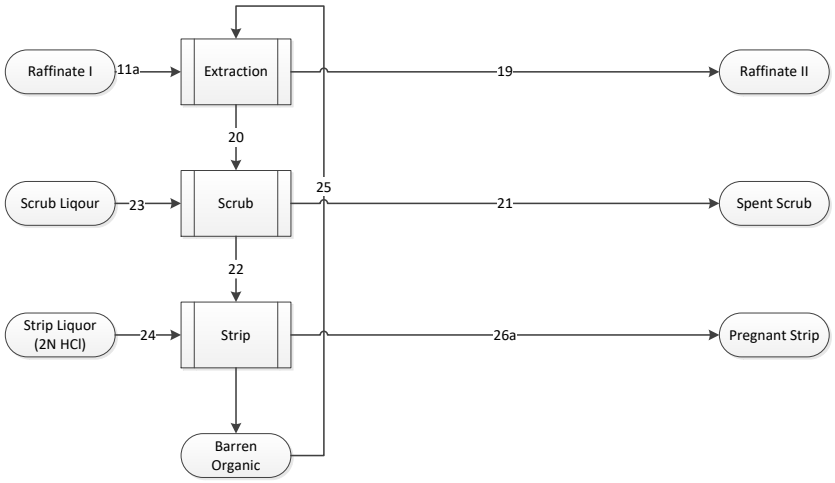

	Stream 11a	Stream 11b	Stream 19	Stream 20	Stream 21	Stream 22	Stream 23	Stream 24	Stream 25	Stream 26a	Stream 26b	Stream 26b
	Fe Raffinate	Fe Raffinate	Ti Raffinate	Loaded Organic	Scrub Liquor	Refined Organic	Scrub Solution	Barren Strip Solution	Fresh Organic	Ti Preg Strip	Ti Preg Strip	Ti Preg Strip
Temperature (C)	ambient	ambient	35 35	35 35	35	35	35	35 ambient	ambient	35	35 35	35
Pressure (bar)	1 1	1 1	1 1	1 1	1	1	1	1 1	1	1 1	1 1	1
Mass Flowrate (tonne/h)	9.299	1.302	9.075 9.075	17.705 17.705	2.499 2.499	18.121 18.121	2.499 2.499	4.291 4.291	17.496	17.496 3.799	3.799 0.950	0.950
Mass Flowrate (M3/h)	7.439	1.041	7.439 7.439	20.829 20.829	2.083 2.083	20.829 20.829	2.083 2.083	4.166 4.166	20.829	20.829 3.333	3.333 0.833	0.833
Density	1.250	1.250	1.220 1.220	0.850 0.850	1.200 1.200	0.870 0.870	1.200 1.200	1.030 1.030	0.840	0.840 1.140	1.140 1.140	1.140
HCl (N)	1.200	1.200	1.000 1.000	0.071 0.071	2.036 2.036	0.071 0.071	2.036 2.036	2.000 2.000	0.000	0.000 2.357	2.357 2.357	2.357
Ti (g/l)	26.797	26.797	0.000 0.000	9.570 9.570	37.085 37.085	9.570 9.570	37.085 37.085	0.000 0.000	0.000	0.000 47.373	47.373 47.373	47.373
Fe (g/l)	0.449	0.449	0.209 0.209	0.046 0.046	0.289 0.289	0.046 0.046	0.289 0.289	0.000 0.000	0.000	0.000 0.228	0.228 0.228	0.228
Mg (g/l)	63.192	63.192	63.192 63.192	0.520 0.520	32.896 32.896	0.520 0.520	32.896 32.896	0.000 0.000	0.000	0.000 2.600	2.600 2.600	2.600
Mn (g/l)	0.278	0.278	0.236 0.236	0.153 0.153	0.522 0.522	0.153 0.153	0.522 0.522	0.000 0.000	0.000	0.000 0.765	0.765 0.765	0.765
V (g/l)	0.168	0.168	0.152 0.152	0.156 0.156	0.474 0.474	0.156 0.156	0.474 0.474	0.000 0.000	0.000	0.000 0.780	0.780 0.780	0.780

Figure 102e. Mass balance (continued).

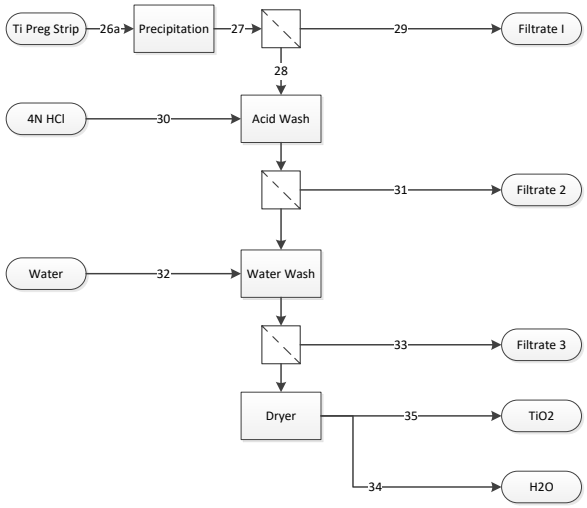

	Stream 26a	Stream 27	Stream 28	Stream 29	Stream 30	Stream 31	Stream 32	Stream 33	Stream 34	Stream 35	Stream 36
	Ti Preg Strip	Slurry	Cake1	Filtrate 1	Acid Wash	Filtrate 2	Wash Water	Filtrate 3	H2O vapor	Dry TiO2 product	Total Filtrate
Temperature (C)	ambient	80	ambient	ambient	ambient	ambient	ambient	ambient		ambient	ambient
Pressure (bar)	1		1	1	1	1	1	1		1	1
Mass Flowrate (tonne/h)	3.799	3.799	0.407	4.342	0.122	0.122	0.116	0.116	0.122	0.475	4.580
Mass Flowrate (M3/h)	3.333	3.333	0.116	3.618	0.116	0.116	0.116	0.116	0.122		3.817
Density	1.140	1.140	3.500	1.200	1.050	1.100	1.000	1.000	1.000		1.200
HCl (N)	2.357	2.357	0.675	4.959	4.000	4.000	0.000	1.200	0.000		4.860
Ti (g/l)	47.373	47.373	47.326	0.047	0.000	0.480	0.000	0.075	0.000		0.061
Fe (g/l)	0.228	0.228	8.167	0.000	0.000	0.000	0.000	0.000	0.000		0.000
Mg (g/l)	2.600	2.600	8.096	2.755	0.000	0.090	0.000	0.000	0.000		2.591
Mn (g/l)	0.765	0.765	23.084	0.140	0.000	0.000	0.000	0.000	0.000		0.132
V (g/l)	0.780	0.780	26.859	0.035	0.000	0.000	0.000	0.000	0.000		0.033

Figure 102f. Mass balance (continued).

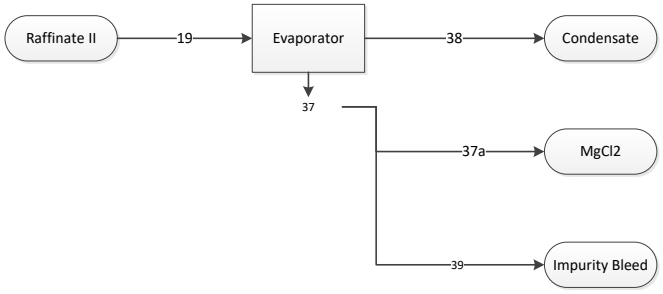

	Stream 19	37 Stream 37	Stream 37a	Stream 39	Stream 38
	Ti Raffinate II	Raffinate Output	Raffinate to Leach	Impurity Bleed	Condensate
Temperature (C)	ambient	ambient	ambient	ambient	ambient
Pressure (bar)	1	1	1	1	1
Mass Flowrate (tonne/h)	9.075	5.445	4.999	0.447	3.630
Mass Flowrate (m3/h)	7.439	3.835	3.520	0.314	3.559
Density	1.220	1.420	1.420	1.420	1.020
Density	1.000	0.919	0.919	0.919	1.420
HCl (N)	1.000	0.919	0.919	0.919	1.100
Ti (g/l)	0.000	0.000	0.000	0.000	0.000
Fe (g/l)	0.209	0.406	0.406	0.406	0.000
Mg (g/l)	63.192	122.585	122.585	122.585	0.000
Mn (g/l)	0.236	0.459	0.459	0.459	0.000
V (g/l)	0.152	0.294	0.294	0.294	0.000
Al (g/l)	0.448	0.869	0.869	0.869	0.000
Ca (g/l)	0.384	0.744	0.744	0.744	0.000
Cr (g/l)	0.101	0.196	0.196	0.196	0.000
MgCl2 (tph)	0.000	1.844	1.692	0.151	0.000

Figure 102g. Mass balance (continued).

Feed

The feed assumed for this exercise is milled ore. The ore most probably also contains other elements such as sodium and potassium, but in this work those were ignored. The mineral suite shown was calculated by searching for plausible minerals and mineral proportions that back-calculated the measured elemental analysis of the sample taken as the feed.

Model

The CTL Process entails leaching; iron solvent extraction; titanium solvent extraction, hydrolysis and calcination; iron hydro-hydrolysis/acid recovery; and Ti raffinate evaporation/impurity bleed.

The information upon which the mineralogical composition of the feed and the extractions in the leach are based was taken from laboratory work done on a sample of the ore in question.

Leach

The incoming ore (stream 1) is leached with hydrochloric acid (stream 2) and brine containing magnesium chloride (stream 3) at a solids content of 10% wt. The reaction stoichiometry and extent of the stoichiometric reaction are listed in Table 91. The leached slurry is filtered and the filter cake is washed with water (stream 6). The washed residue (stream 7) leaves the circuit.

Table 91. Leach.

Stoichiometry	Extent of Stoichiometric Reaction
$FeV_2O_4 + 2Fe^{3+} + 4HCl \rightarrow 3Fe^{2+} + 2VO^{2+} + 4Cl^- + 2H_2O$	1.000
$FeTiO_3 + 4HCl \rightarrow Fe^{2+} + TiOCl_2 + 2Cl^- + 2H_2O$	1.000
$Fe_2TiO_4 + 6HCl \rightarrow 2Fe^{2+} + TiOCl_2 + 4Cl^- + 3H_2O$	1.000
$Fe_3O_4 + 8HCl \rightarrow Fe^{2+} + 2Fe^{3+} + 8Cl^- + 4H_2O$	0.114
$MgAl_2O_4 + 8HCl \rightarrow Mg^{2+} + 2Al^{3+} + 8Cl^- + 4H_2O$	0.000
$FeAl_2O_4 + 8HCl \rightarrow Fe^{2+} + 2Al^{3+} + 8Cl^- + 4H_2O$	0.210
$Mn_3O_4 + 8HCl + 2Fe^{2+} \rightarrow 2Fe^{3+} + 3Mn^{2+} + 8Cl^- + 4H_2O$	0.095
$MgO + 2HCl \rightarrow Mg^{2+} + 2Cl^- + H_2O$	0.500
$CaO + 2HCl \rightarrow Ca^{2+} + 2Cl^- + H_2O$	0.096

Oxidation

The PLS contains iron primarily in the form of Fe^{2+}, which must be oxidized to Fe^{3+} to be amenable to the organic extractant used in Fe SX. Oxygen is sparged into the solution (stream 9), and conversion efficiency was taken as 100%. The oxidized PLS (stream 10) then proceeds to Fe removal.

Iron Removal

The filtrate from the leach filter (stream 10) is subjected to solvent extraction to remove ferric chloride. The resulting raffinate (stream 11) proceeds to the titanium recovery section. The loaded organic solvent is stripped with 0.05M HCl in water (stream 17). Table 92 shows the overall stoichiometry used to represent the solvent extraction of iron.

Table 92. Iron removal.

Stoichiometry		Extent of Stoichiometric Reaction
Extraction	$Fe^{3+} + 3Cl^- \rightarrow \mathbf{FeCl_3}$	1.000
Stripping	$\mathbf{FeCl_3} \rightarrow Fe^{3+} + 3Cl^-$	1.000

The loaded strip liquor (stream 18) is then processed in the Fe recovery stage.

Iron Recovery

The pregnant Fe strip solution is evaporated from ~100 g/L to ~200 g/L total iron. For energy efficiency, a two-stage evaporation sequence is recommended. The condensate (stream 18a) is used as part of the strip solution going to the titanium solvent extraction stage. The concentrated Fe strip solution is sent to the reactor where HCl is produced (stream 18c) and iron oxide is formed (stream 18d).

Titanium Recovery

Solvent extraction is used to remove titanium from the raffinate (stream 11a) from the iron solvent extraction step. The loaded solvent is stripped with aqueous hydrochloric acid (stream 24), such that the loaded strip solution contains ~50 g/L Ti and 2M HCl. The strip solution is made up from process water and recycled hydrochloric acid from the Ti precipitation step. The loaded strip solution (stream 26a) is heated to 95°C, causing the titanium to hydrolyze and precipitate as hydrated titanium dioxide. The resulting slurry (stream 28) is filtered, and the filter cake is washed several times and is calcined to titanium dioxide (stream 35) that leaves the circuit as a product. The filtrates (streams 29, 31, and 33) are reused in areas that require HCl.

Raffinate Recycle

The raffinate from the titanium solvent extraction step (stream 19) is evaporated to control the volume of solution being recycled. The resulting hydrochloric acid and steam (stream 38) is condensed to produce a dilute HCl stream that can be used in the process as strip solution.

The concentrated solution (stream 37) is split into a $MgCl_2$ recycle stream to the leach (stream 37a) and an impurity bleed stream (stream 39).

Numerical Results

The process model was used to generate a mass balance representing the application of the CTL Process to the feed in question.

Leach

The process model produced the leach numbers listed in Table 93.

Table 93. Predicted leach data.

Dry ore into the circuit, t/h	1.00
Solids into the leach, mass %	10
Total HCl to leach, tph	1.6
$MgCl_2$ in lixiviant to leach, g/L	220
HCl in $MgCl_2$ lixiviant to leach, M	0.12
HCl in recovered acid to leach, tph	0.56
Recycled HCl in Other streams, tph	0.13
HCl Make up Requirement, tph	0.94
HCl consumption, t/t ore	1.09
Residual HCl ex leach, g/L	73

Solvent Extraction

Table 94 lists the concentrations of iron, titanium, and vanadium into and out of the respective solvent extraction stages of the circuit.

Table 94. Solvent extraction data, g/L.

Fe in feed to Iron SX	34.9
Fe in loaded strip ex Iron SX	126.7
Fe in evaporated srip ex Iron SX	213.3
Ti in feed to Titanium SX	26.8
Ti in strip ex Titanium SX	47.4

Acid Recovery

Table 95 lists the numbers predicted for the acid recovery section. Many of the streams produce dilute HCl and cannot be cycled back into the leach due to water balance. As the flowsheet is currently set up, the Fe product recovery and HCl regeneration filtrate and a portion of the TiO_2 precipitation filtrate can be utilized with the balance made up of fresh acid. Determination of the recycled lixiviant makeup is presented in Table 96.

Table 95. Acid recovery.

Inputs(TPH)	**Components (tph)** HCl	Water
Lixiviant	1.629	5.679
Leaching residue wash water	0	0.239
Fe strip solution	0.004	2.025
Ti strip solution	0.304	3.994
TiO_2 precipitation acid wash	0.017	0.099
TiO_2 precipitation water wash	0.000	0.116
Total	1.953	12.036
Outputs (TPH)		
Fe evap Condensate	0.062	0.807
Fe product/HCl regen filtrate	0.559	0.761
Ti evap condensate	0.143	2.829
Ti raffinate output	0.129	2.995
TiO_2 precipitation total filtrate	0.677	3.903
Total	1.570	11.294

Table 96. Makeup acid requirement.

		Components (tph)		
Inputs(TPH)	**Utilization**	**HCl**	**Water**	**MgCl2**
Lixiviant		1.629	5.679	1.69
Recovered Streams				
HCl regeneration	1	0.559	0.761	
Ti PPT Filtrate	0.02	0.015	0.086	
Ti Raff Evap	1	0.118	2.749	1.69
Recovered Streams Total		0.693	3.596	
Makeup HCl Required		0.936	2.083	
Final		1.629	5.679	1.69

Production

Table 97 lists the products from the circuit as calculated by the process model.

Table 97. Results of lithogeochemical analyses on two-stage leach residues.

Products	Tonnes/Hour
100% TiO_2	0.47
100%Fe_2O_3	0.37
Leach residue	0.29
Bleed	0.45

OVERALL FLOWSHEET

The overall hydrometallurgical process flowsheet developed in this program for the treatment of Minnesota ilmenite is presented in Figure 103. A visual representation of the various process streams is shown in Figure 104.

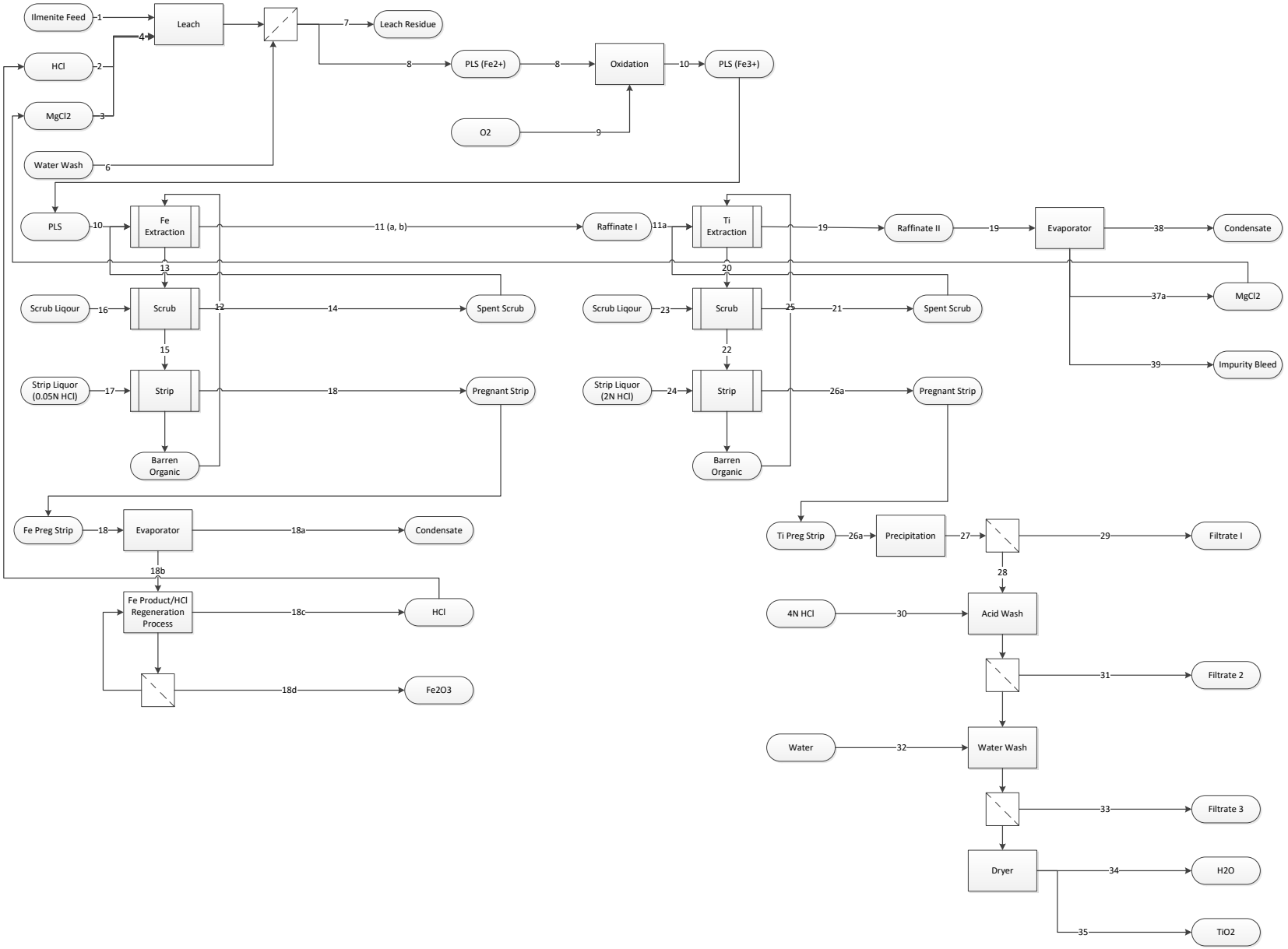

Figure 103. PRO TiO2 process flowsheet.

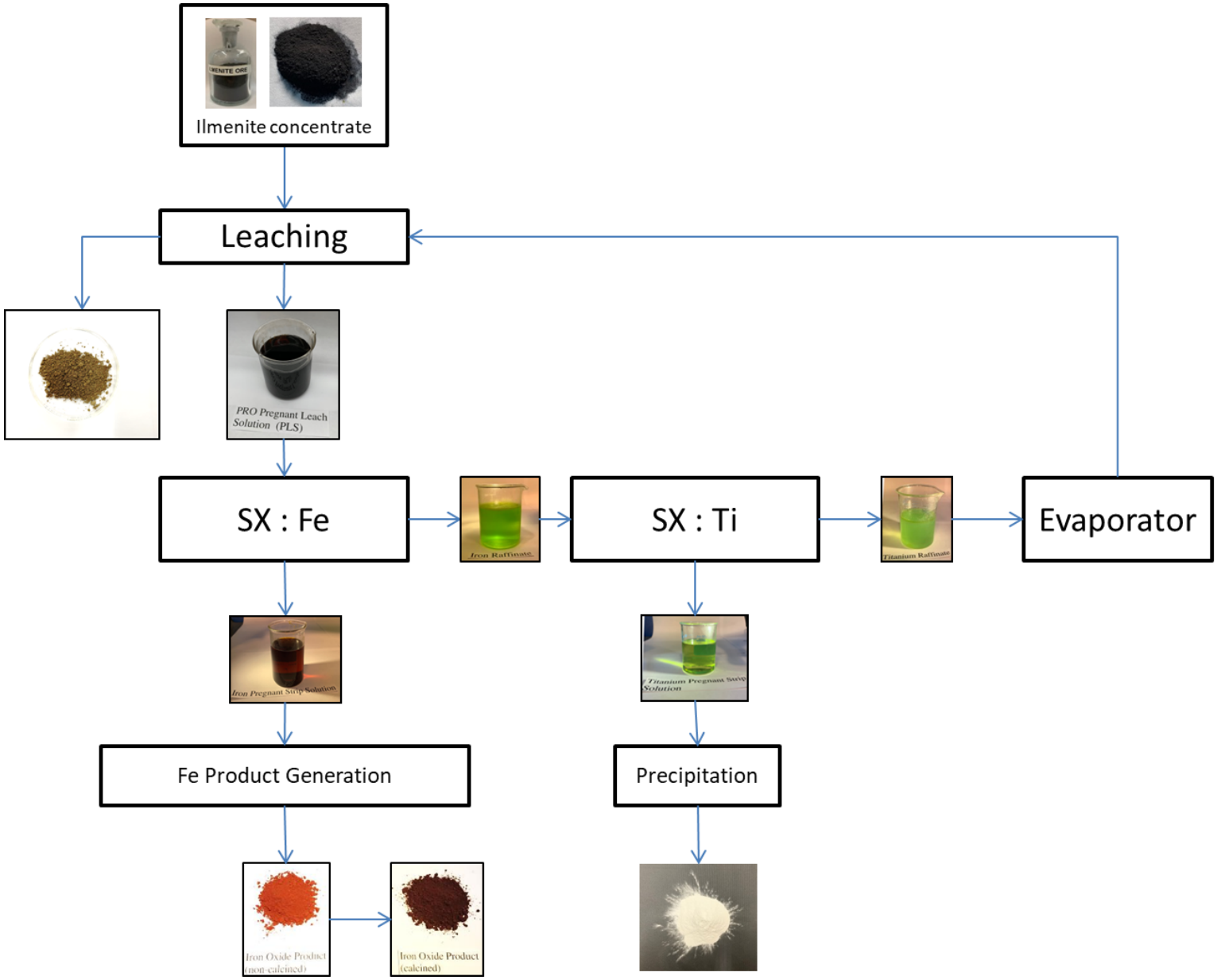

Figure 104. Process solutions and solids.

PROCESS BENCHMARKING

The CTL process was benchmarked against existing process technologies according to some of the major process parameters and are presented in Table 98.

Table 98. Benchmarking of CTL process to major competitors.

Parameter	Chloride	Sulphate	CTL	Upgraded Slag
Raw material	High cost	Low cost	Lowest cost	Medium Cost
($/ton of TiO_2 feed)	($2000 +)	Ilmenite ($250)	Ilmenite ($250)	Ilmenite ($250)
TiO_2 product	High value	Low value	High value	Low Value intermediate
($/ton of TiO_2)	+$3000		+$3000	
Capex	Highest (including front-end)	Medium	Lowest	Medium
Opex	Highest (including front-end)	Medium	Lowest	Medium
Environmental	Medium challenges	Major challenges	Most environmentally friendly	Medium challenges
Raw material	High cost, rutile	Low cost, ilmenite	Lower cost, ilmenite	Low cost, ilmenite
Flexibility in processing raw material	Limitation (Mn, Mg, size)	Limitation (Cr, V)	Can process (Flexible)	Limitation on Ca, Mg content
Process Condition	High Temp. Chlorine (800-1000°C)	High Temp. (140-180°C)	Atmospheric Mixed Chloride (70°C)	High temp. (1600°C)
Technology	Old	Old	Patented, New	Old
End to end in one location	Not practiced	Possible	Possible	Not practiced
Pigment production	Rutile	Rutile/Anatase	Rutile/Anatase	
Commercially Proven process	In practice	In practice	In Development	In practice
Environmental challenges	Disposal of iron and other byproduct chlorides	Disposal of large iron sulphate product and dilute acid	Minimum environmental impact, Iron oxide as byproduct Inert residue	Intermediate process to either sulphate or chloride processes
Safety Requirements	High (Cl_2 at high and low temperature)	High (High temperature acid digestion)	Low (No pressurized vessel and low temperature)	Medium (High temperature melting)
Chlorine and carbon/ carbon containing chemicals at high temperature	Challenges to handle	N/A	N/A	N/A
Energy consumption	High	High	Efficient	High
Sulfur price	No effect	Substantial effect	No effect	No effect

CONCLUSION

Process Research Ortech (PRO) and the Natural Resources Research Institute (NRRI) have completed a combined characterization effort and hydrometallurgical testing program on an ilmenite mineral concentrate produced by the NRRI Coleraine Lab in 2016 from the 1999 Longnose oxide ultramafic intrusion (OUI) bulk sample. The work described in this report comprises a follow-up study to hydrometallurgical test work conducted by PRO and NRRI that has been described in NRRI Technical Report NRRI/TR-2017/25, "Pilot-Scale Demonstration of Ilmenite Processing Technology" (Mlinar et al., 2017).

The initial work performed by PRO and NRRI on the ilmenite concentrate sample included bench testing and mini-pilot operation. These studies were performed to test the unit process steps involved in batch continuous operation and to produce samples of TiO_2 product for market evaluation (Mlinar et al., 2017). Key findings from that study were:

- Iron oxide (Fe_2O_3) and titanium dioxide (TiO_2) powders that were produced on batch-basis from pilot-scale hydrometallurgical strip solutions via precipitation and calcination included a 98.5% Fe_2O_3 powder and a crystalline rutile TiO_2 powder comprising 99.3% TiO_2.
- A purity optimization study found that a titanium product at a purity level of 99.8% was possible by optimizing the titanium solvent extraction and precipitation parameters.
- A blended sample of the hydrometallurgical process leach tailings sent to a third party lab for Ontario regulation 558 standards for metals and inorganic discharge analysis was found to produce ***metal leachate concentrations below Ontario standards*** and was therefore considered an inert waste stream.
- A high-level capital and operational expenditure (CAPEX and OPEX) study was conducted by NRRI and PRO as a front-end loading number for future economic estimates. A design factor of 60,000 tpa TiO_2 product was chosen as the base case plant size. The high-level cost estimate found that the total CAPEX for a 60,000 tpa TiO_2 facility was approximately $164.2M USD to produce a >99% pure TiO_2 powder product from mining 0.5 Mtpa crude ore. The high-level cost estimate found that the total OPEX for a 60,000 tpa TiO_2 facility was approximately $795 per ton of TiO_2 product. The estimated iron oxide production was estimated at 82,088 tpa Fe_2O_3. The estimated credit for the iron oxide product was approximately $82 per ton of TiO_2 product. This by-product credit has an adjusted production cost of $713 per ton of TiO_2.

This research builds on the findings from the previous study by performing additional steady-state pilot operations to examine:

- How variation in feed composition effects SX processes
- The effect(s) of incorporation of recycled streams such as solvent extraction (SX) process raffinates and filtrates from precipitation stages
- Impurity buildup in the circuit from integrated operation (for example, recycling of raffinates) on the final Fe_2O_3 and TiO_2 products and potential bleed effluents
- Fe_2O_3 and TiO_2 product quality from mineralogical, textural, and mineral chemical/bulk chemical analyses
- Energy and mass balance of the system at steady state

Prior to hydrometallurgical processing for this study, detailed characterization of random grab samples of the 1999 Longnose bulk sample as well as the 2016 Longnose ilmenite concentrate, magnetite-rich low-intensity magnetic separator (LIMS) concentrate, and rougher spiral tails produced during the Mlinar et al. (2017) report were performed. Analysis included hand sample and petrographic lithological characterization (bulk sample only) as well as x-ray diffraction mineralogical analysis, whole rock major and trace element analysis, and/or mineral chemical analysis of various oxide and silicate mineral phases present in these materials by means of electron microprobe analyses.

Results of the characterization of 12 random grab samples of the 1999 Longnose bulk sample include the following:

- Hand sample lithological characterization indicated the presence of four rock types in the bulk sample, including semi-massive oxide, semi-massive to massive oxide, oxide-bearing peridotite, and oxide bearing dunite/peridotite.
- Petrographic analyses mineralogically and texturally characterized the bulk sample. Mineralogy for the various lithologies identified in the bulk sample include:
  - Semi-massive oxide (nine samples): Major silicate and oxide-mineral phases (>10 modal percent) include ilmenite, magnetite, olivine, clinopyroxene, hornblende, chlorite, and serpentine. Minor silicate-, oxide-, and carbonate mineral components (<10 modal percent) include iddingsite, biotite, actinolite, tremolite, anthophyllite, sericite, vermiculite, epidote, clay minerals, rutile, hercynite, and calcite. Trace sulfide minerals (<0.5 modal percent) present include chalcopyrite, pyrrhotite, cubanite, pentlandite, bornite, covellite, and digenite.
  - Semi-massive to massive oxide (one sample): Major mineral components (>10 modal percent) include ilmenite and magnetite. Minor silicate- and oxide mineral components (<10 modal percent) include olivine, clinopyroxene, iddingsite, biotite, serpentine, vermiculite, epidote, hornblende, actinolite, tremolite, chlorite, sericite, clay minerals and rare ulvöspinel. No sulfide mineral phases were identified in the single sample of this lithology.
  - Oxide-bearing peridotite (one sample): Major silicate-and oxide mineral phases (>10 modal percent) include olivine, serpentine, and ilmenite. Minor silicate-, oxide- and carbonate mineral phases (<10 modal percent) include clinopyroxene, iddingsite, biotite, chlorite, sericite, vermiculite, cummingtonite/grunerite, magnetite, ulvöspinel, and calcite. Trace sulfide minerals (<0.5 modal percent) include chalcopyrite, covellite, and pentlandite.
  - Oxide-bearing dunite/peridotite (one sample): Major silicate- and oxide mineral phases (>10 modal percent) include olivine and ilmenite. Minor silicate-, oxide- and carbonate mineral phases include clinopyroxene, iddingsite, biotite, hornblende, tremolite, anthophyllite, chlorite, serpentine, sericite, epidote, actinolite, cummingtonite/grunerite, magnetite, ulvöspinel, rutile, and calcite. Trace sulfide minerals (<0.5 modal percent) include chalcopyrite and bornite.
- Mineral chemical analyses of selected mineral phases in four Longnose bulk sample polished thin sections were completed at the Electron Probe Microanalyzer at the Electron Microscopy Laboratory (EML) in the Department of Earth and Environmental Sciences at the University of Minnesota Twin Cities.
  - Ilmenite occurs in a variety of textures and commonly contains submicron-wide exsolution lamellae presumably composed of hematite/titanohematite. Ilmenite compositions were dominated by TiO_2 (48.6–50.9 weight percent, average 49.7 weight percent), FeO (43.8–46.9 weight percent, average 43.4 weight percent), and MgO (2.0–4.0 weight percent, average 3.2

weight percent). Ternary diagrams comprising the FeO-TiO_2-MgO, FeO-TiO_2-V_2O_3, and Fe^{2+}-Ti^{4+}-Fe^{3+} systems illustrate that ilmenite compositions plot above the titanohematite solid solution series (a line between the stoichiometric compositions of pure ilmenite and pure hematite) as a result of Mg^{2+} substitution for Fe^{2+} within the ilmenite crystalline structure.

- Magnetite occurs in a variety of textures. Magnetite was primarily composed of FeO (83.2–93.5 weight percent, average 90.0 weight percent) and TiO_2 (0.0–3.4 weight percent, average 0.9 weight percent), indicating the local presence of titanomagnetite. As well, MgO ranged from 0.0–2.5 weight percent (average 0.2 weight percent), V_2O_3 ranged from 0.0–2.5 weight percent (average 0.6 weight percent), and Cr_2O_3 ranged from 0.0–2.6 weight percent (average 0.5 weight percent). Ternary diagrams comprising the FeO-TiO_2-MgO, FeO-TiO_2-V_2O_3, and Fe^{2+}-Ti^{4+}-Fe^{3+} systems illustrate that magnetites in the bulk sample plot at stoichiometric magnetite or along the titanomagnetite solid solution series (a line between the stoichiometric compositions of ulvöspinel and magnetite). As well, late, cross-cutting magnetite veins within the bulk sample tend to be depleted in MgO and V_2O_3 relative to other textures of magnetite.
- Silicate phases present in the bulk sample indicated during electron microprobe analyses include amphiboles (pargasite to magnesioriebeckite), chlorite (clinochlore), biotite, phlogopite, olivine (average composition $FO_{65.02}FA_{34.58}TP_{0.40}$), and serpentine (antigorite).

- Whole rock major and trace element lithogeochemical analyses performed on 12 grab samples from the Longnose bulk sample indicate the following:
  - Major element oxide analyses (weight percentages) indicate that the overall bulk sample is primarily composed of Fe_2O_3 (33.2%–54.7%, average 42%), TiO_2 (8.9%–38.6%, average 25.73%), MgO (33.2%–54.7%, average 42%), and SiO_2 (2.49%–28.7%, average 14.7%). Sulfur contents ranged from 0.02%–0.15% (average 0.07%).
  - Selected trace elements have the following average compositions in the Longnose bulk sample: As (1.05 ppm), Co (194 ppm), Cr (650 ppm), Cu (1692 ppm), Ni (638 ppm), Pb (8 ppm), Sb (0.06 ppm), V (1658 ppm), and Zn (195 ppm).
  - Rare earth element (REE) concentrations were evaluated relative to standard chondrite and primitive mantle compositions. Relative to chondrites, Longnose bulk samples have REE concentrations that range from 0.1 to 10 times chondritic values. Relative to primitive mantle compositions, Longnose bulk samples tend to be enriched in Nb (15–70 times), zirconium (4–20 times), hafnium (4–20 times), titanium (40–200 times), and vanadium (80–130 times).

Three mineral concentrates resulting from the Mlinar et al. (2017) study include an ilmenite concentrate (used as hydrometallurgical process feed in the current study), a magnetite-enriched low intensity magnetic separator (LIMS) concentrate, and silicate-mineral-rich rougher spiral tails.
Results of the characterization of Longnose ilmenite concentrate include:

- X-ray diffraction studies indicate the presence of ilmenite, antigorite, and zircon.
- Electron microprobe analyses of the ilmenite concentrate indicate the presence of the oxide mineral phases ilmenite, magnetite, and rutile.
  - Ilmenite occurs in a variety of textures and comprises TiO_2 (48.6–51.5 weight percent, average 49.6 weight percent), FeO (41.5–47.2 weight percent, average 45.3 weight percent) and MgO (2.6–4.0 weight percent, average 3.27 weight percent). Ternary diagrams of the FeO-TiO_2-MgO, FeO-TiO_2-V_2O_3, and Fe^{2+}-Ti^{4+}-Fe^{3+} systems illustrate that ilmenite compositions plot above the titanohematite solid solution series (a line between the stoichiometric compositions of pure

ilmenite and pure hematite) as a result of Mg^{2+} substitution for Fe^{2+} within the ilmenite crystalline structure.

- Magnetite occurs in a variety of textures and comprises FeO (80.8–92.7 weight percent, average 87.6 weight percent) and TiO_2 (0.8–6.2 weight percent, average 2.5 weight percent). As well, MgO ranges from 0.0 to 1.4 weight percent (average 0.3 weight percent), V_2O_3 ranges from 0.0 to 2.4 weight percent (average 0.8 weight percent), and Cr_2O_3 ranges from 0.0 to 1.7 weight percent (average 0.5 weight percent). Ternary diagrams comprising the FeO-TiO_2-MgO, FeO-TiO_2-V_2O_3, and Fe^{2+}-Ti^{4+}-Fe^{3+} systems illustrate that magnetite grains in the mineral concentrate plot at stoichiometric magnetite or along the titanomagnetite solid solution tie line.
- One grain of rutile identified in the Longnose mineral concentrate is consistent with petrographic identification of rutile in the Longnose bulk sample. The single analyzed rutile primarily comprises TiO_2 (97.1–97.3 weight percent, average 97.2 weight percent) and FeO (2.3–2.7 weight percent, average 2.6 weight percent).

Whole rock lithogeochemical analyses were performed on the three mineral concentrates produced during the Mlinar et al. (2017) study. Relative results include:

- Major element oxide compositions: SiO_2, Al_2O_3, CaO, MgO, Na_2O, K_2O, P_2O_5, S, and LOI are most highly concentrated in the rougher spiral tails; FeO, Cr_2O_3, and SrO are most highly concentrated in the LIMS concentrate; TiO_2, MnO, and BaO are most highly concentrated in the ilmenite concentrate.
- Selected trace element compositions: Co, Cu, and Ni are most highly concentrated in the rougher spiral tails; Cr, Pb, Sb, V, and Zn are most highly concentrated in the LIMS concentrate; As is most highly concentrated in the ilmenite concentrate.
- Rare earth element concentrations: Chondrite-normalized REE concentrations are higher in the rougher spiral tails (6–9 times chondritic values) relative to the ilmenite concentrate (1.5–4 times chondritic values) relative to the LIMS concentrate (0.5–3 times chondritic values). Primitive mantle-normalized values are highest for Th, La, Ce, Pr, Nd, Sm, Gd, Tb, Dy, Y, Er, Yb, Lu, and Al in the rougher spiral tails; V is most highly concentrated in the LIMS concentrate; Nb, Zr, Hf, Ti, and Sc are most highly concentrated in the ilmenite concentrate.

In the work performed in this program, the PRO mixed chloride was tested in mini pilot to build on the work previously conducted on the Longnose deposit located in Minnesota. Integrated piloting with recycling of process streams to examine the effect of impurity buildup on the robustness of the process and was conducted over three campaigns.

- Campaign 1 included setup of the pilot circuit and buildup of solutions in the various SX circuits so that examination of the effects of impurity buildup in the circuit from subsequent integrated circuit operations could be established.
- Campaign 2 focused on impurity buildup and steady-state operation with the recycling of evaporated Ti-raffinate. Additionally, bench testing using a proprietary technology developed by PRO and NRRI for use in the processing of ilmenite ores was conducted to establish operating conditions and determine potential HCl grade and quality.

- Campaign 3 involved continued pilot circuit operations with recycling streams from Campaign 2 (Ti-raffinate) along with recycling TiO2 precipitation filtrate stream into the circuit as Ti SX barren strip. The focus of the Campaign 3 operation was on impurity buildup and steady-state operation as well as determining the effects of impurity buildup on the selectivity of the SX separation circuits. Bench-scale development of the proprietary process continued to produce Fe2O3 product and establish the quality of the HCl.

It was found that recycling of $MgCl_2$ contained in the Ti raffinate to the leach operation did not adversely affect leach recoveries with average Ti recovery remaining consistent over the 3 campaigns (~70%). ***It was found that particle size played a key role in the leach efficiency and grinding of the material is essential to maintain high Ti leach recovery. A particle size of +90% -43 µm improved Ti leaching to levels of ~90%.***

Operation of the SX circuits was not adversely affected by the build up of impurities such as V, Cr, Al, and Ca. It was found that selectivity was maintained in both the Fe and Ti SX circuits with high purity pregnant strip solutions produced in each campaign. The resultant products Fe_2O_3 and TiO_2 produced from the pregnant strip solutions were of high purity with a TiO_2 product with a purity of ~99.5% TiO_2 produced from both Campaigns 2 and 3 while a Fe_2O_3 product of >95% Fe_2O_3 was produced from Campaigns 2 and 3. The TiO_2 product can be used as a precursor for pigment manufacture while the Fe_2O_3 produced can be used as a feed stock for direct reduced iron (DRI) processes or as a precursor for pigment.

Campaign 1 (not recycled) leach residues were subjected to mineralogical and whole rock and trace element lithogeochemical analysis. Results of the characterization of the Campaign 1 leach residues include:

- X-ray diffraction analysis identified the presence of ilmenite, hornblende, and zircon.
- Duplicate lithogeochemical analysis of Campaign 1 leach residues indicate they are primarily composed of SiO_2 (46.0–47.2 weight percent), TiO_2 (14.5–14.8 weight percent) and Fe_2O_3 (12.5–12.8 weight percent), with MgO, Al_2O_3, and and CaO all comprising less than 4 weight percent of the material. The sulfur contents of the Campaign 1 leach residues ranged from 0.17–0.22 weight percent. Values obtained for Cu, Co, Ni, Cr, Pb, Sb, V, and Zn were 385–704 ppm, 93–102 ppm, 189–209 ppm, 310–320 ppm, 9–12 ppm, 0.06–0.07 ppm, 580–597 ppm, and 428–437 ppm, respectively.
- Chrondrite-normalized REE concentrations range from approximately 2-times to 10-times chondrite normalized values.
- The Campaign 1 leach residues have trace element concentrations ranging from approximately 1–70-times primitive mantle normalized values, with notable enrichments in Nb (~30-times), Zr (~15-times), Hf (~20x), Ti (~70-times) and V (~8-times).

Non-calcined and calcined TiO_2 products from Campaign 2 were characterized by means of x-ray diffraction studies, electron microprobe mineral chemistry studies, and lithogeochemical studies. Results include:

- X-ray diffraction studies indicate the presence of rutile in both the non-calcined and calcined TiO_2 products.
- Electron microprobe analysis was carried out to evaluate the textures and mineral chemistries of various phases in the Campaign 2 TiO_2 precipitates. Non-calcined and calcined Campaign 2 TiO_2 rutile precipitates occurred in a variety of textures, including individual, commonly zoned ~1–30 µm

rounded to oval rutile grains and composite fragments greater than 100 µm in diameter composed of multiple, commonly concentrically zoned rounded to oval rutile grains. Locally, elongate (possibly platy) grains with aspect ratios up to 15 were also present. Within the calcined Campaign 2 TiO_2 rutile precipitates, rare curvilinear elongate fragments with aspect ratios up to 12 were locally observed.

- Mineral chemical analyses of the Campaign 2 TiO_2 precipitates carried out during electron microprobe analysis indicate the precipitates are nearly stoichiometric rutile (TiO2).
- Characteristics of the major- and trace element lithogeochemical analysis the Campaign 2 TiO_2 precipitates include:
  - Major element oxides: Non-calcined TiO_2 precipitates are composed primarily of TiO_2 (~87.4 weight percent) and LOI (~11.3 weight percent). Calcined TiO_2 precipitates are dominantly composed of TiO_2 (~99.0 weight percent) with minor LOI (<0.1 weight percent). Sulfur contents in the non-calcined sample (0.02 weight percent) were higher than sulfur contents in the calcined sample (<0.01 weight percent).
  - Selected Trace Elements: Both the non-calcined and calcined TiO2 precipitates have equivalent concentrations of Co, Cr, Ni, Pb, Sb, V, and Zn. Cu, Nb, and Ta concentrations were found to be marginally higher in the calcined sample than in the non-calcined sample. Relative As values varied between the non-calcined and calcined sample depending on the analytical technique utilized for the analysis.
  - Campaign 2 calcined TiO_2 precipitates have a normalized purity of 99.76 weight percent based on lithogeochemical analysis utilizing x-ray fluorescence.
  - Rare Earth Elements: Chondrite-normalized REE values for both the non-calcined and calcined TiO_2 precipitates were consistently below the analytical method detections limits. Primitive mantle-normalized trace element values for both the non-calcined and calcined TiO_2 precipitates were consistently below the analytical method detection limits except for Nb (non-calcined greater than calcined, ~30–50 times primitive mantle values), Ti (calcined greater than non-calcined, ~400–600 times primitive mantle values), and Al (non-calcined greater than calcined, up to 0.1–0.2 times primitive mantle values).

Non-calcined and calcined iron oxide precipitates from Campaign 2 were characterized by means of x-ray diffraction studies, electron microprobe mineral chemistry studies, and lithogeochemical studies. Results include:

- X-ray diffraction studies indicate the presence of hematite, possibly zircon, and an unknown phase within the non-calcined iron oxide precipitate. Hematite was the only phase identified in the calcined iron oxide precipitate.
- Electron microprobe analysis was carried out to evaluate the texture(s) and mineral chemistries of various phases in the Campaign 2 iron oxide precipitates. A variety of textures occur in the non-calcined Campaign 2 iron oxide precipitate, including composites of massive hematite lathes (up to 1 µm in length) and amorphous composites of hematite with lengths up to 125 µm and widths up to 60 µm. Also present are a “vesicular” Mg- and Cl-bearing unknown and semi-spheres of a Fe- and Cl-bearing unknown that contains nanoparticles of titanohematite. As well, a variety of textures occur in the calcined Campaign 2 TiO_2 precipitates, including polygonal composite fragments and “vesicular” composite fragments <1-2.5 µm hematite lathes and/or grains. As well, rare agglomerates of a SiO_2-Al_2O_3-FeO-bearing unknown phase also are locally present.

- Mineral stoichiometry calculations of the Campaign 2 iron oxide precipitates, assuming all iron as Fe^{3+}, indicate the precipitates are nearly stoichiometric hematite (Fe_2O_3).
- Characteristics of the major- and trace element lithogeochemical analysis the Campaign 2 iron oxide precipitates include:
  - Major element oxides: Non-calcined iron oxide precipitates are composed primarily of Fe_2O_3 (~79.5 weight percent), TiO_2 (~1.3 weight percent) and LOI (~10.9 weight percent). Calcined iron oxide precipitates are dominantly composed of Fe_2O_3 (~98.4 weight percent, TiO_2 (~0.6 weight percent) and LOI (~0.2 weight percent). Sulfur contents in the non-calcined and calcined samples are nearly equivalent (<0.1 weight percent).
  - Selected Trace Elements: The non-calcined sample contains higher concentrations of V and Zn, whereas the calcined sample contains a higher concentration of Sb. Similar concentrations occur in the non-calcined and calcined samples for Cr, Pb, and Ta. Relative values for As, Co, Cu, Nb, and Ni vary between the non-calcined and calcined sample based on the analytical method.
  - Campaign 2 calcined Fe_2O_3 precipitates have a normalized purity of 98.49 weight percent based on lithogeochemical analysis utilizing x-ray fluorescence.
  - Rare Earth Elements: Chondrite-normalized REE values for La, Ce, Pr, Nd, Gd, Dy, and Er are higher in the non-calcined sample relative to the calcined sample. The calcined sample is enriched in Tm relative to the non-calcined sample. Both samples have equivalent values for Sm, Eu, Tb, Ho, Yb, and Lu.
  - Primitive mantle-normalized trace element values are higher in the non-calcined sample than in the calcined sample for Nb, La, Ce, Pr, Nd, Ti, and V. Primitive mantle-normalized trace element values were higher in the calcined sample compared to the non-calcined sample for Al.

Samples of leach residues from Campaign 1 (sample number 1802-BL-10 (ML-71, no recycling)) and Campaign 2 (sample number 1802-BL6 (ML-70, half-recycled) were characterized by means of x-ray diffraction studies, electron microprobe mineral chemistry studies, and lithogeochemical studies. Comparative results include:

- X-ray diffraction study results indicate that Campaign 1 leach residues (not recycled (1802-BL-10/ML-71)) contain ilmenite, zircon and hornblende. Campaign 2 leach residues (half-recycled (1802-BL-6/ML-70)) contain ilmenite, augite, and zircon.
- Electron microprobe mineral chemistry studies were performed to evaluate the texture(s) and mineral chemistries of various phases in the Campaign 1 and Campaign 2 leach residues. Minerals present in the non-recycled Campaign 1 leach residue sample (1802-BL-10/ML-71) include ilmenite, rutile, actinolite, clinochlore, and possibly quartz. Minerals that occur in the half-recycled Campaign 2 leach residue sample (1802-BL-6/ML-70) include ilmenite, pargasite, augite, and possibly quartz. Chip-like morphologies are the dominant texture observed in these samples.
- Characteristics of the major- and trace element lithogeochemical analysis the Campaign 1 and Campaign 2 leach residues include:
  - Major element oxides: The Campaign 1 leach residue (not recycled) has higher concentrations of SiO_2, Al_2O_3, LOI, and S, whereas the Campaign 2 leach residues (half-recycled) has higher concentrations of Fe_2O_3, MgO, TiO_2, MnO and P_2O_5. Concentrations of CaO, Na_2O, K_2O, Cr_2O_3, SrO, BaO, and S are similar in the Campaign 1 and Campaign 2 leach residues.

- Selected Trace Elements: The Campaign 1 leach residues (not recycled) have higher concentrations of Cu, Pb, and Sb, whereas the Campaign 2 leach residues (half-recycled) illustrate higher concentrations of Cr. Relative values for As, Co, Nb, Ni, and Ta vary between the non-calcined and calcined samples based on the analytical method.
- Rare Earth Elements: Chondrite-normalized REE values for Er are higher in the Campaign 1 non-recycled sample relative to the Campaign 2 half-recycled sample. The Campaign 2 (half-recycled) sample is enriched in La, Ce, Pr, and Nd relative to the Campaign 2 (non-recycled) sample. Both samples have similar values for Sm, Eu, Gd, Tb, Dy, Ho, Tm, Yb, and Lu.
- Primitive mantle-normalized trace element values are higher in the Campaign 1 non-recycled sample than in the Campaign 2 half-recycled sample for Hf, Y, Er, and Al. Primitive mantle-normalized trace element values are higher in the Campaign 2 (half-recycled) sample than the Campaign 1 (non-recycled) sample for Nb, La, Ce, Pr, Nd, Ti, V, and Sc. Both samples have similar values for Th, Sm, Eu, Gd, Tb, Dy, Yb, and Lu. The relative values for Zr vary based on the analytical methods for these samples.

Non-calcined and calcined TiO_2 products from Campaign 3 were characterized by means of x-ray diffraction studies, electron microprobe mineral chemistry studies, and lithogeochemical studies. Results include:

- X-ray diffraction study results indicate the presence of rutile in both the non-calcined and calcined TiO_2 products.
- Electron microprobe analysis was carried out to evaluate the texture(s) and mineral chemistries of various phases in the Campaign 3 TiO_2 precipitates. Non-calcined and calcined Campaign 3 TiO_2 rutile precipitates occur in a variety of textures, including individual, commonly concentrically zoned ~2–20 µm rounded to oval rutile grains and composite fragments up to 350 µm in diameter composed of multiple, commonly concentrically zoned rounded to oval rutile grains. Locally, elongate (possibly platy) linear to slightly curved grains with aspect ratios up to 8 are also present. Rounded- to oval, commonly concentrically zoned rutile grains in the calcined sample appear to have more porosity than similar grains in the non-calcined sample.
- Mineral chemical analyses of the Campaign 3 TiO_2 precipitates carried out during electron microprobe analysis indicate the precipitates are nearly stoichiometric rutile (TiO_2).
- Characteristics of the major- and trace element lithogeochemical analysis the Campaign 3 TiO_2 precipitates include:
  - Major element oxides: Non-calcined TiO_2 precipitates are composed primarily of TiO_2 (~87.0 weight percent) and LOI (~11.9 weight percent). Calcined TiO_2 precipitates are dominantly composed of TiO_2 (~98.2 weight percent) with minor LOI (~0.1 weight percent). Sulfur contents in the non-calcined sample (0.03 weight percent) are higher than sulfur contents in the calcined sample (0.02 weight percent).
  - Selected Trace Elements: Both the non-calcined and calcined TiO_2 precipitates have equivalent concentrations of As, Co, Cr, Ni, Sb, V, and Zn. Relative concentrations of Cu, Nb, Pb, and Ta concentrations vary between the non-calcined and calcined sample depending on the analytical technique utilized for the analysis.
  - Campaign 3 calcined TiO_2 precipitates have a normalized purity of 98.74 weight percent based on lithogeochemical analysis utilizing x-ray fluorescence.

- Rare Earth Elements: Chondrite-normalized REE values for both the non-calcined and calcined TiO_2 precipitates are consistently below the analytical method detections limits with the exception of Ce, which is which was approximately equal to the detection limit for the non-calcined TiO_2 precipitate. Primitive mantle-normalized trace element values for both the non-calcined and calcined TiO_2 precipitates are consistently below the analytical method detection limits except for Nb (non-calcined greater than calcined) and Ti (calcined greater than non-calcined).

Non-calcined and calcined iron oxide precipitates from Campaign 3 were characterized by means of x-ray diffraction studies, electron microprobe mineral chemistry studies, and lithogeochemical studies. Results include:

- X-ray diffraction study results indicate the presence of hematite in both the non-calcined and calcined samples of Campaign 3 iron oxide precipitate
- Electron microprobe analysis was carried out to evaluate the texture(s) and mineral chemistries of various phases in the Campaign 3 iron oxide precipitates. Hematite, hematite containing greater than 0.5 weight percent TiO_2 (titanohematite?), and iron-titanium-bearing unknown phases occur in a variety of textures within both the non-calcined and calcined Campaign 3 iron oxide precipitates.
- Mineral stoichiometry calculations of both the non-calcined and calcined Campaign 3 iron oxide precipitates, assuming all iron as Fe^{3+}, indicate the presence of three types of precipitates, including: 1) precipitates that are nearly stoichiometric hematite (Fe_2O_3); and 2) precipitates that contain greater than 0.5 weight percent TiO_2 and most likely represent titanohematite solid solution; and 3) an iron- and titanium-bearing phase that may be ulvöspinel or titanohematite. An iron- and titanium-bearing unknown phase analyzed in the calcined Campaign 3 iron oxide precipitate may be either ulvöspinel (assuming all iron in the Fe^{2+} state) or titanohematite (based on calculations including iron in both the Fe^{2+} or Fe^{3+} state). An iron- and titanium-bearing unknown phase analyzed in the non-calcined Campaign 3 iron oxide precipitates, when plotted on the ternary diagram comprising Fe^{2+}-Ti^{4+}-Fe^{3+}, has a composition that lies along the Fe^{2+} - Ti^{4+} tie line about 2/3 of the way toward rutile from stoichiometric ilmenite.
- Characteristics of the major- and trace element lithogeochemical analysis the Campaign 3 iron oxide precipitates include:
  - Major element oxides: Non-calcined iron oxide precipitates are composed primarily of Fe_2O_3 (~89.3 weight percent), TiO_2 (~1.8 weight percent) and LOI (~5.7 weight percent). Calcined iron oxide precipitates are dominantly composed of Fe_2O_3 (~96.8 weight percent, TiO_2 (~1.8 weight percent) and LOI (~0.2 weight percent). Sulfur contents in the non-calcined and calcined samples are 0.05 and 0.01 weight percent, respectively.
  - Selected Trace Elements: The non-calcined sample contains higher concentrations of Sb, whereas the calcined sample contains higher concentrations of As and V. Similar concentrations occur in the non-calcined and calcined samples for Cr, and Ta. Relative values for Co, Cu, Nb, Ni, and Pb vary between the non-calcined and calcined sample based on the analytical method.
  - Campaign 3 calcined iron oxide precipitates have a normalized purity of 96.84 weight percent Fe_2O_3 based on lithogeochemical analysis utilizing x-ray fluorescence.
  - Rare Earth Elements: Chondrite-normalized REE values for La, Ce, Pr, Nd, Sm, Gd, Tb, Dy, Ho, and Er are higher in the calcined sample relative to the non-calcined sample. Both samples have below detection limit values for Eu, Tm, Yb, and Lu.

- Primitive mantle-normalized trace element values are higher in the non-calcined sample than in the calcined sample for Nb, and Hf. Primitive mantle-normalized trace element values are higher in the calcined sample than the non-calcined sample for Th, La, Ce, Pr, Nd, Sm, Hf, Gd, Tb, Dy, Y, Er, and V. Both samples have similar primitive mantle-normalized trace element values for Zr, Ti, and Al. Both samples also have below detection limit values for Eu, Yb, and Sc.

Samples of leach residues from Campaign 3 (sample numbers BL-19 (ML-72, recycled), 1802-L19R (ML-77, reground and two-stage leach) and 1802-L20R (ML-78, reground and two-stage leach) were characterized by means of x-ray diffraction studies, electron microprobe mineral chemistry studies, and lithogeochemical studies. Results include:

- X-ray diffraction study results indicate that Campaign 3 recycled leach residues (1802-BL-19/ML-72) contain ilmenite, zircon and hornblende. Campaign 3 leach residues that were reground and subjected to two-stage leaching (1802-L19R/ML-77 and 1802-L20R/ML-78) contain ilmenite, rutile, clinochlore, hornblende, and zircon.
- Electron microprobe mineral chemistry studies were completed to evaluate the texture(s) and mineral chemistries of various phases in the Campaign 3 leach residues. Minerals that occur in ***Campaign 3 leach residues (1802-BL-19/ML-72) include ilmenite, augite, actinolite, sepiolite, and possibly quartz.*** Minerals present in the Campaign 3 leach residues that were reground and underwent 2-stage leaching (1802-L19R/ML-77 and 1802-L20R/ML-78) include ilmenite, rutile, augite, actinolite, tremolite, clinochlore, and possibly plagioclase feldspar and quartz. Chip-like morphologies are the dominant texture observed in these samples.
- Characteristics of the major- and trace element lithogeochemical analysis of Campaign 3 single- and two-stage leach residues are as follows:
  - Major element oxides: The Campaign 3 recycled leach residues have higher concentrations of Fe_2O_3, Cr_2O_3, TiO_2, and MnO, whereas the Campaign 3 reground and two-stage leach residues have higher concentrations of SiO_2, Al_2O_3, CaO, MgO, Na_2O, K_2O, LOI and S. Concentrations of SrO and BaO are below detections limits in both the single-and two-stage leach samples. The P_2O_5 concentration in the Campaign 3 recycle leach residue falls between the high- and low-concentrations in the Campaign 3 reground, two two-stage leach samples.
  - Selected Trace Elements: The Campaign 3 recycled leach residues have higher concentrations of Cr and Ni, whereas the Campaign 3 reground and two-stage leach residues have higher concentrations of Ta. The concentrations of Sb in the Campaign 3 recycled and reground/two-stage leach samples are similar. The relative concentrations of As, Co, Cr, Nb, and Pb vary between the recycled and the reground, two-stage leach samples based on analytical methods.
  - Rare Earth Elements: Chondrite-normalized REE values are higher in the Campaign 3 reground and two-stage leach residue relative to the Campaign 3 recycled leach residue for the rare earth elements with the exceptions of Tm, Yb, and Lu. The concentrations of Tm, Yb, and Lu in the Campaign 3 recycled leach residue are equal to, or fall between, the low- and high concentrations identified in the two two-stage-leach residue samples that were analyzed.
  - Primitive mantle-normalized trace element values are higher in Campaign 3 recycled leach residue relative to the Campaign 3 reground and two-stage leach residues for Zr, Hf, and V; all other primitive mantle-normalized trace element values are higher in the Campaign 3 reground and two-stage leach sample relative to the Campaign 3 recycled leach residue sample with the

exception of Nb. The Nb value for the Campaign 3 recycled leach residue falls in between the high- and low-values for the two Campaign 3 reground and two-stage leach samples analyzed.

Ontario Regulation 558 metals and inorganic testing was on conducted on samples of leach residues from Campaigns 1, 2 and 3 of this study. Results indicate that these samples are considered environmentally inert relative to this standard. When compared with Minnesota Rules 7045.0131 Characteristics of Hazardous Waste (revisor.mn.gov/rules/78045.0131), the results obtained for the campaign 1, 2 and 3 residues, as well as the Campaign 3 ground residue, are below the maximum concentrations listed for arsenic, barium, cadmium, chromium, lead, mercury, selenium, and silver. No maximum concentrations are indicated for boron, uranium, fluoride, cyanide or (nitrate/nitrite) as N leachate in Minnesota Rules 7045.0131.

FUTURE CONSIDERATIONS

The technology in its present state has been applied to the Longnose deposit in Minnesota and shown to be successful in producing high grade titanium and iron oxide products. The steady state piloting conducted was successful in demonstrating the robustness of the process with respect to impurity build up and was capable of producing a high purity TiO_2 product and relatively high-purity iron oxide (hematite) powder.

As a result of the recycling of reagents and process streams, a buildup of value impurities such as V takes place and can be a valuable by-product. From the continuous pilot operation levels as high as 450 ppm V were found in the Ti raffinate produced. This is equivalent to ~$78/t of V_2O_5 value per ton of ilmenite ore when using a cost of $6/lb for V_2O_5 which is significant considering the V has already been solubilized during the leach process and only requires a solvent extraction (SX) separation step to produce a high purity V bearing stream for subsequent processing to produce a V product such as V_2O_5. Vanadium has been identified as an element of strategic importance by the USA, Japan, EU and Australia with applications in alloy steels, specialty chemicals (ammonium metavanadate) and high capacity batteries. Further study to recover additional value can be considered.

ACKNOWLEDGEMENTS

The authors express their appreciation to the many individuals and teams that played key roles behind the scenes and that contributed to this research. Steve Monson Geerts and Greg Gargano prepared the polished pucks utilized during electron microprobe analyses. Dr. Rod Johnson (NRRI) oversaw the x-ray diffraction studies and compiled the x-ray diffraction analysis results. Dr. Anette von der Handt (UM Twin Cities Electron Microprobe Laboratory) oversaw the electron microprobe analyses and compilation of the microprobe data, and played a pivotal role in helping the senior author identify appropriate mineral analysis recipes as well as publicly available software for mineral stoichiometry calculations. Janet Legace and the team at ALS Laboratories provided prompt guidance regarding appropriate chemical analytical methods for the oxide products produced during this study. Dr. Donald Fosnacht (NRRI) and Mr. Glenn Barr (Twin Metals Minnesota LLC) provided excellent peer reviews of a draft of this report and these reviews immensely improved the quality of the final report. The University of Minnesota Permanent University Trust Funds supported this research.

REFERENCES

Abbey, S. (1977). Studies in "Standard Samples" for use in the general analysis of silicate rocks and minerals, Part 5: 1977 Edition of "Usable" values: Geological Survey of Canada Paper 77-34, 31 p.

Akhgar, B.N., Pazouki, M., Akhgar, B.N., Ranjbar, M., and Hosseinnia, A. (2013). Preparation of micro and nanostructured titania compounds from ilmenite concentrates: International Journal of Mineral Processing, v. 124, p. 138–140.

Alemany, L.J., Bañares, M.A., Pardo, E., Martín-Jimenéz, F., and Blasco, J.M. (2000). Morphological and structural characterization of a titanium dioxide system: Materials Characterization, v. 44, p. 271–275.

Bayliss, P. (1975). Nomenclature of the trioctahedral chlorites. Canadian Mineralogist, v. 13, p. 178-180.

Benner, B., 2001. Minnesota Ilmenite Processing Using High Pressure Rolls: Natural Resources Research Institute, University of Minnesota Duluth, Technical Report NRRI/TR-2001-25, 57 p.

Chen, K-Y., and Chen, Y-W. (2003). Synthesis of spherical titanium dioxide particles by homogenous precipitation in acetone solution: Jour of Sol-Gel Science and Technology, v. 27, p. 111–117.

Dare, S.A.S., Barnes, S.-J., Beaudoin, G., Méric, J., Boutroy, E., and Potvin-Doucet, C. (2014). Trace elements in magnetite as petrogenetic indicators: Mineralium Deposita, v. 49, p. 785–796.

Deer, W.A., Howie, R A., and Zussman, J. (1992). An Introduction to the Rock Forming Minerals, 2nd Edition: Longman Scientific & Technical, London, 692 p.

Deorsola, F.A., and Vallauri, D. (2009). Study of the process parameters in the synthesis of TiO2 nanospheres through relative microemulsion precipitation: Powder Technology, v. 190, p. 304–309.

Gopal, M., Moberly Chan, W.J., and De Jonghe, L.C., (1997). Room temperature synthesis of crystalline metal oxides: Journal of Materials Science, v. 32, p. 6001–6008.

Ismagilov, Z.R., Tsykoza, L.T., Shikina, N.V., Zarytova, V.F., Zinoviev, V.V., and Sagrebelnyi, S.N. (2009). Synthesis and stabilization of nano-sized titanium dioxide: Russian Chemical Reviews, v. 79, no. 9, p. 1–13.

Karvinen, S. (1995). Method of preparing titanium dioxide: United States Patent 5,443,811, August 22, 1995.

Kerrich, R., and Wyman, D.A. (1996). The trace element systematics of igneous rocks in mineral exploration – an overview: in Wyman, D.A. (ed.), Trace Element Geochemistry of Volcanic Rocks: Applications for Massive Sulphide Exploration: Geological Association of Canada Short Course Notes, v. 50, p. 1–50.

Kim, C.H., Kim, D.K., Moon, Y.T., and Park, H.K. (1998). Process for preparing titania powders from a solution of titanium salt in a mixed solvent of water and alcohol: Unites States Patent 5,846,511, December 8, 1998.

Kim, S-J., Park, S-D., and Jeoun, Y.H. (1999a). Homogenous precipitation of TiO2 ultrafine powders from aqueous TiOCl2 solution: Journal of the American Ceramic Society, v. 82, p. 927–932.

Kim, S-D., Park, S.D., Kim, K.H., Jeong, Y.H., and Kuk, I.H. (1999b). Method for the production of mono-dispersed and crystalline TiO2 ultrafine powders for aqueous TiOCl2 solution using homogenous precipitation: United States Patent 6,001,326, December 14, 1999.

Kirillov, S.A., Lisnycha, T.V., and Chernukhin, S.I. (2011). Precipitated nanosized titanium dioxide for electrochemical applications: Journal of Power Sources, v. 196, p. 2221–2226.

Klein, C., and Hurlbut, C.S. Jr. (1999). Manual of Mineralogy, revised 21st Edition: John Wiley and Sons, Inc., New York, 681 p.

Lawhorne, E.R. (1990). Titanium dioxide with high purity and uniform particle size and method thereof: United States Patent 4,944,936, July 31, 1990.

Leake, B.E., Woolley, A.R., Arps, C.E.S., Birch, W.D., Gilbert, M.C., Grice, J.D., Hawthorne, F.C., Kato, A., Kisch, H.J., Krivovichev, V.G. Linthout, K., Laird, J., Mandarino, J.A., Maresch, W.V., Nickel, E.H., Rock, N.M.S., Schumacher, J.C., Smith, D.C., Stephenson, N.C.N., Ungaretti, L., Whittaker, E.J.W., and Youzhi, G. (1997). Nomenclature of Amphiboles: Report on the Subcommittee on Amphiboles of the Interanational Mineralogical Association, Commission on New Minerals and Mineral Names: The Canadian Mineralogist, v. 35, p. 219–246.

Lechler, P.J., and Desilets, M.O. (1987). A review of the use of loss on ignition as a measurement of total volatiles in whole-rock analysis: Chemical Geology, v. 63, p. 341–344.

Lee, D-U., Jang, S-R., Vittal, R., Lee, J., and Kim, K-J. (2008). CTAB facilitated spherical TiO2 particles and their advantage in a dye-sensitized solar cell: Solar Energy, v. 82, p. 1042–1048.

Lee, J.H., and Yang, Y.S. (2005). Effect of HCl concentration and reaction time on the change in the crystalline state of TiO2 prepared from aqueous TiCl4 solution by precipitation: Journal of the European Ceramic Society, v. 25, p. 3573–3578.

Li, C., Liang, B., and Wang, H.Y. (2008). Preparation of synthetic rutile by hydrochloric acid leaching of mechanically activated Panzhihua ilmenite: Hydrometallurgy, v. 91, p 121–129.

Li, J.-G., Tang, C., Li, D., Haneda, H., and Ishigaki, T. (2004). Monodispersed spherical particles of brookite-type TiO2: synthesis, characterization, and photocatalytic property: Journal of the American Ceramic Society, v. 87, no. 7, p. 1358–1361.

Li, Y., and Demopoulos, G.P. (2008). Precipitation of nanosized titanium dioxide from aqueous titanium (IV) chloride solutions by neutralization with MgO: Hydrometallurgy, v. 90, issue 1, p. 26–33.

Linscheid, E.K. (1991). The petrography of the Longnose peridotite deposit and its relationship to the Duluth Complex: MS Thesis, University of Minnesota, Duluth, 121 p. Milner, D. (n.d.). 3 Manufacturing Applications for Iron (III) Oxide. Retrieved from https://info.noahtech.com/blog/3-manufacturing-applications-for-iron-iii-oxide.

Mainwaring, P.R. (1975). The petrology of a sulfide-bearing layered intrusion at the base of the Duluth Complex, St. Louis County, Minnesota: Unpublished PhD Dissertation, University of Toronto, Ontario, 251 p.

Mainwaring, P.R., and Naldrett, A.J. (1977). Country rock assimilation and genesis of Cu-Ni sulfides in the Water Hen intrusion, Duluth Complex, Minnesota: Economic Geology, v. 72, p. 1269–1284.

McEnroe, S.A., Robinson, P., Langenhorst, F., Frandsen, C., Terry, M.P., and Ballaran, T.B. (2007). Magnetization of exsolution intergrowths of hematite and ilmenite: mineral chemistry, phase relations, and magnetic properties of hemo-ilmenite ores with micron- to nanometer-scale lamellae from Allard Lake, Quebec: Journal of Geophysical Research, v. 112. Retrieved from https://agupubs.onlinelibrary.wiley.com/doi/epdf/10.1029/2007JB004973.

Mehdilo, A. and Irannajad, M. (2013). Effects of mineralogical and textural characteristics of ilmenite concentrate on synthetic rutile production: Arabian Journal of Geoscience, v. 6, p. 3865–3876.

Meinhold, G. (2010). Rutile and its applications in earth sciences: Earth Science Reviews, v. 102, p. 1–28.

Méric, J. (2011). Caractérisation géochimicques des magnetites de la zone critique de l'intrusion magmatique de Sept-Iles (Québec, Canada) et integration a une base de données utilisantla signature géochimique des oxydes de fer comme outil d'exploration: Université du Québec à Chicoutimi – Université Montpellier 2, 48 p.

Minnesota Minerals Coordinating Committee (2016). Explore Minnesota: Titanium: Minnesota Minerals Coordinating Committee, 4p. Retrieved from http://files.dnr.state.mn.us/lands_minerals/mcc_docs/2016_explore_titanium.pdf

Miner, G.C. (1995). Aspects of the petrogenesis of the Longnose Fe-Ti-oxide-rich ultramafic body, Duluth Complex, Minnesota: Unpublished MS Thesis, Washington University, St. Louis, MO, 243 p.

Miner, G.C., and Pasteris, J.D. (1994). Longnose Fe-Ti oxide ultramafic body, Duluth Complex, MN: Evidence for magmatic and metasomatic development [abs.]: Geological Society of America, Abstracts with Programs, v. 26, p. A-294.

Mlinar, M., Rao, S., and Peterson, T. (2017). Pilot-Scale Demonstration of Ilmenite Processing Technology: Natural Resources Research Institute Technical Report NRRI/TR-2017/25, 165 p.

Montino, F. and Spoto, G. (1989). Process for preparing titanium dioxide in the form of spherical particles by hydrolysis of Ti(IV): United States Patent 4,803,064, February 7, 1989.

Mostafa, N.Y., Mahmoud, M.H.H., and Heiba, Z.K. (2013). Hydrolysis of TiOCl2 leached and purified from low-grade ilmenite concentrate: Hydrometallurgy, v. 139, p. 88–94.

Nakade, M., Kameyama, K., and Ogawa, M. (2004). Synthesis and properties of titanium dioxide/polydimehtylsiloxane hybrid particles: Journal of Materials Science, v. 39, p. 4131–4137.

NIST (National Institute of Standards and Technology) (1992). Certificate, Standard Reference Material 278, Obsidian Rock: National Institute of Standards, 3 p. Retrieved from https://hybris-static-assets-production.s3-eu-west-1.amazonaws.com/sys-master/pdfs/he5/hce/9872370040862/en_ST-WB-CERT-2828065-1-1-1.PDF.

Nickel, E.H., and Nichols, M.C. (1991). Mineral Reference Manual: Van Nostrand Reihhold, New York, 250 p.

Niles, H.B. (1996). Beneficiation of the Longnose Ilmenite Deposit: Preliminary, Unpublished Report, Natural Resources Research Institute Coleraine Minerals Research Laboratory CMRL/TR-96/29.

Ohno, T., Sarukawa, K., Tokieda, K., and Matsumura, M. (2001). Morphology of a TiO2 photocatalyst (Degussa, P-25) consisting of anatase and rutile crystalline phases: Journal of Catalysis, v. 203, p. 82–86.

Ookubo, A., Ooi, K., and Tomita, T. (1989). New types of hydrous titanium oxides obtained by homogenous precipitation from (titanium (III) chloride + urea) solutions: Journal of Materials Science, v. 24, p. 3599–3604.

Park, H.K., Kim, D.K., and Kim, C.H. (1997). Effect of solvent on titania particle formation and morphology in thermal hydrolysis of TiCl4: Journal of the American Ceramic Society, v. 80, p. 743–749.

Phillips, W.R., and Griffen, D.T. (1981). Optical Mineralogy – The Nonopaque Minerals: W. H. Freeman and Company, San Francisco, 677 p.

Potts, P.J. (1987). A Handbook of Silicate Rock Analysis: Blackie & Son, Ltd, Glasgow, 622 p.

Process Research Ortech Inc. (2017) UMD Ilmenite Project: Final Report (PRO 16-05): Mississauga, Process Research Ortech Inc.

Razieh, R., Hosseini, S.M.A., and Ranjbar, M. (2014). Production of nanosized synthetic rutile from ilmenite concentrate by Sonochemical HCl and H2SO4 leaching: Iran. J. Chem. Chem. Engineering, v. 33, no. 2, p. 29–36.

Reyes-Coronado, D., Rodriguez-Gattorno, G., Espinosa-Pesqueira, M. E., Cab, C., de Coss, R., and Oksam, G. (2008). Pure-phase TiO2 nanoparticles: anatase, brookite, and rutile: Nanotechnology, v. 19, no. 14, p. 145605–145615.

Rittner, M.N., Abraham, T. (1999). Iron oxide powders: Ceramic Industry, v. 149, no. 1, p. 27

Rollinson, H. (1993). Using Geochemical Data: Evaluation, Interpretation, Presentation: Longman Group U.K. Limited, Essex, England, 352 p.

Severson, M.J. (1995). Geology of the southern portion of the Duluth Complex: Natural Resources Research Institute, University of Minnesota Duluth, Technical Report NRRI/TR-95/26, 185 p.

Severson, M., and Hauck, S. (1990). Geology, geochemistry and stratigraphy of a portion of the Partridge River intrusion: Natural Resources Research Institute, University of Minnesota Duluth, Technical Report NRRI/GMIN-TR-89-11, 236 p. + plates.

SRK Consulting (2012). Technical Report on the Longnose Ilmenite Project, Minnesota, 94 p. Retrieved from https://www.sedar.com/GetFile.do?lang=EN&docClass=24&issuerNo=00005623&issuerType=03&projectNo=01854057&docId=3042490.

Šubrt, J., Štengl, V., Barkardijieva, S., and Szatmary, L. (2006). Synthesis of spherical metal oxide particles using homogeneous precipitation of aqueous solutions of metal sulfates with urea: Powder Technology, v. 169, p. 33–40.

Sun, S.S., and McDonough, W.F. (1989). Chemical and isotopic systematics of ocean basalts: implications for mantle composition and processes: in Saunders, A.D., and Norry, M.J., Magmatism in Ocean Basins: Geological Society, London, Special Publications, v. 42, p. 313–345.

Tadros, M.E., Adkins, C.L.J., Russick, E.M., and Youngman, M.P. (1996). Synthesis of titanium dioxide particles in supercritical CO2: Journal of Supercritical Fluids, v. 9, issue 3, p. 172–176.

Thangavelu, K., Rajendran, A., and Arulnandhi, D. (2013). Preparation and characterization of nanosized TiO2 powder by sol-gel precipitation route: International Journal of Emerging Technology and Advanced Engineering, v. 3, issue 1, p. 636–639.

Tsuchida, H., Narita, E., Takeuchi, H., Adachi, M., and Okabe, T. (1982). Manufacture of high pure titanium (IV) oxide by the chloride process: I. Kinetic study of leaching of ilmenite ore in concentrated hydrochloric acid solution: The Chemical Society of Japan, v. 55, p. 1934–1938.

Visca, M., and Matijević, E. (1979). Preparation of uniform colloidal dispersions by chemical reactions in Aerosols: Journal of Colloid and Interface Science, v. 68, no. 2, p. 308–319.

Werts, M.P.L., Badila, M., Brochon, C., Hébraud, A., and Hadziioannou, G. (2008). Titanium dioxide – polymer core-shell particles dispersion as electronic inks for electrophotoretic displays: Chemistry of Materials, v. 20, p. 1292–1298.

Wiewiora, A. and Wiess, Z. (1990). Crystallochemical classifications of Phyllosilicates based on the Unified system of project of chemical composition: II. The Chlorite Group: Clay Minerals, v. 25, p. 83–92.

Woodruff, L.G., Nicholson, S.W., and Fey, D.L. (2010). A Deposit Model for Magmatic Iron-Titanium-Oxide Deposits Related to Proterozoic Massif Anorthosite Plutonic Suites: U. S. Geological Survey Scientific Investigations Report 2010-5070-K, 47 p., http://pubs.usgs.gov/sir/2010/5070/k.

Wu, F., Li, Z., Wang, Z., Xu, C., He, H., Qi, A., Yin, X., and Guo, H. (2013). Preparation of high-value TiO2 nanowires by leaching of hydrolyzed titania residue from natural ilmenite: Hydrometallurgy, v. 140, p. 82–88.

Xu, J.S., Zhang, H., Zhang, J., He, X.K., Xu, D.L., Qian, J.H., Liu, L., and Liu, X.Y. (2013). Fabrication of anatase titanium dioxide microspheres via homogeneous precipitation method, Materials Research Innovations, 17:2, 117–121, DOI: 10.1179/1433075X12Y.0000000038.

Yamabi, S and Imai, H. (2002). Crystal phase control for titanium dioxide films by direct deposition in aqueous solutions: Chemistry of Materials, v. 14, p. 609–614.

Yavuz, F., Kumral, M., Karakaya, N., Karakaya, M.C., and Yildirim, D.K. (2015). A Windows program for chlorite calculation and classification: Computers and Geosciences, v. 81, p. 101–113 (WinCcac program retrieved from https://www.sciencedirect.com/science/article/pii/S009830041500103X?via%3Dihub).

LIST OF APPENDICES

The following appendix files are attached to this document:

Appendix 1: NRRI Sample Description Sheets – Bulk Sample
Appendix 2: Petrography Description Sheets – Bulk Sample
Appendix 3: ALS Laboratory Analytical Certificates
Appendix 4: Electron Microprobe Mineral Chemistry
Appendix 5: PRO Leaching
Appendix 6: Campaign 1 Fe SX
Appendix 7: Campaign 1 Ti SX
Appendix 8: Campaign 2 Fe SX
Appendix 9: Campaign 2 Ti SX
Appendix 10: Campaign 3 Fe SX
Appendix 11: Campaign 3 Ti SX
Appendix 12: Fe SX Sample Set Assay
Appendix 13: Ti SX Sample Set Assay